Magmatic evolution and platinum potential of SW Yunnan, China

Doctoral Thesis

(Dissertation)

to be awarded the degree of

Doctor rerum naturalium (Dr. rer. nat.)

submitted by

Daniel Hennig

from Dortmund, Germany

approved by the Faculty of Energy and Management,

Clausthal University of Technology,

Date of oral examination

7th of May, 2010

Chairperson of the Board of Examiners:	Prof. Dr.-Ing. Norbert Meyer
Chief Reviewer:	Prof. Dr. Bernd Lehmann
Reviewer:	Prof. Dr. Kurt Mengel

D 104

This dissertation was undertaken at the Mineral Resources Department of the Institute of Disposal Research of the Technical University of Clausthal.

This thesis is dedicated to Mika and my family.

Thank you for being there.

Abstract

Southwestern Yunnan is a key region for the understanding of the complex geological evolution of the Paleo-Tethys at the end of the Paleozoic and the formation of the 260 Ma-old Emeishan Large Igneous Province (ELIP), which hosts several important magmatic ore deposits. The same region is also intensively affected by Himalayan escape tectonics, with large-scale strike-slip movements. The most prominent Cenozoic fault zone in SW China is the NW–SE trending Red River-Ailaoshan Shearzone (RRASSZ) with left-lateral displacement of at least 300 km. The RRASSZ is generally believed to represent the southern boundary of the ELIP.

This thesis investigates the possible continuation of the ELIP south of the RRASSZ, and tries to assess the platinum potential of mafic to ultramafic rock complexes along the Lancang River (further south known as Mekong). From north to south the target areas comprise the Banpo complex about 80 km NW of Simao, the Nanlianshan and Huijingfang complexes at Jinghong, and the Paleng complex close to the border with Laos. Lithogeochemical and geochronological data on these volcano-plutonic complexes were compared with PGE-bearing mafic to ultramafic intrusions associated with the ELIP and elsewhere.

The MORB-like basaltic andesite to microgabbro of the Nanlianshan complex has a U–Pb zircon age of 292 ±1 Ma and indicates Early Permian sea-floor spreading. The calc-alkaline, mafic to ultramafic Banpo intrusion hosts arc-related harzburgites and gabbros with a U–Pb zircon age of 286 ±2 Ma. The mafic to ultramafic Paleng complex at the border to Laos is similar in composition to the Banpo complex and hosts amphibole gabbro cumulates with island-arc signature. U–Pb zircon ages for this complex are 262 ±3 to 258 ±2 Ma, and Ar–Ar ages on hornblende range from 259 ±2 to 251 ±4 Ma. The amphibole gabbro is associated with arc-type basaltic andesite and within-plate basalt of 262 ±2 Ma (U–Pb on zircon) which resembles in major and trace element characteristics the lavas of the ELIP. It appears likely that the Permian arc magmatism and the formation of the ELIP are part of the same tectonomagmatic cycle.

Chalcophile trace elements and platinum-group elements of the Banpo and Paleng complexes depict drastic depletion, which is in the range of the sulfide-saturated Nadezhdinsky Formation of the Siberian Trap (host to the Noril`sk Ni–PGE deposit), of the sulfide-depleted northern Deccan Trap, and of the ELIP. The 286 ±2 Ma-old Banpo gabbro shares geologic and geochemical similarities with the host rocks of a number of ELIP-

associated ore deposits, such as Yangliuping and Jinbaoshan (PGE), and Hongge and Baimazhai (Fe–Ti–V oxide) in SW China, as well with Ban Phuc (Ni–PGE) in Vietnam. The Paleng cumulate sequence shows similarities to the Panzhihua and Baimazhai Fe–Ti–V deposits. Both the Banpo and Paleng mafic-ultramafic intrusive complexes have high platinum potential which needs testing by detailed exploration.

Keywords: Platinum potential, China, Emeishan Large Igneous Province, Paleo-Tethys

Zusammenfassung

Die Grenzregion China-Burma-Laos-Vietnam hat eine komplexe geologische Geschichte, die von permo-triassischen Kollisionen einzelner Krustenfragmente mit dem Yangtze-Block und damit einhergehender Subduktion devonischen bis triassischen Ozeanbodens der Paläotethys bestimmt ist. Zudem wurde diese Collage durch weiträumige, känozoische Blattverschiebungen in Verbindung mit der Indien-Eurasien-Kollision überprägt. Die bedeutendste Blattverschiebung in Südwest-China ist die NNW-SSO streichende Red River-Ailaoshan Scherzone (RRASSZ) mit einem sinistralen Versatzbetrag von ca. 400 km. Ihr schließen sich im Norden und Nordosten auf einer Fläche von ca. 250.000 km^2 die Flutbasalte der Emeishan LIP (Large Igneous Province; ca. 260 Ma) an. Sie enthalten wirtschaftlich wichtige magmatische Sulfid- (Ni, Cu, PGE) und Oxid-Lagerstätten (Ti, V, Fe). Die vorliegende Arbeit zielt auf die mögliche Fortsetzung der Emeishan LIP südlich der RRASSZ entlang des Lancang-Flusses.

Von Nord nach Süd umfassen die Zielbereiche den Banpo-Komplex, ca. 80 km nordwestlich von Simao, die Nanlianshan- und Huijingfang-Komplexe bei Jinghong und den Paleng-Komplex nahe der laotischen Grenze. Die gewonnenen lithogeochemischen und geochronologischen Daten werden mit Platinmetall-führenden Gesteinskomplexen der ELIP verglichen.

Die E-MORB ähnlichen basaltischen Andesite und Mikrogabbros des Nanlianshan-Komplexes mit U–Pb Zirkonaltern von 292 ±1 Ma deuten auf frühpermische Neubildung ozeanischer Kruste. Der kalkalkaline Banpo-Komplex - Teil eines ehemaligen aktiven Kontinentalrandes - besteht aus Harzburgiten und Gabbros mit U–Pb Zirkonaltern von 286 ±2 Ma. Der Paleng-Komplex wird überwiegend von Hornblende-Gabbro-Kumulaten aufgebaut. Er ähnelt in seiner geochemischen Zusammensetzung dem Banpo-Komplex. Die

U–Pb Zirkonalter dieses Komplexes sind 262 ±3 Ma and 258 ±2 Ma; Ar–Ar Alter variieren von 259 ±2 bis 251 ±4 Ma. Kleine Vorkommen von porphyrischen Basalten im Paleng Komplex (262 ±2 Ma) zeigen typische Flutbasalt-Signatur, sehr ähnlich zu den Laven der ELIP. Es erscheint denkbar, dass der permische Bogen-Magmatismus und die Bildung der ELIP in einem geotektonischen Kontext stehen.

Spurenelement- und Platingruppenelement-Analysen an Gabbros der Banpo- und Paleng-Komplexe zeigen eine deutliche Abreicherung der Platingruppenelemente und der chalkophilen Spurenelemente, womit die Entmischung einer Sulfidschmelze angezeigt ist. Die Elementkonzentrationen sind in Bereichen wie sie typisch für die Sulfid-gesättigte Nadezhdinsky-Formation der Sibirischen Flutbasalte (Wirtsgestein der Noril`sk Ni–PGE Lagerstätten), für die Sulfid-verarmten nördlichen Deccan Trappbasalte und der ELIP sind. Der Banpo-Gabbro ähnelt in seinem geologischen Aufbau sowie in seinen geochemischen Signaturen Wirtsgesteinen der ELIP-gebundenen Lagerstätten Yangliuping, Jinbaoshan (PGE Lagerstätten) und Hongge und Baimazhai (Fe–Ti–V Oxid Lagerstätten) in SW China, sowie Ban Phuc (Ni–PGE) in Vietnam.

Die Paleng-Kumulatsequenz hat petrographische und geochemische Gemeinsamkeiten mit den Fe–Ti–V-Lagerstätten Panzhihua und Baimazhai. Die Banpo- und Paleng-Komplexe haben ein hohes Platinmetall-Potenzial, dem durch weitere Detailexploration nachgegangen werden sollte.

Acknowledgements

I am grateful to my supervisor Professor Bernd Lehmann for confidence and help during the preparation of this PhD thesis, which presents the results of the Hochschulvergabeprojekt "Platinmetall-Potential Yünnan" funded by Bundesanstalt für Geowissenschaften und Rohstoffe, Hannover (contract no. 204-4500029770 of 10 August 2006).

For second reviewing, valuable petrologic criticism and support I sincerely thank Professor Kurt Mengel. Dr. Kai Schmidt is thanked for the ICP-MS analysis.

Field work was realized by help of the Yunnan Geological Survey and the Geology Department of the University of Hong Kong. Field sessions in July/August 2007 and March 2008 involved Alexandre Cabral, Bernd Lehmann, Wenchang Li, Pusheng Zeng, Fuliang Zhang, Xinfu Zhao and Meifu Zhou. Thin and polished sections were prepared by Ulf Hemmerling, Clausthal. IT support was given by Fred Türck. Electron microprobe work was guided by Klaus Herrmann. X-ray fluorescence spectrometry on all rock powders was done at Bundesanstalt für Geowissenschaften und Rohstoffe. Nd and Sr isotopes were analyzed by Boris Belyatsky at the Institute for Precambrian Geology and Geochronology in St Petersburg, Russia. U–Pb zircon dating by LA-ICP-MS was done by Dirk Frei at the Geological Survey of Denmark and Greenland, Copenhagen, Denmark. Ar–Ar and K–Ar dating was done by Ray Burgess at the University of Manchester, UK. I am grateful to Dr. Thomas Oberthür for help in the organization of the project as well as for analytical support.

This thesis would maybe not exist without the support of my family, friends and collegues. My special thanks go to my brothers and their families, to my parents, to Jörg, Anja, Kim, Betti, Markus, Axel, Steffi, Ingo, Jana, Ulf, Fred, Konni, Lucas, Lingang, Etienne, Farhad, Mohammed, Kermit, Uwe, Christine, Saleem, Kea and Frau Schulze.

Dirk Frei and his lovely family are thanked for accommodation during U–Pb zircon analysis at Copenhagen.

Contents

List of Figures

List of Tables

1 Geology, petrology and geochronology of magmatic rocks from SW Yunnan, China

1.1 PLATE TECTONIC FRAMEWORK

Southwestern China has a complex geological history with the Paleozoic evolution of the Paleo-Tethys orogen and the Mid-Late Permian Emeishan continental flood basalt event standing out. The Paleo-Tethys orogen is a patchwork of Gondwana-derived continental terranes such as Sibumasu, Qiangtang, Lancang, Simao, Indochina and Yangtze (Fig. 1). These blocks are presently bounded by sutures with relictic ophiolite material (Metcalfe, 2006).

Paleomagnetic and paleo-faunal/floral investigations suggest that Simao-Indochina-Yangtze (yellow blocks in Fig. 1) were rifted from East Gondwana prior to the Early Devonian and generated the Paleo-Tethys Ocean, whereas Sibumasu-Qiangtang remained part of Gondwana until the Early Permian (orange blocks in Fig. 1). The main oceanic branch of the Paleo-Tethys is believed to follow the Lancangjiang, Changning-Menglian, Chiang Mai and Bentong-Raub sutures in Tibet, South China, Myanmar and Thailand, respectively (Fig. 1), and was closed by mid-Triassic times.

The Emeishan Large Igneous Province (~0.3 x 10^6 km^3) extends in the Sichuan, Yunnan and Guizhou Provinces, i.e. northeast of the Red River-Ailaoshan Shearzone (Fig. 2; Ali *et al*., 2005). There is general consensus about the timing of the main magmatic event at ~260 Ma, but there is still much debate on the genesis of the ELIP (e.g. Anderson, 1994; Campbell & Griffith, 1990). Recently, first attempts were published to link the onset of the ELIP extrusion with the Paleo-Tethys orogeny (Jian *et al*., 2009a,b). Their data suggest an overlap of the two processes; precise indicators, however, are still lacking.

1.2 GEOLOGICAL SETTING

The Paleo-Tethys Ocean was a complexly built, archipelagic ocean that separated the Simao-Indochina-Yangtze Blocks from the Sibumasu-Qiangtang Blocks (Fig. 1). The suture zone of the former ocean is evident by the major Late Paleozoic Gondwana-Cathaysia Divide, which likely represents the boundary between high latitude, cold climate Gondwana faunas

(on Sibumasu-Qiangtang) and low latitude, warm climate Cathaysia faunas (on Simao, Indochina and Yangtze). In southern China the divide largely coincides with the Lancang River (Lancangjiang) fault and the Changning-Menglian belt (Metcalfe, 2006; Fig. 2).

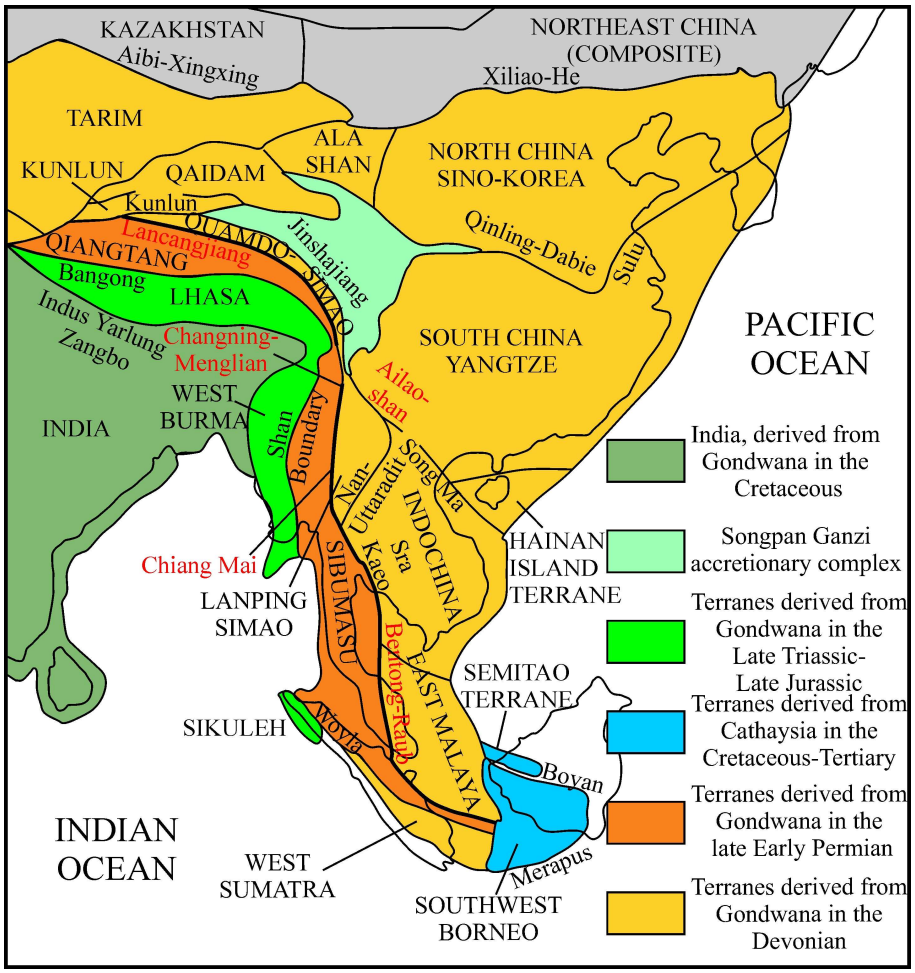

Fig. 1: Simplified plate tectonic configuration of SE Asia (adapted from Metcalfe, 2006).

Besides the Changning-Menglian main-ocean (present western position; 270-264 Ma), the eastern Paleo-Tethys was most likely characterized by two tributary, branch-oceans, which probably opened by rifting of continental fragments (Simao and Lancang) from the western Yangtze Block (e.g. Hennig *et al.*, 2009; Jian *et al.*, 2009a/b; Fig. 2 and references therein). The poorly-defined Lancangjiang Ocean is located between the Lancang and Simao Blocks, i.e. further east of the Changning-Menglian main ocean, and the Jinshajiang-Ailaoshan Ocean (403-282 Ma) is located in an easternmost position, between the Simao and Yangtze Blocks (Fig. 2 and references therein; Feng *et al.*, 2005; Liu *et al.*, 1993; Metcalfe, 2006; Zhang *et al.*, 2008a; Zhong, 1998). The existence of the Lancangjiang Ocean is indicated by E-MORB

like basaltic andesites at Nanlianshan of 292 ±1 Ma (2σ) and by arc-like granodiorites of 284 ±1 Ma (2σ) to 282 ±1 Ma (2σ) at Jinghong (Hennig *et al*., 2009).

The currently favored paleotectonic models for Southwest China were recently summarized by Jian *et al.* (2009b), based on earlier work by Zhang *et al*. (1993), Jian *et al*. (2003a), Peng *et al*. (2006, 2008) and Zhang *et al*. (2008a). These studies propose eastward-dipping subduction of the Changning-Menglian oceanic basin/plate beneath the western edge of the Simao Block in the Carboniferous (Fig. 2). Remnants of the subducted oceanic crust are believed to be seen in Carboniferous to Late Permian primitive oceanic rocks along the Changning-Menglian belt (Fang & Niu, 2003; Feng, 2002; Jian *et al.*, 2009a,b). The Jinshajiang-Ailaoshan oceanic basin was likely subducted westward in the Permian to Late Triassic, feeding an active continental margin to the west (Fig. 2) (Zhang *et al.*, 2008a; Jian *et al.*, 2009a,b). Closure of the oceanic basins is post-dated by the large Triassic syn- to post-collisional Lincang granite, which is part of a regionally distributed granite belt extending from Tibet to northern Thailand and Peninsular Malaysia (Cobbing *et al.*, 1992; Fig. 2B), and by Late Triassic conglomerates unconformably covering the Paleo-Tethys ophiolites (Zhong, 1998).

The dominant faults of the Lancangjiang (Lancang River) area are related to the Paleo-Tethyan orogenesis and to escape tectonics of the Tertiary India-Eurasia collision. The central, north–south trending Lancangjiang fault extends along the Lancang River (jiang is the Chinese term for river; Fig. 2) and separates the Lancang Block from the Simao Block. To the west, the upper reaches of the Nu River (further south named Salween) correlate with a major fault separating the Baoshan and Tengchong Blocks (both blocks are part of Sibumasu). The Red River (Hongjiang/Yuanjiang)-Ailaoshan fault to the east separates the Simao Block from the Yangtze Block and is morphologically enhanced by the Jinshajiang in the north and the Red River in the south. Cenozoic left-lateral displacement along the reactivated Red River-Ailaoshan fault, subsequent to the India-Eurasia collision, is estimated at more than 500 km by Tapponnier *et al.* (1990). Results from comparative petrological studies on the Lincang granite and the Jinghong granodiorite with felsic intrusive rocks from the northern Lancangjiang zone suggest left-lateral displacement of at least 300 km (Hennig *et al*., 2009).

The dominant rock complex of the Lancangjiang zone is the Lincang granite surrounding the town of Lincang (Fig. 2). To the west, the batholith intrudes the Proterozoic Lancang group consisting of metasedimentary and arc-like metavolcanic rocks with Sm–Nd model ages (T_{DM}) of 1.3-1.0 Ga. $^{40}Ar/^{39}Ar$ ages of 294.0 ±1.0 Ma on phengites of a blueschist belt within the Lancang group document a Late Carboniferous high-P/low-T

tectonometamorphic event (Heppe, 2006; Zhai *et al.*, 1990; Zhang *et al.*, 1993; Zhao *et al.*, 1994; Zhong, 1998; Fig. 2).

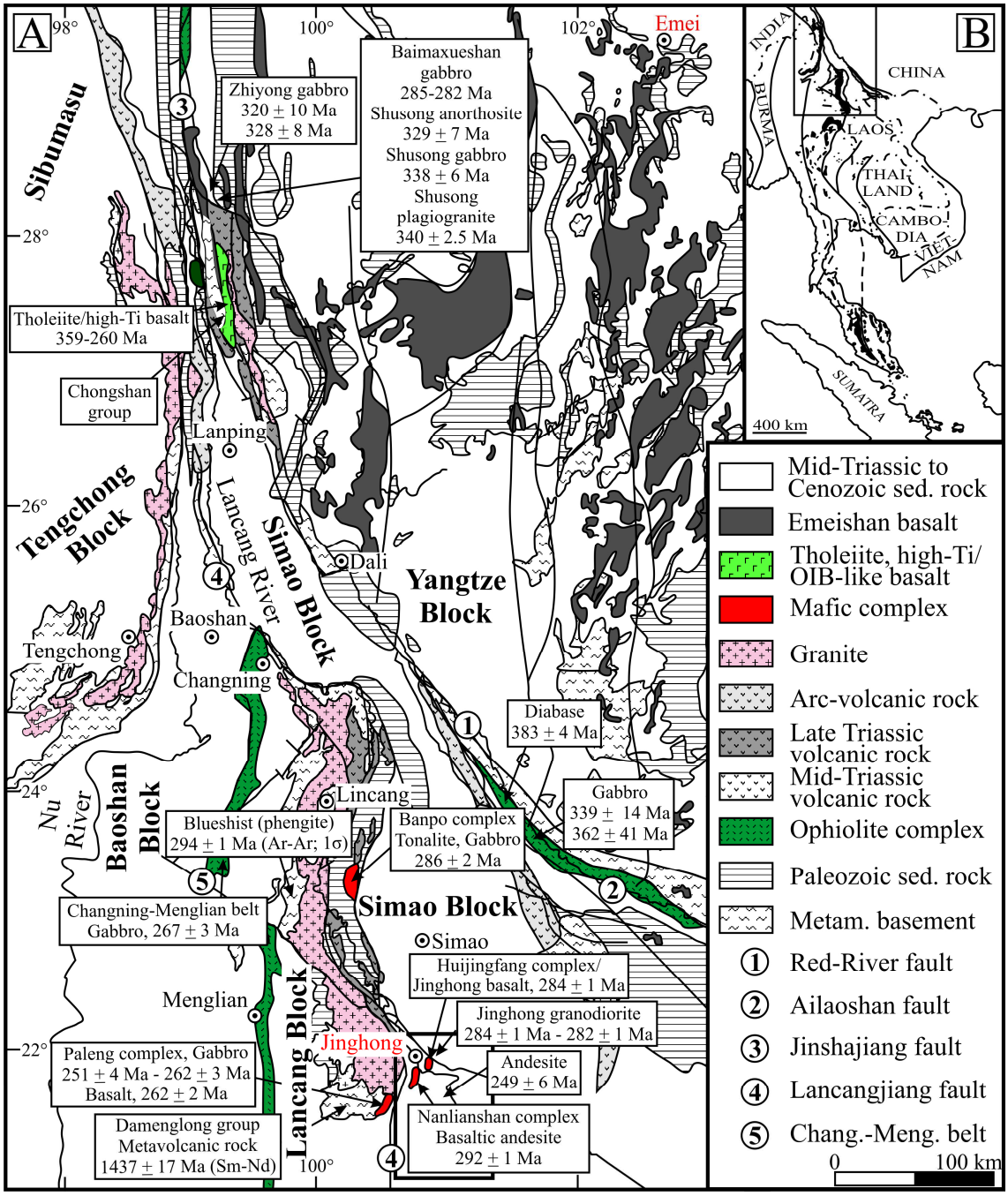

Fig. 2: Simplified geological map of the Lancangjiang zone in southwestern Yunnan (adapted from Ali *et al.*, 2005; Huang *et al.*, 2002; Jian *et al.*, 2004, 2009a,b; Peng *et al.*, 2006, 2008). Labeled age data are SHRIMP U–Pb zircon ages of Jian *et al.* (1998, 2003a,b, 2004, 2008), Peng *et al.* (2006, 2008), Wang *et al.* (2000b,c), and Zhong (1998, 2000). Ar–Ar age data are from Heppe (2006). The black box at Jinghong refers to more detailed geological maps discussed in the following chapters and the red bodies indicate the studied mafic to ultramafic rock complexes. B: The location map shows major faults and cratonic blocks in SW China, as well as the Triassic granite belt extending from Tibet to Indonesia, of which the Lincang granite in the Lancangjiang zone is part (adapted from Cobbing *et al.*, 1992).

To the south, east and north, the Lincang granite is hosted by Meso- to Neoproterozoic arc-like metavolcanic and metasedimentary rocks of the Damenglong and Chongshan groups, consisting of gneiss, mica schist, amphibolite, migmatite and marble with increasing metamorphic grade from east (lower amphibolite facies) to west (lower granulite facies) (Zhang *et al*., 1993; Zhong, 1998). The best outcrops of the Damenglong and Chongshan groups are located south of the Lincang granite and around the towns of Lanping and Dali (Fig. 2). Rock ages published on the Damenglong group range from 1437 ±17 Ma (Sm–Nd on metavolcanic rock) to 716 Ma (Rb–Sr on gneiss) (YBGMR, 1990; Zhai *et al*., 1990; Fig. 2). Sm–Nd model ages (T_{DM}) on granitic gneisses of the Damenglong and Chongshan groups are 1.9-1.7 Ga (Zhai *et al*., 1990). Genetically, the Damenglong and Chongshan groups are related to the Paleo- to Mesoproterozoic active continental margin of the Yangtze Block (Cong & Zhai, 2000).

Likewise, to the east of the Lincang granite a phyllite belt - assigned to be of Late Permian age (P_2) - extends from Manyan (~50 km north of Lincang) down to Myanmar (Heppe, 2006; YBGMR, 1990). This belt is part of the Paleozoic sedimentary rocks shown in Figure 2. In contrast to the Damenglong and Chongshan groups, the metamorphic grade within this Paleozoic belt decreases from west to east, corresponding to a sequence of quartz-veined phyllite to unmetamorphosed turbidite, radiolarite and limestone. These rocks were likely deposited in a complex marginal basin (Heppe, 2006). Helmcke *et al*. (2001) obtained Carboniferous K–Ar ages of 328 ±7 Ma to 311 ±7 Ma (2σ) and suggest a major Late Carboniferous tectono-metamorphic event with uplift and major landmass formation.

Incorporated into the (meta-) sedimentary strata is a voluminous magmatic belt composed of basalt (partly alkalic), hawaiite, basaltic andesite, andesite, rhyolite, felsic ignimbrite and minor dacite and granodiorite (Hennig *et al*., 2009; Heppe, 2006; Peng *et al*., 2008). There is still much debate about the age and petrogenesis of the magmatic rocks. Heppe (2006) suggests - without having robust age constraints - a sequence of Late Permian basaltic to predominantly Triassic felsic magmatic rocks. Hennig *et al*. (2009) relate their Early Permian granodiorites from the vicinity of Jinghong (Fig. 2) to arc-magmatism, in accord with likely arc-derived andesite with a U–Pb zircon age of 249 ±6 Ma (2σ) from Jingha, about 50 km SSE of Jinghong (Peng *et al*., 2008) and recently obtained age data on likely arc-related dacite from the same region of 248.5 ±3.3 Ma (this study).

The basaltic rocks have a striking geochemical mantle signature and Helmcke *et al*. (2001) interpreted the volcanic sequence as related to a postcollisional failed rifting event of the peripheral Emeishan mantle plume. Similar basalts, i.e. thick, high-Ti within-plate basalts

(359-260 Ma, age determinations by fossils in interlayered sedimentary rocks) (Xiao *et al.*, 2008; Zhong, 1998) are reported from the Xiaruo-Tuoding area further north and were interpreted to have formed along a volcanic rifted margin (Sun & Jian, 2004; Xiao *et al.*, 2008; Fig. 2). The Jurassic to Paleogene evolution of the Lancangjiang zone is characterized by extension with km-thick red-bed sedimentary sequences (Helmcke *et al.*, 2001).

1.3 NANLIANSHAN VOLCANO-PLUTONIC COMPLEX (292 ±1 Ma)

The north–south trending Nanlianshan volcano-plutonic complex - about 5 kilometers south of the city of Jinghong - covers an area of ca. 12 x 3 km. Exposure is poor due to deep tropical weathering and all samples are from boulders. According to the available geological maps, the Nanlianshan complex is delimited to the west by a north–south trending apophyse of the Lincang granite and to the east by mid-Triassic diorite. To the north the intrusion is overlain by Quaternary fluvial sediments of the Lancang River (YBGMR, 1990; Fig. 3).

1.3.1 PETROGRAPHIC DESCRIPTION

The dominant rock type of the Nanlianshan volcano-plutonic complex is basaltic andesite in porphyritic and equigranular fine-grained variants (samples JI-1-JI-5, JI-36, JI-37, JI-39, JI-41-JI-43, JI-45, JI-47; Fig. 4A/B). The rock is affected by pervasive propylitic alteration with disseminated and vein-type carbonate (mostly dolomite), epidote, chlorite, pyrite and quartz. The modal composition is 55-65 vol% plagioclase, 30-45 vol% amphibole, 0-10 vol% diopside, 0-10 vol% K-feldspar, 0-10 vol% quartz and up to 5 vol% opaque minerals.

Tectonically twinned, subhedral plagioclase shows varying intensities of sericitization, epidotization and carbonatization. Amphibole and diopside depict actinolitization. Sample JI-3 has some strongly altered olivine. Amphibole is altered to chlorite (Fig. 4C/D). Acessory minerals include titanite, zircon and rutile. Opaques are pyrite, chalcopyrite, chalcocite, hematite and ilmenite, whereas hematite and ilmenite are derived from decomposition of titanium-rich magnetite (Fig. 4G/H).

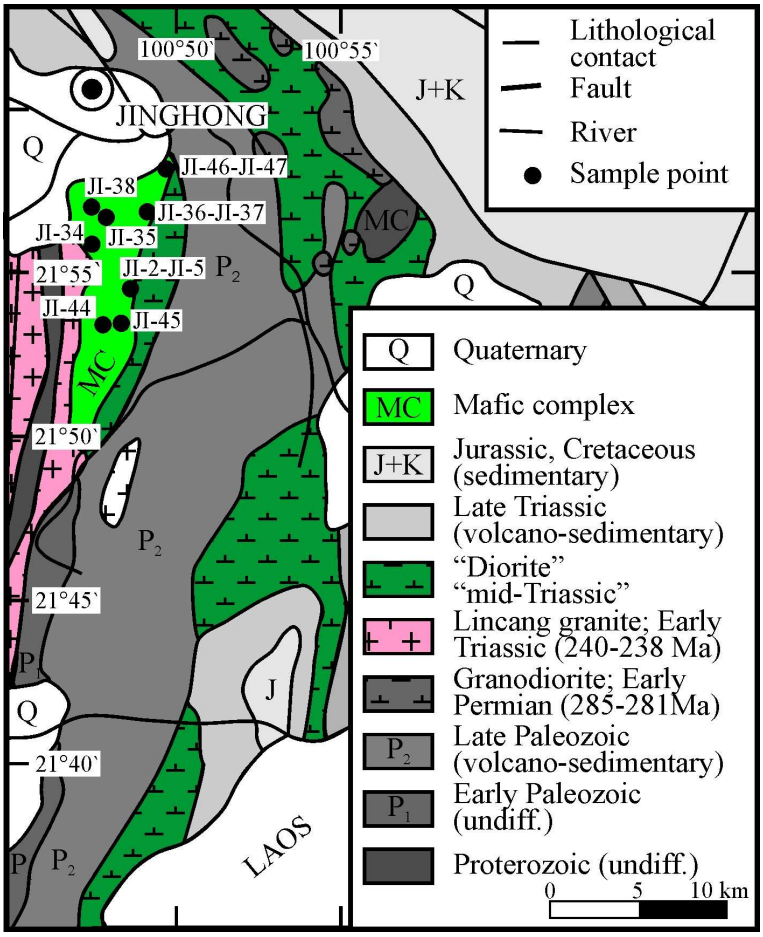

Fig. 3: Geological overview map of the Jinghong area with the Nanlianshan complex (MC) highlighted in light green (adapted from the geologic and magmatic maps of the YBGMR, published in 1990).

The basaltic andesite is intruded by fine- to medium-grained gabbro (microgabbro; samples JI-35, JI-38, JI-40, JI-44, JI-46). The hypidiomorphic to xenomorphic-granular rock is of similar mineralogy as the basaltic andesite, i.e. it has 50-55 vol% of eu- to subhedral plagioclase, 30-45 vol% of subhedral amphibole, 0-15 vol% of eu- to subhedral diopside, 0-10 vol% of subhedral K-feldspar, 0-5 vol% of sub- to anhedral quartz and 0-3 vol% of opaques. In general, the microgabbro depicts stronger alteration than the basaltic andesite. Plagioclase is variably sericitized, carbonatized and epidotized. Amphibole alters to chlorite, epidote and dolomite (Fig. 4E/F). Sample JI-38 stands out with about 5-10 vol% of sub- to anhedral olivine. Due to the very similar rock mode and geochemical composition, the two rock variants were not treated separately in the following studies.

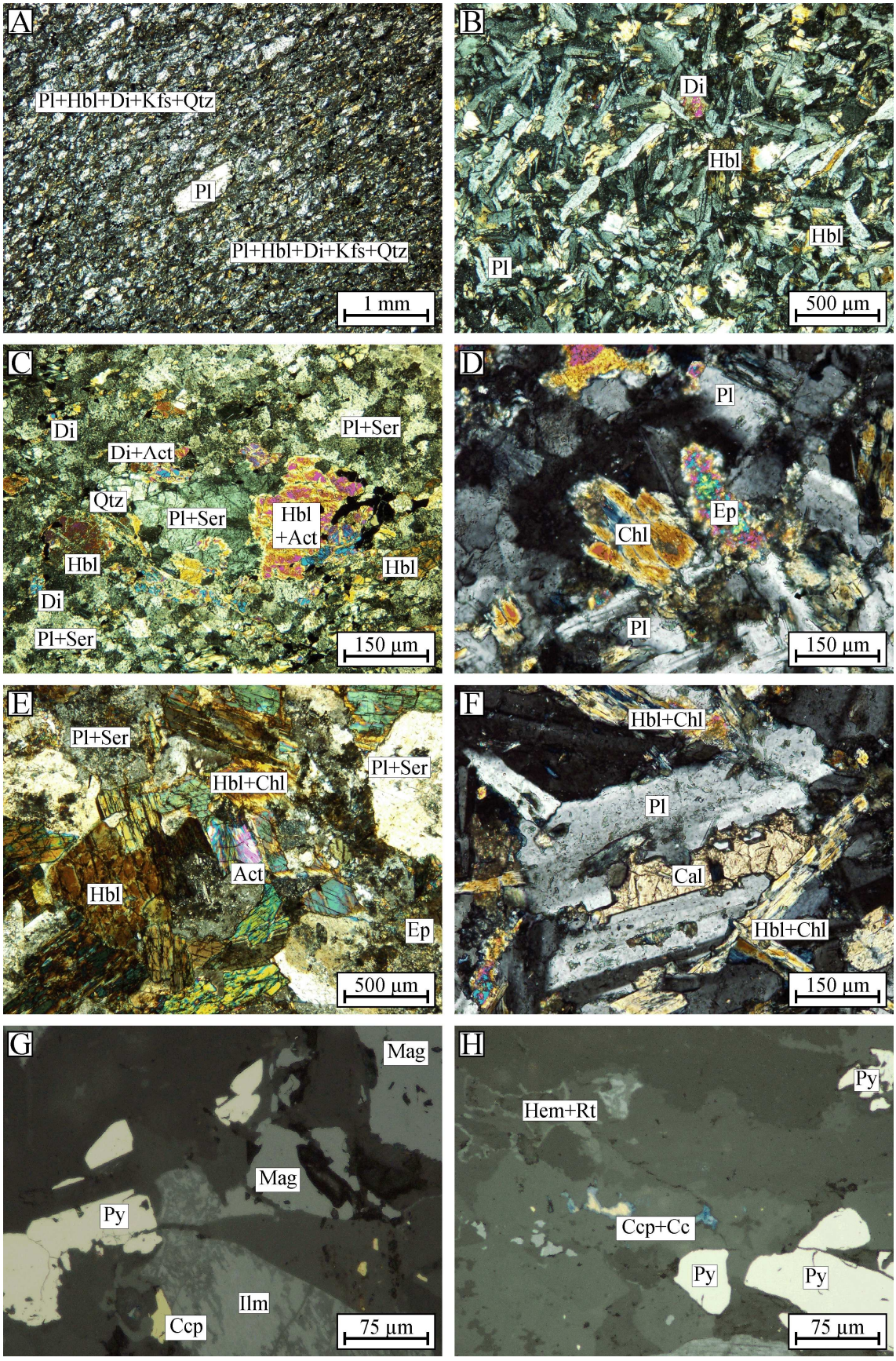

Fig. 4: Photomicrographs of the Nanlianshan basaltic andesite samples (A: JI-39, B: JI-37, C/G/H: JI-2, D: JI-47) and the Nanlianshan microgabbro samples (E: JI-35, F: JI-38); A-F: transmitted light/crossed polars, G/H: reflected, plane-polarized light.

1.3.2 MAJOR AND TRACE ELEMENT COMPOSITION

The Nanlianshan complex has suffered hydrothermal alteration and most samples have LOI values of ≥2.5 wt%. Therefore, the Nanlianshan dataset is reduced, based on petrographic and geochemical criteria, to a "least-altered dataset", which includes samples JI-1, JI-4, JI-5, JI-37, JI-39, JI-41, JI-43 and JI-47.

According to the Total Alkalis vs. Silica (TAS) diagram for volcanic and plutonic rocks (Cox *et al*., 1979; Le Maitre, 1989; MacDonald, 1968; MacDonald & Katsura, 1964; Wilson, 1989) the Nanlianshan least-altered rocks classify as subalkaline basaltic andesite and subalkaline gabbro to diorite, respectively (anhydrous basis; Fig. 5A/B). Immobile element plots of the complete Nanlianshan dataset, such as the Zr/Ti vs. Nb/Y diagram of Winchester & Floyd (1977), and modal and normative mineral compositions support the rock classification (Fig. 5C; Streckeisen, 1976). The least-altered rocks are low in potassium (0.08-0.59 wt% K_2O) and plot as low-K tholeiitic on the K_2O vs. SiO_2 diagram (Fig. 5D; Appendix Tables 5 and 6).

The least-altered rock suite of the Nanlianshan volcano-plutonic complex has 1.0-2.0 wt% TiO_2, 9.2-12.5 wt% Fe_2O_3(t) and 3.6-6.3 wt% MgO. Trace element compositions are 0.6-14.6 ppm Rb, 203-426 ppm Sr, 28-185 ppm Ba, 77-176 ppm Zr and 3.4-8.7 ppm Nb. Ni ranges from 6 to 33 ppm and Cr from 5 to 96 ppm. Both trace elements correlate with MgO.

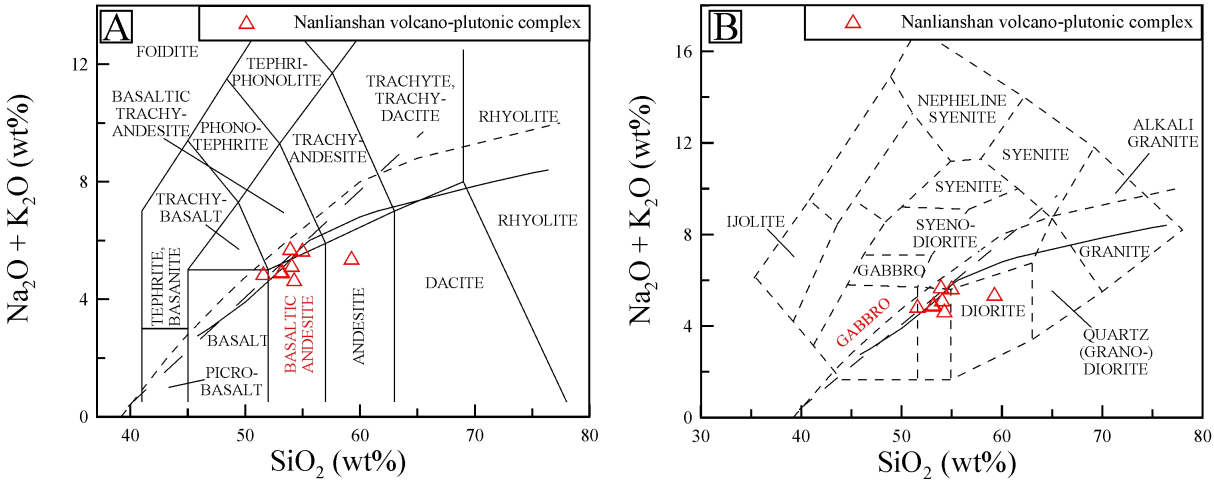

Fig. 5A/B: The least-altered rock suite of the Nanlianshan volcano-plutonic complex on the Total Alkalis versus Silica (TAS) diagrams for volcanic and plutonic rocks (Cox *et al*., 1979; Le Maitre, 1989; Wilson, 1989). Subdivisions into alkaline and subalkaline rocks: continuous line Kuno (1966), widely dashed line MacDonald (1968) and MacDonald & Katsura (1964); narrowly dashed line Irvine & Baragar (1971).

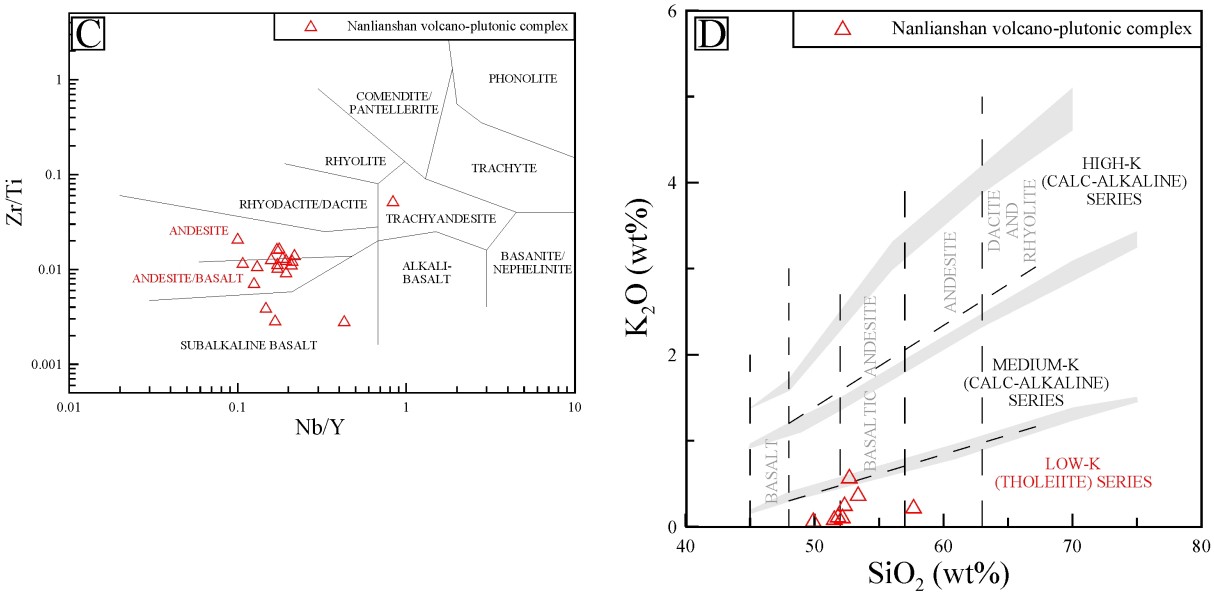

Fig. 5 continued; C: All Nanlianshan volcano-plutonic rock samples on the Zr/Ti vs. Nb/Y plot of Winchester & Floyd (1977). D: The Nanlianshan least-altered rocks on the K_2O vs. SiO_2 diagram for subalkaline rocks. Subdivisions: Le Maitre (1989) and Rickwood (1989) (nomenclature in parentheses). Shaded bands: Boundary lines of Carr (1985), Ewart (1982), Innocenti *et al.* (1982), Middlemost (1985) and Peccerillo & Taylor (1976).

In general, these major element and trace element characteristics are suggestive for a MORB and ocean-island tholeiite affinity (Wilson, 1989). The MORB-normalized trace element patterns of Figure 6 show moderate enrichments in the large low-valence cations, such as Rb, Pb and Ba, and in the large high-valency cations Th and U. These patterns are suggestive for a transitional to E-MORB composition, but exclude a typical N-MORB composition. However, an island-arc setting cannot be ruled out by trace-element characteristics, as evidenced by the broad, light grey shaded polygon in Figure 6.

The least-altered rocks of the Nanlianshan volcano-plutonic complex have an intermediate Zr/Nb ratio of 19-23, in between typical N-type MORB (>30) and typical oceanic-island basalts (<10) (Wilson, 1989). This transitional to enriched MORB composition is also seen in the Y/Nb ratios of 4.6-8.0, with most values around 5, which is typical of a transitional MORB composition (Le Roex *et al.*, 1983; Wilson, 1989).

The low concentrations in ferromagnesian elements such as Ni, Co, Sc and Cr, and their correlation with MgO point to an evolved state of the basaltic melt, which likely has undergone olivine, spinel and clinopyroxene fractionation (Appendix Tables 5 and 6).

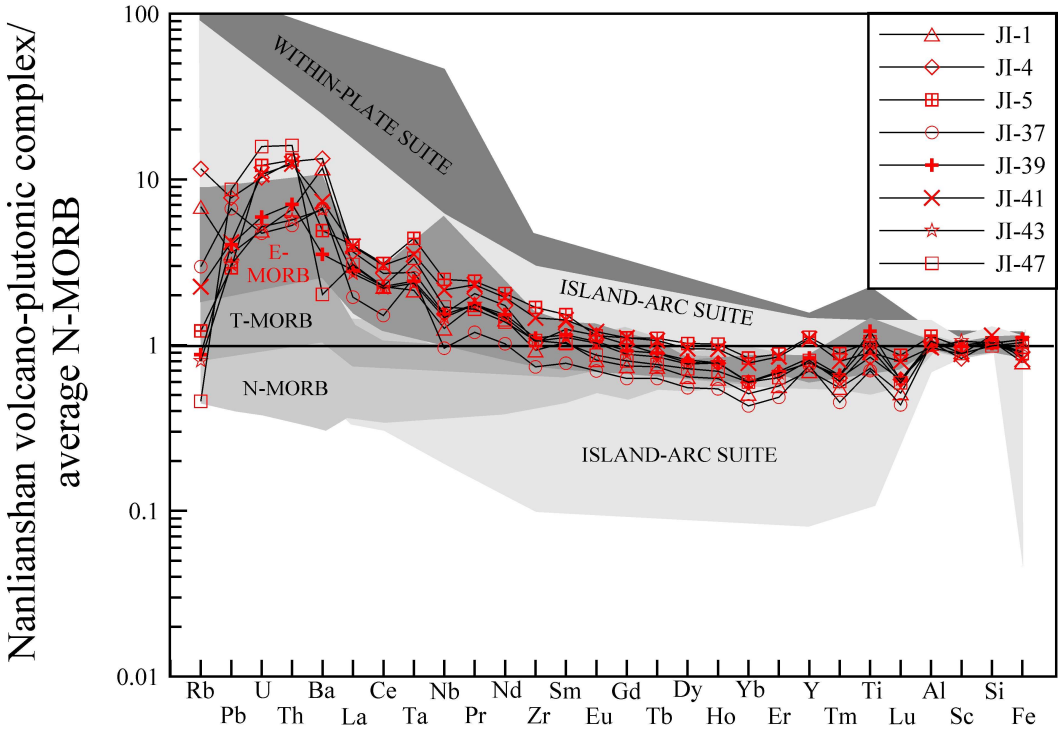

Fig. 6: Average N-MORB-normalized multi-element patterns for the least-altered rock suite of the Nanlianshan volcano-plutonic complex. Average N-MORB data are from Hofmann (1988). The "Within-Plate Suite", "Island-Arc Suite" and "E-", "T-" and "N-MORB"-polygons include several datasets cited by Wilson (1989).

Chondrite-normalized REE patterns for the least-altered rock suite of the Nanlianshan complex plot predominantly in a coherent group, only samples JI-37 and JI-46 stand out with lower REE concentrations (Fig. 7). The patterns are characterized by moderate enrichments of the light rare earth elements (LREE) relative to heavy rare earth elements (HREE). $(La/Sm)_N$ varies for the least-altered rocks from 1.6 to 2.0, which again excludes a classic N-MORB composition and points to a transitional MORB (T-MORB) or enriched MORB (E-MORB) composition (Schilling *et al*., 1983; Winter, 2001). The REE composition of the Nanlianshan volcano-plutonic complex is strikingly different to published data of the Jinshajiang-Ailaoshan and Changning-Menglian oceanic basins (Jian *et al*. 2009a,b; Fig. 7B).

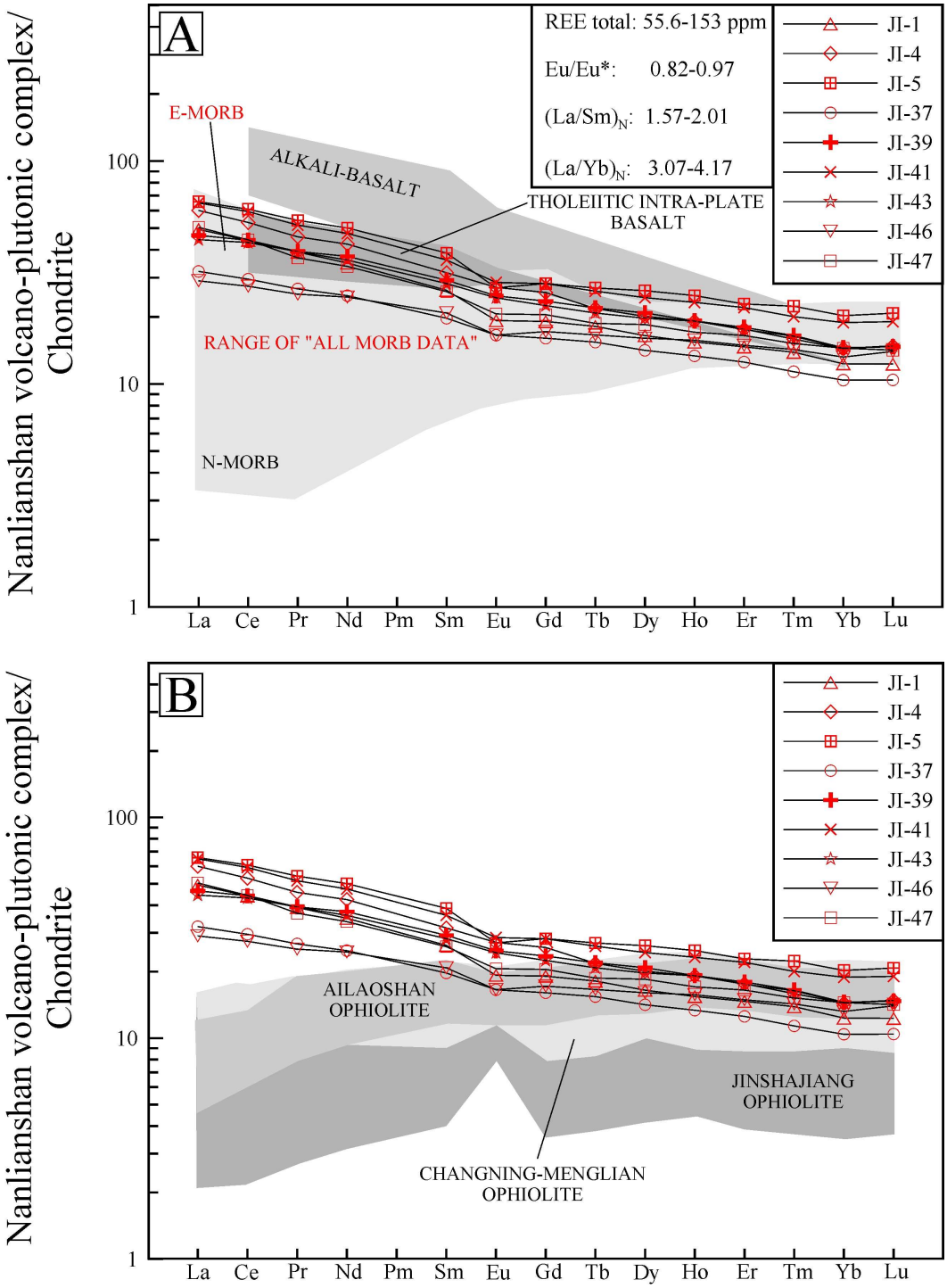

Fig. 7: Chondrite-normalized REE patterns of the Nanlianshan least-altered rock suite (McDonough & Sun, 1995). Reference data are from Wilson (1989) and Jian *et al.* (2009a,b).

1.3.3 U–Pb ZIRCON GEOCHRONOLOGY

Twenty-four single zircon grains from the Nanlianshan microgabbro (sample JI-46) were spot-analyzed (30 µm) by Laser-Ablation Magnetic-Sector ICP-MS at the Geological Survey of Denmark and Greenland (GEUS) in Copenhagen. Details on the U–Pb dating technique are given in Appendix chapter 4.1.2. The U–Pb data for the Nanlianshan gabbro are compiled in Appendix Table 16 and the concordia plot is shown in Figure 8.

The Th/U ratios for zircon from the gabbro sample of the Nanlianshan volcano-plutonic complex have only little spread and indicate a magmatic origin (Th/U = 0.53-1.01). The weighted mean $^{206}Pb/^{238}U$ age of the Nanlianshan gabbro is 292.4 ±1.4 Ma (n = 24; Fig. 8) and is interpreted as the crystallization age of the rock.

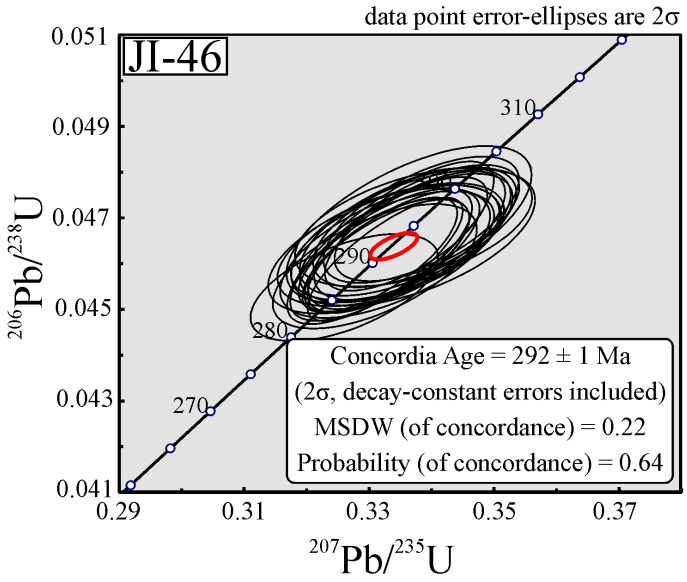

Fig. 8: U–Pb concordia plot for zircon from the Early Permian microgabbro of the Nanlianshan volcano-plutonic complex (sample JI-46).

1.3.4 Sr–Nd ISOTOPIC COMPOSITION

The gabbro sample JI-46 was analyzed for its Sr–Nd whole-rock isotope composition. The data was obtained at the Institute of Precambrian Geology and Geochronology, Russian Academy of Sciences (RAS) in St Petersburg, Russia. Details on the isotopic analysis are given in Appendix chapter 4.1.4. The data are shown in Table 1 and plotted in Figure 9. The Nanlianshan gabbro is altered, and the Sr budget could be modified by both ocean-seafloor alteration and weathering. Both processes would result in higher $^{87}Sr/^{86}Sr$ ratios (Hart *et al.*,

1974, 1999). However, it is unlikely that the Sm and Nd concentrations were significantly affected by hydrothermal alteration and weathering as Nd and Sm are largely immobile.

The isotopic data of the Nanlianshan gabbro indicates a primitive composition with initial ε_{Nd} of 5.3 and initial $^{87}Sr/^{86}Sr$ of 0.7041 (calculated for 290 Ma). Figure 9 compares the isotopic signature of the Nanlianshan gabbro with reference data for the Shuanggou and Jinshajiang Paleo-Tethyan ophiolites, the Xigaze and Troodos Neo-Tethyan ophiolites, as well as "Old Pacific MORB" from Alexander Island, "Old Western Indian MORB", and "Tethyan basalts" (from Masirah and Xigaze) (Mahoney *et al*., 1998; Xu & Castillo, 2004). The Nanlianshan gabbro has an "Old-Tethyan" and "Old Pacific MORB" signature and is similar in its isotopic composition to the Paleo-Tethyan Jinshajiang ophiolite.

Table 1: Sr–Nd isotopic composition of the Nanlianshan microgabbro sample JI-46.

Sample ID	Rock type	Age	Sm	Nd	$^{147}Sm/^{144}Nd$	$^{143}Nd/^{144}Nd$	2σ	$\varepsilon_{Nd}(t)$	Rb	Sr	$^{87}Rb/^{86}Sr$	$^{87}Sr/^{86}Sr$	2σ	$(^{87}Sr/^{86}Sr)t$
		Ma	ppm	ppm					ppm	ppm				
JI-46	Gabbro	290	3.8	13.6	0.16883	0.512856	0.000005	5.29	29.7	219.6	0.391790	0.705730	0.000006	0.704113

$\varepsilon_{Nd}(t)$ was calculated relative to CHUR values: $^{147}Sm/^{144}Nd = 0.1967$, $^{143}Nd/^{144}Nd = 0.512638$ (DePaolo & Wasserburg; 1976; Wasserburg *et al*., 1981).

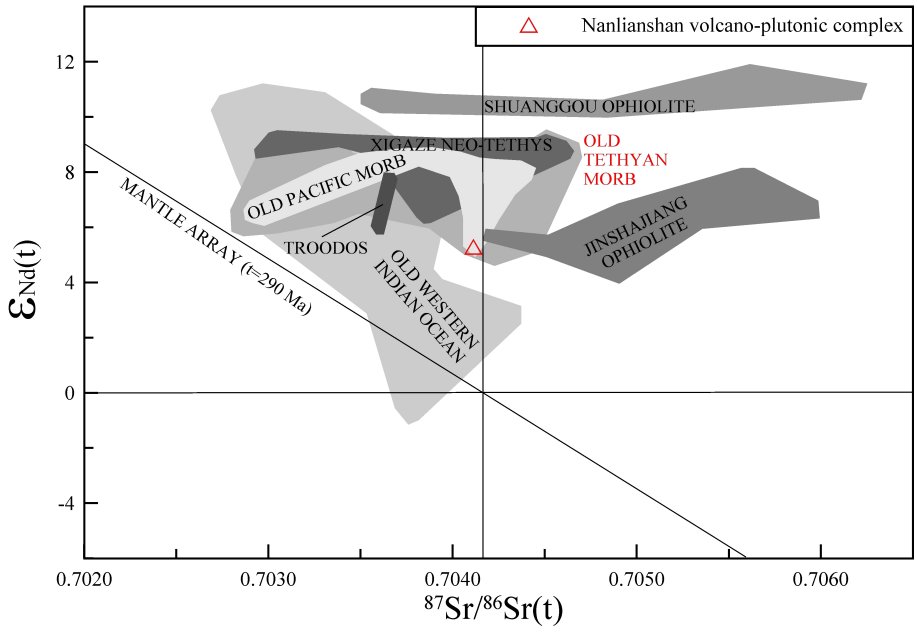

Fig. 9: $\varepsilon_{Nd}(t)$ vs. $^{87}Sr/^{86}Sr(t)$ diagram for the Nanlianshan gabbro (t = 290 Ma). Bulk Silicate Earth and Mantle array (Faure, 1986) are shown for 290 Ma. Data for Old Pacific MORB (shown for 200 and 150 Ma), Old Western Indian MORB (shown for 140-46 Ma) and Old Tethyan MORB (shown for 150 and 120 Ma) are from Mahoney *et al*. (1998). Data for the Shuanggou Paleo-Tethyan ophiolite (339 Ma), Jinshajiang Paleo-Tethyan ophiolite (339 Ma) and Troodos Neo-Tethyan ophiolite (90 Ma) are from Xu & Castillo (2004). Data for the Xigaze Neo-Tethyan ophiolite (110 Ma) are from Mahoney *et al*. (1998) and from Xu & Castillo (2004).

1.3.5 DISCUSSION OF AGE DATA

The Nanlianshan volcano-plutonic complex, dominated by basaltic andesite, represents the oldest recorded igneous event in the southern Lancangjiang zone and suggests seafloor spreading at 293-291 Ma. Interestingly, Yan *et al*. (2005) reported a U–Pb zircon age of 292 ±4 Ma on a gabbro sample of the Garzê ophiolite block, some kilometers southwest of Garzê, i.e. ~900 km north of Nanlianshan. This ophiolite is part of the Garzê-Litang tectonic mélange, separating the Yidun arc massif and the Zhongza Block from the eastward following Songpan-Garzê Block, the northward continuation of the Yangtze Block. Heppe (2006) published a $^{40}Ar/^{39}Ar$ age of 294 ±1 Ma on a blueschist sample from the area between Lancang and Menglian (Fig. 2). Maybe, the blueschist represents ancient subducted oceanic crust.

Much geological and geochronological work was done on the Jinshajiang-Ailaoshan ophiolitic sequence to the east, and especially to the north of the Lancangjiang area (Fig. 2). Jian *et al*. (2003b, 2008) and Wang *et al*. (2000a,b) report SHRIMP U–Pb zircon ages on anorthosites, layered gabbros and plagiogranites from the Dequin-Weixi area. All rocks are interpreted as oceanic crust. The ages include 340 ±3 Ma for the Shusong plagiogranite, 329 ±7 Ma for the Shusong anorthosite, 328 ±8 Ma and 320 ±10 Ma for the Zhiyong gabbro, and 285-282 Ma for the Baimaxueshan gabbro. Age data on oceanic rocks from the Ailaoshan area were presented by Zhong (1998, 2000), which include a $^{40}Ar/^{39}Ar$ plateau age of 339 ±14 Ma for clinopyroxene from a gabbro sample of the Shuanggou ophiolite. This rock age is strikingly similar to the age of the Shusong gabbro and the Shusong plagiogranite. Jian *et al*. (1998) obtained a SHRIMP zircon U–Pb age of 362 ±41 Ma on the Ailaoshan gabbro, which is within the error range of the $^{40}Ar/^{39}Ar$ age of the Shuanggou gabbro, and Jian *et al*. (2009b) published a U–Pb age of 383 ±4 Ma on diabase of the Ailaoshan ophiolite, which represents the currently favored age estimate on the Ailaoshan Ocean (Fig. 2).

The oceanic plutonic rocks of Late Devonian to Early Carboniferous age (403-310 Ma) were interpreted to represent a mid-ocean ridge environment of the Jinshajiang-Ailaoshan oceanic basin. This period of sea-floor spreading was followed by a late phase of spreading above an intraoceanic subduction zone in the Early Permian (285-282 Ma). Continued spreading along this axis is thought to have produced a plutonic arc complex in the Mid- to Late Permian (Jian *et al*., 2008). Rocks from the Changning-Menglian Ocean were recently dated at 267 ±2 Ma (Jian *et al*., 2009a,b; Fig. 2).

1.3.6 TECTONOMAGMATIC ENVIRONMENT

The Nanlianshan volcano-plutonic complex characterizes the earliest recorded tectonomagmatic event in the Paleo-Tethys evolution of the southern Lancangjiang zone known to date. On the Ti–Zr–Y tectonic discrimination diagram (Fig. 10A) all samples except one plot in or closely around the “MORB, island-arc tholeiite and calc-alkali basalt field”. This plot excludes a within-plate setting for the Nanlianshan volcano-plutonic complex (Pearce & Cann, 1973). Further subdivision was done on the Zr vs. Ti diagram, which clearly shows a MORB signature (Fig. 10B) (Pearce, 1982). These results are in accord with the Zr vs. Zr/Y diagram (not shown) and the Ti/Y vs. Nb/Y diagram (Fig. 10C) (Pearce, 1982, 1983; Pearce & Cann, 1973).

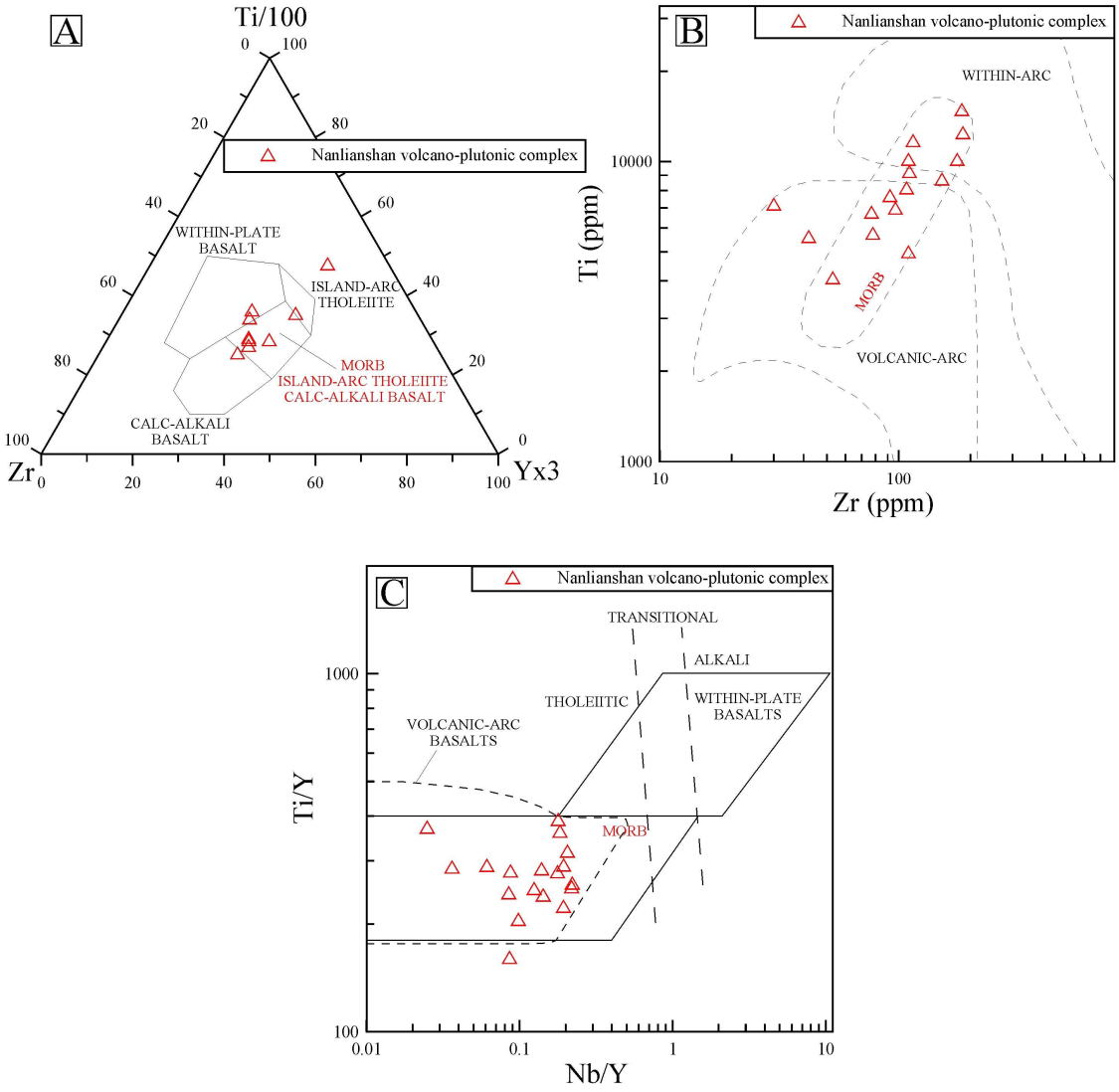

Fig. 10: Ti–Zr–Y discrimination diagram for basalts (Pearce & Cann, 1973). All, except one sample plot in/close to the MORB, island-arc tholeiite and calc-alkali basalt field. B: Ti vs. Zr discrimination diagram (Pearce, 1982); the samples plot in the “MORB cigar”. C: Ti/Y vs. Nb/Y discrimination diagram (Pearce, 1982). Nearly all rock samples plot in the MORB field.

The tectonic discrimination plots suggest a MORB affinity for the Nanlianshan rock suite. This is in accord with La/Yb ratios of 4.5-6.1 and La/Nb ratios of 1.8-2.6 for the least-altered rocks. The average Th/Ta ratio for all Nanlianshan rock samples is 2.4 (3.2 for the least-altered rock suite), which is either supportive for a T- to E-MORB character or might indicate a weak supra-subduction zone environment (Elthon, 1991).

The geochemical and geochronologic results on the Nanlianshan volcano-plutonic complex point to Early Permian oceanic crust in the southern Lancangjiang zone, which is strikingly different in composition to the younger Changning-Menglian Ocean to the west and the older Jinshajiang-Ailaoshan Ocean to the east. Therefore, it is very likely that the Nanlianshan complex indeed mirrors the beginning evolution of an independent branch ocean between the Lancang and Simao Blocks, which is referred to in the literature as Lancangjiang Ocean.

1.4 BANPO COMPLEX (286 ±2 Ma)

The mafic to ultramafic Banpo complex, about 80 km north of Simao, is little studied so far (Heppe, 2006; Jian *et al*., 2009a,b; Fig. 2). Jian *et al*. (2009a) classify the Banpo complex as Early Permian plutonic arc, which is located next to the Damenglong complex, a continental fragment of the Proterozoic Simao Block. The Damenglong complex is in fault contact with Devonian to Permian sedimentary rocks, which are in turn unconformably overlain by mid- to Late Triassic volcano-sedimentary rocks (Jian *et al*., 2009a).

Jian *et al*. (2009a) classify the Banpo complex as calc-alkaline with predominantly medium- to coarse-grained clinopyroxene peridotite, subordinate dunite, harzburgite and pyroxenite. Associated gabbroic rocks include two-pyroxene gabbro, olivine gabbro, leucogabbro, anorthosite and small bodies of tonalite (Jian *et al*., 2009a).

The samples of Jian *et al*. (2009a,b) include serpentinite/harzburgite (BP02), gabbro (BP04) and tonalite (BP01). The gabbro and tonalite gave identical Early Permian U–Pb zircon ages of 285.6 ±1.7 Ma and 285.8 ±2.0 Ma, respectively (Jian *et al*., 2009a).

We could sample at Banpo chromite-bearing harzburgite (8 samples), two-pyroxene gabbro (15 samples), anorthosite (2 samples), hornblendite (1 sample), porphyritic rhyolite (18 samples) and calcsilicate rock (2 samples). The latter two rock units are not discussed in this thesis. Dating of the rhyolite by in situ LA-ICP-MS analysis was just successful on one single zircon grain, which gave a $^{206}Pb/^{238}U$ age estimate of about 269 Ma.

1.4.1 GEOLOGICAL MAPPING

1.4.1.1 LOCAL GEOLOGY AND STRATIGRAPHY

During the sampling campaign at Banpo a geologic map was compiled and tectonic data were collected. Map base for field work was the georectified topographic map NF 47-3 (sheet Mien-Ning) at a scale of 1:250.000 (Army map service, 1956), available at the University of Texas (Austin) (http://www.lib.utexas.edu/maps/ams/china).

The Banpo complex is predominantly built-up of Early Permian gabbro which intrudes slate, andesite, rhyolite, conglomerate and sandstone (Fig. 11; YBGMR, 1990). Harzburgites are restricted to small areas in the northern and southern parts of the complex. Major outcrops of whitish rhyolite could be mapped in the northern and southern part of the complex and are locally accompanied by minor occurrences of calcsilicate rock. Field relationships suggest that the rhyolite is younger than the gabbro (Fig. 11).

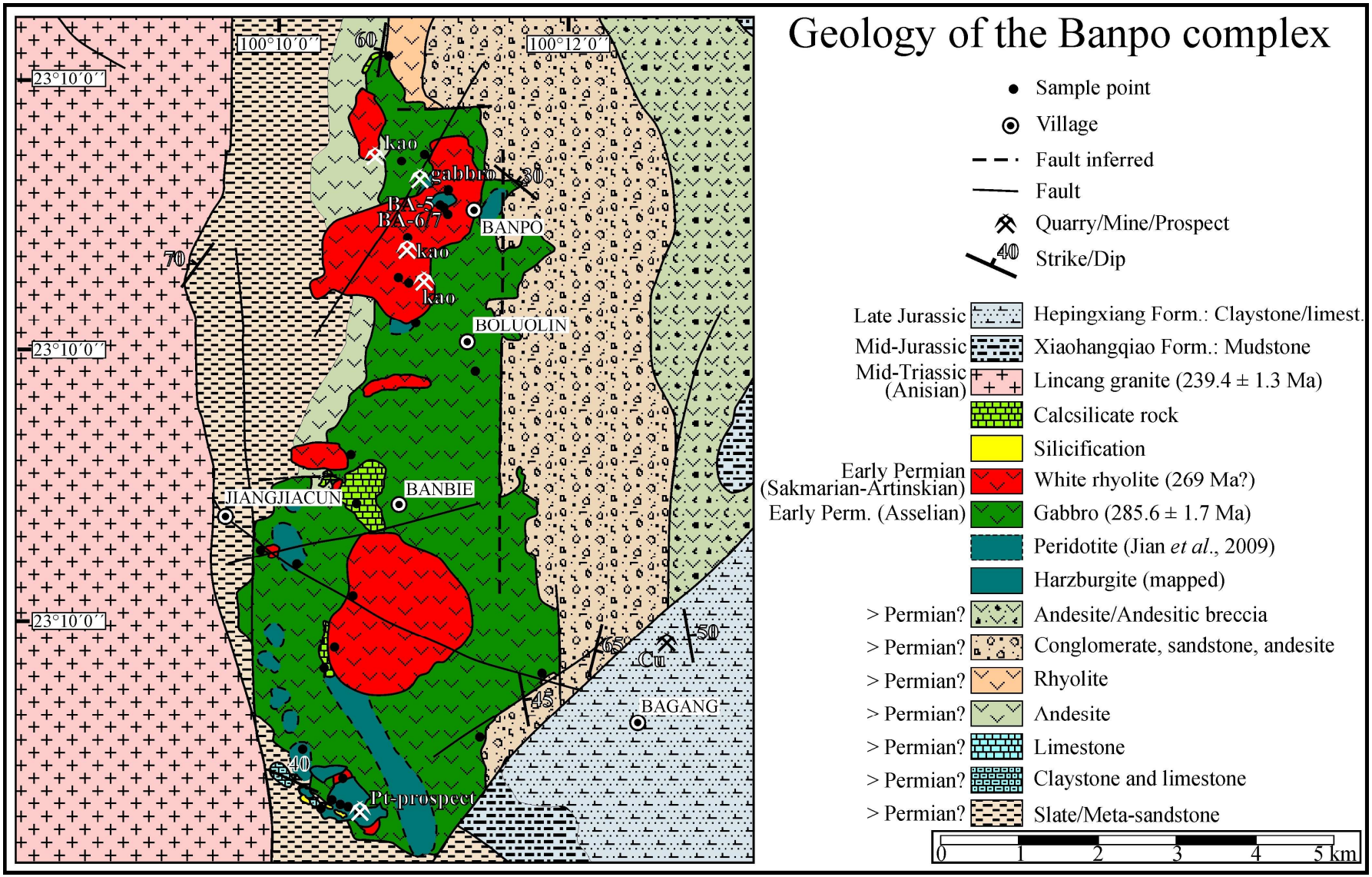

Fig. 11: Geological overview map of the Banpo complex. The Banpo anorthosite (BA-6/7) and hornblendite (BA-5) sample locations are indicated. The map combines own field data, data of Jian *et al*. (2009a,b) and data from geological overview maps of the YBGMR (1990).

1.4.1.2 TECTONICS

The strata show - as indicated on the geologic map - predominant west-dip on the west side of the complex and predominant east-dip on the east side, suggesting an anticline with its core along the N–S axis of the Banpo complex (Figs. 11 and 12A; Appendix Table 4). The measured, predominantly NNW–SSE striking fold hinge lineaments correspond well to this scenario (Fig. 12A/B; Appendix Table 4). These folds have partly box shape and show kink bands. There appears to be a second, perpendicular oriented NE–SW population, as indicated by one measurement (70/20; Fig. 12A/B; Appendix Table 4).

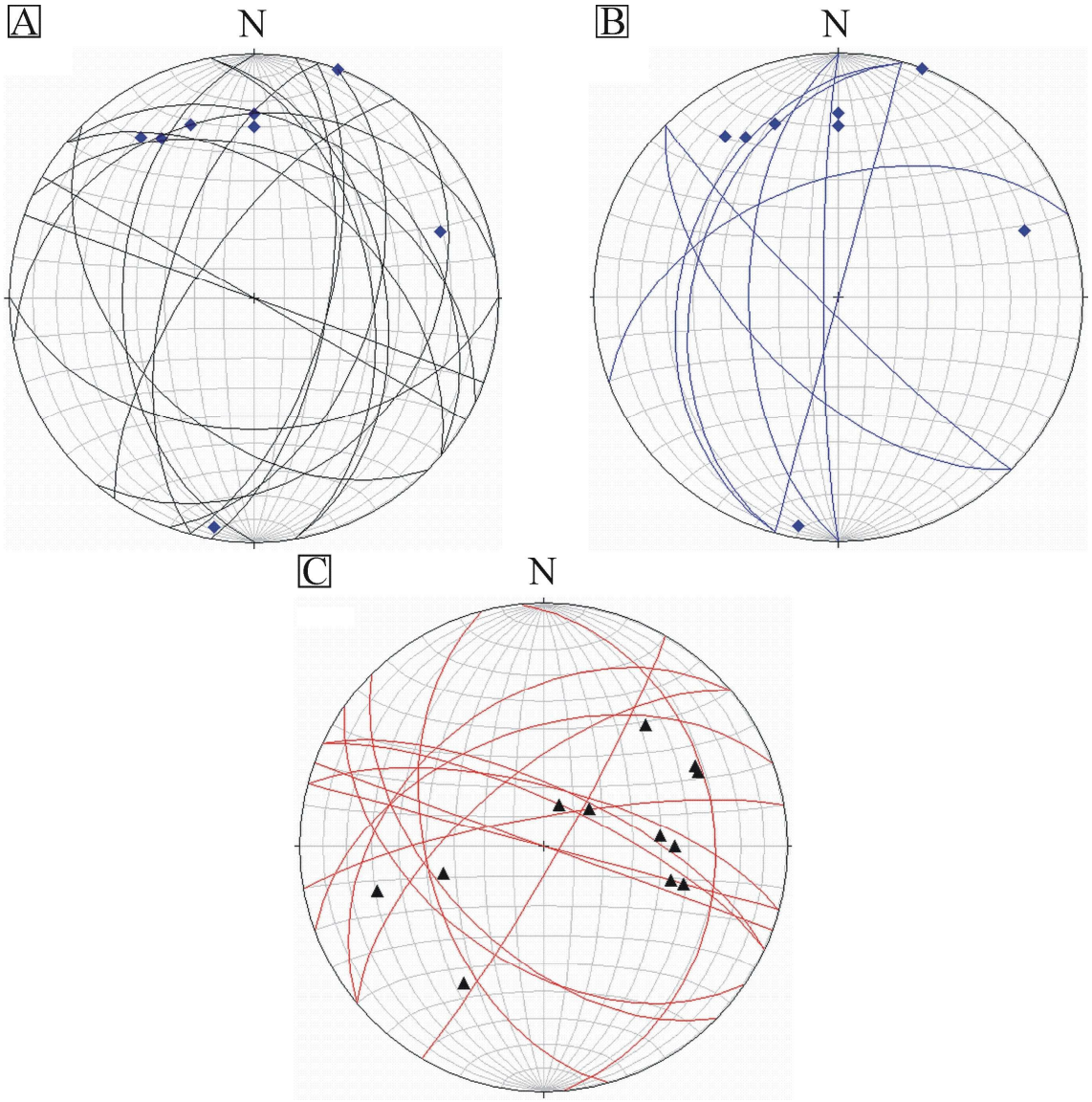

Fig. 12: Tectonic data for the Banpo complex (8 localities) and host rocks (25 localities) plotted on stereonets (equal area/lower hemisphere). A: Bedding data plotted as black planes (n = 18) and fold hinge lineaments plotted as blue lineaments (n = 9). B: Foliation data plotted as blue planes (n = 8) and fold hinge lineaments plotted as blue lineaments (n = 9). C: Fault data plotted as red planes (n = 13) and fault lineaments (striation) plotted as black triangles.

The predominant foliation has N–S strike and is likely the axial plane cleavage of the predominant folds (Fig. 12B). As the foliation shows dominantly west-dip, fold vergence is believed to be to the east. One foliation measurement suggests, in accordance to the fold hinge lineament data, a suppressed NE–SW system. The major faults in the Banpo region have N–S strike. There is a predominant WNW–ESE and again a NE–SW system (Fig. 12C).

In the Lancang group three deformational episodes (D1, D2 and D3) are distinguished (Zhang *et al*., 2000). D1 is characterized by SSW-vergent isoclinal folds, a penetrative axial plane cleavage and faults with northern dip. D1 is attributed to the "Jinningian tectonothermal event" which is believed to have shaped the Yangtze basement at ~900 Ma (Zhang *et al*., 2000). D2 is attributed to the "Hercynian orogeny" and consists of W–E striking fold hinges and S-dipping faults (Heppe, 2006; Zhang *et al*. 2000). D3 is characterized by complex folds with E-vergence and N–S trending fold hinges. D3 is related to the closure of the Changning-Menglian Ocean i.e. to the Paleotethyan orogeny (Zhang *et al*., 2000). As no further ductile deformation structures can be found in the Lancang group, the Himalayan overprint is believed to be predominantly of brittle nature. Most measured structures in the Banpo area correspond to the D3 deformational episode. Maybe there are relics of the D2 event.

1.4.2 CHROMITE-BEARING HARZBURGITE

1.4.2.1 PETROGRAPHIC DESCRIPTION

The inequigranular harzburgite (samples JI-1-JI-4, BA-16, BA-18-BA-20, BA-45) is of idiomorphic to xenomorphic-granular texture and has a very variable mineralogy of 45-90 vol% olivine, 5-45 vol% orthopyroxene (predominantly enstatite), <10 vol% clinopyroxene (predominantly augite), <15 vol% plagioclase and <5 vol% chromite (Fig. 13A-G). The rock shows strong to pervasive serpentinization, partly accompanied by prehnitization, chloritization and carbonatization (Fig. 13A-F).

The harzburgite samples depict a distinct range from a predominantly dunitic composition (<5 vol% pyroxene; sample BA-18) to nearly equal amounts of pyroxene and olivine (sample BA-4). The whole series was sorted by microscopic observations from olivine- to pyroxene-rich as BA-18, BA-20, BA-45, BA-16, BA-2, BA-3, BA-1, BA-4. The intensity of hydrothermal alteration varies from strong - among the pyroxene-rich rocks - to intensive in the olivine-dominated samples and includes cross-cutting serpentine, carbonate, prehnite, saponite and ironoxyhydroxide veins (Fig. 13A-F). In the olivine-dominated

samples pyroxene is serpentinized, whereas in the pyroxene-rich rocks carbonatization, chloritization and hematitization predominate (Fig. 13B/C).

In all rocks, euhedral olivine (0.3-5.0 mm) is altered to serpentine fibers and meshes (lizardite by RDA analysis) with only the crystal outline preserved (Fig. 13A-F). Its primary crystal shape suggests a forsteric composition (Fig. 13E/F). Orthopyroxene (0.2-6.0 mm) forms anhedral patches in between the olivine crystals and shows clinopyroxene exsolution lamellae (Fig. 13B-D). As extinction of pyroxene is partly straight and partly inclined, and interference colors are partly diagnostic for orthopyroxene and partly diagnostic for clinopyroxene, primary clinopyroxene (augite) with orthopyroxene exsolution lamellae cannot be excluded as well (diallag formation). It appears, however, that clinopyroxene is predominantly of secondary origin, as the freshest rocks have orthopyroxene and depict only minor clinopyroxene exsolution (Fig. 13B). Orthopyroxene shows partly oriented pseudomorphs of lizardite (bastitization) (Fig. 13A). Both pyroxenes depict limonite exsolution lamellae as well (Fig. 13A-D), and weathering leads to a fine-grained mineral assemblage of carbonate, ilmenite and hematite grains (e.g. Fig. 13D/E). Relics of tectonized plagioclase (0.2-3.0 mm) altered to prehnite could be detected in sample BA-4 (15 vol%). As samples BA-1 and BA-2 have minor prehnite (1-3 vol%) it is reasonable to assume a primary plagioclase content for these pyroxene-rich samples as well. Prehnite suggests hydrothermal/metamorphic overprint (Fig. 13B).

Euhedral to subhedral chromite (0.04-3.0 mm) has cracks filled by serpentine (Fig. 13G). The modal chromite content and crystal size appear to correlate positively with modal olivine content. Some crystals depict ferritchromit formation along the crystal outline and intensive chromite alteration includes spongy ferritchromit with only relictic chromite preserved. Some chromite crystals have magnetite rims. All rocks have pyrrhotite (<0.12 mm; Fig. 13H), which alters in the pyroxene-rich samples BA-1-BA-4 predominantly to pyrite, and subordinately to "zwischenprodukt". Samples BA-3 and BA-4 appear to have some tiny minute grains of chalcopyrite and secondary covellite. Additional oqaques are magnetite, hematite and ilmenite - partly developed as veins. Accessories include titanite (BA-1, BA-2), zircon (BA-1, BA-2, BA-4) and rutile.

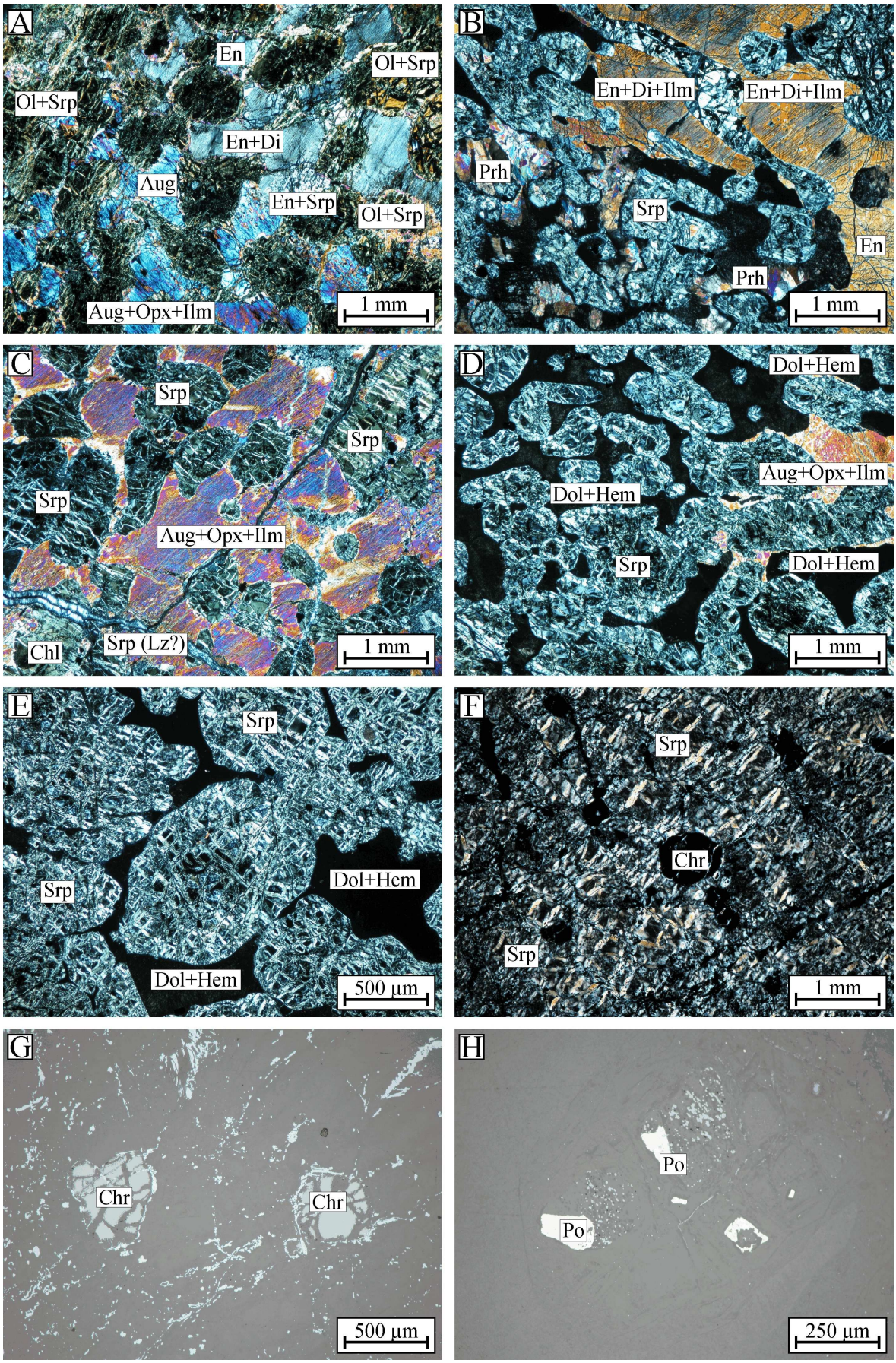

Fig. 13: Photomicrographs of the Banpo harzburgite (A/C: BA-1, B: BA-4, D: BA-2, E/F/G: BA-20, H: BA-3; A-F: transmitted light/crossed polars, G/H: reflected, plane-polarized light).

1.4.2.2 MAJOR AND TRACE ELEMENT COMPOSITION

The major element composition of the Banpo harzburgite (samples BA-1-BA-4, BA-16, BA-18-BA-20, BA-45) corresponds well to published peridotite and harzburgite reference data (Le Maitre, 1976), and the petrographically assessed intensive alteration is expressed by LOI values of 12.0-13.9 wt% (Appendix Table 6). The geochemical data validates the petrographic subdivision in orthopyroxene-rich (partly plagioclase-bearing) and olivine-rich harzburgites, respectively. The (partly plagioclase-bearing) orthopyroxene-rich samples BA-1 to BA-3 are higher in Ti, Al, Mn, Ca and K (0.04-0.06 wt% TiO_2, 3.4-4.6 wt% Al_2O_3, 0.16-0.18 wt% MnO, 0.1-1.3 wt% CaO, 0.03 wt% K_2O) and lower in Mg and Cl (30.9-33.9 wt% MgO and 0.008-0.013 wt% Cl). The olivine-rich harzburgite samples BA-16, BA-18, BA-20 and BA-45 are lower in Ti, Al, Ca and K (0.03-0.05 wt% TiO_2, 0.9-1.4 wt% Al_2O_3, 0.01-0.04 wt% CaO and 0.01-0.02 wt% K_2O) and higher in Mg, Mn and Cl (33.9-37.1 wt% MgO, 0.04-0.07 wt% MnO and 0.016-0.024 wt% Cl). The plagioclase-rich sample BA-4 is set apart from the orthopyroxene-rich rocks by very high Al, Ca and Mn, and low Fe and Mg (Appendix Table 6).

Calculated CIPW norms (anhydrous basis) give for the pyroxene-rich and olivine-rich harzburgites 1.9-4.4 and 1.1-1.7 wt% corundum, 0.18-0.21 and 0.06-0.12 wt% orthoclase, 0.1 wt% albite, 0.4-17.5 and 0-0.1 wt% anorthite, 24.6-29.1 and 16.3-27.8 wt% hypersthene, 57.7-67.3 and 65.3-69.4 wt% olivine, 2.3-3.8 wt% magnetite, 0.1 wt% ilmenite and 0.02-0.05 wt% apatite, with the plagioclase-bearing harzburgite BA-4 standing out from the pyroxene-rich harzburgites by high normative anorthite and low hypersthene/olivine contents.

Table 2: Calculated CIPW norms and Mg-numbers of the Banpo and Jinbaoshan harzburgites. Calculations are according to Kelsey (1965) and Middlemost (1989).

Sample ID	Corundum	Orthoclase	Albite	Anorthite	Hypersthene	Olivine	Magnetite	Ilmenite	Apatite	Mg#
BA-1	1.92	0.18	0.10	7.46	27.78	57.66	3.42	0.13	0.02	83.42
BA-2	3.73	0.18	0.10	0.39	23.20	67.28	3.60	0.10	0.02	83.87
BA-3	4.36	0.20	0.10	2.48	22.85	65.83	2.94	0.08	0.02	86.64
BA-4	2.76	0.21	0.10	17.49	16.31	59.56	2.51	0.08	0.02	86.83
BA-16	1.58	0.08	0.10	0.10	24.61	68.53	3.50	0.12	0.02	84.80
BA-18	1.66	0.07	0.10	0.00	29.12	65.73	2.31	0.10	0.02	90.15
BA-20	1.05	0.06	0.10	0.04	24.99	69.35	3.10	0.08	0.02	86.77
BA-45	1.26	0.12	0.10	0.11	27.81	65.26	3.76	0.07	0.05	83.41
JBS-2	2.90	1.42	0.10	3.08	26.85	59.67	3.64	0.73	0.19	82.71
JBS-3	2.41	1.23	0.10	3.17	28.49	58.46	3.65	0.93	0.14	82.67

In general, the calculated CIPW norms for the Banpo harzburgite correspond well to the petrographic observations. The CIPW norms and Mg-numbers of the Banpo harzburgite are similar to those of the Jinbaoshan harzburgite reference samples (refer to chapter 2.2.1.5; Table 2; Fig. 14).

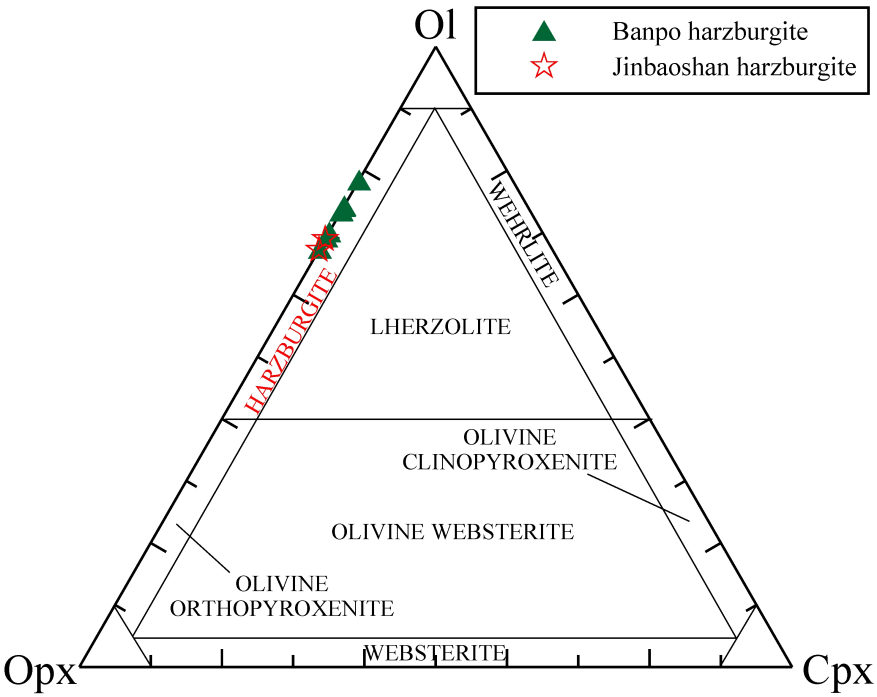

Fig. 14: Rock classification of the Banpo harzburgite and the Jinbaoshan harzburgite based on normative mineral contents (Streckeisen, 1973).

The Banpo harzburgite shows characteristic trace element variations (Fig. 15; Appendix Table 6). The (plagioclase-bearing) orthopyroxene-rich harzburgites are higher in Ba and Sr, likely representing fractionating plagioclase, and lower in Cr and V, likely due to chrome-spinel fractionation, as evidenced by petrography. The primitive mantle-normalized multi-element patterns of Figure 15 show for most orthopyroxene-rich harzburgites (samples BA-1, BA-2 and BA-4) positive Zr-anomalies, suggesting zircon fractionation. Samples BA-1 and BA-2 depict drastic Ta-enrichment, decoupled from Nb, which suggests in combination with high Th of sample BA-2, fractionating titanite (Luhr & Carmichael, 1980).

All olivine-rich harzburgite samples exhibit a clear negative Zr-anomaly and plot similar to the Banpo peridotite reference sample of Jian *et al*. (2009a). All samples have a negative Ti-anomaly, likely reflecting titanite and magnetite fractionation (Fig. 15).

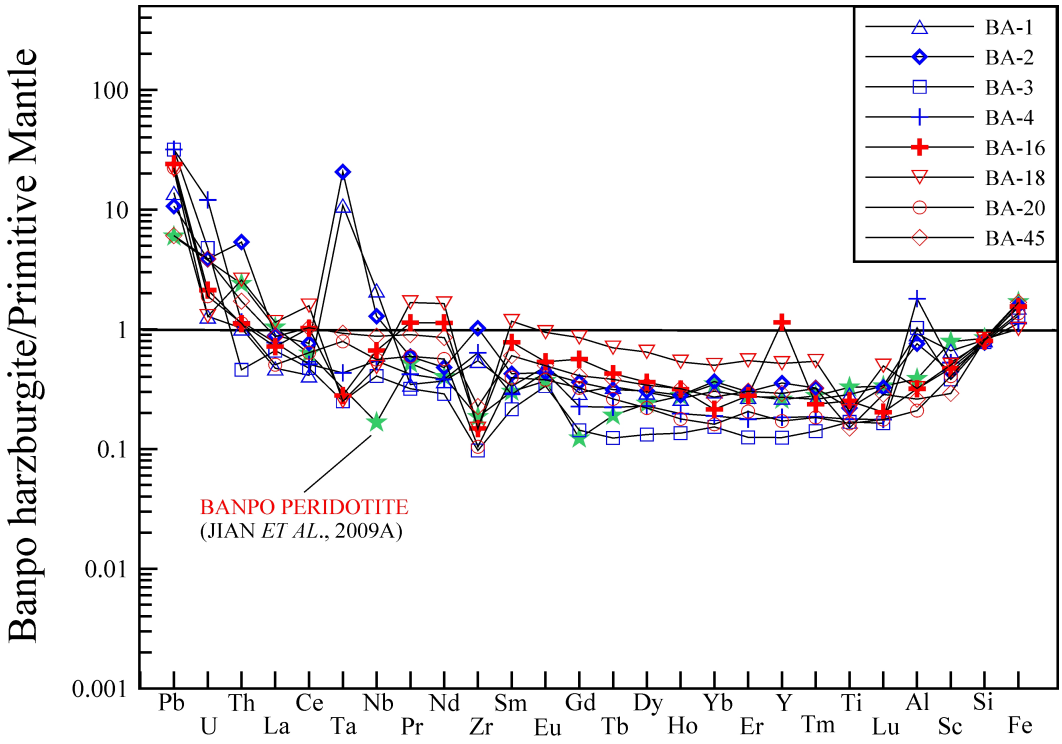

Fig. 15: Primitive mantle-normalized multi-element patterns for the Banpo harzburgite samples. The pyroxene-rich harzburgites are shown in blue and the olivine-rich harzburgites in red. Primitive mantle data are from Palme & O`Neill (2004).

Compared to worldwide peridotite data, the Banpo harzburgite has an intermediate composition, i.e. it is neither as enriched as dunites from the Pechenga Pasik greenstone belt (Kola Peninsula; Brügmann *et al*. 2000), harzburgites from New England (Bruce *et al*., 2000; Bruce & Niu, 2002; not shown) or the ELIP-related reference samples from the Jinbaoshan deposit, nor as depleted as harzburgites and dunites from the Greater Antilles and the Kurile Arc (Frey *et al*., 1991; Marchesi *et al*., 2006; Matsumoto *et al*., 2001; Morishita *et al*., 2004; Saal *et al*., 2001; Shiotani & Niida, 1997; Takazawa *et al*., 2000; Yoshida & Takahashi, 1997; Yoshikawa & Nakamura, 2000; Fig. 16). In addition, the patterns are more vivid and depict a wider range in concentrations than, e.g., dunites from the Trans-Hudson orogen. The more depleted samples depict similarities to harzburgites from the Central Massif (red stars) and Argentina (green stars). The more enriched samples are similar to lherzolites from the Central Massif (blue stars; Conceicao *et al*., 2005; Femenias *et al*., 2003). An “ultramafic rock” reference sample of the Changning-Menglian belt (yellow star) has distinctly lower LREEs and Ti contents than the Banpo harzburgite (Jian *et al*., 2009a).

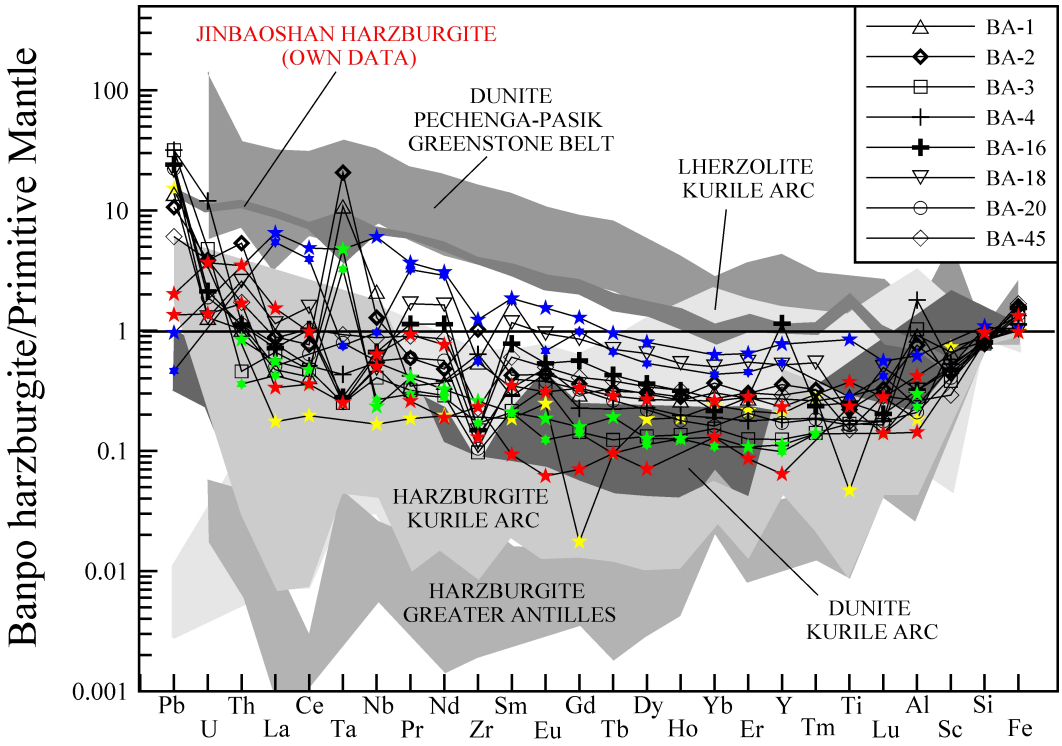

Fig. 16: Primitive mantle-normalized multi-element patterns for the Banpo harzburgite. The Banpo harzburgite is markedly depleted in comparison to the Jinbaoshan harzburgite.

Chondrite-normalized REE patterns of the Banpo harzburgite samples clearly distinguish the two harzburgite groups (Fig. 17). The orthopyroxene-rich samples (BA-1-BA-4) are very low in REEs (REE total of 2.3-3.9 ppm) and all samples depict positive Eu-anomalies (Eu/Eu* = 1.1-1.9) and positive $(La/Ce)_N$ ratios of 1.1-1.5. Both criteria fit to plagioclase, as identified by petrography and as suggested by the calculated CIPW norms.

The olivine-rich samples (BA-16, BA-18, BA-20, BA-45) are higher in REEs (REE total of 3.2-8.5 ppm) and depict negative $(La/Ce)_N$ and $(La/Nd)_N$ of 0.7-0.8 and 0.6-1.0, respectively, illustrating the increasing contents of orthopyroxene and olivine.

The drastic U-shaped REE pattern (including a marked negative Gd-anomaly) as described by Jian *et al.* (2009a) could not be confirmed for the Banpo harzburgite. Based on this pattern Jian *et al.* (2009a) identified the peridotites either as harzburgites of residual origin (Harnois & Morency, 1989), as crustally contaminated, or as low-T altered during magma ascent (Gruau *et al.*, 1998).

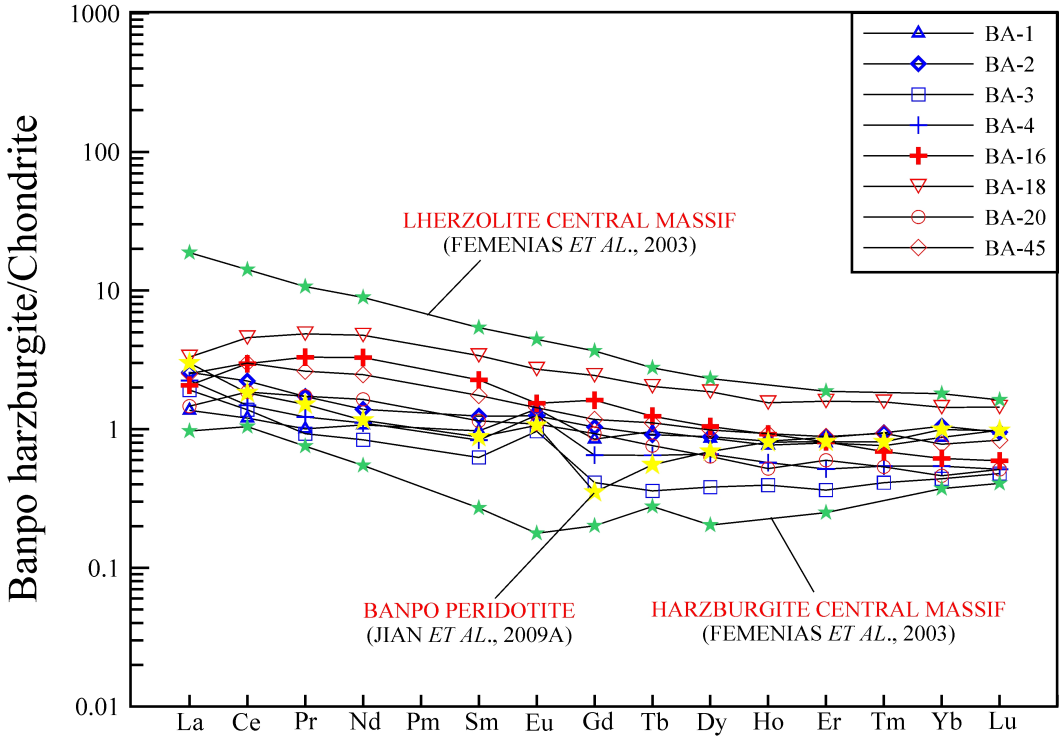

Fig. 17: Chondrite-normalized REE patterns of the Banpo harzburgite (McDonough & Sun, 1995). The olivine-rich (red) and pyroxene-rich harzburgites (blue) are clearly separated from each other by their total REE budget, opposed Eu-anomalies and $(La/Ce)_N$ ratios.

1.4.2.3 Sr–Nd ISOTOPIC COMPOSITION

The olivine-rich Banpo harzburgite sample BA-18 was analyzed for its whole-rock Sr–Nd isotopic composition (Table 3). The sample depicts a very low initial $^{87}Sr/^{86}Sr$ ratio of 0.6880, likely due to alteration. Heppe (2006) reported a similar, but even lower initial Sr-ratio of 0.6745 for a Banpo peridotite sample (calculated for 286 Ma). The initial ε_{Nd} ratio of 6.1 for BA-18 and 4.6 for the reference sample of Heppe (2006) are consistent and are in the range of typical MORB. The ε_{Nd} ratios of the two samples are indicated by dashed horizontal lines in Fig. 18, as the $^{87}Sr/^{86}Sr$ ratios are obviously disturbed.

Table 3: Sr–Nd isotopic compositions of the Banpo harzburgite sample BA-18 and a Banpo peridotite reference sample (Heppe, 2006). Parameter calculation as cited in Table 1.

Sample ID	Rock type	Age	Sm	Nd	$^{147}Sm/^{144}Nd$	$^{143}Nd/^{144}Nd$	2σ	ε_{Nd} (t)	Rb	Sr	$^{87}Rb/^{86}Sr$	$^{87}Sr/^{86}Sr$	2σ	$(^{87}Sr/^{86}Sr)t$
		Ma	ppm	ppm					ppm	ppm				
BA-18	Harzburgite	286	0.5	2.2	0.14468	0.512854	0.000007	6.12	1.5	0.8	5.42561	0.710102	0.000085	0.688023
01/131	Peridotite	286	2.4	8.2	0.17629	0.512837	0.000015	4.63	9.0	3.4	7.65950	0.705700	0.000012	0.674530

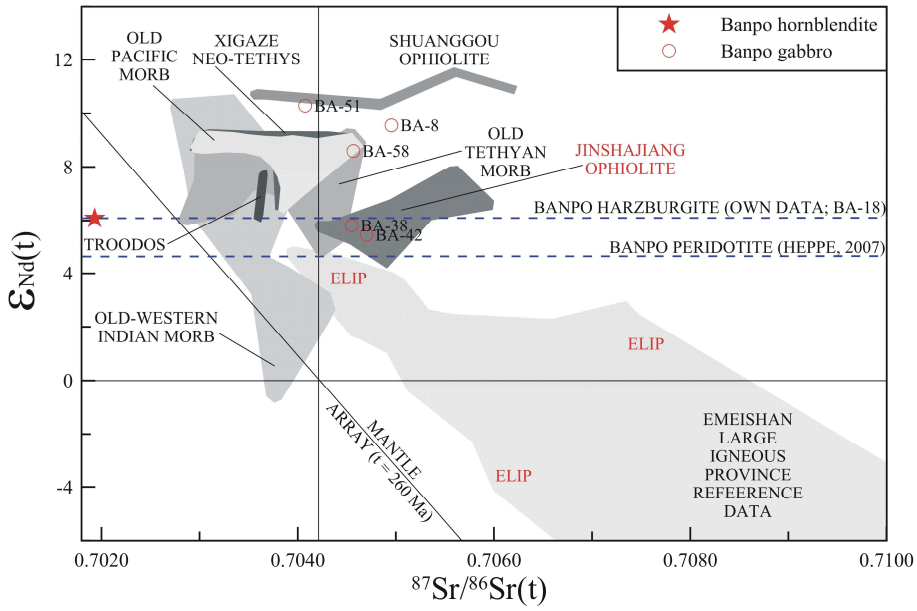

Fig. 18: $\varepsilon_{Nd}(t)$ vs. $^{87}Sr/^{86}Sr(t)$ diagram for the Banpo complex sample suite. Peridotite, harzburgite, gabbro and hornblendite data are shown for t = 286 Ma. ELIP reference data are from Qi & Zhou (2008), Xu *et al*. (2001), Zhong *et al*. (2004) and Zhou *et al*. (2006). Other reference data as cited in Fig. 9.

1.4.3 BANPO GABBRO

1.4.3.1 PETROGRAPHIC DESCRIPTION

The inequigranular, hypidiomorphic to xenomorphic-granular, altered and metamorphosed gabbro has a very variable modal composition of 55-65 vol% plagioclase, 10-40 vol% clinopyroxene, 0-30 vol% amphibole, 0-15 vol% olivine, 0-5 vol% orthopyroxene, 0-3 vol% quartz and 0-5 vol% opaques (samples BA-8, BA-9, BA-11, BA-13, BA-14, BA-24, BA-37, BA-38, BA-41, BA-42, BA-48, BA-49, BA-56 and BA-58; Fig. 19). As the rock suite is variably altered (incl. actinolitization, uralitization and diallag formation), an accurate determination of primary and secondary amphibole, clinopyroxene and orthopyroxene modes is hampered and the gabbros were not further subdivided. It appears, however, that the strongly altered gabbros depict beside highest olivine, the highest amphibole contents, which suggests major impact on rock mineralogy by hydrothermal alteration. Gabbro sample BA-8 is strongly actinolitized and prehnitized (prehnite plates 0.03-0.6 mm, mosaics, fan-shaped, leaved, rosette- and frostwork-like aggregates). This rock sample, with a LOI value of 6.2 wt%, has been omitted for further petrographic and geochemical interpretations.

Subhedral, sericitized, carbonatized, tectonized and prehnitized plagioclase (0.1-6.0 mm) has some poikilitic hornblende (Fig. 19A). Chloritized clinopyroxene (0.1-1.2 mm) is of

both diopsidic and augitic composition, whereas diopside appears to predominate over augite (Fig. 19A/B). Clinopyroxene depicts orthopyroxene exsolution (diallag formation), minor ilmenite exsolution (Fig. 19B/C) and uralitization. Subhedral to anhedral, chloritized amphibole (0.15-0.8 mm) weathers to limonite and is locally actinolitized. Primary subhedral orthopyroxene (hypersthene?) is up to 1.2 mm in diameter. Euhedral to subhedral olivine (0.02-0.5 mm) is serpentinized. Subhedral quartz is 0.02-0.3 mm in size (Fig. 19C).

Opaques include 0-1.5 vol% eu- to anhedral pyrite (0.02-0.5 mm) and 0-0.5 vol% sub- to anhedral chalcopyrite (0.02-0.4 mm; predominantly on veinlets), sub- to anhedral pyrrhotite (0.02-0.4 mm), magnetite (<0.6 mm), hematite (<0.3 mm) and ilmenite. Sample BA-41 stands out with very high pyrite (5 vol%; <1 mm) and chalcopyrite contents (1-2 vol%; <0.5 mm) and sample BA-49 with very high magnetite (25 vol%; <2 mm). Sample BA-13 has some galena on veinlets (<0.3 mm). Accessories include apatite (<0.15 mm), zircon (<0.1 mm), rutile and titanite (<0.15 mm). The rock is cut by dolomite, fine-grained prehnite, sericite, epidote, quartz, chlorite, pyrite and chalcopyrite veinlets (Fig. 19C-F).

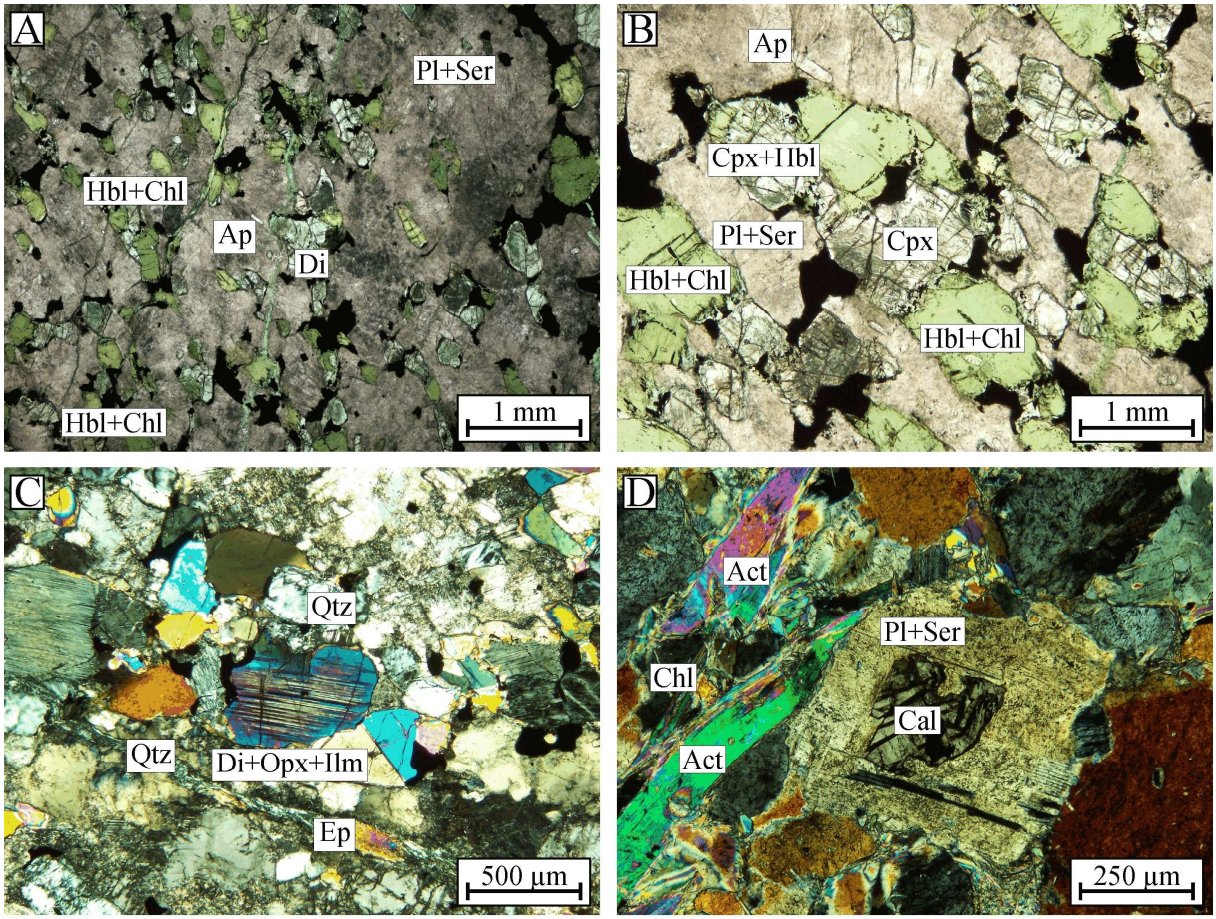

Fig. 19: Photomicrographs of the Banpo gabbro (A/B: BA-11, C: BA-13, D: BA-9; A/B: transmitted, plane-polarized light, C/D: transmitted light/crossed polars).

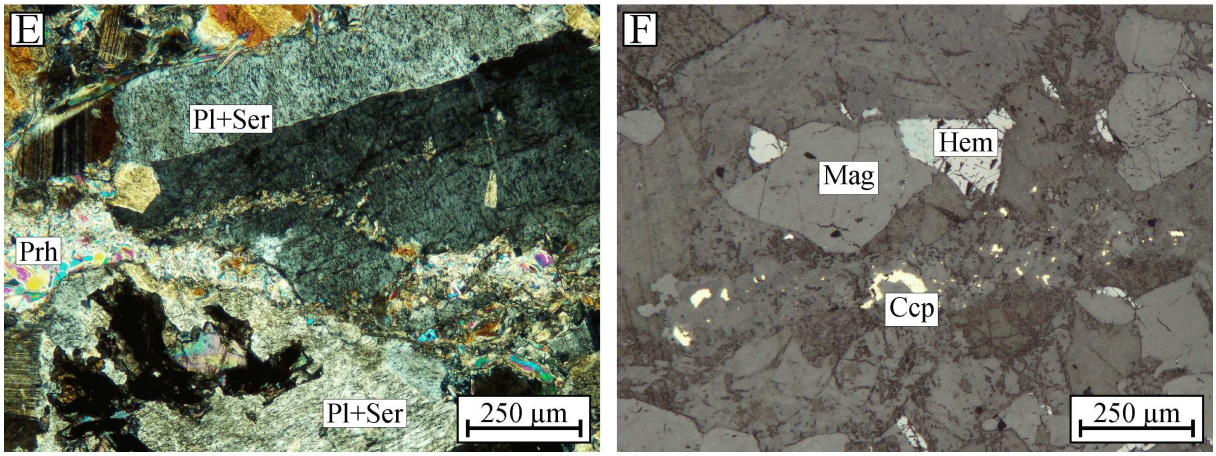

Fig. 19 continued; photomicrographs of the Banpo gabbro (E: BA-9, F: BA-41; E: transmitted light/crossed polars, F: reflected, plane-polarized light).

1.4.3.2 MAJOR AND TRACE ELEMENT COMPOSITION

The Banpo gabbro is variably altered and metamorphosed (LOI values of 2.0-5.3 wt% for samples BA-11, BA-13, BA-14, BA-24, BA-37, BA-38, BA-41-BA-43, BA-48, BA-49, BA-56 and BA-58). To avoid misinterpretations, the sample suite has been split up for some plots into a least-altered rock suite with LOI values <3 wt% (samples BA-11, BA-13, BA-24, BA-42, BA-48, BA-49 and BA-56) and an altered rock suite with LOI values of >3 wt% (samples BA-14, BA-37, BA-38, BA-41, BA-43, BA-51 and BA-58).

TAS classifies all rock samples as gabbro, whereas the least-altered rock samples suggest alkaline character, and the altered samples depict a transitional to subalkaline character (Cox *et al.*, 1979; Irvine & Baragar, 1971; Kuno, 1966; Le Maitre, 1989; MacDonald, 1968; MacDonald & Katsura, 1964; Wilson, 1989; Fig. 20A). The R1 vs. R2 diagram confirms the gabbroic composition and suggests most altered rocks to be olivine gabbros (Fig. 20B; De la Roche *et al.*, 1980). This corresponds to the petrographic observation. On immobile element plots, such as the SiO_2 vs. Zr/Ti and Zr/Ti vs. Nb/Y diagrams, the gabbroic composition is confirmed. These plots suggest subalkalinity for the gabbros (Winchester & Floyd, 1977; Fig. 20C/D).

On the SiO_2 vs. K_2O diagram for subalkalic rocks the Banpo gabbro plots as low-K type (Fig. 21A). The AFM diagram suggests calc-alkalinity for the Banpo gabbro samples (Fig. 21B) and the Alkali index vs. Al_2O_3 diagram favors calc-alkalinity for the Banpo gabbro as well (not shown). Considering all this information, it appears likely that the Banpo gabbro is of low-K type of the calc-alkaline series.

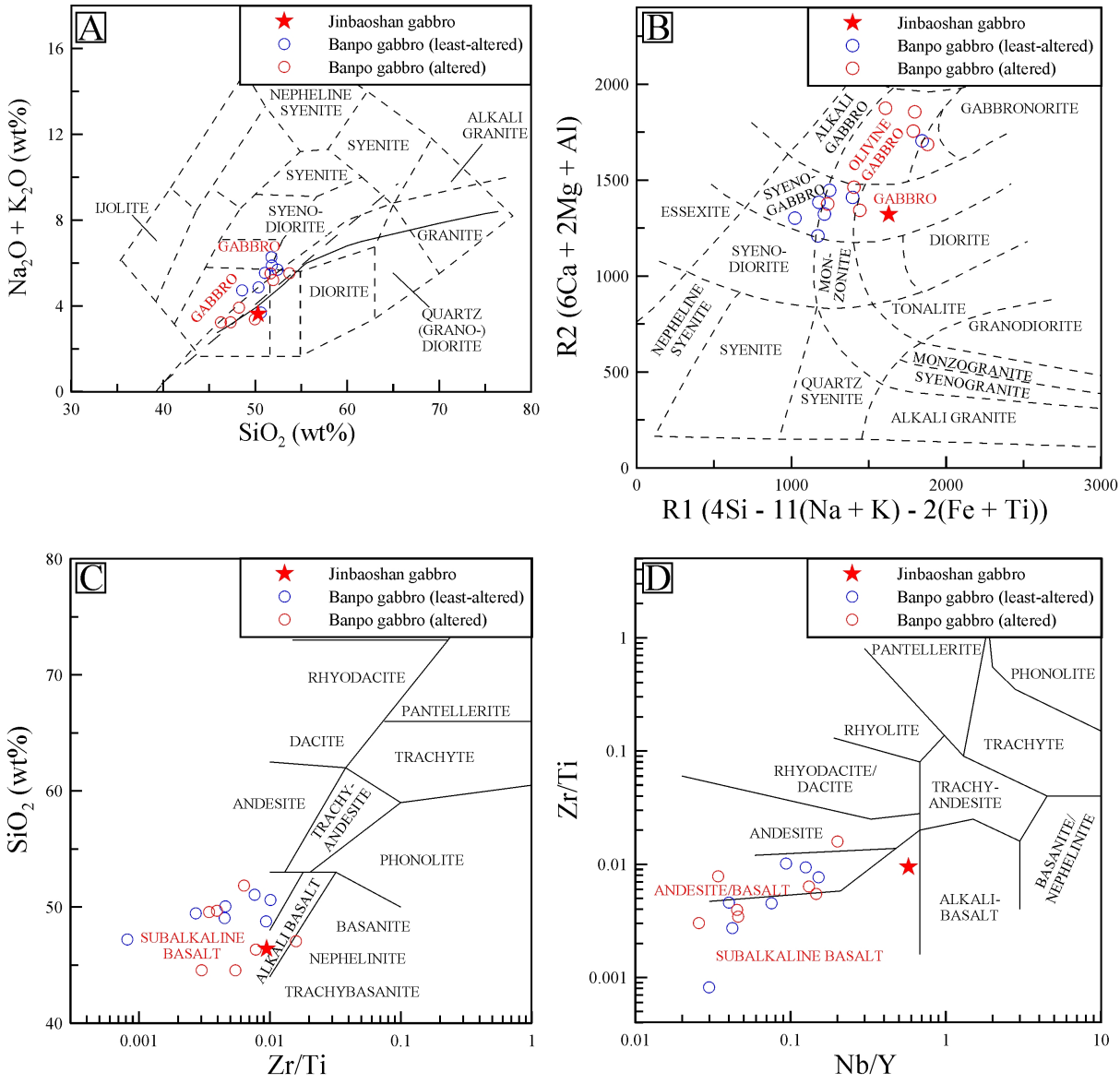

Fig. 20A: The Banpo and Jinbaoshan gabbro samples on the TAS diagram for plutonic rocks (Cox *et al*., 1979; Le Maitre, 1989; MacDonald, 1968; MacDonald & Katsura, 1964; Wilson, 1989). B: The R1 vs. R2 diagram of De la Roche *et al*. (1980). C/D: Immobile element plots for volcanic rocks. These plots verify the gabbroic composition as classified by mobile major elements (Winchester & Floyd, 1977). Reference data as cited in Fig. 5.

Despite the wide range of major element contents, the data of the Banpo gabbro correspond well to published gabbro reference data (Le Maitre, 1976; Appendix Tables 7 and 8). Calculated CIPW norms (anhydrous basis) vary accordingly, but suggest for all samples silica-undersaturation. Only sample BA-41 is alumina-oversaturated (normative corundum/no diopside). Most samples, however, have normative diopside, hypersthene and olivine. Sample BA-13 is weakly more silica-undersaturated (no hypersthene and nepheline). Samples BA-48 and BA-58 have normative nepheline. The norms correspond to the petrographic observation.

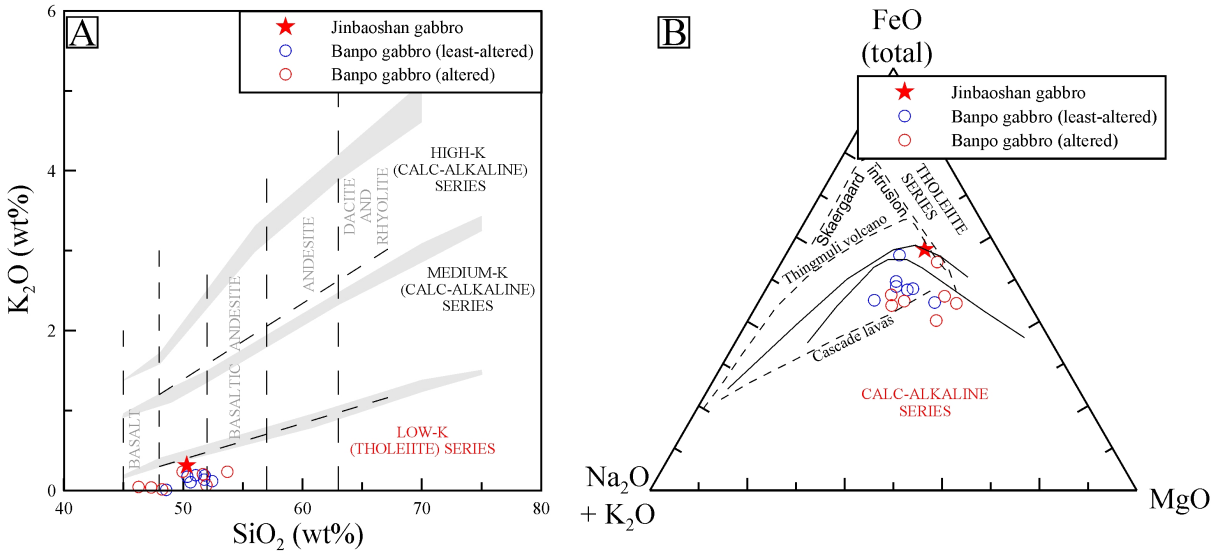

Fig. 21A: The K_2O vs. SiO_2 plot for subalkaline rocks classifies the Banpo gabbro as low-K type of the calc-alkaline series. B: The AFM diagram classifies the Banpo gabbro as calc-alkaline as well (Rickwood, 1989). Upper heavy line by Kuno (1968) separates the calc-alkaline field and the tholeiitic field; lower heavy line by Irvine & Baragar (1971). Data of the Thingmuli volcano, Iceland, and average Cascade lavas are taken from Carmichael (1964). Other reference data as cited in Fig. 5.

The calculated CIPW norm for the gabbro reference sample from Jinbaoshan (JBS-1) differs markedly from those of the Banpo gabbro samples. The Jinbaoshan gabbro has normative quartz, lowest orthoclase, highest hypersthene, magnetite, ilmenite and apatite and no olivine. The Mg-number is accordingly distinctly lower.

Table 4: Calculated CIPW norms and Mg-numbers of the Banpo and Jinbaoshan gabbros.

Sample ID	Quartz	Corundum	Orthoclase	Albite	Anorthite	Nepheline	Diopside	Hypersthene	Olivine	Magnetite	Ilmenite	Apatite	Mg#
BA-48	-	-	1.30	47.65	14.13	0.13	14.16	-	11.91	5.43	4.00	0.44	55.76
BA-49	-	-	2.73	44.22	16.58	-	7.00	10.40	9.73	5.58	2.59	0.27	58.52
BA-24	-	-	3.41	35.09	29.77	-	6.89	0.83	14.67	6.08	2.27	0.02	49.16
BA-11	-	-	5.58	38.87	23.99	-	5.71	5.60	11.67	5.36	1.92	0.44	54.57
BA-56	-	-	1.98	28.38	35.74	-	7.59	15.94	3.91	4.12	1.45	0.24	65.20
BA-13	-	-	11.08	35.79	25.94	-	7.74	-	11.84	4.34	1.50	0.32	54.63
BA-42	-	-	4.27	35.03	28.98	-	2.81	10.16	10.51	5.08	1.95	0.40	59.20
BA-38	-	-	4.24	40.67	24.67	-	6.13	15.27	1.98	4.10	1.75	0.54	59.33
BA-58	-	-	2.41	22.04	32.33	1.01	17.82	-	15.33	6.05	1.96	0.10	57.63
BA-51	-	-	9.50	19.55	44.24	-	4.33	2.86	14.53	3.61	0.76	0.03	68.88
BA-14	-	-	1.53	44.44	27.61	-	4.29	2.05	12.93	4.52	1.44	0.47	56.76
BA-37	-	-	3.25	39.37	26.42	-	8.61	5.19	10.52	4.44	1.34	0.16	60.48
BA-41	-	0.05	3.42	22.47	42.12	-	-	10.20	14.96	4.65	1.29	0.09	67.94
BA-43	-	-	2.25	25.33	34.13	-	6.95	21.80	1.23	4.54	2.50	0.55	65.26
JBS-1	4.02	-	1.13	28.99	21.77	-	7.66	22.18	-	6.63	5.84	0.72	52.97

Note: Banpo gabbro samples are sorted by increasing LOI values (as alteration index). For all samples a Fe_2O_3/FeO ratio of 0.3 was assumed (Middlemost, 1989).

On the primitive mantle-normalized multi-element plot of Figure 22 most Banpo gabbro samples depict drastic depletion in the high field strength elements (HFSEs) U, Th, Ta, Nb and Zr, and enrichment in the large ion lithophile elements (LILEs), e.g. Pb. These characteristic features suggest an arc-signature for the Banpo gabbro (e.g. Pearce & Cann, 1973). The Banpo gabbro samples depict similarities to the Gicha complex of the northern Lancangjiang zone, which is interpreted by Jian *et al.* (2009a) as back-arc complex (Fig. 22). In analogy to the Banpo harzburgite, the Banpo gabbro reference sample of Jian *et al.* (2009a) is distinctly depleted in REEs and Ti compared to our gabbro samples.

Samples BA-43 and BA-48 are more enriched and are set apart from the other gabbro samples by a slight positive Zr anomaly, by depressed Th–U and Nb–Ta troughs, and by marked Ti enrichment. These samples are similar in composition to the Jinbaoshan gabbro reference sample and depict similarities to low-Ti gabbroic intrusions of the ELIP, such as the Anding, Yapai and Baimazhai intrusions (Wang *et al.*, 2008; Zhou *et al.*, 2006).

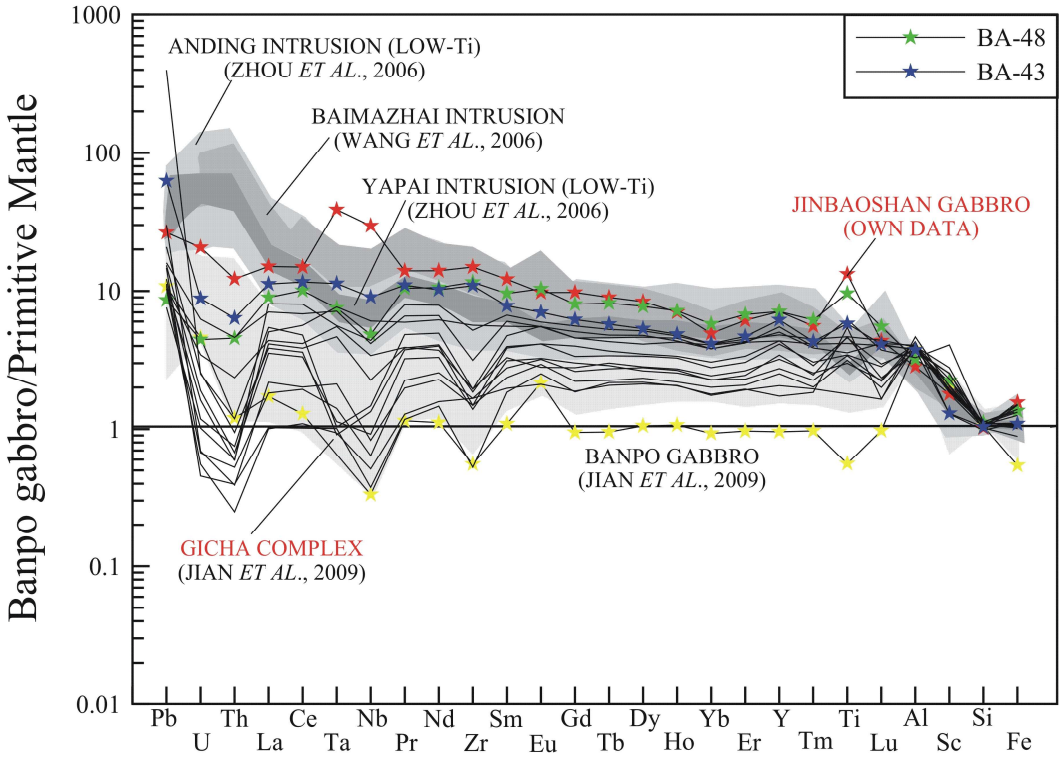

Fig. 22: Primitive mantle-normalized multi-element patterns of the Banpo and Jinbaoshan gabbro samples. Primitive mantle data are from Palme & O`Neill (2004).

The positive Ti-anomaly corresponds to titanite, rutile and magnetite, as evidenced by the microscopic observation. The gabbros were affected by zircon fractionation. Evidence comes from sample BA-48 where zircon and magnetite (5 vol%) are enriched (petrographic

observation). The remarkable spread in Nb/Ta ratios might be either caused by titanite fractionation (Kd_{Nb} tit = 3.9-5.7; Kd_{Ta} tit = 10.8-18.9; Benett *et al.*, 2004; Foley *et al.*, 2000; Green & Pearson, 1987; Klemme *et al.*, 2005; McCallum & Charette, 1987) or by analytical problems, such as Ta–Nb complexation or Ta-flocculation.

Chondrite-normalized REE patterns of the Banpo gabbro (Fig. 23) stress the similarity of the Banpo samples to gabbroic rock samples of the Gicha complex (Jian *et al.*, 2009a). Gabbro samples BA-43 and BA-48 are identical in REE composition to low-Ti Emeishan basalts and very similar to the Jinbaoshan gabbro reference sample (Xiao *et al.*, 2003; Xu *et al.*, 2001). The marked positive Eu-anomaly and $(La/Ce)_N$ >1 suggest that the Banpo gabbro reference sample of Jian *et al.* (2009) is much richer in plagioclase and therefore likely not representative.

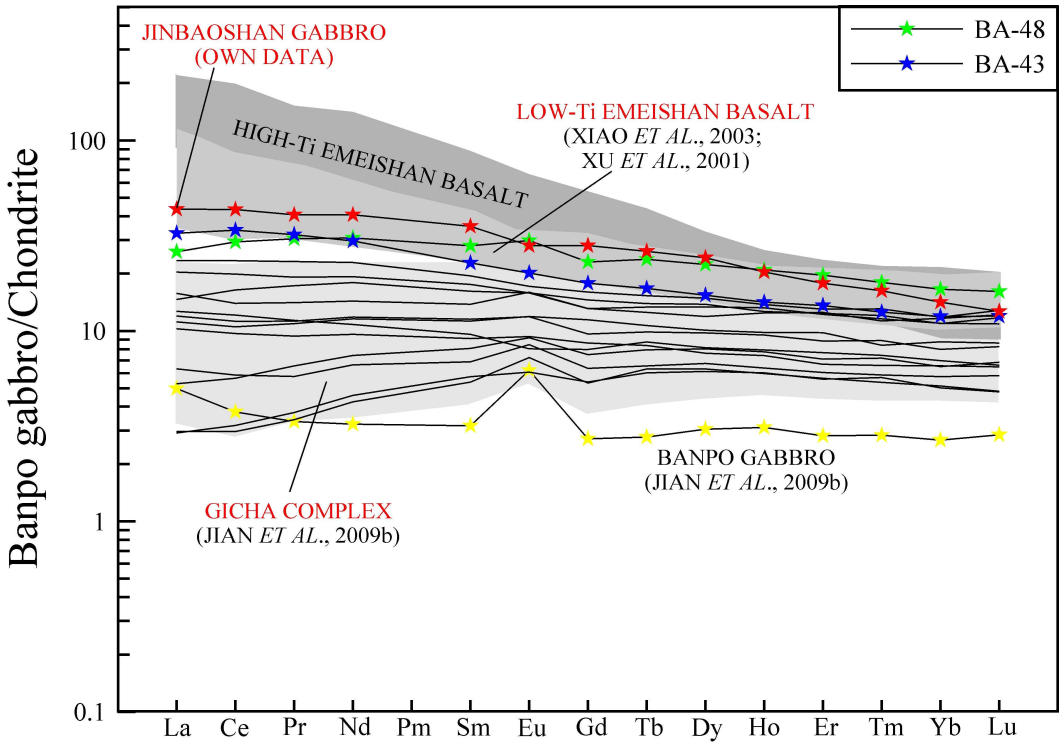

Fig. 23: Chondrite-normalized REE patterns of the Banpo gabbro (McDonough & Sun, 1995).

1.4.3.3 U–Pb ZIRCON GEOCHRONOLOGY

Due to the low Zr-content of sample BA-8 only four single grains could be spot-analyzed (30 µm). The data are given in Appendix Table 17 and the concordia plot is shown in Figure 24. The Th/U ratios for the analyzed zircons are 0.13-1.09 and indicate a magmatic origin.

We obtained a low-precision intercept age of 453 ±170 Ma on the four zircons analyzed. Much better concordia ages of 285.6 ±1.7 Ma and 285.8 ±2.0 Ma for gabbro and tonalite were defined by Jian *et al*. (2009a,b) on a larger zircon population. These ages likely reflect the crystallization age of the complex.

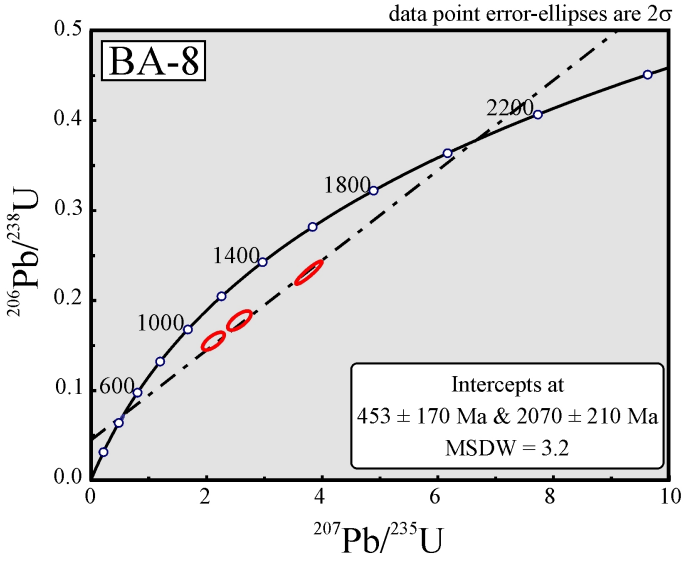

Fig. 24: U–Pb concordia plot for the strongly altered Banpo gabbro sample BA-8.

1.4.3.4 $^{40}Ar/^{39}Ar$ GEOCHRONOLOGY

$^{40}Ar/^{39}Ar$ geochronology by incremental heating was performed on the whole-rock gabbro sample BA-24. The age data are provided in Appendix Table 24 and the age spectrum is shown in Figure 25. It is noteworthy that the data do not fulfill the criteria for a plateau age, i.e. they do not include ≥3 contiguous steps with ≥60% of the ^{39}Ar released. However, there are three distinct degassing ages, which are discussed below.

About 56% of the total ^{39}Ar are already released at 600°C and define a “plateau date” of 127.9 ±6.7 Ma (2σ). This age likely reflects the decomposition of sericite, that has been detected petrographically and affects all plagioclase crystals in sample BA-24 (refer to chapter 1.4.3.1). Sericitization is interpreted to be related to a major metamorphic event.

The second group of ages includes about 40% of the total ^{39}Ar released at temperatures of 700-1400°C. These degassing steps all gave low-error ages ranging from 207.1 ±4.9 to 252.8 ±2.4 Ma with Ca/K and Cl/K of 1.9 to 7.6 and 0.002 to 0.04. The high age of 378.5 ±12.9 Ma, obtained at 1600°C, likely reflects excess ^{40}Ar with Ca/K of 8.2 and Cl/K of 0.03.

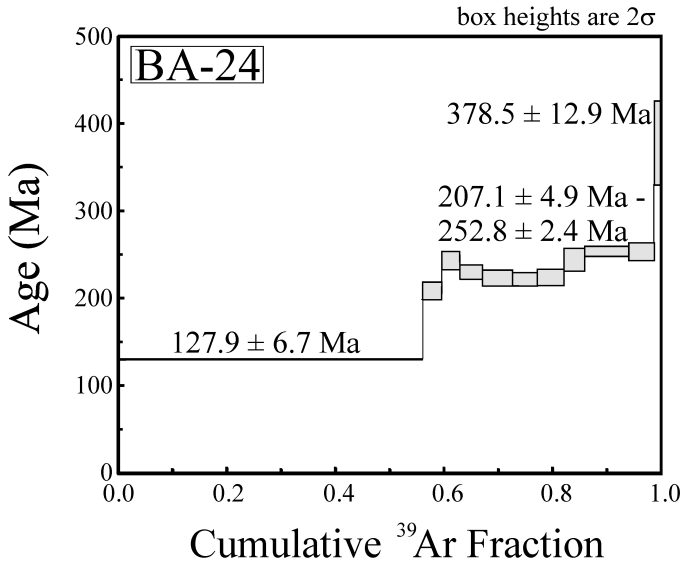

Fig. 25: $^{40}Ar/^{39}Ar$ age spectrum of the Banpo gabbro. Note the distinctly low temperature interval around 130 Ma, likely reflecting metamorphic overprint, the bowl-shaped pattern of Triassic degassing ages and the final high-temperature/high-date, which points to excess ^{40}Ar.

1.4.3.5 Sr–Nd ISOTOPIC COMPOSITION

The gabbro samples BA-8, BA-38, BA-42, BA-51 and BA-58 were analyzed for their whole-rock Sr–Nd isotope composition. The data are shown in Table 5 and plotted in Figure 18.

Although the analyzed Banpo gabbro samples are altered (i.e. all, except BA-42, have LOI values of >3 wt%), they depict a well defined, narrow range in $^{87}Sr/^{86}Sr(t)$ ratios of 0.70407-0.70495 (calculated for t = 286 Ma). Initial ε_{Nd} values vary from 5.5 to 10.3. It is noteworthy to mention, that the strongly altered samples BA-8, BA-51 and BA-58 are set apart from the less altered samples BA-38 and BA-42 with higher ε_{Nd}. The latter two samples have Nd-isotopic compositions similar to the Banpo harzburgite (blue dashed lines in Fig. 18), which suggests that the harzburgite and gabbro might be derived from the same mantle source. The gabbros have $^{143}Nd/^{144}Nd$ ratios higher than those typical of the Emeishan LIP, but are in the range of MORB data from China (Fig. 18).

Table 5: Sr–Nd isotopic compositions of the Banpo gabbro samples BA-8, BA-38, BA-42, BA-51, BA-58 and the Banpo gabbro reference sample 01/135 of Heppe (2006).

Sample ID	Rock type	Age	Sm	Nd	$^{147}Sm/^{144}Nd$	$^{143}Nd/^{144}Nd$	2σ	ε_{Nd} (t)	Rb	Sr	$^{87}Rb/^{86}Sr$	$^{87}Sr/^{86}Sr$	2σ	$(^{87}Sr/^{86}Sr)t$
		Ma	ppm	ppm					ppm	ppm				
BA-8	Gabbro	286	0.3	0.8	0.20637	0.513145	0.000014	9.54	25.7	398.0	0.18695	0.705716	0.000011	0.704955
BA-38	Gabbro	286	2.9	9.9	0.17862	0.512902	0.000006	5.81	21.4	299.8	0.20689	0.705392	0.000008	0.704550
BA-42	Gabbro	286	3.0	10.8	0.17021	0.512868	0.000006	5.46	16.7	269.5	0.17884	0.705428	0.000011	0.704700
BA-51	Gabbro	286	0.9	2.3	0.24846	0.513262	0.000007	10.29	26.0	317.8	0.23619	0.705036	0.000011	0.704075
BA-58	Gabbro	286	1.3	3.7	0.22009	0.513122	0.000006	8.59	21.5	371.8	0.16736	0.705248	0.000008	0.704567
01/135	Gabbro	286	6.3	28.0	0.13628	0.512355	0.000011	-3.32	16.0	265.5	0.17450	0.715919	0.000013	0.715209

1.4.4 BANPO ANORTHOSITE

1.4.4.1 PETROGRAPHIC DESCRIPTION

The Banpo anorthosite samples BA-6 and BA-7 are from the northern Banpo complex, just south of the northern harzburgite body (Fig. 11). The field relationships suggest that the anorthosite is together with harzburgite and gabbro part of the Banpo cumulate series.

The samples are strongly altered. Prehnite is ubiquitous (80-95 vol%). The larger crystals are fan-like, rosette-like and frostwork-like grown (0.3-4.0 mm). Fine-grained prehnite (<0.2 mm) is restricted to the groundmass. Relics of primary minerals are predominantly restricted to sample BA-6 and include plagioclase (0.3-4.5 mm), clinopyroxene (0.6-3.0 mm) and amphibole (2.0 mm).

Plagioclase is predominantly prehnitized, but exhibits minor sericitization as well. Some former euhedral clinopyroxene depicts chloritization. Eu- to subhedral amphibole is corroded and broken and shows partly ghost texture. Amphibole is altered to chlorite fibers and prehnite. Accessories include apatite, zircon, titanite (especially in BA-6), rutile and minor epidote. The rock is cut by prehnite, muscovite, sericite, chlorite and dolomite veinlets. BA-7 hosts some minute grains of pyrite and chalcopyrite. The primary rock mode is estimated at 80 vol% plagioclase, 10 vol% clinopyroxene and 10 vol% amphibole for BA-6, and at 95 vol% plagioclase for BA-7.

1.4.4.2 MAJOR AND TRACE ELEMENT COMPOSITION

The intensive alteration of the Banpo anorthosite samples is expressed in LOI values of 4.5 wt% (BA-6) and 5.6 wt% (BA-7). However, the major element composition of the two samples still corresponds to published anorthosite reference rock and to anorthite mineral reference data (Le Maitre, 1976; Meeker, 1995; Mikouchi *et al*., 1999; Mittlefehldt *et al*., 1998; Appendix Table 8). The calculated CIPW norms (anhydrous basis) are shown in Table 6 and confirm the petrographic observation.

Table 6: Calculated CIPW norms of the Banpo anorthosite samples. Calculations as cited in Table 2.

Sample ID	Quartz	Orthoclase	Albite	Anorthite	Nepheline	Diopside	Magnetite	Ilmenite	Apatite	CaDiSilicate	Wollastonite	Hematite	Titanite
BA-6	0.78	0.25	7.63	54.77	-	10.85	-	0.59	0.40	-	23.38	0.89	0.38
BA-7	-	-	-	73.34	0.24	6.69	0.41	0.06	0.01	3.42	3.89	0.10	-

The chondrite-normalized REE patterns of the Banpo anorthosite samples are in accord to published anorthosite rock and anorthite mineral data (Fig. 26). The amphibole-bearing sample BA-6 is more enriched in REEs and depicts similarities to the “plagioclase-rich end-member” of the Paleng cumulate series (green star; Paleng complex is discussed in chapter 1.6). Amphibole might also cause a “weakening” of the positive “plagioclase” Eu-anomaly. The nearly pure anorthosite sample BA-7, in contrast, is accordingly similar in REEs to anorthite mineral reference data and depicts a pronounced positive Eu-anomaly (Floss *et al.*, 1998).

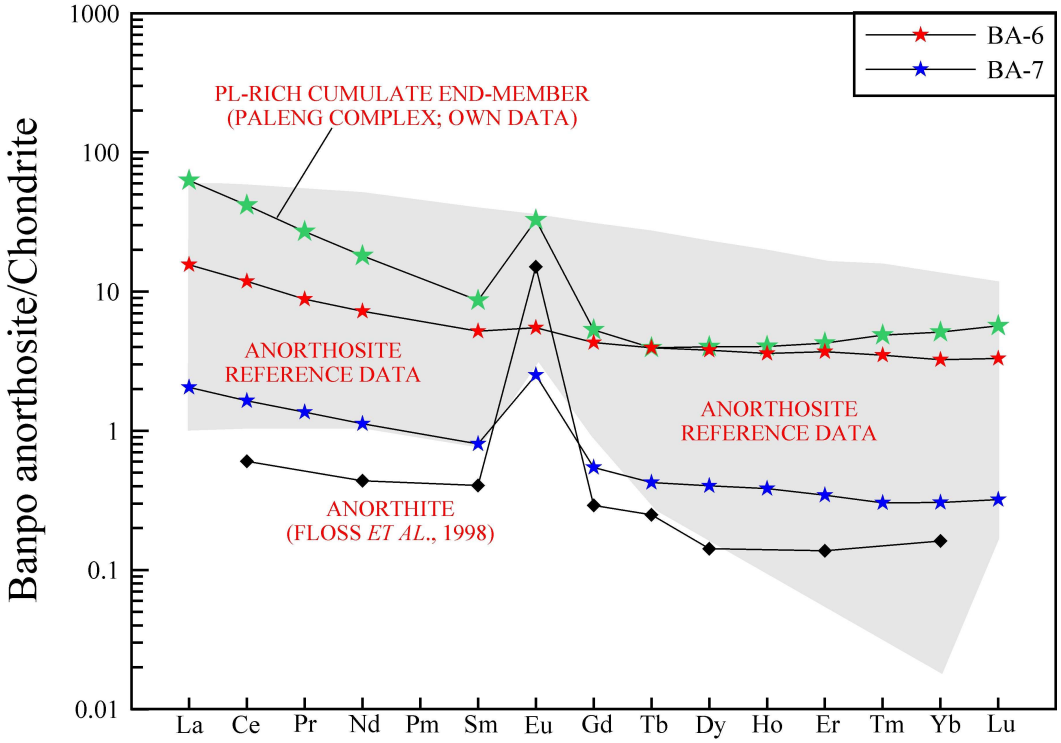

Fig. 26: Chondrite-normalized REE patterns of the Banpo anorthosite samples BA-6 and BA-7 (McDonough & Sun, 1995). The shaded polygon of “anorthosite reference data” comprises REE data of Blake *et al.* (1992), Cliff *et al.* (1983), McBirney (2002), Melezhik & Sturt (1994), Morrison *et al.* (1983) and Polat *et al.* (2008).

1.4.5 BANPO HORNBLENDITE

1.4.5.1 PETROGRAPHIC DESCRIPTION

The Banpo hornblendite sample BA-5 is from the same sample site as the Banpo anorthosite (Fig. 11). The field relationships suggest that the hornblendite forms together with the harzburgite, gabbro and anorthosite a cumulate series.

The hornblendite has about 75 vol% green hornblende, 15 vol% prehnite and 10 vol% of chlorite. The primary rock mode might have been 85 vol% green hornblende and about 15 vol% plagioclase. Eu- to subhedral green hornblende (0.08-1.2 mm) depicts actinolitization and chloritization. Petrography suggests a hastingsitic composition. Brown chlorite is developed in fibers, needles and depicts locally radiolithic growth. Prehnite occurs as plates and fans (<0.6 mm), but is mostly fine-grained (<0.2 mm). The rock has rutile and zircon. Opaques include ilmenite and some tiny grains of chalcopyrite.

1.4.5.2 MAJOR AND TRACE ELEMENT COMPOSITION

The high LOI value of 4.4 wt% for the Banpo hornblendite sample BA-5 is well explained by the high modal amounts of hornblende and by chloritic and prehnitic alteration. Nevertheless, the recast major element compositions of the hornblendite still match published reference data of magnesiohornblende and ferrohornblende, i.e. 47.6 vs. 51.2-44.4 wt% SiO_2, 11.1 vs. 10.9-9.4 wt% Al_2O_3, 9.4 vs. 2.4-35.82 wt% Fe_2O_3 (t), 18.2 vs. 19.6-0 wt% MgO, 12.1 vs. 10.9-9.4 wt% CaO (http://webmineral.com). The relatively high Al and Ca contents are explained by prehnite and primary plagioclase, respectively, whereas the high Fe content is most likely a combined feature of Fe-bearing magnesiohornblende and ilmenite.

The trace element composition of the Banpo hornblendite is generally in agreement to published hornblendite reference data (Fig. 27 and references therein). High Th and U contents are typical of hornblendite, as the partition coefficients are high for hornblende in basaltic melts (Arth, 1976). The low Nb and Ta concentrations, however, might point, similar to the Banpo gabbro, to a subduction environment (e.g. Pearce & Cann, 1973).

The chondrite-normalized REE pattern of the Banpo hornblendite sample BA-5 is relatively flat in comparison to the hornblendite datasets compiled (Cordier *et al*., 2005; Corriveau, 2005; Frimmel, 1996; Grenne, 2003; Neumann *et al*., 2000; Suda, 2004; Fig. 28). The Banpo hornblendite has relatively low REE contents, which especially applies to the REEs Ce-Tb. Both features can be explained by the presence of primary plagioclase (now present as secondary prehnite).

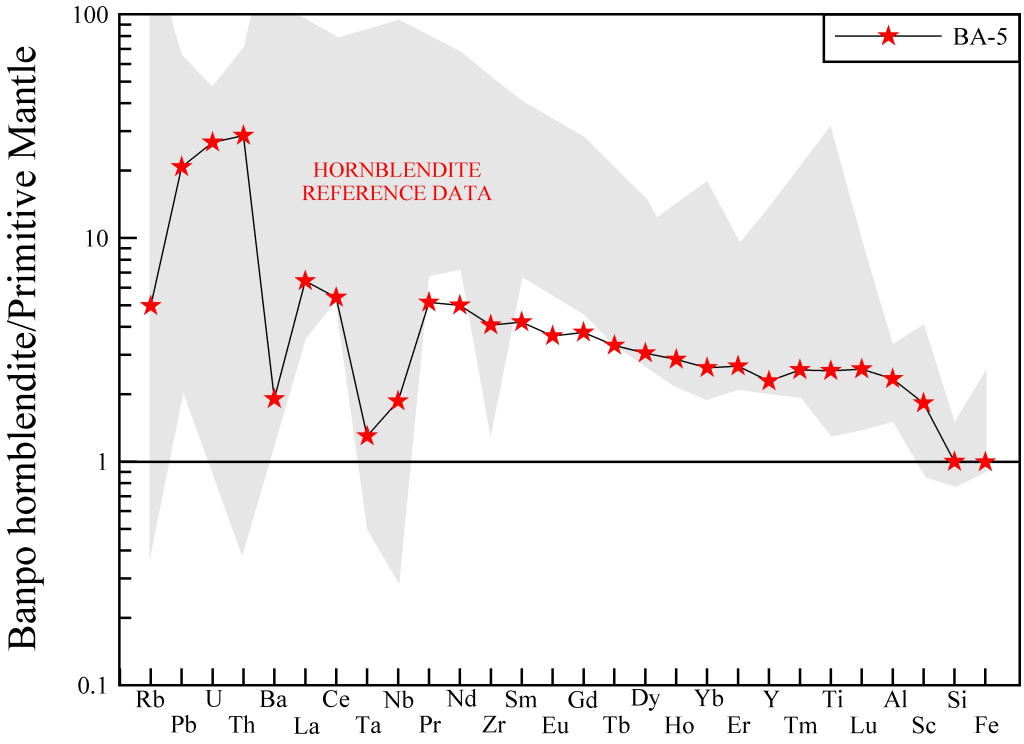

Fig. 27: Primitive mantle-normalized multi-element pattern of the Banpo hornblendite sample BA-5. The shaded polygon of "hornblendite reference data" includes datasets of Cordier *et al*. (2005), Corriveau & Bonnet (2005), Frimmel *et al*. (1996), Grenne *et al*. (2003), Neumann *et al*. (2000) and Suda (2004). Primitve mantle data are from Palme & O`Neill (2004).

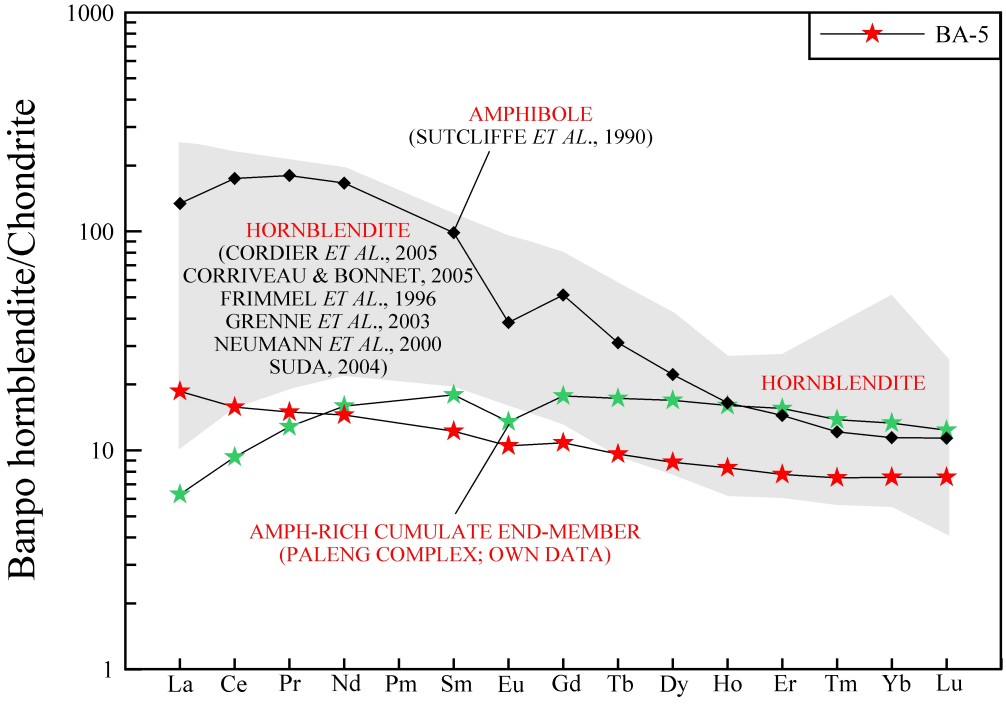

Fig. 28: Chondrite-normalized REE pattern of the Banpo hornblendite sample BA-5 (McDonough & Sun, 1995).

1.4.5.3 Sr–Nd ISOTOPIC COMPOSITION

The whole-rock Sr–Nd isotopic data of the Banpo hornblendite sample BA-5 is shown in Table 7 and plotted in Figure 18 (red star). The very low initial Sr-isotopic ratio of 0.70193 (calculated for t = 286 Ma) is likely due to hydrothermal overprint (Rb addition at very low Rb abundance). The initial ε_{Nd} value of 6.1 corresponds exactly to the data of the Banpo harzburgite sample BA-18 and is very similar to those of the least-altered Banpo gabbro samples BA-38 and BA-42 (Fig. 18). These ratios give further evidence for one cumulate series of harzburgite, gabbro, hornblendite and anorthosite.

Table 7: Sr–Nd isotopic composition of the Banpo hornblendite sample BA-5. Parameter calculation as cited in Table 1.

Sample ID	Rock type	Age	Sm	Nd	$^{147}Sm/^{144}Nd$	$^{143}Nd/^{144}Nd$	2σ	ε_{Nd} (t)	Rb	Sr	$^{87}Rb/^{86}Sr$	$^{87}Sr/^{86}Sr$	2σ	$(^{87}Sr/^{86}Sr)t$
		Ma	ppm	ppm					ppm	ppm				
BA-5	Hornblendite	286	1.9	6.5	0.17135	0.512902	0.000003	6.08	4.5	23.8	0.55244	0.704178	0.000009	0.701930

1.4.6 TECTONOMAGMATIC ENVIRONMENT

The Banpo gabbro is a cumulate rock, which excludes the usage of tectonic discrimination diagrams sensu stricto. Nevertheless, we plotted the data and most samples depict relatively low scatter and affinity to arc-magmatic rocks (Fig. 29; Pearce, 1982, 1983; Pearce & Cann, 1973; Shervais, 1982). In general, the HFSEs (e.g. Zr) are more depleted than for typical N-MORB and the resulting very high LILE/HFSE ratios, such as Ba/Ce ratios of 9-115 and Ba/Zr ratios 2-19 clearly favor an arc-setting, most likely even a continental arc-setting, as suggested by Jian *et al*. (2009a,b) for the Banpo complex.

The Banpo complex/gabbro is geochemically similar to the Gicha complex/gabbro of the northern Lancangjiang zone (e.g. Fig. 62). The two complexes have roughly the same age (the Gicha complex is 306 ±5 Ma to 280 ±3 Ma old) and both complexes are interpreted as magmatic arcs. They are located between continental blocks. For the Gicha complex these are the Tengchong Block and the Chongshan metamorphic complex of Simao affinity, and for the Banpo complex these are the Lancang Block and the Damenglong complex, a continental fragment of the Proterozoic Simao Block (Jian *et al*., 2009a,b).

Samples BA-43 and BA-48 are set apart from the other Banpo gabbro samples on the tectonic discrimination diagrams. As shown in the geochemistry chapter, these samples are very similar in composition to reference data of basalts from the ELIP, which are indicated in

different grey shades on the tectonic discrimination diagrams (Fig. 29). The two samples plot on four out of five diagrams congruent to the ELIP reference data (Fig. 29A-D). Especially sample BA-48 has high Ti, Y, Zr and V, and correspondingly high Zr/Y and Ti/Y ratios, which classify this rock on all plots as within-plate basalt.

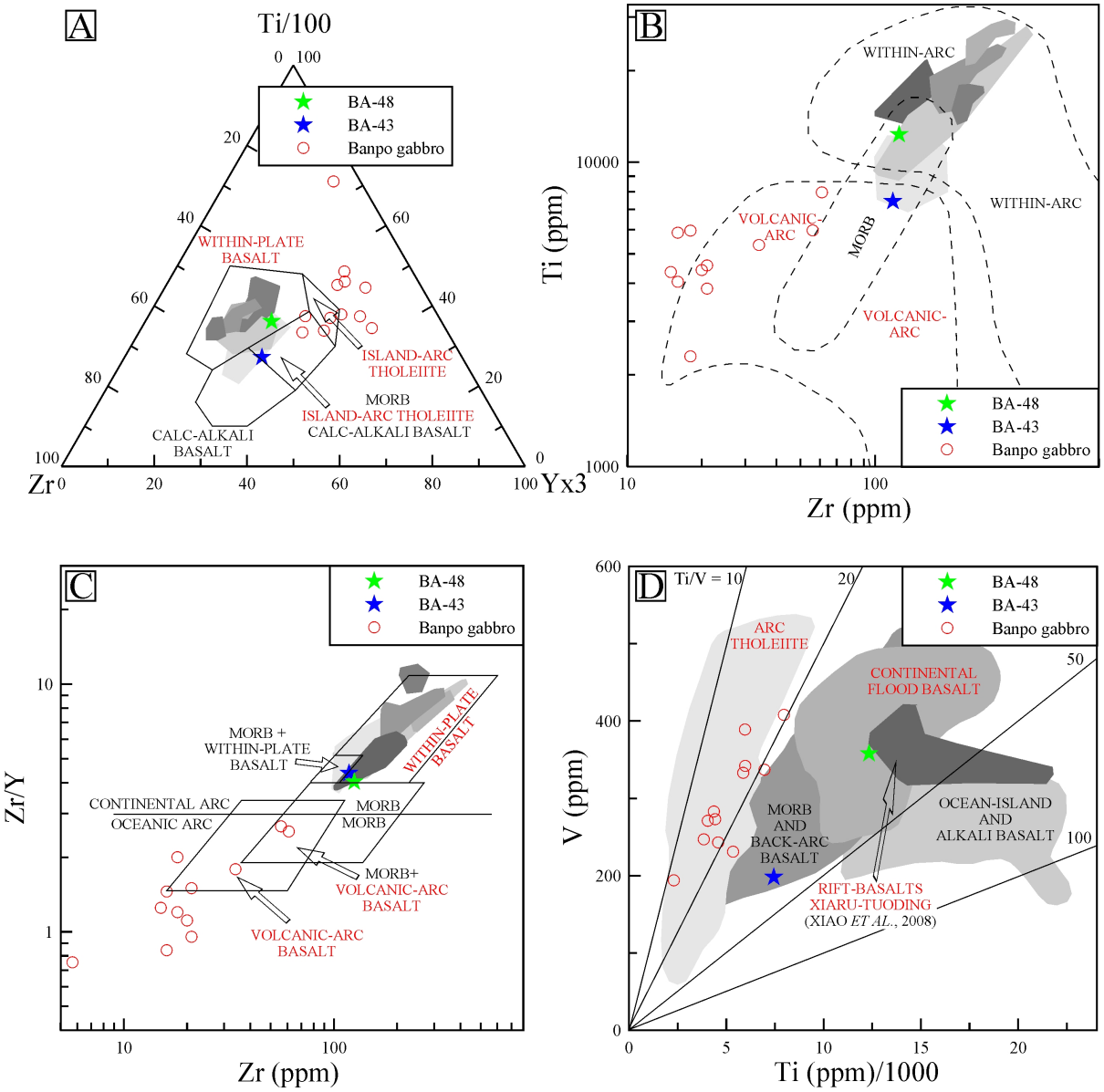

Fig. 29A: Ti–Zr–Y discrimination diagram (Pearce & Cann, 1973); B: Ti vs. Zr discrimination diagram (Pearce, 1982); C: Zr/Y vs. Zr discrimination diagram (Pearce & Norry, 1979); D: V vs. Ti discrimination diagram (Shervais, 1982). These plots suggest for most Banpo gabbro samples a volcanic-arc setting. For gabbro sample BA-48, in contrast, a within-plate setting is suggested. Data of the ELIP are plotted in shaded polygons (light to dark: low Ti1, low Ti2, high Ti1, high Ti2, high Ti3; Xiao *et al.*, 2003; Xu *et al.*, 2001).

1.5 JINGHONG GRANODIORITE (285-281 Ma)

There are several km-sized, medium-grained, equigranular granodiorite intrusions 6-15 km east and southeast of Jinghong (Fig. 30; YBGMR, 1990). Several quarries provide excellent exposure, but the intrusions are invariably affected by tectonic overprint accompanied by propylitic alteration and silicification.

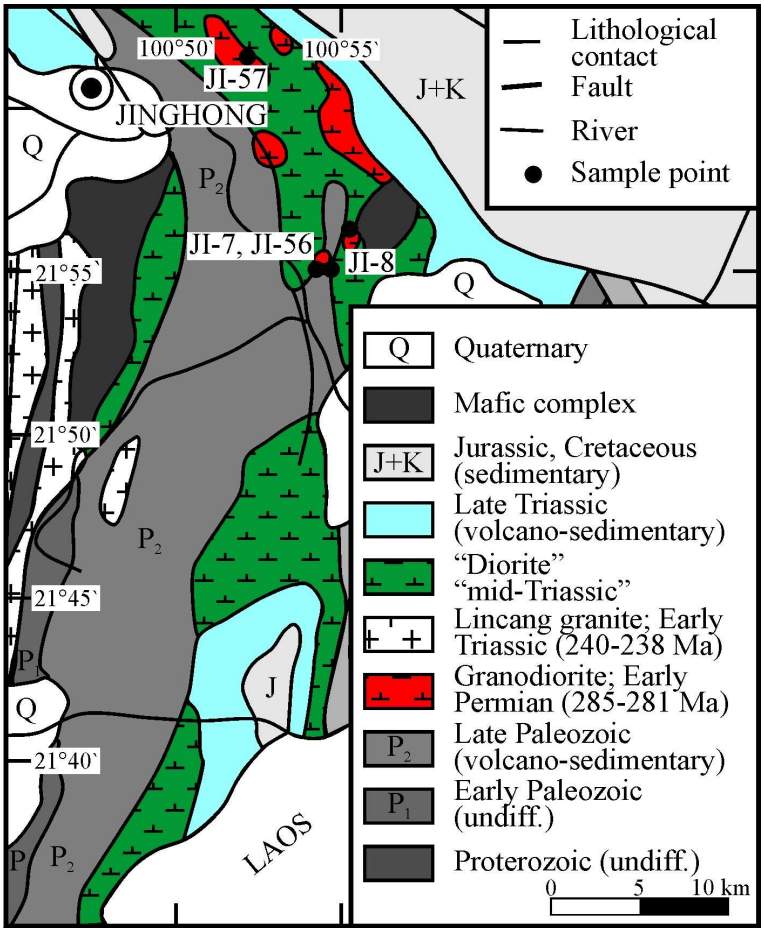

Fig. 30: Geological overview map of SW China (adapted from the YBGMR, 1990). The Jinghong granodiorite is shown in red and appears to intrude the belt of "Mid-Triassic diorite" of which the Jinghong dacite and Jinghong trachyandesite (both discussed below) are part.

1.5.1 PETROGRAPHIC DESCRIPTION

The studied rock samples JI-7, JI-8, JI-56 and JI-57 have 40-50 vol% plagioclase (0.2-2.5 mm), 20-25 vol% quartz (<0.8 mm), 10-20 vol% K-feldspar (0.2-1.6 mm), 15-20 vol% biotite and amphibole combined (0.2-1.4 mm), and about 5 vol% of a secondary quartz-chlorite-carbonate-sericite-limonite-pyrite assemblage (Fig. 32). These modal compositions

classify the rock as granodiorite on the QAPF diagram for plutonic rocks (Streckeisen, 1976; Fig. 31).

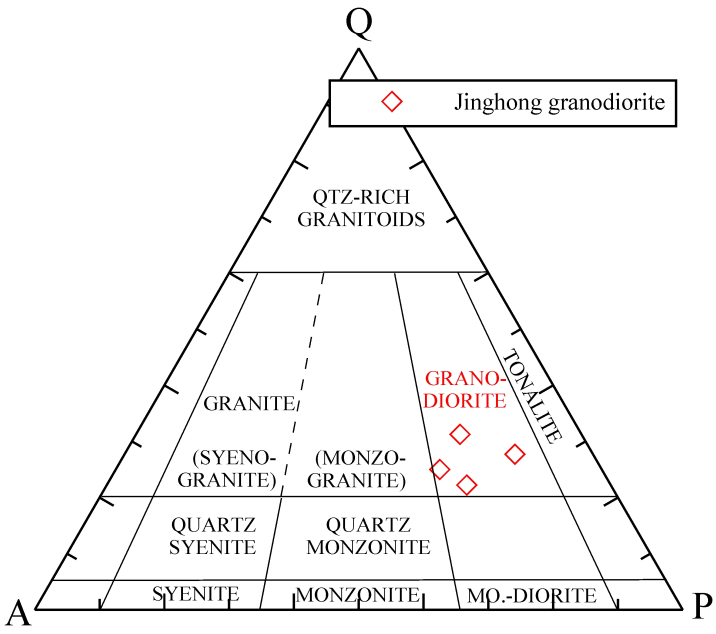

Fig. 31: The Jinghong granodiorite on the QAPF diagram for plutonic rocks (based on Streckeisen, 1976).

Alteration intensity - as assessed by microscopy - increases from JI-57 over JI-8 and JI-56 to JI-7. JI-56 and JI-7 depict moderate quartz flooding (Fig. 32). Carbonatized and sericitized, subhedral to anhedral plagioclase is bended and complexly twinned, which suggests tectonic overprint (e.g. Fig. 32B). Some crystals depict glomerocrystic growth. Sericitized, sub- to anhedral K-feldspar shows partly perthitic exsolution (Fig. 32A). Subhedral to anhedral amphibole and biotite are chloritized and weather to carbonate and limonite (Fig. 32A-D). Accessories include apatite, zircon, and minor titanite (e.g. Fig. 32C). The rock is cut by quartz, carbonate, sericite and pyrite veinlets and has euhedral to subhedral pyrite (<0.05 mm) in the groundmass (Fig. 32B-F).

1.5.2 MAJOR AND TRACE ELEMENT COMPOSITION

The granodiorite samples are affected by propylitic alteration and silicification. Propylitic alteration is expressed in elevated LOI values of 2.1-3.5 wt%. The major element composition corresponds according to the TAS diagram for plutonic rocks to subalkaline quartz diorite

(granodiorite) and granite, respectively (Cox *et al*., 1979; MacDonald, 1968; MacDonald & Katsura, 1964; Wilson, 1989; Fig. 33A). TAS for volcanic rocks suggests a dacitic to rhyolitic composition for the sample suite (Le Maitre, 1989; Fig. 33B). Immobile element plots for volcanic rocks, such as the SiO_2 vs. Zr/Ti and the Zr/Ti vs. Nb/Y diagrams favor a dacitic to rhyodacitic composition (Winchester & Floyd, 1977; Fig. 33C/D). Following the IUGS classification, the immobile element plots - and bearing in mind the silicification of samples JI-7 and JI-56 - the rocks are classified as granodiorite. The granodioritic composition is confirmed by the R1 vs. R2 diagram of De la Roche *et al*. (1980) (Fig. 33E).

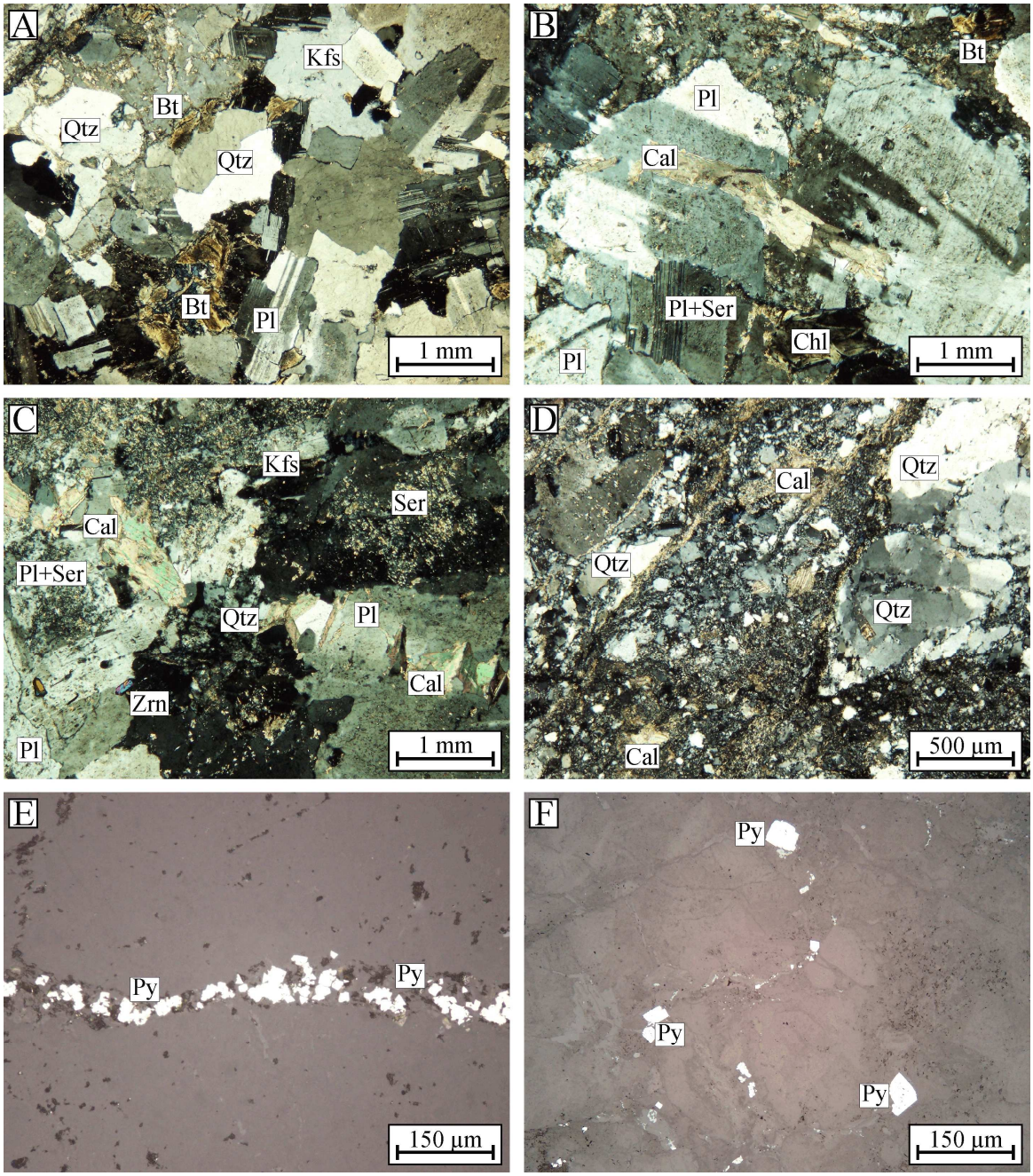

Fig. 32: Photomicrographs of the Jinghong granodiorite samples (A/E: JI-7, B/C/F: JI-8, D: JI-56; A-D: transmitted light/crossed polars, E/F: reflected light/crossed polars).

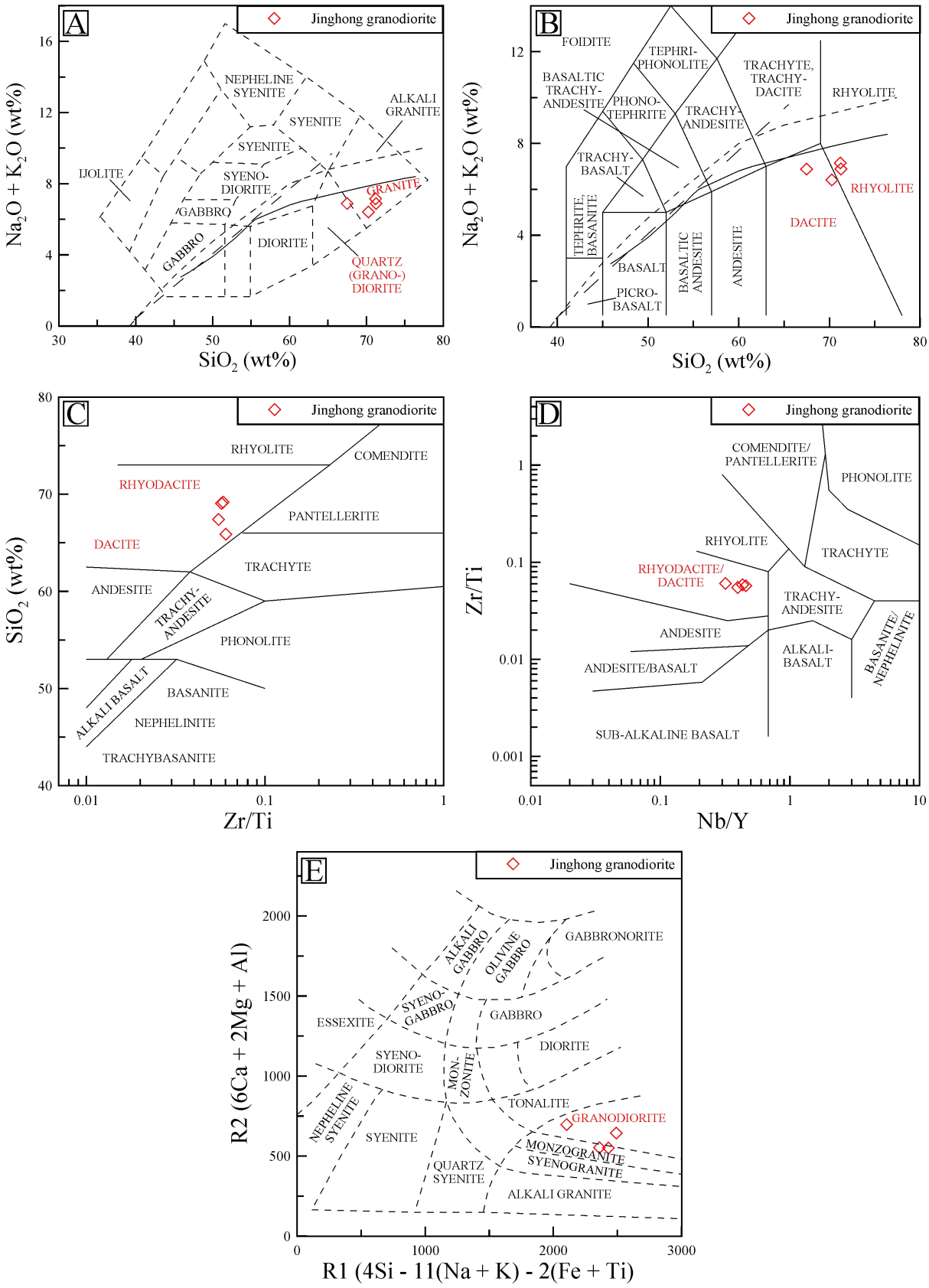

Fig. 33A/B: The Jinghong granodiorite on the TAS diagrams for plutonic and volcanic rocks (Cox *et al*., 1979; Le Maitre, 1989; MacDonald, 1968; MacDonald & Katsura, 1964; Wilson, 1989). C/D: The Jinghong granodiorite on immobile element plots for volcanic rocks of Winchester & Floyd (1977). E: The Jinghong granodiorite on the R1 vs. R2 diagram of De la Roche *et al*. (1980). Subdivisions and reference data are given in Fig. 5.

The granodiorite is relatively low in Ti (0.39-0.41 wt% TiO_2), Al (14.1-17.0 wt% Al_2O_3), Fe (3.3-3.7 wt% Fe_2O_3 total), Mg (1.1-1.2 wt% MgO), Ca (1.9-2.7 wt% CaO), K (1.3-2.0 wt% K_2O) and P (0.07-0.08 wt% P_2O_5), but high in Na (4.6-5.5 wt% Na_2O) (Le Maitre, 1976; Nockolds, 1954). These trends might be explained by a relatively evolved granodiorite melt, which had undergone magnetite fractionation followed by sericitization and kaolinitization of feldspar and chloritization of mafic minerals - as proven by the microscopic observations (refer to chapter 1.5.1).

Calculated CIPW norms of the Jinghong granodiorite give high corundum and low orthoclase and anorthite (Table 8; Le Maitre, 1976). These features are well explained by hydrothermal alteration. The relatively high albite contents are due to the high Na contents of the rocks and may be suggestive for albitization. Rock classification based on normative mineral contents mirror the predominant carbonatization and may be suggestive for albitization as well (Fig. 34).

Table 8: Calculated CIPW norms of the Jinghong granodiorite. Calculations as cited in Table 2.

Rock type	Jinghong granodiorite			
Sample ID	JI-7	JI-8	JI-56	JI-57
Quartz	28.29	27.69	27.13	21.46
Corundum	0.90	0.68	0.70	2.02
Orthoclase	11.29	9.54	12.27	7.69
Albite	42.09	40.57	42.93	47.24
Anorthite	9.18	12.83	9.25	13.12
Nepheline	-	-	-	-
Diopside	-	-	-	-
Hypersthene	5.19	5.51	4.86	5.43
Olivine	-	-	-	-
Magnetite	1.86	1.94	1.71	1.88
Ilmenite	0.80	0.81	0.75	0.75
Apatite	0.18	0.18	0.17	0.19
Mg #	45.80	46.62	46.94	47.17

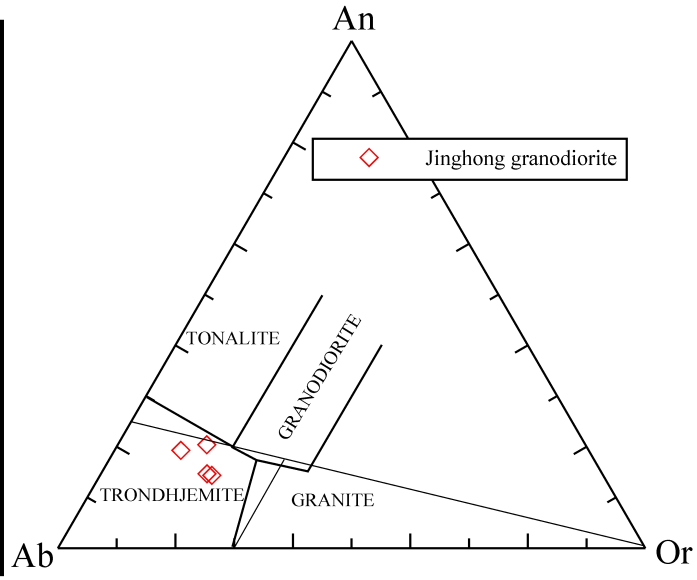

Fig. 34: The Jinghong granodiorite samples on the Or–An–Ab diagram of O`Connor (1965) and Barker (1979). Faint lines are from O`Connor (1965); heavy lines from Barker (1979).

On the K_2O vs. SiO_2 diagram the granodiorite plots in the medium-K field of the calc-alkaline series (Fig. 35A). Calc-alkalinity is confirmed by the AFM diagram, on which the granodiorite samples mimic the trend for the Cascade lavas (Fig. 35B; Carmichael, 1964).

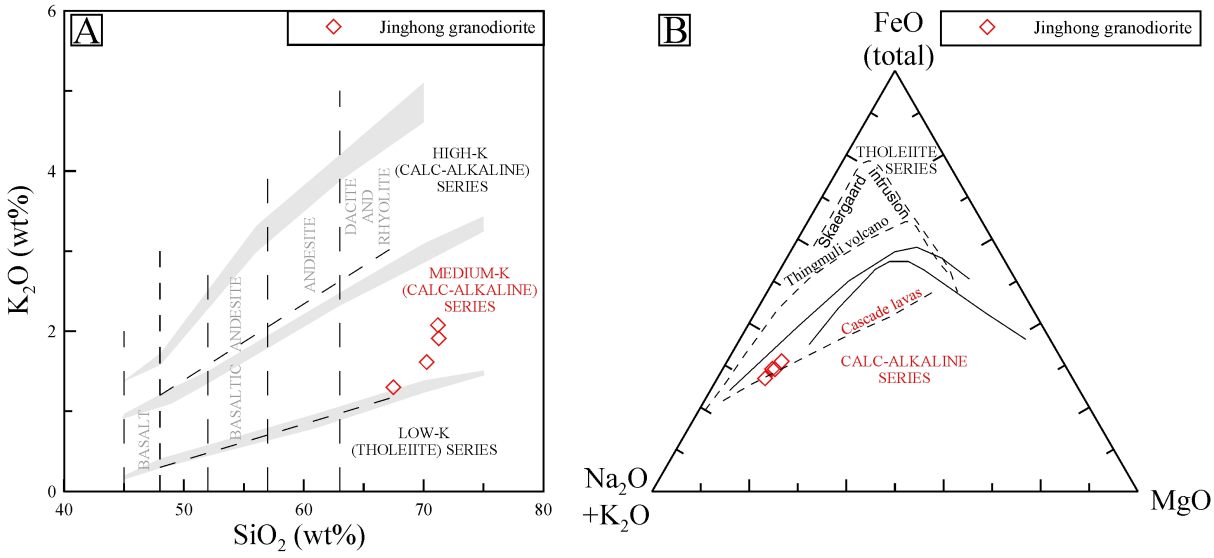

Fig. 35A: The Jinghong granodiorite on the K_2O vs. SiO_2 diagram for subalkaline rocks. B: The Jinghong granodiorite on the AFM diagram. Reference data and subdivisions as cited in Figs. 5 and 21.

Alumina saturation of the Jinghong granodiorite is affected by hydrothermal overprint. Microscopic observation shows the predominance of carbonatization and only minor sericitization, which is in accord to the mostly invariable Al contents (Appendix Table 10). The Ca, Na and K contents suggest only minor element mobility with respect to the alumina saturation index. The altered samples are slightly peraluminous but still show an I-type signature with Al_2O_3 / CaO + Na_2O + K_2O (mol) of 1.03-1.12 and correspondingly normative corundum of 0.70-2.0 wt% only (Chappel & White, 1974; Shand, 1947).

The primitive mantle-normalized multi-element plot of Figure 36 shows coherent patterns with enriched LILEs, such as Sr, K, Rb, Ba, and depleted HFSEs, such as Ta, Nb, Ce, Zr, Hf, Sm, Y and Yb, close to average crustal levels (Rudnick & Gao, 2004). Cr contents are in the range of 7 to 15 ppm, and Ni contents range from <3 to 5 ppm. The Nb content of the Jinghong granodiorite is distinctly low (6.5-8.7 ppm Nb), and Ta is in between 0.62 and 0.95 ppm. These trace-element characteristics are typical of arc magmas (e.g. Pearce, 1983).

The chondrite-normalized REE data of the Jinghong granodiorite plot in coherent patterns as well (Fig. 37). The granodiorite is moderately fractionated with a total REE content of 75-102 ppm, $(La/Sm)_N$ of 4.7-5.1, and $(La/Yb)_N$ of 5.3-8.2. The patterns exhibit shapes typical of arc magmas (Kimura & Yoshida, 2006; Luhr & Haldar, 2006). The moderate negative Eu-anomaly (Eu/Eu* = 0.7-0.9) suggests high-level fractionation of plagioclase and/or K-feldspar.

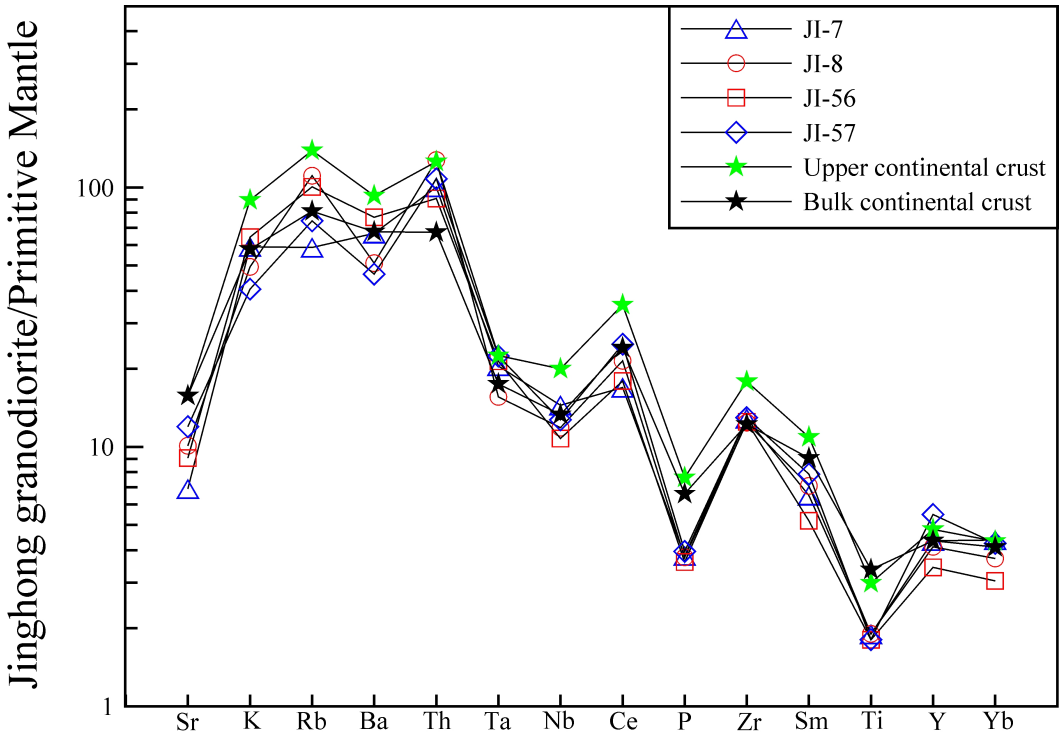

Fig. 36: Primitive mantle-normalized multi-element patterns for the Jinghong granodiorite. Primitive mantle data are from Palme & O`Neill (2004). Bulk continental crust and upper continental crust data are from Rudnick & Gao (2004).

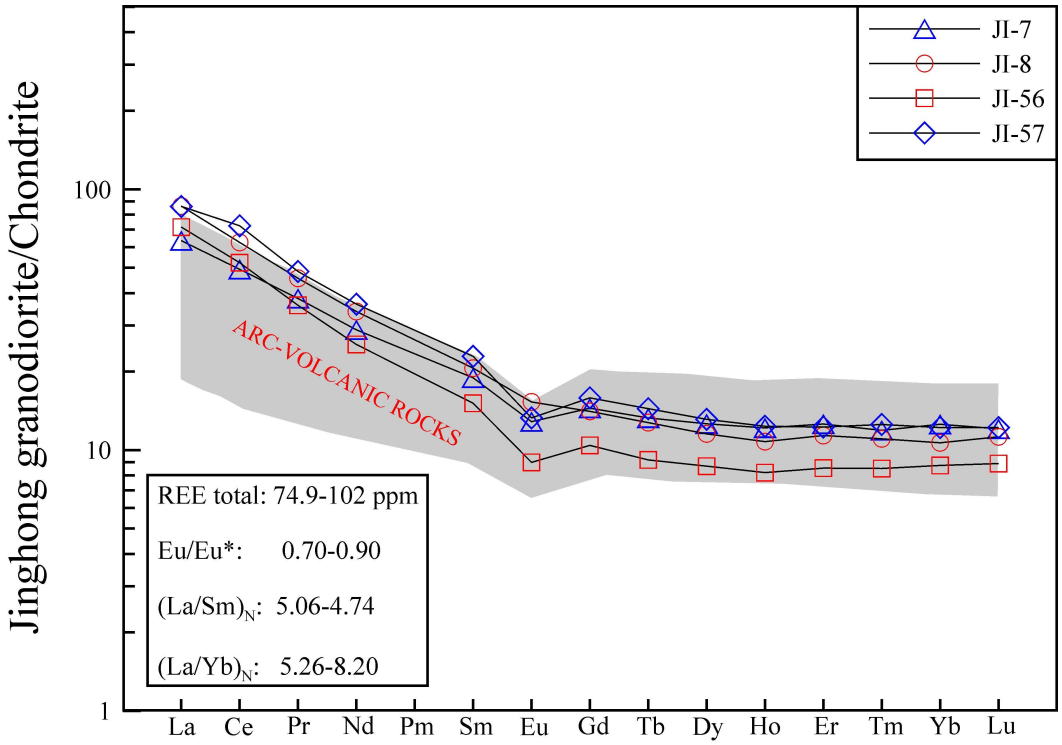

Fig. 37: Chondrite-normalized REE patterns of the Jinghong granodiorite samples (McDonough & Sun, 1995). Reference data for arc-volcanic rocks (shaded field) are from Kimura & Yoshida (2006) and Luhr & Haldar (2006).

1.5.3 U–Pb ZIRCON GEOCHRONOLOGY

Zircon mounts of the Jinghong granodiorite samples JI-7, JI-8 and JI-56 were spot-analyzed (30 µm). The data are compiled in Appendix Table 18 and plotted in Figure 39. A few measurements with low signal quality were omitted for age calculations. The Th/U ratios for zircon from the granodiorite samples show only little spread and indicate a magmatic origin, i.e. 0.43-0.74 for JI-7, 0.37-0.97 for JI-8 and 0.42-0.77 for JI-56.

All zircon populations form single, tight clusters on the concordia plot. The weighted mean $^{206}Pb/^{238}U$ ages of the Jinghong granodiorite samples are 283.7 ±1.1 Ma (n = 25; two low-quality signals), 283.0 ±1.3 Ma (n = 26; one low-quality signal) and 282.0 ±1.2 Ma (n = 25; Fig. 38).

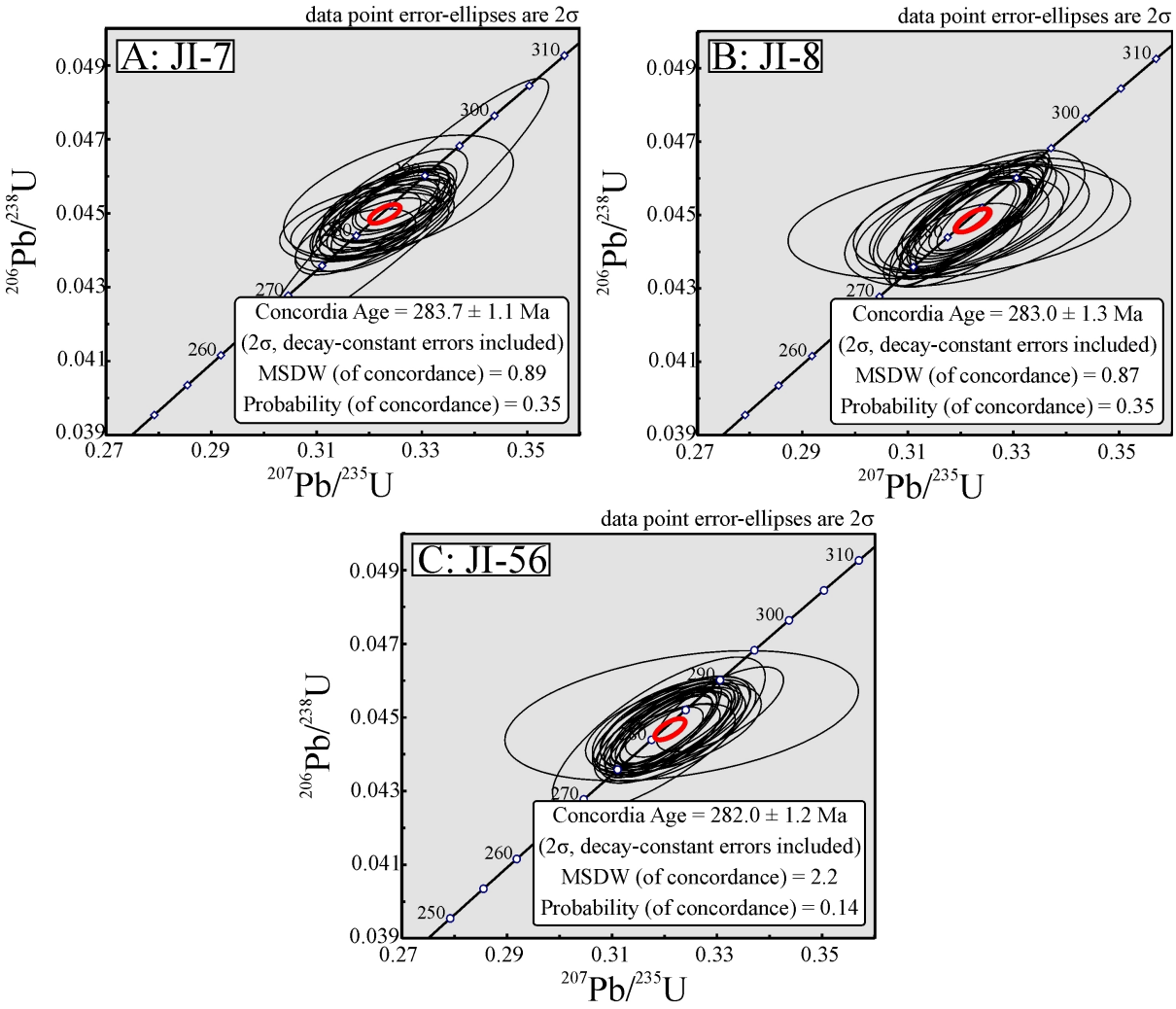

Fig. 38A-C: U–Pb concordia plots for the Early Permian Jinghong granodiorite samples JI-7, JI-8 and JI-56. The plots depict well defined ages which overlap within the analytical error of 2σ.

1.5.4 Sr–Nd ISOTOPIC COMPOSITION

The Jinghong granodiorite samples JI-7 and JI-56 have initial Sr isotopic ratios of 0.709 and 0.710, and εNd(t) of -3.1 and -3.6, respectively (Table 9; calculated for 280 Ma). The corresponding single-stage depleted-mantle model ages are 1.3 and 1.4 Ga. In Figure 39 the isotopic composition of the Jinghong granodiorite is compared to andesite data of Peng *et al*. (2008) from Jinghong (for sample locations refer to Figs. 2 and 63). These rocks are assigned to be "arc-like", but are about 35 million years younger. In terms of $^{143}Nd/^{144}Nd$ both the andesite and granodiorite have identical compositions. However, the Jinghong granodiorite is more enriched in radiogenic Sr compared to the andesites. This trend is most likely due to hydrothermal alteration.

Table 9: Sr–Nd isotopic compositions of the Jinghong granodiorite samples JI-7 and JI-56. Parameters are calculated as cited in Table 1.

Sample ID	Rock type	Age	Sm	Nd	$^{147}Sm/^{144}Nd$	$^{143}Nd/^{144}Nd$	2σ	ε_{Nd} (t)	Rb	Sr	$^{87}Rb/^{86}Sr$	$^{87}Sr/^{86}Sr$	2σ	$(^{87}Sr/^{86}Sr)t$
		Ma	ppm	ppm					ppm	ppm				
JI-7	Granodiorite	280	2.9	13.7	0.12733	0.512351	0.000004	-3.12	65.4	145.3	1.30285	0.714117	0.000020	0.708927
JI-56	Granodiorite	280	3.1	16.4	0.11409	0.512304	0.000003	-3.56	72.4	194.6	1.07754	0.713869	0.000013	0.709576

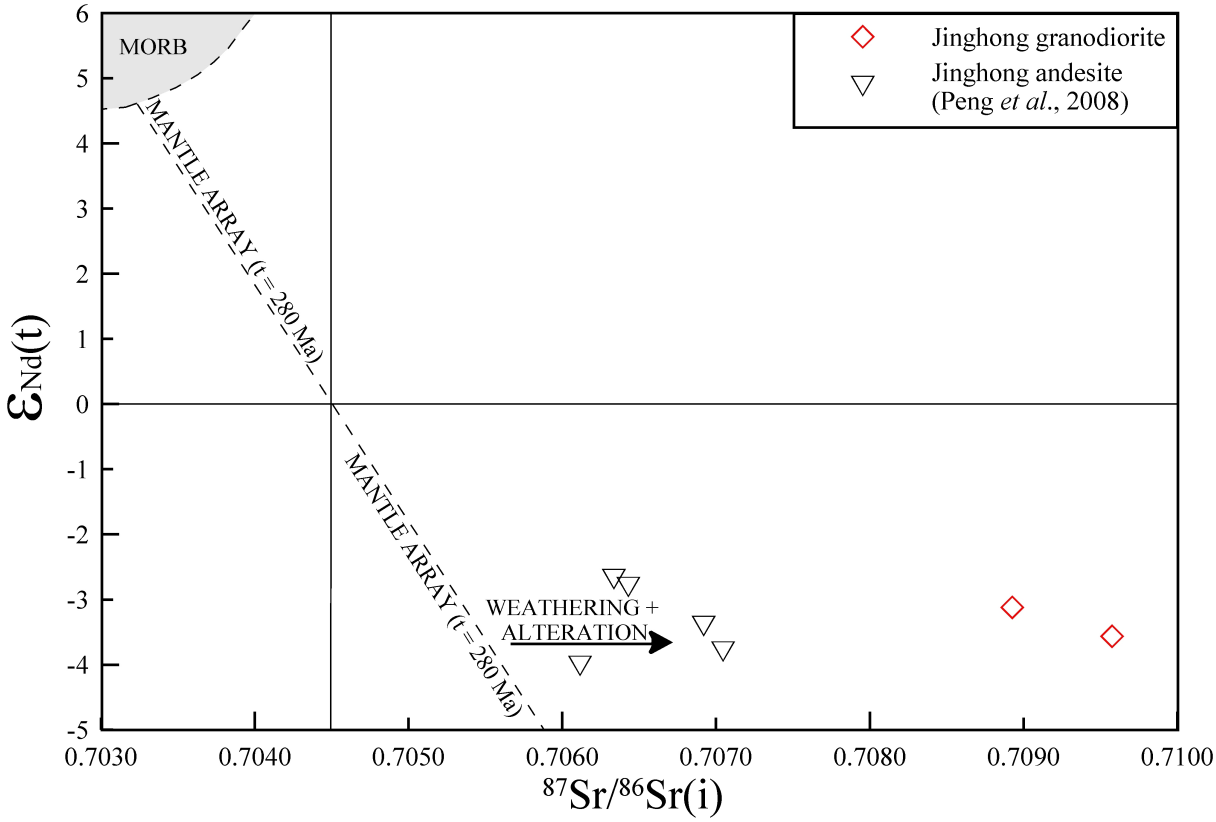

Fig. 39: εNd(t) vs. initial $^{87}Sr/^{86}Sr(t)$ diagram for the Jinghong granodiorite (t = 280 Ma, this study). The Early Triassic andesite data (t = 249) are from Peng *et al*. (2008)

1.5.5 DISCUSSION OF AGE DATA AND TECTONOMAGMATIC ENVIRONMENT

The Jinghong granodiorite intrusions with a U–Pb zircon age of 285-281 Ma document the oldest felsic magmatism known so far in the southern Lancangjiang zone. Interestingly, Jian *et al*. (2008) reported a SHRIMP U–Pb zircon age on the Liangjiuding trondhjemite of 285 ±6 Ma from the Dequin-Weixi area ~750 km north, and interpreted the trondhjemite by geochemical characteristics as a product of arc magmatism (Fig. 40).

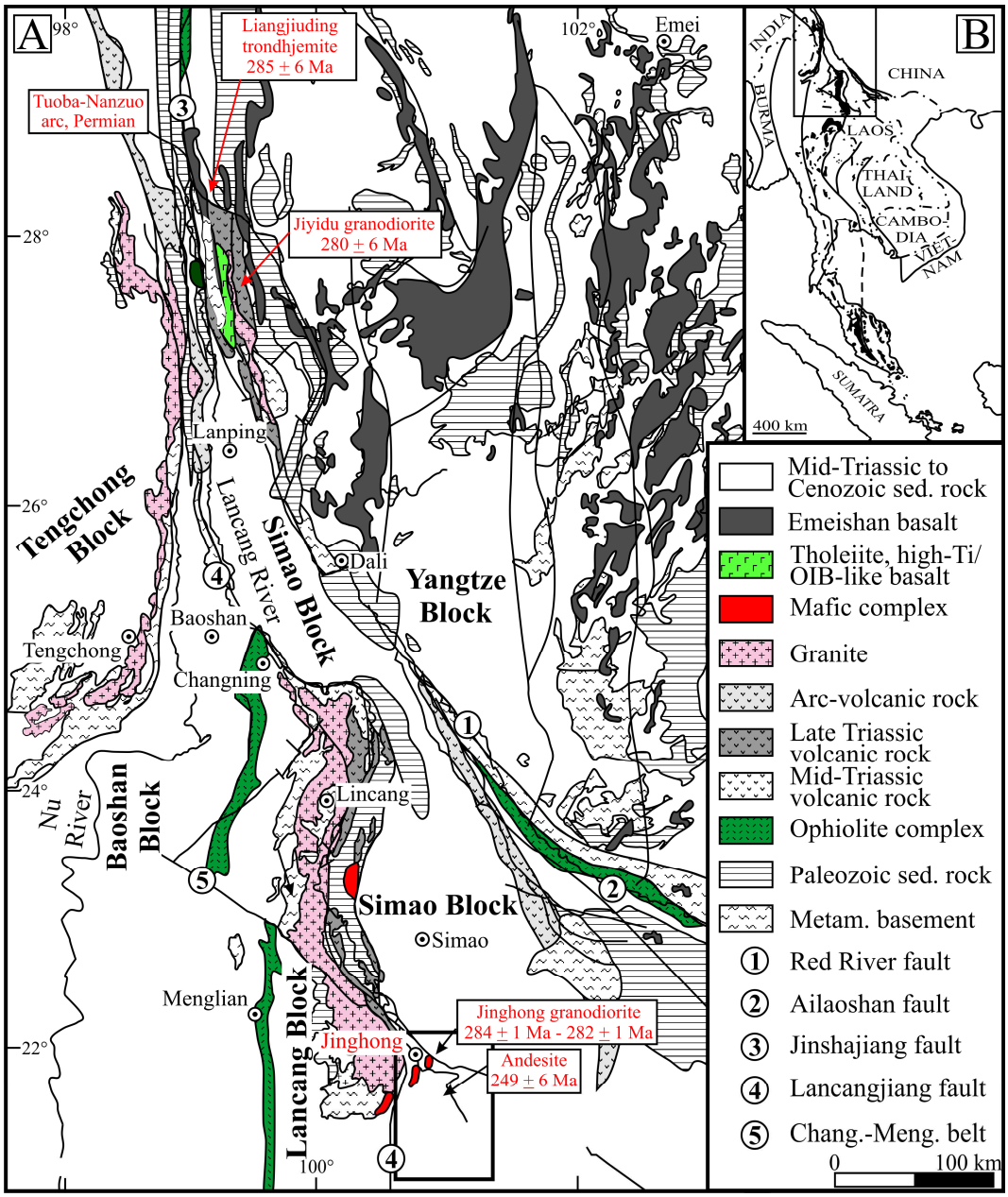

Fig. 40: Simplified geological map of the Lancangjiang zone in southwestern Yunnan. Labeled age data are SHRIMP U–Pb zircon ages of Jian *et al*. (2003b, 2008) and Peng *et al*. (2008). Jinghong granodiorite ages are from this study.

The Jiyidu granodiorite of the Jinshajiang ophiolite is located between Dequin and Weixi and has a SHRIMP U–Pb zircon age of 280 ±6 Ma (Jian *et al*., 2003b). The geochemical signature of this rock was interpreted as arc magmatic as well (Jian *et al*., 2008). West of these granodiorite bodies - attached to the Tengchong Block of Sibumasu - extends the distinct Permian Tuoba-Nanzuo arc. Maybe, all these bodies originally belonged to one continous arc along the eastern edge of Sibumasu (Fig. 40).

The Jinghong granodiorite plots in the "volcanic-arc granite" field of the Nb vs. Y and Ta vs. Yb diagrams of Pearce *et al*. (1984) (Fig. 41A/B). The Rb vs. (Y + Nb) and Rb vs. (Yb + Ta) plots give the same results (not shown). On the La/Yb vs. Sc/Ni diagram of Bailey (1981) the Jinghong granodiorite depicts an island-arc signature as well (Fig. 41C).

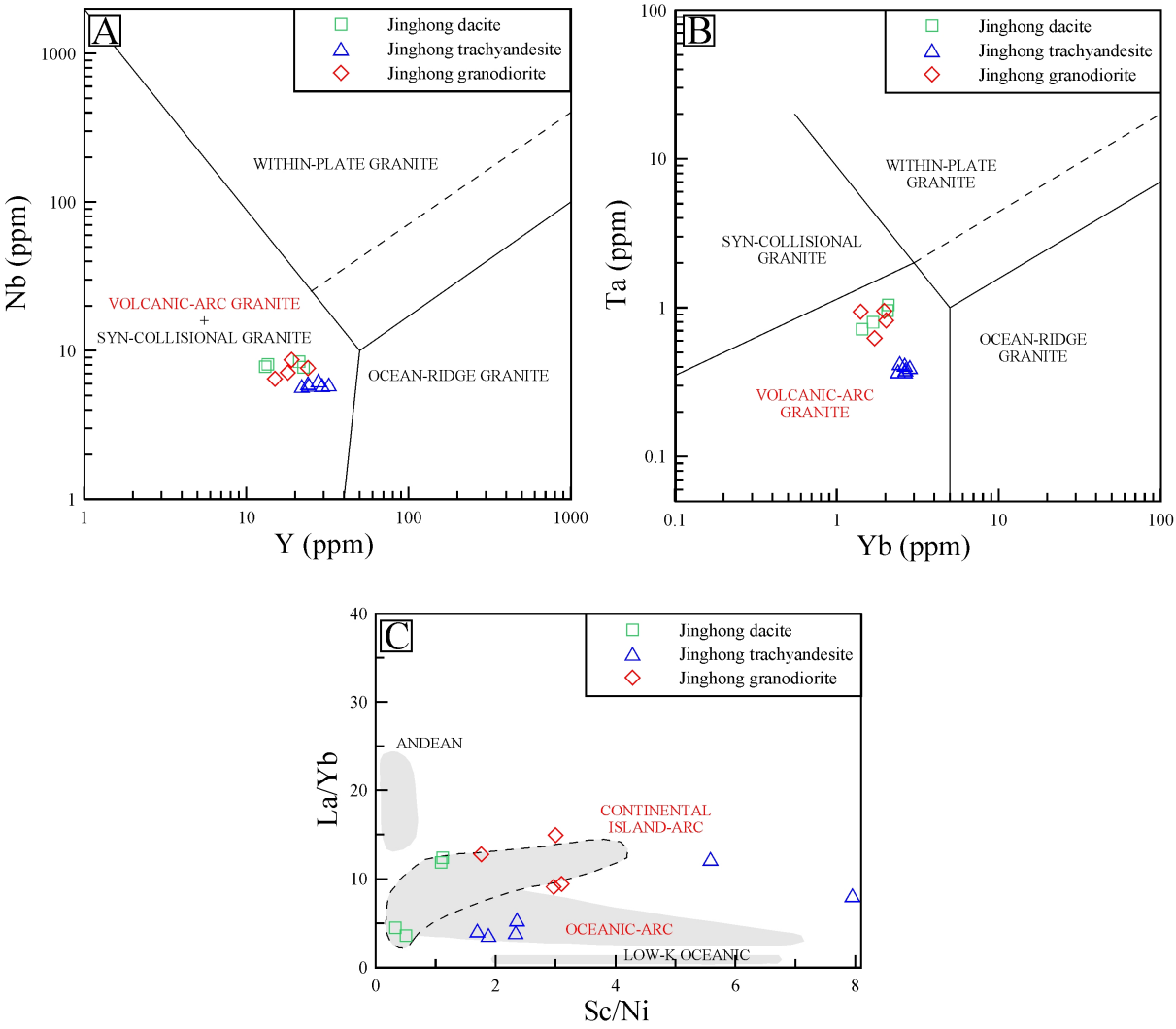

Fig. 41A/B: The Jinghong granodiorite, trachyandesite and dacite on the Nb vs. Y and Yb vs. Ta tectonomagmatic discrimination diagrams for granitic rocks (Pearce *et al*., 1984). All rocks depict a volcanic-arc signature. C: On the La/Yb vs. Sc/Ni plot of Bailey (1981) the Jinghong granodiorite samples span up a polygon covering the "continental island-arc" field. The Jinghong dacite plots in the transition of "oceanic-" to "continental island-arc". For the Jinghong trachyandesite samples an "oceanic-arc" affinity is suggested.

1.6 PALENG COMPLEX (263-257 Ma)

The Paleng complex is located in the southernmost Lancangjiang zone and is little studied to date (Zhao *et al.*, 1991; Figs. 2 and 42). Dense tropical vegetation and deep weathering allow for very few outcrops only. According to the field observations the Paleng complex is ~10 km long and ~6 km wide and has predominant NNE-SSW strike. The geological map of Zhao *et al*. (1991) defines fault-contacts to the west with the Lancang group, which consists in southwestern Yunnan of meta-andesites with island-arc signature, mica schists, pelitic schists, greenschists and blueschists (Peng & Luo, 1982). To the north, the intrusion is in magmatic contact with the Lincang granite. To the east and south, the geological situation is complex and doubtful. At least in places, the intrusion is bordered by the Damenglong group.

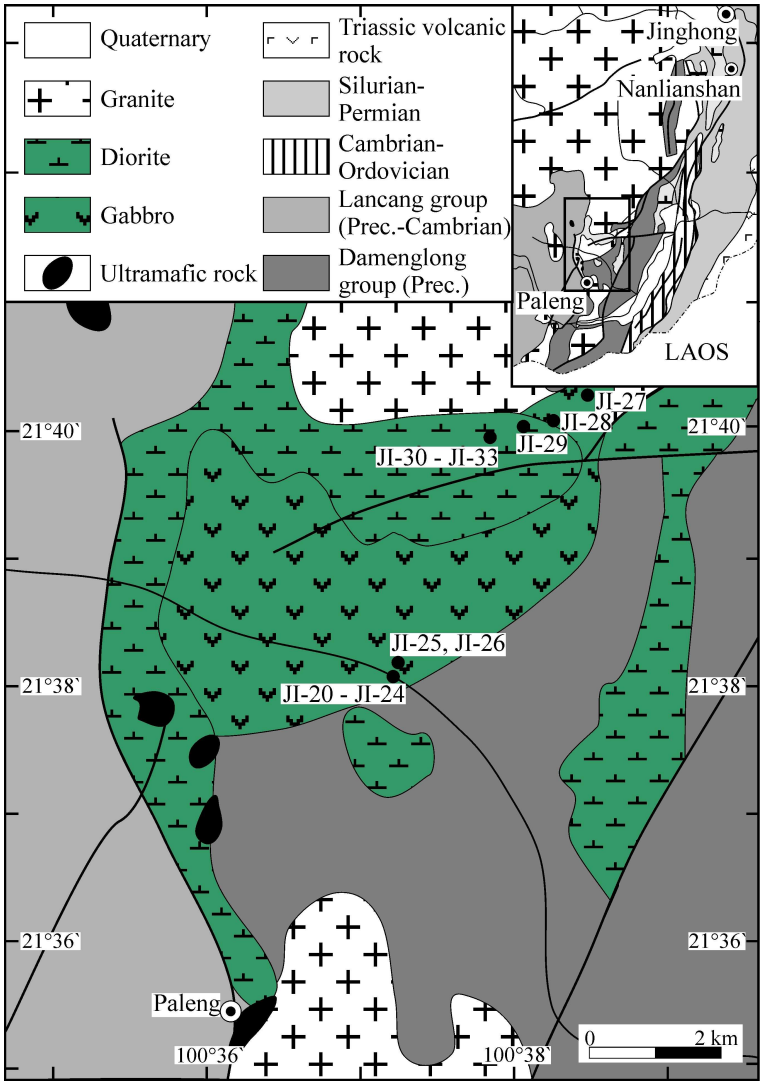

Fig. 42: Geological sketch map of the Paleng complex in southern Yunnan (adapted from Huang *et al*., 2002 and Zhao *et al*., 1991). Sample locations are indicated. Note: Inset shows the Lincang granite and the Nanlianshan volcano-plutonic complex at Jinghong.

According to Zhao *et al.* (1991), the Paleng complex is a ring-shaped structure with some minor occurrences of amphibole peridotite, pyroxenite and amphibolite in the center (all <200 m in diameter), surrounded by gabbro (1000 x 500 m) and the predominant diorite phase. Zhao *et al.* (1991) interpret the Paleng complex as root zone of an island arc or active continental margin and estimate the age of the Paleng complex by field relationships at 350-175 Ma.

We could sample at Paleng a series of amphibole gabbro cumulates with varying proportions of amphibole and plagioclase, which likely represent the amphibolites, gabbros and diorites of Zhao *et al.* (1991). We failed to locate the reported ultramafic rocks. However, we identified basaltic andesite and porphyritic basalt not reported so far.

1.6.1 PALENG AMPHIBOLE GABBRO CUMULATE SERIES

1.6.1.1 PETROGRAPHIC DESCRIPTION

The amphibole gabbro samples JI-23-JI-24 and JI-27-JI-33 of the Paleng complex show a distinct range from a plagioclase-dominated end-member (sample JI-30) to an amphibole-dominated end-member (sample JI-31). The intensively altered rock sample JI-25 shows pervasive sericitization and chloritization and could not be classified reliably. It has been omitted for petrographic and geochemical studies. The amphibole gabbro cumulate series could be determined by microscopic mineral mode estimations from plagioclase- to amphibole-rich as JI-30, (JI-23, JI-32), JI-24, JI-29, (JI-28, JI-27), JI-33 and JI-31. The intensity of hydrothermal alteration varies from moderate - in general prevalent among the more plagioclase-rich samples - to strong in the amphibole-dominated samples, and includes cross-cutting quartz, plagioclase, epidote and pyrite veins.

The rocks have 20-75 vol% sericitized and tectonized, subhedral plagioclase (0.15-8.0 mm), 20-80 vol% sub- to anhedral amphibole (0.15-5.0 mm), <3 vol% euhedral apatite (0.05-0.5 mm) and <3 vol% anhedral quartz (0.1-1.0 mm) (Fig. 43). Hornblende hosts some poikilitic plagioclase and is mostly of hastingsitic composition in the plagioclase-rich rocks, whereas brown hornblende becomes prevalent in the amphibole-dominated rocks. Some hornblende crystals depict fibrous and mosaic-like actinolite, suggesting tectono-magmatic overprint. Apatite is prevalent in the amphibole-dominated rocks (Fig. 43B-D). Primary quartz is restricted to the plagioclase-rich end-member sample JI-30. Opaque

minerals include pyrrhotite, chalcopyrite, hematite and magnetite (Fig. 43E/F). Accessory minerals are titanite “eggs”, rutile and zircon (<0.05 mm).

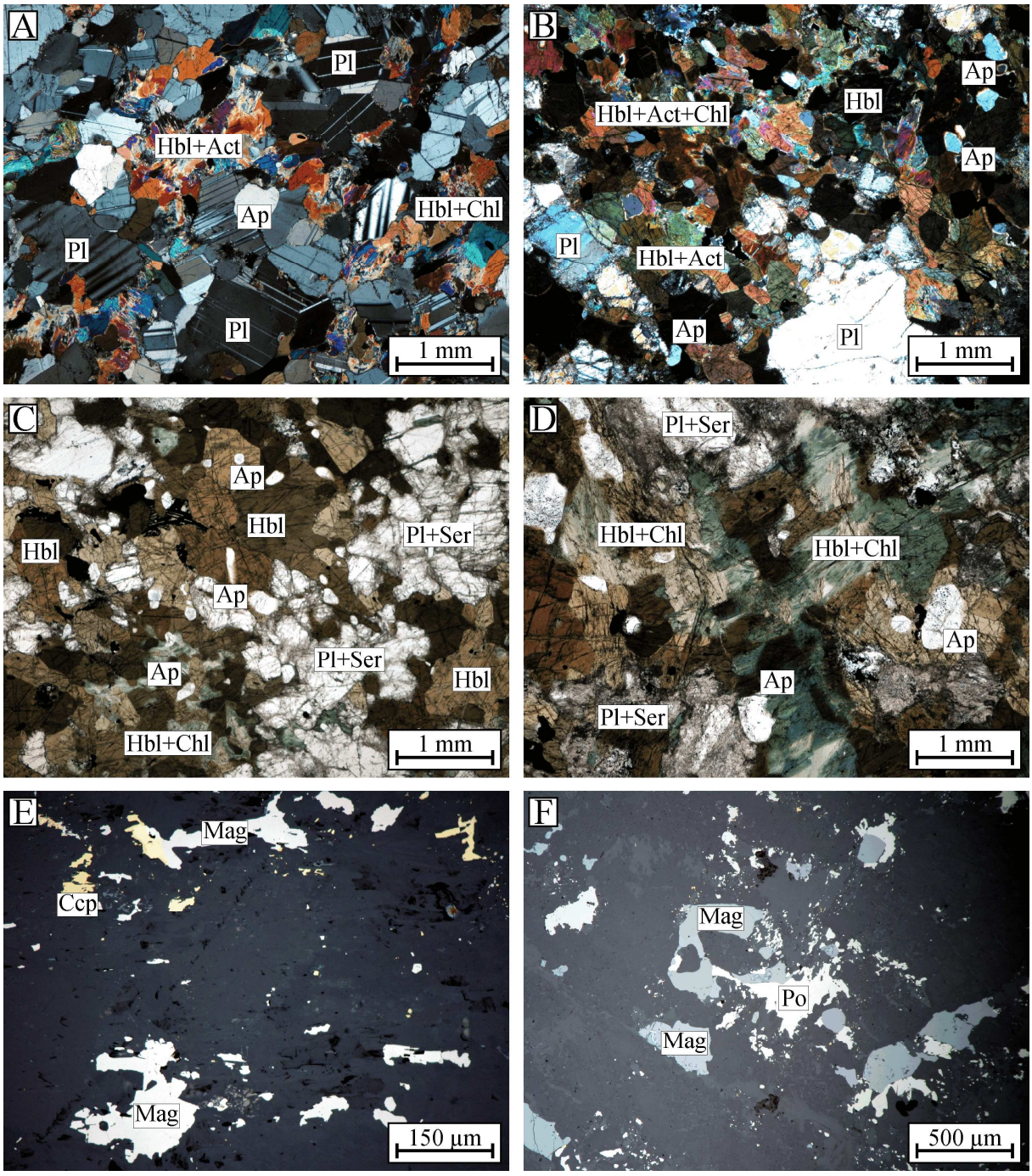

Fig. 43: Photomicrographs of the Paleng amphibole gabbro (A: JI-23, B/C: JI-29, D: JI-33, E: JI-24, F: JI-30; A/B: transmitted light/crossed polars, C/D: transmitted, plane-polarized light, E/F: reflected light/crossed polars).

1.6.1.2 MAJOR AND TRACE ELEMENT COMPOSITION

The amphibole gabbro samples JI-23, JI-24, JI-27-JI-33 are variably altered. The intensively altered rock sample JI-25 (LOI of 3.9 wt%) has been omitted for the geochemical studies.

All studied rock samples plot as subalkaline gabbro on the TAS diagram for plutonic rocks (Cox *et al*., 1979; Irvine & Baragar, 1971; Kuno, 1966; Le Maitre, 1989; MacDonald, 1968; MacDonald & Katsura, 1964; Wilson, 1989; Fig. 44A). The R1 vs. R2 diagram verifies the gabbroic composition (De la Roche *et al*., 1980; Fig. 44B), similar to immobile element plots, such as the SiO_2 vs. Zr/Ti and the Zr/Ti vs. Nb/Y diagrams, which suggest for all, except one amphibole gabbro sample, a subalkaline basaltic composition (Winchester & Floyd, 1977; Fig. 44C/D). On the SiO_2 vs. K_2O diagram the amphibole gabbro plots as medium-K type of the calc-alkaline series (Fig. 44E). AFM suggests for most samples (except for the amphibole-rich samples JI-28 and JI-29) calc-alkalinity (Fig. 44F), and the Alkali index vs. Al_2O_3 diagram gives calc-alkalinity for all rocks as well (not shown).

The major element compositions of the gabbro samples suggest a subdivision into two groups. The first group comprises samples JI-30, JI-23, JI-32 and JI-24 and is referred to here as the plagioclase-dominated gabbro cumulate group and corresponds to petrographically determined plagioclase to amphibole ratios of 70/20 to 50/45. These rocks are higher in Si, Al and Na (48.6-51.1 wt% SiO_2, 19.4-21.3 wt% Al_2O_3, 1.9-3.1 wt% Na_2O) and lower in Ti, Fe, Mn, Mg, P and Cl (0.7-1.3 wt% TiO_2, 6.5-9.3 wt% Fe_2O_3(t), 0.14-0.17 wt% MnO, 3.8-7.2 wt% MgO, 0.01-0.17 wt% P_2O_5 and 0.011-0.013 wt% Cl). The amphibole-dominated gabbro cumulate group (samples JI-33, JI-27, JI-28, JI-29 and JI-31) with plagioclase to amphibole ratios of 50/45 to 20/80, in contrast, has lower Si, Al and Na (42.7-46.9 wt% SiO_2, 11.3-18.0 wt% Al_2O_3, 0.8-2.0 wt% Na_2O), and higher Ti, Fe, Mn, Mg, P and Cl (0.9-1.7 wt% TiO_2, 10.8-15.0 wt% Fe_2O_3(t), 0.17-0.24 wt% MnO, 6.1-10.1 wt% MgO, 0.08-0.55 wt% P_2O_5 and 0.014-0.040 wt% Cl). The higher P and Cl contents correspond to the observed abundance of apatite in the amphibole-rich gabbro cumulates.

Evidence for a continuous cumulate series - as suggested by microscopy - comes from calculated CIPW norms, which give normative quartz for the plagioclase-dominated gabbro cumulate samples JI-30, JI-23 and JI-32 of 4.5-0.5 wt%. This corresponds to the microscopic observations (refer to chapter 1.6.1.1; Table 10). Sample JI-24 has normative olivine (3.7 wt%), which increases within the amphibole-dominated group to 19.1 wt% (JI-29). The whole series has constant normative orthoclase of 1.4-3.5 wt%. The albite content is high in the plagioclase-rich samples JI-30, JI-23 and JI-32 (21.8-26.8 wt%) and decreases to 7.3 wt% in the amphibole-dominated end-member sample JI-31.

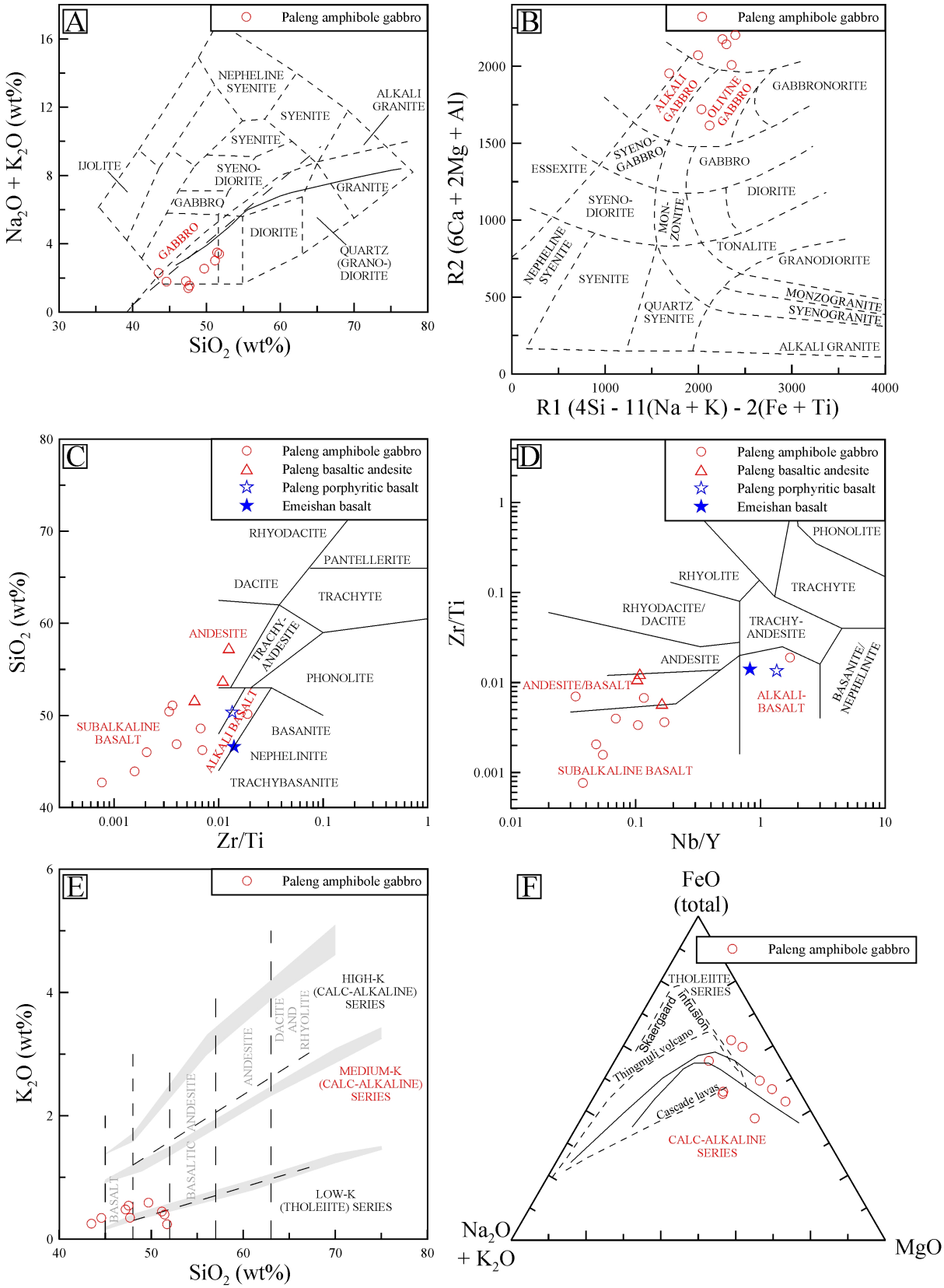

Fig. 44A: The Paleng amphibole gabbro samples on the TAS diagram for plutonic rocks (Cox *et al.*, 1979; Le Maitre, 1989; MacDonald, 1968; MacDonald & Katsura, 1964; Wilson, 1989); B: The Paleng amphibole gabbro samples on the R1 vs. R2 diagram of De la Roche *et al.* (1980); C/D: The Paleng amphibole gabbro samples on immobile element plots for volcanic rocks (Winchester & Floyd, 1977); E: K_2O vs. SiO_2 diagram for subalkaline rocks; F: AFM diagram. References as cited in Figs. 5 and 21.

As expected, the normative anorthite content is highest in the plagioclase-dominated end-member JI-30 (46.1 wt%) and lowest in the amphibole-dominated end-member JI-31 (26.2 wt%). Normative diopside increases from 0 wt% in the plagioclase-rich end-member to 27.2 wt% in the amphibole-rich end-member. Normative magnetite and ilmenite contents decrease within the plagioclase-dominated gabbro cumulate sample group from the plagioclase-rich end-member JI-30 to JI-24 (2.8-1.9 wt% magnetite and 2.4-0.9 wt% ilmenite, respectively), to increase again within the amphibole-dominated cumulate group up to the amphibole-rich end-member JI-31 (3.1-3.7 wt% magnetite and 1.7-3.3 wt% ilmenite, respectively). This corresponds also to the petrographic observations. Normative apatite shows a vague increase from the plagioclase-rich end-member (0 wt%) to the amphibole-rich rocks (1.3 wt%). In general, the sequence defined by CIPW norms and geochemical data supports the series defined by the microscopic observations. Alumina saturation is indicated by

Al_2O_3 / K_2O + Na_2O + CaO (molar) <1 and Al_2O_3 / K_2O + Na_2O (molar) >1 (Kelsey, 1965; Middlemost, 1989).

Table 10: Calculated CIPW norms and Mg-numbers of the Paleng amphibole gabbro.

Rock type	Paleng amphibole gabbro								
Sample ID	JI-30	JI-23	JI-32	JI-24	JI-33	JI-27	JI-28	JI-29	JI-31
Quartz	4.54	0.45	1.06	-	-	-	-	-	-
Corundum	0.05	-	-	-	-	-	-	-	-
Orthoclase	2.64	2.35	1.42	3.49	2.04	2.83	2.03	1.47	3.20
Albite	21.75	26.16	26.81	16.53	10.16	11.29	12.19	16.52	7.31
Anorthite	46.14	38.81	39.40	44.79	39.39	38.14	42.49	39.75	26.16
Nepheline	-	-	-	-	-	-	-	0.43	-
Diopside	-	8.75	6.78	15.31	11.62	21.25	16.39	13.61	27.19
Hypersthene	18.96	18.54	19.73	12.54	26.69	13.53	4.59	-	17.59
Olivine	-	-	-	3.91	3.67	6.45	15.50	19.07	12.23
Magnetite	2.76	2.43	2.47	1.91	3.32	3.21	3.07	3.31	3.65
Ilmenite	2.37	1.44	1.33	0.91	2.03	1.74	2.04	3.26	1.68
Apatite	0.03	0.41	0.34	0.11	0.18	0.69	0.51	1.29	0.03
Mg #	48.86	61.20	60.73	72.10	67.62	64.06	51.87	47.65	71.80

Note: Paleng gabbro is sorted from plagioclase- to amphibole-rich by geochemical criteria.

The plagioclase dominated rocks are higher in Sr (409-518 ppm Sr) and lower in the transition metals Sc, V, Cr, Co, Ni and Cu (13-33 ppm Sc, 136-184 ppm V, 85-354 ppm Cr, 25-34 ppm Co, 59-88 ppm Ni and 6-120 ppm Cu) than the amphibole dominated rocks (108-476 ppm Sr, 38-59 ppm Sc, 245-466 ppm V, 51-806 ppm Cr, 34-54 ppm Co, 24-141 ppm Ni and 97-169 ppm Cu). These trends reflect the higher partition coefficients of the transition

metals for amphibole and of Sr for plagioclase in basaltic melts (Aignertorres *et al.*, 2007; Bindemann *et al.*, 1998; Dostal *et al.*, 1983; Higuchi & Nagasawa 1969; Luhr & Carmichael, 1980; Sisson, 1994). Yttrium is 5-12 ppm in the plagioclase-dominated cumulates, and 13-31 ppm in the amphibole-dominated cumulates, which likely reflects its higher affinity to amphibole in basaltic melts (Arth, 1976).

On the primitive mantle-normalized multi-element plot of Figure 45, the two gabbro end-members JI-30 (plagioclase-rich: blue star) and JI-31 (amphibole-rich: red star) show complementary patterns, embracing the "mixed patterns" of samples JI-23, JI-24, JI-27, JI-28, JI-29, JI-32 and JI-33 for La, Sm, Gd, Tb, Dy, Ho, Er, Y, Tm, Al, and Sc. However, the HFSEs Ta, Nb, Zr, Th and U are drastically depleted for the amphibole-rich rocks. Ti and Y show both enrichment and depletion.

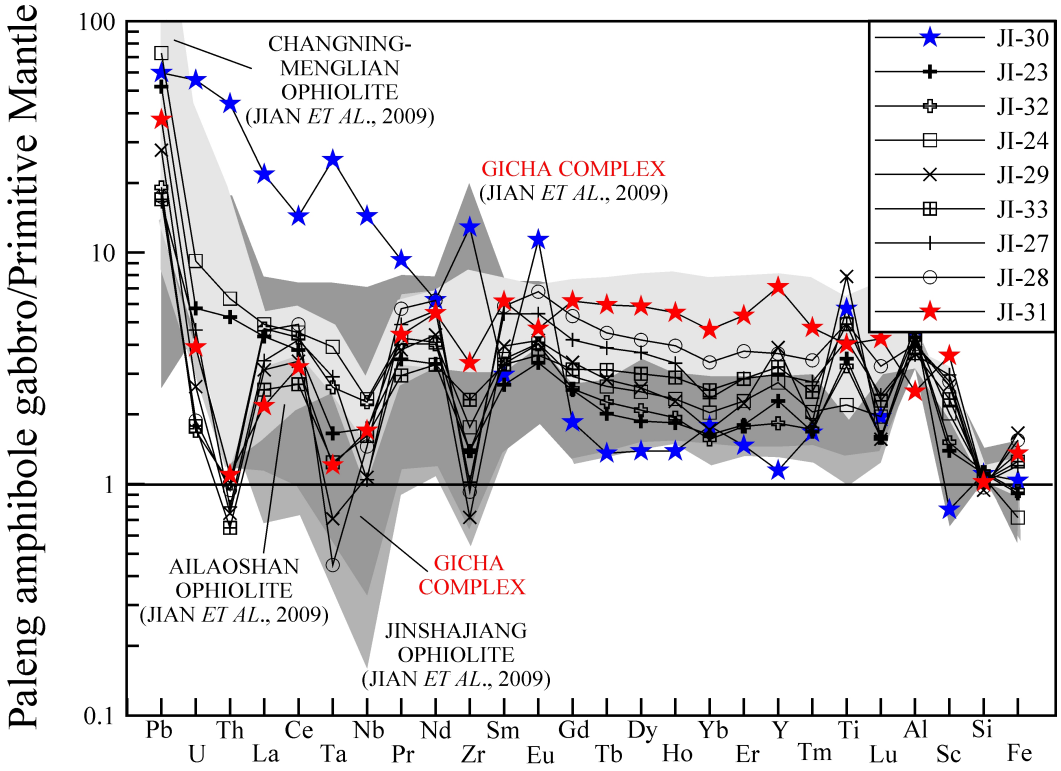

Fig. 45: Primitive mantle-normalized multi-element patterns for the Paleng amphibole gabbro. Primitive mantle data are from Palme & O`Neill (2004).

There is a remarkable spread in the Nb/Ta ratios, whereas most samples of the amphibole dominated group have lower ratios (9-16) than the plagioclase-dominated rocks (19-49). Titanite is known to fractionate Nb and Ta in basaltic liquids (Kd_{Nb} tit: 3.9-5.7; Kd_{Ta} tit: 10.8-18.9) (Benett *et al.*, 2004; Foley *et al.*, 2000; Green & Pearson, 1987; Klemme *et al.*, 2005; McCallum & Charette, 1987). In combination with the petrographic descriptions and major

element geochemistry, however, it appears likely that Ta/Nb fractionation is - at least partly - due to apatite fractionation (~3 vol% apatite in samples JI-27-JI-29). Disappointingly, we cannot exclude analytical problems due to Nb- and Ta-complexation. The positive Ti-anomaly suggests titanite, rutile and magnetite as fractionating phases. Both P and Ti correlate negatively with Th, Ta, Nb and Zr (not shown). It appears likely that the gabbros were affected by zircon fractionation. Evidence comes from sample JI-30, the plagioclase-rich end-member of the series. It stands out with high Ti, Zr, Nb, Ta, Th and U contents (1.2 wt% vs. 0.5-0.7 wt% TiO_2, 139 vs. 15-19 ppm Zr, 8.6 vs. 1.0-1.4 ppm Nb, 1.0 vs. 0.1-0.2 ppm Ta, 3.7 vs. 0.1-0.5 ppm Th and 1.2 vs. 0.0-0.2 ppm U). The transition metals Cu, Zn and Ni are enriched as well (120 vs. 8-59 ppm Cu, 124 vs. 70-88 ppm Zn, 88 vs. 59-76 ppm Ni). Petrography of a rock slab rich in opaques showed the highest zircon, magnetite (3 vol%), chalcopyrite (3 vol%), pyrrhotite (1 vol%) and sphalerite content (0.5 vol%).

From a tectono-magmatic point of view the gabbros are characterized by enrichment of the LILEs, e.g. Pb, over the HFSEs (e.g. Ta), and all samples depict a marked Ta–Nb trough relative to the LREEs and HREEs, which suggests an arc affinity. The Paleng gabbro is similar in composition to the Gicha Complex of the northern Lancangjiang zone, which is interpreted by Jian *et al.* (2009a,b) as back-arc complex (Fig. 45), and similar to the Banpo gabbro, which is interpreted as an active continental margin.

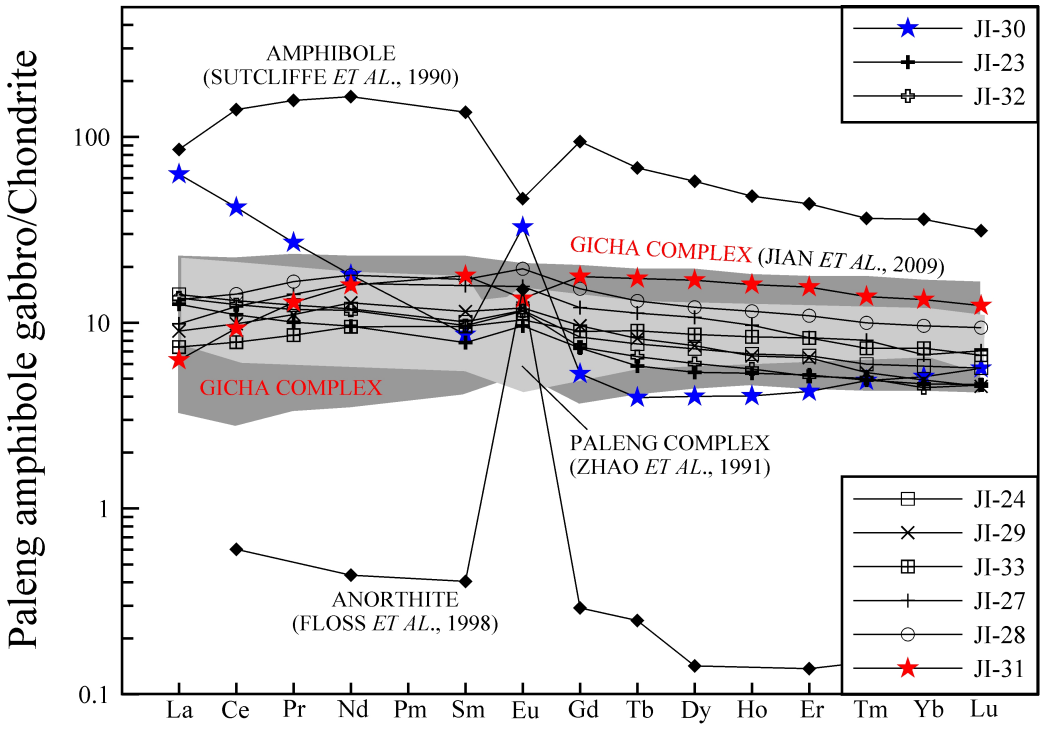

Fig. 46: Chondrite-normalized REE patterns of the Paleng gabbro (McDonough & Sun 1995).

Chondrite-normalized REE patterns of the Paleng amphibole gabbro (Fig. 46) show the plagioclase-dominated samples JI-23, JI-24 and JI-32 plotting in a consistent, moderately fractionated group, characterized by a total REE budget of 21.9-26.5 ppm, $(La/Yb)_N$ of 2.4-3.0, and positive Eu-anomalies of 1.3-1.4, clearly derived from plagioclase accumulation.

The plagioclase-rich end-member (JI-30) stands out with a pattern typical of plagioclase and a strong positive Eu-anomaly (Floss *et al*., 1998). The amphibole-dominated samples JI-27, JI-28, JI-29 and JI-33 have a similar REE composition but show $(La/Nd)_N$ of 0.6-0.8, typical of amphibole (e.g. Suttcliffe *et al*., 1990). These samples still have a positive, but less well developed Eu-anomaly of 1.1-1.2. The amphibole-rich end-member in contrast depicts a negative Eu-anomaly of 0.8 and $(La/Nd)_N$ of 0.4.

1.6.1.3 U–Pb ZIRCON GEOCHRONOLOGY

Single-grain LA ICP-MS U–Pb spot analyses (30 µm) were performed on zircon concentrates of the amphibole gabbro samples JI-25 and JI-32. BSE images are shown in Figure 47. The data are compiled in Appendix Table 19, and concordia plots are shown in Figure 48.

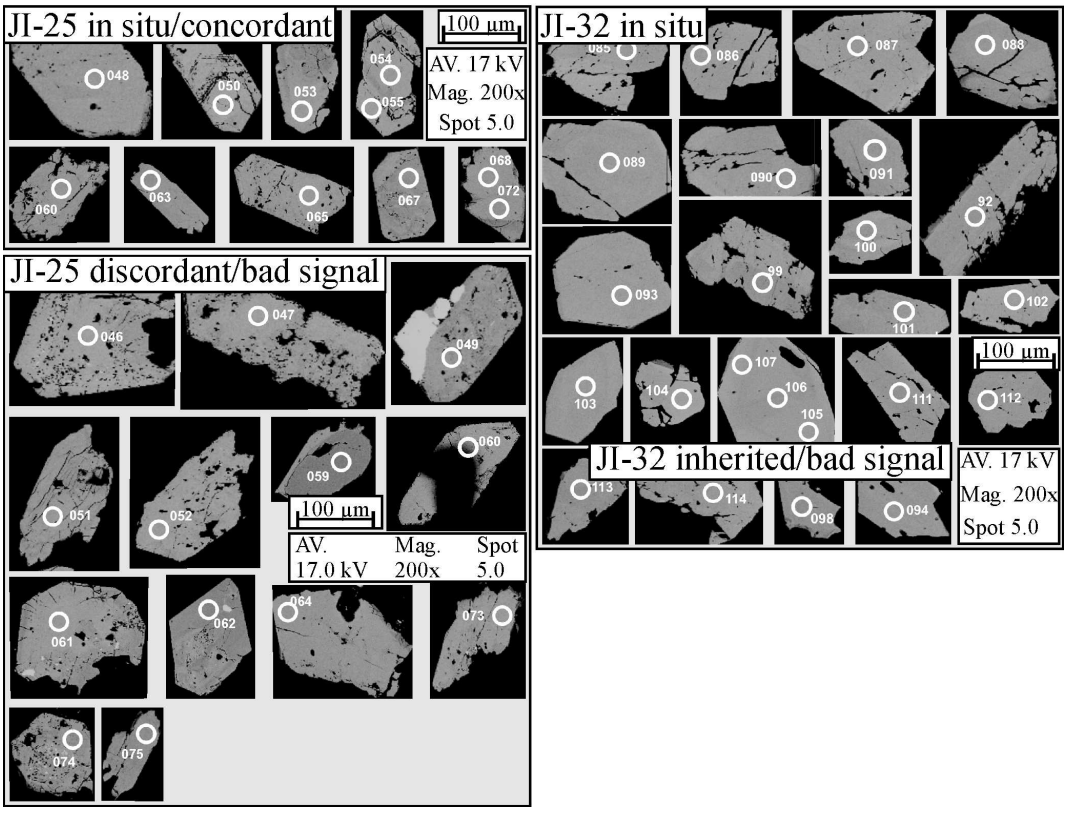

Fig. 47: BSE images of zircons from the Paleng amphibole gabbro samples JI-25 and JI-32. Spot locations are shown. AV.: Acceleration voltage; Mag.: Magnification.

On the strongly altered rock sample JI-25 twenty-two grains were spot-analyzed. The zircon grains are light grey, subhedral and mostly developed as tetragonal pyramides and tabular prisms with length to width ratios of ~2. Most grains exhibit holes, cracks and bay-like corrosion. Magmatic zoning is indicated by corrosion along growth lines (e.g. at spots 50, 54 and 55; Fig. 47). The zircons have 220-1080 ppm Th and high U contents of 4040-11000 ppm, which results in very low Th/U ratios of 0.04-0.11.

Zircons of sample JI-32 appear fresher than those of JI-25. The in situ crystals (n = 20) are lighter in color than the inherited crystal at spot 98. Th ranges for the magmatic zircons from 83 to 590 ppm and U from 94 to 1680 ppm. The resulting Th/U ratios of 0.28-0.88 are suggestive of a magmatic origin. The inherited zircon at spot 98 ($^{207}Pb/^{206}Pb$ age of 2.2 Ga) is strongly corroded and has 165 ppm Th and 188 ppm U, i.e. a Th/U ratio of 0.88, which is suggestive of magmatic origin.

The zircon populations of the Paleng gabbro form single and tight clusters on the concordia plots with weighted mean concordia ages of 260 ±3 Ma for JI-25 (n = 11; thirteen low-quality signals) and 258 ±2 Ma for JI-32 (n = 23; one low-quality signal; Fig. 48). As the zircon ages overlap within the analytical errors and inherited zircons could be easily detected by shape, color and Th/U ratios, the U–Pb zircon ages are interpreted as crystallization ages of the amphibole gabbro.

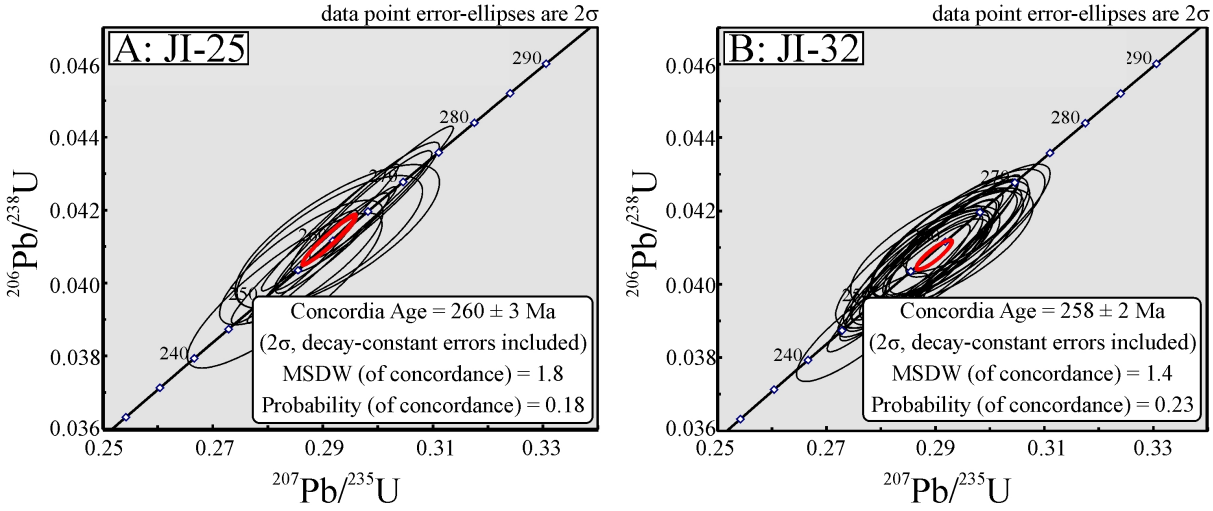

Fig. 48A/B: U–Pb concordia plots for the Paleng amphibole gabbro (samples JI-25and JI-32).

1.6.1.4 $^{40}Ar/^{39}Ar$ GEOCHRONOLOGY

$^{40}Ar/^{39}Ar$ geochronology by incremental heating was performed on hornblende mineral separates of the Paleng amphibole gabbro samples JI-27, JI-31 and JI-33. The age data are provided in Appendix Table 26 and the age spectra are plotted in Figure 49. It is noteworthy that none of the "plateau dates" fulfill the criteria for plateau ages sensu stricto, i.e. none of the degassing spectra include ≥3 contiguous steps with ≥60% of the ^{39}Ar released. However, the degassing spectra of all samples depict one well defined degassing step with highest ^{39}Ar release and lowest error. Based on these steps the $^{40}Ar/^{39}Ar$ ages were calculated. Two of the three obtained ages (samples JI-31 and JI-33) overlap with the U–Pb zircon ages. The "plateau date" of sample JI-27 is ~10 Ma lower and likely corresponds to metamorphic overprint.

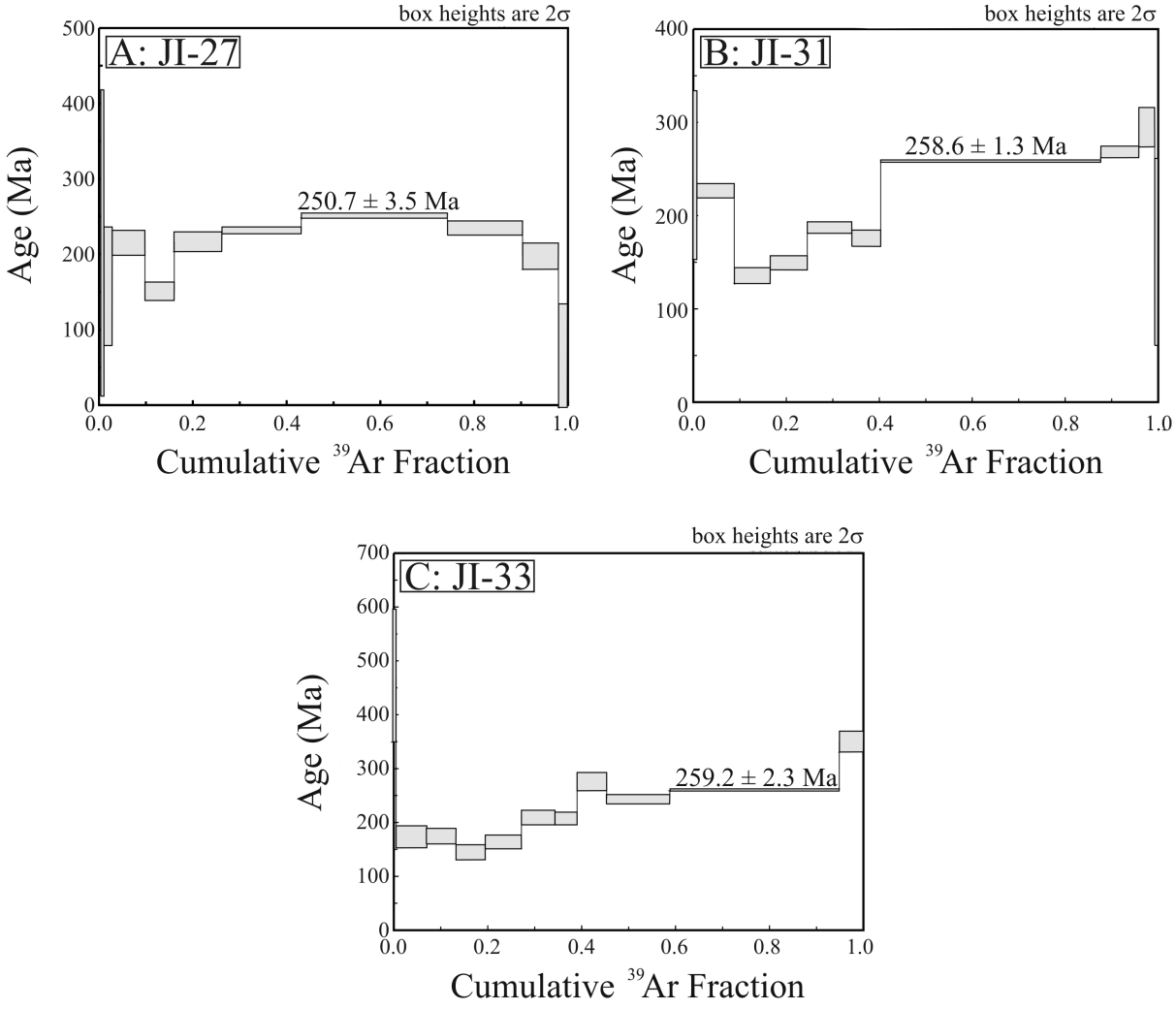

Fig. 49: Ar–Ar age spectra for the Paleng amphibole gabbro (samples JI-27, JI-31, JI-33).

JI-27 has a maximum plateau date of 250.7 ±3.5 Ma (2σ) at 1200°C, which comprises 31% of the total ^{39}Ar released. This plateau is rimmed by two lower plateaus of 231.1 ±4.7 Ma (2σ) at 1100°C and 234.0 ±9.4 Ma (2σ) at 1300°C with 17% and 16% of ^{39}Ar released (Fig. 49A). It appears likely that hornblende of JI-27 has suffered partial loss of radiogenic ^{40}Ar by alteration or metamorphic overprint. Moderate hydrothermal overprint of JI-27 is well established on geochemical grounds, e.g. LOI of 2.1 wt% and SO_3 of 0.06 wt%, and by petrographic studies, as the amphibole crystals show varying intensities of actinolitization and chloritization.

Hornblende of sample JI-31 gave a precise age of 258.6 ±1.3 Ma (2σ). This step includes 47% of the total ^{39}Ar, released at 1175°C. The Ca/K and Cl/K ratios of 39 and 0.14 suggest minor hydrothermal alteration and are in accord to the petrographic studies. Similar to JI-27, about 40% of the ^{39}Ar was released, before the plateau date was obtained (Fig. 49B).

Based on geochemical grounds, JI-33 appears to be the freshest of the three rock samples. It has a low LOI value of 1.4 wt% and low SO_3 content of 0.03 wt%. Microscopic investigations defined weak actinolitization and chloritization of the amphiboles. The age spectrum shows a well defined plateau at 259.2 ±2.3 Ma (2σ) at 1300°C, after 60% of precedent ^{39}Ar release and includes 36% of the total ^{39}Ar (Fig. 49C). This is about 100°C hotter than the release temperatures of JI-27 and JI-31 and about 20% of precedent ^{39}Ar more than for JI-27 and JI-31. Similar, but less well defined ages of 275.0 ±17.3 Ma (2σ) and 242.1 ±8.9 Ma (2σ) were obtained on the two previous temperature steps of 1160°C and 1200°C. If we include these steps, the major ^{39}Ar release corresponds to those of 40% prededent ^{39}Ar determined for JI-27 and JI-31. The Cl/K ratio of 0.15 at 1300°C is much lower than for JI-27 and similar to JI-31, and gives further evidence for little alteration only.

It appears likely that JI-31 and JI-33 have excess ^{40}Ar, as evidenced by their “saddle-shaped” spectra (e.g. Faure, 1986; Harrison & McDougall, 1981). JI-33 has both a low-temperature/high-date fraction of 472.4 ±124.0 Ma (2σ) at 600°C (Ca/K = 21; Cl/K = 0.2) and a high-temperature/high-date fraction at 1400°C. This step has an age of 349.5 ±19.4 Ma (2σ) with high Ca/K of 194 and Cl/K of 1.58. JI-31 shows two high temperature/high-date steps at 1250°C and 1350°C with ages of 268.5 ±6.1 Ma (2σ) and 294.9 ±21.3 Ma (2σ) and high Ca/K and Cl/K ratios (85 and 132 for Ca/K, and 0.19 and 0.21 for Cl/K). An early, low-temperature/high-date fraction cannot be traced for JI-31, as the determined age at 600°C of 243.4 ±90.5 Ma (2σ) does not necessarily exceed the plateau age.

1.6.1.5 Sr–Nd ISOTOPIC COMPOSITION

Sr–Nd isotopic studies were performed on the whole-rock amphibole gabbro samples JI-27 and JI-31. The data are compiled in Table 11 and plotted in Figure 50. The gabbro samples JI-27 and JI-31 have initial Sr isotopic ratios of 0.705 and 0.707, and εNd(t) of 3.4 and -0.7.

Table 11: Sr–Nd isotopic composition of the amphibole gabbro samples JI-27 and JI-31.

Sample ID	Rock type	Age	Sm	Nd	$^{147}Sm/^{144}Nd$	$^{143}Nd/^{144}Nd$	2σ	εNd(t)	Rb	Sr	$^{87}Rb/^{86}Sr$	$^{87}Sr/^{86}Sr$	2σ	$(^{87}Sr/^{86}Sr)t$
		Ma	ppm	ppm					ppm	ppm				
JI-27	Gabbro	260	2.5	8.6	0.17869	0.512781	0.000005	3.39	19.9	416.4	0.138010	0.705888	0.000016	0.705378
JI-31	Gabbro	260	3.6	9.8	0.22064	0.512644	0.000003	-0.68	24.2	112.5	0.622130	0.709019	0.000012	0.706718

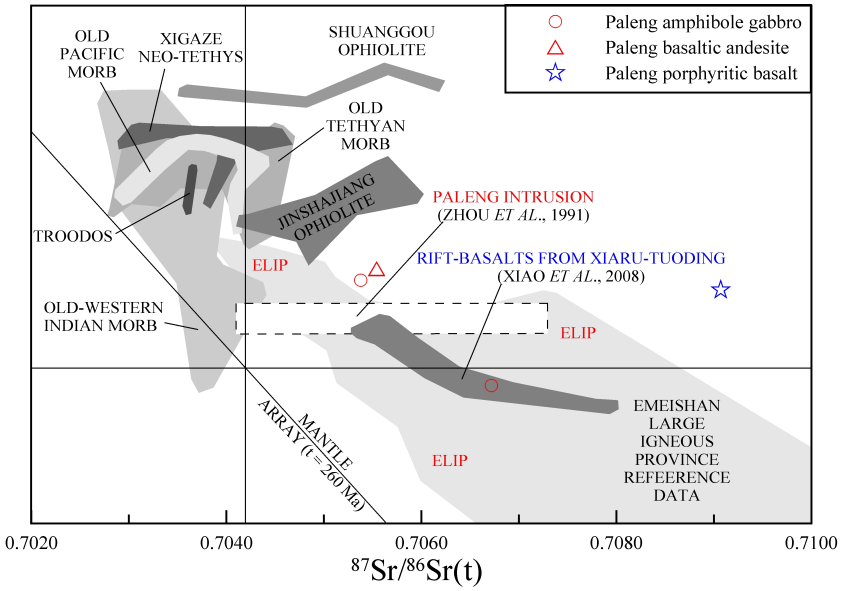

Fig. 50: $\varepsilon_{Nd}(t)$ vs. $^{87}Sr/^{86}Sr(t)$ diagram for the Paleng amphibole gabbro, Paleng basaltic andesite and the Paleng porphyritic basalt (t = 260 Ma). Bulk silicate earth and mantle array (Faure, 1986) are shown for 260 Ma as well. Reference data as cited in Figs. 9 and 18.

The spread in the Sr isotopic ratios is likely caused by hydrothermal overprint, as the two gabbro samples have high LOI values of 2.1 and 2.2 wt%, respectively, and show drastic variation in their Sr concentrations as well (108-518 ppm Sr). Hydrothermal alteration and weathering result in higher $^{87}Sr/^{86}Sr$ ratios (e.g. Hart *et al.* 1974, 1999). Zhao *et al*. (1991) reported for the Paleng diorite/gabbro similar initial $^{87}Sr/^{86}Sr$ ratios of 0.7041-0.7073 (t not given) and explain the wide datarange by alteration. Their $^{143}Nd/^{144}Nd$ ratios of 0.5121-0.5128 and εNd(t) of 1.3-2.5 plot in an intermediate position to our data. The low εNd(t) and high $^{87}Sr/^{86}Sr(i)$ of sample JI-31 may be suggestive for crustal contamination of this sample (Table 11). The $^{143}Nd/^{144}Nd$ ratios are in the range of those published for the ELIP (Fig. 50).

1.6.2 PALENG BASALTIC ANDESITE

1.6.2.1 PETROGRAPHIC DESCRIPTION

The porphyritic basaltic andesite (samples JI-20-JI-22) has about 25 vol% phenocrysts (Fig. 51). Euhedral, zoned and sericitized plagioclase (0.5-4.0 mm), subhedral, actinolitized and chloritized (clinochlore - identified by RDA) green hornblende (0.6-5.0 mm), subhedral biotite (<1.5 mm) and subhedral clinopyroxene (0.6-1.6 mm) are set in a holocrystalline, trachytic matrix of euhedral to subhedral plagioclase, green hornblende, subhedral quartz (all <0.25 mm) and accessories such as apatite (<0.09 mm) and zircon (<0.03 mm) (Fig. 51A-D). Optical analysis of plagioclase phenocrysts revealed a labradoritic to andesinic composition (Rittmann, 1929). Rock mode is 50-60 vol% plagioclase, 30-40 vol% green hornblende, <10 vol% biotite and quartz each, <5 vol% clinopyroxene and <2 vol% opaques, which include pyrite cubes (<0.15 mm), magnetite (<0.1 mm) and hematite (0.02-0.06 mm) from amphibole decomposition. The rock is cut by quartz veinlets (e.g. Fig. 51C).

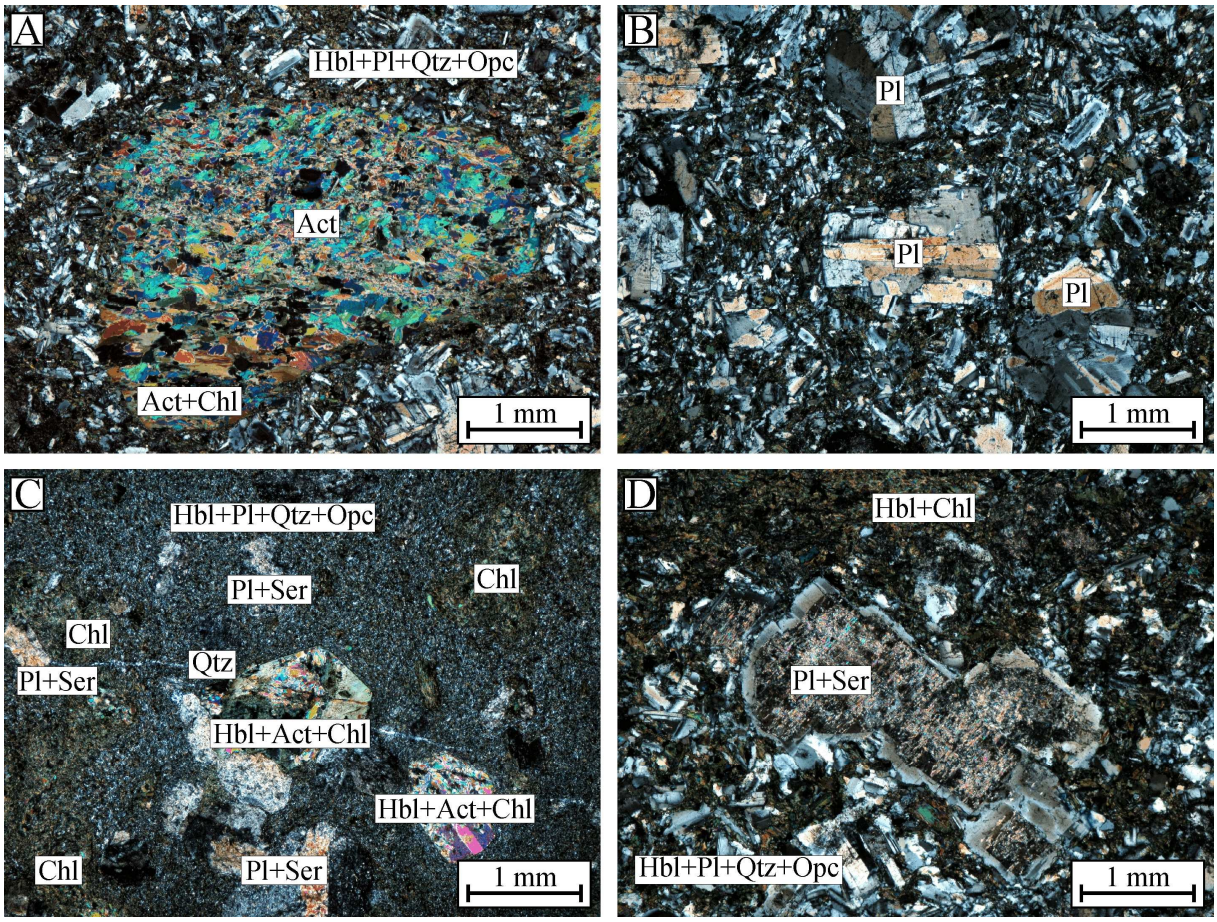

Fig. 51: Photomicrographs of the Paleng basaltic andesite (A/B/D: JI-20, C: JI-21; all photographs: transmitted light/crossed polars).

1.6.2.2 MAJOR AND TRACE ELEMENT COMPOSITION

The samples have a typical basaltic-andesitic to andesitic composition in terms of SiO_2, Al_2O_3, Fe_2O_3(t), MnO and CaO contents, i.e. 52-57 wt% SiO_2, 16-19 wt% Al_2O_3, 8-10 vol% Fe_2O_3(t), 0.2 wt% MnO and 8-9 wt% CaO, but are relatively low in Ti, Na, K and P (0.6-0.8 wt% TiO_2, 3.0-3.2 wt% Na_2O, 0.4-0.5 wt% K_2O, 0.1 wt% P_2O_5). Mg contents have a wide range (3-6 wt% MgO) (e.g. Bailey, 1981; Nockolds, 1954).

TAS (Le Maitre, 1989) classifies the Paleng basaltic andesite as subalkaline basaltic andesite to andesite (Fig. 52A), which is confirmed by immobile element plots, such as the Zr/Ti vs. Nb/Y and the SiO_2 vs. Zr/Ti diagrams of Winchester & Floyd (1977; refer to Fig. 44C/D). On the K_2O vs. SiO_2 diagram, the basaltic andesite is of calc-alkaline low-K type or part of the tholeiitic magma series (Fig. 52B). The AFM (Fig. 52C) and Alkali index vs. Al_2O_3 diagrams (not shown) suggest calc-alkaline composition.

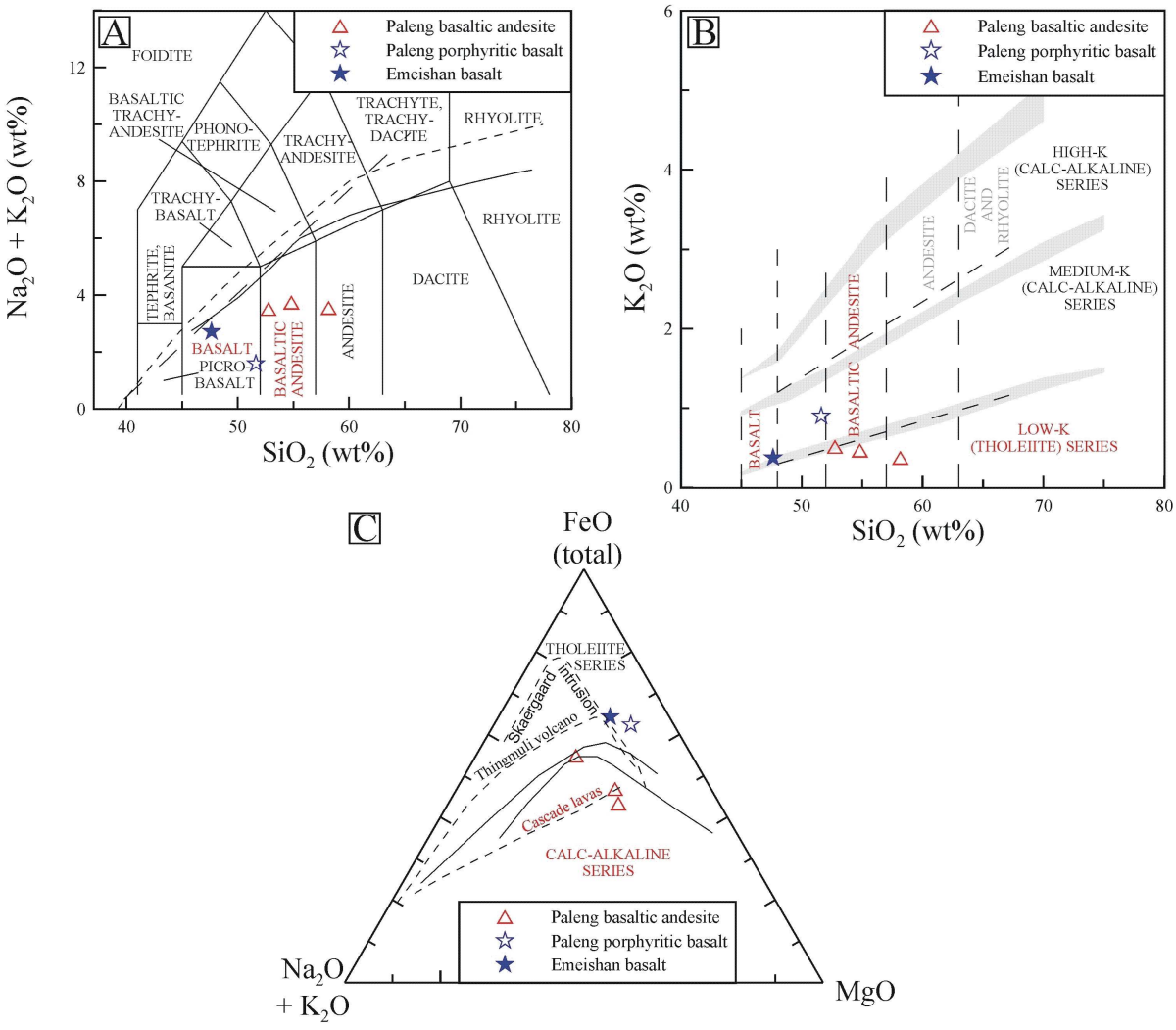

Fig. 52: The Paleng basaltic andesite, porphyritic basalt (JI-26) and Emeishan basalt reference sample (BI-2) on (A) the TAS diagram (Le Maitre, 1989); (B) the K_2O vs. SiO_2 diagram for subalkaline rocks and (C) the AFM diagram. Reference data as cited in Figs. 5 and 21.

The rock mode is in accord to calculated CIPW norms with normative quartz (3.3-15.7 wt%), orthoclase (2.2-3.1 wt%), albite (25.4-27.7 wt%), anorthite (27.3-37.6 wt%), diopside (6.0-13.1 wt%) and hypersthene (10.7-17.8 wt%), and correspondingly $K_2O + Na_2O + CaO > Al_2O_3 > K_2O + Na_2O$ (molar) (Kelsey, 1965; Middlemost, 1989; Table 12). The variation in Mg-numbers of 47.9-65.4 is due to the wide range in Mg contents. It appears likely, and corresponds to the microscopic observation, that MgO of the fresh rock was ~5-6 wt% and has been lowered in sample JI-20 by actinolitization during metamorphic overprint (e.g. Bailey, 1981; Nockolds, 1954).

Table 12: Calculated CIPW norms and Mg-numbers for the Paleng basaltic andesite.

Sample ID	Quartz	Orthoclase	Albite	Anorthite	Diopside	Hypersthene	Magnetite	Ilmenite	Apatite	Mg #
JI-20	15.68	2.22	26.86	31.68	5.99	10.74	4.53	1.46	0.26	47.94
JI-21	5.76	2.78	27.67	27.32	13.11	17.24	4.22	1.09	0.15	61.91
JI-22	3.29	3.05	25.38	37.63	7.32	17.80	3.49	1.15	0.33	65.35

The primitive mantle-normalized multi-element patterns of the Paleng basaltic andesite plot coherently with minor variations in the Ba, Ta and Zr abundances (Fig. 53). The rocks are more enriched in the large, low-valence cations, such as Rb, Pb, and Ba than E-MORB, and are moderately enriched in the large high-valency cations U and Th (0.3-0.6 ppm U, 1.0-2.3 ppm Th). In contrast, the high field strength elements (HFSEs), such as Ta, Nb, Zr and Ti show marked depletions (0.1-0.4 ppm Ta, 1.8-2.6 ppm Nb, 21-57 ppm Zr, 0.6-0.8 wt% TiO_2). These trace and major element characteristics are suggestive of an island-arc setting (e.g. Pearce, 1982). For reference, volcanic arc data are plotted on the multi-element plot of Figure 53 (Wilson, 1989 and references therein). Additional diagnostic trace element contents for the Paleng basaltic andesite are 149-253 ppm V, low Cr (37-113 ppm Cr), low Co (21-32 ppm Co), low Ni (8-75 ppm Ni), low Sc (23-44 ppm Sc) and low Y (14-24 ppm Y). In combination with the low Ti/Y ratios of 189-255, an intra-plate setting can be ruled out.

The weakly fractionated REE patterns of the Paleng basaltic andesite plot coherently at 15-25 times chondritic composition with a total REE content of 36-57 ppm, $(La/Sm)_N$ of 1.4-1.9, and $(La/Yb)_N$ of 1.5-3.8 (Fig. 54). The slight bow-shaped patterns of samples JI-20 and JI-21 might be suggestive of amphibole and clinopyroxene fractionation. There is no marked europium anomaly (Eu/Eu* = 0.9-1.1). The total REE content and the shape of the patterns are typical of island-arc magmas (Bailey, 1981; Kimura & Yoshida, 2006; Luhr & Haldar, 2006).

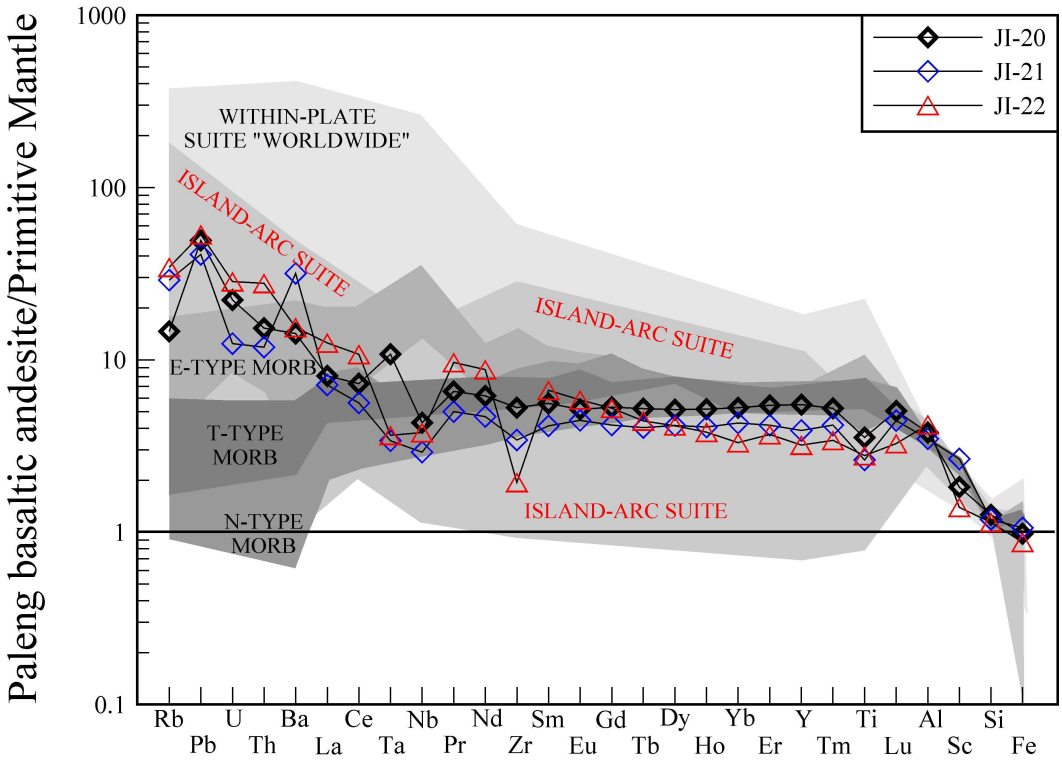

Fig. 53: Primitive mantle-normalized multi-element patterns of the Paleng basaltic andesite. Reference data are from Wilson (1989) and sources cited therein. Primitive mantle data are from Palme & O`Neill (2004).

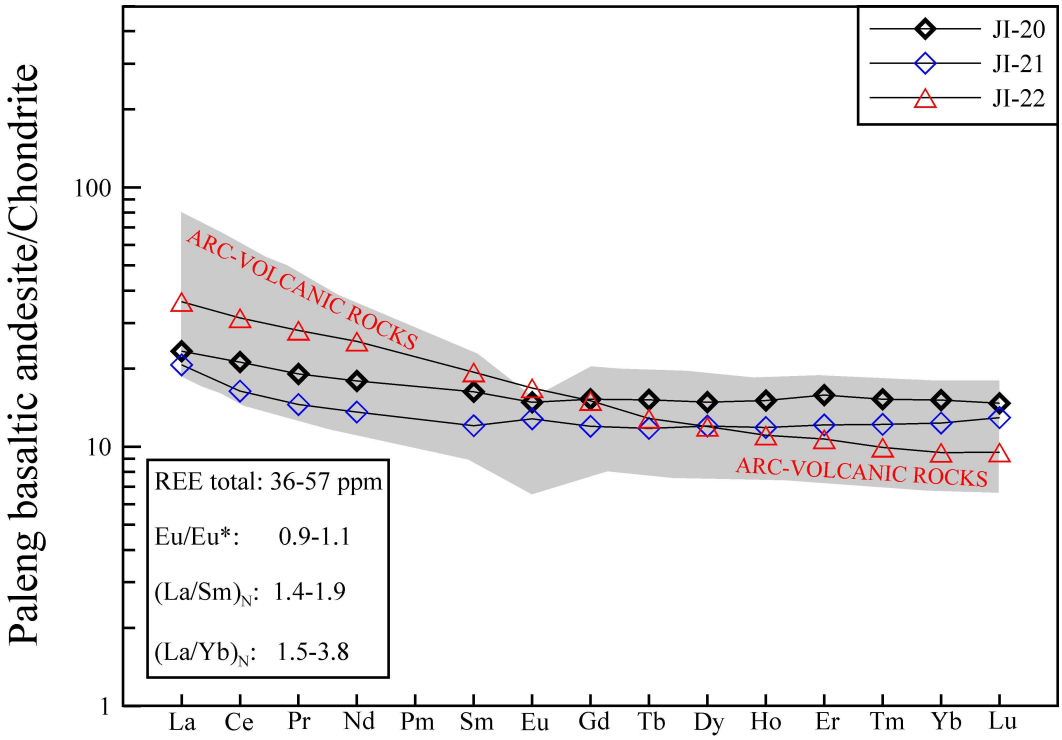

Fig. 54: Chondrite-normalized REE patterns of the Paleng basaltic andesite (McDonough & Sun, 1995). Reference data for volcanic-arc rocks are from Kimura & Yoshida (2006) and Luhr & Haldar (2006).

1.6.2.3 Sr–Nd ISOTOPIC COMPOSITION

The Paleng basaltic andesite sample JI-20 has been analyzed for its whole rock Sr–Nd isotopic composition. The isotopic signature is very similar to that of the amphibole gabbro sample JI-27, i.e. $^{87}Sr/^{86}Sr(i)$ of 0.706 vs. 0.705, and εNd(t) of 3.8 vs. 3.4 (calculated for t = 260 Ma; Tables 11, 13; Fig. 50). The petrographic studies and the low LOI value of 1.2 wt% point to minor alteration only and suggest that the Sr isotopic ratio is predominantly undisturbed. Although we are aware of the significance of just one data point, the similarity of the isotopic data might be suggestive of a common source of the amphibole gabbro and the basaltic andesite. In general, the isotopic composition of the basaltic andesite is in accord to published Sr–Nd isotopic data from island-arc rocks (e.g. Davidson, 1986).

Table 13: Sr–Nd isotopic composition of the Paleng basaltic andesite sample JI-20.

Sample ID	Rock type	Age	Sm	Nd	$^{147}Sm/^{144}Nd$	$^{143}Nd/^{144}Nd$	2σ	εNd(t)	Rb	Sr	$^{87}Rb/^{86}Sr$	$^{87}Sr/^{86}Sr$	2σ	$(^{87}Sr/^{86}Sr)t$
		Ma	ppm	ppm					ppm	ppm				
JI-20	Basaltic andesite	260	2.5	8.4	0.17933	0.512805	0.000004	3.84	11.6	203.2	0.706148	0.706148	0.000007	0.705540

1.6.3 PALENG PORPHYRITIC BASALT AND EMEISHAN BASALT REFERENCE SAMPLE

1.6.3.1 PETROGRAPHIC DESCRIPTION

1.6.3.1.1 PALENG PORPHYRITIC BASALT

The porphyritic basalt sample JI-26 distinctly stands out in terms of texture and geochemical composition from the Paleng amphibole gabbro and the Paleng basaltic andesite. The rock is flow textured with mafic phenocrysts (<7 mm) set in a strongly altered, white to greenish groundmass. Patches of hydrothermal quartz (<5 mm) and minute grains of chalcopyrite occur sporadically. Minor relics of clinopyroxene and actinolitized amphibole with some poikilitic plagioclase are altered to chlorite, epidote, quartz, carbonate and hematite (Fig. 55A). Former plagioclase, up to 1.5 mm in diameter, is pervasively altered to sericite, muscovite, carbonate and prehnite. Some plagioclase relics show tectonic twinning (Fig. 55B). Patches of quartz have partly a mosaic-structure. The primary rock mode is difficult to assess but might have been 45 vol% plagioclase and 50 vol% amphibole and clinopyroxene combined. The rock has pyrite, chalcopyrite, magnetite and hematite (Fig. 55C/D).

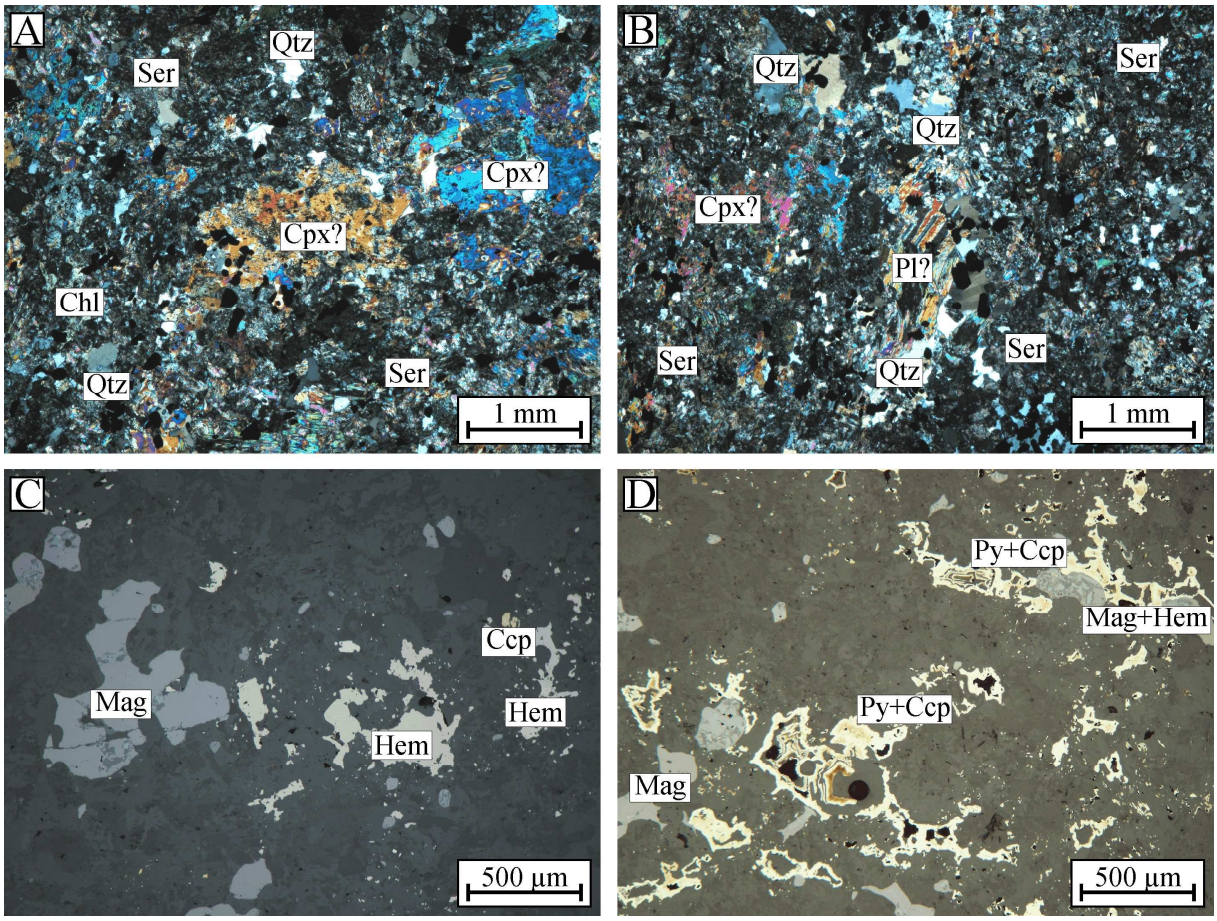

Fig. 55: Photomicrographs of the Paleng porphyritic basalt sample JI-26 (A/B: transmitted light/crossed polars, C/D: reflected light/crossed polars).

1.6.3.1.2 EMEISHAN BASALT REFERENCE SAMPLE

One representative Emeishan basalt sample from Binchuan was analyzed. The Binchuan section is a reference locality in the Emeishan literature, with flow thickness >6 km and well documented chemostratigraphy (e.g. Xiao *et al.*, 2003; Xu *et al.*, 2001).

The moderately altered porphyrogranulitic basalt has amygdules of 1-15 mm in size filled with chlorite, quartz and carbonate (Fig. 56A). Phenocrysts of euhedral to subhedral augite (0.2-1.0 mm) and of euhedral, zoned, seriate plagioclase (<1.5 mm) are set in a trachytic, holo- to hypocrystalline groundmass of clinopyroxene (predominantly augite and some minor diopside), plagioclase, titano-magnetite, ilmenite and rutile. Clinopyroxene shows varying intensities of chloritization and is intersertal to intergranular in the groundmass (Fig. 56B). Weak sericitization and carbonatization of plagioclase is mostly restricted to the anorthite-rich crystal-core. Parts of the chloritized groundmass might be derived from altered

volcanic glass. The mode of the rock is ~50 vol% plagioclase, ~45 vol% clinopyroxene and ~5 vol% opaques. Carbonate and chlorite veinlets are cross-cutting.

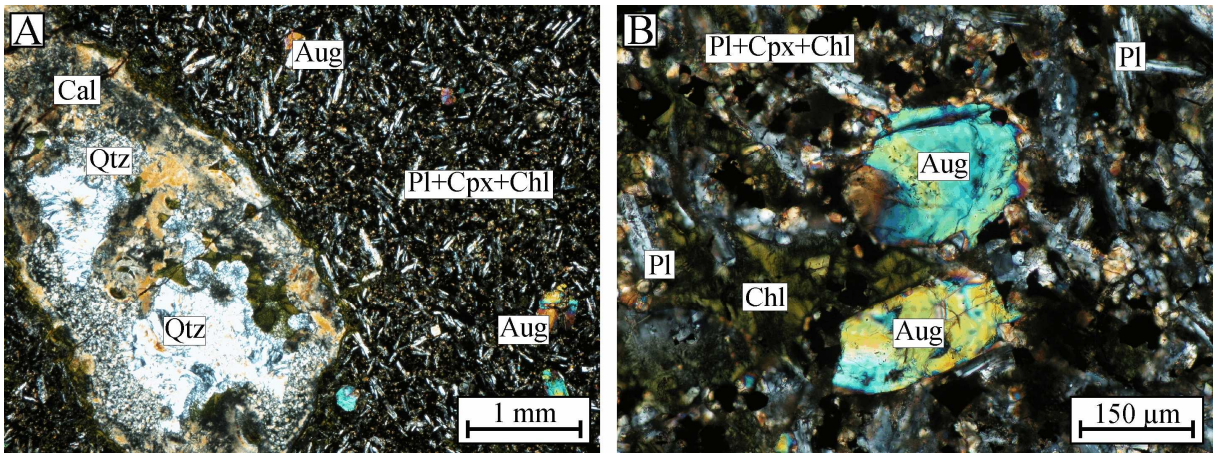

Fig. 56: Photomicrographs of the Emeishan basalt reference sample BI-2 (A/B: transmitted light/crossed polars).

1.6.3.2 MAJOR AND TRACE ELEMENT COMPOSITION

The major and trace element characteristics of the Paleng porphyritic basalt (sample JI-26) are similar to those of the Emeishan basalt reference sample from Binchuan (BI-2). The porphyritic basalt has 50.3 wt% SiO_2, 2.6 wt% TiO_2, 11.9 wt% Fe_2O_3(t), 4.9 wt% MgO and 9.7 wt% CaO. The Emeishan basalt reference sample (BI-2) has 46.6 wt% SiO_2, 3.0 wt% TiO_2, 15.3 wt% Fe_2O_3(t), 5.0 wt% MgO and 10.8 wt% CaO (Appendix Table 10). The LOI values of the two rocks are 2.0 wt% and 1.8 wt%, and suggest only minor hydrothermal alteration. However, it appears likely that the Paleng porphyritic basalt (JI-26) has suffered sodium loss, as it has only 0.7 wt% Na_2O. The Mg-numbers are 49.1 for the porphyritic basalt and 43.3 for the Emeishan basalt reference sample (Table 14).

According to TAS, the Paleng porphyritic basalt and the Emeishan basalt are classified as subalkaline basalt (refer to Fig. 52A). The rocks are low in potassium (0.6 and 0.9 wt% K_2O) and plot in the medium-K field of the calc-alkaline series (Fig. 52B). The basaltic character is confirmed by immobile element plots such as the SiO_2 vs. Zr/Ti and the Zr/Ti vs. Nb/Y diagrams of Winchester & Floyd (1977) (refer to Fig. 44C/D).

The normative mineral composition of the Paleng porphyritic basalt was calculated on the basis of the sodium content of the Emeishan basalt reference sample BI-2, i.e. 2.1 wt% Na_2O. The normative compositions (Kelsey, 1965; Middlemost, 1989) of the two rock units are very similar and are in accord with the microscopic observations, i.e. little normative

quartz, much anorthite-rich plagioclase and pyroxene, no olivine and no corundum (Table 14). The data match the petrographic descriptions published on basaltic lavas of the Emeishan flood basalt province (e.g. Ali *et al.*, 2005).

Table 14: CIPW norms and Mg-numbers for the Paleng porphyritic basalt sample JI-26 and the Emeishan basalt reference sample BI-2.

Sample ID	Quartz	Orthoclase	Albite	Anorthite	Diopside	Hypersthene	Magnetite	Ilmenite	Apatite	Mg #
JI-26	6.89	5.32	17.77	32.13	11.68	16.93	3.54	5.11	1.08	49.07
BI-2	2.17	3.65	17.73	27.60	20.43	15.92	4.52	5.88	0.87	43.25

Diagnostic trace element compositions for the two rocks are similar, e.g. 28 and 30 ppm Sc, 314 and 379 ppm V, 46 and 31 ppm Cr, 36 and 54 ppm Co, 42 and 56 ppm Ni, 343 and 409 ppm Sr, 35 and 38 ppm Y, 47 and 31 ppm Nb, 212 and 255 ppm Zr, and 374 and 348 ppm Ba. The rocks have high Ti/Y ratios of 449 and 478, and low Zr/Nb ratios of 4.5 and 8.1. The Th/Nb ratios are 0.12 and 0.19.

In general, the high Sr, Nb, Zr and Ba contents are suggestive of an intra-plate setting. On the primitive mantle-normalized multi-element plot of Figure 57 the Emeishan basalt reference sample and the porphyritic basalt of the Paleng complex show astonishing congruency and plot within the field of high-Ti Emeishan basalt reference data (Xiao *et al.*, 2003; Xu *et al.*, 2001). The strong enrichments over the whole element spectrum exclude an E-MORB setting (Wilson, 1989 and references therein). Further evidence comes from the low Zr/Nb ratios of 4.5 and 8.1 (Zr/Nb of MORB: 10 to >30; Wilson, 1989). The low concentrations in ferromagnesian elements such as Sc, Co, Ni and Cr suggest a rather evolved state of the basaltic melt, which likely has undergone olivine, spinel and clinopyroxene fractionation.

On the chondrite-normalized REE plot of Figure 58 the Paleng porphyritic basalt and the Emeishan basalt plot within the range of published Emeishan high-Ti basalt reference data (Xiao *et al.*, 2003; Xu *et al.*, 2001). However, for the porphyritic basalt a low-Ti affinity cannot be ruled out. $(La/Sm)_N$ for JI-26 and BI-2 are 2.8 and 2.9, and $(La/Yb)_N$ are 7.0 and 8.8. The Paleng porphyritic basalt has a slight negative Eu-anomaly of 0.9, which might be suggestive of plagioclase fractionation.

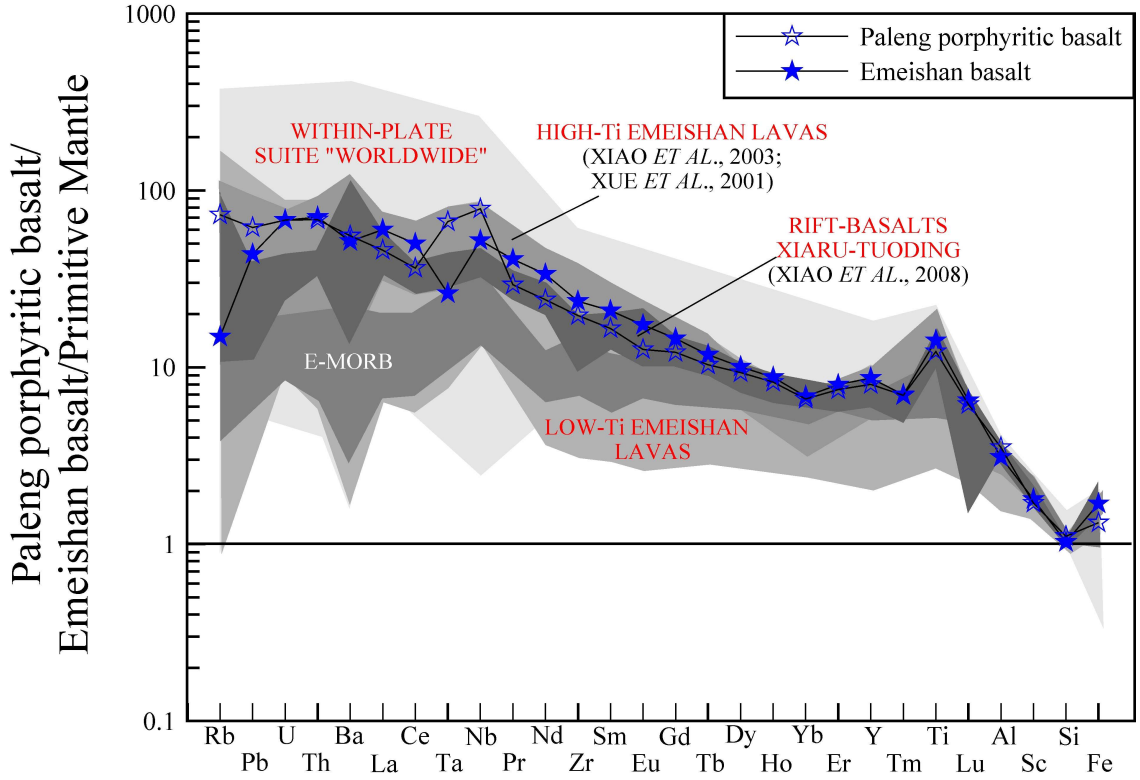

Fig. 57: Primitive mantle-normalized multi-element patterns for the Paleng porphyritic basalt and the Emeishan basalt reference sample BI-2. Additional reference data as cited in Fig. 53.

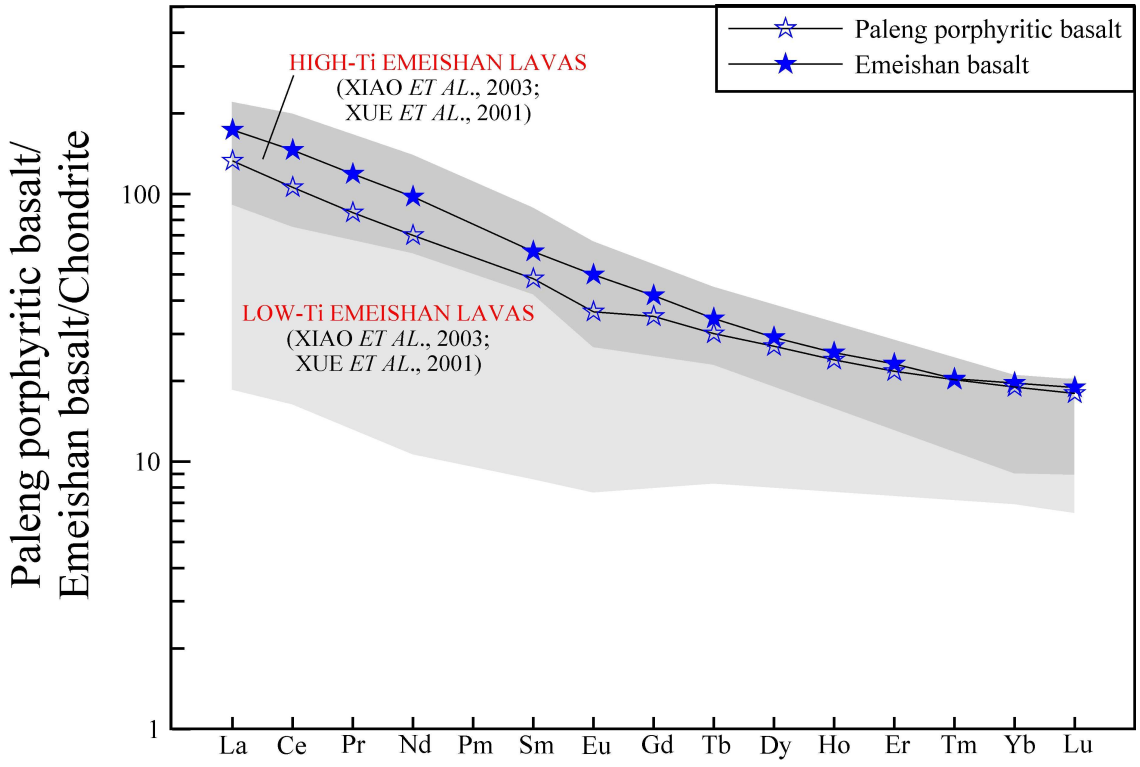

Fig. 58: Chondrite-normalized REE patterns of the Paleng porphyritic basalt and the Emeishan basalt reference sample BI-2 (McDonough & Sun, 1995).

If the Paleng porphyritic basalt is part of the ELIP, it cannot be classified with certainty as a member of the low-Ti or high-Ti basalt groups, as proposed by Xiao *et al.* (2003) for the Binchuan section. The TiO_2 content, as well as the Ti/Y ratio, are elevated, but not as high to be characteristic for high-Ti basalts, i.e. TiO_2 >3.7 wt% and Ti/Y >500, and not as low to be characteristic for low-Ti basalts, i.e. TiO_2 <2.5 wt%. This interestingly also applies for the Emeishan reference sample BI-2 from Binchuan, which suggests that the dataset of Xiao *et al.* (2003) is incomplete.

1.6.3.3 U–Pb ZIRCON GEOCHRONOLOGY

Analyzed zircons of the porphyritic basalt sample JI-26 appear very fresh on BSE images (Fig. 59). The light grey crystals (n = 15) are euhedral to subhedral and have typical magmatic shape. The zircons have 170-570 ppm Th and 370-3350 ppm U. The corresponding Th/U ratios range from 0.06 to 0.62 and provide evidence for the igneous origin.

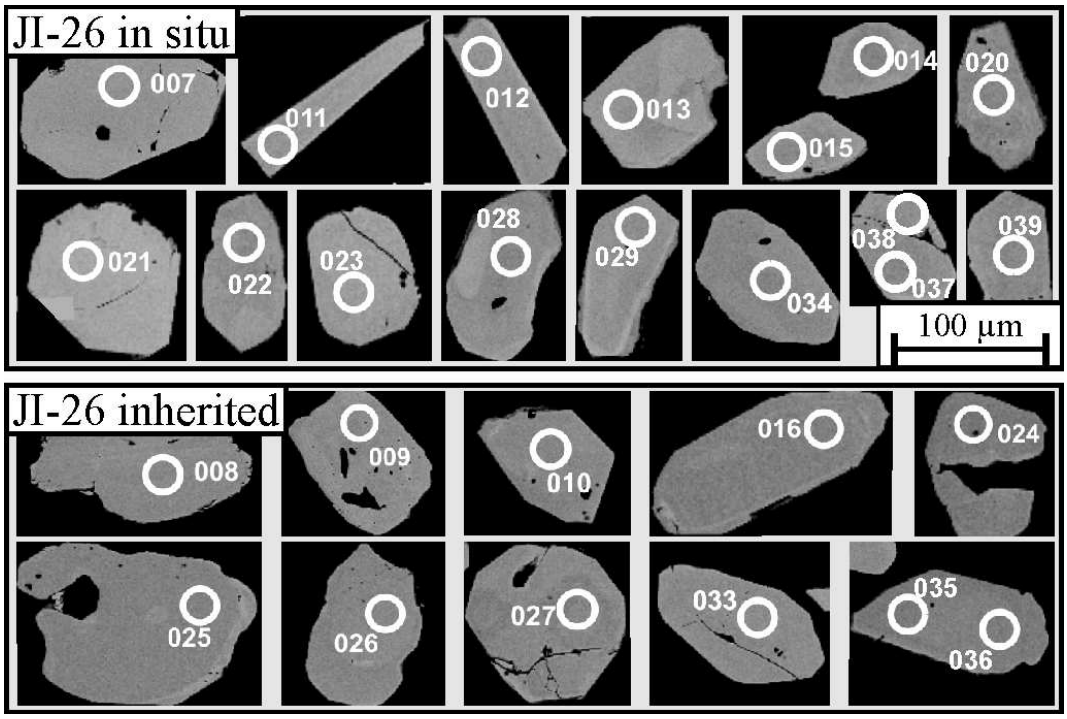

Fig. 59: BSE images of zircons of the Paleng porphyritic basalt. Spot locations are indicated.

Some inherited crystals appear darker on the BSE images and are characterized by cracks and enhanced corrosion (Fig. 59). Poor signals are restricted to the most corroded and broken crystals at spot locations 9, 24 and 33 and are possibly due to Pb loss. All other grains have

55-390 ppm Th and 31-510 ppm U. The resulting Th/U ratios of 0.22-2.77 are suggestive for a magmatic origin. The lowest Th/U ratios were obtained from the zircon grain at spot locations 35 and 36. The highest age of 2.75 Ga was obtained on spot 27.

The concordia age of the porphyritic basalt is 262 ±2 Ma (n = 17; four low-quality signals; Fig. 60A). The crystal shapes and the possible distinction between in situ and inherited crystals allow to interpret this age with confidence as the crystallization age.

The $^{206}Pb/^{238}U$ and $^{207}Pb/^{235}U$ ages for the inherited zircons are plotted in Figure 60B. The age data plot in three distinct groups at ~500-600 Ma, 850-1050 Ma and ~2.0-2.2 Ga. One zircon stands out with a Late Archean age of ~2.75 Ga.

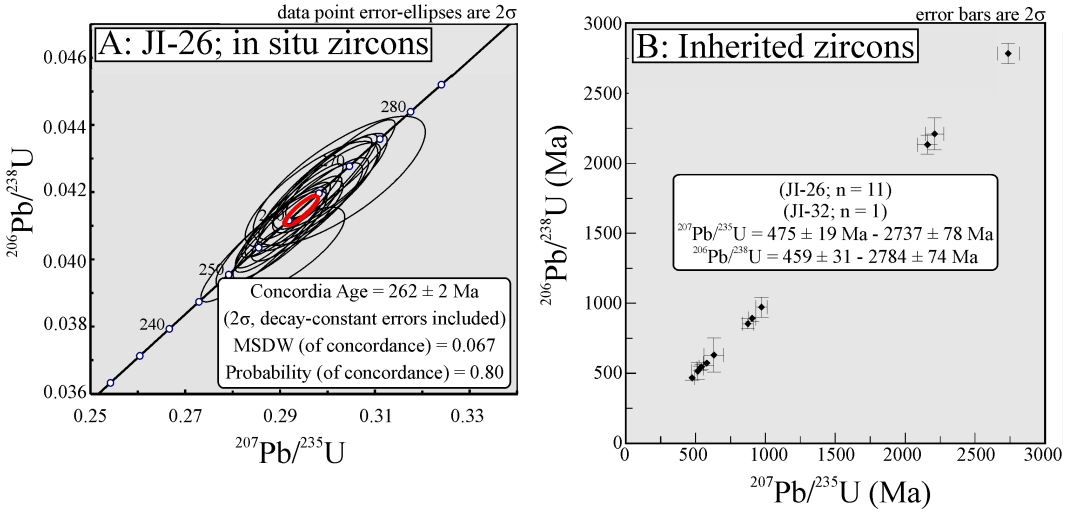

Fig. 60A: U–Pb concordia plot for the Paleng porphyritic basalt. B: $^{206}Pb/^{238}U$ vs. $^{207}Pb/^{235}U$ plot for inherited zircons of the Paleng porphyritic basalt sample JI-26 and of the Paleng amphibole gabbro sample JI-32.

1.6.3.4 Sr–Nd ISOTOPIC COMPOSITION

The initial εNd-value for the whole-rock sample JI-26 of the Paleng porphyritic basalt is 3.0 (calculated for t = 260 Ma; Table 15; refer to Fig. 50). This is within the data range of the ELIP and "old" Western Indian MORB (Mahoney *et al.*, 1998; Xu & Castillo, 2004). The high initial Sr isotopic composition of 0.709 is likely due to hydrothermal overprint or weathering, but may also be suggestive of crustal contamination.

Table 15: Sr–Nd isotopic composition of the Paleng porphyritic basalt sample JI-26.

Sample ID	Rock type	Age	Sm	Nd	$^{147}Sm/^{144}Nd$	$^{143}Nd/^{144}Nd$	2σ	εNd(t)	Rb	Sr	$^{87}Rb/^{86}Sr$	$^{87}Sr/^{86}Sr$	2σ	$(^{87}Sr/^{86}Sr)t$
		Ma	ppm	ppm					ppm	ppm				
JI-26	Porphyritic basalt	260	7.2	31.6	0.13716	0.512691	0.000004	3.01	49.7	357.9	0.401760	0.710556	0.000010	0.709070

1.6.4 DISCUSSION OF AGE DATA

1.6.4.1 INHERITED ZIRCONS

The Archean zircon (2.75 Ga) correlates in age with various Late Archean (Randian) rocks and zircons on the Yangtze Block. For instance, with Archean gneiss from the Kongling complex at Yichang (3.0-2.9 Ga; Qiu *et al*., 2000), with detrital zircons of 3.0-2.9 Ga from bentonite at Kunming (Compston *et al*., 1992), with zircons of 3.2-2.5 Ga from trachyandesite at Maanshan (Anhui Province; Zhang *et al*., 2003), with inherited zircons from lamproite dikes in Hubei, Hunan and Guizhui Provinces (2.9-2.5 Ga; Zheng *et al*., 2006a), with inherited zircons of 2.8-2.7 Ga from alkaline rocks at Miyi, southern Sichuan Province (Liu & Zhang, 2004), with zircon grains of 2.8-2.5 Ga from the Cavinh Complex of northern Vietnam (Lan *et al*., 2003), and with an inherited zircon of 2.4 Ga from the Jinshajiang ophiolite (Jian *et al*., 2009b).

All these rock and zircon ages suggest widespread Late Archean crust on the Yangtze Block and the Randian inherited zircon adds additional evidence for cratonal blocks with Yangtze affinity in southern Yunnan.

The Paleoproterozoic zircons of 2.2-2.0 Ga correlate well with a Paleoproterozoic thermal event on the Yangtze Block assigned to the assembly of the supercontinent Columbia (Zhang *et al*., 2006a; Zhao *et al*., 2004). Zhang *et al*. (2006b) reported zircon overgrowths of 2.0 Ga from Liantuo (Kongling), Bryant *et al*. (2004) zircons of 2.0-1.8 Ga from granite at Dabie, and Zheng *et al*. (2006a) zircons of 2.0 Ga from lamproites on the central Yangtze Block. Upper intercept ages are given by Huang *et al*. (2006) for the Wulian granite of 2.0 Ga, for zircon cores of 1921 ±22 Ma on the Shuanghe quartzite (Ayers *et al*., 2002) and for zircon cores of 1816 ±14 Ma from the Shuanghe eclogite at Dabie (Wu *et al*., 2006). Zheng *et al*. (2006b) obtained on the Wumiao eclogite, Wumiao gneiss and Shuanghe gneiss depleted mantle and crust Hf model ages of 2.2-1.8 Ga. Inherited Paleoproterozoic zircons (1977 ±44 Ma) and Nd model ages (2.1-1.7 Ga) are reported from the close-by Lincang granite (Hennig *et al*., 2009; Peng *et al*., 2006). Helmcke *et al*. (2001) reported inherited zircons of 2.0-1.2 Ga from rhyolites east of the Lincang granite.

The third group of Neoproterozoic inherited zircons (1070-850 Ma) corresponds in age to a Neoproterozoic thermal event known on the Yangtze Block, for instance seen in depleted mantle Hf model ages of 1.24-0.82 Ga of inherited zircons at Wumiao and Shuanghe (Zheng *et al*., 2006b), Sm–Nd ages of 1057 and 820 Ma on eclogites of the Dabie orogen

(Jahn *et al*., 2005), granitic gneiss of 1007 ±14 Ma and zircon overgrowth of 1.3-1.0 Ga at Panzhihua (Li *et al*., 2002).

Probably, this event is related to the collision of the Yangtze and Cathaysia Blocks which resulted in the formation of the South China Block, correlating in time and space with the Grenville orogeny which formed the megacontinent Rodinia (e.g. Li *et al.*, 2002). The corresponding orogenic belt in southern China is referred to as Sibao or Jiangnan orogen and runs from Shanghai to the SW. Evidence for the suture zone is given by the 1-Ga-old Gan-Wan ophiolite belt (Chen *et al.*, 1991). The data (inherited zircons and Nd model ages) suggest that the Jiangnan orogen indeed can be traced southwestwards of the Red River-Ailaoshan Shearzone.

The Vendian to lower Cambrian zircons of ~600-500 Ma are similar in age to Neoproterozoic zircons of 691-622 Ma from alkaline rocks at Miyi (Liu *et al*., 2004), similar to inherited zircons of ~800-600 Ma from magmatic rocks of the Shusong area (Jian *et al*. 2009b), and similar in age to various granitoids in southern China. Genetic interpretations include a Neoproterozoic mantle plume beneath South China (Li *et al*., 2003), and post-orogenic collapse of the Yangtze-Cathaysia orogen (Wu *et al*., 2006).

1.6.4.2 THE PALENG COMPLEX AS POSSIBLE TEMPORAL LINK TO THE EMEISHAN LARGE IGNEOUS PROVINCE

The $^{40}Ar/^{39}Ar$ and U–Pb ages obtained for the Paleng gabbro are highly consistent, i.e. all ages, except those of JI-27, overlap within their analytical errors and define an age interval of 263-257 Ma for the intrusion/cooling of the Paleng gabbro. This is the first age constraint given on the Paleng complex and basically confirms the vague age estimate of Hercynian to Indo-China age (ca. 350-175 Ma) by Zhao *et al*. (1991).

SHRIMP U–Pb zircon studies on mafic to ultramafic intrusions related to the ELIP gave ages of 269-256 Ma and show significant clustering at ~260 Ma (e.g. Zhou *et al.*, 2002, 2005; Zhong & Zhu, 2006; for more detailed information refer to chapter 2.2). These ages are identical to the ages obtained for the Paleng gabbro and the porphyritic basalt, and suggest a genetic link of the Paleng complex with the ELIP.

1.6.4.3 TRIASSIC METAMORPHIC OVERPRINT

The $^{40}Ar/^{39}Ar$ age of 250.7 ±3.5 Ma on the Paleng amphibole gabbro sample JI-27 likely dates metamorphic overprint, as actinolitized hornblende is well known from retrograde greenschist metamorphosed rocks in SW China (e.g. Heppe, 2006). Interestingly, the obtained age is in accord to a Triassic metamorphic event (258 ±6 Ma to 243 ±5 Ma) reported from the Indochina Block, believed to be related to the Paleo-Tethys orogeny (Carter *et al*., 2001; Nam *et al*., 2001) and to published $^{40}Ar/^{39}Ar$ ages from the ELIP of 256-42 Ma, assigned to Mesozoic and Cenozoic overprint (Ali *et al.*, 2004; Boven *et al.*, 2002, Lo *et al.*, 2002).

1.6.5 TECTONOMAGMATIC ENVIRONMENT

1.6.5.1 AMPHIBOLE GABBRO CUMULATE SERIES

The Paleng gabbro is a cumulate rock, i.e. the usage of tectonic discrimination diagrams is sensu stricto not indicated. Nevertheless, the samples were plotted and most of them show the expected large scatter typical of cumulates combined with an affinity to arc magmatic rocks (Fig. 61A-E; Pearce, 1982, 1983; Pearce & Cann, 1973; Shervais, 1982). In general, the HFSEs (e.g. Y, Zr) are more depleted than for typical N-MORB, and the resulting high LILE/HFSE ratios, such as high Ba/Ce ratios of 2-20 and Ba/Zr ratios of 0.4-8, favor an arc setting over MORB or back-arc setting. The low Cr content of the rock suite suggests an island-arc setting as well (Pearce, 1982).

The Paleng amphibole gabbro has many features in common with the 306 ±5 Ma to 280 ±3 Ma-old Gicha complex (Fig. 62; Jian *et al.*, 2009a). 1) Both complexes are associated with a Permian arc, i.e. the Tuoba-Nanzuo Arc west of the Gicha complex, and the “Jinghong arc” east of the Paleng complex (Fig. 62; Hennig *et al.*, 2009; Mo *et al.*, 1993). 2) Both complexes are located between continental blocks. For the Gicha complex these are the Tengchong Block and the Chongshan metamorphic complex of Simao affinity, and for the Paleng complex these are the Lancang Block and the Simao Block. 3) Both complexes show a similar range in major and trace element compositions. However, the Paleng gabbro is not as rich in Na (<3.1 wt% Na_2O vs. >3.4 wt% Na_2O), inter alia a criterion that led Jian *et al.* (2009a) to classify the Gicha complex as back-arc rift related. The predominance of amphibole and plagioclase and their varying amounts in the Paleng amphibole gabbro cumulate are also known from other root zones of magmatic arcs (i.e. H_2O saturated

conditions), e.g. from the Bonanza arc on Southern Vancouver Island and from the Hohe Tauern Region in the Alpes (Carl *et al*., 1988; Larocque & Canil, 2008).

1.6.5.2 BASALTIC ANDESITE

For the basaltic andesite, the tectonic discrimination plots favor an island-arc regime, in accord with the major, trace and REE characteristics (Fig. 61A-F; Bailey, 1981; Gill, 1981; Pearce, 1982, 1983; Pearce & Cann, 1973; Pearce & Norry, 1979; Shervais, 1982). On the Sc/Ni vs. La/Yb diagram the andesite samples plot in the transition zone of “low-K oceanic-“ and “other oceanic island-arc” (Fig. 61F).

1.6.5.3 PORPHYRITIC BASALT

The Paleng porphyritic basalt has a chemical composition and age typical of the Emeishan flood basalt province. This is the first discovery of such rocks in the southern Lancangjiang zone (Fig. 62). On the Ti–Zr–Y diagram (Fig. 61A) the rock sample classifies as within-plate basalt (Pearce & Cann, 1973). Further evidence comes from the Ti vs. Zr; Zr/Y vs. Zr; Ti/Y vs. Nb/Y, Cr vs. Y, and Ti vs. Y/Nb diagrams (Fig. 61B-D; latter two not shown; Pearce, 1982, 1983; Pearce & Cann, 1973; Pearce & Norry, 1979; Winchester & Floyd, 1977). On the Ti vs. V plot an ocean island affinity is suggested for the porphyritic basalt (Shervais, 1982), however, it can be seen that the data of Xiao *et al*. (2008) show a wide spread from continental flood basalt to ocean island basalt and that the reference sample from Binchuan plots in between these two fields. The porphyritic basalt sample shows on most plots a marked similarity to Emeishan basalt reference data and to reference data of Xiao *et al*. (2008) from Xiaru-Tuoding (Fig. 61). All except one of the documented inherited zircons are from the porphyritic basalt sample JI-26. This applies to the petrogenetic interpretation as within-plate basalt as well, considering that the mantle melt might have entrained large amounts of crustal material during the onset/early phases of the ELIP formation.

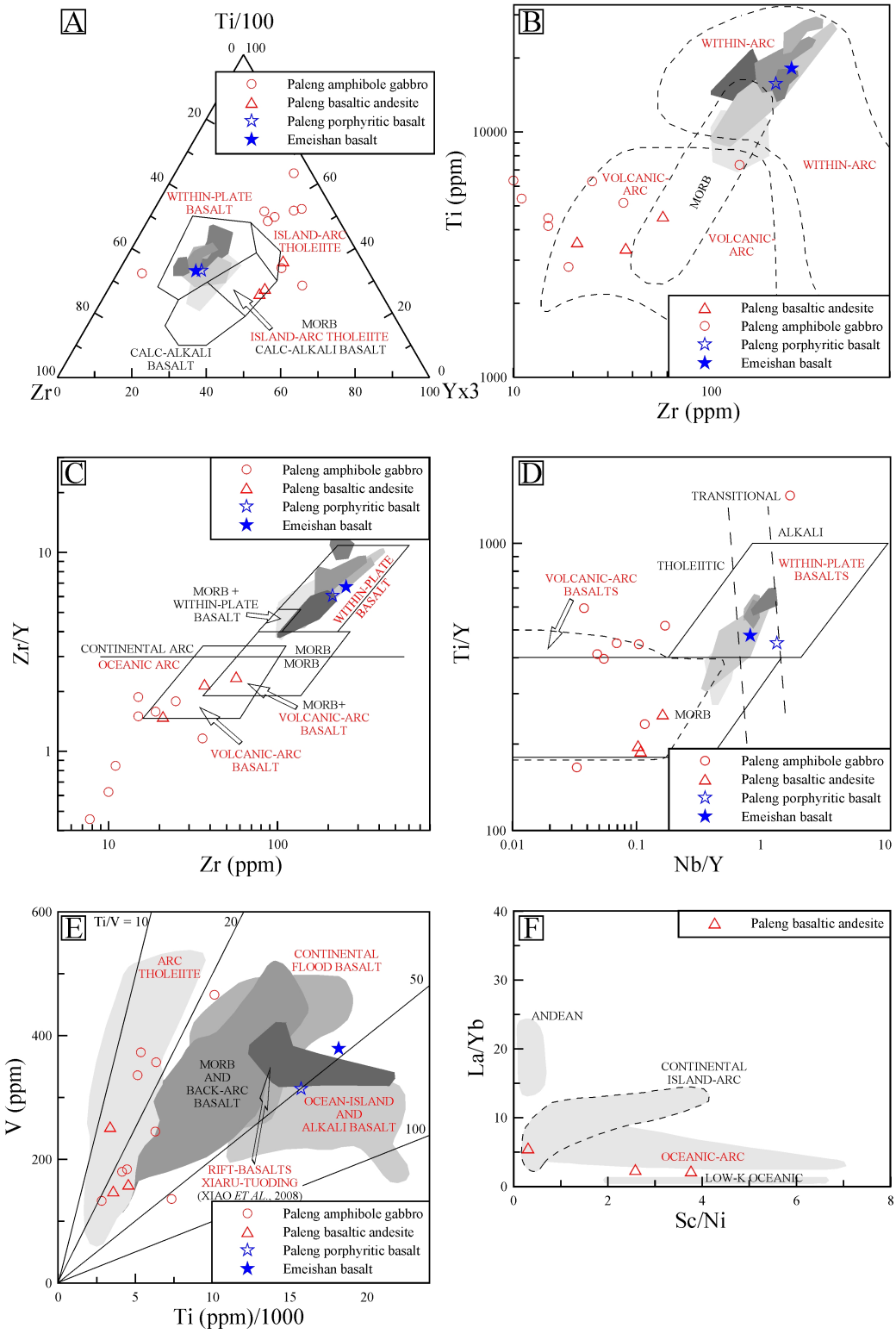

Fig. 61A-D: Tectonic discrimination diagrams for the Paleng rock suite. The Paleng amphibole gabbro shows an affinity to “volcanic-arc basalt”, the Paleng basaltic andesite plots as “volcanic-arc basalt”, and the porphyritic basalt and the Emeishan basalt reference sample plot as “within-plate basalt”. E: The V vs. Ti diagram classifies the Paleng gabbro and the Paleng basaltic andesite as arc magmatic. The Paleng porphyritic basalt and the reference sample of the Emeishan Large Igneous Province have a composition typical of continental flood and ocean-island basalts, and they are very similar to rift basalts of the Xiaru-Tuoding area. F: The tectonic discrimination diagram for andesites suggests for the Paleng basaltic andesite a composition typical of oceanic-arcs. References as cited in the text and in Fig. 29.

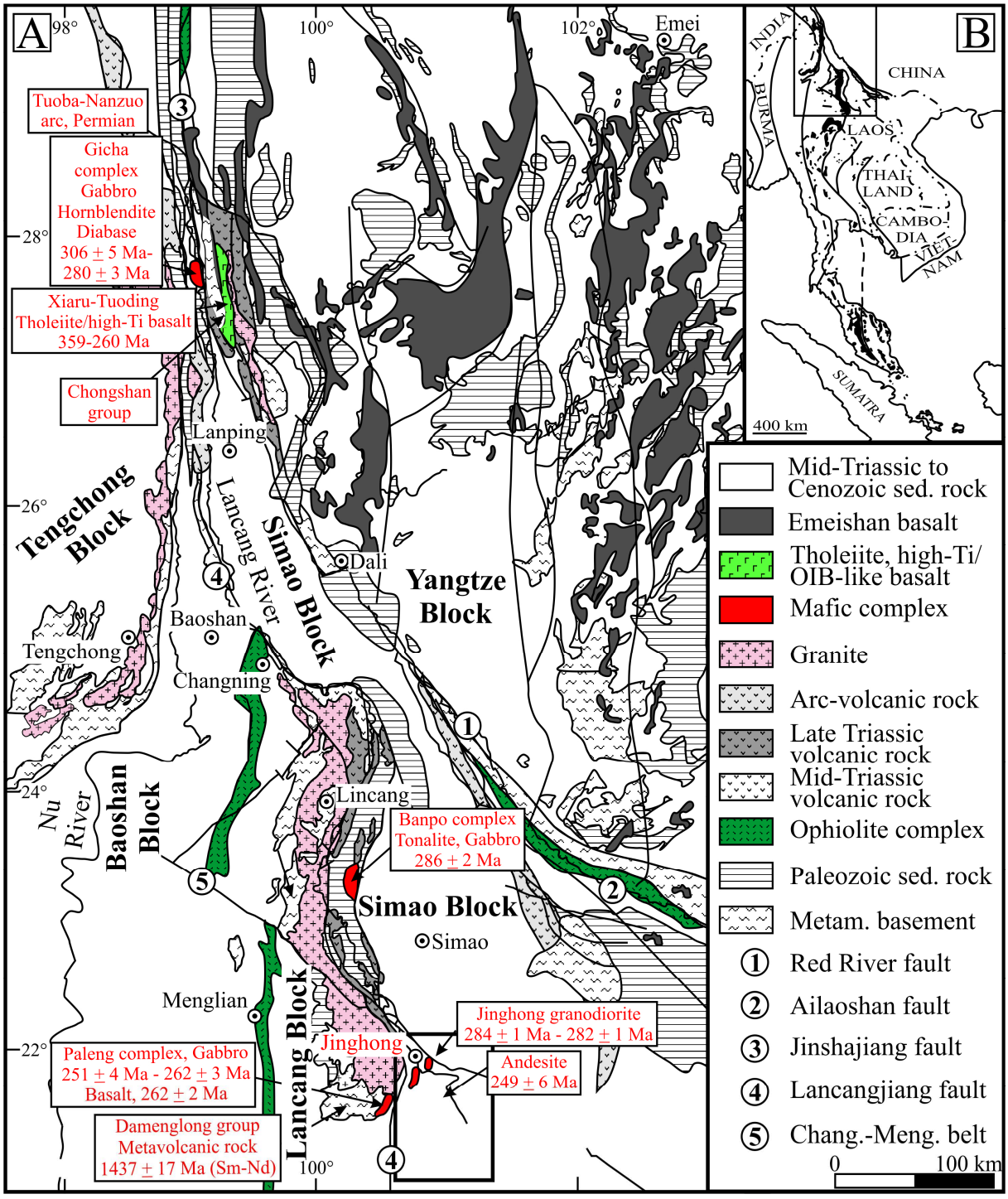

Fig. 62: Simplified geological map of the Lancangjiang zone in southwestern Yunnan (adapted from Ali *et al.*, 2005; Jian *et al.*, 2004, 2009a,b; Huang *et al.*, 2002 and Peng *et al.*, 2006, 2008). Labeled age data are SHRIMP U–Pb ages of Jian *et al.* (2009a,b), Peng *et al.* (2008) and own data.

1.7 JINGHONG TRACHYANDESITE SEQUENCE (PERMIAN/TRIASSIC?)

The Jinghong trachyandesite samples JI-12-JI-14 and JI-16-JI-18 plot in a ~3 km-long, N–S extending corridor on the magmatic map of Yunnan (Fig. 63; YBGMR, 1990). This map shows for the sample localities a mid-Triassic magmatic belt composed of diorite. Zhou (personal communication, 2007) classifies the Jinghong trachyandesite by field relationships as fractionated Emeishan basalt. The trachyandesite rests - similar to the Emeishan basalt - on an extensive suite of limestone. Peng *et al*. (2008) obtained on a very close-by, arc-related andesite an Early Triassic U–Pb zircon age of 248.5 ±6.3 Ma.

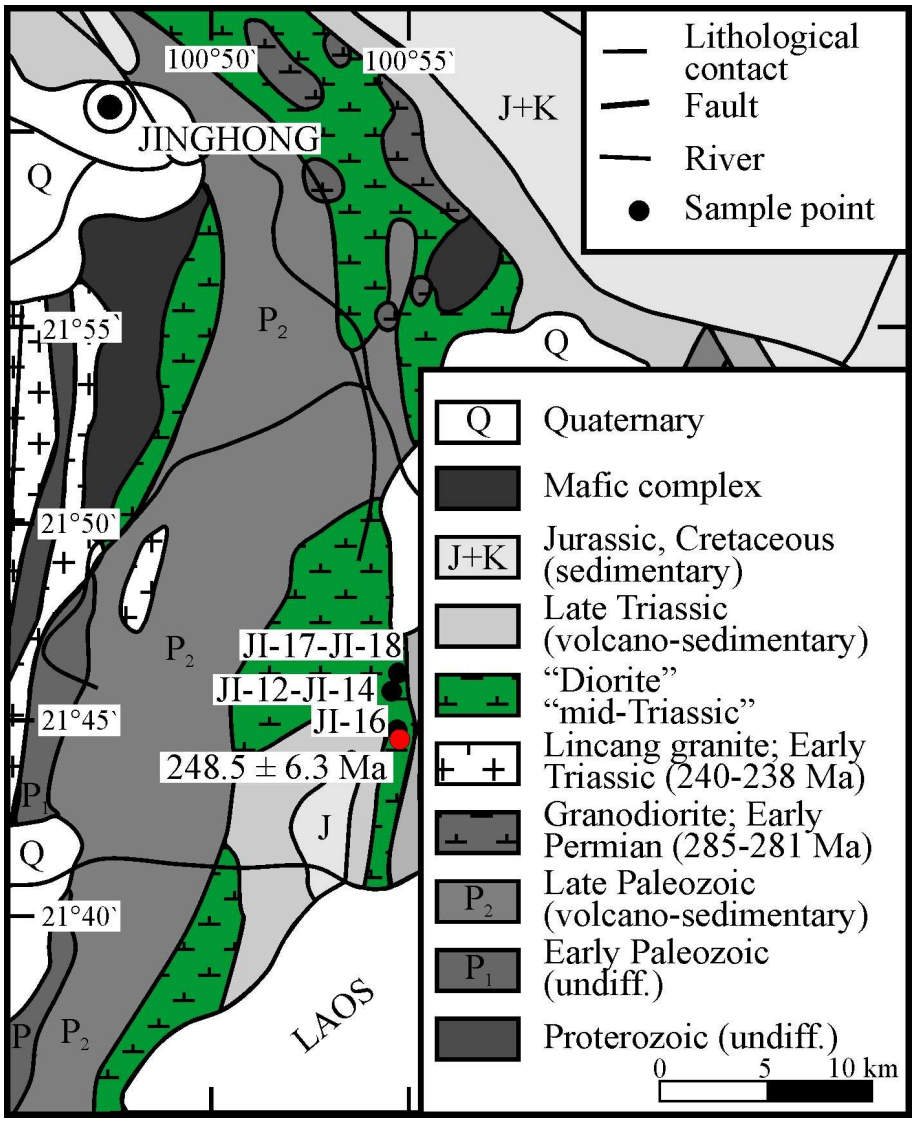

Fig. 63: Geologic overview map of the Jinghong area with sample locations of the Jinghong trachyandesite. Labeled U–Pb zircon age is from Peng *et al*. (2008).

1.7.1 PETROGRAPHIC DESCRIPTION

The trachyandesite samples JI-12 to JI-14 and JI-16 to JI-18 are composed of 30-70 vol% plagioclase, amphibole, clinopyroxene, biotite, K-feldspar and quartz phenocrysts, set in a trachytoid groundmass of very similar mineralogy (Fig. 64).

The plagioclase phenocrysts (0.2-4.0 mm) are sericitized, carbonatized and epidotized, and amount to ~60 vol% of the phenocryst total. Relics exhibit zoning, glomerocrystic growth and tectonic twinning (Fig. 64A-D). Optical analysis (on sample JI-14) gave an andesinic composition (33 mol% anorthite; Rittmann, 1929). Seriate, subhedral amphibole phenocrysts, altered clinopyroxene and biotite relics (30 vol% of phenocryts; 0.2-3 mm) are opacitized and altered to chlorite (clinochlore by XRD), carbonate, epidote, quartz and limonite (Fig. 64E/F). K-feldspar phenocrysts (predominantly orthoclase) are moderately sericitized (15 vol% of phenocrysts; 0.2-2.5 mm). Subhedral quartz is 0.2-0.5 mm in size.

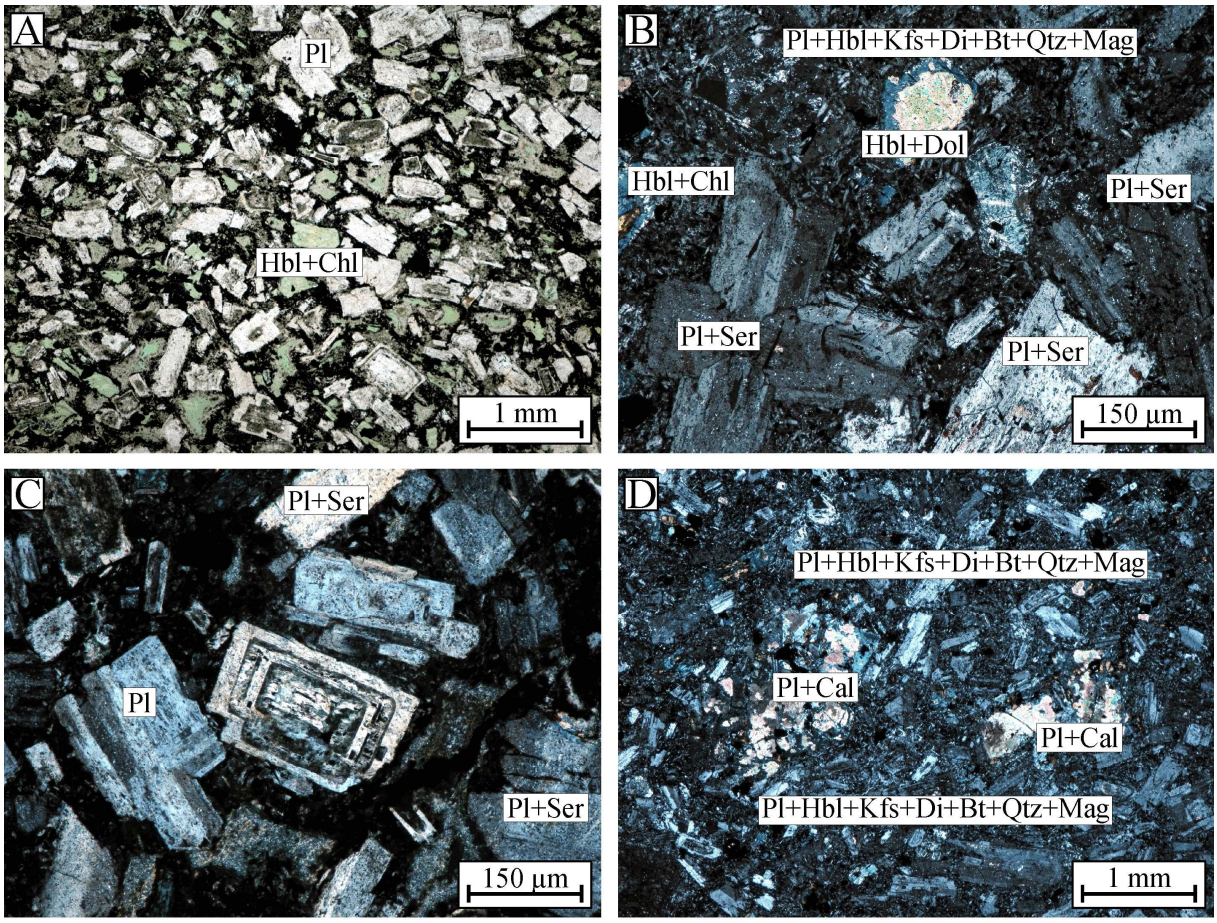

Fig. 64: Photomicrographs of the Jinghong trachyandesite samples (A/C: JI-13, B/D: JI-16; A: transmitted, plane-polarized light, B-D: transmitted light/crossed polars).

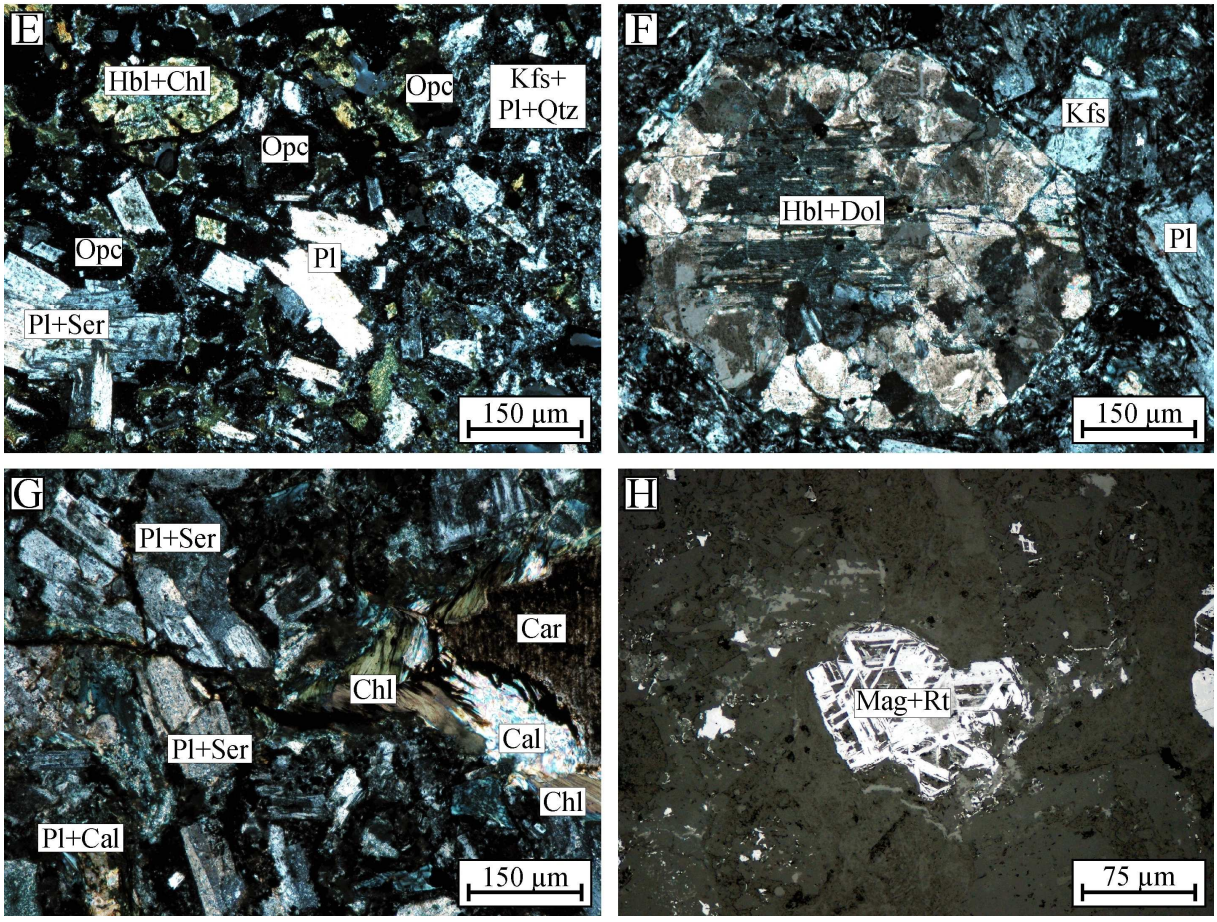

Fig. 64 continued: Photomicrographs of the Jinghong trachyandesite samples (E/F/H: JI-14, G: JI-13; H: reflected, plane-polarized light, E-G: transmitted light/crossed polars).

The seriate, moderately to strongly altered groundmass is composed of subhedral amphibole, plagioclase, K-feldspar, clinopyroxene, biotite and quartz (0.015-0.2 mm). Accessories include secondary titanite, rutile and zircon (all <0.01 mm). The rock mode is estimated at 30 vol% plagioclase, 20-25 vol% amphibole, 20-25 vol% K-feldspar, <15 vol% clinopyroxene, <10 vol% quartz, <5 vol% biotite and 5 vol% opaques, including hematite tons (<0.04 mm) and needles (<0.03 mm) from amphibole decay plus magnetite. The rock is cut by chlorite, carbonate, limonite and pyrite veinlets (Fig. 64B/C/G). Ti-rich magnetite depicts Ti-exsolution to rutile (Fig. 64H).

Samples JI-17 and JI-18 are set apart by two phenocryst generations. The first one comprises ~1 vol% of amphibole and plagioclase phenocrysts (2.0-3.0 mm) and the second includes subhedral, sericitized plagioclase (<0.6 mm), subhedral, kaolinitized K-feldspar, subhedral, chloritized amphibole and some pyroxene (all <1.0 mm).

1.7.2 MAJOR AND TRACE ELEMENT COMPOSITION

Hydrothermal alteration of the Jinghong trachyandesite samples JI-12-JI-14 and JI-16-JI-18 is confirmed by high LOI values of 3.3-6.6 wt%. However, on the TAS diagram, most samples plot coherently and suggest an alkaline trachyandesitic composition with affinity to basaltic trachyandesitic (Irvine & Baragar, 1971; Kuno, 1966; Le Maitre, 1989, MacDonald, 1968; MacDonald & Katsura, 1964; Fig. 65A). Rock classification by immobile element plots, such as the Zr/Ti vs. Nb/Y and Zr/Ti vs. SiO_2 diagrams indicate trachyandesitic and andesitic compositions (Winchester & Floyd, 1977; Fig. 65B/C).

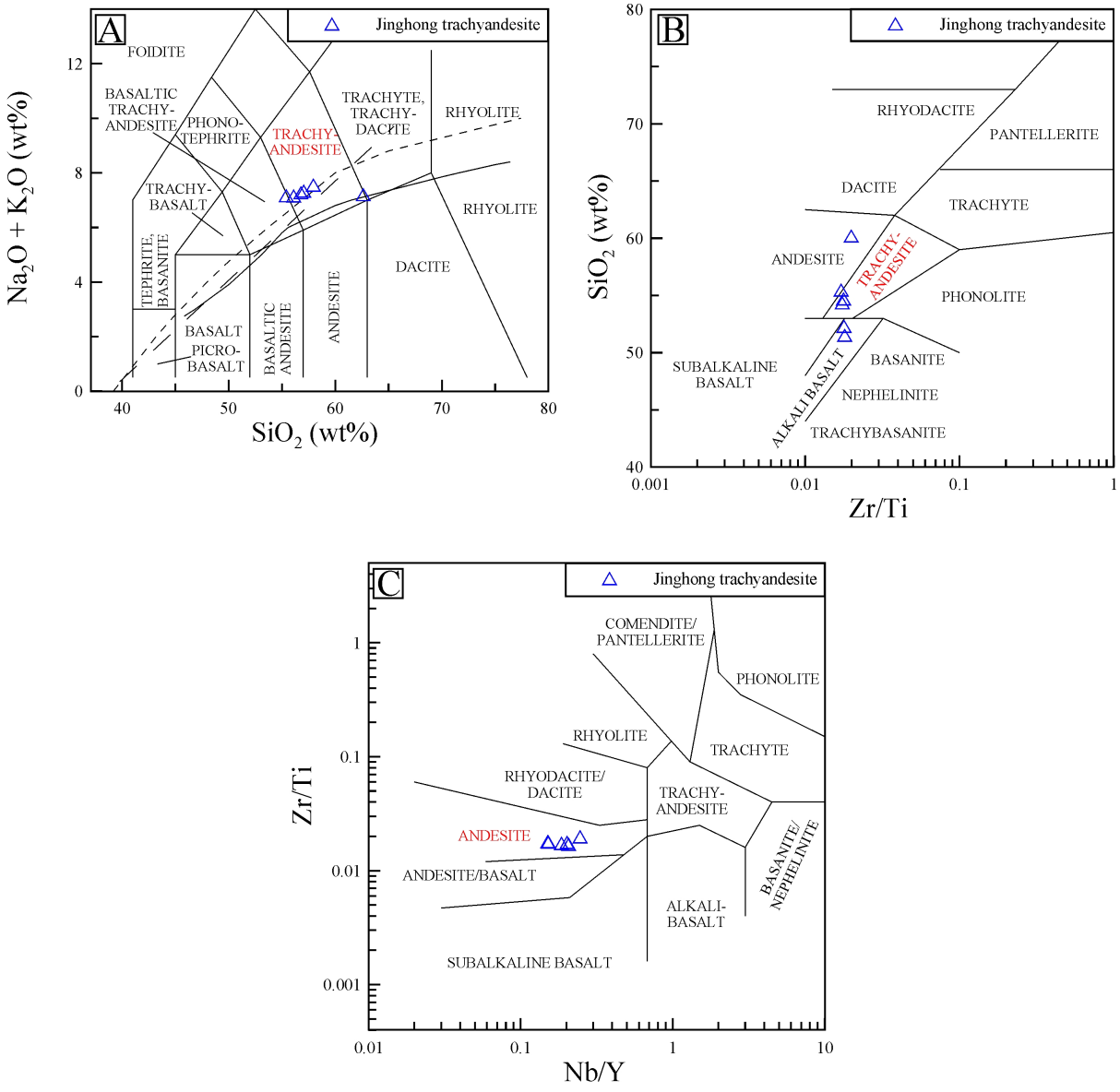

Fig. 65A: The Jinghong trachyandesite on the TAS diagram (Le Maitre, 1989). B/C: The Jinghong trachyandesite on immobile element plots of Winchester & Floyd (1977). All plots give a trachyandesitic to andesitic composition. References as cited in Figs. 5 and 21.

Trachyandesites can be subdivided into benmoreites (Na_2O-2 $\geq$ K_2O) and latites (Na_2O-2 < K_2O), i.e. samples JI-12 to JI-14 and JI-16 are benmoreitic, and samples JI-17 and JI-18 latitic in composition (Le Maitre, 1989). However, it cannot be ruled out that this feature may represent an alteration artefact, and I stay for simplicity with trachyandesite. The "latite", for instance, also has the highest LOI values of 6.3-6.6 wt%, in contrast to 3.3-3.9 wt% for the "benmoreitic" samples. Most likely, the high LOI values for the "latite" reflect water in kaolinite (refer to chapter 1.7.1). However, it cannot be excluded that the high K content may reflect crustal contamination.

Caculated CIPW norms for the sample suite are listed in Table 16. Samples JI-17 and JI-18 have correspondingly the highest normative quartz, corundum, orthoclase, and lowest albite and anorthite contents, and suggest a more evolved composition (Kelsey, 1965; Middlemost, 1989). In general, the norms are, except for high corundum (likely due to kaolinitization), in accord to published CIPW norms for trachyandesite and latite (Le Maitre, 1976).

Table 16: Calculated CIPW norms and Mg-numbers for the Jinghong trachyandesite samples. Calculations as cited in Table 2.

Sample ID	Quartz	Corundum	Orthoclase	Albite	Anorthite	Hypersthene	Magnetite	Ilmenite	Apatite	Mg #
JI-12	4.88	1.67	10.43	47.12	12.90	13.73	6.07	2.18	0.40	47.66
JI-13	5.58	3.97	10.39	46.67	9.20	15.23	5.69	2.26	0.41	54.57
JI-14	13.58	1.51	6.97	50.97	8.79	10.58	4.98	1.74	0.36	45.05
JI-16	4.95	0.87	11.19	47.90	15.20	11.48	5.22	2.25	0.41	47.63
JI-17	9.34	6.58	16.49	37.03	8.11	12.21	6.86	2.23	0.44	36.97
JI-18	10.83	6.71	17.58	35.38	7.82	11.72	6.59	2.26	0.44	37.34

The primitive mantle-normalized multi-element patterns of the Jinghong trachyandesite in Figure 66 plot coherently with minor variations for JI-17 and JI-18 to higher Rb and for JI-14 to lower Y, Ti, Sc and Fe, which generally suggests, in accord with petrography and calculated CIPW norms, a more evolved composition of these rocks. The drastic positive Ba offset of JI-14 (3396 vs. 1058-1209 ppm), however, points undoubtfully to hydrothermal alteration, as seen in barite on veinlets.

All patterns exhibit enrichments in the LILEs Rb, Pb and Ba over E-MORB (21.9-105 ppm Rb, 17.3-28.5 ppm Pb, 1058-3396 ppm Ba). The HFSEs, such as Th and U are markedly depleted (0.58-0.91 ppm U, 2.3-3.1 ppm Th). Ta and Nb show weak to moderate depletion relative to LREEs and MREEs (0.37-0.43 ppm Ta, 5.8-6.3 ppm Nb) and Y shows slight enrichment relative to the HREEs (22.0-32.2 ppm Y). These trace element

characteristics might suggest an island-arc setting for the Jinghong trachyandesite (e.g. Pearce, 1982). The trachyandesite data is in the range of volcanic arc reference data (Wilson, 1989, and references therein).

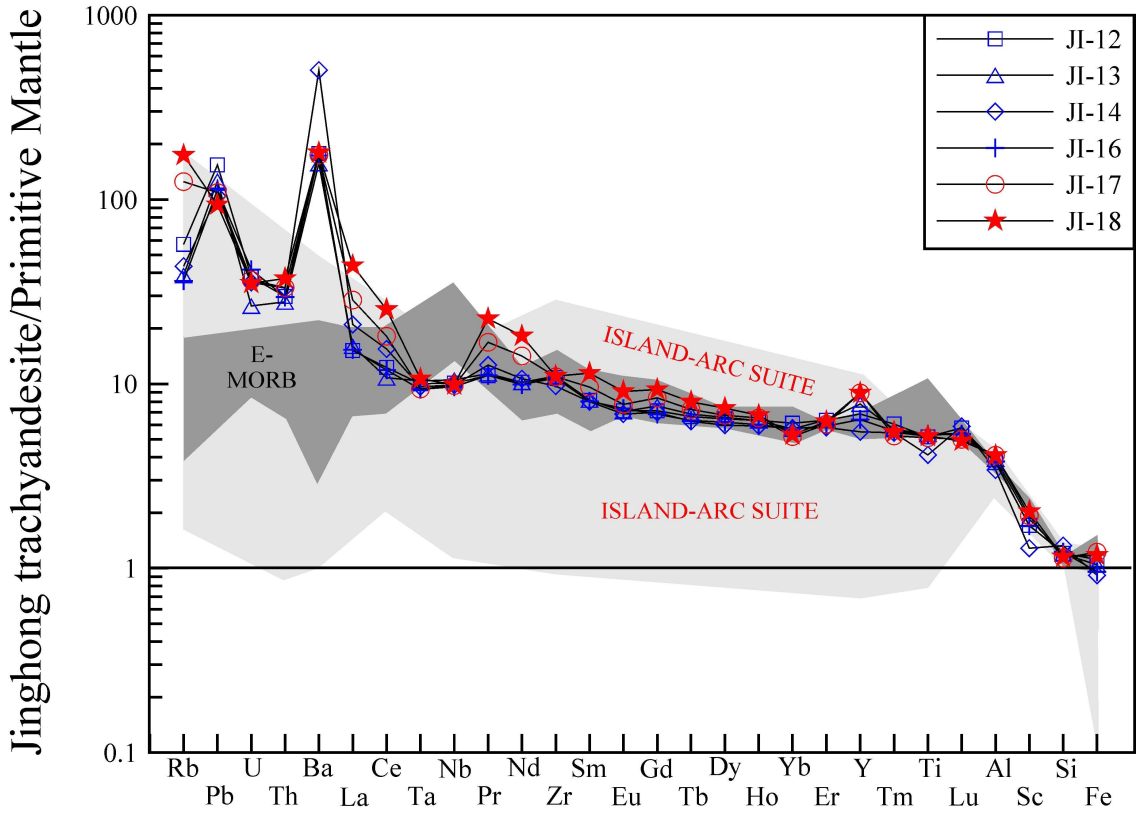

Fig. 66: Primitive mantle-normalized multi-element patterns for the Jinghong trachyandesite samples. Pb and Ba peaks are due to barite and galena (disseminated and on veinlets).

Trachyandesite reference data sorted by tectonic setting are plotted in Figure 67 (http://georoc.mpch-mainz.gwdg.de/georoc/Entry.html). Even though the data compilation does not allow a clear distinction by tectonic setting, the relatively high Sc contents (21.2-33.5 ppm Sc) argue against a classic rift-setting (medium grey polygon with black dashed line). Additional diagnostic trace element contents include 157-319 ppm V, low Cr (9-44 ppm Cr), low Co (14-26 ppm Co), low Ni (4-18 ppm Ni), and in combination with the low Ti/Y ratios of 168-242 and relatively low Zr contents (105-119 ppm Zr), an intra-plate setting appears unlikely, but cannot be ruled out.

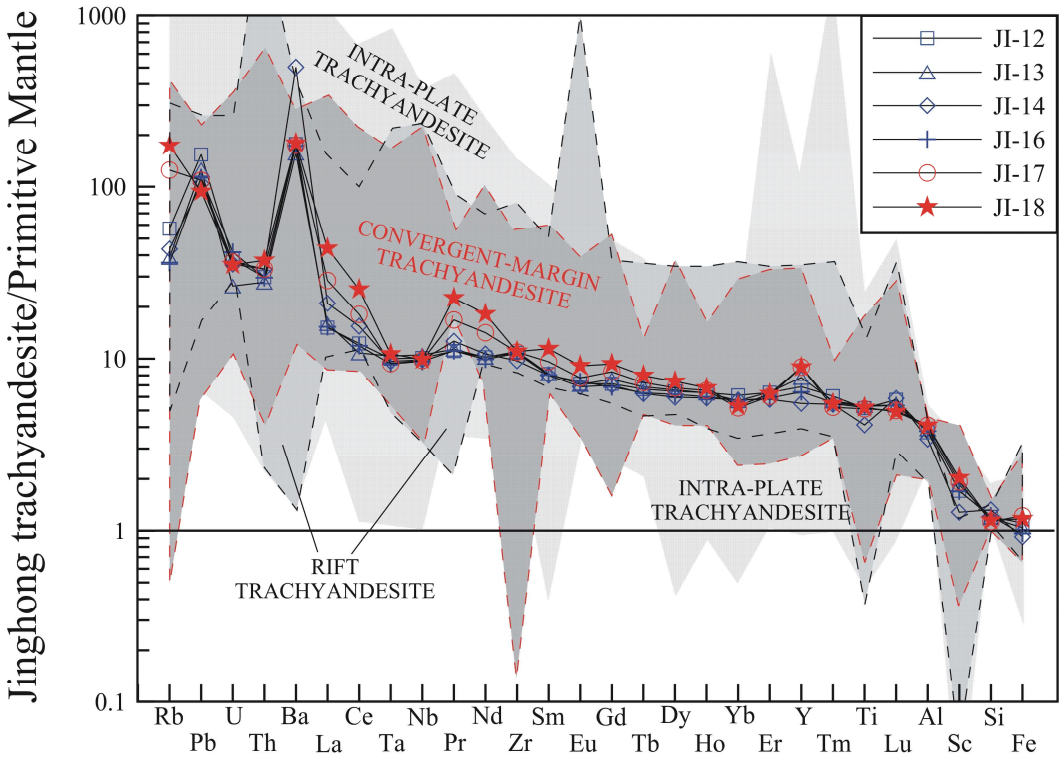

Fig. 67: Primitive mantle-normalized multi-element patterns for the Jinghong trachyandesite samples. Reference data are taken from the trachyandesite dataset of georoc (http://georoc.mpch-mainz.gwdg.de/georoc/Entry.html) containing 307 references and 1338 samples. Note: “Intra-plate” includes continental-flood basalt, ocean-island, seamount, oceanic plateau and intra-plate data. Primitive mantle data are from Palme & O`Neill (2004). Ba and Pb peaks for the trachyandesite samples are from hydrothermal barite and galena (veinlets and disseminated).

The chondrite-normalized REE patterns of the Jinghong trachyandesite samples in Figure 68 depict a well developed fractional crystallization series, ranging from the weakly fractionated samples JI-12, JI-13 and JI-16 (total REE: 69-70 ppm, $(La/Sm)_N$ = 1.9-2.0, $(La/Yb)_N$ = 2.5-2.8) to the moderately fractionated sample JI-18 (total REE: 130 ppm, $(La/Sm)_N$ = 3.8, $(La/Yb)_N$ = 8.3). All samples are characterized by a slight negative Eu-anomaly of 0.8-0.9, likely derived by plagioclase fractionation.

In comparison to worldwide latite and benmoreite REE data (http://georoc.mpch-mainz.gwdg.de/georoc/Entry.html) the composition of the Jinghong trachyandesite suggests a continental margin or intra-plate setting. A rift setting is less likely due to high HREE abundances of ~20 times chondritic, which favor a non-garnetiferous source in the upper mantle. The negative Ce-anomalies of the “latitic” samples JI-17 and JI-18 stress the higher alteration state of these samples.

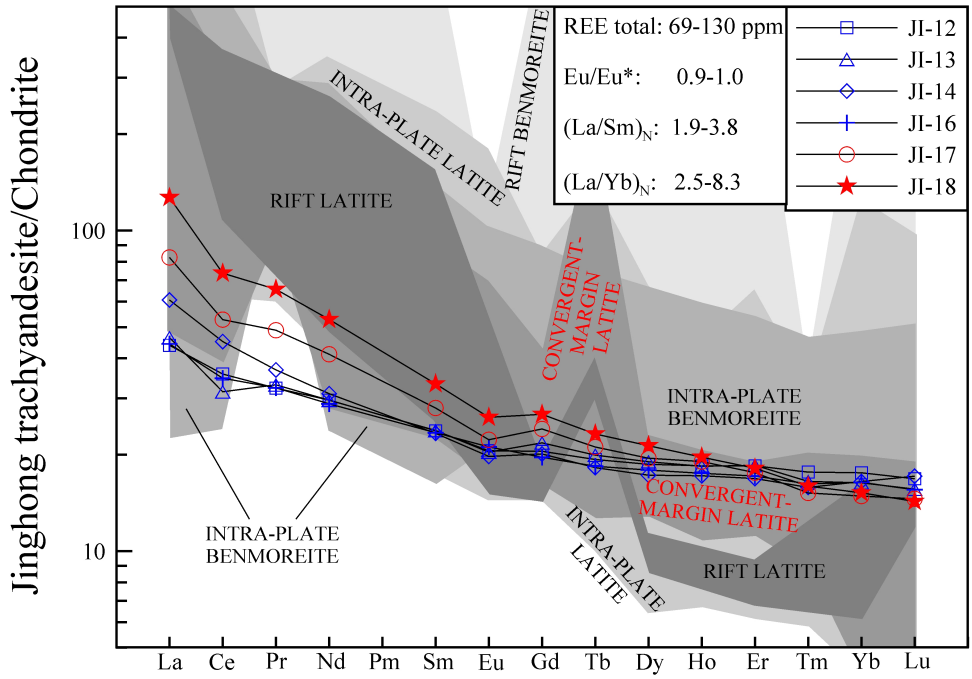

Fig. 68: Chondrite-normalized REE patterns of the Jinghong trachyandesite (McDonough & Sun, 1995). Reference data are taken from the benmoreite and latite datasets of georoc (http://georoc.mpch-mainz.gwdg.de/georoc/Entry.html) containing 124 and 114 references with 321 and 720 samples, respectively. Data screening includes filtering for whole-rock data, and sorting by geotectonic setting. Note: "Intra-plate" includes continental flood basalt, ocean-island, seamount, oceanic plateau and intra-plate data.

1.7.3 K–Ar GEOCHRONOLOGY

$^{40}Ar/^{39}Ar$ dating by incremental heating failed for the Jinghong trachyandesite sample JI-13, which is presumably due to the predominant carbonatization of this sample (refer to chapter 1.7.1). Carbonate causes large interferences in the mass spectrometer during thermal decomposition. Therefore two K–Ar age determinations (JI-13a and JI-13b) were tried on rock powders, which resulted in well defined, coherent ages of 103.2 ±5.2 and 100.1 ±5.0 Ma (Table 17). The K–Ar ages are interpreted to represent metamorphic overprint. The rock is believed to be older. Disappointingly, the samples have no zircon (proven by EMPA analysis), i.e. LA ICP-MS U–Pb age determinations on zircons were not possible.

Table 17: K–Ar age data for the Jinghong trachyandesite. For calculations see $^{40}Ar/^{39}Ar$ data tables in the Appendix.

	$^{40}Ar^*$ (divs)	2σ	Mass (g)	$^{40}Ar^*$ (cc/g)	2σ	K_2O (wt%)	2σ	t (Ma)	2σ
JI-13a	17342.49	32.42	0.00557	5.76E-06	1.08E-08	1.68	0.084	103.2	5.2
JI-13b	32800.51	104.76	0.01088	5.58E-06	1.78E-08	1.68	0.084	100.1	5.0

1.7.4 Sr–Nd ISOTOPIC COMPOSITION

The Jinghong trachyandesite sample JI-16 has initial ε_{Nd} of 3.4 and high initial $^{87}Sr/^{86}Sr$ of 0.7080 (calculated for t = 249 Ma; Table 18). As can be seen in Figure 69, the rock depicts similarities to the Jinghong dacite (refer to chapter 1.8) and affinity to the ELIP reference data (Qi & Zhou, 2008; Xu *et al*., 2001; Zhong *et al*., 2004; Zhou *et al*., 2006).

Table 18: Sr–Nd isotopic composition of the Jinghong trachyandesite.

Sample ID	Rock type	Age	Sm	Nd	$^{147}Sm/^{144}Nd$	$^{143}Nd/^{144}Nd$	2σ	ε_{Nd} (t)	Rb	Sr	$^{87}Rb/^{86}Sr$	$^{87}Sr/^{86}Sr$	2σ	$(^{87}Sr/^{86}Sr)t$
		Ma	ppm	ppm					ppm	ppm				
JI-16	Trachyandesite	249	3.7	14.9	0.15199	0.512741	0.000006	3.43	64.0	572.3	0.32337	0.709179	0.000005	0.708034

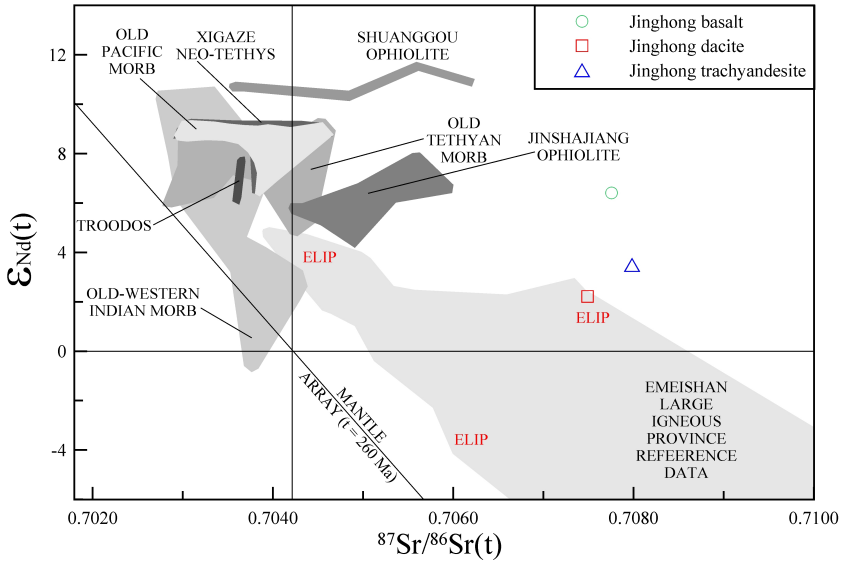

Fig. 69: $\varepsilon_{Nd}(t)$ versus $^{87}Sr/^{86}Sr(t)$ diagram for the Jinghong trachyandesite (t = 249 Ma), the Jinghong dacite (t = 249 Ma; refer to chapter 1.8) and the Jinghong basalt (t = 194 Ma; refer to chapter 1.10). Reference data as cited in Figs. 9 and 18.

1.7.5 DISCUSSION OF AGE DATA AND TECTONOMAGMATIC ENVIRONMENT

The Jinghong trachyandesite samples plot similar to the Jinghong granodiorite samples as arc-magmatic rocks on the tectonic discrimination diagrams of Pearce *et al*. (1984) (Fig. 41A/B). On the La/Yb vs. Sc/Ni tectonic discrimination diagram of Bailey (1981), especially the least-altered "benmoreitic" samples plot coherently in the "oceanic-arc" field (Fig. 41C). The age of the trachyandesite samples is probably identical to the Early Triassic U–Pb zircon age of 248.5 ±6.3 Ma on nearby arc-related andesite by Peng *et al*. (2008).

1.8 JINGHONG DACITE (249 ±3 Ma)

The porphyritic dacite samples JI-9-JI-10 and JI-48-JI-49 are derived from two different localities (Fig. 70). JI-9 and JI-10 plot on the combined geological and magmatic map of Yunnan next to the lithological boundary of Late Paleozoic volcano-sedimentary strata (P_2) and “mid-Triassic diorite” (YBGMR, 1990; Fig. 70). Samples JI-48 and JI-49 plot further north along the lithological contact of the mafic Huijingfang complex, “mid-Triassic diorite” and satellite intrusions of the Jinghong granodiorite. Peng *et al*. (2008) obtained on the same magmatic belt an Early Triassic U–Pb zircon age of 248.5 ±6.3 Ma on andesite.

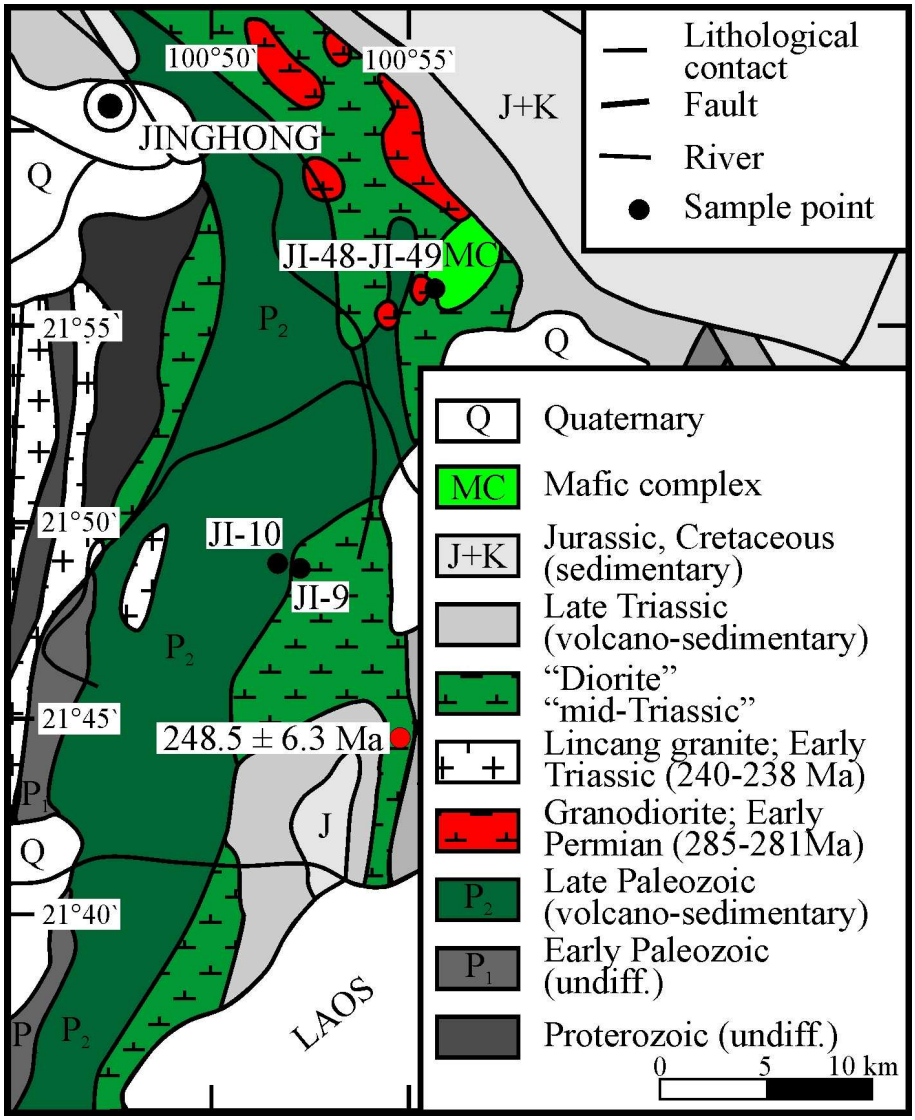

Fig. 70: Geologic overview map of the Jinghong area with sample locations of the Jinghong dacite. Labeled U–Pb zircon age is from Peng *et al*. (2008).

1.8.1 PETROGRAPHIC DESCRIPTION

The porphyritic dacite has 25-40 vol% of predominantly subhedral phenocrysts including tectonized, sericitized, partly zoned and corroded, glomerocrystic plagioclase (~30 vol% of phenocrysts; 0.1-5.0 mm), sericitized, muscovitized and kaolinitized orthoclase (~15 vol% of phenocrysts; 0.5-3.0 mm), opacitized and chloritized amphibole (~10 vol% of phenocrysts; <6.0 mm), chloritized biotite (~10 vol% of phenocrysts; <4.0 mm) and chloritized clinopyroxene (<5 vol% of phenocrysts; <2.0 mm). Corroded quartz (5-10 vol% of phenocrysts; 0.3-1.5 mm) is restricted to samples JI-9 and JI-10 (Fig. 71A-C). Alteration intensity increases from JI-9 over JI-10 to JI-48 and JI-49. The latter two samples depict intensive tourmalinization, affecting predominantly plagioclase phenocrysts by rosette-like mineral overgrowths (Fig. 71E). The second type of hydrothermal tourmaline is coarse-grained and fills vugs (Fig. 71F). The tourmalinized samples depict intensive opacitization of amphibole, which leads to calcite, chlorite, quartz, hematite and subordinate tourmaline (Fig. 71G).

The holocrystalline groundmass (<0.25 mm) of all rock samples is less altered but still exhibits hematitization, limonitization, epidotization and carbonatization, and consists predominantly of quartz, K-feldspar, chloritized amphibole, plagioclase, pyroxene and opaques. Accessories include apatite needles (0.06-0.5 mm), rutile “eggs” and titanite. The total rock mode is estimated at 10-25 vol% quartz, 30-40 vol% orthoclase, 20-25 vol% plagioclase, 10-15 vol% hornblende, <10 vol% biotite, <5 vol% clinopyroxene and <2 vol% opaques, whereas both magnetite and hematite could be localized in samples JI-9 and JI-10 (Fig. 71D). In samples JI-48 and JI-49 in contrast, hematite distinctly predominates (<5 vol%; 0.02-0.06 mm) (Fig. 71H). Hematite is partly derived from amphibole decomposition. Sample JI-9 has minute grains of sub- to anhedral chalcopyrite (<0.05 mm).

1.8.2 MAJOR AND TRACE ELEMENT COMPOSITION

TAS classifies the least-altered porphyritic dacite samples JI-9 and JI-10 as subalkaline dacite and the tourmalinized samples JI-48 and JI-49 as peralkaline (comenditic) trachyte (q = 9.4 wt%, A/CNK = 1.2, 100 x q / (q + an + ab + or) = 11.5 and Al_2O_3 >1.33 x $FeO_{(t)}$ + 4.4) (Irvine & Baragar, 1971; Kuno, 1966; Le Maitre, 1989; MacDonald, 1968; MacDonald & Katsura, 1964; Middlemost, 1975; Fig. 72A).

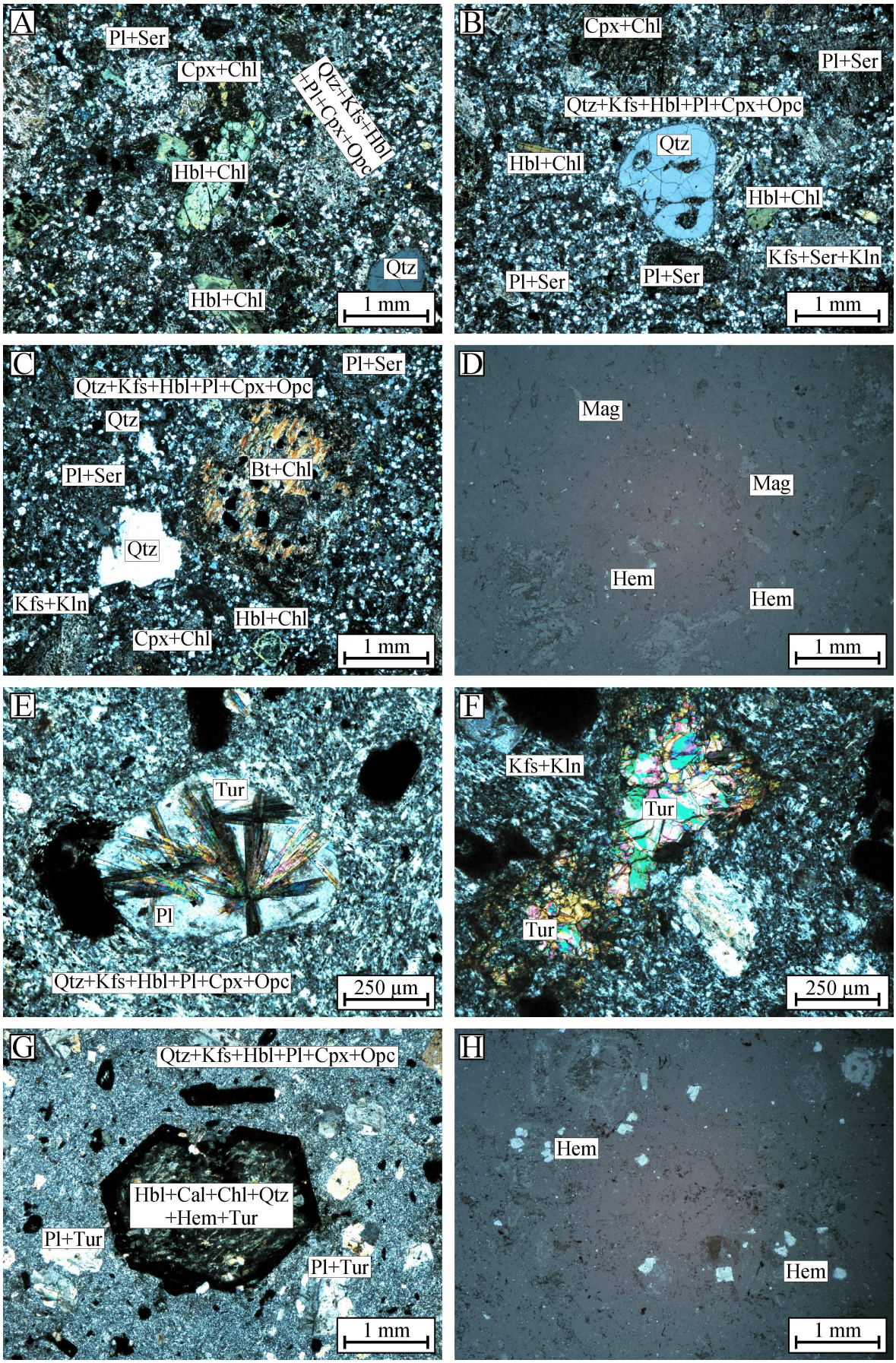

Fig. 71: Photomicrographs of the Jinghong dacite samples (A/C: JI-10, B/D: JI-9, E/F: JI-49, G/H: JI-48; A-C/E-G: transmitted light/crossed polars, D/H: reflected light/crossed polars).

The SiO_2 vs. Zr/Ti diagram suggests a dacitic composition for the least-altered and an andesitic composition for the tourmalinized samples, and the Zr/Ti vs. Nb/Y plot gives a dacitic composition for the complete dataset (Winchester & Floyd, 1977; Fig. 72B/C). The SiO_2 vs. K_2O plot suggests a high-K, calc-alkaline composition for samples JI-9 and JI-10, and a transitional, low-K/medium-K type for the tourmalinized samples (Fig. 72D; Carr, 1985; Ewart, 1982; Innocenti *et al.*, 1982; Le Maitre, 1989; Middlemost, 1985; Peccerillo & Taylor, 1976). On the AFM and FeO/MgO vs. SiO_2 diagrams the samples mimic the trend of the calc-alkaline Cascade lavas (Carmichael, 1964; Irvine & Baragar, 1971; Kuno, 1968; Fig. 72E) and for the Marianas calc-alkaline suite, respectively (Miyashiro, 1974; Fig. 72F).

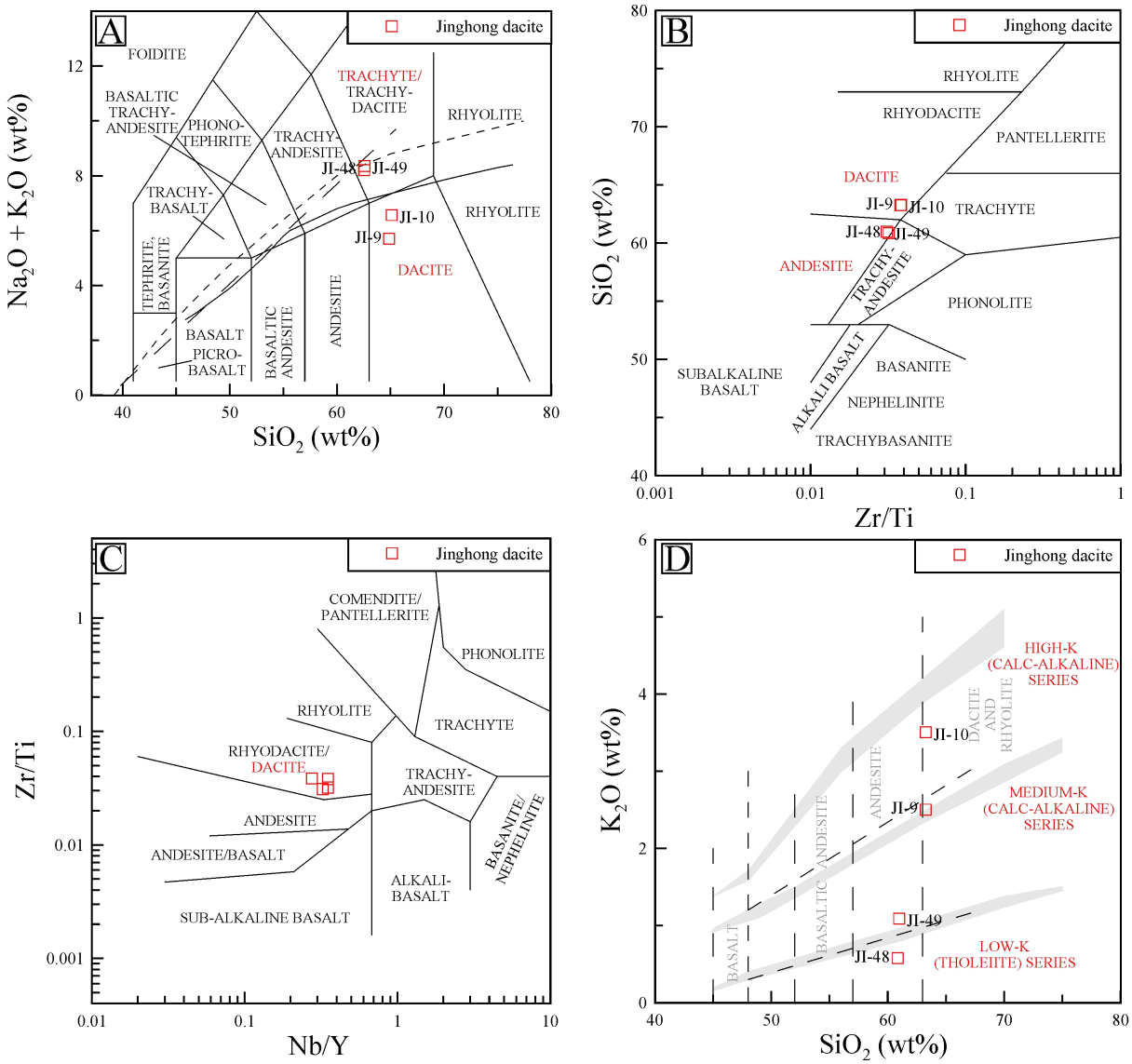

Fig. 72A: The Jinghong dacite samples on the TAS diagram (Le Maitre, 1989). B/C: The Jinghong dacite samples on immobile element plots of Winchester & Floyd (1977). D: The SiO_2 vs. K_2O plot for subalkaline rocks classifies the least-altered rocks of the Jinghong dacite as high-K type of the calc-alkaline series.

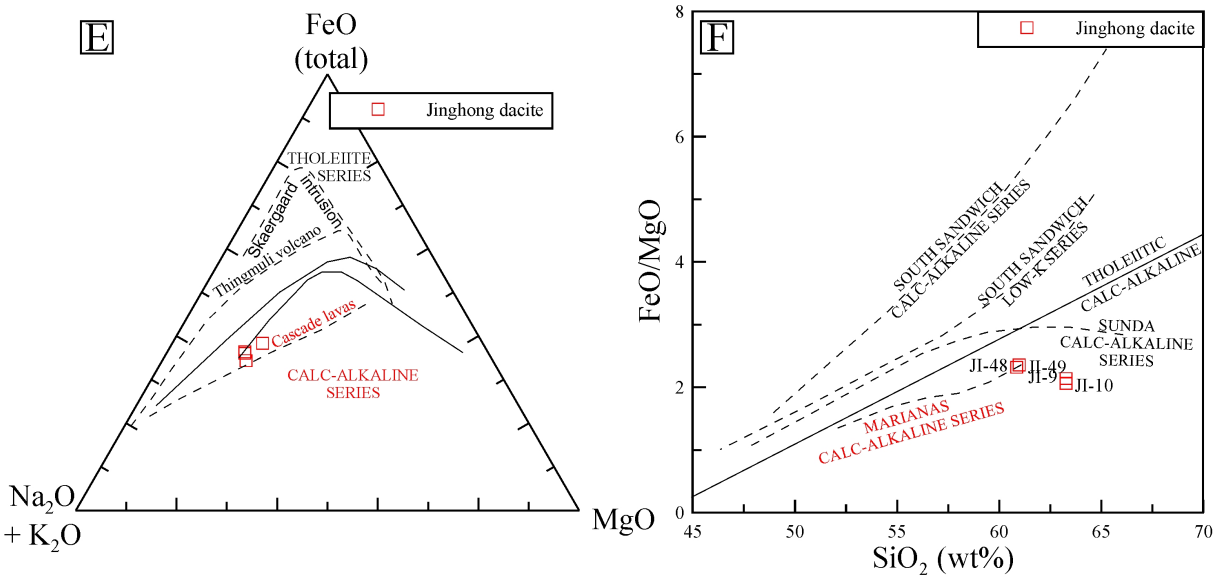

Fig. 72 continued; E: On the AFM diagram the Jinghong dacite samples mimic the fractionation trend for the calc-alkaline Cascade lavas (Carmichael, 1964; Irvine & Baragar, 1971; Kuno, 1968). F: The Jinghong dacite on the FeO/MgO vs. SiO_2 diagram. This plot suggests calc-alkalinity with a trend similar to the Marianas island arc (Miyashiro, 1974). Further reference data and subdivisions as cited in Figs. 5 and 21.

Samples JI-9 and JI-10 have a typical dacitic composition in terms of Ti, Al, Fe, Mg, Ca and P, i.e. 63.3 wt% SiO_2, 0.56-0.59 wt% TiO_2, 15.7-15.8 wt% Al_2O_3, 5.0-5.4 wt% Fe_2O_3, 2.2-2.3 wt% MgO, 3.9-4.4 wt% CaO and 0.15 wt% P_2O_5, but are relatively low in Mn and Na (0.07-0.08 wt% MnO, 2.9-3.1 wt% Na_2O) and high in K (2.5-3.5 wt% K_2O) (Le Maitre, 1976; Nockolds, 1954; Appendix Table 12). The LOI values of 2.2 wt% for JI-9 and 2.5 wt% for JI-10 correlate with the alteration assessment by petrographical studies and suggest moderate alteration only. CIPW norms are shown on Table 19 and correspond for the least-altered rocks to a typical dacite (Kelsey, 1965; Le Maitre, 1976; Middlemost, 1989).

Table 19: Calculated CIPW norms and Mg-numbers for the Jinghong dacite samples.

Sample ID	Quartz	Corundum	Orthoclase	Albite	Anorthite	Hypersthene	Magnetite	Ilmenite	Apatite	Mg #
JI-9	22.92	0.56	15.16	26.55	21.10	8.64	3.22	1.15	0.37	54.35
JI-10	21.34	0.37	21.30	25.08	19.06	8.12	2.97	1.09	0.35	55.27
JI-48	9.38	3.09	3.51	64.45	4.24	8.40	4.92	1.31	0.37	55.15
JI-49	9.39	2.63	6.61	61.20	4.51	8.61	5.07	1.27	0.36	54.75

The tourmalinized samples are lower in Si and K (60.9-61.0 wt% SiO_2, 0.58-1.1 wt% K_2O; and higher in Ti, Al, Fe, Mn, Mg and Na (0.65-0.67 wt% TiO_2, 17.0-17.3 wt% Al_2O_3,

6.6-6.8 wt% Fe_2O_3 (total), 0.1 wt% MnO, 2.6 wt% MgO and 7.1-7.4 wt% Na_2O). These systematic trends are well explained by a more primitive state of the two samples and correspond to the petrographic descriptions (e.g. no modal quartz). On Harker plots of MgO vs. immobile major elements such as TiO_2, Al_2O_3 and Fe_2O_3 (t) the dacite samples depict clear trends suggestive of fractional crystallization (not shown). The low Ca (1.0-1.1 wt% CaO) and high Na contents are likely artefacts of the prevalent tourmalinization.

The mantle-normalized multi-element plot of Figure 73 shows samples JI-9 and JI-10 plotting consistently with strong enrichments in the LILEs such as Rb, Pb and Ba (96-138 ppm Rb, 25.8-28.7 ppm Pb, 469-591 ppm Ba), and the strongly tourmalinized samples JI-48 and JI-49 with distinctly lower LILE abundances (17-26 ppm Rb, 3.2-3.3 ppm Pb, 271-475 ppm Ba). In immobile element concentrations, the samples are similar (0.7-1.0 ppm Ta, 7.7-8.4 ppm Nb, 121-135 ppm Zr, 23-28 ppm Y, 0.59-0.67 wt% TiO_2, 13.1-15.3 ppm Sc). Hence, it appears likely that the tourmalinization is, at least partly, responsible for the characteristic trace element pattern.

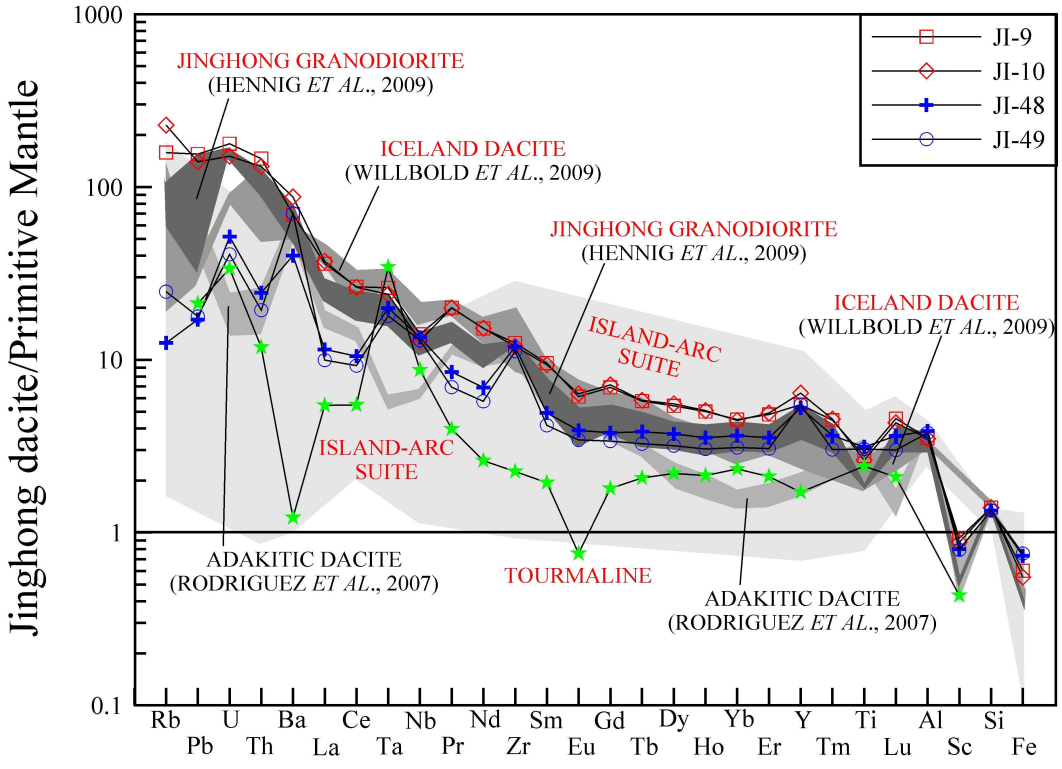

Fig. 73: Primitive mantle-normalized multi-element patterns for the Jinghong dacite (Palme & O`Neill, 2004). The least-altered Jinghong dacite samples JI-9 and JI-10 resemble arc-related granodiorite from the Jinghong area (Hennig *et al.*, 2009). The plotted tourmaline represents the average of three tourmaline analyses by Roberts *et al.* (2006). It appears likely that tourmalinization affected the primary element inventory of the Jinghong dacite.

In general, the low abundances of Nb, Ti and Sc are suggestive of a volcanic-arc setting (e.g. Pearce & Peate, 1995), and the low Sr/Y ratios of 11-17 generally exclude direct slab melting (e.g. Rodríguez *et al.*, 2007; Fig. 73). The least-altered rocks JI-9 and JI-10 depict marked similarities to the island arc related, nearby Jinghong granodiorite (Hennig *et al.*, 2009). For reference, dacite data from Iceland is plotted in Figure 73 (Willbold *et al.*, 2009). The Jinghong dacite samples JI-9 and JI-10 resemble - except for the HREEs - the Iceland dacite.

On the REE plot of Figure 74 the least-altered and more evolved dacite samples JI-9 and JI-10 are clearly set apart from the altered and more mafic samples JI-48 and JI-49. The negative Eu-anomalies of JI-9 and JI-10 (Eu/Eu* = 0.7-0.8) are likely due to plagioclase fractionation. The melts are not depleted in HREEs (Gd-Lu), which implies that they were not formed in the garnet-stability field, as adakitic rocks do (e.g. Rodríguez *et al.*, 2007).

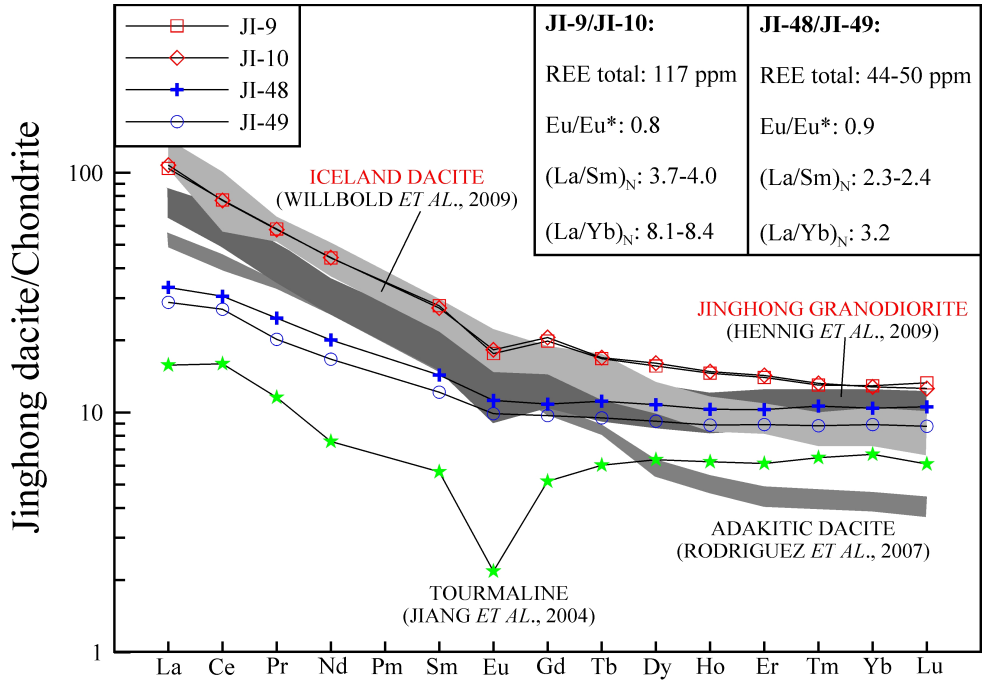

Fig. 74: Chondrite-normalized REE patterns of the Jinghong dacite samples (McDonough & Sun, 1995). The plotted tourmaline represents the arithmetic mean of five tourmaline analyses by Jiang *et al.* (2004).

1.8.3 U–Pb ZIRCON GEOCHRONOLOGY

U–Pb zircon geochronology was performed on a polished rock slab of the Jinghong dacite sample JI-49. Zircon location and documentation was done by EMPA. Three single zircon grains were analyzed at eight spot locations (15-20 µm). The isotopic data are compiled in Appendix Table 21 and the age data plots are shown in Figure 75.

The analyzed zircon grains are light grey in color, euhedral to subhedral and mostly developed as tetragonal pyramides, dipyramides and tabular prisms with length to width ratios of ~2. The grains appeared very fresh on the BSE images and have Th/U ratios of 0.49-2.11. Especially the $^{206}Pb/^{238}U$ ages are highly conclusive (probability of 1) and give an Early Triassic mean $^{206}Pb/^{238}U$ age of 248.5 ±3.3 Ma (Fig. 75A). The concordia plot verifies the age constraint and gives an identical lower intercept age of 248.8 ±3.7 Ma (Fig. 75B). The ages correspond exactly to the "higher error" age constraint on arc-related andesite of Peng e*t al*. (2008). The dates are interpreted as crystallization ages of the rocks.

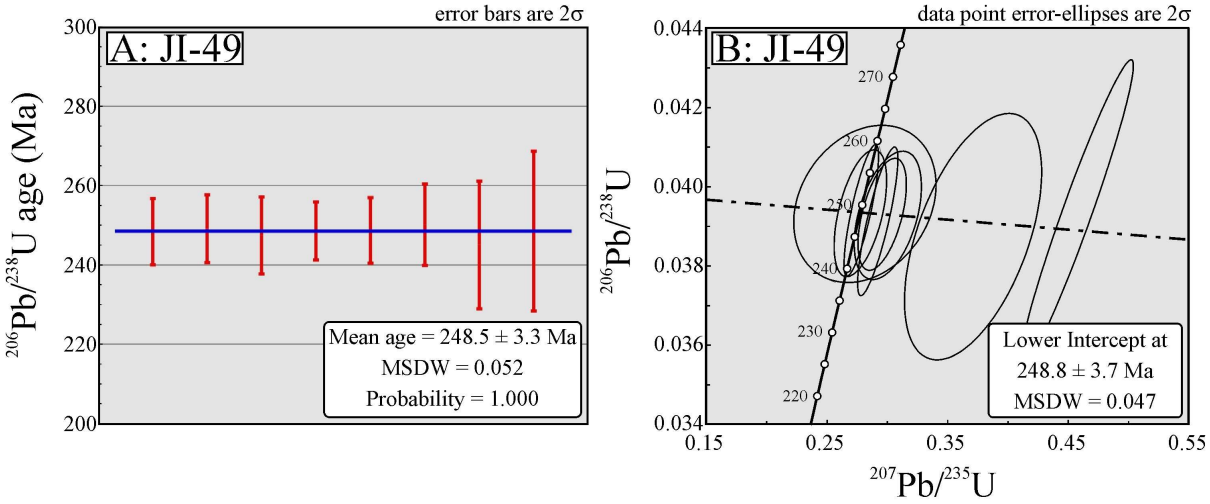

Fig. 75A: Mean $^{206}Pb/^{238}U$ age of eight spots analyzed on three zircon grains of the Jinghong dacite sample JI-49. B: Concordia plot of the Jinghong dacite. Both plots give identical rock ages.

1.8.4 Sr–Nd ISOTOPIC COMPOSITION

The strongly altered Jinghong dacite sample JI-49 has initial ε_{Nd} of 2.2 and high initial $^{87}Sr/^{86}Sr$ of 0.7075 (calculated for 249 Ma; Table 20; refer to Fig. 69). Based on the petrographic studies and the major and trace element compositions, it appears likely that the Sr isotopic signature is disturbed. Nevertheless, the isotopic characteristics link the Jinghong dacite to the Jinghong trachyandesite (refer to chapter 1.7).

Table 20: Sr–Nd isotopic composition of the tourmalinized Jinghong dacite sample JI-49.

Sample ID	Rock type	Age	Sm	Nd	$^{147}Sm/^{144}Nd$	$^{143}Nd/^{144}Nd$	2σ	ε_{Nd} (t)	Rb	Sr	$^{87}Rb/^{86}Sr$	$^{87}Sr/^{86}Sr$	2σ	$(^{87}Sr/^{86}Sr)t$
		Ma	ppm	ppm					ppm	ppm				
JI-49	Dacite	249	3.1	14.2	0.13254	0.512647	0.000006	2.22	29.3	263.6	0.32190	0.708630	0.000013	0.707490

1.8.5 TECTONOMAGMATIC ENVIRONMENT

The trace element characteristics of the Jinghong dacite suggest an arc environment, which is in good agreement with the tectonic discrimination diagram of Pearce *et al*. (1984) (refer to Fig. 41A/B; note: for clarity reasons, the Jinghong dacite samples are shown in green). On these diagrams the Jinghong dacite plots - similar to the Jinghong granodiorite and Jinghong trachyandesite - as “volcanic-arc granite”.

As the dacite has exactly the same age as arc-related andesite closeby (Peng *et al*., 2008), we suggest that the Jinghong dacite, the Jinghong trachyandesite and the andesite of Peng *et al*. (2008) together form an Early Triassic magmatic arc (Figs. 62 and 70).

1.9 LINCANG GRANITE (239 ±1 Ma)

The dominant geological unit of the Lancangjiang zone is the Lincang granite, a composite granite batholith of Triassic age (Liu *et al*., 1989; Fig. 2). Rock varieties include monzonitic biotite granite, K-feldspar granite, granodiorite and late aplite phases (Hennig *et al*., 2009; Liu *et al*., 1989; Peng *et al*., 2006). The Lincang granite is characterized by N–S strike, a length of 370 km and a width of 10-50 km. It extends from Jinghong to Lincang, with the small Pinhejie satellite intrusion to the north at Changning. The Lincang granite can be followed northwards to the Baimaxueshan granodioritic intrusions, which are 250 km north, and to the granites of the Yidun arc, ~500 km north. Southwards, the Lincang granite can be correlated with the Triassic Mai Thai and Main Range granite province extending from northern Thailand to Peninsular Malaysia and on to the Indonesian islands (Cobbing *et al*., 1992; Wen *et al*., 2001).

The batholith is intruded into Meso- to Neoproterozoic metavolcanic and metasedimentary rocks to the west (Damenglong and Chongshan groups; Zhong, 1998). To the east the intrusion is delimited by a major mylonitic fault zone beyond which phyllites of the Lancang group document a Late Carboniferous high-P/low-T tectonometamorphic event (Heppe *et al*., 2007; Zhang *et al*., 1993; Zhao *et al*., 1994). The Lincang granite became uplifted and eroded in the Late Triassic to Early Jurassic, as evidenced by Early Jurassic basal conglomerates with granite gravels.

1.9.1 PETROGRAPHIC DESCRIPTION

The Lincang granite samples LI-2 to LI-7 can be subdivided into three distinct groups. The assumed main-phase rock (*sensu* Cobbing *et al*., 1992; LI-2 to LI-4) is a weakly altered, xenomorphic-granular, slightly K-feldspar porphyritic, medium-grained biotite monzogranite with a mode of 30 vol% quartz, 20-25 vol% K-feldspar, 25-30 vol% plagioclase and 15-20 vol% biotite (Figs. 76/77A-D; Streckeisen, 1976). Anhedral quartz (0.03-3.0 mm) exhibits undulatory extinction, parquet-like mineral growth and occurs locally in disc-shapes (Fig. 77A-D). These features suggest metamorphic overprint. Weakly sericitized, subhedral to anhedral, tectonized K-feldspar (microcline and orthoclase; 0.4-5.0 mm) shows perthitic exsolution (Fig. 77A). Variably sericitized, carbonatized, epidotized and silicified plagioclase (0.06-4.0 mm) exhibits oscillatory zoning and minor antiperthitic exsolution (Fig. 77A-D).

Bended, undulatory brown biotite (0.06-2.0 mm) is weakly chloritized and depicts sagenite structure (rutile formation by Ti-exsolution) (Fig. 77B/D/E). Accessories include apatite, titanite “eggs” and zircon (all <0.1 mm). Opaques are magnetite (<0.15 mm), ilmenite and some minute grains of pyrite (<0.1 mm). The rock is cut by quartz veinlets.

Samples LI-5 and LI-7 are medium-grained, tectonized and more altered and evolved. Plagioclase depicts strong sericitization, and biotite shows strong chloritization (Fig. 77F/G). These samples have higher modes in K-feldspar (35-40 vol%) and quartz (35-40 vol%), and less plagioclase (15-20 vol%) and biotite (<5 vol%), respectively. K-feldspar is strongly perthitic (Fig. 77F/G). Accessories include zircon (partly hosted by biotite; <0.1 mm), minor apatite and limonite. On the QAPF diagram of Streckeisen (1976), these samples plot in the transition of syeno- to monzogranite (Fig. 76).

All granite samples are cut by late-phase aplite veins (LI-6), similar in mineralogy to the more evolved granites (Fig. 77H). The fine-grained rock has 40 vol% K-feldspar (microcline and orthoclase, <0.4 mm), 40 vol% anhedral quartz (<0.4 mm), 15 vol% sericitized plagioclase (0.03-0.5 mm) and up to 5 vol% anhedral biotite (<0.05 mm) altered to chlorite. Accessories include euhedral apatite (<0.08 mm), subhedral zircon and titanite (both <0.04 mm). The Lincang granite aplite plots on the QAPF diagram (Streckeisen, 1976) as syenogranite (Fig. 76). The magnetic susceptibility of the rock variants is low (<0.3 x 10^{-3} SI units) and defines the granite as part of the ilmenite series (Ishihara, 1977, 1981).

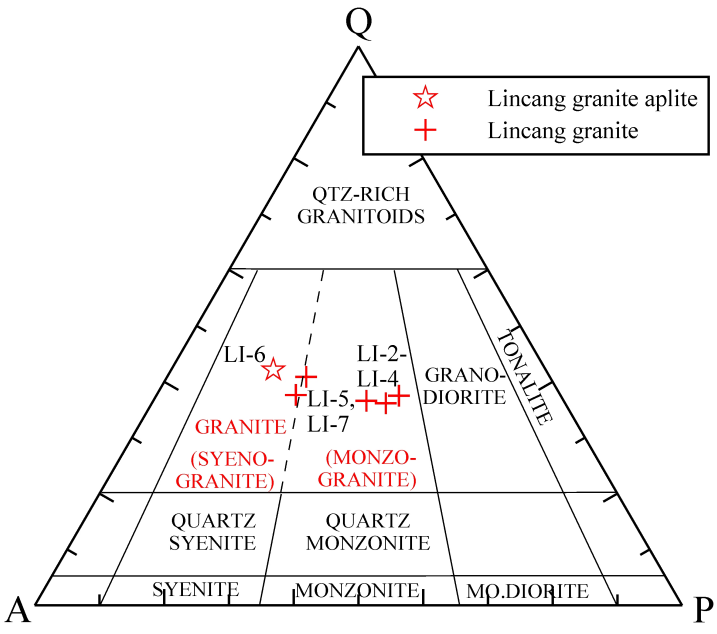

Fig. 76: The Lincang granite samples on the modified QAPF diagram of Streckeisen (1976). The less evolved samples LI-2 to LI-4 plot as monzogranite with affinity to granodiorite. The more evolved samples LI-5 and LI-7 plot as syeno- to monzogranite, and the highly evolved Lincang granite aplite (sample LI-6) plots as syenogranite.

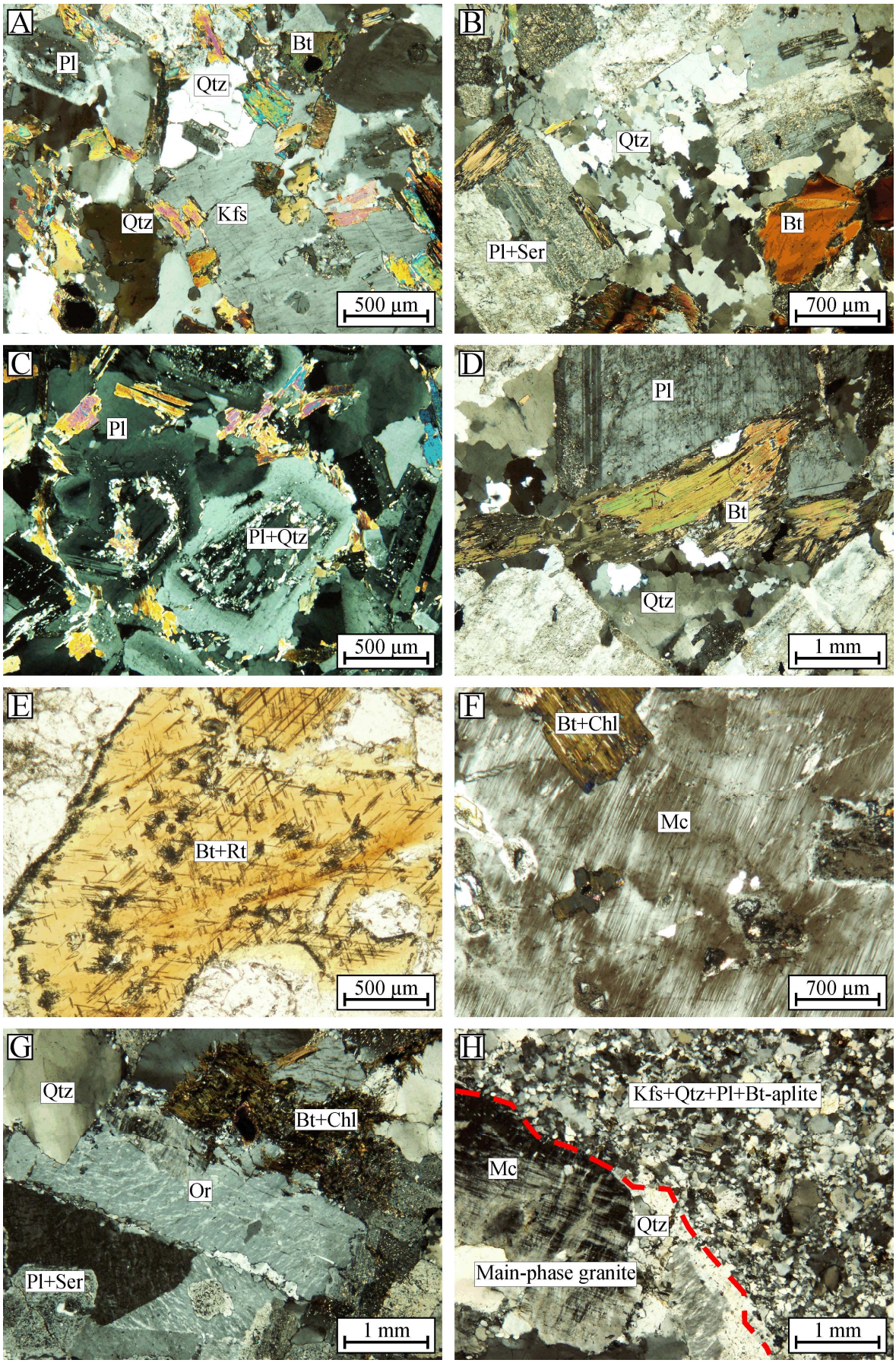

Fig. 77: Photomicrographs of the Lincang granite samples (A-D: LI-2, E: LI-4, F/G: LI-5, H: LI-6; A-D and F-H: transmitted light/crossed polars, E: transmitted, plane-polarized light).

1.9.2 MAJOR AND TRACE ELEMENT COMPOSITION

The QAPF classification for the Lincang granite is in accord to rock classifications by major and trace elements (Fig. 78A-D). The TAS diagram for plutonic rocks suggests for all Lincang granite samples a subalkaline granitic composition with affinity to subalkaline granodiorite (Cox *et al.*, 1979; Irvine & Baragar, 1971; Kuno, 1966; Le Maitre, 1989; MacDonald, 1968; MacDonald & Katsura, 1964; Wilson, 1989). The R1 vs. R2 diagram favors for the main-phase granite a granodioritic to monzogranitic and for the more evolved samples - similar to the QAPF classification - a syenogranitic composition (De la Roche *et al.*, 1980). Immobile element plots give a dacitic to rhyodacitic composition for the main-phase suite and a rhyolitic composition for the more evolved rocks (Winchester & Floyd, 1977).

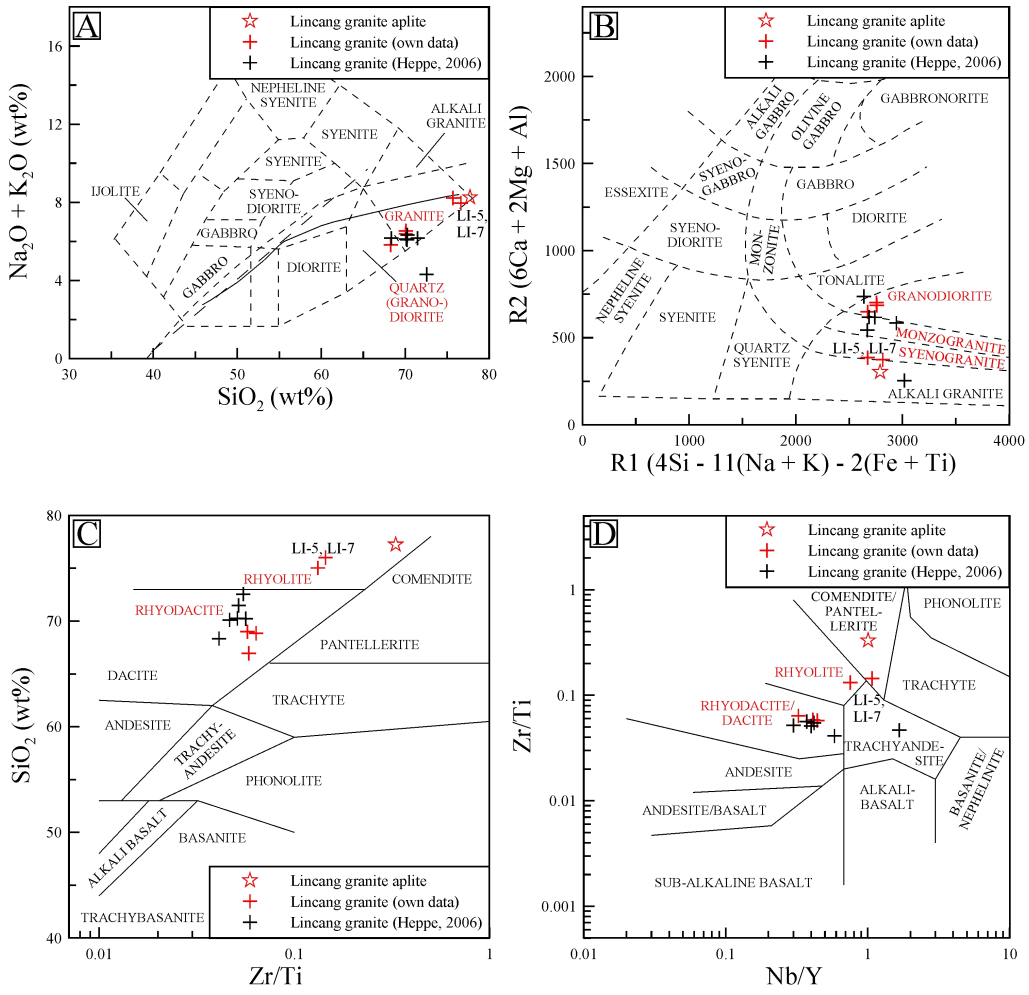

Fig. 78A: The Lincang granite samples on the TAS diagram for plutonic rocks (Cox *et al.*, 1979; Le Maitre, 1989; Wilson, 1989). B: The Lincang granite samples on the R1 vs. R2 diagram of De la Roche *et al.*, (1980). C/D: The Lincang granite samples on immobile element plots for volcanic rocks of Winchester & Floyd (1977). Note: Data is complemented by data of Heppe (2006). Additional references are given in Figs. 5 and 21.

The complete sample suite of the Lincang granite (samples LI-2-LI-7) has 67.0-77.2 wt% SiO_2, 2.3-3.6 wt% Na_2O and 3.5-4.8 wt% K_2O, which defines the granite as member of the high-K (calc-alkaline) series (Fig. 79A; Appendix Table 12). On the AFM diagram the granite samples (in red) lie on a well defined calc-alkaline fractionation trend (Fig. 79B).

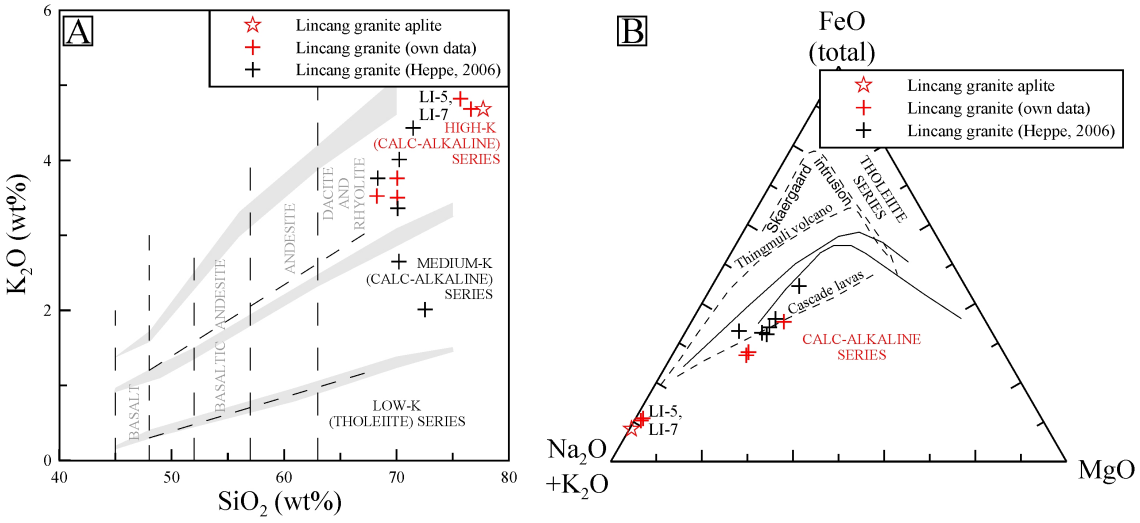

Fig. 79A: The K_2O vs. SiO_2 diagram classifies the Lincang granite as high-K, calc-alkaline. The data of Heppe (2006) depict K-loss, likely caused by hydrothermal alteration. B: On the AFM diagram the Lincang granite samples define a distinct calc-alkaline fractionation trend, from which some altered samples of Heppe (2006) deviate. References as in Figs. 5 and 21.

As shown by petrography and as can be seen on the various classification plots, the Lincang granite samples allow a subdivision into two distinct groups. The main-phase group (*sensu* Cobbing *et al*., 1992; samples LI-2 to LI-4) is characterized by low Si (<69 wt% SiO_2), high Ti (>0.4 wt% TiO_2), high Al (≥14.3 Al_2O_3), high Fe (≥3.4 wt% Fe_2O_3 total), high Mg (>1.8 wt% MgO), high Ca (≥2.4 wt% CaO), low Na (<3.0 wt% Na_2O), low K (<3.7 wt% K_2O) and high P (≥0.1 wt% P_2O_5). The more evolved equigranular granite, including aplite (samples LI-5 to LI-7), is characterized by high Si (>75 wt% SiO_2), low Ti (≤0.1 wt% TiO_2), low Al (<13.5 wt% Al_2O_3, low Fe (≤1.1 wt% Fe_2O_3 total), low Mg (<0.2 wt% MgO), low Ca (≤1.0 wt% CaO), high Na (≥3.3 wt% Na_2O), high K (≥4.7 wt% K_2O) and low P (≤0.02 wt% P_2O_5). This systematic pattern suggests that these samples indeed represent residual melt portions from the main-phase system (Cobbing *et al*., 1992).

It is noteworthy that average granite reference data lie for most major elements between the two groups, which points to a primitive composition for the main-phase samples (e.g. Le Maitre, 1976; Nockolds, 1954). Accordingly, calculated CIPW norms and parameters such as solidification index, differentiation index, color index, agpaitic coefficient and

Mg-number show the distinct subdivision of the two rock suites as well (Table 21; Kelsey, 1965; Middlemost, 1989). In general, the CIPW norms verify the petrographic interpretation.

Rock classification by normative mineral constituents, as shown in Figure 80, gives further evidence for the primitive character of the Lincang granite main-phase rocks as these samples plot with relatively high normative anorthite content above the granite-field boundary line of O`Connor (1965). All Lincang granite samples have normative corundum (0.7-3.0 wt%; Table 21). The alumina-saturation index (A/CNK molar) is 1.05-1.21 and A/NK molar is 1.14-1.93. These characteristics define the Lincang granite as peraluminous. According to the classification of Chappel & White (1974) all Lincang granite samples are of S-type affinity (Al / (0.5 x Ca + Na + K) > 1.1).

Table 21: Calculated CIPW norms and additional parameters for the Lincang granite samples. Differentiation index is calculated according to Thornton & Tuttle (1960).

Rock type	Lincang granite					
Sample	LI-2	LI-3	LI-4	LI-5	LI-7	LI-6
Quartz	31.60	30.70	30.64	34.89	37.09	37.69
Corundum	2.95	2.09	0.92	0.92	0.70	0.65
Orthoclase	20.82	20.70	22.22	28.48	27.68	27.66
Albite	19.41	25.61	22.22	28.77	27.72	30.23
Anorthite	11.11	11.23	14.32	5.04	5.09	2.53
Hypersthene	8.98	6.24	6.38	0.76	0.67	0.49
Magnetite	2.99	1.99	2.04	0.83	0.75	0.60
Ilmenite	1.37	0.90	0.82	0.21	0.20	0.10
Apatite	0.45	0.32	0.24	0.05	0.04	0.01
Solidification Index	18.96	20.07	23.77	10.07	10.49	5.40
Differentiation Ind.	71.83	77.01	75.08	92.14	92.49	95.58
Color Index	13.35	9.13	9.24	1.80	1.63	1.19
Agpaitic Index	0.52	0.59	0.58	0.80	0.80	0.87
Mg#	59.35	60.64	60.15	29.62	28.57	13.39

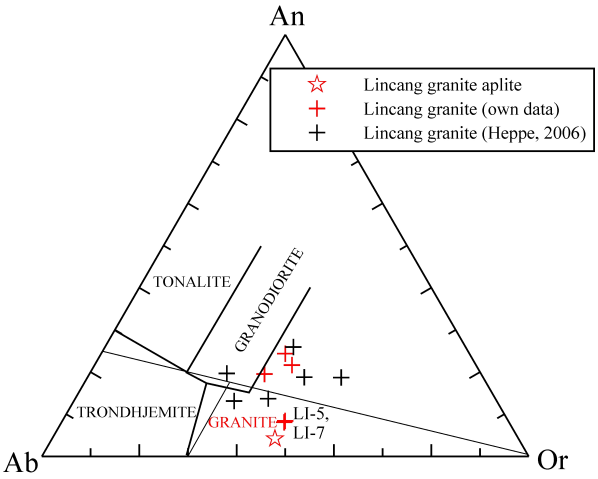

Fig. 80: The Lincang granite on the Or–An–Ab diagram of O`Connor (1965) and Barker (1979). For explanations see Fig. 34.

The primitive mantle-normalized multi-element plot for the Lincang granite shows compositions more evolved than bulk and upper continental crust (Fig. 81; Rudnick & Gao, 2004). In contrast to the main-phase granite (blue samples), the more evolved samples LI-5 and LI-7 depict enrichment in K and Rb due to their higher amounts of K-feldspar, and lack a Ta–Nb trough. Likewise, these samples are markedly depleted in Ba - which might be explained by the higher K_D in felsic melts for Ba in biotite than for Ba in K-feldspar. These samples are markedly depleted in P and Ti, as they have little apatite only and no magnetite (Arth, 1976; Mahood & Hildreth, 1983; Nash & Crecraft, 1985; Pearce & Norry, 1979). The

aplite sample stands out in terms of very low Ba, Sr, P and Ti concentrations and elevated Rb, Th, Ta, Nb and HREE concentrations, resulting in a very high Rb/Sr ratio of 29.

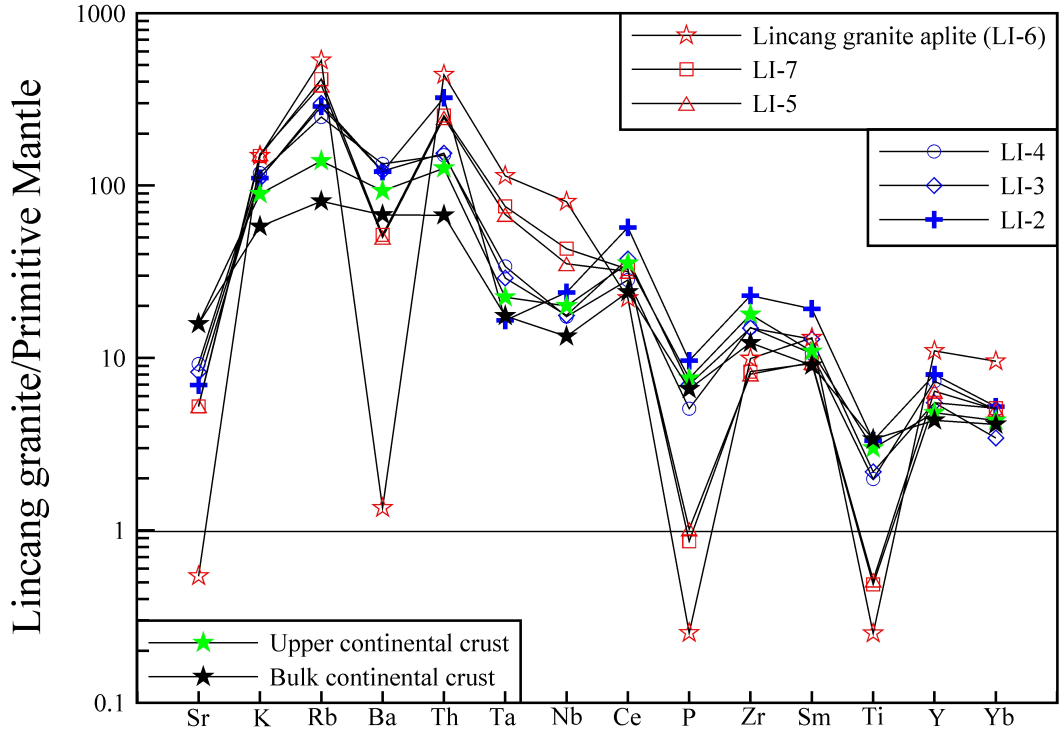

Fig. 81: Primitive mantle-normalized multi-element patterns of the Lincang granite. Continental crust is from Rudnick & Gao (2004) and PM from Palme & O`Neill (2004).

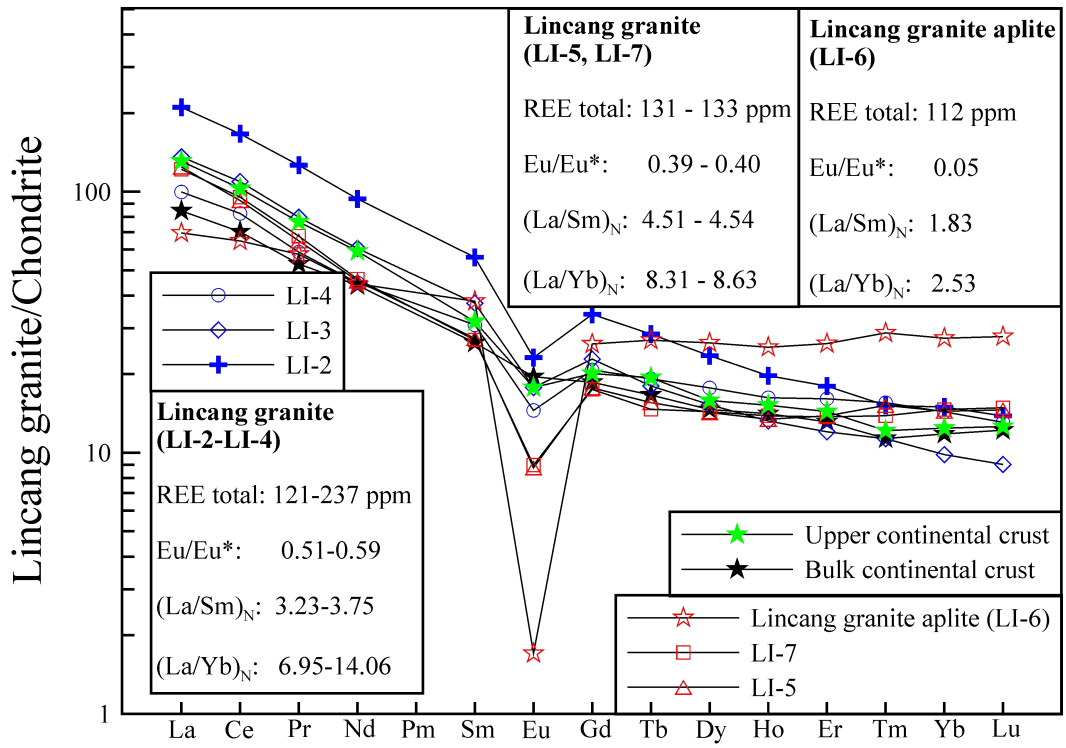

Fig. 82: REE patterns of the Lincang granite (McDonough & Sun, 1995).

On the chondrite-normalized REE plot of Figure 82 the Lincang granite samples exhibit consistent, strongly fractionated patterns similar to upper and bulk continental crust (Rudnick & Gao, 2004). All samples are characterized by strong negative Eu-anomalies of Eu/Eu* = 0.4-0.6. The drastic Eu-anomaly of the Lincang granite aplite (Eu/Eu* = 0.05) supports the hypothesis that this rock type formed from a residual melt portion of the main-phase Lincang granite melt, that has undergone intensive feldspar fractionation.

1.9.3 U–Pb ZIRCON GEOCHRONOLOGY

Twenty-five zircon grains from the Lincang granite sample LI-5 were spot-analyzed (30 µm). The data are compiled in Appendix Table 22. The Th/U ratios for zircon from the Lincang granite show a wide range of 0.06-7.81. However, if the lowest value of 0.06 and the two highest values of 7.81 and 2.08 are regarded as outliers, the data range from 0.38-1.15 and suggest magmatic origin only. The weighted mean $^{206}Pb/^{238}U$ age for the Lincang granite is 239.4 ±1.3 Ma (n = 25; Fig. 83).

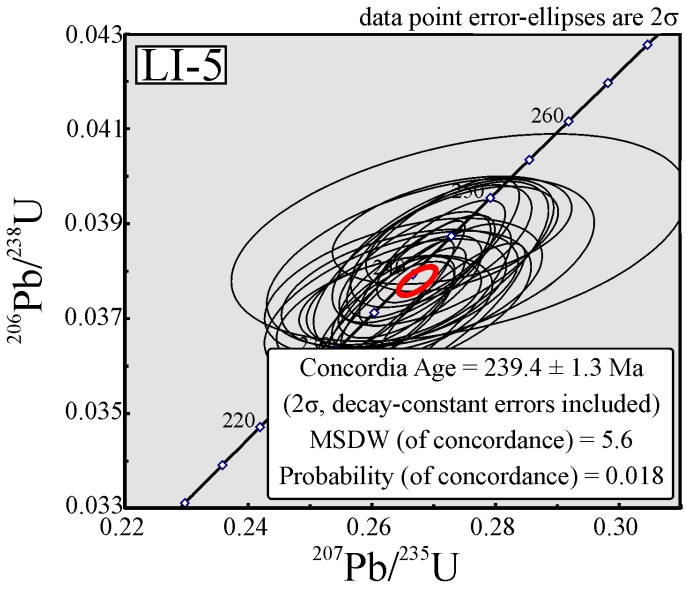

Fig. 83: U–Pb concordia plot for the Early Triassic Lincang granite (sample LI-5).

1.9.4 Sr–Nd ISOTOPIC COMPOSITION

The Lincang granite has high initial $^{87}Sr/^{86}Sr$ ratios and very low εNd values. Figure 84 gives a set of isotopic reference data for the Lincang granite and its northern satellite intrusion, the Pinhejie granite. Published depleted mantle model ages range from 2.1-1.5 Ga (Heppe, 2006; Lehmann *et al.*, 2005; Li, 1996). These model ages are in accord with SHRIMP U–Pb ages of inherited zircons from the Lincang granite which are up to 1977 ±44 Ma in age (Peng *et al.*, 2006). Paleoproterozoic model ages are typical of the Southern Yangtze Block (Zhang *et al.*, 2006a), and it appears likely that the Lincang Block is a fragment of the Yangtze Block (for more detailed information refer to chapter 1.6.4).

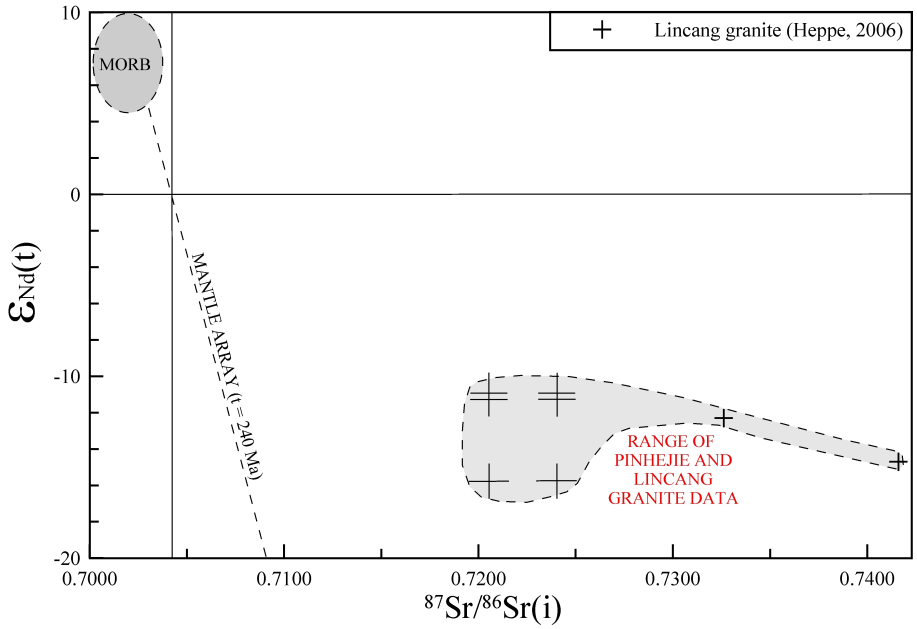

Fig. 84: $\varepsilon_{Nd}(t)$ vs. initial $^{87}Sr/^{86}Sr$ diagram for the Lincang granite (data are from Heppe, 2006; t = 220 Ma). The large black crosses represent composite isotopic data for the Lincang granite and its northward following satellite intrusion, the Pinhejie granite. The Nd data for the Lincang granite are from Lehmann *et al.* (2005) and Li (1996) (both for t = 240 Ma), and the Sr data are from Liu *et al.* (1989); whereas the lower Sr value is for the Pinhejie granite (t = 294 Ma), and the higher value for the Lincang granite (t = 275 Ma).

1.9.5 DISCUSSION OF AGE DATA

The new U–Pb zircon age on the Lincang granite of 239 ±1 Ma is in the range of previously published age determinations. It is slightly older than the reported SHRIMP zircon ages of 229.4 ±3.0 Ma and 230.4 ±3.6 Ma on the northern and southern Lincang granite, respectively (Peng *et al*., 2006; Fig. 85), and it is slightly younger than the age of 245 Ma (no error given) reported by Wen *et al*. (2001). Rb–Sr whole-rock and Ar–Ar ages on biotite for the Lincang granite range from 300 to 200 Ma (Liu *et al*., 1989; Wen *et al*., 2001) and are likely affected by post-intrusive tectonothermal overprint. The Xuedui trondhjemite dike of the Jinshajiang area gave a SHRIMP U–Pb zircon age of 238 ±10 Ma, which is indistinguishable from our age on the Lincang granite as well as from the age data on the Baimaxueshan granodioritic intrusion (Jian *et al*., 2003a, 2008).

It appears likely that the trondhjemite dike postdates arc magmatism and is synchronous with crustal thickening in the region. Age data on syn- to postcollisional granites of the Yidun arc, about 500 km to the north of the sample site of the Lincang granite, are 224 ±3 Ma, 222 ±3 Ma and 213 ±3 Ma (Yan *et al*., 2005).

The ~240-210 Ma granite magmatism along the Lancangjiang zone is part of a more than 4000 km long granite province, which extends from Tibet to the Indonesian islands in the Sunda Shelf. These peraluminous granites are best studied in the Main Range Province of Peninsular Malaysia where they formed at 230-200 Ma with a peak around 220 Ma (Cobbing *et al*., 1992; Liew & Page, 1985).

1.9.6 TECTONOMAGMATIC ENVIRONMENT

On the Ta vs. Yb diagram of Pearce *et al*. (1984) the Lincang granite samples span up a plane covering the “syn-collisional granite” field (Fig. 86A). Similar to the Ta vs. Yb diagram, the samples define on the Rb vs. Yb + Ta diagram a population close to the triple point of “volcanic-arc granite”, “syn-collisional granite” and “within-plate granite” (Fig. 86B). This position is typical of late-collisional to post-collisional granites (Pearce *et al*., 1984). The Lincang granite aplite is enriched in incompatible elements and plots accordingly as within-plate granite on both plots. In accordance to previous genetic interpretations, the Lincang granite is therefore regarded as syn- to postcollisional. The Lincang granite likely marks the final closure of the Paleo-Tethys in southern Yunnan, i.e. the collision of the cratonal blocks

Sibumasu and Yangtze - or in a more local context - of Lancang and Simao (refer to Figs. 1 and 85).

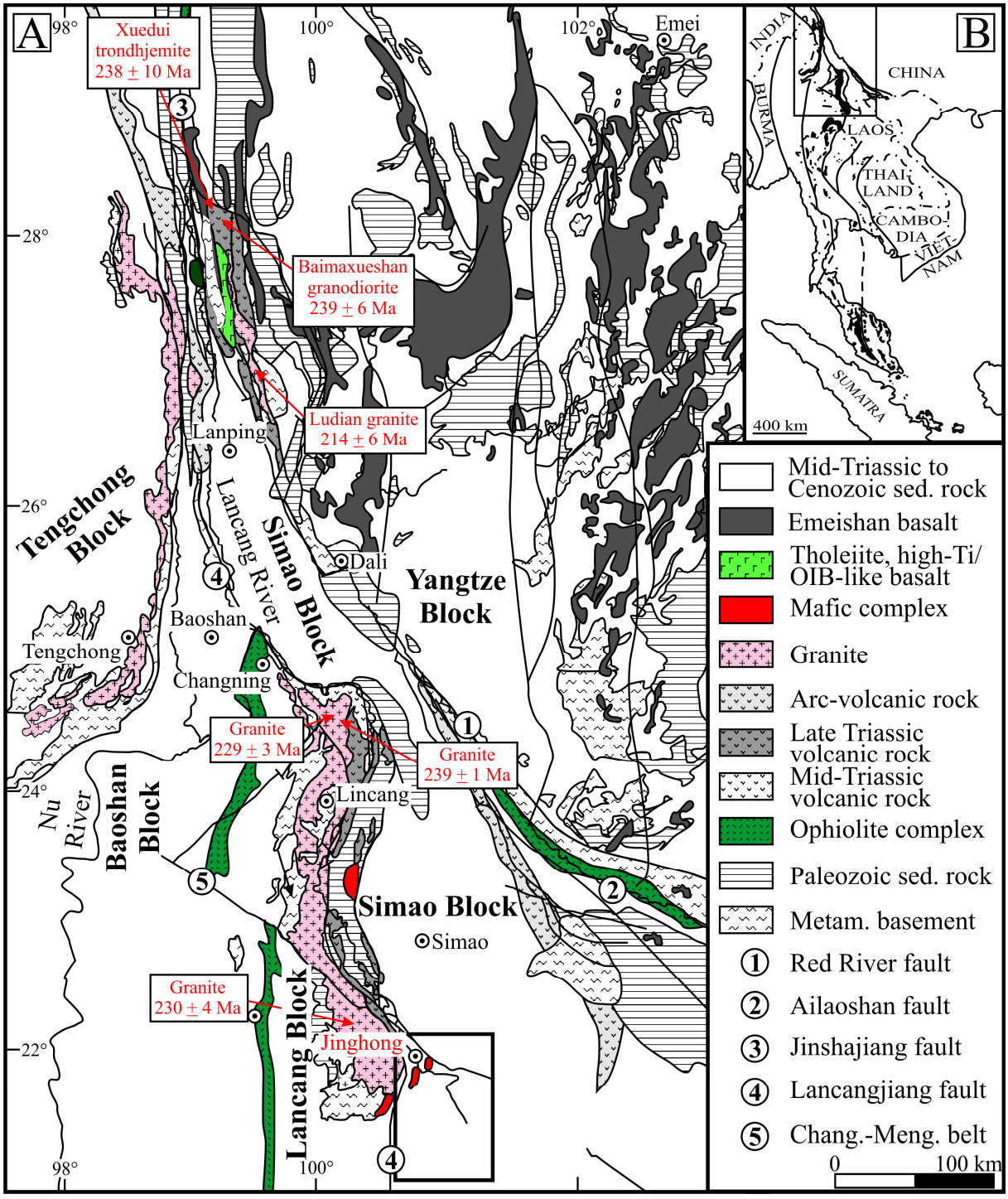

Fig. 85: Simplified geological map of the Lancangjiang zone in southwestern Yunnan. Labeled age data are SHRIMP U–Pb ages of Jian *et al.* (2003a, 2008) and Peng *et al.* (2006). The U–Pb zircon age of 239 ±1 Ma on the Lincang granite is own data.

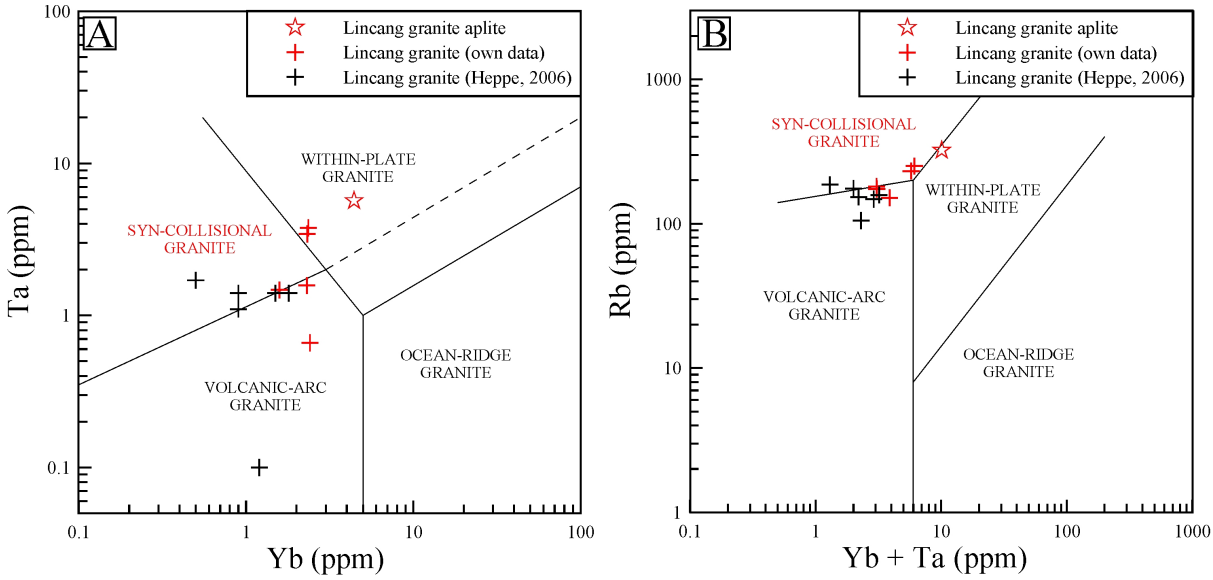

Fig. 86A: The Lincang granite samples in the Ta vs. Yb tectonomagmatic discrimination diagram for granitic rocks of Pearce *et al*. (1984). The samples plot in a position which is suggestive for syn-collisional granites. The highly enriched Lincang granite aplite sample plots as “within-plate granite”. B: Rb vs. Yb + Ta diagram (Pearce *et al*., 1984). All Lincang granite samples plot close to the triple point of “volcanic-arc-“, “syn-collisional-“ and “within-plate granite”, which is typical of late- to post-orogenic granites.

1.10 JINGHONG BASALT/HUIJINGFANG COMPLEX (194 ±2 Ma)

The basalt samples JI-50 to JI-55 and JI-58 are located ~20 km southeast of Jinghong (Fig. 87), within and around the NE–SW trending, 5 x 3 km-large, basaltic Huijingfang complex, which intrudes, similar to the Jinghong granodiorite, the “mid-Triassic diorite” belt (YBGMR, 1990). To the north, the Huijingfang complex has a very limited magmatic contact with a major Jinghong granodiorite intrusion and to the northeast a wider magmatic contact with Late Triassic volcano-sedimentary strata (YBGMR, 1990).

According to the published geological maps of the YBGMR (1990) the basalt samples JI-50, JI-51 and JI-54 plot within the Huijingfang complex and samples JI-52 and JI-53 plot south of it in the “mid-Triassic” diorite belt. Sample JI-55 plots as “Late Triassic volcanic rock” east of the Huijingfang complex and JI-58 north of the Huijingfang complex, within a

triple junction of the lithological units of Jinghong granodiorite, “mid-Triassic diorite” and “Late Triassic volcano-sedimentary strata” (Fig. 87).

Heppe (2006) analyzed basalts in the region as well. These samples (i.e. 02/039, 02/139 and 02/140) plot, similar to sample JI-55, in the contact area of Paleozoic to Mesozoic rocks (YBGMR, 1990; Fig. 87). Heppe (2006) classifies - without having robust age constraints, samples 02/139 and 02/140 as Late Permian, and sample 02/039 as mid-Triassic.

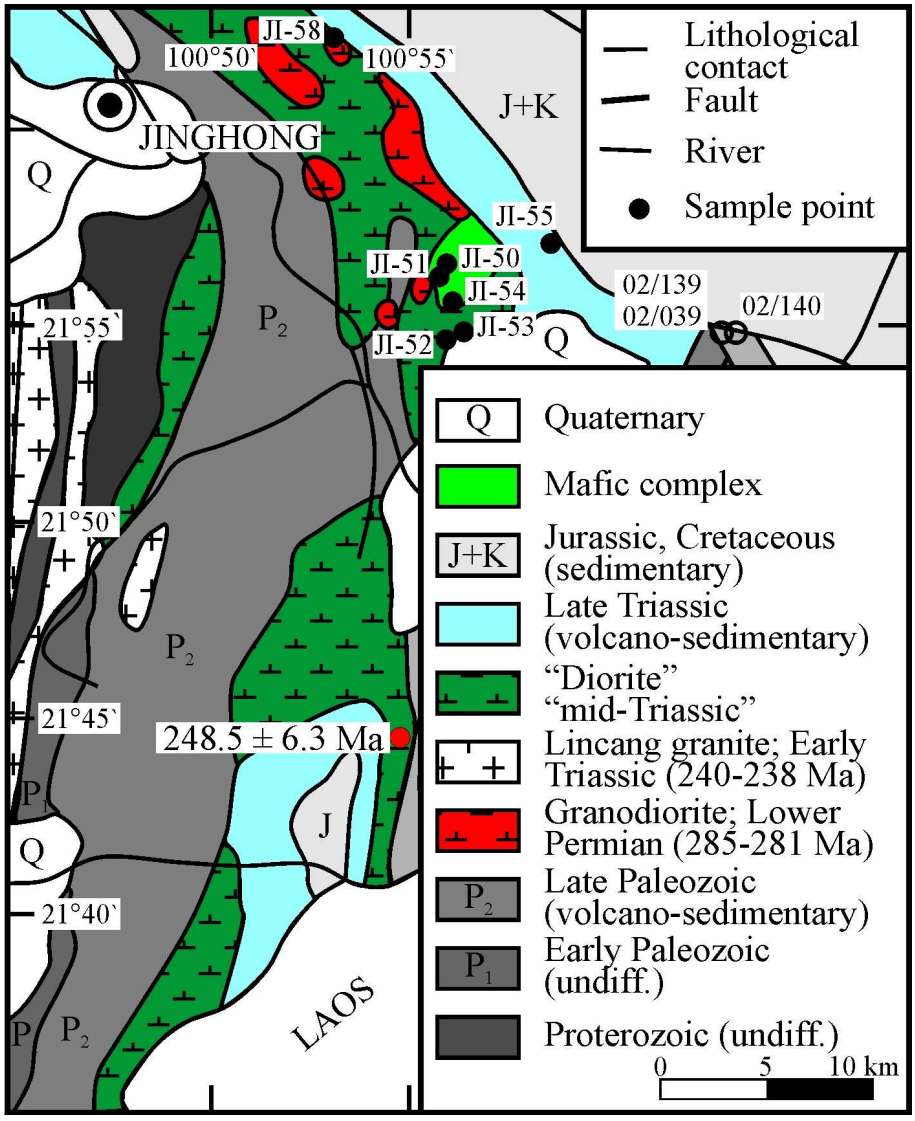

Fig. 87: Geologic overview map of the area south of Jinghong (YBGMR, 1990). The basalt samples are from the mafic Huijingfang complex (samples JI-50, JI-51, JI-54), from the “mid-Triassic diorite” belt north and south of the complex (samples JI-52, JI-53, JI-58), of which the Jinghong trachyandesite and dacite are part, and from “Late Triassic" strata (JI-55). Sample locations of Early Triassic, arc-related andesite with a SHRIMP age of 248.5 ±6.3 Ma (Peng *et al.*, 2008) and basalt reference samples of Heppe (2006) are also plotted (open circles).

1.10.1 PETROGRAPHIC DESCRIPTION

The hypidiomorphic to xenomorphic-granular basalt has 40-60 vol% plagioclase, 35-40 vol% of locally uralitized clinopyroxene, <15 vol% actinolitic amphibole and <5 vol% olivine. Three rock variants occur: Samples JI-50 and JI-55 are fine-grained subophitic (<1.5 mm; Fig. 88A/B). Samples JI-52 and JI-53 are coarser grained and subophitic (<5.0 mm; Fig. 88C/D). Both types appear to be sub-volcanic in origin. JI-58 is fine-grained (<0.6 mm) and has chlorite-, carbonate-, quartz- and sericite-filled amygdules (<10 mm; Fig. 88E/F). This rock has a well preserved, fluidal texture of plagioclase with interstital clinopyroxene (trachyophitic to basiophitic). Due to mineralogical and geochemical similarities, the three rock variants were not treated separately.

All samples have variably sericitized, carbonatized and prehnitized plagioclase. Metamorphic overprint is indicated by bended/broken crystals and tectonic twinning. Predominantly augitic clinopyroxene (0.1-1.0 mm) is moderately altered to high-Fe chlorite (clinochlore by XRD, Fig. 88D). Chloritized amphibole (0.1-1.3 mm) hosts poikilitic plagioclase. Olivine (0.1-0.6 mm) depicts serpentinization. Opaques include subhedral pyrite (<1 vol%; 0.02-0.5 mm) and chalcopyrite (<1 vol%; 0.02-0.33 mm; Fig. 88H). The rock has some apatite and rutile, and is cut by chlorite, carbonate, sericite, quartz and minor prehnite veinlets (Fig. 88C). Sample JI-58 has some fine-grained, likely hydrothermal quartz in the groundmass. Uralitization, actinolitization, chloritization and prehnitization point, together with tectonized plagioclase, to low-grade metamorphism and hydrothermal overprint.

Samples JI-51 and JI-54 are strongly altered and do not allow rock classification by mineral mode estimates. Interestingly, both samples are derived from the contact area of the Huijingfang complex (Fig. 87). JI-51 depicts weak to moderate tourmalinization accompanied by silicification (Fig. 88G) and JI-54 is strongly carbonatized, sericitized and silicified. It is noteworthy that the Jinghong dacite samples JI-48 and JI-49 (refer to chapter 1.8) are from the vicinity of sample JI-51 and depict tourmalinization as well (Figs. 70 and 87).

Except the textural similarity of JI-52 and JI-53 and their higher granularity, no petrographic correlation of the different rock variants with the rock units outlined on the magmatic map of southern Yunnan (YBGMR, 1990) could be made. But, in general, the petrographic observations correspond to the sketchy descriptions of Heppe (2006).

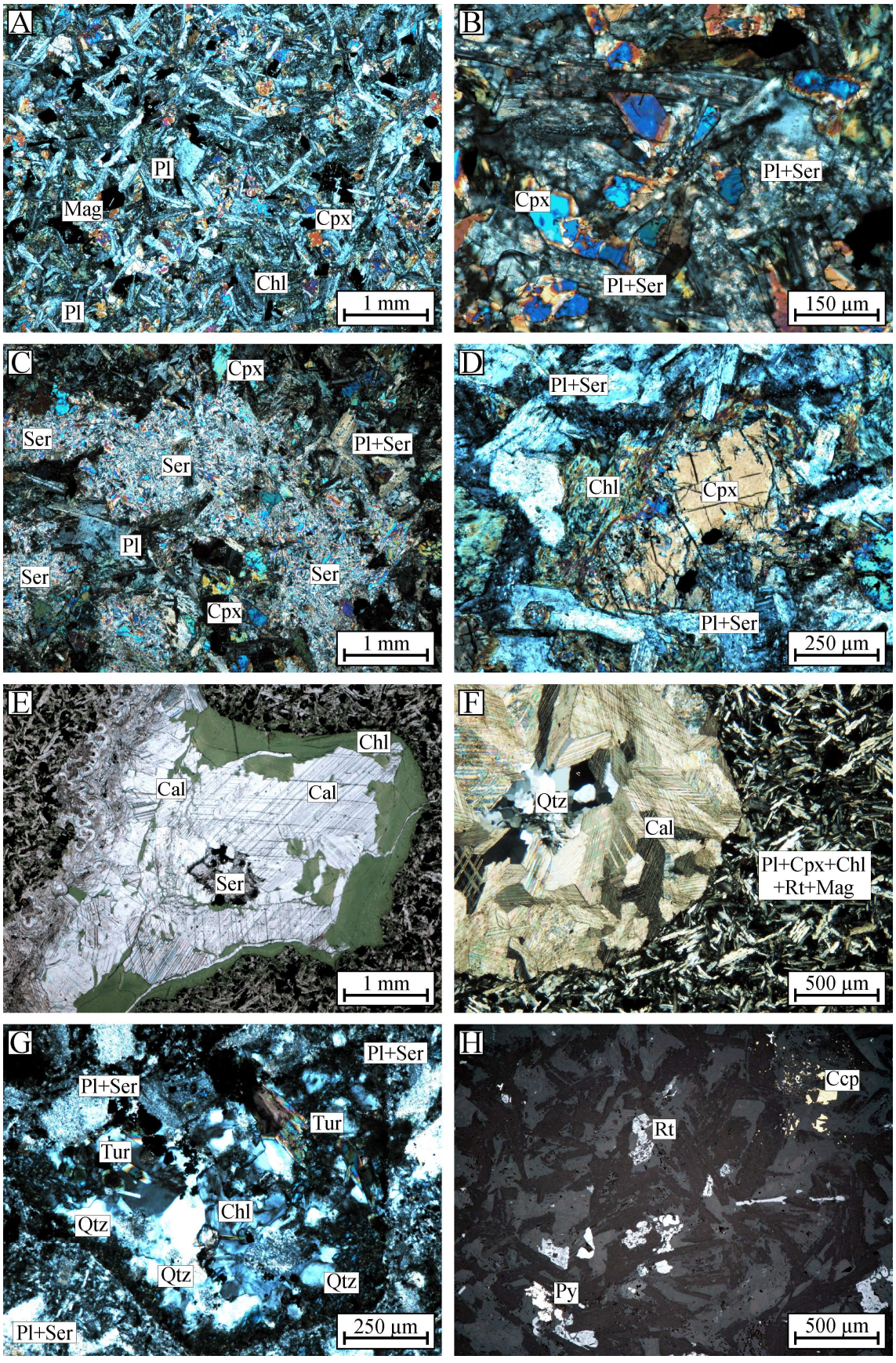

Fig. 88: Photomicrographs of the Jinghong basalt samples (A/H: JI-50, B: JI-55, C: JI-52, D: JI-53, E/F: JI-58, G: JI-51; A-D and F-G: transmitted light/crossed polars, E: transmitted, plane-polarized light, H: reflected light/crossed polars).

1.10.2 MAJOR AND TRACE ELEMENT COMPOSITION

TAS classifies the least-altered Jinghong basalt samples JI-50, JI-52, JI-53, JI-55 and JI-58 as alkaline basalt with affinity to alkaline trachybasalt (Kuno, 1966; Le Maitre, 1989; MacDonald, 1968; MacDonald & Katsura, 1964; Fig. 89A). The SiO_2 vs. Zr/Ti and the Zr/Ti vs. Nb/Y diagrams give an alkali basaltic and a basaltic to andesitic composition, respectively (Fig. 89B/C; Winchester & Floyd, 1977). The Na_2O vs. SiO_2 plot suggests alkalinity as well (not shown). The K_2O vs. SiO_2 diagram, however, favors a subalkaline composition of the medium-K calc-alkaline series (Middlemost, 1975; Fig. 89D).

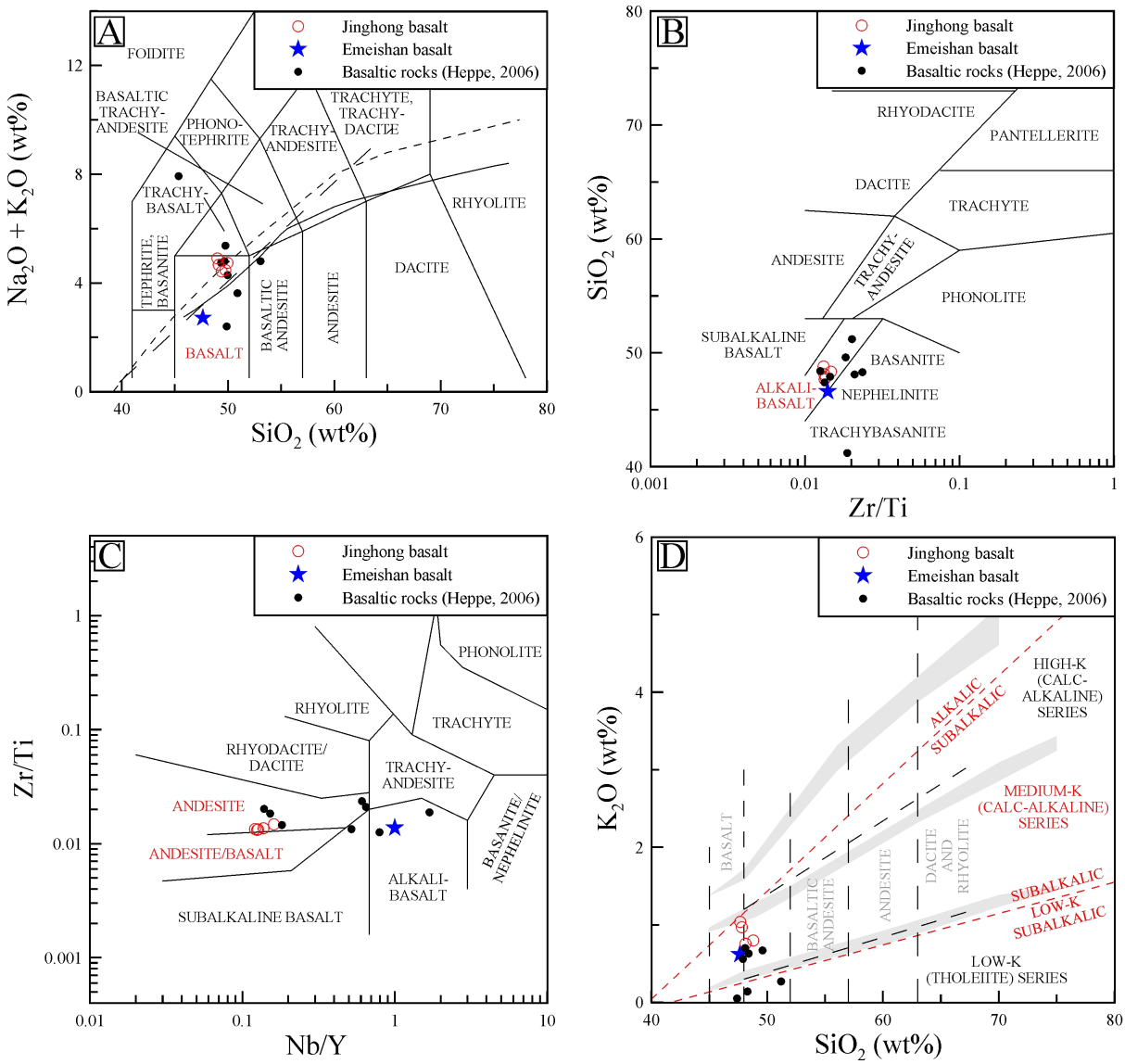

Fig. 89A: The least-altered rock samples of the Jinghong basalt on the TAS diagram (Le Maitre, 1989). B/C: The Jinghong basalt on immobile element plots of Winchester & Floyd (1977). D: The K_2O vs. SiO_2 diagram suggests for the Jinghong basalt a subalkaline composition (Middlemost, 1975). On all plots the samples depict similarities to the basaltic reference samples of Heppe (2006).

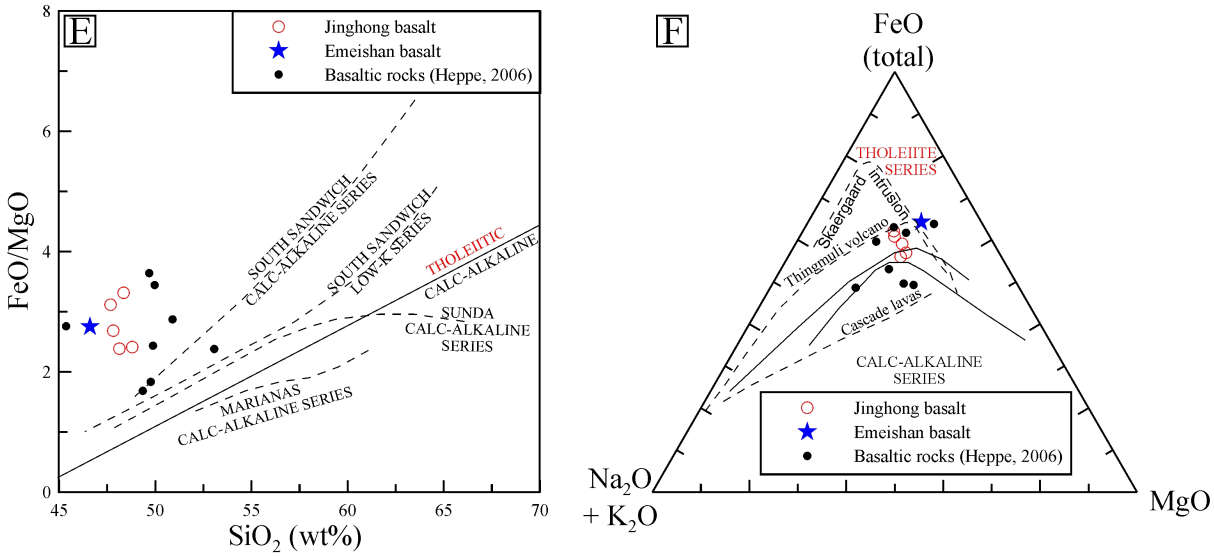

Fig. 89 continued; E: The Jinghong basalt samples on the FeO/MgO vs. SiO_2 diagram. This plot suggests a tholeiitic composition (Miyashiro, 1974). B: The AFM diagram shows for the Jinghong basalt a tholeiitic fractionation trend, similar to that of the Thingmuli volcano (Iceland) (Carmichael, 1964). On both plots the samples depict marked similarities to the basaltic reference samples of Heppe (2006). Further reference data and subdivisions are cited in Figs. 5 and 21.

Overall, a transitional character is assumed for the Jinghong basalt as suggested by the subdivision of Irvine & Baragar (1971) on the TAS diagram (Fig. 89A; narrowly dashed line), by the FeO/MgO vs. SiO_2, by the Alkali index vs. Al_2O_3 (not shown) and by the AFM diagram (Fig. 89E/F). The latter three diagrams favor a tholeiitic trend for the basalts (Middlemost, 1975; Miyashiro, 1974). Especially on the AFM diagram the least-altered samples depict a tholeiitic trend, similar to the Thingmuli volcano in Iceland (Carmichael, 1964; Fig. 89F). Calculated CIPW norms (Table 22) suggest subalkalinity as well (no normative nepheline).

Compared to “intermediate basalt” (Le Maitre, 1976; Nockolds, 1954) the Jinghong basalt has relatively low Si, Al, Mg and Ca (47.7-48.8 wt% SiO_2, 13.0-13.9 wt% Al_2O_3, 4.3-5.4 wt% MgO and 7.3-9.0 wt% CaO) and relatively high Ti, Fe, Mn and Na (2.1-2.9 wt% TiO_2, 13.9-16.4 wt% Fe_2O_3 (total), 0.27-0.57 wt% MnO and 3.6-3.8 wt% Na_2O). These characteristics point to a rather juvenile state of the basaltic suite. The LOI values of 1.9-2.4 wt% for the least-altered basalt samples JI-50, JI-52, JI-53, JI-55 and JI-58 correspond to the alteration assessment by petrographic studies and point to moderate alteration only.

Calculated CIPW norms suggest that the basalt samples are mildly undersaturated in SiO_2 and Al_2O_3, i.e. the rocks have 31.0-33.2 wt% normative albite, 16.0-19.1 wt% anorthite, 14.3-21.0 wt% diopside, 4.8-15.8 wt% hypersthene, 6.4-8.9 wt% olivine,

4.1-4.9 wt% magnetite, 4.1-5.6 wt% ilmenite and 0.6-0.9 wt% apatite (Kelsey, 1965; Middlemost, 1989). The amygdaloid basalt sample JI-58 is set somewhat apart with low orthoclase (4.3 vs. 4.6-6.3 wt%) and olivine (1.5 vs. 6.4-8.9 wt%), and high anorthite (19.1 vs. 16.0-18.9) and hypersthene (15.8 vs. 4.8-12.8 wt%).

The norms generally match the petrographic descriptions and correspond, except for the relatively high albite and low anorthite content, to published CIPW norms for basalts (Le Maitre, 1976). The high albite and low anorthite content might be explained by sericitization of plagioclase.

Table 22: Calculated CIPW norms and Mg-numbers for the least-altered Jinghong basalt samples. Calculations as cited in Table 2.

Sample ID	Orthoclase	Albite	Anorthite	Diopside	Hypersthene	Olivine	Magnetite	Ilmenite	Apatite	Mg #
JI-50	6.31	32.45	15.96	14.83	10.88	6.90	4.89	5.56	0.90	40.22
JI-52	4.59	30.84	18.35	21.00	7.64	6.41	4.22	5.03	0.78	46.77
JI-53	5.88	31.04	17.52	14.26	12.76	6.62	4.69	5.14	0.82	43.85
JI-55	4.83	33.18	18.90	19.42	4.84	8.94	4.11	4.08	0.59	46.51
JI-58	4.29	31.70	19.06	16.04	15.84	1.47	4.67	4.84	0.82	38.75

The primitive mantle-normalized multi-element patterns of the Jinghong basalt plot coherently with some spread in the mobile LILEs, such as Rb and Pb, and in the mobile high field strength element (HFSE) U (Fig. 90). Nevertheless, the rocks are more enriched in the large, low valence cations, such as Rb, Pb and Ba, and in HFSEs, such as Zr, Y and REEs, than E-MORB (Wilson, 1989 and references therein). The patterns depict for the HFSEs both slight depletions relative to the LREEs, such as for Ta and Nb (0.4-0.7 ppm Ta, 5.4-8.5 ppm Nb), and slight enrichments relative to the MREEs and HREEs, as for Zr, Y and Ti (166-229 ppm Zr, 43-61 ppm Y, 2.1-2.9 wt% TiO_2). These characteristic trends are suggestive of an intra-plate setting and limited crustal contamination.

Reference datasets for within-plate rocks span-up fields that embrace the Jinghong basalt samples (Wilson, 1989 and references therein; Xiao *et al.*, 2003; Xu *et al.*, 2001). Additional evidence for an intra-plate setting are high V contents (302-375 ppm V), low Cr (27-81 ppm Cr), low Co (39-46 ppm Co), low Ni (14-37 ppm Ni), low Sc (23-39 ppm Sc), and high Ti/Y ratios of 280-303. The Jinghong basalt resembles basaltic rocks from Yunnan (blue and green crosses in Fig. 90; Heppe, 2006). Especially the green samples, according to Heppe (2006) basaltic andesites and basanites (although they plot as basalt on TAS; Fig. 88A), have a striking resemblance to the Jinghong basalt samples. Heppe (2006) believes

that the basaltic rocks are related to a failed-rifting event caused by the Emeishan mantle plume, and the varying Ta and Nb concentrations are explained by crustal contamination (Heppe, 2006).

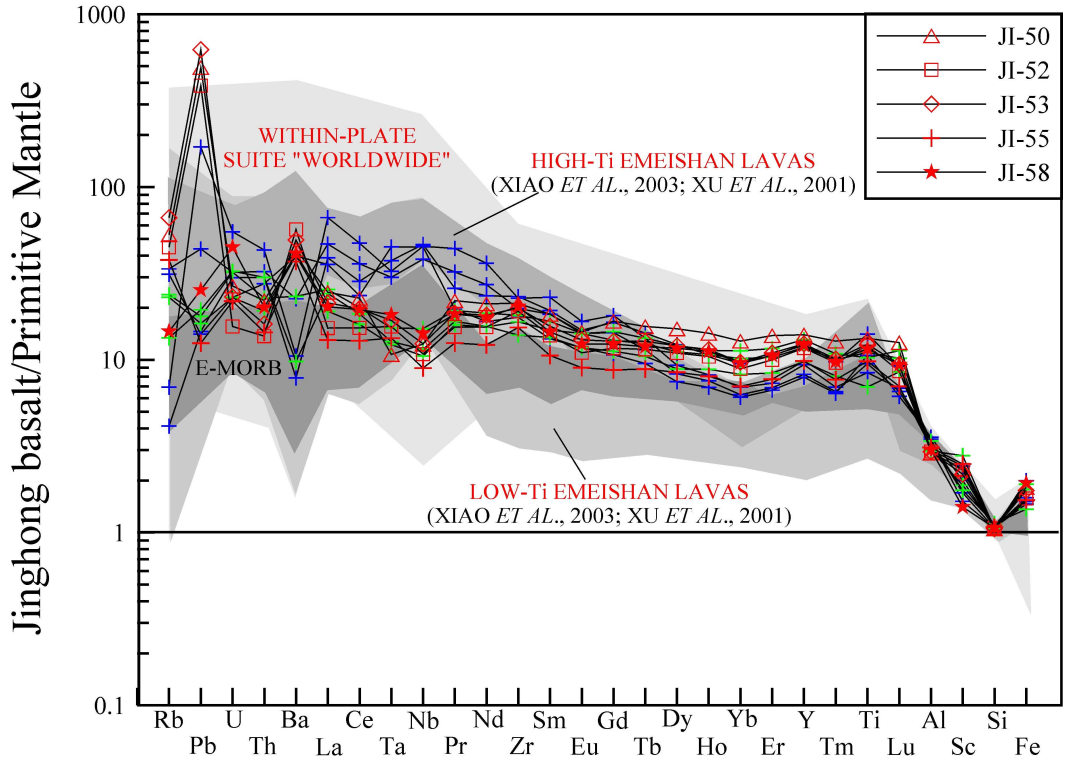

Fig. 90: Primitive mantle-normalized multi-element patterns of the Jinghong basalt. The rocks show marked similarities to basaltic rocks (in green) from SW Yunnan (Heppe, 2006).

The weakly fractionated REE patterns of the Jinghong basalt samples plot coherently at 20-70 times chondritic (Fig. 91). The weak negative Eu-anomaly (Eu/Eu* = 0.8-0.9) is likely due to plagioclase, either as retained phase in the source or as fractionating phase in a high-level magma chamber. Most samples depict slight negative Yb-anomalies, which might be suggestive of minor residual garnet. The total REE content and the shape of the patterns contrast to reference data of volcanic-arc magmas and MORB (Bailey, 1981; Kimura & Yoshida, 2006; Luhr & Haldar, 2006; Wilson, 1989 and references therein) but resemble within-plate igneous rocks, such as those of the ELIP (Xiao *et al.*, 2003; Xu *et al.*, 2001).

Note that the Jinghong trachyandesite, Jinghong dacite and Jinghong granodiorite all have more fractionated patterns (with respect to La/Sm and La/Yb ratios) and lower total REE contents. This provides further evidence - besides the rock age - for a different source of the Jinghong basalt and the Jinghong granodiorite, trachyandesite and dacite.

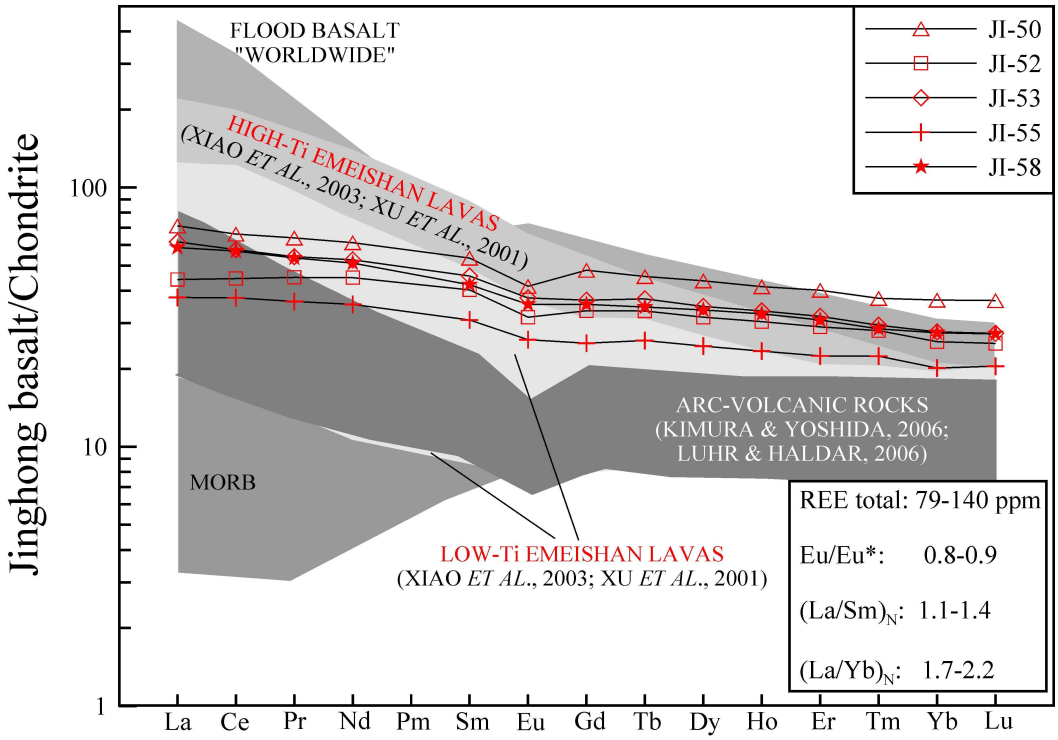

Fig. 91: Chondrite-normalized REE patterns for the Jinghong basalt. The rocks have high REE contents but depict only little fractionation, which suggests a primitive mantle source.

1.10.3 U–Pb ZIRCON GEOCHRONOLOGY

U–Pb zircon geochronology of the Jinghong basalt was performed on a polished rock slab of sample JI-52. Zircon location and documentation was done - similar to the Jinghong dacite - by EMPA. Eleven zircon grains were analyzed at thirteen spots (15-30 µm). The isotopic data are compiled in Appendix Table 23 and age data plots are shown in Figure 92.

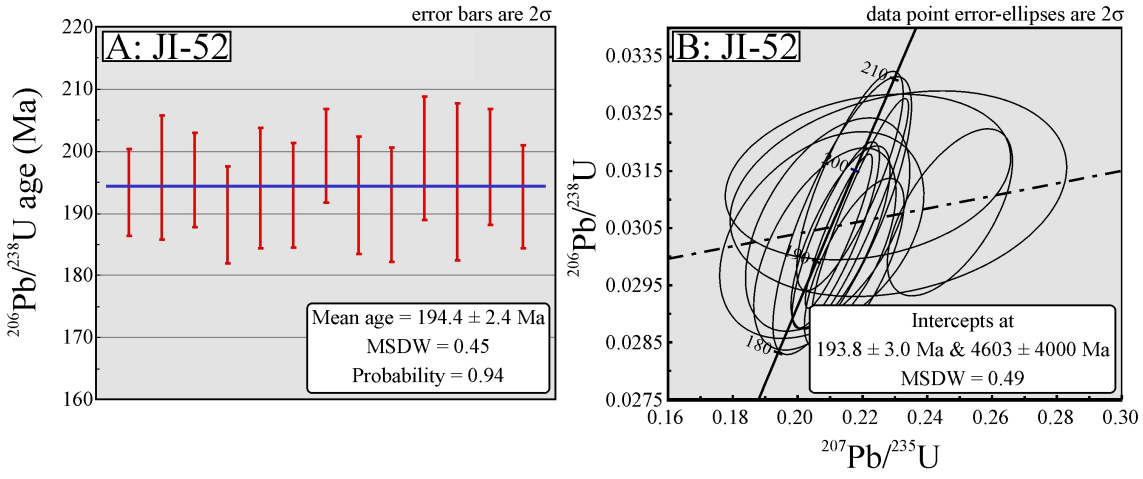

Fig. 92A: Mean $^{206}Pb/^{238}U$ age of thirteen spots analyzed on eleven zircon grains of sample JI-52. B: Concordia plot of sample JI-52. Both plots give identical rock ages.

All zircon grains are light grey in color, show predominantly sharp edges and are partly broken. The analyzed grains have Th/U ratios of 0.25-3.58. The mean $^{206}Pb/^{238}U$ age of all thirteen spots is 194.4 ±2.4 Ma (Fig. 92A). The concordia plot gives a lower intercept age of 193.8 ±3.0 Ma (Fig. 92B). Both ages overlap within the analytical error. The ages are interpreted as crystallization ages of the Jinghong basalt.

1.10.4 $^{40}Ar/^{39}Ar$ GEOCHRONOLOGY

$^{40}Ar/^{39}Ar$ geochronology by incremental heating was performed on rock powder of sample JI-50. The age data are provided in Appendix Table 28 and the age spectrum is shown in Figure 93. The obtained ages at 900-1220°C (^{39}Ar release >1%) are 47.9 ±25.2 to 145.2 ±20.2 Ma. At 1280°C and 1350°C the "lowest-error ages" of 101.9 ±6.7 Ma and 109.6 ±9.5 Ma were obtained, respectively. The final increments at 1450 and 1600°C gave ages of 162.2 ±20.8 and 164.2 ±25.5 Ma.

Petrography and geochemistry (LOI: 2.2 wt%, SO_3: 0.04 wt%) suggest that pyroxene, plagioclase and hornblende of JI-50 may have suffered partial loss of radiogenic ^{40}Ar, which is in accord to the $^{40}Ar/^{39}Ar$ age data, that show two low-temperature/high age dates at 500 and 600°C. The Cl/K ratios of 0.06-0.09 for the temperature intervals of 900-1220°C and 1280-1350°C suggest overprint as well. As seen with other Ar–Ar data in the same region, the time interval of 180-100 Ma is interpreted as a period of tectonothermal overprint.

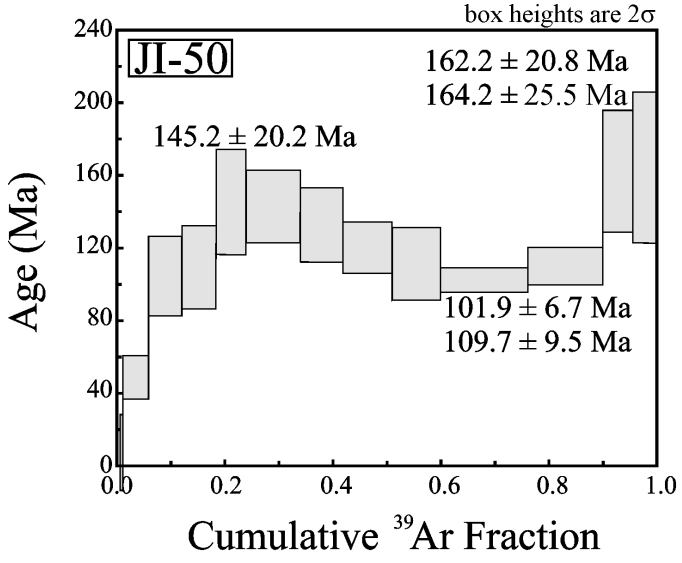

Fig. 93: Ar–Ar age spectrum for the Jinghong basalt sample JI-50. None of the steps fulfills the criteria for a plateau-age. The first three degassing steps at 500-700°C (including <0.2% of the total ^{39}Ar released) with large error are not shown.

1.10.5 Sr–Nd ISOTOPIC COMPOSITION

The Jinghong basalt sample JI-50 has a very primitive composition with high initial ε_{Nd} of 6.4. Interestingly, this is higher than reported for the ELIP (refer to Fig. 69). Beyond that, the rock has high initial $^{87}Sr/^{86}Sr$ of 0.7085 (Table 23; calculated for t = 194 Ma) similar to the Jinghong trachyandesite and the Jinghong dacite.

Table 23: Sr–Nd isotopic composition of the Jinghong basalt sample JI-50. Calculations as cited in Table 1.

Sample ID	Rock type	Age	Sm	Nd	$^{147}Sm/^{144}Nd$	$^{143}Nd/^{144}Nd$	2σ	ε_{Nd} (t)	Rb	Sr	$^{87}Rb/^{86}Sr$	$^{87}Sr/^{86}Sr$	2σ	$(^{87}Sr/^{86}Sr)t$
		Ma	ppm	ppm					ppm	ppm				
JI-50	Basalt	194	7.6	27.0	0.17130	0.512934	0.000004	6.41	34.0	371.7	0.26479	0.708487	0.000004	0.707757

1.10.6 TECTONOMAGMATIC ENVIRONMENT

As suggested by major and trace element geochemistry, most tectonic discrimination diagrams indicate for the Jinghong basalt an intra-plate setting (Fig. 94A-D). On all plots the samples depict marked similarities to reference datasets of the ELIP (plotted in grey shades; Xiao *et al.*, 2003; Xu *et al.*, 2001), to rift basalts from the Xiaru-Tuoding area (Xiao *et al.*, 2008) and to the presumably within-plate related basalt from the Paleng complex (refer to chapter 1.6.3).

1.11 SUMMARY OF THE MAGMATIC EVOLUTION IN THE LANCANGJIANG ZONE

The 292 ±1 Ma-old Nanlianshan complex has a typical “E-MORB composition” and is likely related to the early rift evolution of the Lancangjiang Ocean, a branch ocean of the Paleo-Tethys, which is located between the continental blocks of Simao and Lancang.

The calc-alkaline, 286 ±2 Ma-old Banpo complex (harzburgite, gabbro) likely represents a magmatic arc and points to subduction of oceanic crust beneath the Lancang Block. Additional evidence for Permian to Early Triassic subduction is given by the Paleng complex, the Jinghong granodiorite, the Jinghong trachyandesite, and the Jinghong dacite. These rocks document arc magmatism at least until 249.5 ±3.3 Ma.

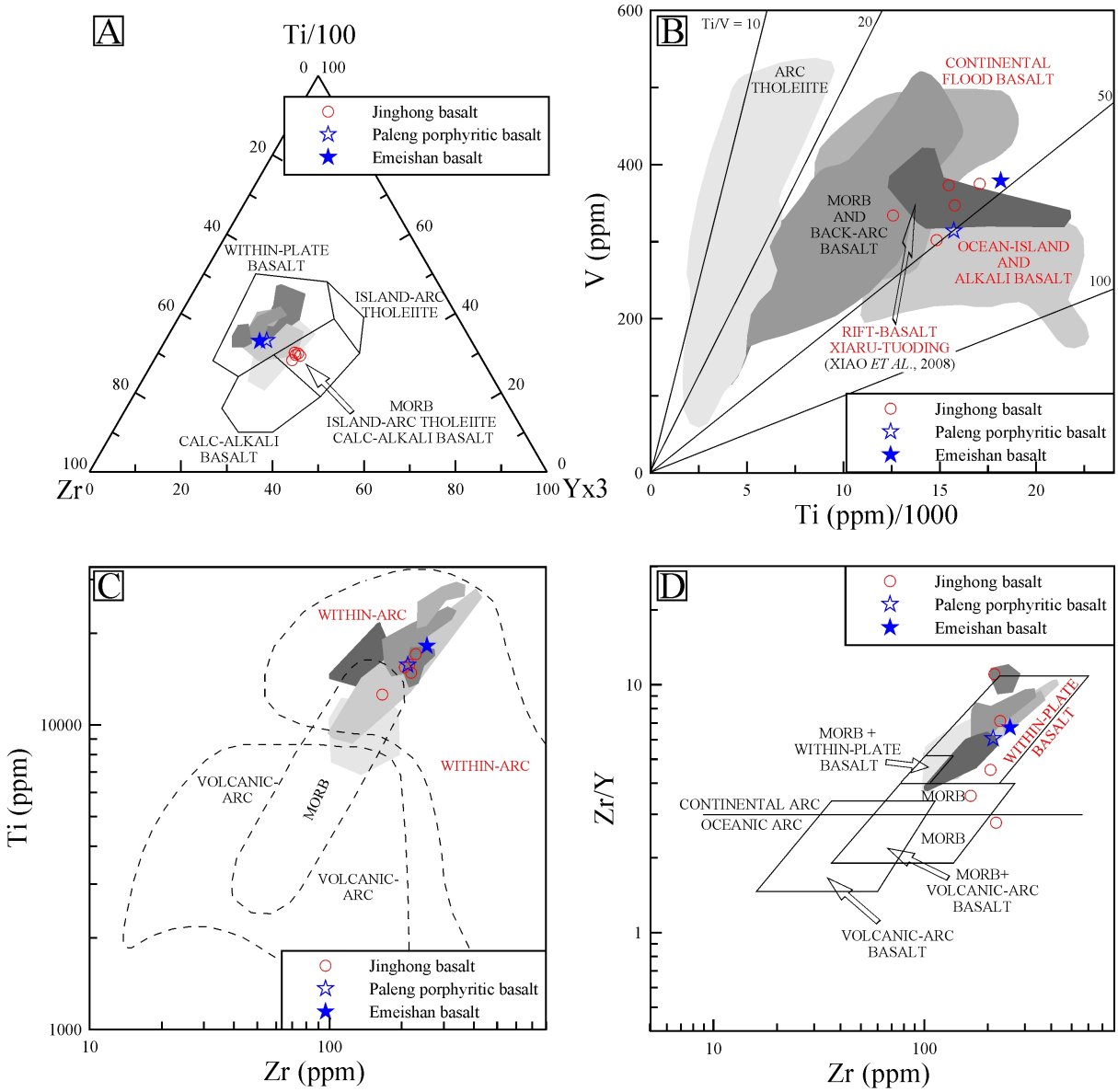

Fig. 94A: The Ti–Zr–Y diagram excludes an intra-plate setting for the Jinghong basalt. Note, however, that reference data for the ELIP (grey shaded polygons) plot partly outside the within-plate basalt field as well (Pearce & Cann, 1973). B: On the V vs. Ti diagram of Shervais (1982) the Jinghong basalt samples plot as “continental flood basalt” and “ocean- island/alkali basalt” and depict marked similarities to the intra-plate basalt from Paleng, to the Emeishan basalt reference sample and to rift basalts from the Xiaru-Tuoding area (Xiao *et al.*, 2008). C/D: Similarities to the Emeishan reference data and to the intra-plate basalt from Paleng are also shown on the Ti vs. Zr and Zr/Y vs. Zr diagrams (Pearce & Cann, 1973; Pearce & Norry, 1979). For additional reference data and further explanations refer to Fig. 61.

The data from the Paleng complex in the southern Lancangjiang zone suggest a temporal and spatial relationship of the arc magmatism of the Paleo-Tethys and the ELIP magmatism at ca. 260 Ma. There are a number of features which point to a causal relationship between these

geological regimes: (1) The ELIP is located, as most large igneous provinces, on the margin of a Precambrian craton (Yangtze Block). 2) There is evidence for accreted terranes (Lancang and Simao Blocks) and for a former oceanic basin in between (Nanlianshan complex, about 40 km to the northeast) (Hennig *et al*. 2009). 4) This oceanic basin was subducted in the Early Permian producing the Jinghong granodiorite and subduction likely went on up to the Permian-Triassic boundary (Hennig *et al*., 2009). 5) The porphyritic basalt from the Paleng complex is astonishingly similar to the Emeishan basalts.

Anderson (1994) suggested a linkage of the extrusion of continental flood basalts with the plate tectonic cycle. One of his models is the ridge-trench collision scenario, where enriched shallow mantle is formed by subduction and dehydration of the oceanic plate beneath “accreted terrane lithosphere” next to a craton. Melting of the fluxed mantle may produce island-arc and back-arc volcanic rocks. When the oceanic ridge finally collides with the trench, the stress regime may change from compressive to extensional and along a weak fracture zone - representing the fissure between the accreted terrane and the craton - the two blocks may break-apart and flood basalts may extrude as a transient result (Anderson, 1994). This model may apply to the situation in SW China. We can however - due to modest outcrop conditions - currently not exclude that the porphyritic basalt of the Paleng complex may represent an oceanic island or seamount component that was incorporated into the Paleng arc-magmatic rocks. But the fact of synchroneity of the Emeishan LIP and the mafic Paleng intrusion remains.

Recently, Peate & Bryan (2008) have shown that the assumed rapid crustal doming before the eruption of the Emeishan flood basalts as claimed by He *et al*. (2003), did not take place. This observation weakens the plume theory for the ELIP generation.

The Lincang granite with an age of 239.4 ±1.3 Ma has a syn- to post-collisional geochemical fingerprint, i.e. it marks the final closure of the Paleo-Tethys in southwest China, which corresponds in the Lancangjiang zone to the closure of the Lancangjiang Ocean. In combination with age data on arc-related volcanic rocks from northern Thailand, it can be assumed that the Paleo-Tethys closed completely by the Early to mid-Triassic (240 ±10 Ma), simultaneously with the collision of the Sibumasu (Shan-Thai) and Indosinian cratonal blocks in southern Vietnam (Barr *et al*., 2000, 2006; Metcalfe, 2002). The collisional event propagated further south into Peninsular Malaysia with a peak around 220 Ma. Postorogenic rifting is evidenced by the Huijingfang mafic complex (194.4 ±2.4 Ma). All rocks studied, including the youngest Huijingfang basalt samples, display Ar–Ar spectra which suggest Cenozoic-Mesozoic tectonothermal overprint.

2 Platinum potential

2.1 PGE ECONOMICS OF CHINA

World resources of platinum-group elements (PGEs) that can be mined economically are estimated to total at more than 100,000 tonnes. The largest resources are in the Bushveld Complex in South Africa, followed by Russia, Canada, Zimbabwe, USA and Australia, which together have >95% PGE resources (USGS, 2010). The PGE resources of China are only <1% of the world`s total.

Three major PGE deposits account for 82% of China's PGE resources. These are the Baijiazuizi/Jinchuan Cu–Ni sulfide deposit, Gansu Province, with reserves of 176 t (57% of China`s total), the Jinbaoshan Pd–Pt deposit, Yunnan Province, with 49 t (16%), and the Yangliuping Ni–Cu deposit, Sichuan Province, with 28 t (9.1%). In general, the PGE grade is very low in China and the PGEs are mostly exploited as by-product in Ni–Co–Cu deposits. The ores have an average composition of 0.34 ppm Pt, 0.39 ppm Pd, 0.041 ppm Os + Ir, and 0.028 ppm Rh + Ru (http://www.chinamining.org).

2.2 THE ELIP AND RELATED DEPOSITS IN SW CHINA AND VIETNAM

The ~260 Ma-old Emeishan Large Igneous Province (ELIP) covers an area of more than 5×10^5 km^2 and is composed of flood basalts and spatially and temporally associated mafic to ultramafic intrusions and sills. These intrusions were exposed by significant uplift and erosion subsequent to the India-Eurasia collision. Some of these intrusions host important Fe–Ti–V oxide, Ni–Cu sulfide or Pt–Pd deposits (Fig. 95). It has been suggested that the ELIP consists of two distinct magma series, one comprising high-Ti basalts and Fe-rich gabbroic intrusions, the other low-Ti basalts and mafic–ultramafic intrusions. Each series is believed to be associated with a distinct type of mineralization, the high-Ti series with predominantly Fe–Ti–V oxide ore deposits, the low-Ti series predominantly with Ni–Cu–(PGE) sulfide deposits (Zhou *et al*., 2002, 2008).

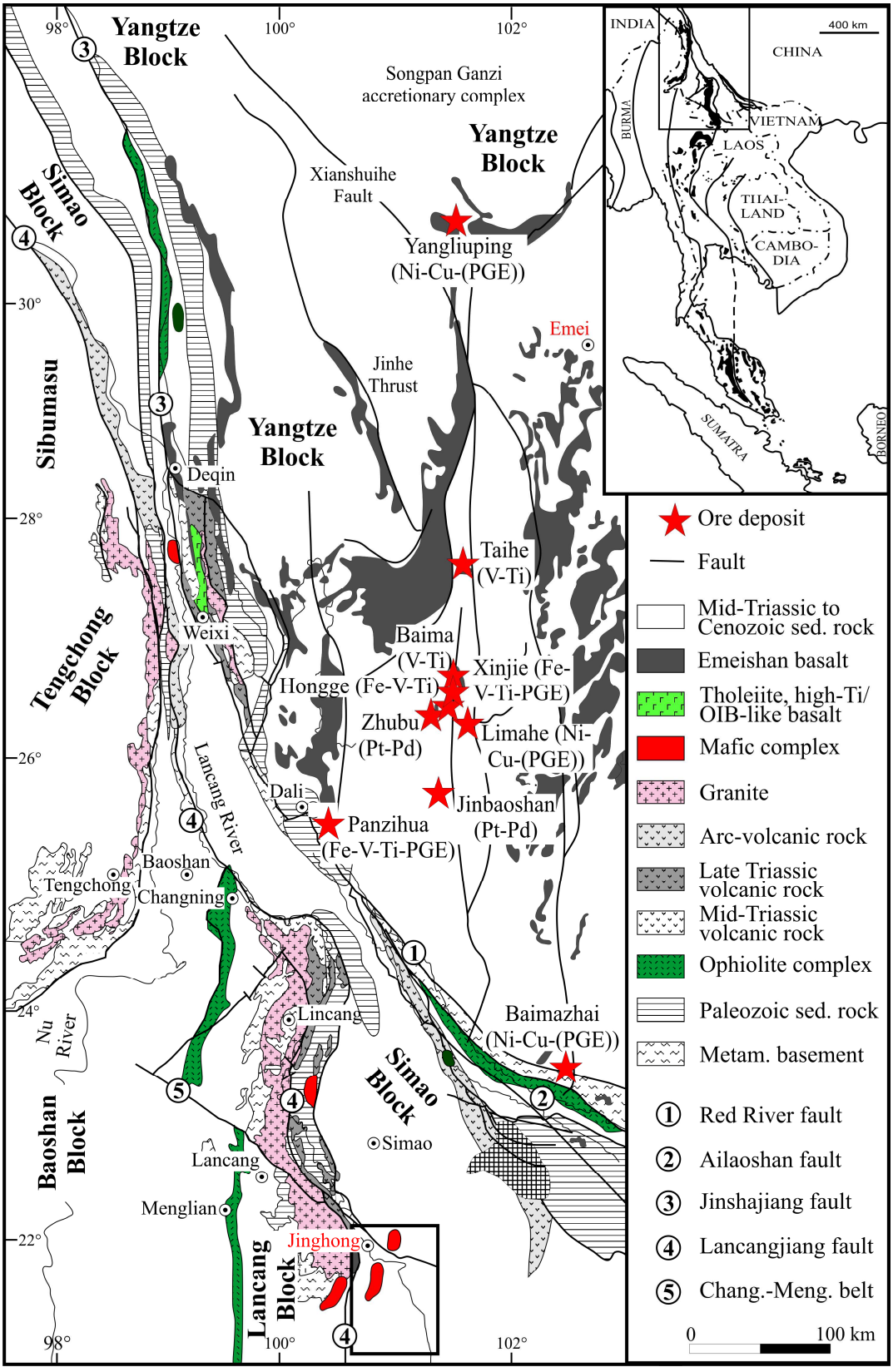

Fig. 95: Geological overview map of SW China with magmatic ore deposits related to the ELIP. In the Panzhihua-Xichang (Pan-Xi) region the Baima, Xinjie, Hongge, Zhubu, Limahe, Jianbaoshan and Panzhihua deposits constitute a mineral belt of ~200 km km length, which is the most important metallogenic district for Fe–Ti–V and Ni–Cu–(PGE) metals in China (Ma *et al.*, 2003). The region was uplifted during the Eurasia-India collision along N–S trending faults.

The four largest Fe–Ti–V oxide deposits in Sichuan and Yunnan are Hongge (4.3 Gt ore resources), Baima (1.5 Gt ore resources), Panzhihua (1.3 Gt ore reserves) and Taihe (~550 Mt ore reserves) (Ganino *et al*., 2008; Ma *et al*., 2003; Tao *et al*., 2007). Hongge was studied by the Sichuan Bureau of Geology and Mineral Resources (SBGMR, 1991), Yao *et al*. (1993), Zhong *et al*. (2002, 2003, 2004, 2005), Zhong & Zhu (2006) and Pang *et al*. (2008); Baima by Zhou *et al*. (2005, 2008), and Panzhihua by Ganino *et al*. (2008), Pang *et al*. (2008), Zhong & Zhu (2006) and Zhou *et al*. (2005, 2008). No English literature exists on Taihe.

The three most important Ni–Cu sulfide deposits in Sichuan and Yunnan are Limahe, Baimazhai and Yangliuping. Little information is available on Limahe (Zaw *et al*., 2007; Zhou *et al*., 2008). English-language publications for Baimazhai are from Pu *et al*. (2007) and Wang *et al*. (2006). Yangliuping was mainly studied by Song *et al*. (2003) and Zheng *et al*. (2004), with some contributions by Deng *et al*. (2002) and Yao *et al*. (2003).

Pt–Pd mineralization is known from several mafic-ultramafic intrusions, including Jinbaoshan, Zhubu, Xinjie and Panzhihua, but Jinbaoshan is the only one with economic Pt–Pd ore. Publications in English about Jinbaoshan are from Wang *et al*. (2005, 2008), Tao *et al*. (2007, 2008), Song *et al*. (2008a) and Zaw *et al*. (2007). Only little English literature is available on Zhubu (Tao *et al*., 2006; Zhou *et al*., 2008; Zhu *et al*., 2004). Xinjie is described by Luo (1981), by the Pan-Xi Geological Team (PXGT, 1981), by Zhang *et al*. (1999), Zhong *et al*. (2004), Zhou *et al*. (2002) and Zhu *et al*. (2010).

The Ban Phuc Ni–Cu–(PGE) deposit in northern Vietnam is likely related to the ELIP as well. The deposit - including its host rocks - was studied by Glotov *et al*. (2001), Hanski *et al*. (2004), Hellman (2005), Polyakov *et al*. (1996, 1998) and Trung *et al*. (2006).

2.2.1 Ni–Cu–(PGE) DEPOSITS

2.2.1.1 YANGLIUPING

In the Yangliuping area, Ni–Cu–PGE sulfide deposits are hosted in four mafic to ultramafic sills, of which the Yangliuping and Zhengziyanwuo sills are the most economic. Each sill is ~1-2 km long, 200-300 m thick and consists of serpentinite, talc schist, tremolite schist and metagabbro. The sills are associated with ELIP-related basalts and intrude Devonian marble and graphite schist of the Yangliuping tectonic dome (Song *et al*., 2003; Zheng *et al*., 2004). Massive Ni–Cu mineralization is restricted to the basal sill parts and to the footwall beneath (Song *et al*., 2003). The mineralization is ~130-250 m thick (Zheng *et al*., 2004).

The Bureau of Geological and Mineral Resources of Sichuan Province (BGMS) discovered the deposits in the 1970s, and subsequent exploration established a combined resource for the Yangliuping and Zhengziyanwuo sills of 275,000 t Ni (average grade: 0.45 wt% Ni), 100,000 t Cu (0.16 wt% Cu), 10,000 t Co (0.016 wt% Co) and 35 t PGEs (0.55 ppm PGE) (BGMS, 1982; Song *et al*., 2003; Zaw *et al*., 2007). Ore minerals include pyrrhotite, chalcopyrite, pentlandite, sphalerite, galena, ilmenite, cobaltite (CoAsS), violarite ($FeNi_2S_4$), sperrylite ($PtAs_2$) and testibiopalladite (PdTe(Sb,Te)) (Song *et al*., 2003; Zaw *et al*., 2007).

2.2.1.2 LIMAHE

The Limahe deposit is hosted by a concentric intrusion with a peridotite core surrounded by pyroxenite and gabbro. The sulfide ore bodies are in the central part of the intrusion (Zhao *et al*., 2008). Zhao et *al*. (2008) obtained a Late Permian $^{206}Pb/^{238}U$ zircon age on gabbro of 263 ±3 Ma and an identical $^{207}Pb/^{235}U$ age of 261 ±5 Ma. Zaw *et al*. (2007) give a resource of 1.5 Mt ore with 1 wt% Ni, 0.5 wt% Cu and about 1 ppm PGEs.

2.2.1.3 ZHUBU

The Zhubu intrusion is similar to the Limahe intrusion, i.e. it forms a concentric body with a peridotite core surrounded by pyroxenite and gabbro/diorite. The sulfides are in the central part (http://www.chinamining.org). Zhou *et al*. (2008) obtained a $^{206}Pb/^{238}U$ zircon age of 261 ±2 Ma. The Zhubu deposit is generally regarded as exploited but PGEs are recovered from slag. Beyond that, Zhubu produces Ca–Mg–P fertilizers and slag cement. The PGE resources are estimated at 6.3 t (http://www.chinamining.org).

2.2.1.4 XINJIE

The Xinjie deposit is hosted by a mafic-ultramafic sill with well developed igneous layering. The sill has NW-trend and is about 7.5 x 1-1.5 km large (Zhang *et al*., 1999). It intrudes Emeishan basalts and has three lithological cycles, each representing a sequence from ultramafic to basic/felsic composition (Zhong *et al*., 2004). Cycle I includes from bottom upwards peridotite, olivine clinopyroxenite, plagioclase clinopyroxenite, gabbro, and quartz-bearing gabbro. Cycle II is characterized by plagioclase-bearing peridotite, olivine

clinopyroxenite, gabbro and quartz-bearing gabbro. Cycle III has plagioclase clinopyroxenite, gabbro and quartz diorite. At the chilled bottom of the intrusion, i.e. at the contact with the Emeishan basalts, fine-grained gabbro and olivine gabbro are developed (Mao & Sun, 1981).

V–Ti magnetite ores occur mainly at the top of Cycles I and II and are composed of Ti-bearing chromite, Cr-magnetite, magnetite and ilmenite. The PGE mineralization is located at the base of the intrusion and in the upward following pyroxenite, with disseminated Cu and Ni sulfides and thin Ti-bearing chrome-magnetite and chromite layers (Luo, 1981; PXGT, 1981; Zhang *et al*., 1998).

There are two 5-10 m-thick PGE-enriched layers at the bottom of Cycle I that contain 0.3-1.8 ppm PGEs (PXGT, 1981). These layers have up to 2 vol% sulfides including pyrrhotite, pentlandite, chalcopyrite and cubanite, and 5-20 vol% Fe–Ti oxides. Platinum-group minerals (PGMs) include native platinum, sperrylite, merenskyite $(Pd,Pt)(Te,Bi)_2$, moncheite ($(Pt,Pd)(Te,Bi)_2$), michenerite ((Pd,Pt)BiTe), erlichmanite (OsS_2) and Ru-rich erlichmanite (Luo, 1981; Zhu *et al*., 2010). The Xinjie intrusion is dated at 259 ±3 Ma by SHRIMP U–Pb on zircon (Zhou *et al*., 2002).

2.2.1.5 JINBAOSHAN

2.2.1.5.1 Introduction

The Jinbaoshan deposit was discovered in 1971 and was mined by the Yunnan Nickel Company since the 1980s. Currently it is under exploration by Jinshan Gold Mines. The deposit is hosted by a large sill-like ultramafic body (4760 x 1240 x 8-170 m) of wehrlite and plagioclase hornblendite (Wang *et al*., 2008; Zaw *et al*., 2007). Tao *et al*. (2008) obtained SHRIMP U–Pb zircon ages of 260.6 ±3.5 and 260.7 ±5.6 Ma on wehrlite and hornblendite, respectively.

The geologic situation at Jinbaoshan is complex. There are 11 ultramafic and 21 mafic sill-like bodies that intrude Devonian and Lower Permian limestone, sandstone and slate. The country rocks form a dome and are in fault contact with the overlying Triassic sedimentary rocks (Wang *et al*., 2008). Economic ore grades are restricted to five ultramafic sills, of which the largest is ~2100 x 400-600 x 4-16 m and accounts for 44% of the total resource.

The ores have 9-20 vol% oxides and <3 vol% base metal sulfides (BMS). Net textured ores with >5 vol% BMS are rare and located in the lower part of the intrusion (Wang *et al*., 2008). The enrichment of Pt and Pd is spatially associated with disseminated

BMS that occur as discontinuous layer within the wehrlite. A sub-horizontal layer of 5-15 m thickness with 5-12 vol% chromite occurs in the middle part of the wehrlite (Tao *et al*., 2007).

The resource is estimated by Chinese geologists at 1.3 Mt ore grading 0.65 ppm Pt, 1.1 ppm Pd, 0.19 wt% Ni and 0.19 wt% Cu (http://www.jinshanmines.com; SEGNL, 2005). The cut-off at Jinboashan is 0.5 ppm Pt + Pd. PGMs are moncheite ($PtTe_2$), atokite (Pd_3Zn), kotulskite (PdTe), sperrylite ($PtAs_2$), irarsite (IrAsS), cooperite (PtS), sudburyite (PdSb), rustenbergite (Pd_3Sn), paolovite (Pd_2Sn), biopalladinite, mertieite ($Pd_{11}(Sb,As)_4$), arsenopalladinite ($Pd_8(As,Sb)_3$), Pt–Fe alloy and native platinum (Song *et al*., 2008; Wang *et al*., 2008). BMSs include violarite ($FeNi_2S_4$), pentlandite ($(Ni,Fe)_9S_8$), siegenite ($(Ni,Co)_3S_4$), rammelsbergite ($NiAs_2$), cobaltite (CoAsS), chalcopyrite, tetrahedrite ($(Cu,Fe)_{12}Sb_4S_{13}$), bornite and covellite (Song *et al*., 2008; Wang *et al*., 2008).

2.2.1.5.2 Petrographic description of the Jinbaoshan reference samples

2.2.1.5.2.1 Chromite-bearing peridotite

The inequigranular, idiomorphic to xenomorphic-granular peridotite (samples JBS-2 to JBS-6) has 50-60 vol% olivine, 20-30 vol% orthopyroxene (predominantly enstatite), 10-20 vol% clinopyroxene (predominantly augite), 2-3 vol% hornblende and <2 vol% phlogopite (Fig. 95A-I). The rock is intensively serpentinized and carbonatized (Fig. 96A-J).

Euhedral olivine (0.2-5.0 mm) is altered to serpentine fibers and meshes. The crystal shape suggests a forsteritic composition (Fig. 96A-F). Enstatite (0.2-2.0 mm) forms anhedral patches in between the olivine crystals, similar to the Banpo harzburgite, but shows only minor clinopyroxene exsolution (Fig. 96B/D). Exsolution of clinopyroxene to orthopyroxene (diallag) is abundant (Fig. 96F). Orthopyroxene exhibits locally oriented pseudomorphs of lizardite (bastitization) (Fig. 96B/F), and both pyroxenes have ilmenite exsolution lamellae (Fig. 96B/D/F/I). Clinopyroxene depicts uralitization and chloritic alteration (Fig. 96E). Pyroxene weathering leads to a fine-grained mineral assemblage of carbonate, ilmenite and hematite (Fig. 96D/E). Mg-rich, brown hornblende (0.05-1.0 mm) fills together with phlogopite (0.1-1.0 mm) the interstices of olivine crystals (Fig. 96G/H). Hornblende appears to be predominantly derived from uralitization of augite and enstatite (Fig. 96A/E/G). Hornblende weathers to hematite (Fig. 96M). Intensive weathering of the rock suite leads to vermiculite formation, predominantly from olivine decay (Fig. 96I). The rock is cut by carbonate veinlets (Fig. 96J).

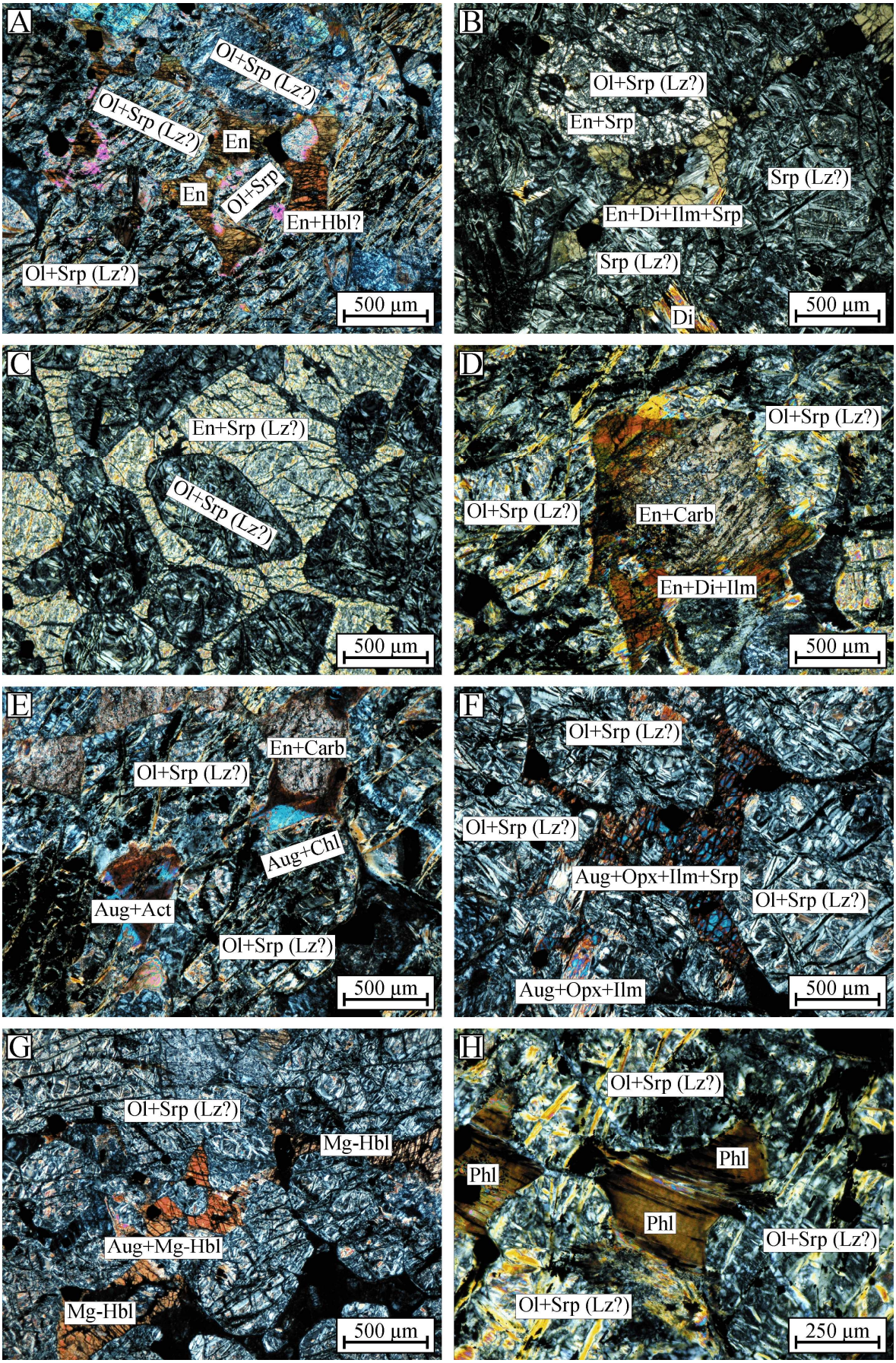

Fig. 96: Photomicrographs of the Jinbaoshan peridotite samples (A/D/E: JBS-2, B/C/F/G/H: JBS-3. All photographs are taken at transmitted light/crossed polars).

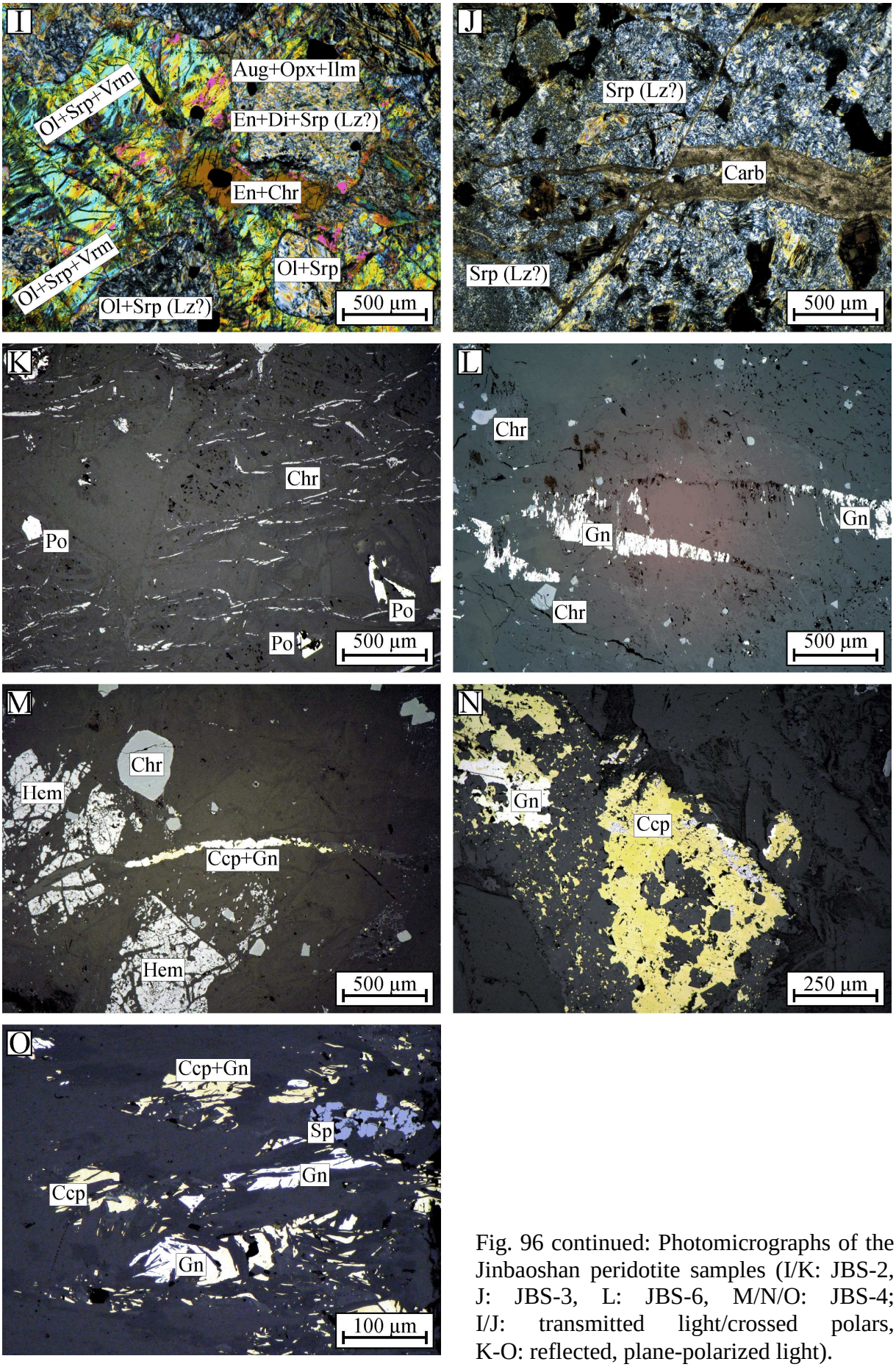

Fig. 96 continued: Photomicrographs of the Jinbaoshan peridotite samples (I/K: JBS-2, J: JBS-3, L: JBS-6, M/N/O: JBS-4; I/J: transmitted light/crossed polars, K-O: reflected, plane-polarized light).

Euhedral to subhedral chromite occurs as thin seams (<0.05 mm-thick) and as euhedral to subhedral crystals (0.04-3.0 mm; Fig. 96K-M). Some crystals depict cracks, predominantly filled by serpentine (Fig. 95L/M). Most of the rock samples have pyrrhotite (<0.5 mm; Fig. 95K), that is partly altered to pyrite. On vein locations, rock samples JBS-4 to JBS-6 have syntectonic galena (0.04-0.6 mm) and chalcopyrite (0.05-0.7 mm; Fig. 96L-N). JBS-4 has some minor sphalerite (0.02-0.2 mm; Fig. 96O). Accessories include titanite, zircon and rutile.

2.2.1.5.2.2 Gabbro

The inequigranular, hypidiomorphic to xenomorphic-granular gabbro reference sample JBS-1 is strongly altered. The primary modal composition is estimated at 55 vol% plagioclase, 35 vol% clinopyroxene (predominantly diopside) and 5 vol% amphibole (Fig. 97A-C). The rock is intensively cut by chlorite, calcite and quartz veinlets (Fig. 97A).

Subhedral plagioclase (0.3-2.0 mm) is bended and broken, which suggests tectonic overprint (Fig. 97A-C). Plagioclase alters to sericite and carbonate (Fig. 97A/B). Diopside is predominantly fine-grained (0.02-0.5 mm; basiophitic rock texture) and alters to chlorite (Fig. 97A/B). Subhedral brown hornblende (0.1-1.0 mm) depicts actinolitization, chloritization and hematitization (Fig. 97C/D). Opaques include 5 vol% hematite, 0.5 vol% chalcopyrite (0.02-0.15 mm) and 0.1 vol% pyrrhotite (0.01-0.4 mm; Fig. 97E/F). Accessories are apatite (<0.015 mm), zircon (<0.1 mm), rutile and titanite (<0.15 mm).

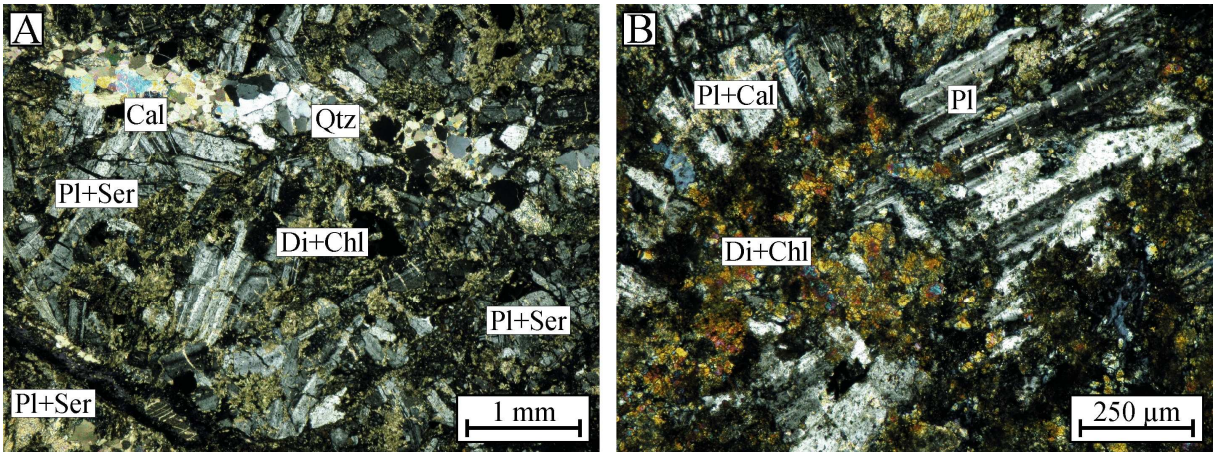

Fig. 97: Photomicrographs of the Jinbaoshan gabbro sample JBS-1 (A/B: transmitted light/crossed polars).

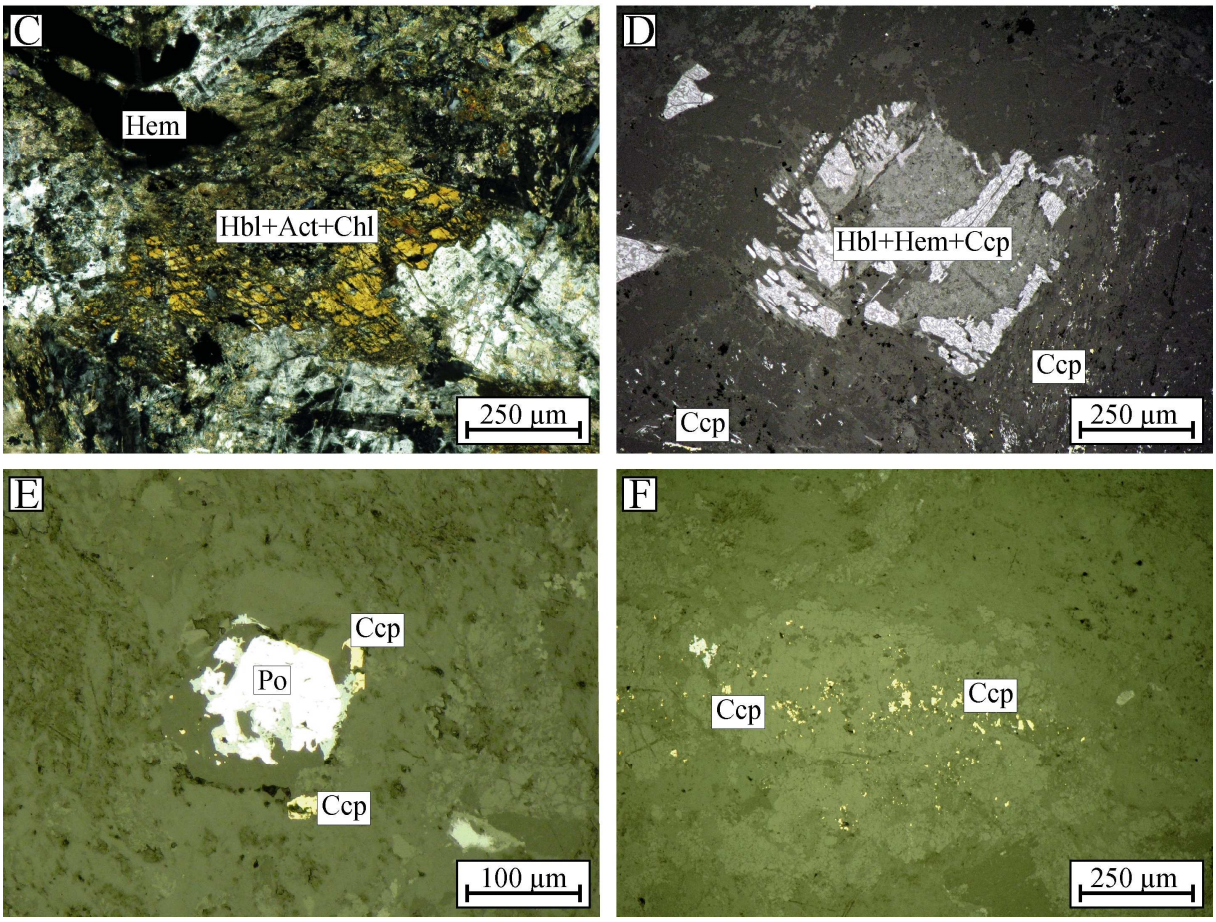

Fig. 97 continued: Photomicrographs of the Jinbaoshan gabbro sample JBS-1 (C: transmitted light/crossed polars, D-F: reflected, plane-polarized light).

3.2.1.5.3 $^{40}Ar/^{39}Ar$ geochronology of the Jinbaoshan peridotite

$^{40}Ar/^{39}Ar$ geochronology by incremental heating was performed on a serpentine mineral separate of sample JBS-2. The age data are provided in Appendix Table 27 and the plots are shown in Fig. 98. The ^{39}Ar data do not fulfil the criteria for a plateau age, and the spectra indicate tectonothermal overprint.

At about 1025°C, i.e. after 25% of the total ^{39}Ar released, the age spectrum gives a maximum date of 259.9 ±11.6 Ma (2σ), which corresponds to the SHRIMP U–Pb zircon ages on wehrlite and hornblendite of 260.6 ±3.5 and 260.7 ±5.6 Ma, respectively (Tao *et al.*, 2008).

The age spectrum identifes younger age intervals (in blue). The older, more distinct interval of 213-176 Ma (including the errors) comprises five successive heating steps of 1140-1280°C with about 47% of the total ^{39}Ar released. The second age interval of 168-142 Ma includes 26% of the total ^{39}Ar released with three non-successive heating steps (Fig. 98A). Ar/Ar correlation diagrams suggest, in accordance to the complicated Ar–Ar

spectrum and petrographic descriptions, metamorphic overprint. The $^{40}Ar/^{39}Ar$ isochron age of the rock is 183 ±17 Ma, and the $^{36}Ar/^{39}Ar$ isochron age is 178 ±29 Ma (Fig. 98B/C).

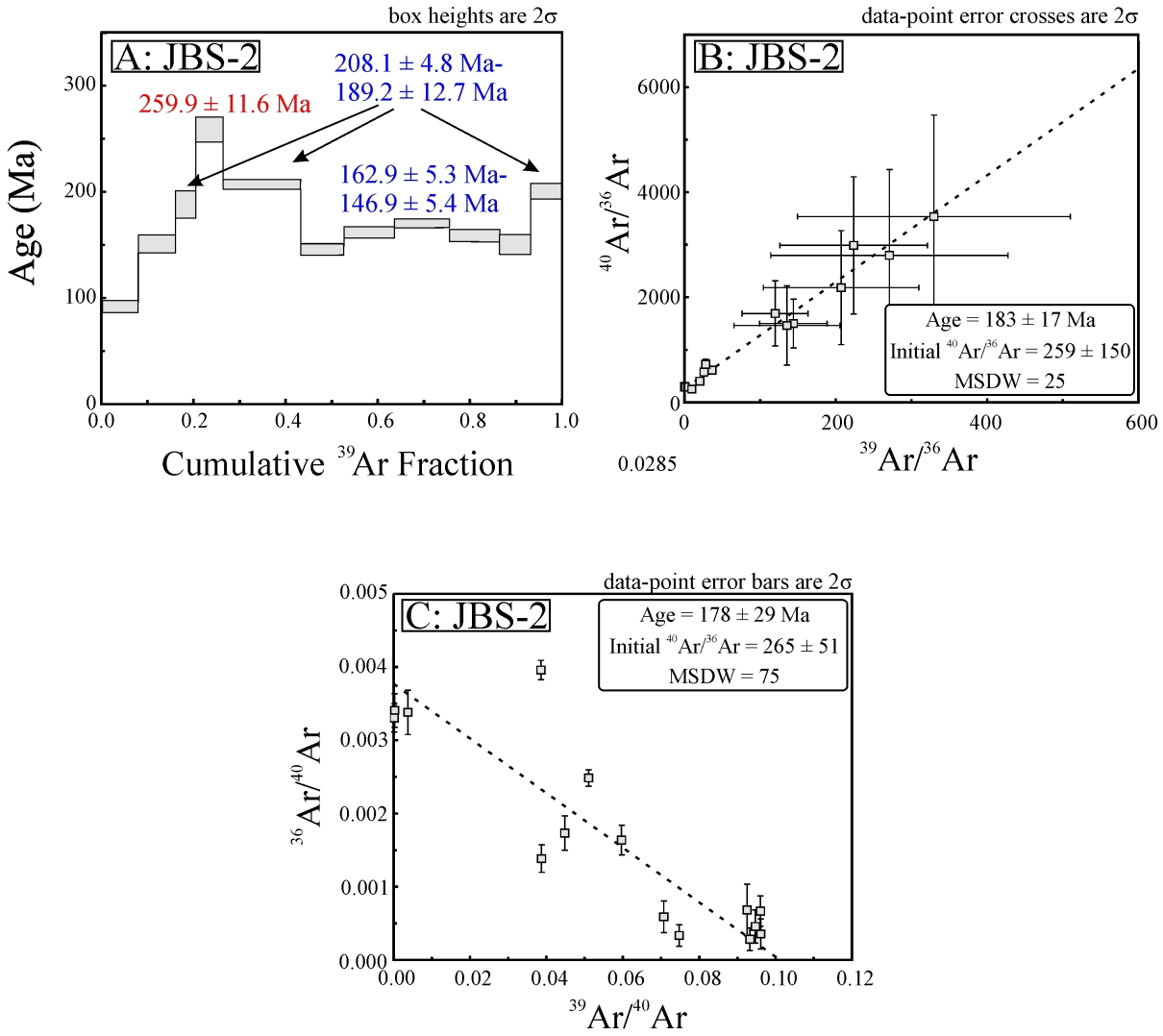

Fig. 98A: Ar–Ar age spectrum for the Jinbaoshan peridotite (sample JBS-2). Note: For clarity, the first high error steps are omitted. The plot gives a typical "Emeishan date" and suggests metamorphic overprint in between ~200 and 140 Ma. B/C: Ar–Ar correlation diagrams for the Jinbaoshan peridotite.

2.2.1.6 BAIMAZHAI

The Baimazhai Ni–Cu deposit, south of the Red River-Ailaoshan Shearzone, within the Jinping-Song Da rift, is hosted by a mafic to ultramafic sill-like intrusion (500 x 200 x 24-64 m) emplaced into Early Ordovician sedimentary rocks of the Xiangyang Formation (Fig. 95; Wang *et al.*, 2006). The intrusion has a core of olivine pyroxenite and peridotite, surrounded by orthopyroxenite and websterite and rimmed by gabbro. There are

three types of ore: disseminated, altered disseminated and massive (Pu *et al*., 2007). The disseminated ore is restricted to gabbro and pyroxenite (6-12 vol% sulfides) and includes pyrrhotite, pentlandite, chalcopyrite, violarite, magnetite, ilmenite and chromite. The altered ore forms tabular bodies within the disseminated ore and has sulfide contents of 15-30 vol%. Additional ore minerals to the disseminated ore are galena, Ni-cobaltite ((Ni,Co)AsS), and parkerite ($Ni_3(Bi,Pb)_2S_2$). The massive ore forms flat, tabular bodies in the center of the intrusion and has, in addition to the previous ores argentopentlandite ($Ag(Fe,Ni)_8S_8$), mackinawite ($(Fe,Ni)S_{0.9}$), altaite (PbTe) and electrum. The deposit has reserves of 50,000 t Ni and resources of about 100,000 t Ni (unpublished data, cited in Pu *et al*., 2007). Wang *et al*. (2006) obtained a SHRIMP $^{206}Pb/^{238}U$ zircon age of 258.5 ±3.5 Ma on a gabbro sample.

2.2.1.7 BAN PHUC

Ban Phuc is the largest Cu–Ni deposit of Vietnam and was discovered by Vietnamese geologists in 1959 (http://www.asianminres.com). The deposit is related to the NW-trending, oval (940 x 420 m) Ban Phuc intrusion, in the central part of the Song Da rift (Glotov *et al*., 2001). The intrusion is built up of serpentinized dunite and wehrlite, lying concordantly to the folded (anticline structure) Devonian metasedimentary host rocks (Glotov *et al*., 2001).

Massive sulfide mineralization is related to a vein in hornfels along the S-margin of the Ban Phuc intrusion. The vein has NW-strike, and dips steeply to the NE. It is 730 m long, 450 m deep and on average 1.3 m thick (Glotov *et al*., 2001). Mineralization consists of pyrrhotite (70 vol%), pentlandite (10 vol%), chalcopyrite (5 vol%), magnetite (4 vol%), pyrite (3 vol%), violarite (2.5 vol%), siderite, ilmenite, sphalerite and galena (all <1 vol%) (http://www.asianminres.com). Glotov *et al*. (2001) give in addition cobaltite (CoAsS), gersdorffite (NiAsS), glaucodote ((Cu,Fe)AsS), lautite (CuAsS), alloclasite ((Co,Fe)AsS)), hexatestibiopanickelite ((Ni,Pd)(Te,Sb)), parkerite ($Ni_3(Bi,Pb)_2S_2$), tsumoite (BiTe), breithauptite (NiSb), sperrylite ($PtAs_2$) and michenerite ((Pd,Pt)BiTe), and estimate the grade of the massive sulfide ore at 0.3 ppm Au, 3 ppm Ag and 0.1 ppm Pt.

Low-grade ore is restricted to two units in the lower part of the dunite body (UB1, UB2). The overlying UB1 contains in contrast to the UB2 only limited mineralization (http://www.asianminres.com). Total thickness of the two bodies is 2-40 m (Glotov *et al*., 2001). The massive sulfide mineralization contains ~2.6 Mt ore with 2.4-2.6 wt% Ni and 1.0-1.2 wt% Cu, which results in a tonnage of ~65,000 t Ni and ~28,400 t Cu. Estimates for the disseminated sulfide ore are - with a cut-off of 0.25 wt% Ni - 48 Mt ore

with 0.38-0.4 wt% Ni resulting in 112,000 t of Ni (Hellman, 2005). Polyakov *et al*. (1996, 1998) give a Rb–Sr age of 257 ±24 Ma on related komatiitic basalts of the Na Muoi region and Hanski *et al*. (2004) obtained a Re–Os isochron age on komatiite of 270 ±21 Ma.

2.2.2 Fe–Ti–V OXIDE DEPOSITS

2.2.2.1 HONGGE

The Hongge deposit hosts the largest vanadium resource of China (Zhong *et al*., 2005; Zhong & Zhu, 2008) and was extensively explored from 1966 to 1980. However, the deposit has not been exploited yet due to its low Fe-ore grade and poor infrastructure (Zhong *et al*., 2002).

Hongge is hosted by a sill-like, layered mafic-ultramafic body that covers an area of ~60 km^2 and has a thickness of ~1.7 km (Pang *et al*., 2008). The body intrudes the Mesoproterozoic Huili group, which consists of metasedimentary/metavolcanic rocks and Emeishan basalts, and is itself intruded by Emeishan-related Permian basalt and syenite (SBGMR, 1991; Zhong & Zhu, 2006). Emplacement appears to have followed the N–S striking Xigeda fault (Fig. 95). The Hongge intrusion consists of three zones: A lower olivine clinpyroxenite zone (LOZ), a middle clinopyroxenite zone (MCZ) and an upper gabbro zone (UGZ) (Zhong *et al*., 2002, 2004). Thick (14-84 m), MCZ- and UGZ-hosted layers of V- and Ti-rich magnetite are the most important ores (Yao *et al*., 1993; Zhong & Zhu, 2006).

PGE-enriched horizons in the lower parts of the LOZ and MCZ are associated with Cu- and Ni-rich sulfides (Zhong *et al*., 2002). The intrusion contains 1.83 x 10^9 t Fe, 1.96 x 10^8 t Ti and 1.45 x 10^7 t V. The ore has 27 wt% FeO (t), 10.6 wt TiO_2 and 0.24 wt% V_2O_5 (Yao *et al*., 1993). Zhong & Zhu (2006) obtained a U–Pb zircon age of 259.3 ±3.0 Ma on a gabbro sample of the Hongge intrusion.

2.2.2.2 BAIMA

The Baima deposit is hosted by a layered gabbroic intrusion of >50 km^2 in size. The lower sequence of the intrusion is composed of olivine gabbro and gabbro, and the upper portion includes pegmatitic pyroxenite and pegmatitic gabbro (Ma *et al*., 2003). Both the Baima and the Panzhihua intrusions are spatially associated with unmineralized syenitic plutons (Ma *et al*., 2003). U–Pb age dating on zircon of such a syenite yielded a $^{206}Pb/^{238}U$ age of 262 ±2 Ma and a $^{207}Pb/^{235}U$ age of 263 ±4 Ma (Zhou *et al*., 2008).

2.2.2.3 PANZHIHUA

The Panzhihua deposits are hosted by a sill-like, 2 km-thick layered gabbro, which dips 50-60° to NW and extends for ~20 km along strike. The lower parts of the intrusion are mined for Ti- and V-rich magnetite by open pit and underground mining since the 1960s (Ganino *et al*., 2008).

The gabbro has in its basal parts magnetite, hornblende-bearing microgabbro and olivine gabbro (~40 m), and is overlain by gabbro and melagabbro with major m-thick Fe–Ti oxide horizons (~70 m), overlain by apatite (<5 vol%) and ilmenite-rich olivine gabbbro (~800 m). Upwards follows barren leucogabbro with cumulus clinopyroxene and plagioclase and interstitial Fe–Ti oxides (500-1500 m) (Ganino *et al*., 2005; Pang *et al*., 2008; Zhou *et al*., 2005). The gabbro intrudes concordantly Late Neoproterozoic dolomitic limestone, which is metamorphosed to forsterite and diopside marble along the footwall contact. The hanging wall is composed of thrust-bounded Late Permian syenites, Triassic shales and coal measures.

Several mines are in production (Zujiabaobao, Lanjian, Damakan, Gongshan and Nalaqing). The major ore zone in the basal part extends for >15 km along strike and for >850 m down dip. The Panzhihua deposits contain 1.333 Mt of ore grading 43 wt% FeO(t), 12 wt% TiO_2 and 0.3 wt% V_2O_5 (Zhou *et al*., 2005). Zhou *et al*. (2005) obtained a SHRIMP $^{206}Pb/^{238}U$ zircon age of 263 ±3 Ma on a leucogabbro from the Upper Zone.

2.3 INTRODUCTION TO PGE CHEMISTRY AND PGE ORE FORMATION

The PGEs (Ru, Rh, Pd, Os, Ir and Pt) are Group VIII to X transition metals, together with Fe, Co and Ni. Therefore, the PGEs share with Fe and Ni the affinity for metallic bonds over ionic bonds, which is typical of siderophile (iron-loving) elements (Barnes & Maier, 1999). The PGEs also share with Cu, Ag and Au the tendency for covalent bonds with sulfur which places them in the group of chalcophile (sulfur-loving) elements.

These features imply that the fundamental controls for PGE distribution in the Earth are metallic and sulfide phases. Due to their siderophile nature, the PGEs were enriched in the Earth`s core during the early evolution of the Earth, leaving only very low PGE concentrations in the bulk silicate earth (primitive mantle) of 1-7 ppb. Since core formation,

the distribution of the PGEs in the silicate part of the Earth is strongly affected by sulfide liquids.

PGEs in silicate magma are primarily concentrated in immiscible sulfide liquids, due to the very high partition coefficients between sulfide and silicate melts (Bezmen *et al*., 1994; Campbell & Barnes, 1984). Major PGE mineralization in magmatic ore deposits is related to large mafic-ultramafic intrusions, such as the Bushveld Complex in South Africa, the Noril`sk Ni–Cu–(PGE) district in Russia and the Stillwater Complex in the USA (Campbell *et al*., 1983; Naldrett, 2004). There is evidence for hydrothermal overprint of the magmatic PGE enrichment that has likely remobilized base metals and PGEs (e.g. Ballhaus & Stumpfl, 1986; Boudreau & McCallum, 1992; Li & Ripley, 2005; Marshall *et al*., 1999; Meurer *et al*., 1998; Molnár *et al*., 2001; Polovina *et al*., 2004).

Some giant Ni–Cu–(PGE) deposits are developed in sub-volcanic intrusions beneath flood basalts of Large Igneous Provinces (LIPs; Lightfood & Hawkesworth, 1997; Naldrett, 1999; Stribrny, 1996). For instance, the Noril`sk Ni–Cu–(PGE) deposit, the largest Ni and second-largest PGE concentration in the world, is related to the 251 Ma-old Siberian flood basalts (Naldrett, 1999; Naldrett & Lightfoot, 1999). In the flood basalt related deposits, the large volume of sulfide melt has likely been concentrated from a volume of magma several hundred times more in volume than the host intrusion itself. Current models explain the formation of these deposits in magmatic feeder conduits (Naldrett *et al*., 1995).

2.3.1 PGEs IN THE EARTH MANTLE AND THEIR BEHAVIOR DURING PARTIAL MELTING

Olivine and Cr-spinel have appropriate crystal-chemical properties to accommodate PGEs, as divalent Os and Ir ions (0.74 A) might substitute for base metals in octahedral olivine sites (e.g. Brenan *et al*., 2005), and Ir, Ru and Rh might substitute for trivalent cations in Cr-spinel (Capobianco & Drake, 1990; Righter *et al*., 2004). For olivine, PGE concentrations of 0.03-0.1 ppb were suggested, which is insufficient to account for the total PGE budget of the mantle (Burton *et al*., 2002; Handler & Bennett, 1999; Luguet *et al*., 2007). Cr-spinel might accommodate 10-100 ppb Ir, Ru and Rh, but accounts only for 2-3 vol% of the mantle and is therefore likely of minor importance as well (Lorand *et al*., 2008).

However, the upper mantle contains ~0.1 vol% Fe–Ni–Cu sulfides (BMS) with PGE concentrations at the ppm level (Burton *et al*., 2002; Morgan, 1986; Pattou *et al*., 1996) and in

situ analyses confirmed that more than 90% of the PGEs of lherzolites reside in BMS (Alard *et al*., 2000; Ballhaus *et al*., 2001; Lorand & Alard, 2001). Therefore, there is general consensus that sulfides play a key role in controlling the PGE abundances of mantle-derived magmas (e.g. Mungall & Naldrett, 2008).

As the PGE sulfide-silicate partition coefficients are extremely high (i.e. 10^3-10^6; e.g. Bezmen *et al*., 1994; Brenan *et al*., 2005; Crocket *et al*., 1997; Fleet *et al*., 1991, 1996, 1999; Peach *et al*., 1990, 1994; Stone *et al*., 1990), a silicate melt segregating from a mantle source with residual sulfide should be nearly PGE free. Melting experiments with sulfide saturated mantle material show, however, that sulfide is, at least partially, molten in the asthenosphere and behaves physically incompatible during melt segregation, i.e. a silicate melt segregating from a mantle residue will entrain molten residual sulfide (and PGEs) in suspension and incorporate it in the basaltic melt (Ballhaus *et al*., 2006; Bockrath *et al*., 2004).

This model, however, does not explain why all primitive basalts - regardless of melting degree and tectonic setting - are depleted in the refractory platinum-group elements Os, Ir and Ru (also called Ir-group PGEs or IPGEs) which results in a characteristic positively sloped chondrite-normalized noble metal pattern (e.g. shown in Fig. 102), non-explainable from published sulfide-silicate partition coefficients. This problem is elegantly explained by primary PGE fractionation in the mantle and is in agreement with mantle samples that have noble metal spectra complementary to those of basalts. Obviously, a sulfide melt must coexist in the mantle with a residual sulfide phase allowing for fractionation of Os, Ir and Ru.

In situ analyses on lithospheric mantle xenoliths suggest two different sulfide populations (Alard *et al*., 2000, 2002; Burton *et al*., 1999; Lorand & Conquéré, 1983), namely (1) Os–Ir–Ru- and Rh-rich sulfides as Fe–Ni monosulfide solid solution blebs (mss), predominantly in olivine, with negatively-sloped chondrite-normalized PGE patterns, and (2) Pd-enriched, chemically very variable, but predominantly intergranular Ni-sulfide (pentlandite) and Cu-sulfide (chalcopyrite-isocubanite) intermediate solid solution (iss) with a positively-sloped chondrite-normalized PGE pattern. The latter are believed to be the crystallization products of a Ni–Cu-rich sulfide melt. Potentially, these two sulfide types record ancient partial melting episodes in the two-phase (solid-liquid) field of mantle sulfide, frozen in, when the samples cooled to lithospheric temperatures (Alard *et al*., 2002).

Interestingly, Ryzhenko & Kennedy (1973) could show that $Fe_{1-x}S$ is indeed stable in the asthenospheric upper mantle and can coexist with silicate melt. Ballhaus *et al*. (2006) and Meibom *et al*. (2004) doubt the existence of monosulfide solid solution and suggest instead

Os–Ir–Ru metallic alloys and common PGE phases in podiform and stratiform chromite ores and in the residual mantle, respectively.

In summary, if a sulfide melt coexists with monosulfide solid solution (or other PGE phases) in the mantle source, it will be depleted in Os, Ir, Ru and Rh, imposing a positively sloped PGE pattern onto basalt as commonly observed. This extraction process leads to the typical negatively-sloped pattern of the residual mantle (Ballhaus *et al*., 2006).

2.3.2 PGE FRACTIONATION DURING ASCENT AND AFTER EMPLACEMENT

As the sulfide solubility in basaltic melts increases with falling pressure (Mavrogenes & O`Neill, 1999), sulfide droplets entrained from the mantle might become dissolved during ascent. Likely, all the elements contained in sulfide are released to the silicate melt, and further noble metal fractionation might be controlled by silicates or oxides and, if the silicate melt is PGE-saturated, by discrete PGE phases (e.g. Borisov & Palme, 1997, 2000).

Nucleation experiments in sulfide-free PGE-oversaturated basaltic melts show olivine, euhedral chromite and metallic noble metal alloy crystallization, with Ir and Ru forming small metallic nuggets attached to chromite microliths (Ballhaus *et al*., 2006). Pt and Pd, in contrast, crystallize to fewer and larger metallic phases suspended in silicate glass, and Rh shows a behavior in between, i.e. there is a negative correlation of melting point and grain size. The higher the melting point of the PGE alloy, the smaller the nugget and the more pronounced the affinity to chromite surfaces.

It is noteworthy to mention that this style of nugget formation is only possible at S-undersaturation, independent of oxidation state. If sulfide is present in addition to chromite, PGEs will partition into the sulfide melt (Ballhaus *et al*., 2006; Borisov & Palme 1997; Sattari *et al*., 2002). Nugget fractionation may also work within the mantle when chromite is precipitated by incongruent melting of Cr-diopside (Onuma & Tohara, 1983). Beyond that, it has been suggested that Os, Ir and Ru are fractionated by substitution in the crystal lattice of chromite (see above) - a process which is believed to reign especially at high fO_2 (Capobianco & Drake, 1990; Capobianco *et al*., 1994), and it is known that the solubility of IPGEs in silicate magma is drastically reduced when oxygen fugacity increases, e.g. due to chromite precipitation (Amossé & Allibert, 1993), which could account for the association of IPGEs with chromite.

2.3.3 ROLE OF SULFIDE SATURATION

It appears likely that only the “last stages” of PGE fractionation are controlled by sulfide-silicate partitioning. Most basaltic melts emplaced in the crust or on the Earth`s surface reach sulfide saturation at some stage, either by cooling and/or olivine fractionation (Li & Ripley, 2005). PGEs in solution in silicate melt are then immediately transferred to the sulfide melt. There will be no relative PGE fractionation at this stage. The sulfide-silicate partition coefficients, although different, are so high that an exsolving sulfide melt will not fractionate the PGEs. However, on fractional crystallization of the sulfide melt, early formed mss will enrich IPGEs, while later formed iss will enrich base metals and Pt and Pd.

2.4 PGEs AND Au IN MAFIC COMPLEXES OF SW YUNNAN

Ten rock samples were analyzed by lead fire assay ICP-MS for Au, Pd and Pt at Actlabs, Canada, and twelve selected rock samples were analyzed by a low-blank high-precision Carius tube ID ICP-MS technique at the University of Hongkong (analytical details in Appendix). All samples were low in Au and PGE (<100 ppb).

2.4.1 NANLIANSHAN VOLCANO-PLUTONIC COMPLEX

Samples JI-3 and JI-38 of the Nanlianshan volcano-plutonic complex have 0.1 and 4.8 ppb Pd, 0.3 and 4.6 ppb Pt and 1.0 ppb Au, respectively (Pb fire assay ICP-MS), which is typical of MORB (Appendix Table 15; Fig. 99). The PGE concentrations are in the range of ELIP-related basaltic and gabbroic (Baimazhai) rocks, of sulfide-saturated northern Deccan trap basalts, and of the sulfide-saturated Nadezhdinsky Formation, which hosts the Noril´sk Ni–(PGE) deposits (Fig. 99A-D).

The drastic negative Pd-anomalies (Pd/Pd* = Pd/Pt x Au) of 0.004 and 0.014, as well as the variable and high Pt/Pd ratios of 1.0 and 3.0 are likely due to weathering, as Pt dissolves in surface waters less readily than Pd (Bowles *et al*., 1994; Cameron & Hattori, 2005; Oberthür, 2002). This hypothesis corresponds to the strongly altered nature of these samples, as defined by petropraphic studies (refer to chapter 1.3.1).

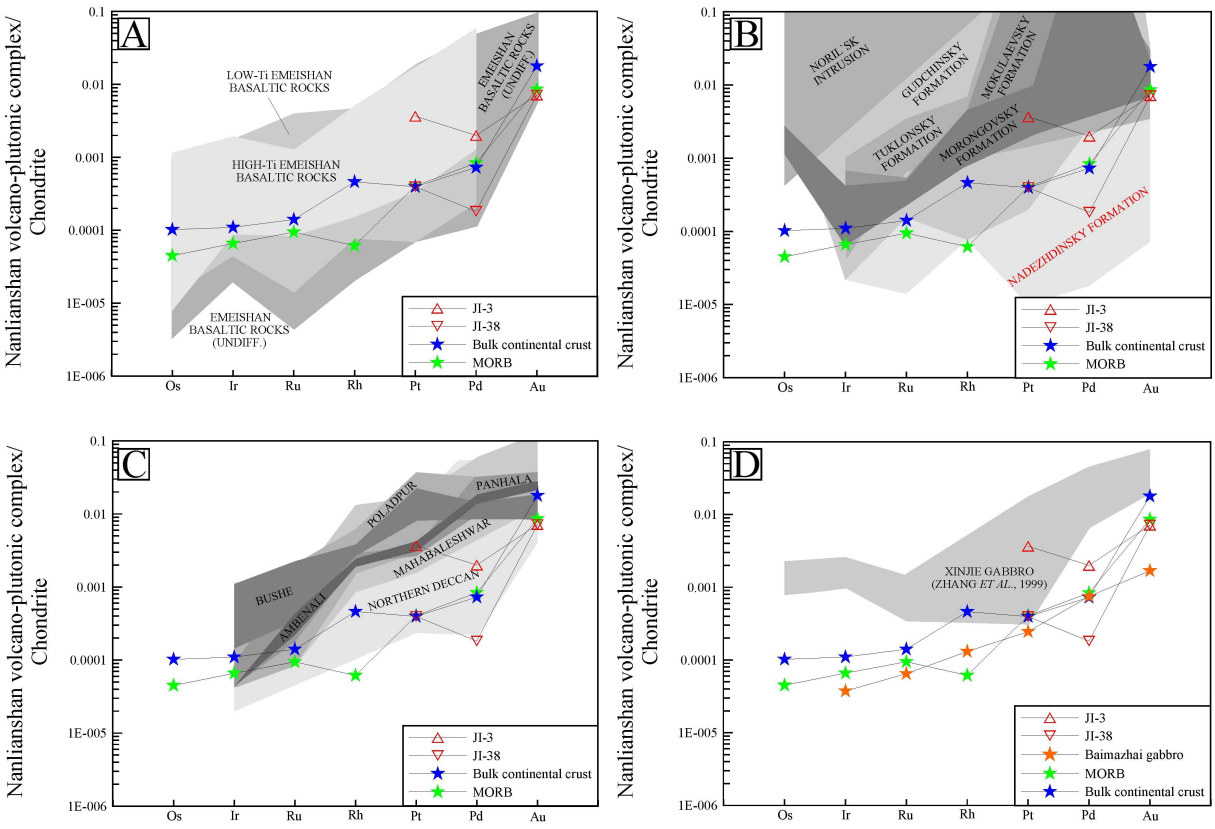

Fig. 99: Chondrite-normalized Pt, Pd and Au concentrations of the two samples from the Nanlianshan volcano-plutonic complex (McDonough & Sun, 1998). The PGEs are sorted in order of descending melting point. Emeishan basaltic rock reference data are from Qi & Zhou (2008), Song *et al*. (2006, 2009) and Zhang *et al*. (2008b). Siberian trap data are from Brügmann *et al*. (1993), Horan *et al*. (1995), Keays & Lightfoot (2009), Walker *et al*. (1994, 1997), Wooden *et al*. (1993) and Zolotukhin & Al`Mukhamedov (1991). Deccan trap data are from Crocket & Paul (2004, 2008), Crocket & Skippen (1966), Keays & Lightfoot (2009) and Paul *et al*. (1984). Baimazhai gabbro data is from Sun *et al*. (2008). MORB data is from Crocket (2002), and bulk continental crust data is from Wedepohl (1995).

2.4.2 BANPO COMPLEX

2.4.2.1 BANPO HARZBURGITE

The five Banpo harzburgite samples analyzed by Carius tube digestion ID ICP-MS have total PGE contents of 5.2-21.9 ppb, and show basalt-like, positively-sloped patterns, i.e. they are strongly depleted and fractionated compared to primitive mantle reference data. Pd/Ir ratios for the pyroxene-rich harzburgites BA-1 and BA-4 are 20-40, and for the olivine-rich harzburgites they are 11-13 (Fig. 100). The Ir concentrations in the olivine/chromite-rich harzburgites are higher (blue samples, 0.27-0.32 ppb) than those of the pyroxene-rich/chromite-poor harzburgites (red samples, 0.11-0.19).

As olivine and chromite are believed to preferably concentrate the Ir-group PGEs (IPGEs = Os, Ir and Ru) over the Pd-group PGEs (PPGEs = Rh, Pt and Pd) (Barnes *et al*., 1988; Capobianco *et al*., 1994; Hertogen *et al*., 1980), these features suggest chromite and olivine fractionation. That chromite fractionation indeed plays a role is indicated by the microscopic observations, by major and trace element characteristics, by positive correlation of Mg with Cr (Fig. 101D), by the strong, negative Ru-anomaly of the pyroxene-rich/chromite-poor sample BA-4 (Ru/Ru* = 0.16) and by the positive Ru-anomaly of the olivine rich/chromite-rich sample BA-20 (Ru/Ru* = 1.34; Maier, 2005).

The Banpo harzburgite has PGE concentrations typical of the S-unsaturated Morongovsky Formation of the Siberian trap (Fig. 100A), of the S-unsaturated southern Deccan traps including the Bushe, Poladpur, Panhala, Ambenali and Mahabaleshwar Formations (Fig. 100B) and of ultramafic rocks of the giant Hongge Fe–V–Ti deposit in the Pan-Xi area, which is related to the ELIP (Fig. 100C).

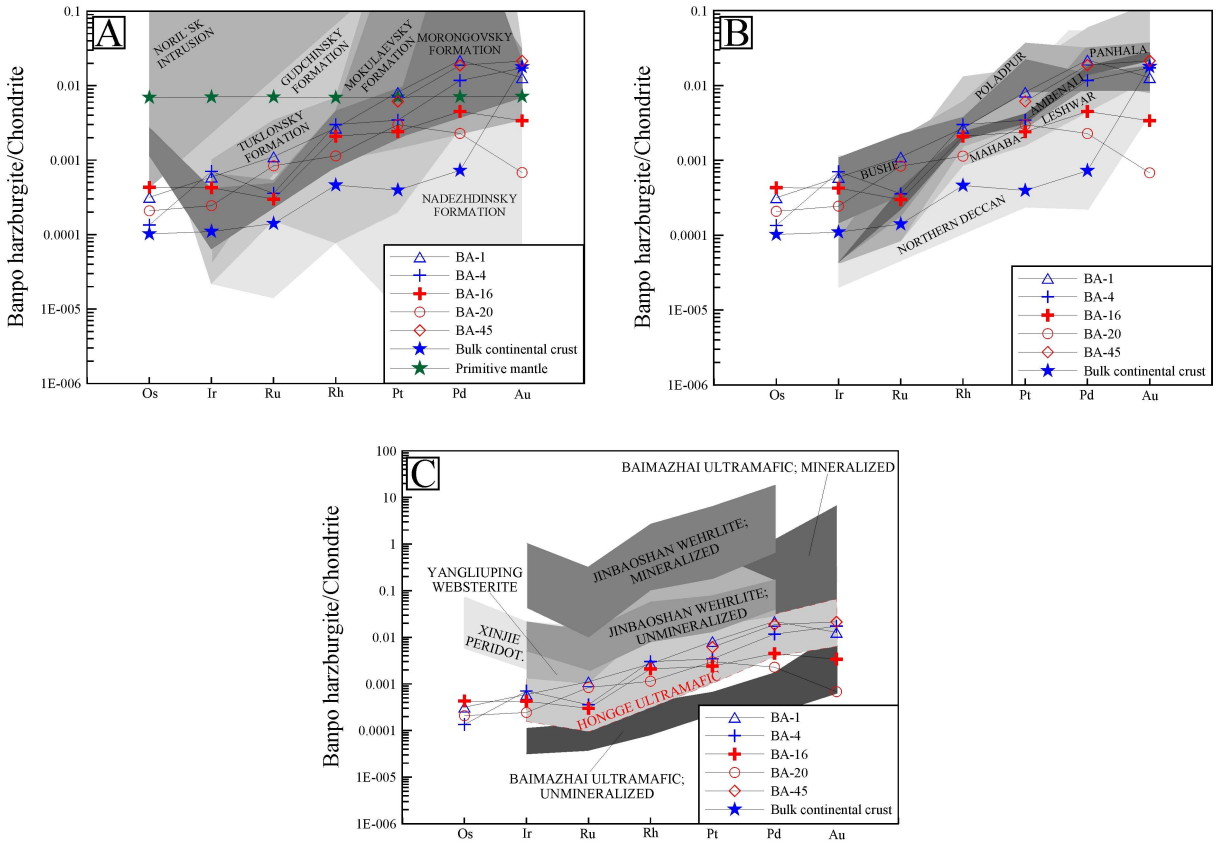

Fig. 100: Chondrite-normalized PGE-patterns of the Banpo harzburgite (McDonough & Sun, 1995). Baimazhai reference data are from Sun *et al*. (2008) and Wang & Zhou (2006), Hongge data are from Zhong *et al*. (2002), Jinbaoshan data from Tao *et al*. (2007), Xinjie from Zhang *et al*. (1999) and Yangliuping from Zheng *et al*. (2004). Other reference data as cited in Fig. 99.

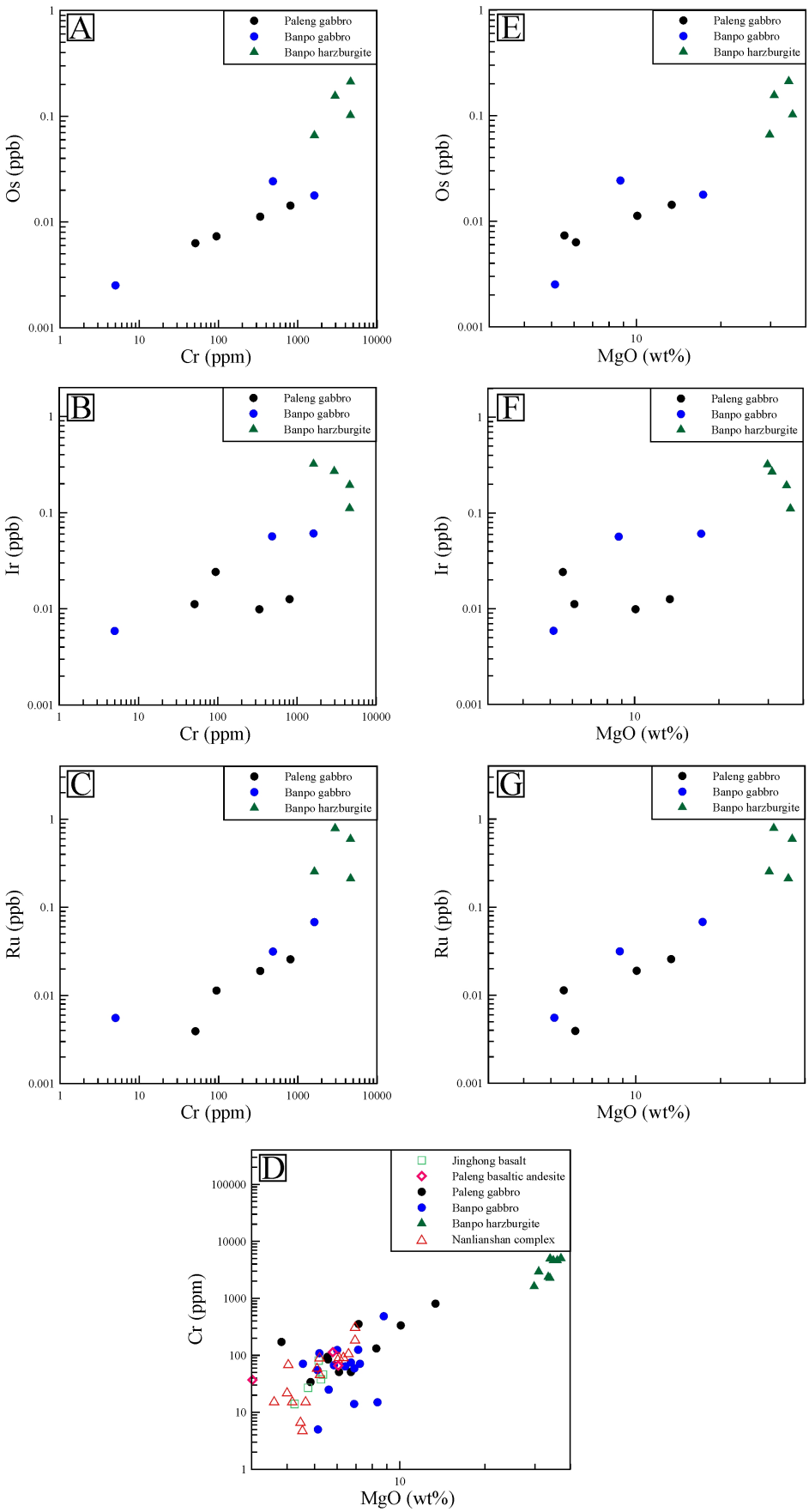

Fig. 101A-C: Correlation diagrams of the IPGEs and Cr. D: The Cr vs. MgO diagram suggests chromite as fractionating phase for the Banpo and Paleng complexes. E-G: Correlation diagrams of the IPGEs and MgO.

2.4.2.2 BANPO GABBRO/HORNBLENDITE

The Banpo gabbro/hornblendite samples BA-5, BA-8, BA-24 and BA-53 (analyzed by Carius tube digestion ID ICP-MS) and BA-41, BA-43, BA-48, BA-51, BA-58 (analyzed by Pb fire assay ICP-MS) show a wide range in PGE concentrations, namely 0.006-0.068 ppb Ru, 0.002-0.046 ppb Rh, 0.047-4.6 ppb Pd, 0.003-0.024 ppb Os, 0.006-0.061 ppb Ir, 0.022-4.2 ppb Pt, and 0.853-3.0 ppb Au (Fig. 102).

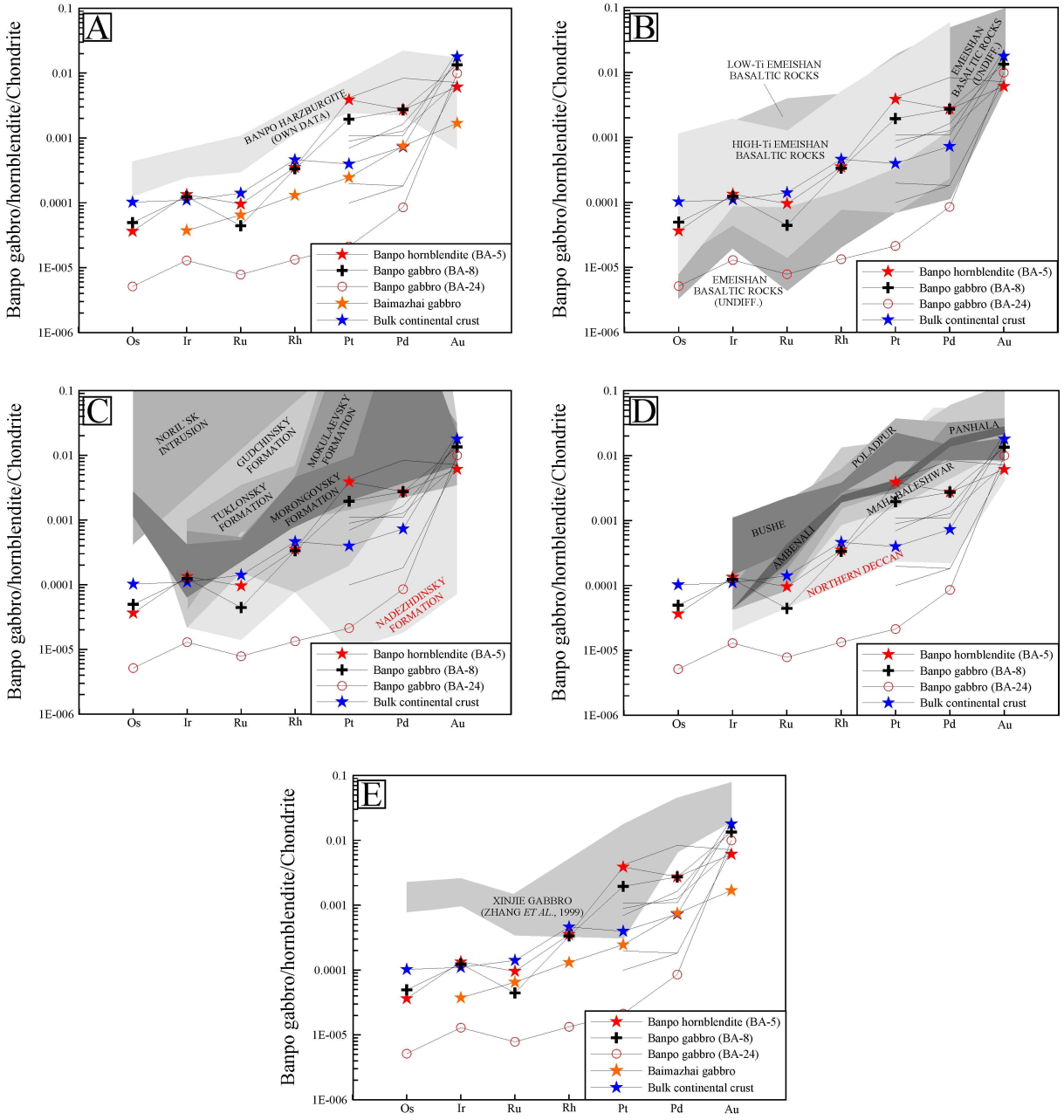

Fig. 102: Chondrite-normalized PGE-patterns of the Banpo gabbro and hornblendite samples. Lines without symbols indicate samples analyzed by fire assay ICP-MS.

The Banpo hornblendite sample BA-5 is very similar in PGE concentrations to the Banpo gabbro sample BA-8, which gives further evidence for a “Banpo cumulate series” comprising gabbro, hornblendite and anorthosite (Fig. 102). The total PGEs of BA-5 and BA-8 are 5.6 and 3.6 ppb, respectively. Gabbro sample BA-24 is set apart with much lower concentrations (total PGEs of 0.08 ppb) and is linked by sample BA-43 to the relatively more concentrated samples plotting together (Fig. 102). In general, all samples are distinctly lower in PGEs than the Banpo harzburgite (Fig. 102A) and depict moderately fractionated slopes with Pd/Ir ratios of 8.0-26.5. All samples have a marked negative Ru-anomaly (Ru/Ru*) of 0.2-0.4.

We suggest that the fractionated patterns of the Banpo gabbro/hornblendite are predominantly driven by partial melting of the upper mantle, followed by chromite fractionation and sulfide saturation. Chromite fractionation is indicated by correlations of Ir and Ru with Cr (Fig. 101B/C) and by the distinct negative Ru-anomalies of the sample suite. The varying Pt/Pd ratios of 0.5-2.6 and the Pd-anomalies (0.02-1.5) might point to a subduction environment (e.g. Kepezhinskas *et al*., 2002) and/or might be governed by hydrothermal alteration and weathering effects (e.g. Bowles *et al*., 1994; Cameron & Hattori, 2005; Oberthür, 2002). The wide range in PGE concentrations and the distinct Pd–Au fractionation are suggestive of sulfide saturation or slab-fluid metasomatism.

All samples have suffered from partial Os loss, which either suggests weathering and hydrothermal alteration (e.g. Hannignan & Peucker-Ehrenbrink, 1999), or Os mobility in subduction zone environments (Brandon *et al*., 1996; Kepezhinskas *et al*., 2002).

The Banpo gabbro has PGE concentrations in the range of the ELIP, of the S-depleted Nadezhdinsky Formation and the northern Deccan flood basalts (Fig. 102B-D). The Banpo gabbro is similar in its PGE inventory to the Baimazhai gabbro, but contrasts with the Xinjie gabbro (Fig. 102E).

2.4.3 PALENG AMPHIBOLE GABBRO

The Paleng amphibole gabbro (4 samples analyzed by Carius tube digestion ID ICP-MS, 6 samples analyzed by Pb fire assay ICP-MS) is very low in PGEs. The total PGE concentrations of the Carius tube ID ICP-MS analyzed samples are 0.3-1.6 ppb (Appendix Table 15).

Chondrite-normalized PGE plots of the Paleng amphibole gabbro samples depict moderately to strongly fractionated patterns with Pd/Ir ratios of 4.4-54.5 (Fig. 103A-D). In general, for the Paleng gabbro, similar fractionation processes as for the Banpo gabbro are inferred, i.e. partial melting of the upper mantle, followed by chromite fractionation and sulfide saturation. Chromite fractionation is indicated by positive correlations of Os and Ru with Cr (Fig. 101A/C), and by the negative Ru-anomalies of the sample suite (Fig. 103A-D).

Samples JI-23 and JI-29 are set apart from samples JI-31 and JI-33 by lower Os contents (0.007 and 0.006 ppb Os vs. 0.014 and 0.011 ppb Os), marked negative Ru anomalies (0.20 and 0.08 ppb Ru vs. 0.81 and 0.71 ppb Ru), and by less developed negative Pd-anomalies (0.41 and 0.60 ppb Pd vs. 0.14 and 0.11 ppb Pd). Samples JI-23 and JI-29 are enriched in Rh, Pt and Pd. Interestingly, the PGE patterns can be correlated with the petrographically determined plagioclase/amphibole ratios of the cumulate series, i.e. samples JI-23 and JI-29 are plagioclase-richer than samples JI-31 and JI-33, which have been identified as the amphibole-richest samples (refer to chapter 1.6.1). As Mg correlates positively with Cr in the Paleng gabbro amphibole samples, there appears to be indeed a genetic link between the modal contents of amphibole and chromite. The amphibole-rich rock JI-33 shows Pt–Pd fractionation, as expressed by high Pt/Pd ratio of 4.9 (vs. 1.0-1.6 for JI-23, JI-29 and JI-31). As the rock appears very fresh under the microscope and the LOI is 1.4 wt% only, the Pt and Pd contents probably reflect the igneous situation. The high Pt/Pd ratio may point to a subduction environment for the Paleng complex (e.g. Kepezhinskas *et al*., 2002). The strongly varying and partly very high Pt/Pd ratios of the fire assay ICP-MS data (1.0-7.5; samples JI-24, JI-25, JI-27, JI-28, JI-30, JI-32), however, are best explained by weathering, as most samples from the Paleng complex are derived from boulders.

An interesting feature is that Os and Ru correlate negatively with P_2O_5, whereas Rh, Pd and Pt correlate positively (Fig. 104). This might be due to the fact that the modal amphibole content is related to modal apatite in the Paleng cumulate series (up to 5 vol% apatite; see chapter 1.6)

The PGE concentrations of the Paleng amphibole gabbro samples are in the range of the ELIP, the sulfide-saturated Nadezhdinsky Formation of the Siberian Trap, the sulfide-saturated Northern Deccan trap basalts, and the sulfide-saturated Baimazhai gabbro (Fig. 103A-D).

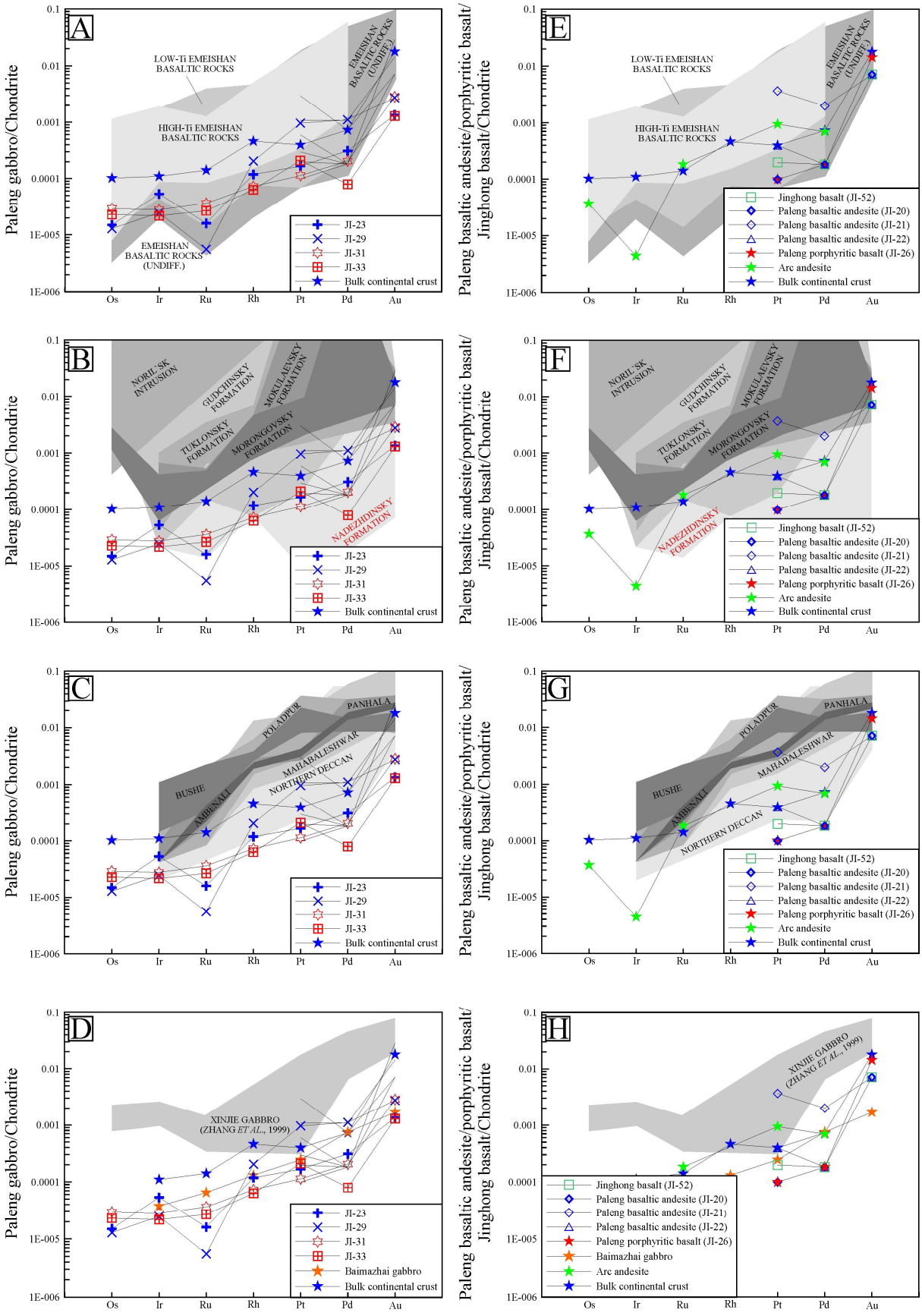

Fig. 103: Chondrite-normalized PGE-patterns of the Paleng amphibole gabbro (A-D), Paleng basaltic andesite, porphyritic basalt and Jinghong basalt (E/F).

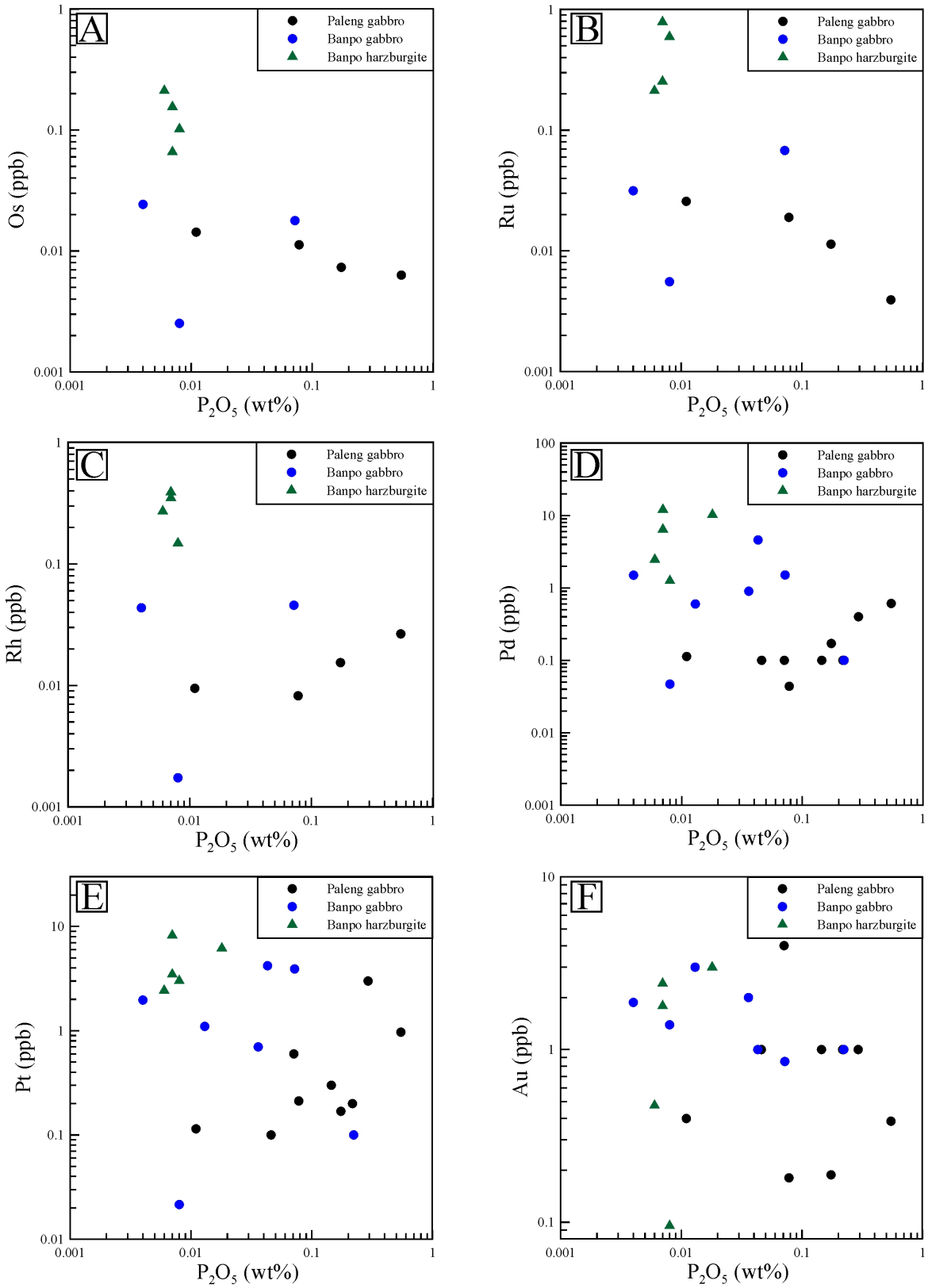

Fig. 104: Correlation diagram of Os, Ru, Rh, Pd, Pt and Au vs. P_2O_5. The plots suggest distinct correlations of the PGEs with phosphorus in the Paleng amphibole gabbro.

2.4.4 PALENG BASALTIC ANDESITE/PORPHYRITIC BASALT/ JINGHONG BASALT

The three Paleng basaltic andesite samples (JI-20 to JI-22) were analyzed by Pb fire assay ICP-MS for Pt, Pd and Au. Pt is <0.1-3.7 ppb, Pd is <0.1-1.1 ppb, and Au is <1-1 ppb, which results in Pt/Pd ratios of 1-4, that are in good agreement to the assumed arc setting for the Paleng basaltic andesite (refer to chapter 1.6). The Pt and Pd basaltic andesite data is enclosing PGE reference data for arc-andesite (Fig. 103E-H; Pearson & Woodland, 2000).

The Paleng porphyritic basalt (sample JI-26) has Pt and Pd concentrations below the analytical detection limit of the Pb fire assay ICP-MS analysis of 0.1 ppb Pt and Pd, and 2 ppb Au. The Jinghong basalt sample JI-52 of the Huijingfang complex was analyzed by Pb fire assay ICP-MS. It has 0.2 ppb Pt, <0.1 ppb Pd and 1 ppb Au.

The Paleng basaltic andesite, porphyritic basalt and the Jinghong basalt have PGE concentrations in the range of the ELIP, and in the range of sulfide-saturated reference data from Siberia and India (Fig. 103E-H).

2.5 SULFIDE SEGREGATION

Multi-element plots of chalcophile elements (except for the PGEs) plus some other elements are shown in Fig. 105. All mafic rocks - except for the Banpo harzburgite and hornblendite - show drastic Cr, Ni (and Co) depletion. These features can be explained by olivine, clinopyroxene and chromite fractionation, which is proven for all rock units studied (e.g. Bougault & Hekinian, 1974; Duke, 1976; Kloeck & Palme, 1988; Luhr & Carmichael, 1980; Paster *et al*., 1974; Villemant *et al*., 1981; Zack & Brumm, 1998). The Banpo harzburgite has high and invariable olivine and chromite content per se.

Compared to MORB and “Average oceanic crust” (green and red stars) the Nanlianshan rock suite is drastically depleted in Cr, Co, Ni and Cu (Fig. 105A; Edmond *et al*., 1979; Kelemen *et al*., 2004; Oppenheimer, 2004). The Banpo harzburgite depicts variations in S, Mn, Cu und Zn. Samples with high Cu content generally have high Zn (and S) contents (predominantly the pyroxene-rich rocks), which corresponds to the observed chalcopyrite in samples BA-3 and BA-4, and to higher Zn partition coefficients for clinopyroxene than for olivine in basaltic liquids (Ewart & Griffin, 1994; Luhr & Carmichael, 1980). The Banpo harzburgite is similar in chalcophile elements to our Jinbaoshan peridotite reference samples.

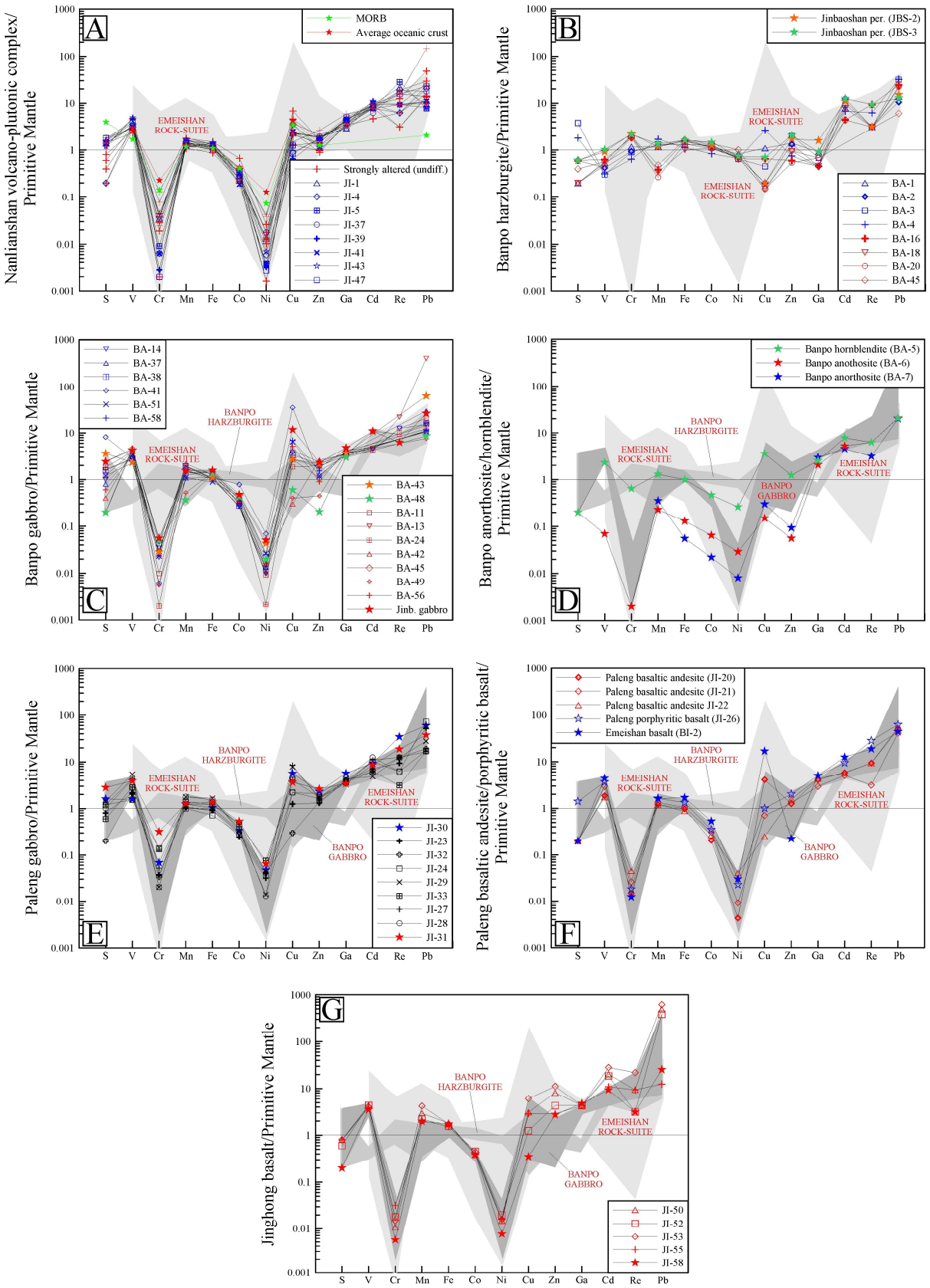

Fig. 105: Chalcophile multi-element plots for mafic/ultramafic rocks of SW Yunnan. Reference data for the Emeishan rock suite are from Fan *et al*. (2008), Guo *et al*. (2004), Hanski *et al*. (2004), Qi & Zhu (2008), Shellnut *et al*. (2008), Song *et al*. (2001, 2004, 2006, 2008b, 2009), Wang *et al*. (2007), Xiao *et al*. (2003, 2004), Xu *et al*. (2001, 2007), Zhang *et al*. (2006c, 2008b), Zhou *et al*. (2006, 2008) and Zi *et al*. (2008).

The Banpo gabbro depicts the widest range in S concentrations of all mafic rock units (Fig. 105C). The very high S, Co, Ni and Cu concentrations of sample BA-41 correspond to the petrographic observations, as this sample has the highest pyrite and chalcopyrite content.

The Banpo anorthosite samples BA-6 and BA-7 depict nearly congruent patterns (Fig. 105D). Due to the low amount of mafic phases and opaques, the two rock samples are very low in V, Cr, Fe, Co and Ni. In contrast, the Banpo hornblendite has high V, Cr, Mn, Fe, Co and Ni, similar to the Banpo harzburgite and primitive-mantle (Fig. 105D), corresponding to the high partition coefficients of these elements for hornblende in basaltic liquids.

The Paleng gabbro samples are sorted in Figure 105E by their plagioclase to amphibole ratios. The amphibole-rich end-member (shown in red) has - as expected - a pattern similar to the Banpo hornblendite (Fig. 105D). As the chalcophile element compositions cannot be explained by simple mixing of the two end-members (amphibole-rich and plagioclase-rich) it appears very likely that there is an additional sulfide mineral/melt control. This corresponds to the petrographic observation, as some of these samples have pyrrhotite, chalcopyrite, hematite and magnetite.

The basaltic andesite samples have chalcophile element concentrations in the range of the Paleng gabbro (Fig. 105F). The Paleng porphyritic basalt is relatively high in S. Nevertheless, it resembles both in major and trace elements - except for Cu - the Emeishan basalt reference sample BI-2. The high S content is well explained by microscopically detected pyrite and minor chalcopyrite. The Jinghong basalt has very low S concentrations (Fig. 105G). In general, the patterns are similar to those of the Banpo gabbro.

All mafic complexes have chalcophile element concentrations similar to those of the ELIP and to the gabbro reference samples from Jinbaoshan (Fig. 105 and references therein).

Variation diagrams of Cu/Au/PGEs (Co/Cr/Ni) vs. MgO/SiO_2 (Figs. 106-107) show predominantly positive correlation with MgO, and negative correlation with SiO_2 (and TiO_2 and Zr; not shown). These trends are suggestive of sulfide saturation on fractional crystallization (Keays & Lightfoot, 2009). The Banpo harzburgite shows little variation in terms of degree of fractional crystallization, but large scatter in some chalcophile element concentrations which may indicate a variable degree of sulfide saturation. Co and Ni remain constant which suggests fixation in olivine and pyroxene. Additional evidence for sulfide saturation for the Paleng gabbro comes from the Ni vs. MgO plot (Fig. 106F). As the gabbro series is predominantly composed of the rock forming minerals amphibole, plagioclase and apatite, major depletion, as shown for JI-28 and JI-29, is very likely due to sufide phases.

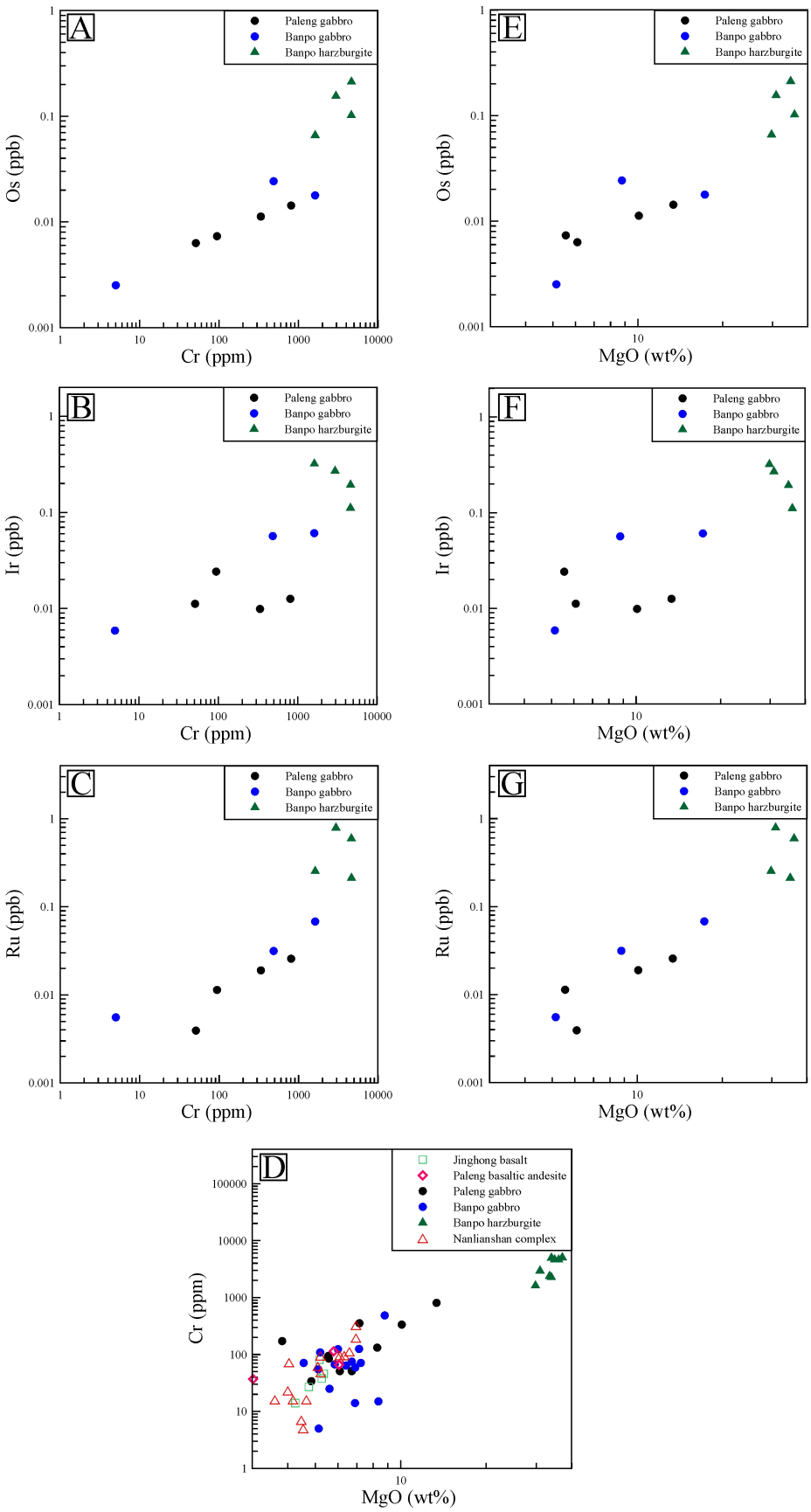

Fig. 106: Correlation diagrams of the PPGEs/Co/Ni/Cu with MgO. The positive correlation for the mafic rock units suggests sulfide saturation on fractional crystallization, while the Banpo harzburgite shows large scatter in Au, Cu, PGEs (variable sulfide segregation), and Ni and Co remain constant (silicate control).

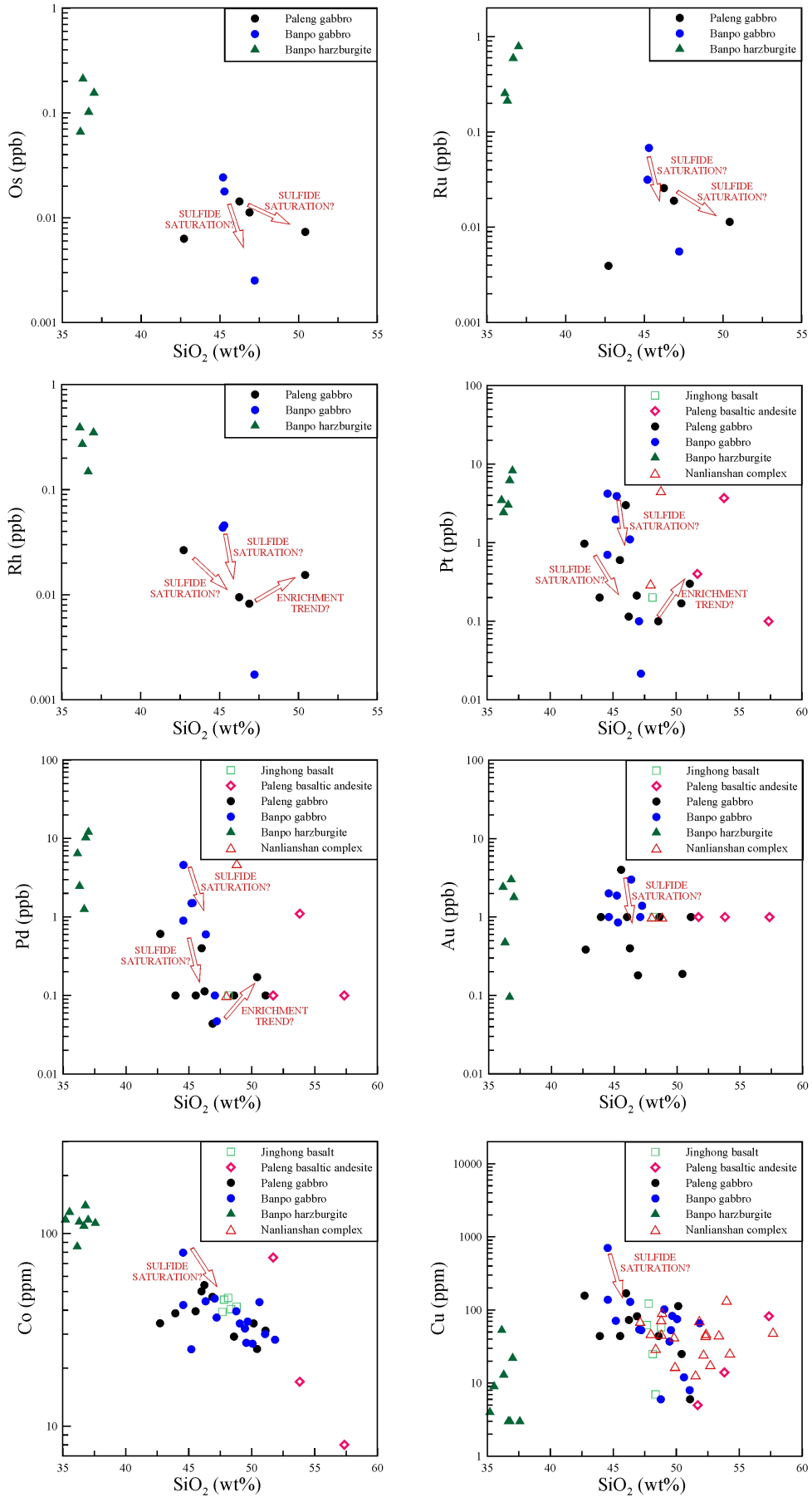

Fig. 107: PGEs/Au/Co/Cu vs. SiO_2 diagrams. Negative correlation suggests sulfide saturation on fractional crystallization.

Further evidence for sulfide saturation comes from the absence of a clear and consistent Pd–Pt fractionation throughout the different mafic rock series, as one would expect in S-undersaturated magmas (Keays, 1995). Momme *et al*. (2002) showed that Pd is incompatible in S-undersaturated, fractionating magmas and Pt is more compatible (bulk partition coefficient of silicate solid/liquid = 2.5) (Figs. 106-107).

As Cu is chalcophile, the Cu/Zr ratios decrease with fractionation in sulfide-saturated magmas (Lightfoot & Hawkesworth, 1997; Naldrett & Lightfoot, 1993). For the Nanlianshan complex, the Banpo gabbro and the Paleng gabbro, the Cu/Zr ratios correlate positively with MgO, and negatively with SiO_2 and TiO_2 (Fig. 108A-C). The Banpo harzburgite gives a scatter distribution suggestive of variable degree of sulfide saturation (Fig. 108). Figure 108D shows, that the Ni/MgO and Cu/Zr ratios of the Nanlianshan complex, Banpo gabbro and Jinghong basalt are similar to the sulfide saturated (depleted) Nadezhdinsky Formation.

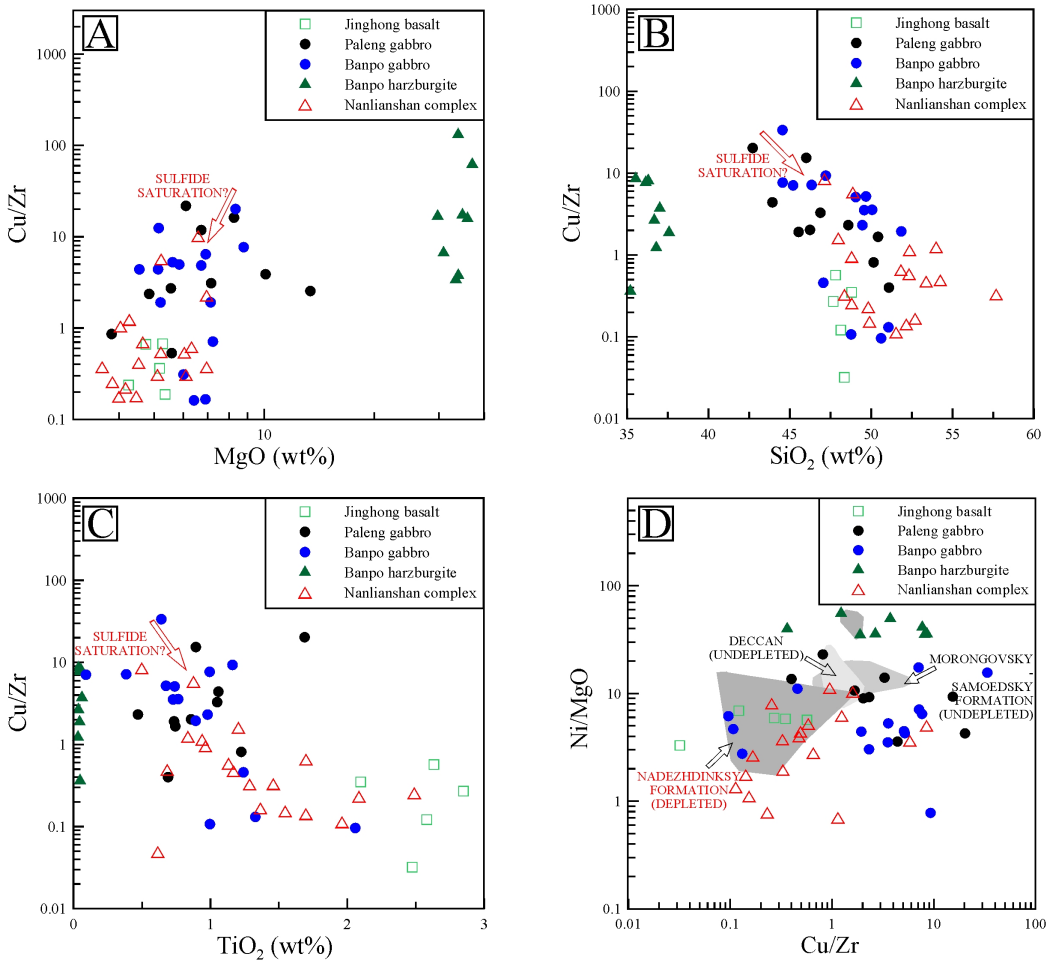

Fig. 108: A-C: Variation diagrams of Cu/Zr vs. MgO, SiO_2 and TiO_2. Decreasing Cu/Zr with increasing fractionation is suggestive of sulfide saturation. D: Variation diagram of Ni/MgO vs. Cu/Zr. The Nanlianshan and Huijingfang complexes have Ni/MgO and Cu/Zr ratios similar to the sulfide-depleted Nadezhdinsky Formation of the Siberian trap basalts. The Banpo and Paleng gabbros show predominantly depletion in Ni/MgO. Reference data are by Keays & Lightfoot (2009).

Because Ir behaves as a compatible element, entering Ir–Os alloys, chromite and olivine or becoming attached to chromite, respectively, while Pd is highly incompatible in S-undersaturated, fractionating magmas (Keays, 1995; Momme *et al.*, 2002), the Pd/Ir ratios increase with fractionation and decreasing Mg-number. The indicated positive correlation of the Banpo gabbro samples on the Pd/Ir vs. Mg# diagram suggests sulfide saturation (Fig. 109A). For the Banpo harzburgite and the Paleng gabbro there are no clear trends, which might be explained by combined fractionation and sulfide saturation.

The Cu and Pd contents of the Banpo gabbro, Paleng gabbro and Jinghong basalt are - considering the mobile character of Cu - in the range of the Nadezhdinsky Formation and clearly contrast with the upper Siberian Trap (Morongovsky, Mokulaevsky, Tuklonsky and Samoedsky Formations; Keays & Lightfoot, 2009), and with the S-undepleted southern Deccan traps (Brügmann *et al.*, 1993; Lightfoot & Keays, 2005; Fig. 109B). The Nanlianshan complex shows its typical MORB composition, i.e. depletion in Cu and PGEs (Bézos *et al.*, 2005; Hertogen *et al.*, 1980).

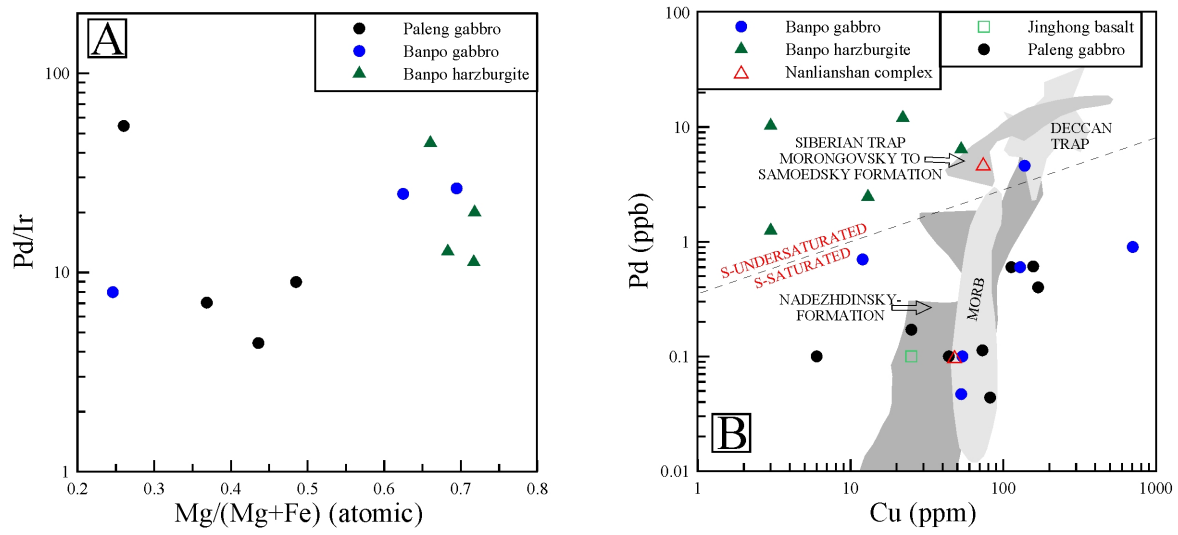

Fig. 109A: The Pd/Ir vs. Mg# plot suggests sulfide saturation for the Banpo gabbro. B: The Pd vs. Cu diagram stresses S-saturation for the Banpo gabbro, Paleng gabbro, and Jinghong basalt. The Nanlianshan complex has a composition typical of MORB.

As the partition coefficients for Ni and Cu (sulfide melt/silicate melt) are at least two orders of magnitude lower than those for the PGEs, base-metal/PGE ratios are sensitive indicators for sulfide fractionation (e.g. Fleet *et al.*, 1991, 1996, 1999; Peach *et al.*, 1990, 1994; Stone *et al.*, 1990).

The high Ni/Pd and Cu/Ir ratios of the Nanlianshan, Banpo, Paleng and Huijingfang complexes suggest that the magmas have experienced sulfide segregation (Fig. 110A). Interestingly, this plot confirms chromite as major PGE-fractionating phase for the Banpo harzburgite, which plots in a position close to the mantle and komatiite fields. Beyond that, the plot shows the Banpo gabbro and Paleng gabbro having typical Cu/Ir ratios of calc-alkaline basalts, which corresponds to the tectonic classifications.

Especially the Cu/Pd ratio is widely adopted as sensitive indicator for sulfide mineral segregation and is useful in local or regional Ni, Cu and PGE exploration (Barnes *et al.*, 1993). Without sulfide segregation, Cu behaves similar to Pd, and the Cu/Pd ratio for both fractionated magma and cumulates is the same as for the primary magma (Cu/Pd = 1000-10000; Barnes *et al.*, 1993). Similarly, primary magmas should have Ti/Pd ratios close to mantle values (3 x 10^5; Sun *et al.*, 1991). The Banpo harzburgite has Ni/Pd, Cu/Pd, Cu/Ir and Ti/Pd ratios close to mantle values (Fig. 110). It appears, therefore, unlikely that the Banpo harzburgite attained major sulfide saturation. The Nanlianshan complex, Banpo gabbro, Paleng gabbro and Jinghong basalt have Cu/Pd and Ti/Pd ratios greater than mantle values, providing further evidence for sulfide segregation. Specifically, the Banpo gabbro matches the Ni/Pd, Cu/Ir and Cu/Pd ratios of the Hongge layered intrusion (Zhong *et al.*, 2002), which hosts a titanomagnetite deposit and has horizons enriched in PGEs.

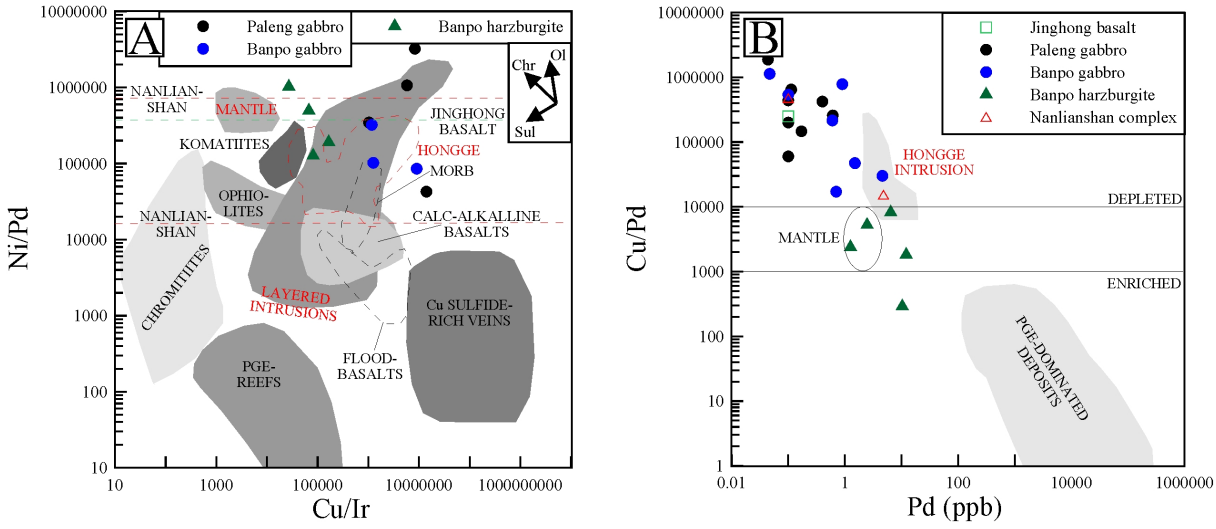

Fig. 110A: Ni/Pd vs. Cu/Ir plot showing the compositions of the studied mafic to ultramafic rocks of the southern Lancangjiang zone. B: Cu/Pd vs. Pd plot for the mafic to ultramafic complexes of the southern Lancangjiang zone. Reference data are from Barnes *et al.* (1988, 1993) and Zhong *et al.* (2002).

2.6 CONTROLS ON SULFIDE SATURATION

Previous studies have shown that sulfide saturation in layered intrusions might be related to magma mixing (Campbell *et al*., 1983; Harney & von Gruenewaldt, 1995; Hoatson & Keays, 1989; Naldrett *et al*., 1990; Naldrett & Wilson, 1990; von Gruenewaldt *et al*., 1989), crustal contamination (e.g. Keays & Lightfoot, 2009; Lesher & Keays, 2002; Lightfoot & Keays, 2005; Wilson & Chunnett 2006) or fractional crystallization (Holzheid & Groove, 2002; Mavrogenes & O`Neill, 1999).

It is generally accepted, that decreasing $(Nb/Th)_{PM}$ with increasing $(Th/Yb)_{PM}$ is indicative of crustal contamination (Fig. 111A; Lightfoot & Hawkesworth, 1988; Lightfoot *et al*., 1990). The Nanlianshan complex shows a clear negative correlation of $(Nb/Th)_{PM}$ with $(Th/Yb)_{PM}$. The ratios range from typical N-MORB composition to ratios typical of upper continental crust. The Banpo harzburgite has ratios ranging from primitive mantle to bulk continental crust. These trends suggest crustal contamination for the Nanlianshan complex rock suite and the Banpo harzburgite.

Most of the Banpo gabbro and Paleng gabbro samples have $(Nb/Th)_{PM}$ and $(Th/Yb)_{PM}$ ratios in the range of MORB and primitive mantle. Only two samples (for the Banpo gabbro) and three samples (for the Paleng gabbro) stand out with lower $(Nb/Th)_{PM}$ and higher $(Th/Yb)_{PM}$ ratios. These trends generally suggest minor crustal contamination for the Banpo and Paleng gabbros. The wider data range for the Banpo gabbro suggests that crustal contamination was more intensive than for the Paleng gabbro. This is in agreement with the $^{143}Nd/^{144}Nd$ vs. $^{87}Sr/^{86}Sr(i)$ diagram, where the variation range and correlation indicate crustal contamination (Fig. 111B). The $(Nb/Th)_{PM}$ vs. $^{87}Sr/^{86}Sr(i)$, $(Th/Yb)_{PM}$ vs. $^{87}Sr/^{86}Sr(i)$ and $(Nb/Th)_{PM}$ vs. $^{143}Nd/^{144}Nd(i)$ diagrams (Fig. 111C-E) show trends for the Banpo gabbro suggestive of crustal contamination as well. The Paleng gabbro in contrast depicts on these diagrams and on the $(Th/Yb)_{PM}$ vs. $^{143}Nd/^{144}Nd(i)$ diagram of Figure 111F, trends contradicting crustal contamination. This pattern corresponds to the petrographic and petrologic descriptions, which suggest predominantly simple mixing of the two cumulate end-members plagioclase-rich and amphibole-rich.

The Jinghong basalt samples depict negative correlation of $(Nb/Th)_{PM}$ and $(Th/Yb)_{PM,}$ with ratios in the range of primitive mantle and lower continental crust, implying moderate crustal contamination. Moderate crustal contamination corresponds to the relatively high Sr isotopic ratio and to the trace element characteristics (Fig. 111).

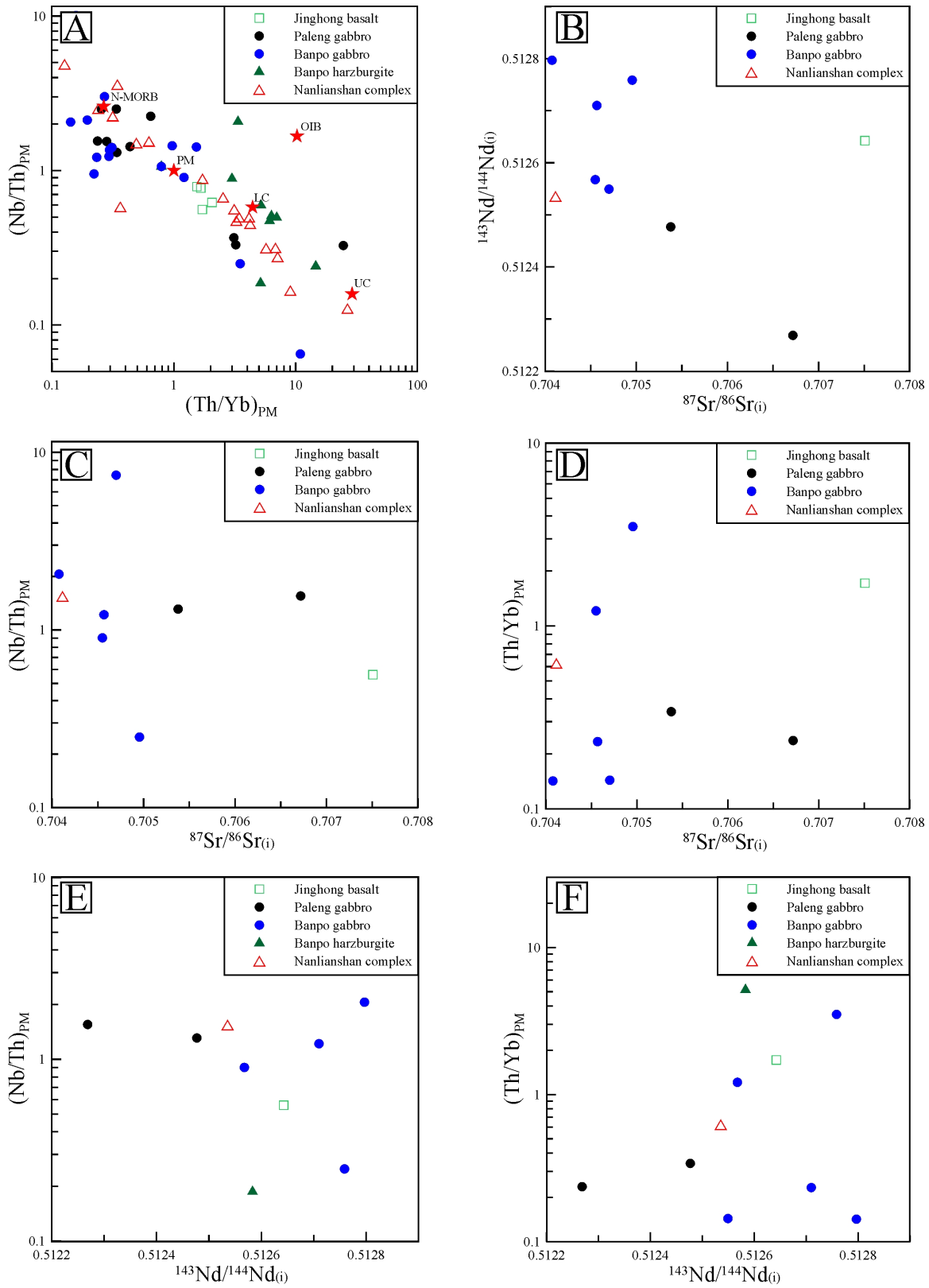

Fig. 111A: The $(Nb/Th)_{PM}$ vs. $(Th/Yb)_{PM}$ diagram suggests crustal contamination for all studied rock complexes of SW China. B-F: The isotopic correlation diagrams suggest that crustal contamination was for the Banpo gabbro more intensive than for the Paleng gabbro.

Lesher & Stone (1996) estimated the depleted mantle to contain 150-215 ppm S. Partial melting of 10-20% (Langmuir *et al*., 1992) would then lead to MORB magma with ~1000-2000 ppm S (Li & Ripley, 2005). Experimental data indicate that about half of this amount (i.e. ~1000 ppm S) could be present as immiscible sulfide liquid.

As sulfide solubility increases with decreasing pressure, a magma that is sulfur saturated at its source might be undersaturated when it reaches the surface. Mantle derived mafic magma should arrive at the surface sulfide saturated only if the magma had undergone fractional crystallization or if assimiliation of S from the country rock occurred (Holzheid & Groove, 2002; Mavrogenes & O`Neill, 1999). The common presence of immiscible sulfide globules in mid-ocean ridge basalts shows that the magmas are indeed saturated or nearly sulfide saturated at the time of eruption (Mathez, 1976; Wallace & Carmichael, 1992). Li *et al*. (2003) estimate the amount of crystallization necessary to drive a MORB magma to sulfide saturation at <10 wt%, i.e. an initially sulfide saturated basaltic liquid should easily maintain sulfide saturation during fractional crystallization.

2.6.1 SULFUR CONTENT AT SULFIDE SATURATION

The sulfur content at sulfide saturation (SCSS) can be estimated from the following equation of Li & Ripley (2005):

1) $lnXs = 1.229 - 0.74(10^4 / T) - 0.021(P) - 0.311\ lnX_{FeO} - 6.166\ X_{SiO2} - 9.153\ X_{Na2O+K2O} - 1.914X_{MgO} + 6.594\ X_{FeO}$

Where T is in degrees Kelvin, X is mole fraction and P is in kbar.
The following steps lead to the sulfur concentration in ppm.

2) Moles S = (Xs) x (moles oxides in magma) / (1 - Xs)

3) wt% S = Moles S x 32.07

The approach of Li & Ripley (2005) works best for primitive, anhydrous MORBs at fO_2 conditions below QFM where sulfide is the predominant S species. The accuracy decreases for temperatures <1030°C and for more evolved MORB samples. The SCSS has been studied for hydrous basaltic magmas as well, and its behavior appears to be more complex and difficult to predict (e.g. Bradbury, 1983; Burnham, 1979; Gorbachev & Kashiceva, 1986).

For the Nanlianshan basaltic andesite and gabbro samples, which represent according to Li & Ripley (2005) primitive MORBs (<2.8 wt% TiO_2, <14 wt% FeO) a pressure of 1 kbar and a temperature of 1200°C was assumed (Wallace & Carmichael, 1992), which leads to SCSS of 534-1043 ppm with a mean of 739 ppm S. For 0.38 kbar (the hydrostatic pressure for the present average depth of the oceans) the SCSS for the basaltic andesite samples is 541-1028 ppm S (mean 715 ppm S). The measured mean S concentration in the Nanlianshan complex is 231 ppm, which is a minimum value due to loss of sulfur on sample preparation for XRF analysis.

The porphyritic basalt of the Paleng complex has a SCSS of 1089 ppm S compared to 280 ppm measured by XRF. The calculated SCSS value for the Jinghong (Huijingfang) basalt is 951-1101 ppm S (mean: 1044 ppm S), compared to the measured S content of 126 ppm S (XRF). Although the Banpo and Paleng gabbros were likely generated under hydrous conditions, the SCSS calculated for dry magmas is 605-1295 ppm S (mean: 859 ppm) and 810-1793 ppm S (mean: 1176 ppm S), respectively. These samples have mean XRF concentrations of 325 and 276 ppm, respectively.

2.7 ASSESSMENT OF THE MINERAL POTENTIAL

2.7.1 Cu–Ni–Co–(PGE) AND Fe–Ti–V POTENTIAL

2.7.1.1 NANLIANSHAN VOLCANO-PLUTONIC COMPLEX

The geochemical data suggest an E-MORB setting of the Early Permian Nanlianshan volcano-plutonic complex. The rocks appear to have undergone sulfide-saturation. However, as already mentioned, nearly all MORB melts are sulfide-saturated, which limits the significance of these results. The rock textures suggest that the Nanlianshan complex represents ancient ocean-seafloor and upper oceanic crust. Such an environment is not favorable for podiform Cr, Ni and PGE deposits which occur in layered magma chambers, i.e. much lower in the crust, or below the oceanic crust. Therefore the platinum-potential of the Nanlianshan complex can be regarded as minor. However, there might be potential for Cyprus-type VMS (Zn-Cu) mineralization in the Nanlianshan complex.

2.7.1.2 BANPO COMPLEX

The Early Permian Banpo complex is the largest of all complexes studied and consists of harzburgite, gabbro, hornblendite, anorthosite, and rhyolite (Fig. 11). All geological and geochemical data suggest that the Banpo complex represents a Lower Permian continental arc (refer to chapter 1.4). Arc zones are in general regarded as unfavorable targets for Cu–Co–Ni–PGE mineralization.

On the other hand, there is little doubt that the Banpo complex represents a well exposed magma chamber, with clear cumulate structures and striking evidence for both drastic PGE depletion and slight enrichment in gabbro. The Banpo harzburgite is very similar in PGE concentrations to ultramafic rocks of the Hongge Fe–V–Ti deposit in the Pan-Xi area, and the Banpo gabbro resembles in major and trace elements the reference gabbro samples from the Jinbaoshan Pt–Pd deposit. The low PGE concentrations of the Banpo gabbro resemble the sulfide-saturated Nadezhdinsky Formation of the Siberian Trap, the northern Deccan Trap and the ELIP. The geochemical complexity of the Banpo gabbro might point to magma mixing and - as proven - to crustal contamination, processes regarded as crucial for attaining sulfide saturation and concomitant PGE enrichment.

The geologic situation, i.e. that the Banpo intrusion is related to a N–S striking anticlinal core, relates the Banpo intrusion to the Yangliuping and Ban Phuc intrusions with associated Ni–PGE mineralization. A clear zoning of ultramafic and mafic rocks, as described for most mineralized intrusions in SW China, is less evident for the Banpo complex.

In summary, the platinum potential of the Banpo complex is judged to be favorable. In contrast to previous exploration campaigns, however, which focussed on the weakly mineralized southern harzburgite body (Fig. 11), the lowest parts of the Banpo gabbro are regarded as the most promising targets, which should be tested by exploration drilling.

Two gabbro samples with intra-plate-like signature (Ti–V–Y–Zr–Nb discrimination plots) are similar to ELIP rocks and strengthen the argument for elevated platinum potential of the Banpo gabbro.

2.7.1.3 PALENG COMPLEX

The economic potential of the Paleng complex appears to be most favorable of all rock units studied, despite the fact that this intrusion probably represents a Permian island arc. The Paleng amphibole gabbro has a typical Emeishan age of 263-256 Ma (U–Pb ages including the errors) and forms an undisturbed, well developed cumulate series with features such as high apatite content, linking it to gabbro of the ELIP-related Panzhihua Fe–Ti–V deposit (Ganino *et al*., 2005; Pang *et al*., 2008; Zhou *et al*., 2005). At Panzhihua massive magnetite ores are located below the apatite-rich gabbro (Ganino *et al*., 2005; Pang *et al*., 2008; Zhou *et al*., 2005).

The Paleng complex also comprises basalt of intra-plate setting with an age of ~262 ±2 Ma that is geochemically strikingly similar to basalt of the ELIP, and gives a further clue for ELIP-related rocks south of the Red River-Ailaoshan Shear Zone. The Paleng amphibole gabbro is distinctly depleted in chalcophile trace elements and especially in the PGEs, similar to the sulfide-saturated Nadezhdinsky Formation of the Siberian Trap which hosts the Noril`sk Ni–Cu–PGE deposits. The Paleng gabbro depicts slight enrichment trends of Cu and PGEs as well. These features might point to sulfide saturation and to an elevated platinum potential.

2.7.1.4 HUIJINGFANG COMPLEX

The geochemical data suggest an intra-plate setting for the Early Jurassic Huijingfang complex, and the rocks appear to have undergone sulfide saturation. Rock textures suggest that the Jinghong basalt extruded sub-aerially or intruded in the uppermost continental crust. Sulfide segregation, i.e. Cu–Ni–Co–(PGE) mineralization, or fractional crystallization in layered magma chambers, i.e. Fe–Ti–V mineralization, would have to be expected at deeper levels currently not exposed.

2.7.2 POTENTIAL OF INTERMEDIATE TO FELSIC ROCKS

2.7.2.1 JINGHONG GRANODIORITE

The petrographic and geochemical data suggest for the Early Permian Jinghong granodiorite an oxidized, I-type composition (Chappel & White, 1974) and indicate an active continental margin setting. High level fractionation is supported by the REE data. These features point to general potential for porphyry Cu–Mo mineralization.

2.7.2.2 JINGHONG TRACHYANDESITE AND JINGHONG DACITE

The Jinghong trachyandesite and Jinghong dacite point to Early Triassic subduction of oceanic crust in an island-arc setting. This setting has in general potential for porphyry Cu–Au, epithermal Au, and Kuroko-type Zn–Cu VMS deposits.

It appears likely that the Paleo-Tethys in SW China was a complex archipelagic ocean, with several back-arc basins. This situation involves mineral potential for e.g. podiform Cr and orogenic Au deposits in the compressed accretionary wedge, as well as Cyprus- and Besshi-type Cu–Fe VMS deposits related to the back-arc basin.

2.7.2.3 LINCANG GRANITE

The Lincang granite is peraluminous with S-type and ilmenite-series affinity (Chappell & White 1974; Ishihara, 1977, 1981). These characteristics favor the Lincang granite for Sn–W–(U–Th) mineralization (Ishihara, 1981). The Lincang granite presents a broad chemical spectrum from relatively primitive to highly evolved granite portions, and the most evolved intrusive phases may be associated with hydrothermal tin mineralization, as present in the southern continuation of the granite belt into peninsular Malaysia.

3 REFERENCES

Aignertorres, M., Blundy, J., Ulmer, P. & Pettke, T. (2007). Laser Ablation ICPMS study of trace element partitioning between plagioclase and basaltic melts: an experimental approach. *Contributions to Mineralogy and Petrology* 153, 647-667.

Alard, O., Griffin, W.L, Lorand, J.P., Jackson, S.E. & O'Reilly, S.Y. (2000). Non-chondritic distribution of the highly siderophile elements in mantle sulphides. *Nature* **407**, 891-894.

Alard, O., Griffin, W.L., Pearson, N.J., Lorand, J.P. & O'Reilly, S.Y. (2002). New insights into the Re–Os systematics of sub-continental lithospheric mantle from in situ analyses of sulphides. *Earth and Planetary Science Letters* **203**, 651-663.

Ali, J.R., Lo, C.H., Thompson, G.M. & Song, X. (2004). Emeishan basalt Ar–Ar overprint ages define several tectonic events that affected the western Yangtze platform in the Mesozoic and Cenozoic. *Journal of Asian Earth Sciences* **23**, 163-178.

Ali, J.R., Thompson, G.M., Zhou, M.F. & Song, X. (2005). Emeishan large igneous province, SW China. *Lithos* **79**, 475-489.

Amossé, J. & Allibert, M. (1993). Partitioning of iridium and platinum between metals and silicate melts: evidence for passivation of the metals depending on fO_2. *Geochimica et Cosmochimica Acta* **57**, 2395-2398.

Anderson, D.L. (1994). The sublithospheric mantle as the source of continental flood basalts; the case against the continental lithosphere and plume head reservoirs. *Earth and Planetary Science Letters* **123**, 269-280.

Aoki, K.I. (1968). Petrogenesis of ultrabasic and basic inclusions in alkali basalts, IKI Island, Japan. *American Mineralogist* **53**, 241-256.

Arth, J.G. (1976). Behaviour of trace elements during magmatic processes - a summary of theoretical models and their applications. *Journal of Research of the United States Geological Survey* **4**, 41-47.

Ayers, J.C., Dunkle, S., Gao, S. & Miller, C.F. (2002). Constraints on timing of peak and retrograde metamorphism in the Dabie Shan Ultrahigh-Pressure Metamorphic Belt, east-central China, using U–Th–Pb dating of zircon and monazite. *Chemical Geology* **186**, 315-331.

Bailey, J.C. (1981). Geochemical criteria for a refined tectonic discrimination of orogenic andesites. *Chemical Geology* **32**, 139-154.

Ballhaus, C., Bockrath, C., Wohlgemuth-Ueberwasser, C., Laurenz, V. & Berndt, J. (2006). Fractionation of the noble metals by physical processes. *Contributions to Mineralogy and Petrology* **152**, 667-684.

Ballhaus, C.G. & Stumpfl, E.F (1986). Sulfide and platinum mineralization in the Merensky Reef: evidence from hydrous silicates and fluid inclusions. *Contributions to Mineralogy and Petrology* **94**, 193-204.

Ballhaus, C., Tredoux, M. & Spaeth, A. (2001). Phase relations in the Fe-Ni-Cu-PGE-S system at magmatic temperature and application to massive sulphide ores of the Sudbury Igneous Complex. *Journal of Petrology* **42**, 1911-1926.

Barker, F. (1979). Trondhjemite: Definition, environment and hypotheses of origin. In: Barker, F. (Ed.) *Trondhjemites, dacites and related rocks*. Elsevier, Amsterdam, 1-12.

Barnes, S.J., Naldrett, A.J. & Gorton, M.P. (1985). The origin of the fractionation of platinum-group elements in terrestrial magmas. *Chemical Geology* **53**, 303-323.

Barnes, S.J., Boyd, R., Korneliussen, A., Nilsson, L.P., Often, M., Pederson, R.B. & Robins, B. (1988). The use of mantle normalization and metal ratios in discriminating between the effects of partial melting, crystal fractionation and sulphide segregations on platinum-group elements, gold, nickel and copper: examples from Norway. In: Prichard, H.M., Potts, P.J., Bowles, J.F.W. & Cribb, S. (Eds.) *Geo-platinum* **87**. Elsevier, Barking, 113-143.

Barnes, S.J., Couture, J.F., Sawyer, E.W. & Bouchaib, C. (1993). Nickel-copper occurrences in the Belleterre–Angliers belt of the Pontiac subprovince and the use of Cu–Pd ratios in interpreting platinum-group element distributions. *Economic Geology* **88**, 1402-1418.

Barnes, S.J. & Maier, W. (1999). The fractionation of Ni, Cu and the noble metals in silicate and sulphide liquids. In: Keays, R.R., Lesher, C.M., Lightfoot, P.C. & Farrow, C.E.G. (Eds.) *Dynamic Processes in Magmatic Ore Deposits and their Application in Mineral Exploration*. Geological Association of Canada Short Course Notes **13**, 69-106.

Barr, S.M., MacDonald, A.S., Ounchanum, P. & Hamilton, M.A. (2006). Age, tectonic setting and regional implications of the Chiang Khong volcanic suite, northern Thailand. *Journal of the Geological Society* **163**, 1037-1046.

Barr, S.M., MacDonald, A.S., Ounchanum, P. & Yaowanoiyothin, W. (2000). Petrochemistry, U-Pb (zircon) age, and paleotectonic setting of the Lampang volcanic belt, northern Thailand. *Journal of the Geological Society* **157**, 553-563.

Beard, J.S. & Barker, F. (1989). Petrology and tectonic significance of gabbros, tonalites, shoshonites and anorthosites in a Late Paleozoic Arc-root complex in the Wrangellia Terrane, Southern Alaska. *Journal of Geology* **97**, 667-683.

Bennett, S., Blundy, J. & Elliott, J. (2004). The effect of sodium and titanium on crystal-melt partitioning of trace elements. *Geochimica et Cosmochimica Acta* **68**, 2335-2347.

Bernstein, S., Kelemen, P.B., Tegner, C. & Kurz, M.D. (1998). Post-breakup basaltic magmatism along the East Greenland Tertiary Rifted Margin. *Earth and Planetary Science Letters* **160**, 845-862.

Bezmen, N.I., Asif, M., Brugmann, G.E., Romanenko, I.M. & Naldrett, A.J. (1994). Distribution of palladium, rhodium, ruthenium, iridium, osmium and gold between sulphide and silicate melts. *Geochimica et Cosmochimica Acta* **58**, 1251-1260.

Bézos, A., Lorand, J.P., Hummler, E. & Gros, M. (2005). Platinum-group element systematics in Mid-Oceanic Ridge basaltic glasses from the Pacific, Atlantic, and Indian Oceans. *Geochimica et Cosmochimica Acta* **69**, 2613-2627.

Bindeman, I.N., Davis, A.M. & Drake, M.J. (1998). Ion microprobe study of plagioclase-basalt partition experiments at natural concentration levels of trace elements. *Geochimica et Cosmochimica Acta* **62**, 1175-1193.

Blake, D.H., Peterman, Z.E. & Thieben, S.E. (1992). Possible crustal contamination of mid-continent rift igneous rocks: Examples from the Mineral Lake Intrusion. *Canadian Journal of Earth Sciences* **29**, 1140-1153.

Bockrath, C., Ballhaus, C. & Holzheid, A. (2004). Fractionation of the platinum-group elements during mantle melting. *Science* **305**, 1951-1953.

Borisov, A. & Palme, H. (1997). Experimental determination of the solubility of platinum in silicate melts. *Geochimica et Cosmochimica Acta* **61,** 4349-4357.

Borisov, A. & Palme, H. (2000). Solubilities of noble metals in Fe-containing silicate melts as derived from experiments in Fe-free systems. *American Mineralogist* **85**, 1665-1673.

Boudreau, A.E. & McCallum, I.S. (1992). Concentration of platinum-group elements by magmatic fluids in layered intrusions. *Economic Geology* **87**, 1830-1848.

Bougault, H. & Hekinian, R. (1974). Rift valley in the Atlantic Ocean near 36 degrees 50'N; petrology and geochemistry of basalt rocks. *Earth and Planetary Science Letters* **24**, 249-261.

Boven, A., Pasteels, P., Punzalan, L.E., Liu, J., Luo, X., Zhang, W., Guo, Z. & Hertogen, J. (2002). $^{40}Ar/^{39}Ar$ geochronological constraints on the age and evolution of the Permo-Triassic Emeishan Volcanic Province, Southwest China. *Journal of Asian Earth Sciences* **20**, 157-175.

Bowles, J.F.W., Gize, A.P. & Cowden, A. (1994). The mobility of the platinum group elements in the soils of the Freetown Peninsula, Sierra Leone. *Canadian Mineralogist* **32**, 957-967.

Bradbury, J.W. (1983). Pyrrhotite solubility in hydrous albite melts. PhD Thesis, The Pennsylvania State University, 136 pp.

Brandon, A.D., Creaser, R.A., Shirey, S.B. & Carlson, R.W. (1996). Osmium recycling in subduction zones. *Science* **272**, 861-864.

Brenan, J.M., McDonough, W.F. & Ash, R. (2005). An experimental study of the solubility and partitioning of iridium, osmium and gold between olivine and silicate melt. *Earth and Planetary Science Letters* **237**, 855-872.

Bruce, M.C., Niu, Y., Harbort, T.A. & Holcombe, R.J. (2000). Petrological, geochemical and geochronological evidence for a Neoproterozoic ocean basin recorded in the Marlborough Terrane of the Northern New England Fold Belt. *Australian Journal of Earth Sciences* **47**, 1053-1064.

Bruce, M.C. & Niu, Y. (2000). Early Permian supra-subduction assemblage of the South Island Terrane, Percy Isles, New England Fold Belt; Queensland. *Australian Journal of Earth Sciences* **47**, 1077-1085.

Brügmann, G.E., Hanski, E.J., Naldrett, A.J. & Smolkin, V.F. (2000). Suphide segregation in ferropicrites from the Pechenga Complex, Kola Peninsula; Russia. *Journal of Petrology* **41**, 1721-1742.

Brügmann, G.E., Naldrett, A.J., Asif, F., Lightfoot, P.C., Gorbachev, N.S. & Fedorenko, V.A. (1993). Siderophile and chalcophile metals as tracers of the evolution of the Siberian Trap in the Noril`sk Region; Russia. *Geochimica et Cosmochimica Acta* **57**, 2001-2018.

Bryant, D.L., Ayers, J.C., Gao, S., Miller, C.F. & Zhang, H. (2004). Geochemical, age, and isotopic constraints on the location of the Sino–Korean/Yangtze Suture and evolution of the Northern Dabie Complex, east central China. *Geological Society of America Bulletin* **116**, 698-717.

Bureau of Geological and Mineral Resources of Sichuan Province (BGMS) (1982). *Exploration report of the Zhengziyanwuo and Yangliuping Pt-Ni deposits, Danba, Sichuan* (in Chinese).

Burgess, R., Kiviets, G.B. & Harris, J.W. (2004). $^{40}Ar/^{39}Ar$ age determinations of eclogitic clinopyroxene and garnet inclusions in diamonds from the Venetia and Orapa kimberlites. *Lithos* **77**, 113-124.

Burnham, C.W. (1979). Magmas and hydrothermal fluids. In: Barnes, H.L. (Ed.) *Geochemistry of hydrothermal ore deposits*. Wiley, New York, 71-136.

Burton, K.W., Gannoun, A., Birck, J.L., Allegre, C.J., Schiano, P., Clocchiatti, R. & Alard, O. (2002). The compatibility of rhenium and osmium in natural olivine and their behaviour during mantle melting and basalt genesis. *Earth and Planetary Science Letters* **198**, 63-76.

Burton, K.W., Schiano, P., Birck, J.L. & Allegre, C.J. (1999). Osmium isotope disequilibrium between mantle minerals in a spinel-lherzolite. *Earth and Planetary Science Letters* **204**, 385-402.

Cameron, E.M. & Hattori, K.H. (2005). Platinum Group Elements in Geochemical Exploration. In: Raeside, R. (Ed.) *Exploration for Platinum-Group Element Deposits*. Mineralogical Association of Canada Short Course Series Volume **35**. Oulu, Finland. 287-308.

Campbell, I.H. & Barnes, S.J. (1984). A model for the geochemistry of the platinum group elements in magmatic sulphide deposits. *Canadian Mineralogist* **22**, 151-160.

Campbell, I.H. & Griffith, R.W. (1990). Implications of mantle plume structure for the origin of flood basalts. *Earth and Planetary Science Letters* **99**, 79-93.

Campbell, I.H., Naldrett, A.J. & Barnes, S.J. (1983). A model for the origin of the platinum-rich sulfide horizons in the Bushveld and Stillwater Complexes. *Journal of Petrology* **21**, 133-165.

Capobianco, C.J. & Drake, M.J. (1990). Partitioning of ruthenium, rhodium, and palladium between spinel and silicate melt and implications for platinum-group element fractionation trends. *Geochimica et Cosmochimica Acta* **54**, 869-874.

Capobianco, C.J., Hervig, R.L. & Drake, M.J. (1994). Experiments on crystal/liquid partitioning of Ru, Rh and Pd for magnetite and hematite solid solutions crystallized from silicate melt. *Chemical Geology* **113**, 23-43.

Carl, R.R.B., Höll, R. & Schroll, E. (1988). Ein Metadioritvorkommen in der Habachformation westlich der Achselalm/Hollersbachtal (Hohe Tauern, Österreich). *Mittteilungen der Österreichischen Geologischen Gesellschaft* **81**, 123-132.

Carmichael, I.S.E. (1964). The petrology of Thingmuli, a Tertiary volcano in Eastern Iceland. *Journal of Petrology* **5**, 435-460.

Carr, P.F. (1985). Geochemistry of Late Permian shoshonitic lavas from the southern Sydney Basin. In: Sutherland, F.L., Franklin, B.J. & Waltho, A.E. (Eds.) *Volcanism in Eastern Australia: with case histories from New South Wales*. Geological Society of Australia, 165-183.

Carter, A., Roques, D., Bristow, C. & Kinny, P. (2001). Understanding Mesozoic accretion in Southeast Asia: Significance of Triassic thermotectonism (Indosinian orogeny) in Vietnam. *Geology* **29**, 211-214.

Chappel, B.W. & White, A.J.R. (1974). Two contrasting granite types. *Pacific Geology* **8**, 173-174.

Chen, J., Foland, K.A., Xing, F., Xu, X. & Zhou, T. (1991). Magmatism along the southeast margin of the Yangtze block: Precambrian collision of the Yangtze and Cathaysia block of China. *Geology* **19**, 815-818.

Cliff, R.A., Gray, C.M. & Huhma, H. (1983). A Sm–Nd isotopic study of the South Harris Igneous Complex, Outer Hebrides. *Contributions to Mineralogy and Petrology* **82**, 91-98.

Cobbing, E.J., Pitfield, P.E.J., Darbyshire, D.P.F. & Mallick, D.I.J. (1992). The granites of the South-East Asian tin belt. *Overseas Memoir of the British Geological Survey* **10**.

Compston, W., Williams, I.S., Kirschvink, J.L., Zhang Z. & Ma, G. (1992). Zircon U–Pb ages for the Early Cambrian time scale. *Journal of the Geological Society* **149**, 171-184.

Conceicao, R.V., Mallmann, G., Koester, E., Schilling, M.E., Bertotto, G.W. & Rodriguez-Vargas, A. (2005). Andean subduction-related mantle xenoliths: Isotopic evidence of Sr–Nd decoupling during metasomatism. *Lithos* **82**, 273-287.

Cong, B. & Zhai, M. (2000). Metamorphic petrology and metamorphism in western Yunnan. In: Zhong, D. (Ed.) *Paleotethysides in west Yunnan, China*. Science Press, Beijing.

Conticelli, S., D`Antonio, M., Pinarelli, L. & Civetta, L. (2002). Source contamination and mantle heterogeneity in the genesis of Italian potassic and ultrapotassic volcanic rocks: Sr-Nd-Pb isotope data from Roman Province and Southern Tuscany. *Mineralogy and Petrology* **74**, 189-222.

Cordier, C., Clement, J.P., Caroff, M., Hemond, C., Blais, S., Cotton, J., Bollinger, C., Launeau, P. & Guille, G. (2005). Petrogenesis of coarse-grained intrusives from Tahiti Nui and Raiatea (Society Islands, French Polynesia). *Journal of Petrology* **46**, 2281-2312.

Corriveau, L. & Bonnet, A.L. (2005). Pinwarian (1.5 Ga) volcanism and hydrothermal activity at the eastern margin of the Wakeham Group, Grenville Province, Quebec. *Canadian Journal of Earth Sciences* **42**, 1749-1782.

Cox, K.G., Bell, J.D. & Pankhurst, R.J. (1979). *The interpretation of igneous rocks*. George, Allen and Unwin, London.

Crocket, J.H. (2002). Platinum group element geochemistry of mafic and ultramafic rocks. In: Cabri, L.J. (Ed.) *The Geology, Geochemistry, Mineralogy and Benefication of PGE*. CIM Special Volume **54**, 177-210.

Crocket, J.H., Fleet, M.E. & Stone, W.E. (1997). Implications of composition for experimental partitioning of platinum-group elements and gold between sulphide liquid and basalt melt: the significance of nickel content. *Geochimica et Cosmochimca Acta* **61**, 4139-4149.

Crocket, J.H. & Paul, D.K. (2004). Platinum-group elements in Deccan mafic rocks: A comparison of suites differentiated by Ir content. *Chemical Geology* **208**, 273-291.

Crocket, J.H. & Paul, D.K. (2008). Platinum-group elements in igneous rocks of the Kutch Rift Basin; NW India: Implications for relations with the Deccan volcanic Province. *Chemical Geology* **248**, 239-255.

Crocket, J.H. & Skippen, G.B. (1966). Radioactivation determination of palladium in basaltic and ultrabasic rocks. *Geochimica et Cosmochimica Acta* **30**, 129-141.

Davidson, J.P. (1986). Isotopic and trace element constraints on the petrogenesis of subduction related lavas from Martinique, Lesser Antilles. *Journal of Geophysical Research* **91**, 5943-5962.

De la Roche, H., Leterrier, J., Grande Claude, P. & Marchal, M. (1980). A classification of volcanic and plutonic rocks using R1-R2 diagrams and major element analyses - its relationships and current nomenclature. *Chemical Geology* **29**, 183-210.

Deng, H.L., Campbell, A.J. & Humayun, M. (2002). Platinum Group Elements in sulfides from Yangliuping Cu-Ni-Pt-Pd Deposit in Sichuan, China. *Goldschmidt Conference Abstracts*, A177.

DePaolo, D.J. & Wasserburg, G.J. (1976). Nd isotopic variations and petrogenetic models. *Geophysical Research Letters* **3**, 249-252.

Dostal, J., Dupuy, C., Carron, J.P., Dekerneizon, M.L. & Maury, R.C. (1983). Partition-Coefficients of Trace-Elements - Application to Volcanic-Rocks of St-Vincent, West-Indies. *Geochimica et Cosmochimica Acta* **47**, 525-533.

Duke, J.M. (1976). Distribution of the period four transition elements among olivine, calcic clinopyroxene and mafic silicate liquid; experimental results. *Journal of Petrology* **17**, 499-521.

Dunn, T. (1987). Partitioning of Hf, Lu, Ti, and Mn between Olivine, Clinopyroxene and Basaltic Liquid. *Contributions to Mineralogy and Petrology* **96**, 476-484.

Dunn, T. & Sen, C. (1994). Mineral/matrix partition coefficients for orthopyroxene, plagioclase, and olivine in basaltic to andesitic systems: A combined analytical and experimental study. *Geochimica et Cosmochimica Acta*, **58**. 717-733.

Edmond, J.M., Measures, C., McDuff, R.E., Chan, L.H., Collier, R. & Grant, B. (1979). Ridge crest hydrothermal activity and the balances of the major and minor elements in the ocean; the Galapagos data. *Earth and Planetary Science Letters* **46**, 1-18.

Elthon, D. (1991). Geochemical evidence for formation of Bay of Islands ophiolite above a subduction zone. *Nature* **354**, 140-143.

Ewart, A. (1982). The mineralogy and petrology of Tertiary-Recent orogenic volcanic rocks with special reference to the andesitic-basaltic composition range. In: Thorpe, R.S. (Ed.) *Andesites*. John Wiley, Chichester, 25-95.

Ewart, A. & Griffin, W.L. (1994). Application of Proton-Microprobe Data to Trace-Element Partitioning in Volcanic-Rocks. *Chemical Geology* **117**, 251-284.

Fan, W.M., Zhang, C., Wang, Y., Guo, F. & Peng, T. (2008). Geochronology and geochemistry of Permian basalts in Western Guangxi Province, Southwest China: Evidence for Plume-Lithosphere interaction. *Lithos* **102**, 218-236.

Fang, N.Q. & Niu, N.F. (2003). Late Palaeozoic ultramafic lavas in Yunnan, SW China, and their geodynamic significance. *Journal of Petrology* **44**, 141-157.

Faure, G. (1986). *Principles of Isotope Geology*. John Wiley.

Femenias, O., Coussaert, N., Bingen, B., Whitehouse, M.J., Mercier, J.C.C. & Demaiffe, D. (2003). A Permian underplating event in late- to post-orogenic tectonic setting. Evidence from the mafic-ultramafic layered xenoliths from Beaunit (French Massif Central). *Chemical Geology* **199**, 293-315.

Feng, Q.L. (2002). Stratigraphy of volcanic rocks in the Changning-Menglian Belt in southwestern Yunnan, China. *Journal of Asian Earth Sciences* **20**, 657-664.

Feng, Q.L., Chonglakmani, C., Helmcke, D., Ingavat-Helmcke, R. & Liu, B. (2005). Correlation of Triassic stratigraphy between the Simao and Lampang-Phrae Basins: implications for the tectonopaleogeography of Southest Asia. *Journal of Asian Earth Sciences* **24**, 777-785.

Fleet, M.E., Crocket, J.H. & Stone, W.E. (1996). Partitioning of platinum-group elements (Os, Ir, Pt, Pd) and gold between sulphide liquid and basalt melt. *Geochimica et Cosmochimica Acta* **60**, 2397-2412.

Fleet, M.E., Stone, W.E. & Crocket, J.H. (1991). Partitioning of palladium, iridium, and platinum between sulphide liquid and basalt melt; effects of melt composition, concentration, and oxygen fugacity. *Geochimica et Cosmochimica Acta* **55**, 2545-2554.

Fleet, M.E., Crocket, J.H., Liu, M. & Stone, W.E. (1999). Laboratory partitioning of platinum-group elements (PGE) and gold with application to magmatic sulphide-PGE deposits. *Lithos* **47**, 127-144.

Floss, C., James, O.B., McGee, J.J. & Crosaz, G. (1998). Lunar ferroan anorthosite petrogenesis: clues from trace element distribution in FAN subgroups. *Geochimica et Cosmochimica Acta* **62**, 1255-1283.

Foley, S.F., Barth, M.G. & Jenner, G.A. (2000). Rutile/melt partition coefficients for trace elements and an assessment of the influence of rutile on the trace element characteristics of subduction zone magmas. *Geochimica et Cosmochimica Acta* **64**, 933-938.

Frei, D. & Gerdes, A. (2009). Precise and accurate *in situ* U–Pb dating of zircon with high sample throughput by automated LA-SF-ICP-MS. *Chemical Geology* **261**, 261-270.

Frei, D., Hollis, J.A., Gerdes, A., Harlov, D., Karlsson, C., Vasquez, P., Franz, G., Johansson, L. & Knudsen, C. (2006). Advanced in-situ trace element and geochronological microanalysis of geomaterials by laser ablation techniques. *Geological Survey of Denmark and Greenland Bulletin* **10**, 25-28.

Frimmel, H.E., Hartnady, C.J.H. & Koller, F. (1996). Geochemistry and tectonic setting of magmatic units in the Pan-African Gariep Belt, Namibia. *Chemcial Geology* **130**, 101-121.

Frey, F.A., Shimizu, N., Leinbach, A., Obata, A. & Takazawi, E. (1991). Compositional variations within the Lower Layered Zone of the Horoman Peridotite, Hokkaido, Japan: Constraints on models for melt-solid segregation. *Journal of Petrology* (Special Volume 2/Lherzolites Issue), 211-227.

Fuster, J.M., Ibarrola-Muno, E., Snelling, N.J., Cantagrel, J.M., Huertas, M.J., Coello, J. & Ancochea, E. (1994). K–Ar Chronology of the Canadas Formation in the southeastern sector of Tenerife: Implications of pyroclastic episodes in volcanic evolution. *Boletín de la Real Sociedad Española Historia Natural Seccion Geología* **89**, 25-41.

Ganino, C., Arndt, N.T., Zhou, M.F., Gaillar, F. & Chauvel, C. (2008). Interaction of magma with sedimentary wall rock and magnetite ore genesis in the Panzhihua mafic intrusion, SW China. *Mineralium Deposita* **43**, 677-694.

Garde, A.A. (1997). Accretion and evolution of an Archean high-grade grey gneiss-amphibolite complex: The Fiskey Jord Area, southern West Greenland. *Geological Survey of Denmark and Greenland Bulletin* **177**, 1-114.

Garuti, G., Fershatater, G., Bea, F., Montero, P., Pushkarev, E.V. & Zaccarani, F. (1997). Platinum-group elements as petrological indicators in mafic–ultramafic complexes of the central and southern Urals: preliminary results. *Tectonophysics* **276**, 181-194.

Gerdes, A. & Zeh, A. (2006). Combined U-Pb and Hf isotope LA-(MC)-ICP-MS analyses of detrital zircons: Comparison with SHRIMP and new constraints for the provenance and age of an Armorican metasediment in Central Germany. *Earth Planetary Science Letters* **249**, 47-61.

Gill, J.B. (1981). *Orogenic andesites and plate tectonics*. Springer. Berlin.

Glotov, A.I., Polyakov, G.V., Hoa, T.T., Balykin, P.A., Akimtsev, V.A., Krivenko, A.P., Tolstykh, N.D., Phuong, N.T., Tranh, H.H., Hung, T.Q. & Petrova, T.E. (2001). The Ban Phuc Ni-Cu-PGE deposit related to the Phanerozoic komatiite-basalt association in the Song Da Rift, Northwestern Vietnam. *The Canadian Mineralogist* **39**, 573-589.

Gorbachev, N.S. & Kashiceva, G.A. (1986). Fluid-magmatic differentiation of basaltic magma and equilibrium with magmatic sulfides. In: *Experiments in the study of important problems in geology*. Nauka, Moscow, 98-119.

Govindaraju, K. (1994). *Geostandards Newsletter,* Special Issue **18**.

Green, T.H. & Pearson, N.J. (1987). An experimental study of Nb and Ta partitioning between Ti-rich minerals and silicate liquids at high pressure and temperature. *Geochimica et Cosmochimica Acta* **51**, 55-62.

Grenne, T., Pedersen, R.B., Bjerkgard, T., Braathen, A., Selassie, M.G. & Worku, T. (2003). Neoproterozoic evolution of western Ethiopia: Igneous geochemistry, isotope systematics and U–Pb ages. *Geological Magazine* **140**, 373-395.

Gros, M., Lorand, J.P. & Luguet, A. (2002). Analysis of platinum-group elements and gold in geological materials using NiS fire assay and Te coprecipitaion; the NiS dissolution step revised. *Chemical Geology* **185**, 179-191.

Gruau, G., Bernard-Griffiths, J. & Lécuyer, C. (1998). The origin of U-shaped rare earth patterns in ophiolite peridotites: assessing the role of secondary alteration and melt/rock reaction. *Geochimica et Cosmochimica Acta* **62**, 3545-3560.

Guo, F., Fan, W.M., Wang, Y. & Li, C. (2004). When did the Emeishan Mantle Plume activity start? Geochronological and geochemical evidence from ultramafic-mafic dykes in southwestern China. *International Geology Review* **46**, 226-234.

Handler, M.R. & Bennett, V.C. (1999). Behaviour of platinum-group elements in the subcontinental mantle of eastern Australia during metasomatism and melt depletion. *Geochimica et Cosmochimica Acta* **63**, 3597-3618.

Hannigan, R.E. & Peucker-Ehrenbrink, B. (1999). Black Shale Weathering and the Mobility of Osmium Isotopes, Rhenium, and Platinum Group Elements. *Goldschmidt Conference Abstracts*, A452.

Hanski, E., Walker, R.J., Huhma, H., Polyakov, G.V., Balykin, P.A., Tran, T.H. & Ngo, T.P. (2004). Origin of the Permian-Triassic komatiites, northwestern Vietnam. *Contributions to Mineralogy and Petrology* **147**, 453-469.

Harney, D.M.W. & von Gruenewaldt, G. (1995). Ore-forming processes in the upper part of the Bushveld Complex, South Africa. *Journal of African Earth Sciences* **20**, 77-89.

Harnois, L. & Morency, M. (1989). Geochemistry of Mount Orford ophiolite complex, Northern Appalachians, Canada. *Chemical Geology* **77**, 133-147.

Harrison, T.M. & McDougall, I. (1981). Excess ^{40}Ar in metamorphic rocks from Broken Hill, New South Wales: implications for $^{40}Ar/^{39}Ar$ age spectra and the thermal history of the region. *Earth and Planetary Science Letters* **55**, 123-149.

Hart, S.R., Blusztajn, J., Dick, H.J.B., Meyer, P.S. & Muehlenbachs, K. (1999). The fingerprint of seawater circulation in a 500-meter section of ocean crust gabbros. *Geochimica et Cosmochimica Acta* **63**, 4059-4080.

Hart, S.R., Brooks, C., Krogh, T.E., Davis, G.L. & Nava, D. (1974). Sea floor alteration: Some chemical and Sr isotopic effects. *Contributions to Mineralogy and Petrology* **44**, 219-230.

He, B., Xu, Y.G., Chung, S.L. & Wang, Y. (2003). Sedimentary evidence for rapid crustal doming before the eruption of the Emeishan flood basalts. *Earth and Planetary Science Letters* **213**, 389-403.

Hellman, P.L. (2005). *Mineral Resource Update Ban Phuc Nickel-Copper Prospect, Vietnam*. Hellman & Schofield PTY LTD. 50 pp.

Helmcke, D., Ingavat-Helmcke, R., Feng, Q., Wagner, B. & Heppe, K. (2001). On geodynamic evolution of Simao region (southwestern Yunnan, China) during Late Paleozoic and Triassic. *Journal of China University of Geosciences* **12**, 195-200.

Hennig, D., Lehmann, B., Frei, D., Belyatski, B., Zhao, X.F., Cabral, A.R., Zheng, P., Zhou, M.F. & Schmidt, K. (2009). Early Permian seafloor to continental-arc magmatism in the eastern Paleo-Tethys: U–Pb age and Nd–Sr isotope data from the southern Lancangjiang zone, Yunnan, China. *Lithos* **113**, 408-422.

Heppe, K. (2006). Plate Tectonic evolution and mineral resource potential of the Lancang River Zone, southwestern Yunnan, People`s Republic of China. *Geologisches Jahrbuch* **SD 7**, 1-159.

Heppe, K., Helmcke, D. & Wemmer, K. (2007). The Lancang River zone of southwestern Yunnan, China: a questionable location for the active continental margin of Paleotethys. *Journal of Asian Earth Sciences* **30**, 706-720.

Hertogen, J., Janssen, M.J. & Palme, H. (1980). Trace elements in ocean ridge basalt glasses: implications for fractionation during mantle evolution and petrogenesis. *Geochimica et Cosmochimica Acta* **44**, 2125-2143.

Higuchi, H. & Nagasawa, H. (1969). Partition of trace elements between rock-forming minerals and the host volcanic rocks. *Earth and Planetary Science Letters* **7**, 281-287.

Hoatson, D.M. & Keays, R.R. (1989). Formation of platiniferous sulfide horizons by crystal fractionation and magma mixing in the Munni layered intrusion, west Pilbara block, Western Australia. *Economic Geology* **84**, 1775-1804.

Hoffmann, E.L. (1992). Instrumental neutron activation in geoanalysis. *Journal of Geochemical Exploration* **44**, 297-319.

Hofmann, A.W. (1988). Chemical differentiation of the Earth: the relationship between mantle, continental crust, and oceanic crust. *Earth and Planetary Science Letters* **90**, 297-314.

Holzheid, A. & Grove, T.L. (2002). Sulfur saturation limits in silicate melts and their implications for core formation scenarios for terrestrial planets. *American Mineralogist* **87**, 227-237.

Horan, M.F., Walker, R.F., Fedorenko, V.A. & Czamanske, G.K. (1995). Osmium and Neodymium isotopic constraints on the temporal and spatial evolution of Siberian Flood basalt sources. *Geochimica et Cosmochimica Acta* **59**, 5159-5168.

Horstwood, M.S.A., Foster, G.L., Parrish, R.R., Noble, S.R. & Nowell, G.M. (2003). Common-Pb corrected in situ U–Pb accessory mineral geochronology by LA-MC-ICP-MS. *Journal of Analytical Atomic Spectrometry* **18**, 837-846.

Huang, J., Zheng, Y.F., Zhao, Z.F., Wu, Y.B. & Zhou, J.B. (2006). Melting of subducted continent: Element and isotopic evidence for a genetic relationship between Neoproterozoic and Mesozoic granitoids in the Sulu orogen. *Chemical Geology* **229**, 227-256.

Huang, Z., Ye, T., Wu, K., Ji, X., Gao, Z., Qian, D., Tian, Y., He, Y., Zhang, Q., Cao, B., Li, L., Shao, H., Wang, Y., Yang, M., Zhang, Z., Yao, D. & Zheng, J. (2002). Geological Map of People`s Republic of China; 1:2.500.000. Chinese Geological Survey, Sino Maps Press, Beijing.

Innocenti, R., Manetti, P., Mazzuoli, R., Pasquare, G. & Villari, S. (1982). Anatolia and north-western Iran. In: Thorpe, R.S. (Ed.) *Andesites*. John Wiley, Chichester.

Irvine, T.N. &, Baragar, W.R.A. (1971). A guide to the chemical classification of the common volcanic rocks. *Canadian Journal of Earth Sciences* **8**, 523-548.

Ishihara, S. (1977). The magnetite-series and ilmenite-series granitic rocks. *Mining Geology* **26**, 293-305.

Ishihara, S. (1981). The granitoid series and mineralization. *Economic Geology 75th Anniversary Volume*, 458-484.

Jackson, S., Pearson, N.J., Griffin, W.L. & Belousova, E.A. (2004). The application of laser ablation – inductively coupled plasma – mass spectrometry to in situ U-Pb zircon geochronology. *Chemical Geology* **211**, 47-69.

Jahn, B.M., Liu, X., Yui, T.F., Morin, N. & Bouhnik-Le Coz, M. (2005). High-pressure/ultrahigh-pressure eclogites from the Hong`an Block, East-Central China: geochemical characterization, isotope disequilibrium and geochronological controversy. *Contributions to Mineralogy and Petrology* **149**, 499-526.

Jaques, A.L., Chappel, B.W. & Taylor, S.R. (1983). Geochemistry of cumulus peridotites and gabbros from the Marum Ophiolite complex, Northern Papua New Guinea. *Contributions to Mineralogy and Petrology* **82**, 154-164.

Jian, P., Liu, D., Kröner, A., Zhang, Q., Wang, Y., Sun, X. & Zhang, W. (2009a). Devonian to Permian plate tectonic cycle of the Paleo-Tethys Orogen in southwest China (I): Geochemistry of ophiolites, arc/back-arc assemblages and within-plate igneous rocks. *Lithos* **113**, 748-766.

Jian, P., Liu, D., Kröner, A., Zhang, Q., Wang, Y., Sun, X. & Zhang, W. (2009b). Devonian to Permian plate tectonic cycle of the Paleo-Tethys Orogen in southwest China (II): Insights from zircon ages of ophiolites, arc/back-arc assemblages and within-plate igneous rocks and generation of the Emeishan CFB province. *Lithos* **113**, 767-784.

Jian, P., Liu, D.Y. & Sun, X.M. (2003a). SHRIMP dating of Baimaxueshan and Ludian granitoid batholiths Northwestern Yunnan Province, and its geological implications. *Acta Geoscientica Sinica* **24**, 338-342 (in Chinese with English abstract).

Jian, P., Liu, D.Y. & Sun, X.M. (2003b). SHRIMP dating of Carboniferous Jinshajiang ophiolite in Western Yunnan and Sichuan: Geochronological constraints on the Evolution of the Paleo-Tethys Oceanic Crust. *Acta Geologica Sinica* **77**, 217-228 (in Chinese with English abstract).

Jian, P., Liu, D.Y. & Sun, X.M. (2004). SHRIMP dating of Jicha Alaskan-type gabbro in West Yunnan Province: Evidence for the early Permian subduction. *Acta Geologica Sinica* **78**, 165-170 (in Chinese with English abstract).

Jian, P., Liu, D.Y & Sun, X.M. (2008). SHRIMP dating of the Permo-Carboniferous Jinshajiang ophiolite, southwestern China: Geochronological constraints for the evolution of Paleo-Tethys. *Journal of Asian Earth Sciences* **32**, 371-384.

Jian, P., Wang, X., He, L. & Wang, C. (1998). U-Pb zircon dating of the Shuanggou ophiolite from Xinping County, Yunnan Province. *Acta Petrologica Sinica* **58**, 1-17 (in Chinese with English abstract).

Jiang, S.Y., Yu, J.M. & Lu, J.J. (2004). Trace and rare-earth element geochemistry in tourmaline and cassiterite from the Yunlong tin deposit, Yunnan, China: implication for migmatitic-hydrothermal fluid evolution and ore genesis. *Chemical Geology* **209**, 193-213.

Jourdan, F., Verati, C. & Féraud, G. (2006). Intercalibration of the Hb3gr $^{40}Ar/^{39}Ar$ dating standard. *Chemical Geology* **231**, 77-89.

Kagami, H., Tainosho, Y., Iizumi, S. & Hayama, Y. (1985). High initial Sr-isotopic ratios of gabbro and metadiabase in the Ryoke Belt, Southwest Japan. *Geochemical Journal* **19**, 237-243.

Kagami, H., Masaki, Y., Iizumi, S., Tainosho, Y., Owada, M., Ikeda, Y., Okano, O., Ochi, S., Hayama, Y. & Nureki, T (2000). Continental basalts in the accretionary complexes of the South-West Japan Arc: Constraints from geochemical and Sr and Nd isotopic data of metadiabase. *The Island Arc* **9**, 3-20.

Keays, R.R. (1995). The role of komatiitic and picritic magmatism and S-saturation in the formation of ore deposits. *Lithos* **34**, 1-18.

Keays, R.R. & Lightfoot, P.C. (2009). Crustal sulphur is required to form magmatic Ni–Cu sulphide deposits: evidence from chalcophile element signatures of Siberian and Deccan Trap basalts. *Mineralium Deposita* **152**, 309-321.

Kelemen, P.B., Hanghoj, K. & Greene, A.R. (2004). One View of the Geochemistry of Subduction-related Magmatic Arcs, with an Emphasis on Primitive Andesite and Lower Crust. In: Holland, H.D. & Turekian, K.K. (Eds.) *Treatise on Geochemistry* **3**, Elsevier, Amsterdam, 593-659.

Kelsey, C.H. (1965). Calculation of the C.I.P.W. Norm. *Mineralogical Magazine* **34**, 276-282.

Kepezhinskas, P., Defant, M.J. & Widom, E. (2002). Abundance and distribution of PGE and Au in the island-arc mantle: implications for sub-arc metasomatism. *Lithos* **60**, 113-128.

Kimura, J.I. & Yoshida, T. (2006). Contributions of slab fluid, mantle wedge and crust to the origin of quaternary lavas in the NE Japan arc. *Journal of Petrology* **47**, 745-750.

Klemme, S., Prowatke, S. & Hametner, K. (2005). The partitioning of trace elements between rutile and silicate melts: Implications for subduction zones. *Geochimica et Cosmochimica Acta* **69**, 2361-2371.

Kloeck, W. & Palme, H. (1988). Partitioning of siderophile and chalcophile elements between sulfide, olivine, and glass in a naturally reduced basalt from Disko Island, Greenland. In: Ryder, G. (Ed.) *Proceedings of the Lunar and Planetary Science Conference*. Pergamon, New York, 471-483.

Kretz, R. (1983). Symbols for rock-forming minerals. *American Mineralogist* **68**, 277-279.

Kristmannsdottir, H. (1971). Anorthosite inclusions in Teritary dolerite from the Island Groups Hrappsey and Purkey, West Iceland. *Journal of Geology* **79**, 741-748.

Kuno, J. (1966). Lateral variation of basalt magma type across continental margins and island arcs. *Bulletin of Volcanology* **29**, 195-222.

Lan, C.Y., Chung, S.L., Long, T.V., Lo, C.H., Lee, T.Y., Mertzman, S.A. & Shen, J.J.S (2003). Geochemical and Sr–Nd isotopic constraints from the Kontum massif, central Vietnam on the crustal evolution of the Indochina block. *Precambrian Research* **122**, 7-27.

Langmuir, C.H., Klein, E.M. & Plank, T. (1992). Petrological systematics of mid-ocean ridge basalts: constraints on melt generation beneath ocean ridges. In: Morgan, J.P, Blackman, D.K & Sinton, J.M. (Eds.) *Mantle flow and melt generation at midocean ridges*. *Geophysical Monograph* **71**, 183-280.

Larocque, J. & Canil, D. (2008). Amphibole and mid-crustal differentiation: Evidence from a Jurassic arc section, Vancouver Island, BC. *Goldschmidt Conference Abstracts*, A517.

Leblanc, M. (1991). Platinum-group elements and gold in ophiolitic complexes: distribution and fractionation from mantle to ocean floor. In: Peters, T.J. & Nicolas, A. (Eds.) *Ophiolite genesis and Evolution of the Oceanic Lithosphere*. Kluwer, 231-260.

Lehmann, B., Heppe, K., Shcheka, G. & Gierth, E. (2005). Geochemistry and geotectonic framework of the Dapingzhang polymetallic massive sulfide/stockwork deposit, Lancangjiang zone, Yunnan, China. *Berichte zur Lagerstätten- und Rohstoffforschung* **48**, 1-60.

Le Maitre, R.W. (1976). The chemical variability of some common igneous rocks. *Journal of Petrology* **17**, 589-598.

Le Maitre, R.W. (1989). *Igneous Rocks: A classification and glossary of terms*. Cambridge University Press, Cambridge.

LeRoex, A.P., Dick, H.J.B., Erlank, A.J., Reid, A.M., Frey, A.M. & Hart, S.R. (1983). Geochemistry, Mineralogy and Petrogenesis of Lavas Erupted along the Southwest Indian Ridge Between the Bouvet Triple Junction and 11 Degrees East. *Journal of Petrology* **24**, 267-318.

Lesher, C.M. & Keays, R.R. (2002). Komatiite-associated Ni–Cu-(PGE) deposits: geology, mineralogy, geochemistry and genesis. In: Cabri, L. (Ed.) *The geology, geochemistry, mineralogy and beneficiation of the platinum-group elements*. Canadian Institute of Mining, Metallurgy and Petroleum **54**, 579-618.

Lesher, C.M. & Stone, W.E. (1996). Exploration geochemistry of komatiites. In: Wyman, D. (Ed.) *Igneous trace element geochemistry: applications for massive sulphide exploration*. Geological Society of Canada, Short Course Notes, 153-204.

Li, C. & Ripley, E.M. (2005). Empirical equations to predict the sulfur content of mafic magmas at sulfide saturation and applications to magmatic sulfide deposits. *Mineralium Deposita* **40**, 218-230.

Li, C., Ripley, E.M. & Mathez, E.A. (2003). The effect of S on the partitioning of Ni between olivine and silicate melt in MORB. *Chemical Geology* **201**, 295-306.

Li, X.L. (1996). Basic characteristics and formation structural environment of Lincang granite batholith. *Yunnan Geology* **15**, 1-18 (in Chinese with English abstract).

Li, Z.X., Li, Z.H., Zhou, H.W., Li, W.X., Liu, Y. & Wingate, M.R.D. (2003). Neoproterozoic granitoids in south China: Crustal melting above a mantle plume at ca. 825 Ma? *Precambrian Research* **122**, 45-83.

Li, Z.X., Li, X.H., Zhou, H.W. & Kinny, P.D. (2002). Grenvillian continental collision in south China: New SHRIMP U-Pb zircon results and implications for the configuration of Rodinia. *Geology* **30**, 163-166.

Liew, T.C. & Page, R.W. (1985). U-Pb zircon dating of granitoid plutons from the West Coast Province of Peninsular Malaysia. *Journal of the Geological Society of London* **142**, 515-526.

Lightfoot, P.C. & Hawkesworth, C.J. (1988). Origin of Deccan Trap Lavas: evidence from combined trace element and Sr-, Nd-, and Pb-isotope studies. *Earth and Planetary Science Letters* **91**, 89-104.

Lightfoot, P.C. & Hawkesworth, C.J. (1997). Flood basalts and magmatic Ni, Cu and PGE sulphide mineralisation: comparative geochemistry of the Noril`sk (Siberian Flood Basalts) and West Greenland sequences. *Transactions of the American Geophysical Union*, 357-380.

Lightfoot, P.C, Naldrett, A.J., Gorbachev, N.S., Doherty, W. & Fedorenko, V.A. (1990). Geochemistry of the Siberian Trap of the Noril'sk Area, USSR, with implications for the relative contributions of crust and mantle to flood basalt magmatism. *Contributions to Mineralogy and Petrology* **104**, 631-644.

Lightfoot, P.C. & Keays, R.R. (2005). Siderophile and chalcophile metal variations in flood basalts from the Siberian Trap, Noril`sk Region: implications for the origin of the Ni–Cu–PGE sulfide ores. *Economic Geology* **100**, 439-462.

Liu, H., Xia, B. & Zhang, Y. (2004). Zircon SHRIMP dating of sodium alkaline rocks from Maomaogou area of Huili County in Panxi, SW China and its geological implications. *Chinese Science Bulletin* **16**, 1750-1757.

Liu, C.S., Zhu, J., Xu, X.S., Chu, X.J., Cai, D. & Yang, P. (1989). Study on the characteristics of Lincang composite granite batholith in west Yunnan. *Yunnan Geology* **8**, 189-204 (in Chinese with English abstract).

Lo, C.H., Chung, S.L., Lee, T.Y. & Wu, G. (2002). Age of the Emeishan flood magmatism and relations to Permian–Triassic boundary events. *Earth and Planetary Science Letters* **198**, 449-458.

Lorand J.P. & Alard, O. (2001). Platinum-group element abundances in the upper mantle: new constraints from in situ and whole-rock analyses of Massif Central xenoliths (France). *Geochimica et Cosmochimica Acta* **65,** 2789-2806.

Lorand, J.P. & Conquéré, F. (1983). Contribution à l`étude des sulfures dans les enclaves de lherzolites à spinell des basalts alcalins (Massif Central et du Languedoc, France). *Bulletin de Minéralogie* **106**, 585-606.

Lorand, J.P., Luguet, A. & Alard, O. (2008). Platinum-Group Elements: A New Set of Key Tracers for the Earth Interior. *Elements* **4**, 247-252.

Ludwig, K. (2003). *Isoplot/Ex version 3: A geochronological toolkit for Microsoft Excel*. Geochronology Center, Berkeley.

Luguet, A., Shirey, S.B., Lorand, J.P., Horan, M.F. & Carlson, R.W. (2007). Residual platinum-group minerals from highly depleted harzburgites of the Lherz massif (France) and their role in HSE fractionation of the mantle. *Geochimica et Cosmochimica Acta* **71**, 3082-3097.

Luhr, J.F. & Carmichael, I.S.E. (1980). The Colima volcanic complex, Mexico. I: post-caldera andesites from Volcan Colima. *Contributions to Mineralogy and Petrology* **71**, 343-372.

Luhr, J.F. & Haldar, D. (2006). Barren Island Volcano (NE Indian Ocean): island-arc high-alumina basalts produced by troctolite contamination. *Journal of Volcanology and Geothermal Research* **149**, 177-212.

Luo, Y.N. (1981). The characteristics of Ti-chromite mineralization in Xinjie layered, ultramafic-mafic intrusion in Panzhihua area, China. *Geochimica* **10**, 66-73 (in Chinese with English abstract).

Ma, Y.X., Ji, X.T., Li, J.C., Huang, M. & Min, Z.Z. (2003). *Mineral Resources of Panzhihua, Sichuan Province, SW China*. Chengdu University of Technology, 275 pp.

MacDonald, G.A. (1968). Composition and origin of Hawaiian lavas. In: Coars, R.R., Hay, R.S. & Anderson, C.A. (Eds.) *Studies in volcanology: a memoir in honour of Howel Williams*. Geological Society of America Memoires **116**, 477-522.

MacDonald, G.A. & Katsura, T. (1964). Chemical composition of Hawaiian lavas. *Journal of Petrology* **5**, 83-133.

Mahoney, J.J., Frei, R., Tejada, M.L.G., Mo, X.X., Leat, P.T. & Nägler, T.F. (1998). Tracing the Indian Ocean Mantle Domain through Time: Isotopic Results from Old West Indian, East Tethyan, and South Pacific Seafloor. *Journal of Petrology* **39**, 1285-1306.

Mahood, G.A. & Hildreth, E.W. (1983). Large partition coefficients for trace elements in high-silica rhyolites. *Geochimica et Cosmochimica Acta* **47**, 11-30.

Maier, W.D. (2005). Platinum-group element deposits and occurrences: Mineralization styles, genetic concepts, and exploration criteria. *Journal of African Earth Sciences* **41**, 165-191.

Mao, Y.S. & Sun, S.H. (1981). Petrological characteristics and origin of layered basic–ultrabasic intrusion in Xinjie, Miyi, Sichuan Province. *Mineralogy and Rocks* **6**, 29-40 (in Chinese with English abstract).

Marchesi, C., Garrido, C.J., Godard, M., Proenza, J.A., Gervialla, F. & Blanco-Moreno, J.A. (2006). Petrogenesis of highly depleted peridotites and gabbroic rocks from the Mayarí-Baracoa Ophiolite Belt (Eastern Cuba). *Contributions to Mineralogy and Petrology* **151**, 717-736.

Marshall, D., Watkinson, D., Farrow, C., Molnár, R. & Fouillac, A.M. (1999). Multiple fluid generations in the Sudbury Igneous Complex: fluid inclusion, Ar, O, H, Rb and Sr evidence. *Chemical Geology* **154**, 1-19.

Mathez, E.A. (1976). Sulfur solubility and magmatic sulfides in submarine basalt glass. *Journal of Geophysical Research* **81**, 4269-4276.

Matsumoto, T., Chen, Y. & Matsuda, J.I. (2001). Concomitant occurrence of primordial and recycled noble gases in the Earth`s Mantle. *Earth and Planetary Science Letters* **185**, 35-47.

Mavrogenes, J.A. & O'Neill, H.S.C. (1999). The relative effects of pressure, temperature and oxygen fugacity on the solubility of sulfide in mafic magmas. *Geochimica et Cosmochimica Acta* **63**, 1173-1180.

McBirney, A.R. (2002). The Skaergaard Layered Series. Part VI. Excluded trace elements. *Journal of Petrology* **43**, 535-556.

McCallum, I.S. & Charette, M.P. (1978). Zr and Nb partition coefficients: implications for the genesis of mare basalts, KREEP, and sea floor basalts. *Geochimica et Cosmochimica Acta* **42**, 859-869.

McDonough, W.F. & Sun, S.S. (1995). Composition of the Earth. *Chemical Geology* **120**, 223-253.

McKenzie, D. & O'Nions, R.K. (1991). Partial melt distributions from inversion of rare Earth element concentrations. *Journal of Petrology* **32**, 1021-1091.

Meeker, G.P. (1995). Constraints on formation processes of two coarse-grained calcium-aluminium-rich inclusions: a study of mantles, islands and cores. *Meteoritics* **30**, 71-84.

Meibom, A., Frei, R. & Sleep, N.H. (2004). Osmium isotopic compositions of Os-rich platinum group element alloys from the Klamath and Siskiyou mountains. *Journal of Geophysical Research* **109**, B02203.

Meisel, T. & Moser, J. (2004). Reference materials for geochemical PGE analysis: new analytical data for Ru, Rh, Pd, Os, Ir, Pt and Re by isotope dilution ICP-MS in 11 geological reference materials. *Chemical Geology* **208**, 319-338.

Melezhik, V.A. & Sturt, B.A. (1994). General geology and evolutionary history of the Early Proterozoic Polmak-Pasvik-Pechenga-Imandra/Varzuga-Ustponoy greenstone belt in the northeastern Baltic Shield. *Earth Science Reviews* **36**, 205-241.

Metcalfe, I. (2002). Permian tectonic framework and palaeogeography of SE Asia. *Journal of Southeast Asian Earth Sciences* **20**, 551-566.

Metcalfe, I. (2006). Paleozoic and Mesozoic tectonic evolution and Paleogeography of East Asian crustal fragments: The Korean Peninsula in context. *Gondwana Research* **9**, 24-46.

Meurer, W.P., Willmore, C.C. & Boudreau, A.E. (1998). Metal redistribution during fluid exsolution and migration in the Middle Banded series of the Stillwater Complex, Montana. *Lithos* **47**, 143-156.

Middlemost, E.A.K. (1975). The basalt clan. *Earth Science Reviews* **11**, 337-364.

Middlemost, E.A.K. (1985). *Magmas and magmatic rocks*. Longman Group, London.

Middlemost, E.A.K. (1989). Iron oxidation ratios, norms and the classification of volcanic rocks. *Chemical Geology* **77**, 19-26.

Mikouchi, T., Miyamoto, M. & McKay, G.A. (1999). Mineralogical study of angrite Asuka-881371: its possible relation to angrite LEW87051. *Proceedings of the NIPR Symposium on Antarctic Meteorites* **9**, 174-188.

Mittlefehldt, D.W., McCoy, T.J., Goodrich, C.A. & Kracher, A. (1998). Non-chondritic meteorites from asteroidal bodies. In: Papike, J.J. (Ed.) *Planetary Materials*. Reviews in Mineralogy **36**, 4100-4195.

Miyashiro, A. (1974). Volcanic rock series in island arcs and active continental margins. *American Journal of Science* **274**, 321-355.

Momme, P., Brooks, C.K., Tegner, C. & Keays, R.R. (2002). Platinum-group element behaviour in basalts from East Greenland rifted margin. *Contributions to Mineralogy and Petrology* **143**, 133-153.

Molnár, F., Watkinson, D.H. & Jones, P.C. (2001). Multiple hydrothermal processes in footwall units of the North Range, Sudbury Igneous Complex, Canada, and implications for the genesis of vein-type Cu-Ni-PGE deposits. *Economic Geology* **96**, 1645-1670.

Morgan, J.W. (1986). Ultramafic xenoliths - clues to the Earth`s late accretionary history. *Journal of Geophysical Research* **91B**, 12375-12387.

Morishita, T., Arai, S. & Green, D.H. (2004). Possible non-melted remnants of subducted lithosphere: Experimental and geochemical evidence from corundum-bearing mafic rocks in the Horoman Peridotite Complex, Japan. *Journal of Petrology* **45**, 235-252.

Morrison, D.A., Ashwal, L.D., Phinney, W.C., Shih, C.Y. & Wooden, J.L. (1983). Pre-Keweenawan anorthosite inclusions in the Keweenawan Beaver Bay and Duluth Complexes Northeastern Minnesota. *Bulletin of the Geological Society of America* **94**, 206-221.

Mungall, J.E. (2007). Crustal contamination of picritic magmas during transport through dikes: The Expo Intrusive Suite, Cape Smith Fold Belt; New Quebec. *Journal of Petrology* **48**, 1021-1039.

Mungall, J.M. & Naldrett, A.J. (2008). Ore deposits of the platinum-group elements. *Elements* **4**, 253-258.

Naldrett, A.J. (1999). World-class Ni-Cu-(PGE) deposits: key factors in their genesis. *Mineralium Deposita* **34**: 227-240.

Naldrett, A.J. (2004). *Magmatic Sulfide Deposits: Geology, Geochemistry and Exploration*. Springer, 728 pp.

Naldrett, A.J., Brügmann, G.E. & Wilson, A.H. (1990). Models for the concentration of PGE in layered intrusions. *Canadian Mineralogist* **28**, 389-408.

Naldrett, A.J., Federenko, V.A., Lightfoot, P.C., Kunilov, V.I., Gorbachev, N.S., Doherty, W. & Johan, Z. (1995). Ni-Cu-PGE deposits of the Noril`sk region, Siberia: their formation in conduits for flood basalt volcanism. *Transactions of the American Institute of Mining, Metallurgical, and Petroleum Engineers* **104**, 1-86.

Naldrett, A.J. & Lightfoot, P.C. (1993). A model for giant magmatic sulphide deposits associated with flood basalts. *Society of Economic Geologists Special Publication Number* **2**, 81-124.

Naldrett, A.J. & Lightfoot, P.C. (1999). Ni-Cu-(PGE) deposits of the Noril`sk region, Siberia, dynamic processes. In: Keays, R.R., Lesher, C.M., Lightfoot, P.C. & Farrow, C.E.G. (Eds.) *Magmatic ore deposits and their application to mineral exploration*. Geological Association of Canada, Washington, 195-250.

Naldrett, A.J. & Wilson, A.H. (1990). Horizontal and vertical variations in noble-metal distribution in the Great Dyke of Zimbabwe: a model for the origin of PGE mineralization by fractional segregation of sulfide. *Chemical Geology* **88**, 279-300.

Nam, T.N., Sano, Y., Terada, K., Toriumi, M., Quynh, P.V. & Dung, L.T. (2001). First SHRIMP U–Pb zircon dating of granulites from the Kontum massif (Vietnam) and tectonothermal implications. *Journal of Asian Earth Sciences* **19**, 77-84.

Nash, W.P. & Crecraft, H.R. (1985). Partition coefficients for trace elements in silicic magmas. *Geochimica et Cosmochimica Acta* **49**, 2309-2322.

Neumann, E.R., Soerensen, V.R., Simonsen, S.L. & Johnsen, K. (2000). Gabbroic xenoliths from LaPalma, Tenerife and Lanzarote, Canary Islands: Evidence for reactions between mafic alkaline canary island melts and old oceanic crust. *Journal of Volcanology and Geothermal Research* **103**, 313-342.

Nockolds, S.R. (1954). Average chemical composition of some igneous rocks. *Bulletin of the Geological Society of America* **65**, 1007-1032.

Nutman, A.P., McGregor, V.R., Friend, C.R.L., Bennett, V.C. & Kinny, P.D (1996). The Itsaq Gneiss Complex of southern West Greenland; The world`s most extensive record of Early Crustal Evolution (3900-3600 Ma). *Precambrian Research* **78**, 1-39.

Oberthür, T. (2002). Platinum-group element mineralization of the Great Dyke, Zimbabwe. In: Cabri, L.J. (Ed.) *The Geology, Geochemistry, Mineralogy and Mineral Benefication of Platinum-Group Elements*. Canadian Institute of Mining, Metallurgy and Petroleum, Special Volume **54**, 483-506.

O`Connor, J.T. (1965). A classification for quartz-rich igneous rocks based on feldspar ratios. *U.S. Geological Survey Professional Paper* **525B**, B79-B84.

Oguri, K., Shimoda, G. & Tatsumi, Y. (1999). Quantitative determination of gold and the platinum-group elements in geological samples using improved NiS fire-assay and tellurium coprecipitation with inductively coupled plasma-mass spectrometry (ICP-MS). *Chemical Geology* **157**, 189-197.

Okamoto, K. (1979). Geochemical study on magmatic differentiation of Asama Volcano, central Japan. *Journal of the Geological Society of Japan* **85**, 525-535.

Onuma, K. & Tohara, T. (1983). Effect of chromium on phase relations in the join forsterite-anorthite-diopside in air at 1-atm. *Contributions to Mineralogy and Petrology* **84**,174-181.

Oppenheimer, C. (2004). Volcanic Degassing. In: Holland, H.D. & Turekian, K.K. (Eds.) *Treatise on Geochemistry* **3**. Elsevier, Amsterdam, 123-166.

Palacz, Z.A. (1985). Sr-Nd-Pb isotopic evidence for crustal contamination in the Rhum Intrusion. *Earth and Planetary Science Letters* **74**, 35-44.

Palme, H. & O'Neill, H.S.C. (2004). Cosmochemical estimates of Mantle Composition. In: Holland, H.D. & Turrekian, K.K. (Eds.) *Treatise on Geochemistry* **2**. Elsevier, Amsterdam.

Pang, K.N., Li, C., Zhou, M.F. & Ripley, E.M. (2008). Abundant Fe–Ti oxide inclusions in olivine from the Panzhihua and Hongge layered intrusions, SW China: evidence for early saturation of Fe–Ti oxides in ferrobasaltic magma. *Contributions to Mineralogy and Petrology* **156**, 307-321.

Pan-Xi Geological Team of the Bureau of Geology and Mineral Resources (PXGT) (1981). *Geological Survey Report on the Xinjie V-Ti-Magnetite Ore District in the Miyi county, Sichuan Province*. 15-35 (in Chinese, unpublished).

Paster, T.P., Schauwecker, D.S. & Haskin, L.A. (1974). The behavior of some trace elements during solidification of the Skaergaard layered series. *Geochimica et Cosmochimica Acta* **38**, 1549-1577.

Pattou, L., Lorand, J.P. & Gros, M. (1996). Non-chondritic platinum-group element ratios in the Earth`s mantle. *Nature* **379**, 712-715.

Paul, D.K., Kreston, P., Barman, T.R., McNutt, R.H. & Brunfeld, A.O. (1984). Geochemical and petrological relations in some Deccan basalts, western Maharashtra; India. *Journal of Volcanology and Geothermal Research* **21**, 165-176.

Peach, C.L. & Mathez, E.A. (1990). Sulfide melt silicate melt distribution coefficients for nickel and iron and implications for the distribution of other chalcophile elements. *Geochimica et Cosmochimica Acta* **57**, 3013-3021.

Peach, C.L., Mathez, E.A. & Keays, R.R. (1990). Sulfide melt–silicate melt distribution coefficients for noble metals and other chalcophile elements as deduced from MORB: implications for partial melting. *Geochimica et Cosmochimica Acta* **54**, 3379-3389.

Peach, C.L., Mathez, E.A., Keays, R.R. & Reeves, S.J. (1994). Experimentally determined sulphide melt-silicate melt extraction: a study of massif and xenolith peridotite suites. *Chemical Geology* **208**, 29-59.

Pearce, J.A. (1982). *Trace* element characteristics of lavas from destructive plate boundaries. In: Thorpe, R.S. (Ed.) *Andesites*. John Wiley, Chichester.

Pearce, J.A. (1983). Role of the sub-continental lithosphere in magma genesis at active continental margins. In: Hawkesworth, C.J. & Norry, M.J. (Eds.) *Continental Basalts and Mantle Xenoliths*. Shiva, Nantwich.

Pearce, J.A. & Cann, J.R. (1973). Tectonic setting of basic volcanic rocks determined using trace element analysis. *Earth and Planetary Science Letters* **19**, 290-300.

Pearce, J.A., Harris, N.B.W. & Tindle, A.G. (1984). Trace element discrimination diagrams for the tectonic interpretation of granitic rocks. *Journal of Petrology* **25**, 956-983.

Pearce, J.A. & Norry, M.J. (1979). Petrogenetic implications of Ti, Zr, Y and Nb variations in volcanic rocks. *Contributions to Mineralogy and Petrology* **69**, 33-47.

Pearce, J.A. & Peate, D.W. (1995). Tectonic implications of the compositions of volcanic arc magma. *Annual Review of Earth and Planetary Sciences* **23**, 251-285.

Pearson, D.G. & Woodland, S.J. (2000). Solvent extraction/anion exchange separation and determination of PGEs (Os, Ir, Pt, Pd, Ru) and Re–Os isotopes in geological samples by isotope dilution ICP–MS. *Chemical Geology* **165**, 87-107.

Peate, I.U. & Bryan, S.E. (2008). Re-evaluating plume-induced uplift in the Emeishan large igneous province. *Nature Geoscience* **1**, 625-629.

Peccerillo, R. & Taylor, S.R. (1976). Geochemistry of Eocene calc-alkaline volcanic rocks from the Kastamonu area, northern Turkey. *Contributions to Mineralogy and Petrology* **58**, 63-81.

Pedersen, A.K. (1979). Basaltic Glass with High-Temperature Equilibrated Immiscible Sulfide Bodies with Native Iron from Disko, Central West Greenland. *Contributions to Mineralogy and Petrology* **69**, 397-407.

Peng, X. & Luo, W. (1982). Discovery and tectonic significance of glaucophane schist from the southern section of the Lancang River in western Yunnan. *Regional Geology of China* **2**, 69-75 (in Chinese with English abstract).

Peng, T.P., Wang, Y.P., Fan, W.M., Liu, D., Shi, Y.R. & Miao, L. (2006). SHRIMP zircon U–Pb geochronology of early Mesozoic felsic igneous rocks from the southern Lancangjiang and its tectonic implications. *Science in China* **49**, 1032-1042.

Peng, T.P., Wang, Y.P., Zhao, G.C., Fan, W.M. & Peng, B.X. (2008). Arc-like volcanic rocks from the southern Lancangjiang zone, SW China: Geochronological and geochemical constraints on their petrogenesis and tectonic implications. *Lithos* **102**, 358-373.

Pin, C., Joannon, S., Bosq, C., Le Fèvre, B. & Gauthier, P.J. (2003). Precise determination of Rb, Sr, Ba, and Pb in geological materials by isotope dilution and ICP-quadrupole mass spectrometry following separation of the analytes. *Journal of Analytical Atomic Spectrometry* **18**, 135-141.

Polat, A., Frei, R., Appel, P.W., Dilek, Y., Fryer, B.J., Ordonez-Calderon, J.C., Yang, Z.M. (2008). The origin and compositions of Mesoarchean oceanic crust: Evidence from the 3075 Ma Ivisaartoq Greenstone Belt, SW Greenland. *Lithos* **100**, 293-321.

Polovina, J.S., Hudson, D.M. & Jones, R.E. (2004). Petrographic and geochemical characteristics of postmagmatic hydrothermal alteration and mineralization in the J-M Reef, Stillwater Complex, Montana. *Canadian Mineralogist* **42**, 261-278.

Polyakov, G.V., Balykin, P.A., Tran, T.H, Hoang, H.T., Tran, Q.H., Ngo, T.P., Petrova, T.E. Vu, V.V., Bui, A.N., Tran, T.A. & Hoang, V.H. (1996). *Permian-Triassic mafic-ultramafic associations of Northern Vietnam*. Science and Technics Publishing House, Hanoi, 172 pp (in Vietnamese).

Polyakov, G.V., Balykin, P.A., Tran, T.H., Ngo, T.P., Hoang, H.T., Tran, Q.H., Ponomarchuk, V.A., Lebedev, Y.N. & Kireev, A.D. (1998). Evolution of the Mesozoic-Cenozoic magmatism in the Song Da rift and its contouring structures (northwestern Vietnam). *Russian Geology and Geophysics* **39**, 695-706 (in Russian).

Powell, R. (1978). Crystallisation conditions of low-pressure cumulate nodules from the Lesser Antilles island arc. *Earth and Planetary Science Letters* **39**, 162-172.

Pu, C., Qin, D., Nian, H., Zhang, X., Pirajno, F. & Zhuguo, F. (2007). Geological and geochemical characteristics of the Baimazhai Ni-Cu-(PGE) sulphide deposit in Yunnan, China. *Chinese Journal of Geochemistry* **26**, 374-383.

Qi, L., Wang, C.Y. & Zhou, M.F. (2008). Controls on the PGE distribution of Permian Emeishan alkaline and peralkaline volcanic rocks in Longzhoushan, Sichuan Province, SW China. *Lithos* **106**, 222-236.

Qi, L. & Zhou, M.F. (2008). Platinum-group and Sr–Nd–Os isotopic geochemistry of Permian Emeishan flood basalts in Guizhou Province, SW China. *Chemical Geology* **248**, 83-103.

Qi, L., Zhou, M.F. & Wang, C.Y. (2004). Determination of low concentrations of platinum group elements in geological samples by ID-ICP-MS. *Journal of Analytical Atomic Spectrometry* **19**, 1335-1339.

Qi, L., Zhou, M.F. & Wang, C.Y. (2007). Evaluation of the determination of Re and PGEs abundance of geological samples by ICP-MS coupled with a modified Carius tube digestion at different temperatures. *Geochemical Journal* **41**, 407-414.

Qiu, Y.M., Gao, S., McNaughton, I.J., Groves, D.I. & Ling, W. (2000). First evidence of >3.2 Ga continental crust in the Yangtze craton of south China and its implications for Archean crustal evolution and Phanerozoic tectonics. *Geology* **28**, 11-14.

Rajamani, V. & Naldrett, A.J. (1978). Partitioning of Fe, Co, Ni, and Cu between Sulfide Liquid and Basaltic Melts and Composition of Ni-Cu Sulfide Deposits. *Economic Geology* **73**, 82-93.

Rauscher, K., Voigt, J., Wilke, I. & Wilke, K.T. (2000). Chemische Tabellen und Rechentafeln für die analytische Praxis. Harri Deutsch, Frankfurt.

Renzulli, A. & Santi, P. (2000). Two-stage fractionation history of the alkali basalt-trachyte series of Sete Cidades volcano (São Miguel Island, Azores). *European Journal of Mineralogy* **12**, 469-494.

Revillon, S., Arndt, N.T., Chauvel, C. & Hallot, E. (2000). Geochemical study of ultramafic volcanic and plutonic rocks from Gorgona Island, Colombia: The plumbing system of an oceanic plateau. *Journal of Petrology* **41**, 1127-1153.

Revillon, S., Chauvel, C., Arndt, N.T., Pik, R., Martineau, F., Fourcade, S. & Marty, B. (2002). Heterogeneity of the Caribbean Plateau mantle source: Sr, O and He isotopic composition of olivine and clinopyroxene from Gorgona Island. *Earth and Planetary Science Letters* **205**, 91-106.

Rickwood, P.C. (1989). Boundary lines within petrologic diagrams which use oxides of major and minor elements. *Lithos* **22**, 247-263.

Richard, P., Shimizu, N. & Allègre, C.J. (1976). $^{143}Nd/^{146}Nd$, a natural tracer: an application to oceanic basalts. *Earth and Planetary Science Letters* **31**, 269-278.

Righter, K., Campbell, A,J., Humayun, M. & Hervig, R.L. (2004). Partitioning of Ru, Rh, Pd, Re, Ir, and Au between Cr-bearing spinel, olivine, pyroxene and silicate melts. *Geochimica et Cosmochimica Acta* **68**, 867-880.

Rittmann, A. (1929). Die Zonenmethode. Ein Beitrag zur Methodik der Plagioklasbestimmung mit Hilfe des Theodolithtisches. *Schweizerische Mineralogische und Petrographische Mitteilungen* **9**, 1-46.

Robb, L. (2008). Introduction to Ore-Forming Processes. Blackwell, 373 pp.

Roberts, S., Palmer, M. & Waller, L. (2006). Sm-Nd and REE characteristics of tourmaline and scheelite from Björkdal gold deposit, northern Sweden: Evidence of an Intrusion-related gold deposit? *Economic Geology* **101**, 1415-1425.

Rodríguez, C., Sellés, D., Dungan, M., Langmuir, C. & Leeman, W. (2007). Adakitic dacites formed by intracrustal crystal fractionation of water-rich parent magmas at Nevado de Longaví Volcano (36.2°S; Andean Southern Volcanic Zone, Central Chile). *Journal of Petrology*. DOI:10.1093/petrology/egm049.

Rousseau, R.M. (2001). Detection limit and estimate of uncertainty on analytical XRF results. *The Rigaku Journal* **18**.

Rudnick, R.L. & Gao, S., 2004. The continental crust. In: Holland, H.D., Turekian, K.K. (Eds.) *Treatise on Geochemistry*. Elsevier, Amsterdam, 1-64.

Ryzhenko, B. & Kennedy, G.C. (1973). Effect of pressure on eutectic in system Fe-FeS. *American Journal of Science* **273**, 803-810.

Saal, A.E., Takazawa, E., Frey, F.A., Shimuzu, N. & Hart, S.R. (2001). Re–Os isotopes in the Horoman Peridotite: Evidence for refertilization? *Journal of Petrology* **42**, 25-37.

Sattari, P, Brenan, J.M., Horn, I. & McDonough, W.F. (2002). Experimental constraints on the sulfide-silicate and chromite-silicate melt partitioning behavior of rhenium and platinum-group elements. *Economic Geology* **97,** 385-398.

SBGMR (Sichuan Bureau of Geology and Mineral Resources) (1991). *Regional geology of Sichuan province*. Geological Publishing House, Beijing, China, 1-680 (in Chinese with English abstract).

Schilling, J.G., Thompson, G., Zajac, M., Evans, R., Johnson, T., White, W., Devine, J.D. & Kingsley, R. (1983). Petrologic and geochemical variations along the Mid-Atlantic Ridge from 27°N to 73°N. *American Journal of Science* **283**, 510-586.

Schock, H.H. (1979). Distribution of rare-earth and other trace elements in magnetites. *Chemical Geology* **26**, 119-133.

SEGNL, 2005. Exploration reviews. *SEG Newsletter* **60**, 42.

Shand, S.J. (1947). *The Eruptive Rocks*. Wiley, New York.

Shellnut, J.G., Zhou, M.F., Yan, D.P. & Wang, Y. (2008). Longevity of the Permian Emeishan Mantle Plume (SW China): 1 Ma, 8 Ma or 18 Ma? *Geological Magazine* **145**, 373-388.

Shervais, J.W. (1982). Ti-V plots and the petrogenesis of modern and ophiolitic lavas. *Earth and Planetary Science Letters* **59**, 101-118.

Shiotani, Y. & Niida, K. (1997). Origin of mafic layers in the Horoman Peridotite Complex. *Memoirs of the Geological Society of Japan* **47**, 123-137.

Shirey, S.B. & Walker, R.J. (1995). Carius Tube Digestion for Low-Blank Rhenium-Osmium Analysis. *Analytical Chemistry* **67**, 2136-2141.

Sisson, T.W. (1994). Hornblende-Melt Trace-Element Partitioning Measured by Ion Microprobe. *Chemical Geology* **117**, 331-344.

Snow, J.E. & Schmidt, G. (1998). Constraints on Earth accretion deduced from noble metals in the oceanic mantle. *Nature* **391**, 166-169.

Song, H., He, M., Zhang, S. & Yi, F. (2008a). Chemical composition of the ore and occurrence state of the elements in Jingbaoshan platinum-palladium deposit. *Chinese Journal of Geochemistry* **27**, 104-108.

Song, X.Y., Keays, R.R., Xiao, L., Qi, H.W. & Ihlenfeld, C. (2009). Platinum-group element geochemistry of the continental flood basalts in the central Emeishan Large Igneous Province, SW China. *Chemical Geology* **262**, 246-261.

Song, X.Y., Qi, H.W., Robinson, P.T., Zhou, M.F. & Peng, T. (2008b). Geochronology and geochemistry of Permian basalts in Western Guangxi Province, Southwest China: Evidence for Plume-Lithosphere interaction. *Lithos* **102**, 218-236.

Song, X.Y., Zhou, M.F., Cao, Z.M., Sun, M. & Wang, Y.L. (2003). Ni-Cu-(PGE) magmatic sulphide deposits in the Yangliuping area, Permian Emeishan igneous province, SW China. *Mineralium Deposita* **38**, 831-843.

Song, X.Y., Zhou, M.F., Cao, Z.M. & Robinson, P.T. (2004). Late Permian rifting of the South China Craton caused by the Emeishan Mantle Plume? *Journal of the Geological Society* **161**, 773-781.

Song, X.Y., Zhou, M.F., Hou, Z.Q., Cao, Z.M., Wang, Y.L. & Li, Y.G. (2001). Geochemical constraints on the mantle source of the Upper Permian Emeishan continental flood basalts, southwestern China. *International Geology Review* **43,** 213-225.

Song, X.Y., Zhou, M.F., Keays, R.R., Cao, Z.M., Sun, M. & Qi, L. (2006). Geochemistry of the Emeishan flood basalts at Yangliuping, Sichuan, SW China: implications for sulphide segregation. *Contributions to Mineralogy and Petrology* **152**, 53-74.

Stacey, J.S. & Kramers, J.D. (1975). Approximation of terrestrial lead isotope evolution by a two-stage model. *Earth and Planetary Science Letters* **26**, 207-221.

Stascheit, A., Knipping, B., Engelhardt, H.J., Rühe, S. & Gareis, R. (1994). In-house Reference Samples for Geochemistry and Environmental Sciences. *Zeitschrift der Deutschen Geologischen Gesellschaft* **145**, 402-413.

Stone, W.E., Crocket, J.H. & Fleet, M.E. (1990). Partitioning of palladium, iridium, platinum, and gold between sulphide liquid and basalt melt at 1200 degrees C. *Geochimica et Cosmochimica Acta* **54**, 2341-2344.

Streckeisen, A. (1976). To each plutonic rock its proper name. Earth *Science Reviews. International Magazine for Geo-Scientists* **12**, 1-33.

Stribrny, B. (1996). Platinmetall- und Goldlagerstätten: Vorkommen, Produktion und Reserven. *Erzmetall* **49,** 191-195.

Suda, Y. (2004). Crustal anatexis and evolution of granitoid magma in Permian intra-oceanic island arc. The Asago body of the Yakuno ophiolite, Southwest Japan. *Journal of Mineralogical and Petrological Sciences* **99**, 339-356.

Sun, S.S., Wallace, D.A., Hoatson, D.M., Gilkson, A.Y. & Keays, R.R. (1991). Use of geochemistry as a guide to platinum group element potentials of mafic–ultramafic rocks: examples from the west Pilbara Block and Halls Creek Mobile Zone, western Australia. *Precambrian Research* **50**, 1-35.

Sun, X. & Jian, P. (2004). The Wilson cycle of the Jinshajiang Paleo-Tethys Ocean, in western Yunnan and Sichuan Provinces. *Geological Review* **50**, 343-350 (in Chinese with English abstract).

Sun, S.S. & McDonough, W.F. (1989). Chemical and isotopic systematics of oceanic basalts: implications for mantle composition and processes. In: Saunders, A.D. & Norry, M.J. (Eds.) *Magmatism in the ocean basins*. Geological Society of London, 313-345.

Sun, X., Wang, S., Sun, W., Shi, G., Sun, Y., Xiong, D., Qu, W. & Du, A. (2008). PGE geochemistry and Re–Os dating of massive sulphide ores from the Baimazhai Cu-Ni deposit, Yunnan province, China. *Lithos* **105**, 12-24.

Sutcliffe, R.H., Smith, A.R., Doherty, W. & Barnett, R.L. (1990). Mantle derivation of Archean amphibole-bearing granitoid and associated mafic rocks: evidence from the southern Superior Province, Canada. *Contributions to Mineralogy and Petrology* **105**, 255-274.

Tao, Y., Hu, R., Wang, X., Zhu, D., Song, X. & Feng, J. (2006). The Cu-Ni-PGE Mineralization in the Emeishan Large Igneous Province-Geochemical Study on Some Typical Deposits. *Bulletin of Mineralogy, Petrology and Geochemistry* **25**, 236-244 (in Chinese with English abstract).

Takazawa, E., Frey, F.A., Shimizu, N. & Obata, M. (2000). Whole rock compositional variations in an upper mantle peridotite (Horoman, Hokkaido, Japan): Are they consistent with a partial melting process? *Geochimica et Cosmochimica Acta* **64**, 695-716.

Tao, Y., Li, C., Hu, R., Ripley, E.M., Du, A. & Zhong, H. (2007): Petrogenesis of the Pt–Pd mineralized Jinbaoshan ultramafic intrusion in the Permian Emeishan Large Igneous Province, SW China. *Contributions to Mineralogy and Petrology* **153**, 321-337.

Tao, Y., Ma, Y., Miao, L. & Zhu, F. (2008). SHRIMP U-Pb zircon age of the Jinbaoshan ultramafic intrusion, Yunnan Province, SW China. *Chinese Science Bulletin* **54**, 168-172.

Tapponnier, P., Lacassin, R., Leloup, P.H., Schärer, U., Dalai, Z., Haiwei, W., Xiaohan, L., Shaocheng, J., Lianshang, Z. & Jiayou, Z. (1990). The Ailao Shan/Red River metamorphic belt: Tertiary left-lateral shear between Indochina and South China. *Nature* **343**, 431-437.

Thornton, C.P. & Tuttle, O.F. (1960). Chemistry of igneous rocks. I: Differentiation Index. *American Journal of Science* **258**, 664-684.

Tomlinson, K.Y., Stott, G.M., Percival, J.A. & Stone, D. (2004). Basement terrane correlations and crustal recycling in the western Superior Province: Nd isotopic character of granitoid and felsic volcanic rocks in the Wabigoon Subprovince, N. Ontario, Canada. *Precambrian Research* **132**, 245-274.

Trung, N.M., Tsujimori, T. & Itaya, T. (2006). Honvang serpentinite body of the Song Ma fault zone, Northern Vietnam: A remnant of oceanic lithosphere within the Indochina–South China suture. *Gondwana Research* **9**, 225-230.

Villemant, B., Jaffrezic, H., Joron, J.L. & Treuil, M. (1981). Distribution Coefficients of Major and Trace-Elements - Fractional Crystallization in the Alkali Basalt Series of Chaine-Des-Puys (Massif Central, France). *Geochimica et Cosmochimica Acta* **45**, 1997-2016.

Von Gruenewaldt, G., Hulbert, L.J. & Naldrett, A.J. (1989). Contrasting platinum-group element concentration patterns in cumulates of the Bushveld Complex. *Mineralium Deposita* **24**, 219-229.

Walker, R.J., Morgan, J.W., Horan, M.F., Czamanske, G.K., Krogstad, E.J., Han, B. & Kunilov, V.E. (1994). Re–Os isotopic evidence for an enriched mantle source for the Noril`sk type ore-bearing intrusion, Siberia. *Geochimica et Cosmochimica Acta* **58**, 4179-4197.

Walker, R.J., Morgan, J.W., Beary, E.S., Smoliar, M.I., Czamanske, G.K. & Horan, M.F. (1997). Applications of the ^{190}Pt–^{186}Os isotope system to geochemistry and cosmochemistry. *Geochimica et Cosmochimica Acta* **61**, 4799-4807.

Wallace, P. & Carmichael, I.S.E. (1992). Sulfur in basaltic magmas. *Geochimica et Cosmochimica Acta* **56**, 1683-1874.

Wang, C.Y., Prichard, H.M., Zhou, M.-F. & Fisher, P.C. (2008). Platinum-group minerals from the Jinbaoshan Pd-Pt deposit, SW China: evidence for magmatic origin and hydrothermal alteration. *Mineralium Deposita* **43**, 791-803.

Wang, C.Y. & Zhou, M.F. (2006). Genesis of the Permian Baimazhai magmatic Ni-Cu-(PGE) sulphide deposit, Yunnan, SW China. *Mineralium Deposita* **41**, 771-783.

Wang, C.Y., Zhou, M.F. & Keays, R.R. (2006). Geochemical constraints on the origin of the Permian Baimazhai mafic-ultramafic intrusion, SW China. *Contributions to Mineralogy and Petrology* **152**, 309-321.

Wang, C.Y., Zhou, M.F. & Qi, L. (2007). Permian flood basalts and mafic intrusions in the Jinping (SW China) - Song Da (Northern Vietnam) District: Mantle sources, crustal contamination and sulphide segregation. *Chemical Geology* **243**, 317-343.

Wang, C.Y., Zhou, M.F. & Zhao, D. (2005). Mineral chemistry of chromite from the Permian Jinbaoshan Pt-Pd-sulphide-bearing ultramafic intrusion in SW China with petrogenetic implications. *Lithos* **83**, 47-66.

Wang, Y., Li, X., Tuan, L., Huang, Z. & Chui, C. (2000a). *Geotectonics and Metallogeny in South Nujiang-Lanchang-Jincha Rivers Area*. Geology Press, Beijing (in Chinese with English abstract).

Wang, X., Metcalfe, I., Ping, J., He, L. & Wang, C. (2000b). The Jinshajiang suture zone: tectono-stratigraphic subdivision and revision of age. *Science in China* **43**, 10-22.

Wang, X., Metcalfe, I., Jian, P., He, L. & Wang, C. (2000c). The Jinshajiang-Ailaoshan Suture Zone, China: tectonostratigraphy, age and evolution. *Journal of Asian Earth Sciences* **18**, 675-690.

Wasserburg, G.J., Jacobsen, S.B., DePaolo, D.J., McCulloch, M.T. & Wen, T. (1981). Precise determination of Sm/Nd ratios, Sm and Nd isotopic abundances in standard solutions. *Geochimica et Cosmochimica Acta* **45**, 2311-2323.

Wedepohl, K.H. (1995). The composition of the continental crust. *Geochimica et Cosmochimica Acta* **59**, 1217-1232.

Weiblen, P.W. & Morey, G.B. (1980). A summary of the stratigraphy, petrology and structure of the Duluth Complex. *American Journal of Science* **280**, 88-133.

Wen, D.J., Chung, S.L., Lee, H.Y., Zhang, Y.Q., Xie, Y.W., Li, H.M., Lo, C.H., Lee, T.Y. & Wang, Y.H. (2001). Geochronology and geochemistry of the Lincang Granite Complex: Implications of the Indosinian Orogeny in Southeast Asia. In: Brown, D. (Ed.) EUG XI, Symposium MS02.

Willbold, M., Hegner, E., Stracke, A. & Rocholl, A. (2009). Continental geochemical signatures in dacites from Iceland and implications for models of early Archean crust formation. *Earth and Planetary Science Letters* **279**, 44-52.

Wilson, A. & Chunnett, G. (2006). Trace element and platinum group element distributions and the genesis of the Merensky Reef, Western Bushveld Complex, South Africa. *Journal of Petrology* **47**, 2369-2403.

Wilson, M. (1989). *Igneous Petrogenesis. A global tectonic approach*. Chapman and Hall, London.

Winchester, F.A. & Floyd, P.A. (1977). Geochemical discrimination of different magma series and their differentiation products using immobile elements. *Chemical Geology* **20**, 325-343.

Winter, J.D. (2001). *An introduction to Igneous and Metamorphic Petrology*. Prentice Hall, New Jersey.

Wood, D.A., Comin-Chiaramonti, P., Tarney, J., Joron, J.L., Fryer, P.B. & Treuil, M. (1980). Geochemistry of igneous rocks recovered from a transect across the Mariana trough arc, forearc and trench sites 453-461, DSDP LEG 60. *Initial report of the Deep Sea Drilling Project* **60**, 611-645.

Wooden, J.L., Czamanske, G.K., Fedorenko, A., Arndt, N.T., Chauvel, C., Bouse, R.M., King, B.S.W., Knight, R.J., & Siems, D.F. (1993). Isotopic and trace-element characterization of the Siberian continental flood basalts of the Noril'sk area. *Geochimica et Cosmochimica Acta* **57**, 3677-3704.

Wu, Y.B., Zheng, Y.F., Zhao, Z.F., Gong, B., Liu, X. & Wu, F.Y. (2006). U–Pb, Hf and O isotope evidence for two episodes of fluid-assisted zircon growth in marble-hosted eclogites from the Dabie orogen. *Geochimica et Cosmochimica Acta* **70**, 3743-3761.

Xiao, L., Chung, S.L., He, B. & Mei, H. (2003). Chemostratigraphic correlation of Upper Permian Lavas from Yunnan Province, China: Extent of the Emeishan Large Igneous Province. *International Geology Reviews* **45**, 753-766.

Xiao, L., He, Q., Pirajno, F., Ni, P., Du, J. & Wei, Q. (2008). Possible correlation between a mantle plume and the evolution of Paleo-Tethys Jinshajiang Ocean: Evidence from a volcanic rifted margin in the Xiaru-Tuoding area, Yunnan, SW China. *Lithos* **100**, 112-126.

Xiao, L., Xu, Y.G., Mei, H., Zheng, Y.F., He, B. & Pirajno, F. (2004). Distinct mantle sources for Low-Ti and High-Ti basalts from the western Emeishan Large Igneous Province, SW China: Implications for Plume-Lithosphere interaction. *Earth and Planetary Science Letters* **228**, 525-546.

Xu, J.F. & Castillo, P.R. (2004). Geochemical and Nd-Pb isotopic characteristics of the Tethyan asthenosphere: implications for the origin of the Indian mantle domain. *Tectonophysics* **393**, 9-27.

Xu, J.F., Suzuki, K., Xu, Y.G., Mei, H. & Li, J. (2007). Os, Pb and Nd isotope geochemistry of the Permian Emeishan Continental Flood Basalts: Insights into the source of a large igneous province. *Geochimica et Cosmochimica Acta* **71**, 2104-2119.

Xu, Y., Chung, S.L., Jahn, B.M. & Wu, G. (2001). Petrologic and geochemical constraints on the petrogenesis of Permian-Triassic Emeishan flood basalts in southwestern China. *Lithos* **58**, 145-168.

Yajima, T. (1970). The Sanogawa Gabbro-Diorite Complex. *Science reports of the Saitama University*. *Series B, biology and earth sciences* **5**, 199-230.

Yan, W., Wang, Z., Liu, S., Li, Q., Zhang, H., Wang, T., Liu, D., Shi, Y., Jian, P., Wang, J., Zhang, D. & Zhao, J. (2005). Opening of the Tethys in southwest China and its significance to the breakup of East Gondwanaland in late Paleozoic: Evindence from SHRIMP U-Pb zircon analysis for the Garzê ophiolite block. *Chinese Science Bulletin* **50**, 256-264.

Yao, Y. & Viljoen, M.J. (2003): Intrusion-hosted PGE mineralization in the Sichuan province, China. *Goldschmidt Conference Abstracts*, A560.

Yao, P.H., Wang, K.N., Du, C.L., Lin, Z.T. & Song, X. (1993). *Records of China`s iron ore deposits*. Metallurgic Industry Press, Beijing, 633-649 (in Chinese).

Yasui, M., Togashi, S., Shimomura, Y., Sakamoto, S., Miyaji, N. & Endo, K. (1998). Petrological features and origin of the gabbroic fragments contained in the 1707 pyroclastic fall deposits, Fuji volcano. *Bulletin of the Volcanological Society of Japan, Series 2*, **43**, 43-59.

YBGMR (Yunnan Bureau of Geology and Mineral Resources (1990). *Regional geology of Yunnan Province*. Geological Publishing House, Beijing.

Yoshida, H. & Takahashi, N. (1997). Chemical behaviour of major and trace elements in the Horoman mantle diapir, Hidaka Belt, Hokkaido, Japan. *Journal of the Japanese Association of Mineralogy, Petrology and Economic Geology* **92**, 391-409.

Yoshikawa, M. & Nakamura, E. (2000). Geochemical evolution of the Horoman Peridotite Complex: Implications for melt extraction, metasomatism and compositional layering in the mantle. *Journal of Geophysical Research* **B105**, 2879-2901.

Zack, T. & Brumm, R. (1998). Ilmenite/liquid partition coefficients of 26 trace elements determined through ilmenite/clinopyroxene partitioning in garnet pyroxene. In: Gurney, J.J., Gurney, J.L., Pascoe, M.D. & Richardson, S.H. (Eds.) *7th International Kimberlite Conference*. Red Roof Design, Cape Town, 986-988.

Zaw, K., Peters, S.G., Cromie, P., Burrett, C. & Hou, Z. (2007). Nature, diversity of deposit types and metallogenic relations of South China. *Ore Geology Reviews* **31**, 3-47.

Zhai, M., Cong, B. & Zhang, R. (1990). Distinguishing two volcanic rock series in the Lancang Group, Yunnan Province, SW China and its geological implication. *Science in China* **32**, 968-969.

Zhai, M., Cong, B. & Zhang, R. (1990). Sm–Nd and Rb–Sr geochronology of metamorphic rocks from SW Yunnan orogenic zones, China. *Acta Petrologica Sinica* **4**, 1-11 (in Chinese).

Zhang, C.J., Wang, Y.L., Li, X.L., Xiu, S.Z. & Huang, Y.J. (1999). Geochemistry of Platinum Group Elements in Mafic-Ultramafic Rocks of the Xinjie intrusion. *Chinese Journal of Geochemistry* **18**, 242-249.

Zhang, Q., Jian, P., Dunyi, L., Wang, Y., Qian, Q., Wang, Y. & Xue, H. (2003). SHRIMP dating of volcanic rocks from Ningwu area and its geological implications. *Science in China* **46**, 830-837.

Zhang, Q., Wang, C.Y., Liu, D., Jian, P., Wian, Q., Zhou, G. & Robinson, P.T. (2008a). A brief review of ophiolites in China. *Journal of Asian Earth Sciences* **32**, 308-324.

Zhang, R., Cong, B., Maruayama, S. & Liou, F.G. (1993). Metamorphism and tectonic evolution of the Lancang paired metamorphic belts, southwestern Yunnan. *Journal of Metamorphic Geology* **11**, 605-619.

Zhang, S.B., Zheng, Y.F., Wu, Y.B., Zhao, Z.F., Gao, S. & Wu, F.Y. (2006a). Zircon U–Pb age and Hf–O isotope evidence for Paleoproterozoic metamorphic event in South China. *Precambrian Research* **151**, 265-288.

Zhang, S.B., Zheng, Y.F., Wu, Y.B., Zhao, Z.F., Gao, S. & Wu, F.Y. (2006b). Zircon U–Pb age and Hf isotope evidence for 3.8 Ga crustal remnant and episodic reworking of Archean crust in South China. *Earth and Planetary Science Letters* **252**, 56-71.

Zhang, Z., Zhi, X., Chen, L., Saunders, A.D. & Reichow, M.K. (2008b). Re–Os isotopic compositions of picrites from the Emeishan Flood Basalt Province. *Earth and Planetary Science Letters* **276**, 30-39.

Zhang, Z., Mahoney, J.J., Mao, J. & Wang, F. (2006c). Geochemistry of picritic and associated basalt flows of the western Emeishan Flood Basalt Province, China. *Journal of Petrology* **47**, 1997-2019.

Zhao, D.S., Zhang, Q., Wang, M., Huang, Z.X., Han, S., Jian, X.Q. & Dong, J.Q. (1991). The geochemical features and tectonic setting of Paleng peridotite-diorite complex in Jinghong county, Yunnan. *Chinese Science Bulletin* **36**, 1974-1978.

Zhao, G., Sun, M., Wilde, S.A. & Li, S. (2004). A Paleo-Mesoproterozoic supercontinent: assembly, growth and breakup. *Earth-Science Reviews* **67**, 91-123.

Zhao, J., Zhong, D.L. & Wang, Y. (1994). Metamorphism of Lancang metamorphic belt, the western Yunnan and its relation to deformation. *Acta Petrologica Sinica* **10**, 27-40 (in Chinese with English abstract).

Zheng, J., Cao, Z., Song, X., An, W. & Liu, J. (2004). Platinum-group Elements Geochemistry of the Yangliuping Magmatic Ni-Cu-PGE Sulfide Deposit: Implications of Its Genetic Link with the Extrusive Basalts. *Journal of Ocean University of China* **3**, 93-98.

Zheng, J., Griffin, W.L., O´Reilly, S.Y., Zhang, M., Pearson, N. & Pan, Y. (2006a). Widespread Archean basement beneath the Yangtze craton. *Geology* **34**, 417-420.

Zheng, Y.F., Zhao, Z.F., Qu, Y.B., Zhang, S.B., Liu, X. & Wu, F.Y. (2006b). Zircon U–Pb age, Hf and O isotope constraints on protolith orogin of ultrahigh-pressure eclogite and gneiss in the Dabie orogen. *Chemical Geology* **231**, 135-158.

Zhong, D.L. (1998). *The Paleotethys orogenic belt in west of Sichuan and Yunnan*. Science Publishing House, Beijing.

Zhong, D.L. (2000). *Paleotethysides in west Yunnan and Sichuan*, China. Beijing Science Press, Beijing.

Zhong, H., Hu, R.Z., Wilson, A.H. & Zhu, W.G. (2005). Review of the Link between the Hongge Layered Intrusion and Emeishan Flood Basalts, Southwest China. *International Geology Review* **47**, 971-985.

Zhong, H., Yao, Y., Hu, S.F., Zhou, X.H., Liu, B.G., Sun, M., Zhou, M.F. & Viljoen, M.J. (2003). Trace-element and Sr-Nd isotopic geochemistry of the PGE-bearing Hongge layered intrusion, Southwestern China. *International Geology Review* **45**, 371-383.

Zhong, H., Yao, Y., Prevec, A., Wilson, A.H., Viljoen, M.J., Viljoen, R.P., Liu, B.G. & Luo, Y.N. (2004). Trace-element and Sr–Nd isotopic geochemistry of the PGE-bearing Xinjie layered intrusion in SW China. *Chemical Geology* **203**, 237-252.

Zhong, H., Zhou, X., Zhou, M.F., Sun, M. & Liu, B. (2002). Platinum-group element geochemistry of the Hongge Fe–V–Ti deposit in the Pan-Xi area, southwestern China. *Mineralium Deposita* **37**, 226-239.

Zhong, H. & Zhu, W.G. (2006). Geochronology of layered mafic intrusions from the Pan–Xi area in the Emeishan large igneous province, SW China. *Mineralium Deposita* **41**, 599-606.

Zhou, M.F., Malpas, J., Song, X.Y., Robinson, P.T., Sun, M., Kennedy, A.K., Lesher, C.M. & Keays, R.R. (2002). A temporal link between the Emeishan large igneous province (SW China) and the end-Guadalupian mass extinction. *Earth and Planetary Science Letters* **196**, 113-122.

Zhou, M.F., Robinson, P.T., Lesher, C.M., Keays, R.R., Zhang, C.J. & Malpas, J. (2005). Geochemistry, petrogenesis and metallogenesis of the Panzhihua gabbroic layered intrusion and associated Fe-Ti-V oxide deposits, Sichuan province, SW China. *Journal of Petrology* **46**, 2253-2280.

Zhou, M.F., Zhao, J.H., Qi, L., Su, W. & Hu, R. (2006). Zircon U–Pb geochronology and elemental and Sr–Nd isotope geochemistry of Permian mafic rocks in the Funing area, SW China. *Contributions to Mineralogy and Petrology* **51**, 1-19.

Zhou, M.F., Arndt, N.T., Malpas, J., Wang, C.Y. & Kennedy, A.K. (2008). Two magma series and associated ore deposit types in the Permian Emeishan large igneous province, SW China. *Lithos* **103**, 352-368.

Zhu, D., Luo, T., Xu, Y., Tao, Y. & Huang, Z. (2004). Soret fractionation - A novel process for origin of the PGE mineralization in the Zhubu mafic-ultramafic intrusion in SW China. *Bulletin of Mineralogy, Petrology and Geochemistry* **23**, 109-110 (in Chinese).

Zhu, W.G., Zhong, H., Hu, R.Z., Liu, B.G., He, D.F., Song, X.Y. & Deng, H.L. (2010). Platinum-group minerals and tellurides from the PGE-bearing Xinjie layered intrusion in the Emeishan Large Igneous Province, SW China. *Mineralogy and Petrology* **98**, 167-180.

Zi, J., Fan, W.M., Wang, Y., Peng, T. & Guo, F. (2008). Geochemistry and Petrogenesis of the Permian mafic dykes in the Panxi Region, SW China. *Gondwana Research* **14**, 368-382.

Zolotukhin, V.V. & Al`Mukhamedov, A.I. (1991). Basalts of the Siberian platform: occurrence, composition, and mechanism of formation. In: Polyakov, G.V. (Ed.) *Traps of Siberia and the Deccan: Signatures of Similarity and Diversity*. Nauka, Novosibirsk, 7-39 (in Russian).

INTERNET RESOURSES

http://www.actlabs.com.
http://www.asianminres.com.
http://www.chinamining.org.
http://georoc.mpch-mainz.gwdg.de/georoc/Entry.html.
http://www.jinshanmines.com.
http://www.lib.utexas.edu/maps/ams/china.
http://www.minerals.usgs. gov/minerals/pubs/commodity/platinum/mcs-2009-plati.pdf.
http://www.webmineral.com.

4 APPENDIX

4.1 ANALYTICAL TECHNIQUES

4.1.1 MAJOR AND TRACE ELEMENT DETERMINATIONS

116 rock powders from 2-kg bulk samples were analyzed for major and trace element concentrations by X-ray fluorescence (XRF) analysis on lithium metaborate fused discs at the Bundesanstalt für Geowissenschaften und Rohstoffe (BGR), Hannover, Germany. Relative uncertainties of the XRF analyses are calculated according to the method of Rousseau (2001), with ≤3% for major elements, and 10 to 30% for most trace elements.

Arsenic, Sb and Sc were measured by instrumental neutron activation (INA) analysis at Actlabs, Canada (Hoffmann, 1992). For INAA, a 1 g aliquot is encapsulated in a polyethylene vial and irradiated with flux wires and an internal standard (1 for 11 samples) at a thermal neutron flux of 7×10^{12} n cm^{-2} s^{-1}. After a 7-day decay, the samples are counted on a high purity Ge detector with resolution of better than 1.7 KeV for the 1332 KeV Co-60 photopeak. Using the flux wires, the decay-corrected activities are compared to a calibration developed from multiple certified international reference materials. The standard present is only a check on accuracy and is not used for calibration purposes. 10-30% of the samples are rechecked by re-measurement. One standard is run for every 11 samples. One blank is analyzed per work order (http://www.actlabs.com).

Cadmium, Te and Re were analyzed by “Total digestion-ICP” at Actlabs, Canada, where a 0.25 g sample is digested with four acids beginning with hydrofluoric, followed by a mixture of nitric and perchloric acids, heated using precise programmer controlled heating in several ramping and holding cycles which takes the samples to dryness. After dryness is attained, samples are brought back into solution using hydrochloric acid. With this digestion certain phases may be only partially solubilized. These phases include zircon, monazite, sphene, gahnite, chromite, cassiterite, rutile and barite. The samples were analyzed using a Varian Vista 735 ICP (http://www.actlabs.com).

Most other trace elements were measured by ICP-MS spectrometry at the Technical University of Clausthal. Sample digestion for ICP-MS was performed with a PicoTrace Pressure Digestion System which holds 16 Polytetrafluorethen (PTFE) vessels, i.e. 14 samples, one reference sample and a blank sample. Aliquots of 100 to 120 mg were weighed and wetted with deionized water and treated with 3 ml of cold concentrated

hydrofluoric acid (HF) for 24 hours. Three milliliters of concentrated nitric acid (HNO_3) were added and the vessels were heated to 180°C for 20 hours in the first pressure phase. The following acid-evaporation phase at 180°C lasted 4 hours. During the acid-evaporation phase only filtered air was used to remove the acid vapors. The soluble salts were dissolved in the second pressure step by 5 ml of concentrated hydrochloric acid (HCl) (20h at 180°C) and evaporized again (4h at 180°C). The final salt was dissolved in 1 ml concentrated HCl, 5 ml deionized water, 1 ml concentrated HCl and 10 ml deionized water, transferred to a degreased, 50 ml-large, narrow-necked volumetric flask, and diluted by hydrochloric acid of 0.5 molarity.

ICP-MS trace-element analysis at Technical University of Clausthal was performed with a Perkin-Elmer/Sciex ELAN 6000 instrument equipped with a Meinhardt-nebulizer. The ICP-MS calibration was based on six standard solutions in the range of minimum to maximum concentrations for the elements in question as previously determined by XRF at BGR Hannover, and by commercial ICP/ICP-MS and INA analysis at Actlabs/Canada. The analyte solutions of 5 ml were prepared to contain 2% HCl, an internal standard of 10 ppb Rh, In, Re and 100 ppb Be, and 1 ml of sample solution. The mean value of CeO^+/Ce^+ during the course of the analysis was 0.022. Background on mass 220 was 11 counts and 28900 counts were measured for 1 ppb Rh. The detection limit was determined according to the method of Rauscher *et al*. (2000). After careful data screening it was decided to use the V, Cr, Cu, Ni, Zn, Ga, Sr, Y, Zr and Ba concentrations of the XRF analysis. Low Y, Zr and Ba concentrations (<2 ppm Y, <10 ppm Zr and <20 ppm Ba) from XRF analysis were substituted by ICP-MS data.

4.1.2 U–Pb ZIRCON ICP-MS ANALYSIS

Zircon crystals from nine rock samples of 4 kg each were separated by magnetic techniques and purified by handpicking under a binocular microscope in Guangzhou, China. Only those idiomorphic zircon grains free of inclusions and cracks were selected for U–Pb dating in Copenhagen. The zircon grains were mounted in epoxy, polished, and coated with gold.

In addition, three samples were prepared for U–Pb zircon analysis as polished slab on which zircon location was done by EMPA. All zircon crystals were analyzed by in situ U–Pb zircon analysis at the Geological Survey of Denmark and Greenland in Copenhagen. The methodology essentially follows that described by Frei *et al*. (2006), Gerdes & Zeh (2006)

and Frei & Gerdes (2009). All analyses were carried out using a ThermoFinnigan Element2 single-collector double focusing magnetic sector ICP-MS coupled to a NewWave/Merchantek UP213 laser ablation system. The UP213 laser ablation system is equipped with a frequency quintupled ND-YAG laser emitting at a wavelength of 213 nm. The nominal pulse width of the laser is 5 ns with a pulse-to-pulse stability of 2% (2σ). The laser was operated at a repetition rate of 10 Hz and a nominal energy output of 45%, corresponding to a laser energy of ~0.025 mJ and a laser fluency of ~3.5 J cm^{-2}. During the 30 s ablation the laser ablated the zircon approximately 30 µm deep. Samples and standards were held in a teardrop-shaped low-volume ablation cell specially developed for U–Pb-dating (Horstwood *et al*., 2003). Helium was used to flush the sample cell and was mixed downstream with the Ar sample gas of the mass spectrometer. The washout time for this configuration is <10 s. All analyses were carried out using 1-inch round polished thick sections. The thick sections were cleaned before introduction into the sample cell to remove surface Pb contamination.

The total acquisition time for each isotopic analysis was 75 s with the first 30 s used to measure the gas blank, followed by 30 s ablation and 15 s sample cell flush out. The mass-spectrometer was tuned (using the GJ-1 zircon standard) to give maximum sensitivity for the ^{206}Pb and ^{238}U peaks at low background count rates (typically around 150 counts per second for ^{207}Pb) and low oxide production rates ($^{238}U^{16}O/^{238}U$ well below 1%). All measurements were performed in low-resolution mode using electrostatic scanning (E-scan) with the magnetic field resting at mass ^{202}Hg. The following masses were measured: ^{202}Hg, $^{204}(Pb + Hg)$, ^{206}Pb, ^{207}Pb, ^{208}Pb, ^{232}Th, ^{235}U and ^{238}U. All data were acquired on four samples per peak with a sampling and a settling time of 1 ms for each isotope. Mass ^{202}Hg was measured to monitor the ^{204}Hg interference on ^{204}Pb (using a $^{202}Hg/^{204}Hg$-ratio of 4.36). Because of the large uncertainties in ^{204}Pb determinations due to the Hg contamination of the carrier gas (Jackson *et al*., 2004) a correction for common lead is only applied if the net intensities for mass ^{204}Pb, corrected for ^{204}Hg, are significantly above the limit of detection (i.e.^{204}Pb >3 standard deviations of the background ^{204}Hg signal). The instrumental mass bias on measured isotopic ratios was corrected by matrix-matched external standardization using the GJ-1 zircon standard (Jackson *et al*., 2004), which was analyzed under exactly the same conditions as the samples. All analyses were carried out in sequences, where six standards are analyzed initially, followed by ten samples, followed by three standards.

The raw data were exported in ASCII format and processed offline using in-house developed data reduction spreadsheets that integrate corrections for laser-induced U–Pb fractionation and instrumental mass bias. All errors (2σ confidence level on ratios and ages) are propagated

by quadratic addition of the external reproducibility of the GJ-1 standard over the entire session and the within-run precision of each analysis (2σ). The calculation of concordia ages and plotting of concordia diagrams were performed using Isoplot/Ex 3.0 (Ludwig, 2003).

4.1.3 $^{40}Ar/^{39}Ar$ GEOCHRONOLOGY

Eight samples were analyzed by the $^{40}Ar–^{39}Ar$ stepped heating technique at the University of Manchester using a MS1 mass spectrometer. The rock samples were lightly crushed and sieved down to 100 µm. If single minerals were analyzed, they were hand-picked under a binocular microscope. The sample material was weighed and wrapped in Al foil and was vacuum encapsulated in quartz vials with the neutron fluence monitor Hb3gr (t = 1073.6 ±5.3 Ma; Jourdan *et al.*, 2006). Nuclear irradiation was carried-out in position B2W of the SAFARI-1 reactor at Pelindaba, South Africa, using a fast neutron flux of ~2 x 10^{18} n cm^2. The J values determined from Hb3gr are given in the Appedix data tables (2σ). The MS1 mass spectrometer at the University of Manchester is equipped with a Baur-Signer ion source. The irradiated samples were step-heated in a Ta-resistance furnace over the temperature interval of 400 to 1600°C, using 30 minutes heating steps. During heating, Ar was purified using a Zr-Al getter at 450°C. Raw isotopic data were corrected for mass discrimination using atmospheric argon measurements, radioactive decay and neutron interference corrections. Further experimental details are given in Burgess *et al.* (2004). $^{40}Ar/^{39}Ar$ ages were determined from degassing spectrum diagrams, using the ISOPLOT/Ex 3.0 software (Ludwig, 2003), and all data are reported at 2σ level of uncertainty.

4.1.4 $^{87}Sr/^{86}Sr$ AND $^{143}Nd/^{144}Nd$ ISOTOPE ANALYSIS

About 500 mg of sample powder for each of the 22 samples were washed with dilute nitric acid on a hot plate for 15 minutes. After drying the samples were weighed, spiked with ^{149}Sm-^{150}Nd and ^{87}Rb-^{84}Sr tracer solutions and decomposed in HF + HNO_3 + $HClO_4$ at 120°C for 2-5 days. Rb, Sr, Sm and Nd separation was done following the standard method of two stage ion-exchange and extraction chromatography (Richard *et al.*, 1976) with minor modifications according to Pin *et al.* (2003). Isotope abundance measurements were performed on a Triton (ThermoElectron) mass spectrometer equipped with nine collectors under static mode at CIR VSEGEI, St. Petersburg, Russia. The $^{143}Nd/^{144}Nd$ ratios are

normalized within-run to $^{146}Nd/^{144}Nd = 0.72190$ and adjusted to $^{143}Nd/^{144}Nd = 0.511860$ of the La Jolla standard. Sr isotope composition was normalized within-run to $^{88}Sr/^{86}Sr = 8.375209$. The value of SRM-987 during this work was $^{87}Sr/^{86}Sr = 0.710248 \pm 15$ (2σ, 6 measurements). Assigned errors (2σ) for $^{147}Sm/^{144}Nd$ and $^{143}Nd/^{144}Nd$ were ±0.3 % and ±0.000015, respectively, and for $^{87}Rb/^{86}Sr$ and $^{87}Sr/^{86}Sr$ ±0.5% and ±0.000025, respectively, according to results of multiple standard analyses (external reproducibility). The 2σ errors cited in the data tables for $^{143}Nd/^{144}Nd$ and $^{87}Sr/^{86}Sr$ are in-run precisions. The total procedure blanks were 0.01 ng for Sm, 0.02 ng for Nd, 0.01 ng for Rb and 0.1 ng for Sr. The data obtained for the international standard BCR-2 during this analytical work were $^{143}Nd/^{144}Nd = 0.512648 \pm 4$ (2 σ, 6 runs) and for JNdi-1 $^{143}Nd/^{144}Nd = 0.512106 \pm 5$ (2σ, 6 measurements).

4.1.5 PGE ELEMENT ANALYSIS BY CARIUS TUBE DIGESTION AND ID ICP-MS

In this study, PGEs and Au were measured by isotope dilution (ID) on a VG Plasma-Quad Excell ICP-MS in the Department of Earth Sciences, University of Hong Kong, China. Digestions were done with a modified Carius tube approach, which results in much lower blanks than the common Ni, (Pb) sulfide fire assay, combined with Te-coprecipitation and prevents Os-loss. For details on instrumentation, reagents, labware and analytical techniques see Qi *et al*. (2004, 2007).

Twelve grams of rock powder and the appropriate amount of enriched isotope spike solution containing ^{190}Os, ^{193}Ir, ^{101}Ru, ^{194}Pt and ^{105}Pd were digested with 35 ml aqua regia (15 ml of 10 M HCl and 20 ml of 16 M HNO_3) in a 75 ml Carius tube, which was sealed similar to the procedure described by Shirey & Walker (1995). The Carius tube was placed in a water-filled custom-made high-pressure autoclave. This autoclave holds the same pressure (external) as the Carius tube (internal) to prevent explosion of the tube when heated to 330°C. This modified technique allows a greater volume of aqua regia (2/3 of the Carius tube volume) and a larger sample mass in comparison to the normal Carius tube technique (Meisel & Moser, 2004).

After 10 hours of heating the Carius tube was slowly cooled in air to room temperature and finally in a refrigerator for about 2 hours. Afterwards it was opened and the contents were transferred to a 50 ml centrifuge tube. After the centrifuging process (2200 rpm; 6 minutes),

the upper solution was transferred to a custom-made distillation system for Os. The acid steam (112°C) was cooled and the OsO_4 vapor was trapped with 5 ml of 5% HCl solution. About 95% of the Os was recovered after a 90 minutes lasting distillation and the Os concentration of the solution was measured by ID-ICP-MS.

After the distillation the residual solution with PGEs in the distillation flask was transferred to a 125 ml Savillex Teflon beaker and evaporated to dryness. Six ml of concentrated HCl were added and the solution was evaporated again. The procedure was repeated with HNO_3 and the residue was dissolved with 50 ml of 3 N HCl and became centrifuged (2200 rpm, 6 min). About 10 ml of the solution were used to separate Re from the matrix by an AG 1-X8 exchange resin. The remaining aliquot of 40 ml was used to preconcentrate PGEs by Te-coprecipitation and was filtered through a Millipore membrane filter (type-HA, 0.45 µm; Qi *et al*., 2004).

The membranes were leached by 3 ml aqua regia, which then was evaporated to near-dryness on a hot plate before dissolution in HCl and HNO_3 and were passaged through a mixed ion exchange column with a Dowex 50 WX 8 cation exchange resin and a P507 extraction chromatograph resin to remove the main interfering elements Cu, Ni, Zr and Hf. The elution solution was evaporated to about 3-5 ml on a hot plate and finally analyzed. $^{195}Pt/^{194}Pt$, $^{106}Pt/^{105}Pt$, $^{99}Ru/^{101}Ru$ and $^{191}Ir/^{193}Ir$ ratios were measured by ID ICP-MS and ^{194}Pt served as internal standard to calculate the mono-isotope Rh (Qi *et al*., 2004). The mass bias was corrected with linear interpolation of the measured ratio of ~10 ng/ml natural Pt, Pd, Ru and Ir standard solution.

Background counts for 2% HNO_3 solutions were <20 cps for all PGEs. Relative standard deviations of 10 ppb PGE standard solution are typically less than 3% of raw counts. The sensitivity of the instrument was adjusted to more than 50,000 cps for 1 ng/ml of ^{115}In, in order to achieve the desired detection limits.

The total procedural blanks were lower than 0.002 ng/g for Os, 0.003 ng/g for Re, Ru, Rh and Ir, 0.020 ng/g for Pd, and 0.011 ng/g for Pt. The detection limit (ng/g) was calculated as three times the standard deviation of five individual procedural reagent blanks (ng), divided by the sample weight of 12 grams. The detection limits are 0.0002 ng/g for Os, 0.001 ng/g for Ir, Ru and Rh, 0.009 ng/g for Pt and 0.015 ng/g for Pd.

The analytical results for standard reference materials UMT-1 (ultramafic mine tailing; CANMET) and WPR-1 (peridotite) are shown on Appendix Table 15. The PGE data for UMT-1 are close to the certified values of CANMET and often represent the best fit of all

measured reference data published (e.g. for Ru, Pd, Pt and Os). The Au concentrations, however, are rather high in comparison to the certified data and to published measurements on the reference material. For WPR-1, the Ru, Rh and Os data are in good agreement, our Pd and Pt data appear to be too high, and Ir and Os appear to be too low in comparison to the data of Govindaraju (1994) and Qi & Zhou (2008). However, there is only little data available on WPR-1 reference material.

4.1.6 Pt, Pd AND Au ANALYSIS BY Pb FIRE ASSAY AND ICP-MS

In addition to the PGE Carius tube ID ICP-MS analysis Pt, Pd and Au were analyzed by conventional fire assay and ICP-MS analysis at Actlabs, Canada. The ordered package "1C-Research" is based on oxidative Pb collection.

A sample aliquot of 30 g powder is weighed, mixed with fire assay fluxes (borax, soda ash, silica), litharge (PbO) for oxidation and sodium carbonate for de-sulfurization and transferred to a crucible. The mixture is fused in an assay furnace at 1050°C for 1 hour. The crucibles are removed from the assay furnace and the molten slag (lighter material) is poured into a mould, leaving a lead button at the base. When cooled, the lead button is placed in a cupel at 820-880°C to absorb the lead, leaving a tiny metal bead of Ag (doré bead) which contains the Au, Pt and Pd. The Ag doré bead is digested in hot aqua regia (95°C). After cooling for 2 hours the sample solution is analyzed for Au, Pt, Pd with a Perkin Elmer Sciex ELAN 6100 or 9000 ICP-MS. On a 30 g sample the detection limits given by Actlabs are 0.1 ppb for Pt and Pd and 1 ppb for Au. Accuracies are given in Appendix Table 15.

4.2 ABBREVIATIONS FOR ROCK-FORMING MINERALS

Act	actinolite
Ap	apatite
Aug	augite
Bt	biotite
Carb	carbonate
Cal	calcite
Ccp	chalcopyrite
Cpx	clinopyroxene
Chl	chlorite
Di	diopside
Dol	dolomite
En	enstatite
Ep	epidote
Hbl	hornblende
Hem	hematite
Ilm	ilmenite
Kfs	K-feldspar
Kln	kaolinite
Lz	lizardite
Mag	magnetite
Mc	microcline
Ol	olivine
Or	orthoclase
Opc	opaques (undiff.)
Opx	orthopyroxene
Pl	plagioclase
Po	pyrrhotite
Prh	prehnite
Py	pyrite
Qtz	quartz
Rt	rutile
Sa	sanidine
Srp	serpentine

Ser	sericite
Tur	tourmaline
Zrn	zircon

4.3 GLOSSARY OF TERMS

Basiophitic	The ophitic rock has a mesostasis composed of augite.
Ophitic	Adjective for a texture, or a rock with such a texture, characterized by plagioclase crystals wholly or partly enclosed by augite.
Poikilitic	Adjective for a texture in igneous rocks in which small crystals are irregularly scattered without common orientation in a larger crystal of another mineral.
Porphyrogranulitc	Large phenocrysts of feldspar and augite or olivine in a groundmass of smaller lath-shaped fledspar crystals and irregular augite grains.
Subophitic	Plagioclase and augite are of about equal size, resulting in incomplete enclosure of plagioclase.
Trachyophitic	The enclosed feldspars have a parallel orientation.
Trachytic	Adjective for a texture characteristic of trachytes. The groundmass is commonly holocrystalline or with a small amount of glassy residue. It consists essentially of lath-shaped feldspar microlites with some degree of parallel disposition in consequence of flow.

4.4 DATA TABLES

Table A1: Sample documentation of the Nanlianshan and Banpo complexes.

Paleng	Rock type	Latitude	Longitude	Altitude	Pts	Ps	XRF	ICP-MS	ICP	INAA	PGE (1)	PGE (2)	Sr-Nd	Ar-Ar age	K-Ar age	U-Pb age
JI-20	basaltic andesite	21°38'05.2"	100°37'13.1"	743	x		x	x	x	x	x		x			
JI-21	basaltic andesite	21°38'05.2"	100°37'13.1"	743	x		x	x	x	x	x					
JI-22	basaltic andesite	21°38'05.2"	100°37'13.1"	743	x		x	x	x	x	x					
JI-30	Plg cumulate	21°39'53.6"	100°37'47.1"	803	x		x	x	x	x	x					
JI-23	Plg-amph cumulate	21°38'05.2"	100°37'13.1"	743	x		x	x	x	x		x				
JI-32	Plg-amph cumulate	21°39'53.6"	100°37'47.1"	803	x		x	x	x	x		x				x
JI-24	Plg-amph cumulate	21°38'05.2"	100°37'13.1"	743	x		x	x	x	x	x					
JI-33	amph-plg cumulate	21°39'53.6"	100°37'47.1"	803	x		x	x	x	x	x			x		
JI-27	amph-plg cumualte	21°40'15.0"	100°38'35.3"	758	x		x	x	x	x	x		x	x		
JI-28	amph-plg cumulate	21°40'02.3"	100°38'14.0"	795	x		x	x	x	x	x					
JI-29	amph-plg cumulate	21°39'59.4"	100°38'04.3"	788	x		x	x	x	x		x				
JI-31	amphibole-cumulate	21°39'53.6"	100°37'47.1"	803	x		x	x	x	x		x	x	x		
JI-25	gabbro	21°38'17.0"	100°37'13.2"	755	x		x	x	x	x		x				x
JI-26	porphyritic basalt	21°38'17.0"	100°37'13.2"	755	x		x	x	x	x	x		x			x
Jingh. dacite	**Rock type**	**Latitude**	**Longitude**	**Altitude**	**Pts**	**Ps**	**XRF**	**ICP-MS**	**ICP**	**INAA**	**PGE (1)**	**PGE (2)**	**Sr-Nd**	**Ar-Ar age**	**K-Ar age**	**U-Pb age**
JI-9	dacite	21°48'56.7"	100°51'57.4"	---	x		x	x	x	x						
JI-10	dacite	21°49'00.6"	100°51'51.9"	---	x		x	x	x	x						
JI-48	tourmalinized dacite	21°55'57.4"	100°55'22.3"	763	x		x	x	x	x						
JI-49	tourmalinized dacite	21°55'57.4"	100°55'22.3"	763	x		x	x	x	x			x			x
Jingh. trachy.	**Rock type**	**Latitude**	**Longitude**	**Altitude**	**Pts**	**Ps**	**XRF**	**ICP-MS**	**ICP**	**INAA**	**PGE (1)**	**PGE (2)**	**Sr-Nd**	**Ar-Ar age**	**K-Ar age**	**U-Pb age**
JI-12	trachyandesite	21°45'05.0"	100°54'47.5"	739	x		x	x	x	x						
JI-13	trachyandesite	21°45'05.0"	100°54'47.5"	739	x		x	x	x	x	x				x	
JI-16	trachyandesite	21°44'47.0"	100°54'46.0"	---	x		x	x	x	x			x			
JI-14	trachyandesite	21°45'05.0"	100°54'47.5"	739	x		x	x	x	x						
JI-17	trachyandesite	21°45'34.7"	100°54'44.9"	649	x		x	x	x	x						
JI-18	trachyandesite	21°45'34.7"	100°54'44.9"	649	x		x	x	x	x						
JI-51	basaltic andesite	21°56'17.0"	100°55'35.2"	724	x		x	x	x	x						
JI-54	andesite	21°55'35.4"	100°56'06.8"	589	x		x	x	x	x						
Lincang gra.	**Rock type**	**Latitude**	**Longitude**	**Altitude**	**Pts**	**Ps**	**XRF**	**ICP-MS**	**ICP**	**INAA**	**PGE (1)**	**PGE (2)**	**Sr-Nd**	**Ar-Ar age**	**K-Ar age**	**U-Pb age**
LI-2	granite	23°32'08.4"	100°07'26.0"	1289	x		x	x	x	x						
LI-3	granite	24°15'36.7"	100°03'01.1"	1443	x		x	x	x	x						
LI-4	granite	24°17'22.1"	100°04'41.3"	1578	x		x	x	x	x						
LI-5	granite	24°42'31.5"	100°16'06.7"	1774	x		x	x	x	x						x
LI-7	granite	24°42'31.5"	100°16'06.7"	1774	x		x	x	x	x						
LI-6	aplite	24°42'31.5"	100°16'06.7"	1774	x		x	x	x	x						
Jingh. basalt	**Rock type**	**Latitude**	**Longitude**	**Altitude**	**Pts**	**Ps**	**XRF**	**ICP-MS**	**ICP**	**INAA**	**PGE (1)**	**PGE (2)**	**Sr-Nd**	**Ar-Ar age**	**K-Ar age**	**U-Pb age**
JI-50	basalt	21°56'24.9"	100°55'38.1"	733	x		x	x	x	x			x	x		
JI-52	basalt	21°54'36.4"	100°56'05.9"	611	x		x	x	x	x	x					x
JI-53	basalt	21°54'37.5"	100°56'19.5"	593	x		x	x	x	x						
JI-55	basalt	21°57'03.9"	100°58'36.6"	662	x		x	x	x	x						
JI-58	amygdaloidal basalt	22°02'12.3"	100°53'04.6"	767	x		x	x	x	x						

(Pts = polished thin section; Ps = polished section).

Table A2: Sample documentation of the Banpo complex, Jinghong granodiorite, Jinbaoshan gabbro/peridotite and the Binchuan rhyolite/basalt.

Banpo	Rock type	Latitude	Longitude	Altitude	Pts	Ps	XRF	ICP-MS	ICP	INAA	PGE (1)	PGE (2)	Sr-Nd	Ar-Ar age	K-Ar age	U-Pb age
BA-23	porphyritic rhyolite	23°09'38.6"	100°10'18.7"	1215	x		x	x	x	x			x	x		
BA-32	porphyritic rhyolite	23°12'49.2"	100°10'53.5"	1642	x		x	x	x	x						
BA-44	rhyolite	23°10'30.2"	100°09'52.8"	1178	x		x	x	x	x			x			
BA-10	porphyritic rhyolite	23°12'59.5"	100°11'09.8"	1586	x		x	x	x	x						
BA-25	porphyritic rhyolite	23°12'29.4"	100°10'53.7"	1466	x		x	x	x	x			x			
BA-30	rhyolite	23°13'16.2"	100°11'01.3"	1640	x		x	x	x	x			x			
BA-12	porphyritic rhyolite	23°13'17.8"	100°11'00.4"	1619	x		x	x	x	x				x		
BA-39	porphyritic rhyolite	23°10'53.7"	100°09'58.8"	1276	x		x	x	x	x						
BA-36	porphyritic rhyolite	23°12'32.0"	100°10'49.6"	1511	x		x	x	x	x						
BA-53	porphyritic rhyolite	23°09'48.1"	100°10'22.9"	1249	x		x	x	x	x			x			
BA-54	porphyritic rhyolite	23°09'48.0"	100°10'23.5"	1262	x		x	x	x	x						
BA-55	porphyritic rhyolite	23°10'10.0"	100°10'30.0"	1322	x		x	x	x	x						
BA-57	rhyolite	23°09'08.2"	100°11'23.2"	942	x		x	x	x	x						
BA-47	porphyritic rhyolite	23°08'49.6"	100°10'26.7"	1258	x		x	x	x	x						
BA-40	porphyritic rhyolite?	23°10'30.2"	100°10'00.5"	1273	x		x	x	x	x						
BA-52	calcsilicate	23°10'51.3"	100°10'32.1"	1486	x		x	x	x	x						
BA-35	calcsilicate with pyrite?	23°14'10.5"	100°10'44.8"	1555	x		x	x	x	x						
BA-33	rhyolite?	23°14'10.2"	100°10'45.3"	1555	x		x	x	x	x						
BA-34	rhyolite?	23°13'07.1"	100°08'53.6"	1572	x		x	x	x	x						
BA-50	granite?	23°09'02.7"	100°10'10.0"	1204	x		x	x	x	x						
BA-46	gabbro	23°08'34.8"	100°10'33.1"	1184	x	x	x	x	x	x						
BA-21	calcite vein	23°08'39.9"	100°10'22.2"	1090	x		x	x	x	x						
BA-17	?	23°08'37.6"	100°10'35.7"	1225	x		x	x	x	x						
Jinghong gr.	**Rock type**	**Latitude**	**Longitude**	**Altitude**	**Pts**	**Ps**	**XRF**	**ICP-MS**	**ICP**	**INAA**	**PGE (1)**	**PGE (2)**	**Sr-Nd**	**Ar-Ar age**	**K-Ar age**	**U-Pb age**
JI-7	granodiorite	21°55'14.0"	100°54'28.6"	634	x		x	x	x	x			x			x
JI-8	granodiorite	21°55'14.0"	100°54'28.6"	634	x		x	x	x	x						x
JI-56	granodiorite	21°55'14.0"	100°54'28.6"	634	x		x	x	x	x			x			x
JI-57	granodiorite	22°01'35.8"	100°52'12.8"	710	x		x	x	x	x						
Jinbaoshan	**Rock type**	**Latitude**	**Longitude**	**Altitude**	**Pts**	**Ps**	**XRF**	**ICP-MS**	**ICP**	**INAA**	**PGE (1)**	**PGE (2)**	**Sr-Nd**	**Ar-Ar age**	**K-Ar age**	**U-Pb age**
JBS-1	gabbro	25°00'33.2"	100°45'48.5"	1589	x		x	x	x	x						
JBS-2	peridotite	25°00'30.5"	100°45'58.0"	1471	x		x	x	x	x				x		
JBS-3	peridotite	25°00'30.5"	100°45'58.0"	1471	x		x	x	x	x						
JBS-4	peridotite	25°00'30.5"	100°45'58.0"	1471	x											
JBS-5	peridotite	25°00'30.5"	100°45'58.0"	1471	x											
JBS-6	peridotite	25°00'30.5"	100°45'58.0"	1471	x											
JBS-7	peridotite	25°00'30.5"	100°45'58.0"	1471	x											
Binchuan	**Rock type**	**Latitude**	**Longitude**	**Altitude**	**Pts**	**Ps**	**XRF**	**ICP-MS**	**ICP**	**INAA**	**PGE (1)**	**PGE (2)**	**Sr-Nd**	**Ar-Ar age**	**K-Ar age**	**U-Pb age**
BI-1	porphyritic rhyolite	25°54'22.5"	100°26'29.3"	1817	x		x	x	x	x						
BI-2	Emeishan basalt	25°54'13.8"	100°25'51.3"	1851	x		x	x	x	x						

Table A3: Sample documentation of the Paleng complex, Jinghong dacite, Lincang granite and Jinghong basalt.

Paleng	Rock type	Latitude	Longitude	Altitude	Pts	Ps	XRF	ICP-MS	ICP	INAA	PGE (1)	PGE (2)	Sr-Nd	Ar-Ar age	K-Ar age	U-Pb age
JI-20	basaltic andesite	21°38'05.2"	100°37'13.1"	743	x		x	x	x	x	x		x			
JI-21	basaltic andesite	21°38'05.2"	100°37'13.1"	743	x		x	x	x	x	x					
JI-22	basaltic andesite	21°38'05.2"	100°37'13.1"	743	x		x	x	x	x	x					
JI-30	Plg cumulate	21°39'53.6"	100°37'47.1"	803	x		x	x	x	x	x					
JI-23	Plg-amph cumulate	21°38'05.2"	100°37'13.1"	743	x		x	x	x	x		x				
JI-32	Plg-amph cumulate	21°39'53.6"	100°37'47.1"	803	x		x	x	x	x		x				x
JI-24	Plg-amph cumulate	21°38'05.2"	100°37'13.1"	743	x		x	x	x	x	x					
JI-33	amph-plg cumulate	21°39'53.6"	100°37'47.1"	803	x		x	x	x	x	x			x		
JI-27	amph-plg cumualte	21°40'15.0"	100°38'35.3"	758	x		x	x	x	x	x		x	x		
JI-28	amph-plg cumulate	21°40'02.3"	100°38'14.0"	795	x		x	x	x	x	x					
JI-29	amph-plg cumulate	21°39'59.4"	100°38'04.3"	788	x		x	x	x	x		x				
JI-31	amphibole-cumulate	21°39'53.6"	100°37'47.1"	803	x		x	x	x	x		x	x	x		
JI-25	gabbro	21°38'17.0"	100°37'13.2"	755	x		x	x	x	x		x				x
JI-26	porphyritic basalt	21°38'17.0"	100°37'13.2"	755	x		x	x	x	x	x		x			x
Jingh. dacite	**Rock type**	**Latitude**	**Longitude**	**Altitude**	**Pts**	**Ps**	**XRF**	**ICP-MS**	**ICP**	**INAA**	**PGE (1)**	**PGE (2)**	**Sr-Nd**	**Ar-Ar age**	**K-Ar age**	**U-Pb age**
JI-9	dacite	21°48'56.7"	100°51'57.4"		x		x	x	x	x						
JI-10	dacite	21°49'00.6"	100°51'51.9"		x		x	x	x	x						
JI-48	tourmalinized dacite	21°55'57.4"	100°55'22.3"	763	x		x	x	x	x						
JI-49	tourmalinized dacite	21°55'57.4"	100°55'22.3"	763	x		x	x	x	x			x			x
Jingh. trachy.	**Rock type**	**Latitude**	**Longitude**	**Altitude**	**Pts**	**Ps**	**XRF**	**ICP-MS**	**ICP**	**INAA**	**PGE (1)**	**PGE (2)**	**Sr-Nd**	**Ar-Ar age**	**K-Ar age**	**U-Pb age**
JI-12	trachyandesite	21°45'05.0"	100°54'47.5"	739	x		x	x	x	x						
JI-13	trachyandesite	21°45'05.0"	100°54'47.5"	739	x		x	x	x	x	x				x	
JI-16	trachyandesite	21°44'47.0"	100°54'46.0"	---	x		x	x	x	x			x			
JI-14	trachyandesite	21°45'05.0"	100°54'47.5"	739	x		x	x	x	x						
JI-17	trachyandesite	21°45'34.7"	100°54'44.9"	649	x		x	x	x	x						
JI-18	trachyandesite	21°45'34.7"	100°54'44.9"	649	x		x	x	x	x						
JI-51	basaltic andesite	21°56'17.0"	100°55'35.2"	724	x		x	x	x	x						
JI-54	andesite	21°55'35.4"	100°56'06.8"	589	x		x	x	x	x						
Lincang gra.	**Rock type**	**Latitude**	**Longitude**	**Altitude**	**Pts**	**Ps**	**XRF**	**ICP-MS**	**ICP**	**INAA**	**PGE (1)**	**PGE (2)**	**Sr-Nd**	**Ar-Ar age**	**K-Ar age**	**U-Pb age**
LI-2	granite	23°32'08.4"	100°07'26.0"	1289	x		x	x	x	x						
LI-3	granite	24°15'36.7"	100°03'01.1"	1443	x		x	x	x	x						
LI-4	granite	24°17'22.1"	100°04'41.3"	1578	x		x	x	x	x						
LI-5	granite	24°42'31.5"	100°16'06.7"	1774	x		x	x	x	x						x
LI-7	granite	24°42'31.5"	100°16'06.7"	1774	x		x	x	x	x						
LI-6	aplite	24°42'31.5"	100°16'06.7"	1774	x		x	x	x	x						
Jingh. basalt	**Rock type**	**Latitude**	**Longitude**	**Altitude**	**Pts**	**Ps**	**XRF**	**ICP-MS**	**ICP**	**INAA**	**PGE (1)**	**PGE (2)**	**Sr-Nd**	**Ar-Ar age**	**K-Ar age**	**U-Pb age**
JI-50	basalt	21°56'24.9"	100°55'38.1"	733	x		x	x	x	x			x	x		
JI-52	basalt	21°54'36.4"	100°56'05.9"	611	x		x	x	x	x	x					x
JI-53	basalt	21°54'37.5"	100°56'19.5"	593	x		x	x	x	x						
JI-55	basalt	21°57'03.9"	100°58'36.6"	662	x		x	x	x	x						
JI-58	amygdaloidal basalt	22°02'12.3"	100°53'04.6"	767	x		x	x	x	x						

Table A4: Tectonic data of the Banpo region.

Outcrop	Rock type	Latitude	Longitude	Altitude	Bedding data	Foliation data	Fault data	Fault striation data	Fold hinge data
C1	breccia	23.239750	100.179222	1533	285/60	105/90			
C3	sandstone	23.220667	100.194028	1736	40/30				
C3	sandstone	23.220667	100.194028	1736	130/30				
C5	andesite	23.210611	100.157000	1416	305/70				
C7	claystone	23.148639	100.164972	1125	350/25		255/50		325/20
C7	claystone	23.148639	100.164972	1125	40/50				00/25
C7	claystone	23.148639	100.164972	1125					00/30
C12	claystone	23.147417	100.168583	1246	25/40				340/25
C14	sandstone	23.183278	100.230750	1224	270/45	270/85			360/30
C14	sandstone	23.183278	100.230750	1224	225/45	225/85			330/25
C14	sandstone	23.183278	100.230750	1224	180/45	270/60			
C14	sandstone	23.183278	100.230750	1224		225/60			
C16	sandstone	23.162833	100.203528	1072	105/65	285/35			190/05
C17	sandstone	23.159528	100.197972	1003	100/65	340/50	320/40	210/35	20/00
C17	sandstone	23.159528	100.197972	1003	110/50		15/90	105/45	70/20
C17	sandstone	23.159528	100.197972	1003	30/90		25/70	105/40	
C17	sandstone	23.159528	100.197972	1003	20/90		15/70	90/45	
C17	sandstone	23.159528	100.197972	1003			320/65	85/50	
C17	sandstone	23.159528	100.197972	1003			340/50	40/35	
C17	sandstone	23.159528	100.197972	1003			20/90		
C20	sandstone	23.156833	100.195306	959	80/45				
C22	sandstone	23.163611	100.211833	1162	80/50	285/40			
G16	gabbro	23.175056	100.164667	1178			350/80	50/70	
G16	gabbro	23.175056	100.164667	1178			85/30	64/30	
G16	gabbro	23.175056	100.164667	1178			25/75	20/75	
G16	gabbro	23.175056	100.164667	1178			215/50	255/30	
G16	gabbro	23.175056	100.164667	1178			225/55	255/55	
G16	gabbro	23.175056	100.164667	1178				62/30	
G45	gabbro	23.221167	100.183694	1640			120/85	225/30	
P3	peridotite	23.143000	100.175861	1184	100/65				

Note: All planes are defined by dip-direction and dip, and all linears by plunge direction and plunge, respectively.

Table A5: Whole-rock data of the Nanlianshan basaltic andesite samples.

Rock type	Method	Unit	Nanlianshan basaltic andesite												
Sample			JI-1	JI-2	JI-3	JI-4	JI-5	JI-36	JI-37	JI-39	JI-41	JI-42	JI-43	JI-45	JI-47
SiO_2	XRF	wt%	53.38	52.36	48.80	52.70	52.16	48.81	52.33	51.53	57.68	48.87	51.83	49.82	49.90
TiO_2	XRF	wt%	1.168	0.939	0.963	1.365	1.697	2.489	1.132	1.961	1.459	0.876	1.698	2.085	1.546
Al_2O_3	XRF	wt%	15.55	16.96	16.15	15.82	17.28	12.06	15.50	15.20	14.75	18.50	14.70	16.80	16.12
Fe_2O_3(t)	XRF	wt%	9.15	10.17	11.97	10.57	10.33	13.54	9.93	12.53	9.49	10.73	12.47	11.23	12.01
MnO	XRF	wt%	0.232	0.175	0.247	0.181	0.170	0.239	0.197	0.219	0.164	0.190	0.160	0.184	0.210
MgO	XRF	wt%	6.04	4.27	6.95	4.17	4.00	6.10	6.32	4.46	3.60	5.22	4.65	3.84	4.53
CaO	XRF	wt%	5.81	6.94	7.43	7.48	5.21	9.69	6.22	5.96	4.65	7.80	6.77	6.94	7.47
Na_2O	XRF	wt%	5.14	5.19	3.49	3.96	5.43	2.69	4.74	4.69	5.03	3.68	4.72	5.13	4.65
K_2O	XRF	wt%	0.39	0.65	0.54	0.59	0.13	0.34	0.27	0.11	0.24	0.64	0.14	0.11	0.08
P_2O_5	XRF	wt%	0.227	0.104	0.172	0.282	0.322	0.268	0.175	0.348	0.275	0.179	0.296	0.685	0.228
(SO_3)	XRF	wt%	0.05	0.07	0.09	0.01	0.07	0.06	0.07	0.08	0.07	0.03	0.06	0.08	0.09
(Cl)	XRF	wt%	0.010	0.017	0.032	0.014	0.011	0.009	0.008	0.008	0.012	0.012	0.013	0.008	0.010
LOI		wt%	2.63	1.97	2.87	2.54	2.89	3.45	2.87	2.61	2.33	3.02	2.19	2.78	2.84
Sum		wt%	99.71	99.79	99.67	99.7	99.68	99.68	99.73	99.69	99.72	99.69	99.66	99.69	99.71
Li	ICPMS	ppm	9.9	5.9	21.0	11.2	6.6	15.0	15.2	5.8	4.1	8.1	2.8	8.8	10.4
Sc	INAA	ppm	41.1	41.2	38.5	34.3	40.3	47.4	40.2	40.6	36.5	40.7	43.8	32.8	36.8
V	XRF	ppm	255	201	260	311	287	408	282	393	272	281	424	262	338
Cr	XRF	ppm	88	<4	326	16	23	96	96	7	16	48	16	<4	5
Co	ICPMS	ppm	29.1	24.5	42.0	28.4	25.8	68.4	32.8	31.2	19.1	30.7	33.1	20.1	33.6
Ni	XRF	ppm	24	<3	78	11	7	49	33	6	7	19	13	<3	5
Cu	XRF	ppm	46	48	74	18	25	47	45	13	50	93	72	43	17
Zn	XRF	ppm	100	48	115	92	78	97	104	95	64	92	62	75	96
Ga	XRF	ppm	13	16	14	20	20	16	13	19	20	19	16	21	22
As	INAA	ppm	<0.5	4.4	<0.5	<0.5	<0.5	12.3	<0.5	<0.5	<0.5	<0.5	<0.5	4.7	<0.5
Rb	ICPMS	ppm	8.62	7.14	15.14	14.59	1.54	8.91	3.76	1.11	2.84	5.18	1.01	1.14	0.58
Sr	XRF	ppm	257	365	235	426	267	192	203	223	218	326	261	105	372
Y	XRF	ppm	25	20	20	28	40	61	27	30	39	18	28	48	29
Zr	XRF	ppm	97	42	78	108	176	184	77	115	152	16	110	186	111
Nb	ICPMS	ppm	4.4	1.7	0.7	5.4	8.7	5.2	3.4	5.4	7.5	1.1	5.1	10.6	6.0
Cd	TD-ICP	ppm	0.6	0.5	0.6	0.6	0.5	0.6	0.4	0.7	0.5	0.6	0.7	0.5	0.6
Sb	INAA	ppm	<0.1	<0.1	<0.1	0.8	1.3	3.3	<0.1	<0.1	<0.1	<0.1	<0.1	<0.1	<0.1
Te	TD-ICP	ppm	0.3	0.2	0.2	0.2	0.2	<0.1	<0.1	0.2	<0.1	0.3	0.2	0.4	0.2
Ba	XRF	ppm	162	123	87	185	68	47	93	49	102	150	91	30	28
La	ICPMS	ppm	11.7	5.1	1.1	14.2	15.6	7.3	7.6	11.0	15.4	3.4	10.5	23.2	12.0
Ce	ICPMS	ppm	27.0	12.9	2.9	32.5	37.3	22.7	18.1	27.1	36.4	8.2	26.4	54.8	27.2
Pr	ICPMS	ppm	3.63	1.81	0.49	4.24	5.03	3.68	2.48	3.65	4.79	1.23	3.64	6.98	3.41
Nd	ICPMS	ppm	16.0	8.6	2.8	19.4	22.9	19.2	11.4	17.1	21.7	6.2	16.4	30.6	15.4
Sm	ICPMS	ppm	3.90	2.38	1.01	4.67	5.73	6.28	2.92	4.33	5.33	1.90	4.18	7.23	3.84
Eu	ICPMS	ppm	1.08	0.97	0.45	1.53	1.52	1.93	0.93	1.40	1.61	0.78	1.37	2.10	1.16
Gd	ICPMS	ppm	3.80	2.84	1.27	5.12	5.62	7.49	3.20	4.69	5.61	2.14	4.47	7.68	4.08
Tb	ICPMS	ppm	0.655	0.527	0.255	0.787	0.974	1.46	0.557	0.792	0.942	0.391	0.752	1.25	0.675
Dy	ICPMS	ppm	4.06	3.52	1.70	4.95	6.45	9.88	3.48	5.13	6.00	2.67	4.85	7.79	4.55
Ho	ICPMS	ppm	0.842	0.754	0.352	1.05	1.36	2.12	0.730	1.05	1.27	0.579	1.05	1.64	0.933
Er	ICPMS	ppm	2.35	2.11	1.00	2.82	3.66	5.83	2.01	2.87	3.53	1.55	2.81	4.47	2.64
Tm	ICPMS	ppm	0.343	0.317	0.149	0.393	0.552	0.888	0.281	0.408	0.495	0.235	0.405	0.633	0.376
Yb	ICPMS	ppm	1.98	1.90	0.90	2.32	3.26	5.37	1.68	2.34	3.04	1.41	2.33	3.78	2.33
Lu	ICPMS	ppm	0.302	0.297	0.137	0.365	0.511	0.840	0.257	0.362	0.468	0.224	0.365	0.580	0.349
Ta	ICPMS	ppm	0.41	0.16	0.07	0.53	0.85	0.52	0.49	0.47	0.68	0.10	0.45	1.04	0.64
Re	TD-ICP	ppm	0.007	0.003	0.005	0.002	0.009	0.004	0.006	0.003	0.003	0.001	0.003	0.005	0.005
Pb	ICPMS	ppm	1.75	1.82	27.51	3.79	1.43	8.93	3.25	1.97	2.04	2.47	1.50	2.57	4.25
Th	ICPMS	ppm	1.23	0.11	0.02	2.39	2.44	0.48	0.99	1.32	2.32	0.06	1.06	4.66	3.00
U	ICPMS	ppm	0.35	0.02	0.02	0.73	0.86	0.16	0.34	0.42	0.76	0.02	0.37	1.60	1.12

Note: Br, Hg, Mo, Se and Sn and are below the analytical detection limits of <0.5 ppm Br, <1 ppm Hg, <1 ppm Mo, <3 ppm Se and <100 ppm Sn (all INAA data from Actlabs).

Table A6: Whole-rock data of the Nanlianshan microgabbro and the Banpo harzburgite samples.

Rock type	Method	Unit	Nanlianshan microgabbro					Banpo harzburgite							
Sample			JI-35	JI-38	JI-40	JI-44	JI-46	BA-1	BA-2	BA-3	BA-4	BA-16	BA-18	BA-20	BA-45
SiO_2	XRF	wt%	54.25	47.98	47.13	48.36	53.99	37.01	35.20	35.53	36.14	36.3	37.58	36.67	36.79
TiO_2	XRF	wt%	0.684	1.204	0.498	1.286	0.835	0.061	0.047	0.036	0.038	0.054	0.044	0.035	0.032
Al_2O_3	XRF	wt%	16.25	15.93	18.81	16.99	16.59	4.11	3.40	4.60	8.07	1.43	1.44	0.94	1.17
Fe_2O_3(t)	XRF	wt%	7.89	10.97	9.3	11.14	9.14	13.72	14.34	11.67	10.09	13.94	9.04	12.24	15.06
MnO	XRF	wt%	0.147	0.220	0.167	0.195	0.189	0.160	0.165	0.180	0.230	0.052	0.046	0.036	0.065
MgO	XRF	wt%	5.21	6.95	6.59	5.10	4.04	30.93	33.41	33.91	29.80	34.84	37.05	35.95	33.93
CaO	XRF	wt%	7.67	8.97	10.93	10.38	7.75	1.32	0.08	0.44	3.09	0.03	0.01	0.02	0.04
Na_2O	XRF	wt%	4.43	3.48	1.75	2.36	3.18	0.01	0.01	0.01	0.01	0.01	0.01	0.01	0.01
K_2O	XRF	wt%	0.60	0.37	0.79	0.06	1.41	0.03	0.03	0.03	0.03	0.01	0.01	0.01	0.02
P_2O_5	XRF	wt%	0.083	0.198	0.010	0.205	0.179	0.007	0.007	0.007	0.007	0.006	0.008	0.008	0.018
(SO_3)	XRF	wt%	0.02	0.06	0.04	0.08	0.01	0.01	0.03	0.19	0.09	0.03	0.01	0.01	0.02
(Cl)	XRF	wt%	0.013	0.016	0.015	0.012	0.031	0.008	0.013	0.010	0.007	0.017	0.024	0.022	0.016
LOI		wt%	2.54	3.37	3.84	3.53	2.43	12.01	12.79	12.94	11.99	12.52	13.87	13.29	11.95
Sum		wt%	99.74	99.67	99.82	99.63	99.72	99.23	99.34	99.40	99.45	99.03	98.97	99.04	98.91
Li	ICPMS	ppm	8.57	18.1	15.9	18.5	14.1	12.1	1.80	5.18	12.1	0.35	<0.30	<0.30	0.41
Sc	INAA	ppm	38.4	48.6	45.6	39.6	33.9	10.9	7.3	6.3	8.7	7.8	8.3	6.7	4.8
V	XRF	ppm	236	286	225	320	231	46	36	26	27	54	48	41	48
Cr	XRF	ppm	95	194	112	62	72	2958	2376	2267	1620	4631	5057	4618	4992
Co	ICPMS	ppm	21.9	42.5	40.5	31.8	24.7	118	118	129	85.4	115	113	109	140
Ni	XRF	ppm	23	72	33	19	25	1536	1334	1212	1230	1227	1300	1288	1888
Cu	XRF	ppm	26	48	70	30	137	22	4	9	53	13	<3	<3	<3
Zn	XRF	ppm	52	102	55	142	90	75	71	108	40	32	50	29	51
Ga	XRF	ppm	15	16	15	26	18	4	<2	3	2	<2	<2	3	3
As	INAA	ppm	<0.5	16.3	<0.5	<0.5	<0.5	<0.5	1.5	<0.5	<0.5	<0.5	<0.5	<0.5	1.0
Rb	ICPMS	ppm	13.75	13.99	18.24	0.46	20.04	1.83	1.44	1.25	1.63	0.47	1.32	0.46	0.94
Sr	XRF	ppm	187	319	349	813	211	4.78	3.95	17.7	19.0	2.39	1.38	1.17	< 2
Y	XRF	ppm	17	35	8	27	31	1.18	1.56	0.54	0.80	5.00	2.27	0.75	1.27
Zr	XRF	ppm	53	30	8.25	92	110	5.90	11.02	1.05	6.88	1.60	1.59	1.13	2.44
Nb	ICPMS	ppm	2.42	3.44	0.20	3.76	2.67	1.27	0.77	0.24	0.33	0.40	0.29	0.33	0.52
Cd	TD-ICP	ppm	0.3	0.6	0.5	0.5	0.5	0.50	0.80	0.60	0.30	0.50	0.50	0.40	n.d.
Sb	INAA	ppm	1.0	0.7	<0.1	1.0	0.9	<0.1	<0.1	<0.1	<0.1	2.3	<0.1	<0.1	<0.1
Te	TD-ICP	ppm	<0.1	<0.1	<0.1	0.5	<0.1	< 0.1	< 0.1	< 0.1	0.9	1.3	0.2	0.5	n.d.
Ba	XRF	ppm	149	106	107	30	420	7.02	17.0	13.7	21.8	8.82	9.19	9.82	6.35
La	ICPMS	ppm	7.70	5.76	0.94	7.14	6.88	0.32	0.61	0.45	0.53	0.49	0.78	0.35	0.60
Ce	ICPMS	ppm	13.06	15.32	2.38	18.25	16.83	0.74	1.36	0.85	0.91	1.82	2.80	1.14	1.84
Pr	ICPMS	ppm	1.85	2.32	0.37	2.63	2.35	0.09	0.16	0.09	0.11	0.31	0.45	0.16	0.24
Nd	ICPMS	ppm	7.96	11.53	2.09	12.57	11.21	0.49	0.64	0.38	0.51	1.50	2.17	0.75	1.13
Sm	ICPMS	ppm	1.96	3.30	0.76	3.32	3.08	0.14	0.18	0.09	0.12	0.34	0.50	0.17	0.26
Eu	ICPMS	ppm	0.71	1.08	0.39	1.19	0.93	0.08	0.07	0.05	0.07	0.09	0.15	0.06	0.08
Gd	ICPMS	ppm	2.32	3.63	0.98	3.60	3.42	0.17	0.21	0.08	0.13	0.32	0.49	0.18	0.23
Tb	ICPMS	ppm	0.389	0.683	0.193	0.600	0.600	0.035	0.033	0.013	0.023	0.045	0.073	0.027	0.040
Dy	ICPMS	ppm	2.51	4.26	1.38	4.00	3.95	0.21	0.22	0.09	0.16	0.26	0.46	0.16	0.24
Ho	ICPMS	ppm	0.542	0.885	0.297	0.853	0.858	0.042	0.045	0.022	0.031	0.050	0.085	0.028	0.051
Er	ICPMS	ppm	1.48	2.45	0.80	2.26	2.39	0.13	0.14	0.06	0.08	0.13	0.25	0.10	0.14
Tm	ICPMS	ppm	0.22	0.34	0.12	0.32	0.35	0.019	0.023	0.010	0.013	0.017	0.039	0.013	0.023
Yb	ICPMS	ppm	1.23	2.13	0.72	1.90	2.13	0.14	0.17	0.07	0.09	0.10	0.23	0.07	0.13
Lu	ICPMS	ppm	0.20	0.31	0.12	0.30	0.34	0.024	0.023	0.012	0.013	0.015	0.035	0.013	0.020
Ta	ICPMS	ppm	0.28	0.30	0.05	0.33	0.24	0.43	0.83	0.01	0.02	0.01	0.01	0.03	0.04
Re	TD-ICP	ppm	0.002	0.003	0.001	0.002	0.006	0.001	<0.001	0.001	0.002	0.003	0.001	<0.001	n.d.
Pb	ICPMS	ppm	4.32	4.87	2.65	2.94	5.42	2.55	1.97	5.86	5.88	4.46	3.94	4.12	1.12
Th	ICPMS	ppm	2.01	0.13	0.05	0.59	0.24	0.09	0.45	0.04	0.10	0.09	0.22	0.09	0.14
U	ICPMS	ppm	0.46	0.06	0.02	0.25	0.11	0.03	0.08	0.10	0.26	0.05	0.03	0.04	0.08

Table A7: Whole-rock data of the Banpo gabbro samples.

Rock type	Method	Unit	Banpo gabbro											
Sample			BA-8	BA-11	BA-13	BA-14	BA-24	BA-37	BA-38	BA-41	BA-42	BA-43	BA-48	BA-49
SiO_2	XRF	wt%	45.20	49.46	50.06	49.57	47.21	49.68	51.85	44.55	48.77	47.06	50.61	51.06
TiO_2	XRF	wt%	0.090	0.979	0.764	0.727	1.161	0.675	0.892	0.641	0.996	1.241	2.058	1.328
Al_2O_3	XRF	wt%	19.95	16.83	18.15	18.27	17.84	17.15	17.11	19.28	17.64	16.81	14.39	14.78
Fe_2O_3(t)	XRF	wt%	3.33	11.94	9.66	9.97	13.59	9.77	9.11	10.06	11.31	9.84	12.19	12.5
MnO	XRF	wt%	0.061	0.223	0.265	0.205	0.167	0.251	0.262	0.145	0.292	0.210	0.049	0.071
MgO	XRF	wt%	8.78	5.61	4.55	5.12	5.14	5.85	5.20	8.34	6.42	7.23	6.01	6.90
CaO	XRF	wt%	13.41	6.29	7.07	6.61	7.48	7.22	6.57	8.04	6.55	8.41	6.46	5.10
Na_2O	XRF	wt%	1.98	4.45	4.25	5.04	4.03	4.45	4.64	2.5	4.01	2.82	5.53	5.09
K_2O	XRF	wt%	0.69	0.92	1.81	0.25	0.56	0.53	0.69	0.55	0.70	0.36	0.22	0.45
P_2O_5	XRF	wt%	0.004	0.185	0.132	0.195	0.008	0.064	0.226	0.036	0.167	0.222	0.184	0.114
(SO_3)	XRF	wt%	0.05	0.06	0.08	0.05	0.09	0.04	0.08	0.41	0.02	0.18	0.01	0.01
(Cl)	XRF	wt%	0.009	0.020	0.019	0.021	0.016	0.029	0.024	0.025	0.024	0.020	0.067	0.043
LOI		wt%	6.19	2.76	2.88	3.76	2.47	4.10	3.06	5.13	2.89	5.34	1.97	2.33
Sum		wt%	99.74	99.67	99.67	99.75	99.69	99.76	99.73	99.65	99.72	99.73	99.70	99.77
Li	ICPMS	ppm	17.1	10.9	13.8	28.1	12.7	35.1	18.5	17.7	11.1	29.4	13.1	3.3
Sc	INAA	ppm	19.9	41.8	38.1	32.1	46.0	30.3	31.6	21.2	34.1	21.4	37.1	67.1
V	XRF	ppm	54	333	243	283	337	271	231	247	342	198	358	408
Cr	XRF	ppm	485	25	71	55	5	67	109	15	64	71	124	14
Co	ICPMS	ppm	25.1	32.1	26.8	27.1	36.6	34.9	28.1	79.5	39.5	46.0	44.0	30.1
Ni	XRF	ppm	153	17	24	18	4	25	23	130	30	80	37	19
Cu	XRF	ppm	71	37	75	53	53	83	66	705	6	54	12	8
Zn	XRF	ppm	16	104	96	100	58	127	115	64	139	114	11	24
Ga	XRF	ppm	9	14	19	16	15	16	16	16	15	16	13	16
As	INAA	ppm	<0.5	6.1	9.9	4.9	<0.5	<0.5	4.0	2.0	<0.5	7.0	6.0	<0.5
Rb	ICPMS	ppm	17.5	11.3	18.7	2.85	9.24	5.48	10.3	11.2	11.0	9.68	4.90	5.10
Sr	XRF	ppm	385	419	403	233	390	253	295	330	271	334	199	207
Y	XRF	ppm	2	19	22	12	7.56	11	19	14	21	27	31	24
Zr	XRF	ppm	10	16	21	15	5.69	16	34	21	56	118	125	61
Nb	ICPMS	ppm	0.24	0.80	0.88	0.55	0.23	0.50	2.50	2.05	2.63	5.42	2.90	3.64
Cd	TD-ICP	ppm	0.18	0.32	0.40	0.24	1.23	1.67	1.17	5.80	0.31	11.07	13.30	0.38
Sb	INAA	ppm	<0.3	0.6	0.6	0.5	0.7	n.d.	n.d.	n.d.	n.d.	n.d.	n.d.	n.d.
Te	TD-ICP	ppm	<0.1	<0.1	<0.1	<0.1	1.0	<0.1	<0.1	0.8	<0.1	1.4	<0.1	<0.1
Ba	XRF	ppm	93	202	367	80	108	145	195	181	195	174	48	97
La	ICPMS	ppm	0.61	2.64	3.73	2.43	0.70	1.50	4.83	3.01	5.54	7.72	6.17	3.47
Ce	ICPMS	ppm	1.38	6.44	8.56	5.94	1.82	3.59	12.17	7.43	14.32	20.73	17.98	10.06
Pr	ICPMS	ppm	0.18	1.01	1.31	0.87	0.32	0.54	1.78	1.05	2.15	2.97	2.83	1.60
Nd	ICPMS	ppm	0.95	5.29	6.56	4.39	1.94	3.03	8.80	4.94	10.45	13.56	14.06	8.20
Sm	ICPMS	ppm	0.29	1.67	2.04	1.35	0.80	1.02	2.60	1.42	2.88	3.37	4.14	2.39
Eu	ICPMS	ppm	0.17	0.67	0.90	0.53	0.41	0.48	0.89	0.45	0.97	1.13	1.68	0.89
Gd	ICPMS	ppm	0.38	2.28	2.61	1.72	1.06	1.27	2.89	1.59	3.18	3.54	4.58	2.60
Tb	ICPMS	ppm	0.061	0.385	0.452	0.303	0.228	0.236	0.502	0.316	0.553	0.603	0.858	0.481
Dy	ICPMS	ppm	0.42	2.48	2.93	1.88	1.55	1.66	3.39	2.01	3.66	3.79	5.49	3.29
Ho	ICPMS	ppm	0.086	0.536	0.678	0.405	0.326	0.349	0.690	0.434	0.751	0.773	1.140	0.722
Er	ICPMS	ppm	0.25	1.57	2.00	1.07	0.90	0.97	1.98	1.23	2.08	2.17	3.14	1.95
Tm	ICPMS	ppm	0.030	0.208	0.279	0.163	0.133	0.145	0.298	0.184	0.322	0.310	0.444	0.286
Yb	ICPMS	ppm	0.21	1.41	1.87	1.06	0.83	0.93	1.76	1.12	1.90	1.92	2.66	1.76
Lu	ICPMS	ppm	0.027	0.213	0.299	0.159	0.119	0.143	0.289	0.162	0.315	0.294	0.396	0.268
Ta	ICPMS	ppm	0.02	0.04	0.04	0.05	0.04	0.08	0.29	0.22	0.22	0.45	0.30	0.31
Re	TD-ICP	ppm	0.002	0.004	0.007	0.004	0.003	n.d.	n.d.	n.d.	n.d.	n.d.	n.d.	n.d.
Pb	ICPMS	ppm	2.45	3.85	73.84	2.84	2.72	5.55	2.96	1.99	2.03	11.61	1.59	1.40
Th	ICPMS	ppm	0.13	0.08	0.10	0.06	0.03	0.03	0.38	0.20	0.05	0.53	0.38	0.05
U	ICPMS	ppm	0.04	0.06	0.05	0.04	0.01	0.02	0.14	0.08	0.04	0.19	0.10	0.02

Table A8: Whole-rock data of the Banpo gabbro, hornblendite, anorthosite, and the Jinbaoshan gabbro and peridotite samples.

Rock type	Method	Unit	Banpo gabbro			Hornblendite	Anorthosite		Jinb. gabbro	Jinb. peridotite	
Sample			BA-51	BA-56	BA-58	BA-5	BA-6	BA-7	JBS-1	JBS-2	JBS-3
SiO_2	XRF	wt%	46.34	49.05	44.56	45.29	45.81	42.57	46.40	36.53	36.76
TiO_2	XRF	wt%	0.384	0.738	0.994	0.544	0.445	0.032	2.838	0.340	0.429
Al_2O_3	XRF	wt%	20.90	18.39	16.31	10.51	20.59	28.00	12.75	3.79	3.35
Fe_2O_3(t)	XRF	wt%	7.98	9.17	13.40	8.95	1.18	0.50	14.05	14.72	14.72
MnO	XRF	wt%	0.147	0.206	0.184	0.175	0.031	0.048	0.208	0.158	0.182
MgO	XRF	wt%	6.91	6.72	7.13	17.28	1.92	1.17	6.19	31.54	31.46
CaO	XRF	wt%	9.62	8.95	10.58	11.51	24.28	19.43	6.18	0.64	0.63
Na_2O	XRF	wt%	2.22	3.25	2.72	0.62	0.86	0.05	3.16	<0.01	<0.01
K_2O	XRF	wt%	1.55	0.33	0.39	0.18	0.04	2.40	0.18	0.21	0.18
P_2O_5	XRF	wt%	0.013	0.100	0.043	0.072	0.165	0.004	0.288	0.074	0.054
(SO_3)	XRF	wt%	0.06	0.03	0.12	0.01	0.01	0.01	0.12	0.03	0.03
(Cl)	XRF	wt%	0.021	0.023	0.024	0.037	0.009	0.008	0.014	0.010	0.009
LOI		wt%	3.66	2.87	3.34	4.38	4.54	5.60	7.21	10.93	11.17
Sum		wt%	99.79	99.80	99.73	99.53	99.87	99.78	99.54	98.82	98.83
Li	ICPMS	ppm	17.7	16.8	26.4	28.3	1.48	5.61	17.1	4.54	3.59
Sc	INAA	ppm	33.5	31.1	42.0	30.1	6.8	1.0	29.6	7.9	9.8
V	XRF	ppm	194	273	389	196	<5	<5	365	79	88
Cr	XRF	ppm	59	75	125	1617	<5	5	140	5592	5415
Co	ICPMS	ppm	44.5	34.1	42.5	47.6	6.62	2.25	48.5	128	150
Ni	XRF	ppm	49	30	46	486	54	15	94	1381	1374
Cu	XRF	ppm	129	102	138	71	3	6	235	<3	14
Zn	XRF	ppm	63	48	82	66	3	5	123	92	110
Ga	XRF	ppm	16	18	14	11	9	13	21	7	4
As	INAA	ppm	<0.5	<0.5	7.0	3.7	<0.5	21.7	<0.5	<0.5	<0.5
Rb	ICPMS	ppm	19.7	4.24	18.2	3.00	0.42	12.6	2.73	10.1	8.64
Sr	XRF	ppm	364	270	342	23	22	33	360	17	17
Y	XRF	ppm	9	18	15	10	7	0.44	31	4.29	5
Zr	XRF	ppm	18	20	18	44	249	6.50	161	41	42
Nb	ICPMS	ppm	0.31	1.36	0.39	1.12	3.29	0.23	17.82	4.46	3.91
Cd	TD-ICP	ppm	10.72	1.96	5.88	0.16	10.71	3.71	1.89	<0.3	0.40
Sb	INAA	ppm	n.d.	n.d.	n.d.	0.5	<0.3	<0.3	0.7	0.7	0.8
Te	TD-ICP	ppm	0.1	<0.1	0.4	<0.1	<0.1	<0.1	<0.1	<0.1	<0.1
Ba	XRF	ppm	224	101	60	12.9	10.9	674	368	56	42
La	ICPMS	ppm	0.69	2.84	1.25	4.41	3.70	0.49	10.33	6.77	6.51
Ce	ICPMS	ppm	1.95	6.88	3.46	9.66	7.27	1.01	26.60	14.12	14.27
Pr	ICPMS	ppm	0.35	1.04	0.61	1.39	0.82	0.13	3.78	1.61	1.74
Nd	ICPMS	ppm	2.10	5.40	3.40	6.63	3.31	0.51	18.59	6.26	7.25
Sm	ICPMS	ppm	0.85	1.70	1.20	1.81	0.77	0.12	5.25	1.21	1.55
Eu	ICPMS	ppm	0.34	0.67	0.52	0.59	0.31	0.14	1.58	0.35	0.47
Gd	ICPMS	ppm	1.07	1.92	1.49	2.16	0.86	0.11	5.59	1.12	1.47
Tb	ICPMS	ppm	0.218	0.356	0.287	0.347	0.143	0.015	0.946	0.154	0.216
Dy	ICPMS	ppm	1.51	2.40	1.98	2.17	0.93	0.10	5.95	0.93	1.24
Ho	ICPMS	ppm	0.329	0.519	0.424	0.455	0.196	0.021	1.11	0.165	0.238
Er	ICPMS	ppm	0.89	1.42	1.14	1.24	0.59	0.06	2.85	0.45	0.65
Tm	ICPMS	ppm	0.141	0.220	0.178	0.185	0.086	0.007	0.401	0.067	0.086
Yb	ICPMS	ppm	0.81	1.29	1.05	1.21	0.52	0.05	2.28	0.36	0.51
Lu	ICPMS	ppm	0.118	0.203	0.168	0.186	0.081	0.008	0.312	0.055	0.081
Ta	ICPMS	ppm	0.04	0.19	0.06	0.05	0.13	0.04	1.55	0.40	0.14
Re	TD-ICP	ppm	n.d.	n.d.	n.d.	0.002	0.002	0.001	0.002	0.001	0.003
Pb	ICPMS	ppm	1.94	2.26	2.09	3.84	3.86	3.72	4.90	2.77	2.38
Th	ICPMS	ppm	0.02	0.06	0.04	2.39	0.51	0.11	1.02	0.98	1.10
U	ICPMS	ppm	0.01	0.03	0.01	0.58	0.62	0.07	0.45	0.24	0.23

Table A9: Whole-rock data of the Banpo rhyolite samples.

Rock type	Method	Unit	Banpo rhyolite												
Sample			BA-10	BA-12	BA-23	BA-25	BA-30	BA-32	BA-36	BA-39	BA-44	BA-53	BA-54	BA-55	BA-57
SiO_2	XRF	wt%	74.99	73.80	73.58	74.70	74.53	77.34	71.81	74.39	79.71	74.77	74.46	74.20	73.80
TiO_2	XRF	wt%	0.038	0.039	0.042	0.040	0.044	0.169	0.045	0.041	0.068	0.042	0.041	0.044	0.055
Al_2O_3	XRF	wt%	15.41	14.57	15.43	15.68	15.66	13.07	16.79	15.06	11.59	15.42	15.33	15.45	15.43
Fe_2O_3(t)	XRF	wt%	0.07	1.04	0.76	0.04	0.05	0.90	0.40	0.46	0.63	0.15	0.75	0.77	0.68
MnO	XRF	wt%	0.001	0.009	0.008	0.001	0.004	0.006	0.004	0.003	0.012	0.002	0.008	0.007	0.010
MgO	XRF	wt%	0.02	0.26	0.17	0.01	0.01	0.09	0.10	0.05	0.07	0.05	0.16	0.17	0.19
CaO	XRF	wt%	0.11	0.38	0.37	0.07	0.13	0.35	0.13	0.49	0.93	0.18	0.18	0.22	0.35
Na_2O	XRF	wt%	8.67	4.94	4.07	8.81	8.84	5.99	7.66	6.48	5.49	8.40	3.67	3.54	4.32
K_2O	XRF	wt%	0.08	3.35	3.76	0.12	0.05	0.77	1.56	1.83	0.85	0.17	3.53	3.61	3.57
P_2O_5	XRF	wt%	0.001	0.035	0.010	0.001	0.008	0.014	0.009	0.009	0.019	0.013	0.012	0.009	0.034
SO_3	XRF	wt%	0.01	0.01	0.01	0.01	0.01	0.01	0.01	0.01	0.01	0.01	0.01	0.01	0.01
Cl	XRF	wt%	0.016	0.014	0.019	0.011	0.026	0.035	0.022	0.033	0.019	0.034	0.023	0.028	0.025
LOI		wt%	0.56	1.41	1.62	0.47	0.57	1.20	1.38	1.09	0.53	0.73	1.74	1.87	1.42
Sum		wt%	99.91	99.81	99.83	99.91	99.99	99.91	99.92	99.88	99.89	99.97	99.88	99.90	99.87
Li	ICPMS	ppm	7.04	7.50	12.1	3.90	9.99	3.51	4.06	1.27	0.61	2.71	7.44	6.34	5.33
Sc	INAA	ppm	1.6	1.8	2.0	1.6	1.1	3.3	1.8	1.3	1.2	1.4	1.7	1.7	1.9
V	XRF	ppm	<5	<5	<5	<5	<5	10	<5	<6	<6	<5	<6	<6	<6
Cr	XRF	ppm	<4	<4	<4	8	<4	<4	<4	<4	<4	<4	<4	<4	<4
Co	ICPMS	ppm	0.35	0.43	0.33	0.35	0.70	0.66	1.11	0.35	0.62	0.50	0.34	0.27	0.33
Ni	XRF	ppm	<2	<2	5	5	<2	<2	<2	<2	<2	<2	<2	<2	<2
Cu	XRF	ppm	13	4	<3	<3	6	35	5	6	6	4	6	12	6
Zn	XRF	ppm	9	14	19	16	15	16	16	16	15	16	13	16	16
Ga	XRF	ppm	16	16	19	18	25	12	16	15	10	11	17	19	19
As	INAA	ppm	<0.5	4.7	<0.5	<0.5	<0.5	2.0	<0.5	<0.5	3.0	<0.5	3.0	<0.5	1.0
Rb	ICPMS	ppm	1.24	38.9	1.55	2.96	0.75	24.4	21.9	41.2	8.37	5.39	133	144	134
Sr	XRF	ppm	56	173	243	44	68	63	70	194	134	116	112	135	177
Y	XRF	ppm	2.70	2.04	6	1.59	6	14	1.59	5	14	1.78	5	2.35	2.67
Zr	XRF	ppm	37	38	36	34	44	117	44	37	72	51	40	47	50
Nb	ICPMS	ppm	6.37	5.42	4.94	10.31	11.49	8.18	11.42	11.30	6.46	12.57	11.27	11.90	11.98
Cs	ICPMS	ppm	0.12	1.17	13.38	0.16	0.04	0.18	0.28	0.65	0.07	0.40	7.23	9.50	8.76
Cd	INAA	ppm	<0.3	<0.3	<0.3	<0.3	n.d.	n.d.	n.d.	n.d.	n.d.	n.d.	n.d.	n.d.	n.d.
Sb	TD-ICP	ppm	<0.1	<0.1	0.6	<0.1	<0.1	0.3	<0.1	0.4	1.4	<0.1	0.5	0.5	0.4
Te	ICPMS	ppm	<0.1	<0.1	<0.1	<0.1	n.d.	n.d.	n.d.	n.d.	n.d.	n.d.	n.d.	n.d.	n.d.
Ba	XRF	ppm	16.92	594	559	18.80	16.60	90	212	274	178	21.37	444	450	501
La	ICPMS	ppm	0.69	4.25	9.05	0.58	0.20	5.10	4.92	3.30	10.40	2.24	6.49	4.71	7.22
Ce	ICPMS	ppm	1.51	6.94	8.10	1.18	0.60	6.52	10.62	5.91	21.60	6.12	10.17	7.09	12.58
Pr	ICPMS	ppm	0.17	0.97	2.01	0.15	0.07	1.43	1.07	0.69	2.44	0.52	1.42	0.99	1.55
Nd	ICPMS	ppm	0.73	3.29	7.82	0.60	0.40	5.24	3.90	2.65	8.73	1.89	5.19	3.62	5.86
Sm	ICPMS	ppm	0.27	0.75	2.12	0.22	0.25	1.03	0.83	0.73	1.76	0.43	1.32	0.88	1.25
Eu	ICPMS	ppm	0.12	0.23	0.77	0.08	0.10	0.19	0.22	0.31	0.29	0.13	0.40	0.29	0.36
Gd	ICPMS	ppm	0.36	0.63	1.90	0.26	0.33	0.93	0.58	0.66	1.65	0.36	1.09	0.71	0.98
Tb	ICPMS	ppm	0.064	0.095	0.254	0.053	0.054	0.189	0.070	0.087	0.284	0.059	0.150	0.094	0.123
Dy	ICPMS	ppm	0.40	0.46	1.17	0.31	0.31	1.44	0.36	0.44	1.84	0.33	0.75	0.49	0.61
Ho	ICPMS	ppm	0.080	0.075	0.170	0.055	0.062	0.334	0.053	0.070	0.407	0.056	0.115	0.074	0.090
Er	ICPMS	ppm	0.22	0.20	0.39	0.14	0.14	1.07	0.15	0.18	1.18	0.15	0.25	0.19	0.23
Tm	ICPMS	ppm	0.029	0.023	0.043	0.022	0.020	0.188	0.022	0.024	0.202	0.021	0.031	0.022	0.026
Yb	ICPMS	ppm	0.19	0.15	0.25	0.11	0.12	1.31	0.12	0.14	1.38	0.12	0.19	0.14	0.18
Lu	ICPMS	ppm	0.025	0.022	0.032	0.019	0.019	0.217	0.018	0.022	0.217	0.017	0.024	0.018	0.023
Ta	ICPMS	ppm	0.24	0.42	0.13	1.68	1.72	1.15	1.62	1.60	0.75	1.87	1.73	1.76	1.81
Re	TD-ICP	ppm	0.001	0.002	0.003	<0.001	n.d.	n.d.	n.d.	n.d.	n.d.	n.d.	n.d.	n.d.	n.d.
Pb	ICPMS	ppm	5.99	4.52	23.1	2.70	2.20	3.05	4.17	4.18	2.46	1.28	13.5	13.2	9.95
Th	ICPMS	ppm	3.76	1.42	4.03	2.37	1.95	10.97	2.14	1.88	0.88	1.30	2.10	2.44	2.91
U	ICPMS	ppm	3.17	3.40	3.97	2.32	3.60	3.20	2.17	2.94	0.44	3.61	2.16	2.22	2.84

Table A10: Whole-rock data of the Jinghong granodiorite, the Paleng basaltic andesite, the Paleng porphyritic basalt and the Emeishan basalt reference samples.

Rock type	Method	Unit	Jinghong granodiorite				Paleng bas. andesite			Porph. basalt	Emeishan basalt
Sample			JI-7	JI-8	JI-56	JI-57	JI-20	JI-21	JI-22	JI-26	BI-2
SiO_2	XRF	wt%	69.06	67.40	69.18	65.88	57.35	53.81	51.70	50.33	46.60
TiO_2	XRF	wt%	0.406	0.407	0.386	0.387	0.758	0.561	0.595	2.624	3.030
Al_2O_3	XRF	wt%	14.06	14.41	14.27	17.01	17.00	15.61	18.90	15.80	13.92
$Fe_2O_3(t)$	XRF	wt%	3.56	3.66	3.28	3.61	8.81	9.53	7.86	11.90	15.26
MnO	XRF	wt%	0.060	0.066	0.052	0.061	0.164	0.180	0.162	0.222	0.218
MgO	XRF	wt%	1.12	1.19	1.08	1.20	3.02	6.06	5.80	4.92	4.99
CaO	XRF	wt%	1.89	2.58	1.91	2.68	7.89	8.68	9.41	9.70	10.78
Na_2O	XRF	wt%	4.82	4.60	4.93	5.45	3.13	3.21	2.94	0.67	2.05
K_2O	XRF	wt%	1.85	1.55	2.02	1.27	0.37	0.46	0.51	0.88	0.60
P_2O_5	XRF	wt%	0.075	0.074	0.071	0.078	0.112	0.064	0.138	0.454	0.369
(SO_3)	XRF	wt%	0.09	0.32	0.09	0.06	0.01	<0.01	0.01	0.07	<0.01
(Cl)	XRF	wt%	0.041	0.041	0.008	0.009	0.02	0.014	0.009	0.014	0.009
LOI		wt%	2.81	3.54	2.53	2.13	1.17	1.58	1.69	2.00	1.78
Sum		wt%	99.84	99.78	99.78	99.78	99.75	99.75	99.73	99.57	99.52
Li	ICPMS	ppm	16.3	21.1	15.2	20.7	6.45	9.56	12.4	14.3	17.5
Sc	INAA	ppm	8.9	9.3	9.0	8.8	30.1	43.9	23.0	28.2	29.6
V	XRF	ppm	49	53	48	51	160	253	149	314	379
Cr	XRF	ppm	15	12	10	7	37	66	113	46	31
Co	ICPMS	ppm	7.64	6.72	5.07	4.94	20.9	31.8	27.4	35.7	54.2
Ni	XRF	ppm	<3	3	<3	5	8	17	75	42	56
Cu	XRF	ppm	10	10	10	33	82	14	5	20	208
Zn	XRF	ppm	72	95	37	39	67	69	84	108	121
Ga	XRF	ppm	13	15	15	19	18	13	19	22	22
As	INAA	ppm	<0.5	57.8	4.0	<0.5	7.8	4.1	<0.5	<0.5	<0.5
Rb	ICPMS	ppm	35.5	67.2	60.9	45.0	8.85	17.5	20.8	44.0	9.00
Sr	XRF	ppm	140	205	184	243	211	213	466	343	409
Y	XRF	ppm	19	18	15	24	24	17	14	35	38
Zr	XRF	ppm	139	134	135	140	57	37	21	212	255
Nb	ICPMS	ppm	8.68	7.11	6.47	7.63	2.59	1.75	2.27	47.2	31.3
Cd	TD-ICP	ppm	0.3	0.5	<0.3	<0.3	0.5	0.5	<0.5	<0.5	0.8
Sb	INAA	ppm	1.4	1.7	1.5	1.1	1.3	1.6	<0.1	<0.1	<0.1
Te	TD-ICP	ppm	0.2	0.1	0.1	0.1	<0.1	0.2	0.3	0.3	<0.1
Ba	XRF	ppm	449	345	518	313	96	214	104	374	348
La	ICPMS	ppm	15.1	20.4	17.0	20.4	5.54	4.90	8.59	31.5	41.1
Ce	ICPMS	ppm	30.3	38.3	32.0	44.4	13.0	10.0	19.2	64.9	89.4
Pr	ICPMS	ppm	3.54	4.23	3.33	4.49	1.77	1.35	2.61	7.91	11.0
Nd	ICPMS	ppm	13.2	15.5	11.6	16.6	8.20	6.22	11.6	32.0	44.6
Sm	ICPMS	ppm	2.80	3.05	2.24	3.39	2.41	1.78	2.87	7.14	9.01
Eu	ICPMS	ppm	0.72	0.86	0.50	0.75	0.84	0.72	0.95	2.04	2.81
Gd	ICPMS	ppm	2.88	2.80	2.07	3.15	3.03	2.39	2.99	6.94	8.30
Tb	ICPMS	ppm	0.480	0.460	0.331	0.520	0.547	0.425	0.464	1.09	1.24
Dy	ICPMS	ppm	3.10	2.84	2.13	3.23	3.66	2.95	2.94	6.64	7.16
Ho	ICPMS	ppm	0.664	0.588	0.447	0.674	0.823	0.648	0.604	1.31	1.39
Er	ICPMS	ppm	2.01	1.82	1.36	1.96	2.53	1.94	1.71	3.48	3.70
Tm	ICPMS	ppm	0.294	0.273	0.210	0.309	0.377	0.301	0.246	0.500	0.503
Yb	ICPMS	ppm	2.02	1.72	1.41	1.96	2.44	1.99	1.53	3.06	3.16
Lu	ICPMS	ppm	0.297	0.276	0.218	0.300	0.362	0.318	0.234	0.442	0.465
Ta	ICPMS	ppm	0.82	0.62	0.94	0.95	0.43	0.14	0.15	2.66	1.05
Re	TD-ICP	ppm	0.004	0.002	<0.001	<0.001	0.003	0.001	0.003	0.006	0.006
Pb	ICPMS	ppm	22.57	27.77	8.78	6.18	9.12	7.56	9.85	11.41	8.07
Th	ICPMS	ppm	8.37	10.64	7.57	9.00	1.27	0.99	2.32	5.70	5.88
U	ICPMS	ppm	3.65	3.36	3.18	3.55	0.48	0.27	0.62	1.48	1.48

Table A11: Whole-rock data of the Paleng amphibole gabbro and Jinghong trachyandesite samples.

Rock type	Method	Unit	Paleng amphibole gabbro										Jinghong trachyandesite					
Sample			JI-30	JI-23	JI-32	JI-24	JI-33	JI-27	JI-28	JI-29	JI-31	JI-25	JI-12	JI-13	JI-16	JI-14	JI-17	JI-18
SiO_2	XRF	wt%	50.15	50.42	51.09	48.59	46.88	46.01	43.93	42.72	46.24	45.54	54.71	54.36	55.48	60.20	51.53	52.32
TiO_2	XRF	wt%	1.225	0.743	0.690	0.470	1.049	0.893	1.058	1.688	0.858	0.734	1.102	1.141	1.132	0.881	1.092	1.112
Al_2O_3	XRF	wt%	21.25	19.35	19.67	19.82	16.50	16.27	18.05	17.88	11.28	21.95	16.75	17.54	17.04	15.30	18.39	18.35
$Fe_2O_3(t)$	XRF	wt%	9.32	8.20	8.41	6.45	11.25	10.80	13.92	14.96	12.23	6.74	10.04	9.40	8.62	8.25	11.00	10.59
MnO	XRF	wt%	0.168	0.142	0.145	0.136	0.189	0.165	0.241	0.240	0.172	0.119	0.164	0.170	0.142	0.120	0.111	0.113
MgO	XRF	wt%	3.82	5.55	5.58	7.15	10.08	8.26	6.72	6.10	13.36	4.84	3.23	3.99	2.77	2.39	2.28	2.23
CaO	XRF	wt%	9.13	10.02	9.69	12.64	10.76	13.02	12.66	11.83	11.76	12.26	2.71	2.00	3.16	1.90	1.75	1.70
Na_2O	XRF	wt%	2.52	3.03	3.13	1.91	1.18	1.30	1.42	2.01	0.84	1.17	5.34	5.28	5.42	5.79	4.07	3.90
K_2O	XRF	wt%	0.44	0.39	0.24	0.58	0.34	0.47	0.34	0.25	0.53	2.24	1.69	1.68	1.81	1.13	2.60	2.77
P_2O_5	XRF	wt%	0.011	0.174	0.145	0.046	0.078	0.292	0.217	0.546	0.011	0.071	0.164	0.171	0.169	0.150	0.178	0.176
(SO_3)	XRF	wt%	0.08	0.04	<0.01	0.06	0.03	0.06	0.05	0.07	0.14	0.15	0.01	0.01	0.06	0.01	<0.01	<0.01
(Cl)	XRF	wt%	0.013	0.011	0.012	0.013	0.015	0.021	0.022	0.040	0.014	0.012	0.007	0.010	0.022	0.014	0.010	0.009
LOI		wt%	1.60	1.64	0.99	1.86	1.39	2.13	1.11	1.32	2.20	3.86	3.66	3.88	3.78	3.26	6.60	6.31
Sum		wt%	99.69	99.71	99.77	99.70	99.70	99.69	99.64	99.65	99.60	99.69	99.58	99.60	99.58	99.40	99.60	99.55
Li	ICPMS	ppm	7.93	3.07	5.03	9.11	2.67	14.3	7.34	2.35	5.29	21.5	72.0	88.4	57.3	65.8	44.6	48.0
Sc	INAA	ppm	12.8	23.0	25.0	33.3	38.4	48.8	45.7	44.1	59.2	31.8	28.2	30.5	28.0	21.2	31.8	33.5
V	XRF	ppm	136	184	180	133	245	373	357	466	336	208	306	257	306	157	292	319
Cr	XRF	ppm	172	94	85	354	335	132	51	51	806	34	39	44	33	26	9	10
Co	ICPMS	ppm	34.1	25.1	31.3	29.2	46.9	50.1	38.5	34.2	54.0	39.5	25.3	24.4	20.7	19.4	17.9	16.3
Ni	XRF	ppm	88	59	76	66	141	77	24	26	120	71	15	18	12	9	4	6
Cu	XRF	ppm	113	25	6	44	82	169	44	157	73	44	<3	8	<3	4	8	6
Zn	XRF	ppm	124	70	74	88	93	87	112	93	140	126	162	133	109	87	128	121
Ga	XRF	ppm	25	17	18	17	16	15	20	19	15	17	19	22	20	13	20	20
As	INAA	ppm	2.8	<0.5	3.3	5.0	6.5	1.3	<0.5	<0.5	<0.5	<0.5	7.5	<0.5	7.6	8.6	11.2	8.8
Rb	ICPMS	ppm	16.97	2.59	3.69	16.17	0.85	15.46	16.00	0.94	3.92	74.06	34.53	23.48	21.90	26.30	75.58	105.09
Sr	XRF	ppm	409	512	518	458	301	398	476	452	108	341	484	502	597	533	470	442
Y	XRF	ppm	5	10	8	12	14	13	16	17	31	21	30	34	28	24	39	39
Zr	XRF	ppm	139	15	15	19	25	11	10	7.75	36	23	117	119	116	105	118	119
Nb	ICPMS	ppm	8.62	1.04	1.36	1.40	0.97	0.63	0.87	0.64	1.02	2.03	6.06	6.31	5.79	5.91	5.87	5.94
Cd	TD-ICP	ppm	0.6	0.6	0.4	0.6	0.6	0.7	0.8	0.8	0.7	1.2	0.7	0.5	0.5	0.4	0.6	0.5
Sb	INAA	ppm	0.8	0.8	0.7	1.8	<0.1	<0.1	<0.1	<0.1	<0.1	6.2	2.2	1.8	2.0	1.3	<0.1	1.3
Te	TD-ICP	ppm	<0.1	0.5	<0.1	0.3	0.3	0.2	0.3	0.1	0.5	<0.1	0.2	0.2	0.2	0.1	0.1	0.1
Ba	XRF	ppm	60	83	62	77	42	89	41	31	115	197	1198	1058	1170	3396	1176	1209
La	ICPMS	ppm	14.9	2.98	3.22	3.36	1.75	2.34	3.16	2.14	1.49	2.68	10.4	11.0	10.5	14.4	19.5	30.1
Ce	ICPMS	ppm	25.6	6.76	7.67	8.06	4.82	7.49	8.74	6.05	5.71	7.15	21.9	19.3	21.2	27.6	32.4	45.2
Pr	ICPMS	ppm	2.51	0.93	1.09	1.15	0.79	1.32	1.55	1.03	1.19	1.15	2.99	3.07	3.00	3.41	4.54	6.09
Nd	ICPMS	ppm	8.27	4.38	5.33	5.43	4.35	7.43	8.24	5.85	7.27	6.02	13.5	13.5	13.2	14.2	18.8	24.2
Sm	ICPMS	ppm	1.28	1.16	1.43	1.49	1.41	2.34	2.53	1.70	2.65	2.08	3.52	3.52	3.47	3.45	4.14	4.92
Eu	ICPMS	ppm	1.84	0.54	0.65	0.66	0.58	0.88	1.10	0.68	0.76	0.61	1.16	1.15	1.19	1.11	1.25	1.47
Gd	ICPMS	ppm	1.06	1.45	1.47	1.67	1.79	2.40	3.03	1.92	3.52	2.38	4.08	4.33	3.91	4.00	4.79	5.32
Tb	ICPMS	ppm	0.143	0.211	0.237	0.277	0.327	0.407	0.472	0.297	0.624	0.492	0.698	0.719	0.665	0.658	0.763	0.838
Dy	ICPMS	ppm	0.99	1.33	1.48	1.78	2.13	2.63	2.98	1.85	4.16	3.38	4.59	4.68	4.41	4.25	4.80	5.25
Ho	ICPMS	ppm	0.220	0.292	0.308	0.371	0.459	0.529	0.629	0.362	0.875	0.722	1.008	1.005	0.955	0.939	1.040	1.073
Er	ICPMS	ppm	0.68	0.84	0.82	1.06	1.32	1.33	1.74	1.04	2.49	1.99	2.95	2.97	2.74	2.70	2.81	2.90
Tm	ICPMS	ppm	0.120	0.121	0.124	0.148	0.180	0.199	0.247	0.133	0.341	0.313	0.436	0.408	0.400	0.391	0.375	0.394
Yb	ICPMS	ppm	0.82	0.75	0.72	0.94	1.17	1.08	1.55	0.79	2.14	1.85	2.83	2.63	2.64	2.66	2.39	2.45
Lu	ICPMS	ppm	0.140	0.114	0.114	0.140	0.164	0.174	0.231	0.112	0.304	0.278	0.414	0.384	0.383	0.422	0.358	0.352
Ta	ICPMS	ppm	1.01	0.07	0.10	0.16	0.05	0.12	0.02	0.03	0.05	0.36	0.40	0.42	0.37	0.39	0.37	0.43
Re	TD-ICP	ppm	0.011	0.003	0.004	0.002	<0.001	0.004	0.002	0.004	0.006	0.005	0.001	0.003	0.003	0.003	0.002	0.006
Pb	ICPMS	ppm	11.06	9.65	3.54	13.46	3.14	3.07	3.23	5.12	6.95	29.30	28.48	23.33	20.89	19.28	20.15	17.32
Th	ICPMS	ppm	3.67	0.44	0.08	0.53	0.05	0.07	0.08	0.06	0.09	0.11	2.49	2.32	2.46	2.76	2.77	3.11
U	ICPMS	ppm	1.21	0.13	0.04	0.20	0.04	0.10	0.04	0.06	0.09	0.57	0.83	0.58	0.91	0.77	0.80	0.77

Note: Amphibole gabbro samples are sorted from plagioclase- to amphibole-rich. Sampe JI-25 is strongly altered.

Table A12: Whole-rock data of the Jinghong dacite, the Lincang granite and the Jinghong basalt samples.

Rock type	Method	Unit	Jinghong dacite				Lincang granite					aplite	Jinghong basalt				
Sample			JI-9	JI-10	JI-48	JI-49	LI-2	LI-3	LI-4	LI-5	LI-7	LI-6	JI-50	JI-52	JI-53	JI-55	JI-58
SiO_2	XRF	wt%	63.27	63.27	60.85	60.98	66.95	68.99	68.84	75.03	76.01	77.23	47.67	48.13	47.81	48.80	48.35
TiO_2	XRF	wt%	0.592	0.560	0.669	0.651	0.708	0.467	0.424	0.110	0.104	0.054	2.848	2.580	2.632	2.098	2.475
Al_2O_3	XRF	wt%	15.83	15.68	17.33	16.95	14.33	14.75	14.30	13.46	12.92	12.44	12.95	13.21	13.17	13.93	13.54
$Fe_2O_3(t)$	XRF	wt%	5.42	4.97	6.60	6.81	5.06	3.38	3.45	1.13	1.03	0.82	16.42	14.19	15.73	13.86	15.66
MnO	XRF	wt%	0.079	0.069	0.095	0.096	0.073	0.053	0.059	0.052	0.049	0.076	0.399	0.301	0.573	0.282	0.269
MgO	XRF	wt%	2.28	2.17	2.56	2.60	2.61	1.84	1.84	0.15	0.13	0.04	4.74	5.35	5.27	5.17	4.25
CaO	XRF	wt%	4.35	3.93	1.04	1.09	2.45	2.41	2.97	1.03	1.04	0.51	7.11	9.02	7.25	8.66	7.94
Na_2O	XRF	wt%	3.06	2.88	7.41	7.05	2.25	2.98	2.58	3.37	3.25	3.55	3.73	3.55	3.57	3.83	3.64
K_2O	XRF	wt%	2.50	3.50	0.58	1.09	3.46	3.45	3.69	4.78	4.65	4.65	1.04	0.76	0.97	0.80	0.71
P_2O_5	XRF	wt%	0.154	0.148	0.155	0.153	0.190	0.138	0.100	0.020	0.017	0.005	0.376	0.326	0.345	0.248	0.343
(SO_3)	XRF	wt%	<0.01	<0.01	<0.01	<0.01	0.08	0.02	<0.01	<0.01	<0.01	<0.01	0.04	0.03	0.04	0.04	<0.01
(Cl)	XRF	wt%	0.012	0.017	0.009	0.008	0.016	0.012	0.014	0.013	0.014	0.010	0.029	0.027	0.032	0.015	0.009
LOI		wt%	2.18	2.51	2.52	2.33	1.48	1.20	1.46	0.66	0.67	0.49	2.22	2.12	2.14	1.90	2.42
Sum		wt%	99.71	99.72	99.77	99.75	99.68	99.70	99.70	99.76	99.82	99.84	99.52	99.56	99.47	99.61	99.60
Li	ICPMS	ppm	67.3	72.0	43.5	41.7	31.6	21.5	18.4	6.50	7.33	3.99	48.9	97.1	74.3	34.6	25.5
Sc	INAA	ppm	15.3	14.5	13.2	13.1	13.7	12.1	11.9	2.7	2.4	3.4	38.7	38.0	35.9	41.1	23.2
V	XRF	ppm	103	100	86	85	77	54	54	<5	<5	<5	375	373	347	334	302
Cr	XRF	ppm	36	30	16	9	88	53	58	6	<4	<4	27	46	38	81	14
Co	ICPMS	ppm	15.7	13.6	13.5	13.0	13.1	9.04	7.22	1.06	0.67	0.35	39.1	46.3	45.4	41.7	40.5
Ni	XRF	ppm	14	13	3	4	37	18	17	5	5	6	28	37	30	30	14
Cu	XRF	ppm	13	12	6	6	21	18	8	<3	<3	3	62	25	122	58	7
Zn	XRF	ppm	70	100	106	93	63	59	42	15	15	12	435	231	595	153	147
Ga	XRF	ppm	18	16	16	18	20	20	18	16	13	17	19	19	19	19	21
As	INAA	ppm	<0.5	<0.5	<0.5	<0.5	9.2	7.4	11.4	<0.5	5.3	<0.5	8.7	4.8	5.2	23.5	16.8
Rb	ICPMS	ppm	95.6	138	7.57	15.0	174	181	151	231	250	322	32.0	27.1	40.2	22.9	8.83
Sr	XRF	ppm	343	470	266	259	141	168	187	107	106	11	357	295	370	255	353
Y	XRF	ppm	24	28	23	24	35	24	32	28	24	48	61	51	54	43	53
Zr	XRF	ppm	135	129	128	121	248	161	162	87	90	107	229	206	215	166	219
Nb	ICPMS	ppm	8.42	7.72	8.08	7.79	14.4	10.6	10.4	21.1	25.8	48.4	7.39	6.48	7.43	5.37	8.54
Cd	TD-ICP	ppm	0.4	0.4	0.3	0.4	0.3	<0.3	0.3	<0.3	<0.3	<0.3	1.3	1.2	1.8	0.7	0.6
Sb	INAA	ppm	<0.1	0.6	2.0	1.8	<0.1	<0.1	<0.1	<0.1	0.4	<0.1	2.0	1.3	1.7	<0.1	<0.1
Te	TD-ICP	ppm	1.7	0.1	0.2	< 0.1	0.1	<0.1	<0.1	<0.1	<0.1	<0.1	0.3	0.2	<0.1	<0.1	<0.1
Ba	XRF	ppm	469	591	271	475	813	819	901	338	349	9.09	294	383	333	250	278
La	ICPMS	ppm	24.7	25.5	7.87	6.82	49.9	32.2	23.6	29.5	28.8	16.5	16.9	10.5	14.6	8.92	13.9
Ce	ICPMS	ppm	47.2	46.9	18.7	16.5	102	66.9	50.5	56.6	58.4	39.7	40.6	27.3	35.3	23.0	34.8
Pr	ICPMS	ppm	5.40	5.38	2.30	1.87	11.7	7.40	5.44	6.01	6.27	5.34	5.93	4.17	5.02	3.37	4.96
Nd	ICPMS	ppm	20.1	20.2	9.16	7.63	42.9	27.7	20.4	20.8	21.1	20.3	28.0	20.5	24.0	16.2	23.4
Sm	ICPMS	ppm	4.12	4.03	2.12	1.80	8.30	5.53	4.57	4.05	4.00	5.63	7.91	5.96	6.74	4.56	6.24
Eu	ICPMS	ppm	0.99	1.03	0.63	0.56	1.30	1.00	0.82	0.49	0.50	0.10	2.34	1.78	2.11	1.46	1.99
Gd	ICPMS	ppm	3.95	4.09	2.16	1.93	6.74	4.54	4.13	3.52	3.48	5.19	9.55	6.66	7.31	4.99	7.05
Tb	ICPMS	ppm	0.605	0.611	0.402	0.343	1.03	0.651	0.693	0.562	0.529	0.974	1.64	1.20	1.34	0.928	1.25
Dy	ICPMS	ppm	3.85	3.95	2.65	2.26	5.79	3.76	4.36	3.51	3.53	6.48	10.7	7.77	8.55	6.02	8.29
Ho	ICPMS	ppm	0.796	0.808	0.563	0.484	1.08	0.722	0.887	0.733	0.756	1.38	2.26	1.66	1.82	1.28	1.78
Er	ICPMS	ppm	2.24	2.28	1.65	1.42	2.88	1.92	2.57	2.21	2.19	4.19	6.42	4.64	5.09	3.59	4.93
Tm	ICPMS	ppm	0.321	0.327	0.262	0.217	0.375	0.279	0.384	0.375	0.342	0.710	0.923	0.693	0.727	0.552	0.704
Yb	ICPMS	ppm	2.08	2.06	1.68	1.43	2.41	1.58	2.31	2.32	2.36	4.42	5.93	4.09	4.46	3.24	4.43
Lu	ICPMS	ppm	0.327	0.310	0.260	0.215	0.340	0.222	0.322	0.359	0.366	0.685	0.902	0.616	0.673	0.503	0.670
Ta	ICPMS	ppm	1.04	0.96	0.80	0.72	0.66	1.47	1.57	3.43	3.76	5.67	0.43	0.62	0.68	0.53	0.73
Re	TD-ICP	ppm	0.003	<0.001	<0.001	0.004	0.001	0.002	0.002	0.003	<0.001	<0.001	0.003	<0.001	0.007	0.003	<0.001
Pb	ICPMS	ppm	28.7	25.8	3.2	3.3	37.1	41.1	27.3	24.4	30.1	28.8	91.0	71.3	115	2.31	4.68
Th	ICPMS	ppm	12.2	10.9	2.03	1.61	27.0	12.8	12.5	20.6	21.2	36.6	1.84	1.14	1.34	1.20	1.68
U	ICPMS	ppm	3.88	3.28	1.13	0.89	4.37	6.26	4.74	6.29	6.91	9.97	0.58	0.34	0.50	0.48	0.98

Table A13: Detection limits and accuracies of the whole-rock data.

Rock type	Method	Unit	DL	Uncertainty	JGb-1	JGb-1	JGb-1	JGb-1-1	JGb-1-2	JGb-1-3	JGb-1-4	JGB1-5
Sample				(%)	Gov. (1994)	Dulski (2001)	Imai (1999)					
SiO_2	XRF	wt%	0.01	1								
TiO_2	XRF	wt%	0.001	2								
Al_2O_3	XRF	wt%	0.01	2								
$Fe_2O_3(t)$	XRF	wt%	0.01	1								
MnO	XRF	wt%	0.001	3								
MgO	XRF	wt%	0.01	2								
CaO	XRF	wt%	0.01	2								
Na_2O	XRF	wt%	0.01	2								
K_2O	XRF	wt%	0.01	1								
P_2O_5	XRF	wt%	0.001	3								
(SO_3)	XRF	wt%	0.01									
(Cl)	XRF	wt%	0.01									
LOI		wt%										
Sum		wt%										
Li	ICPMS	ppm	1.66		**4.30**		**4.59**	4.67	5.17	4.83	6.05	6.14
Sc	INAA	ppm	0.1									
V	XRF	ppm	5	15								
Cr	XRF	ppm	4	25								
Co	ICPMS	ppm	0.03									
Ni	XRF	ppm	3	30								
Cu	XRF	ppm	3	20								
Zn	XRF	ppm	2	10								
Ga	XRF	ppm	3	10								
As	INAA	ppm	0.5									
Rb	ICPMS	ppm	0.67		**4.00**	**5.70**	**6.87**	6.69	6.98	6.71	6.02	6.91
Sr	XRF	ppm	2	5								
Y	XRF	ppm	3	25								
Zr	XRF	ppm	2	10								
Nb	ICPMS	ppm	0.66		**2.80**		**3.34**	2.54	2.48	2.50	2.58	2.59
Cd	TD-ICP	ppm	0.3									
Sb	INAA	ppm	0.1									
Te	TD-ICP	ppm	0.1									
Ba	XRF	ppm	5	10								
La	ICPMS	ppm	0.36		**3.74**	**3.40**	**3.60**	3.59	3.31	3.66	3.16	3.53
Ce	ICPMS	ppm	0.68		**7.86**	**8.00**	**8.17**	9.23	8.58	9.15	7.77	8.54
Pr	ICPMS	ppm	0.07		**1.14**	**1.13**	**1.13**	1.20	1.12	1.20	1.24	1.35
Nd	ICPMS	ppm	0.24		**5.65**	**5.00**	**5.47**	5.44	5.13	5.37	5.66	5.84
Sm	ICPMS	ppm	0.06		**1.49**	**1.33**	**1.49**	1.48	1.44	1.46	1.51	1.53
Eu	ICPMS	ppm	0.02		**0.63**	**0.61**	**0.62**	0.61	0.61	0.61	0.64	0.63
Gd	ICPMS	ppm	0.03		**1.63**	**1.67**	**1.61**	1.69	1.63	1.69	1.52	1.58
Tb	ICPMS	ppm	0.005		**0.31**	**0.27**	**0.29**	0.27	0.27	0.27	0.26	0.26
Dy	ICPMS	ppm	0.03		**1.53**	**1.69**	**1.56**	1.75	1.70	1.72	1.71	1.72
Ho	ICPMS	ppm	0.005		**0.32**	**0.34**	**0.33**	0.35	0.34	0.35	0.34	0.34
Er	ICPMS	ppm	0.02		**1.07**	**1.00**	**1.04**	1.02	1.01	1.01	0.97	0.98
Tm	ICPMS	ppm	0.005		**0.15**	**0.14**	**0.16**	0.14	0.14	0.14	0.13	0.14
Yb	ICPMS	ppm	0.02		**0.97**	**0.91**	**1.06**	0.90	0.87	0.88	0.84	0.83
Lu	ICPMS	ppm	0.004		**0.15**	**0.14**	**0.15**	0.14	0.13	0.13	0.13	0.13
Ta	ICPMS	ppm	0.01		**0.17**		**0.18**	0.13	0.13	0.14	0.17	0.26
Re	TD-ICP	ppm	0.001									
Pb	ICPMS	ppm	0.94		**1.90**			1.63	1.77	1.71		
Th	ICPMS	ppm	0.05		**0.53**	**0.45**	**0.48**	0.54	0.49	0.57	0.36	0.56
U	ICPMS	ppm	0.03		**0.15**	**0.10**	**0.13**	0.13	0.14	0.14	0.09	0.13

Note: Certified and proposed values are printed in bold.

Table A13 continued: Detection limits and accuracies of the whole-rock data.

Rock type	Method	Unit	JGb-2	JGb-2	JGb-2	JGB2-1	JGB2-2	JGB2-3	JGB2-4	JGB2-5	JGB2-6
Sample			Govindaraju (1994)	Dulski (2001)	Imai (1999)						
Li	ICPMS	ppm	**16.0**		**15.2**	13.4	11.9	13.6	12.3	13.8	14.6
Co	ICPMS	ppm	**28.0**		**25.8**	31.2	29.4	32.3	32.4		
Rb	ICPMS	ppm		**2.35**	**2.85**	2.06	1.65	2.17	1.72	2.98	2.82
Nb	ICPMS	ppm			**1.91**					0.84	0.87
La	ICPMS	ppm		**1.47**	**1.45**	1.52	1.43	1.38	1.35	1.77	1.98
Ce	ICPMS	ppm		**3.06**	**2.98**	3.18	2.86	2.71	2.28	3.68	4.15
Pr	ICPMS	ppm		**0.415**	**0.385**	0.405	0.406	0.374	0.389	0.489	0.543
Nd	ICPMS	ppm		**1.810**	**1.840**	1.910	1.845	1.809	1.790	2.094	2.302
Sm	ICPMS	ppm		**0.490**	**0.506**	0.495	0.476	0.458	0.521	0.562	0.576
Eu	ICPMS	ppm		**0.610**	**0.585**	0.536	0.505	0.493	0.551	0.598	0.588
Gd	ICPMS	ppm		**0.612**	**0.390**	0.519	0.505	0.481	0.521	0.636	0.653
Tb	ICPMS	ppm		**0.097**	**0.152**	0.089	0.088	0.091	0.095	0.106	0.101
Dy	ICPMS	ppm		**0.640**	**0.598**	0.604	0.583	0.625	0.648	0.681	0.665
Ho	ICPMS	ppm		**0.134**	**0.145**	0.126	0.124	0.129	0.133	0.139	0.137
Er	ICPMS	ppm		**0.389**	**0.362**	0.348	0.356	0.357	0.358	0.417	0.427
Tm	ICPMS	ppm		**0.056**	**0.050**	0.053	0.054	0.054	0.056	0.060	0.063
Yb	ICPMS	ppm		**0.384**	**0.390**	0.339	0.326	0.325	0.356	0.395	0.386
Lu	ICPMS	ppm		**0.058**	**0.062**	0.052	0.048	0.049	0.052	0.063	0.063
Ta	ICPMS	ppm			**0.286**	0.102	0.263	0.115	0.106	0.005	0.005
Pb	ICPMS	ppm		**1.07**	**1.46**	1.70	1.13	1.68	3.10	0.38	1.43
Th	ICPMS	ppm		**0.100**	**0.194**	0.200	0.122	0.136	0.112	0.391	0.432
U	ICPMS	ppm		**0.026**	**0.030**	0.049	0.030	0.037	0.029	0.062	0.081

Table A13 continued: Detection limits and accuracies of the whole-rock data.

Rock type	Method	Unit	JP1	JP1	JP1	JP1	JP1	JP1-1	JP1-2	JP1-3	JP1-4
Sample			Govindaraju (1994)	Dulski (2001)	Imai (1999)	Jochum (1994)	Jochum (1994)				
Li	ICPMS	ppm	1.80		1.79			1.86	2.11	2.51	2.39
Rb	ICPMS	ppm		0.50	0.80	0.36	0.34	0.60	0.75	0.92	0.55
Nb	ICPMS	ppm	1.20		1.48	0.06	0.08	0.14	0.20	0.23	0.18
La	ICPMS	ppm	0.1	0.034	0.084	0.040	0.043	0.279	0.128	0.348	0.414
Ce	ICPMS	ppm	0.2	0.063	0.19		0.056	0.602	0.280	0.749	0.959
Pr	ICPMS	ppm	0.02	0.0089	0.02	0.014	0.014	0.069	0.033	0.086	0.102
Nd	ICPMS	ppm	0.07	0.033	0.072	0.047	0.073	0.250	0.112	0.312	0.331
Sm	ICPMS	ppm	0.02	0.009	0.019	0.021	0.039	0.042	0.025	0.053	0.062
Eu	ICPMS	ppm	0.003	0.0021	0.004			0.007	0.004	0.006	0.009
Gd	ICPMS	ppm	0.02	0.0092	0.015	0.015	0.013	0.039	0.023	0.042	0.055
Tb	ICPMS	ppm	0.003	0.0016	0.003	0.004		0.007	0.004	0.007	0.007
Dy	ICPMS	ppm	0.02	0.0132	0.022	0.024	0.032	0.040	0.027	0.041	0.043
Ho	ICPMS	ppm		0.003	0.018	0.005		0.008	0.006	0.009	0.010
Er	ICPMS	ppm	0.02	0.0112	0.016	0.020	0.019	0.029	0.022	0.028	0.029
Tm	ICPMS	ppm		0.0023		0.0037		0.006	0.003	0.005	0.005
Yb	ICPMS	ppm	0.020	0.021	0.022	0.022	0.027	0.038	0.031	0.034	0.038
Lu	ICPMS	ppm		0.004	0.0044	0.006		0.007	0.005	0.007	0.007
Ta	ICPMS	ppm			0.02			0.01	0.01	0.01	0.01
Pb	ICPMS	ppm		0.114	0.12		0.12	0.303		3.047	2.825
Th	ICPMS	ppm	0.18	0.012	0.19	0.014	0.025	0.121	0.063	0.187	0.214
U	ICPMS	ppm	0.05	0.0116	0.036	0.013	0.027	0.036	0.020	0.066	0.053

Table A13 continued: Detection limits and accuracies of the whole-rock data.

Rock type	Method	Unit	TW	TW-1	TW-2	TW-3	TUCB	TUCB-1	TUCB-2
Sample									
Li	ICPMS	ppm		46.99	48.06	49.61	13.00	13.04	14.38
Rb	ICPMS	ppm		123.68	126.76	129.15	42.00	45.13	43.40
Nb	ICPMS	ppm		15.54	15.46	15.60	60.00	69.20	69.22
La	ICPMS	ppm	31.00	33.51	33.81	34.03	46.00	44.77	43.65
Ce	ICPMS	ppm	78.00	71.06	74.35	74.91	89.00	96.11	93.16
Pr	ICPMS	ppm		9.44	9.45	9.58	9.40	12.13	11.79
Nd	ICPMS	ppm		32.96	33.08	33.64	42.00	44.96	43.97
Sm	ICPMS	ppm	6.40	6.21	6.35	6.40	8.00	8.71	8.43
Eu	ICPMS	ppm	1.13	1.05	1.07	1.06	2.30	2.72	2.58
Gd	ICPMS	ppm		4.56	4.49	4.49	6.60	6.39	6.09
Tb	ICPMS	ppm	0.70	0.76	0.77	0.76	1.10	0.89	0.87
Dy	ICPMS	ppm		4.42	4.56	4.57	4.50	4.72	4.53
Ho	ICPMS	ppm		0.90	0.90	0.91	0.86	0.82	0.80
Er	ICPMS	ppm		2.61	2.57	2.64	2.00	2.04	2.03
Tm	ICPMS	ppm		0.37	0.38	0.38	0.31	0.26	0.25
Yb	ICPMS	ppm	2.60	2.33	2.38	2.38	1.51	1.57	1.53
Lu	ICPMS	ppm	0.45	0.34	0.36	0.35	0.22	0.21	0.21
Ta	ICPMS	ppm	1.10	1.11	1.07	1.05	3.70	3.89	3.38
Th	ICPMS	ppm	10.00	8.21	8.12	8.16	6.15	4.68	4.70
U	ICPMS	ppm		2.11	2.03	2.09	1.55	1.14	1.14

Table A13 continued: Detection limits and accuracies of the whole-rock data.

	Sc	As	Cd	Sb	Te	Re
	INAA	INAA	TD-ICP	INAA	TD-ICP	TD-ICP
	ppm	ppm	ppm	ppm	ppm	ppm
GXR-1			**3.3**		**13**	
GXR-1			3.9		11.8	
GXR-4			**0.86**		**0.97**	
GXR-4			0.8		1.4	
GXR-2			**4.1**		**0.69**	
GXR-2			2.9		1.1	
SDC-1			**0.08**			
SDC-1			0.5			
SCO-1			**0.14**			
SCO-1			0.4			
GXR-6			**1**		**0.018**	
GXR-6			1.2		<0.1	
DMMAS-104	**14.1**	**1570**		**6.2**		
DMMAS-104	14.1	1590		6.5		
DMMAS-104	**14.1**	**1570**		**6.2**		
DMMAS-104	14.2	1560		6.7		
DMMAS-104	**14.1**	**1570**		**6.2**		
DMMAS-104	14	1560		6.5		
DMMAS 107	**14.8**	**2980**		**13.7**		
DMMAS 107	14.1	3080		4		
Method Blank				<0.3		
Method Blank				<0.3		
Method Blank				<0.3		
Method Blank				<0.3		
Method Blank				<0.3		
Method Blank				<0.3		
Method Blank				<0.3		
Method Blank				<0.3		
Method Blank				<0.3		
Method Blank				<0.3		
Method Blank						<0.001

Table A13 continued: Detection limits and accuracies of the whole-rock data.

Rock type	Method	Unit	Blank1	Blank2	Blank3	Blank4	Blank5	Blank6	Blank7	Blank8	Blank9	Blank10	Blank11	Blank12	Blank13
Sample															
Li	ICPMS	ppm	0.103	0.104	0.098	0.102	0.115	-0.034	-0.020	0.064	0.115	0.170	0.167	0.169	0.164
Co	ICPMS	ppm					0.067	0.119	0.040	0.108					
Rb	ICPMS	ppm	0.041	0.020	0.010	0.024	0.014	0.042	0.038	0.038	0.064	0.111	0.067	0.067	0.054
Nb	ICPMS	ppm	0.003	0.005	0.007	0.005	0.001	-0.032	-0.041	-0.014	-0.009	-0.006	-0.014	-0.012	-0.012
La	ICPMS	ppm	0.008	0.004	0.009	0.007	0.001	0.006	0.001	0.017	0.014	0.029	0.014	0.012	0.011
Ce	ICPMS	ppm	0.014	0.010	0.012	0.012	0.001	0.005	0.005	0.040	0.044	0.053	0.016	0.018	0.051
Pr	ICPMS	ppm	0.001	0.001	0.001	0.001	0.000	0.001	0.000	0.007	0.003	0.005	0.002	0.002	0.002
Nd	ICPMS	ppm	0.004	0.004	0.004	0.004	0.001	0.002	0.005	0.029	0.010	0.016	0.007	0.009	0.007
Sm	ICPMS	ppm	0.003	0.005	0.003	0.004	0.000	0.001	0.001	0.006	0.001	0.003	0.000	0.002	0.001
Eu	ICPMS	ppm	0.000	0.000	0.000	0.000	0.000	0.001	0.000	0.002	0.000	0.000	-0.005	-0.001	-0.004
Gd	ICPMS	ppm	0.001	0.002	0.002	0.002	0.000	0.001	0.000	0.009	0.002	0.002	0.001	0.001	0.001
Tb	ICPMS	ppm	0.000	0.000	0.000	0.000	0.000	0.000	0.001	0.002	0.000	0.000	0.000	0.000	0.000
Dy	ICPMS	ppm	0.002	0.002	0.002	0.002	0.000	0.001	-0.001	0.010	0.001	0.002	0.000	0.001	0.001
Ho	ICPMS	ppm	0.000	0.000	0.000	0.000	0.000	0.000	0.000	0.002	0.000	0.001	0.000	0.000	0.000
Er	ICPMS	ppm	0.001	0.001	0.001	0.001	0.000	0.000	0.001	0.005	0.001	0.001	0.001	0.001	0.001
Tm	ICPMS	ppm	0.000	0.000	0.000	0.000	0.000	0.000	0.000	0.001	0.000	0.000	0.000	0.000	0.000
Yb	ICPMS	ppm	0.001	0.001	0.001	0.001	0.000	0.001	0.000	0.002	0.001	0.002	0.003	0.002	0.002
Lu	ICPMS	ppm	0.000	0.000	0.000	0.000	0.000	0.000	0.000	0.000	0.000	0.000	0.000	0.000	0.000
Ta	ICPMS	ppm	0.001	0.000	0.001	0.000	0.002	-0.004	-0.002	0.024	-0.029	-0.028	-0.029	-0.029	-0.029
Pb	ICPMS	ppm	1.750	1.355	2.195	1.766	0.019	0.138	0.184	0.185	0.414	1.491	0.501	1.559	2.656
Th	ICPMS	ppm	0.002	0.001	0.001	0.001	0.000	0.000	0.001	0.003	0.005	0.003	0.002	0.003	0.003
U	ICPMS	ppm	0.009	0.021	0.002	0.011	0.000	0.000	0.001	0.001	0.005	0.020	0.026	0.025	0.022

Table A14: Sr–Nd isotopic data of the Banpo rhyolite (not discussed in this thesis).

Sample	Rock type	Age	Sm	Nd	$^{147}Sm/^{144}Nd$	$^{143}Nd/^{144}Nd$	2σ	ε_{Nd} (t)	Rb	Sr	$^{87}Rb/^{86}Sr$	$^{87}Sr/^{86}Sr$	2σ	$(^{87}Sr/^{86}Sr)t$
		Ma	ppm	ppm					ppm	ppm				
BA-12	Rhyolite	269	2.0	9.5	0.12508	0.512416	0.000004	-1.87	123.5	180.2	1.98299	0.712217	0.000018	0.704628
BA-23	Rhyolite	269	2.2	8.1	0.16618	0.512446	0.000005	-2.70	168.8	255.2	1.91465	0.712957	0.000016	0.705629
BA-25	Rhyolite	269	0.3	0.9	0.21649	0.513034	0.000008	7.05	3.9	42.9	0.26583	0.707575	0.000021	0.706557
BA-30	Rhyolite	269	0.4	0.6	0.38308	0.513479	0.000007	10.01	1.6	68.1	0.06973	0.706074	0.000010	0.705807
BA-44	Rhyolite	269	1.8	8.8	0.12170	0.512707	0.000007	3.92	8.6	134.5	0.18574	0.705654	0.000007	0.704944
BA-53	Rhyolite	269	1.0	4.7	0.13188	0.512478	0.000008	-0.90	14.2	114.4	0.35817	0.707459	0.000010	0.706089

Table A15: PGE data for the mafic to ultramafic complexes of SW Yunnan, China.

Sample	Rock type	Method	Ru (ppb)	Rh (ppb)	Pd (ppb)	Os (ppb)	Ir (ppb)	Pt (ppb)	Au (ppb)
BA-1	Banpo harzburgite	CT-ID-ICP-MS	0.790	0.350	12.1	0.155	0.270	8.25	1.79
BA-4	Banpo harzburgite	CT-ID-ICP-MS	0.254	0.391	6.44	0.066	0.321	3.48	2.42
BA-16	Banpo harzburgite	CT-ID-ICP-MS	0.212	0.272	2.47	0.212	0.194	2.43	0.475
BA-20	Banpo harzburgite	CT-ID-ICP-MS	0.595	0.148	1.26	0.102	0.111	3.02	0.095
BA-5	Banpo hornblendite	CT-ID-ICP-MS	0.068	0.046	1.51	0.018	0.061	3.92	0.853
BA-8	Banpo gabbro	CT-ID-ICP-MS	0.031	0.044	1.50	0.024	0.057	1.97	1.88
BA-24	Banpo gabbro	CT-ID-ICP-MS	0.006	0.002	0.047	0.003	0.006	0.022	1.39
JI-13	Jinghong trachyandesite	CT-ID-ICP-MS	0.003	0.003	0.046	0.033	0.005	0.042	0.379
JI-23	Paleng amphibole gabbro	CT-ID-ICP-MS	0.011	0.015	0.171	0.007	0.024	0.169	0.188
JI-29	Paleng amphibole gabbro	CT-ID-ICP-MS	0.004	0.027	0.609	0.006	0.011	0.970	0.384
JI-31	Paleng amphibole gabbro	CT-ID-ICP-MS	0.026	0.009	0.113	0.014	0.013	0.114	0.399
JI-33	Paleng amphibole gabbro	CT-ID-ICP-MS	0.019	0.008	0.044	0.011	0.010	0.212	0.181
J1-20	Paleng basaltic andesite	FA-ICP-MS	-	-	<0.1	-	-	<0.1	1
J1-21	Paleng basaltic andesite	FA-ICP-MS	-	-	1.1	-	-	3.7	<1
J1-22	Paleng basaltic andesite	FA-ICP-MS	-	-	<0.1	-	-	0.4	<1
J1-24	Paleng amphibole gabbro	FA-ICP-MS	-	-	<0.1	-	-	<0.1	<1
J1-25	Paleng amphibole gabbro	FA-ICP-MS	-	-	<0.1	-	-	0.6	4
J1-27	Paleng amphibole gabbro	FA-ICP-MS	-	-	0.4	-	-	3.0	<1
J1-28	Paleng amphibole gabbro	FA-ICP-MS	-	-	<0.1	-	-	0.2	<1
J1-30	Paleng amphibole gabbro	FA-ICP-MS	-	-	0.6	-	-	1.1	2
J1-32	Paleng amphibole gabbro	FA-ICP-MS	-	-	<0.1	-	-	0.3	<1
J1-26	Paleng porphyritic basalt	FA-ICP-MS	-	-	<0.1	-	-	<0.1	2
Quality control									
UMT-1 (measured)	Ultramafic mine tailing		10.3	10.6	100	7.82	8.31	129	70.6
CANMET			10.9	9.50	106	8.00	8.80	129	48.0
2σ			1.50	1.10	3.00	-	0.200	4.00	2.00
Gros *et al*. (2002)		FA-ICP-MS	8.90	8.90	99.0	7.13	8.50	121	43.50
1σ			0.450	0.110	1.56	1.40	0.330	1.130	2.60
Pattou (1995)		ICP-MS?	7.60	8.00	88.00	1.50	6.60	99.9	37.1
1σ			0.100	0.400	4.80	0.600	0.600	14.9	3.00
Oguri *et al*. (1999)		FA-ICP-MS	8.70	8.80	95.6	-	10.0	132	50.5
1σ			0.760	0.350	3.70	-	0.790	9.00	1.80
Snow & Schmidt (1998)		FA-INAA	8.20	7.57	98.0	6.00	7.31	-	27.0
Snow & Schmidt (1998)			9.60	9.87	93.0	7.23	7.82	-	32.6
Qui *et al*. (2004)		CT-ID-ICP-MS	9.53	9.22	115	-	8.55	123	-
			0.820	0.710	7.00	-	0.650	8.00	-
WPR-1 (measured)	Peridotite		22.1	13.9	258	12.6	11.5	302	67.9
Govindaraju (1994)			22.0	13.4	235	13.0	13.5	285	42.0
Qui & Zhao (2008)		CT-ID-ICP-MS	23.1	12.8	238	14.7	13.8	280	-
			1.90	0.700	17.0	0.500	1.20	13.0	-
Qui *et al*. (2007) n=5		CT-ID-ICP-MS	22.5	12.7	231	14.5	13.4	276	-
			1.90	0.700	17.0	0.500	1.20	13.0	-
Keays & Lightfoot (2009)		FA-ICP-MS	20.3	15.1	267	-	17.3	312	48.7
CDN-PGMS-9 (measured)	Platinum group ore	FA-ICP-MS	-	-	2600	-	-	684	1030
CDN-PGMS-9	reference standard	FA-ICP-MS	-	-	2600	-	-	710	1040
CDN-PGMS-8 (measured)	Platinum group ore	FA-ICP-MS	-	-	1490	-	-	467	937
CDN-PGMS-8	reference standard	FA-ICP-MS	-	-	1500	-	-	440	820

Table A16: Laser Ablation ICP-MS U–Pb data of the Nanlianshan volcano-plutonic complex (sample JI-46).

Sample ID	cPb	$^{207}Pb^{a}$ [cps]	U^{b} [ppm]	Pb^{b} [ppm]	$^{206}Pb/^{204}Pb$	Th/U	$^{207}Pb/^{235}U^{c}$	2σ [%]^{e}	$^{206}Pb/^{238}U^{c}$	2σ [%]^{e}	rho^{d}	$^{207}Pb/^{206}Pb^{f}$	2σ [%]^{e}	$^{207}Pb/^{235}U$ [Ma]	2σ [Ma]	$^{206}Pb/^{238}U$ [Ma]	2σ [Ma]	$^{207}Pb/^{206}Pb$	2σ [Ma]	Conc [%]^{g}
Nanlianshan volcano-plutonic complex																				
JI-46	n	2890	154	8	17938	0.61	0.3260	3.8	0.0455	2.1	0.56	0.0520	3.1	287	11	287	6	285	36	100
JI-46	n	2424	114	6	11338	0.78	0.3345	3.8	0.0464	2.1	0.56	0.0523	3.1	293	11	292	6	299	36	100
JI-46	n	2659	109	6	31063	0.86	0.3309	4.0	0.0459	2.4	0.60	0.0522	3.2	290	12	290	7	296	37	100
JI-46	n	1380	58	3	6031	0.59	0.3333	4.3	0.0463	2.6	0.60	0.0523	3.5	292	13	292	7	296	39	100
JI-46	n	2898	148	8	9167	0.86	0.3358	4.1	0.0467	2.4	0.59	0.0522	3.3	294	12	294	7	292	38	100
JI-46	n	2197	102	5	11831	1.01	0.3373	3.9	0.0468	2.3	0.58	0.0523	3.2	295	12	295	7	298	37	100
JI-46	n	2197	102	5	14100	1.01	0.3329	3.2	0.0462	2.2	0.68	0.0523	2.4	292	9	291	6	299	27	100
JI-46	n	3634	203	11	6803	0.91	0.3371	4.7	0.0466	2.6	0.55	0.0525	3.9	295	14	293	8	307	45	99
JI-46	n	2056	84	4	33843	0.70	0.3392	3.6	0.0469	2.2	0.62	0.0525	2.8	297	11	295	7	306	32	100
JI-46	n	3286	158	8	13609	0.62	0.3316	4.4	0.0463	2.4	0.55	0.0520	3.6	291	13	292	7	284	42	100
JI-46	n	1610	69	3	10265	0.65	0.3360	3.8	0.0465	2.6	0.69	0.0524	2.8	294	11	293	8	303	32	100
JI-46	n	2481	132	7	10493	0.92	0.3334	4.1	0.0465	3.1	0.77	0.0521	2.6	292	12	293	9	288	29	100
JI-46	n	3671	201	10	30206	0.55	0.3339	3.4	0.0463	2.4	0.70	0.0523	2.4	293	10	292	7	300	27	100
JI-46	n	3681	209	11	72117	0.94	0.3317	3.1	0.0462	2.2	0.73	0.0521	2.1	291	9	291	6	289	24	100
JI-46	n	4617	288	15	7889	0.87	0.3319	3.6	0.0462	2.5	0.71	0.0521	2.5	291	10	291	7	290	29	100
JI-46	n	2793	153	8	4634	0.90	0.3332	4.4	0.0464	2.3	0.53	0.0521	3.7	292	13	292	7	289	42	100
JI-46	n	2540	95	5	2687	0.85	0.3364	4.8	0.0469	3.0	0.63	0.0521	3.7	294	14	295	9	288	42	100
JI-46	n	2789	141	8	3877	1.01	0.3371	4.6	0.0468	2.3	0.49	0.0522	4.0	295	14	295	7	296	46	100
JI-46	n	2197	76	4	4112	0.53	0.3345	4.2	0.0465	2.3	0.54	0.0522	3.5	293	12	293	7	294	40	100
JI-46	n	2651	104	5	7851	0.84	0.3383	3.8	0.0470	2.4	0.64	0.0523	2.9	296	11	296	7	297	33	100
JI-46	n	2382	105	6	15278	0.89	0.3326	3.1	0.0461	2.4	0.78	0.0523	1.9	292	9	290	7	300	22	100
JI-46	n	7859	432	22	11290	0.76	0.3359	3.2	0.0466	2.2	0.69	0.0522	2.3	294	9	294	6	295	26	100
JI-46	n	4279	234	12	3815	0.82	0.3371	3.8	0.0466	2.4	0.63	0.0525	3.0	295	11	294	7	306	34	100
JI-46	n	2170	87	5	24697	0.89	0.3324	3.4	0.0462	2.2	0.65	0.0522	2.5	291	10	291	6	293	29	100

[a]Within-run background-corrected mean ^{207}Pb signal in counts per second [cps]. [b]U and Pb concentrations and Th/U ratios are calculated relative to GJ-1 reference zircon. [c]Corrected for background and within-run Pb/U fractionation and normalized to reference zircon GJ-1 (ID-TIMS values/measured value); $^{207}Pb/^{235}U$ calculated using ($^{207}Pb/^{206}Pb$) / ($^{238}U/^{206}Pb$ x 1/137.88). [d]Rho is the error correlation defined as the quotient of the propagated errors of the $^{206}Pb/^{238}U$ and the $^{207}Pb/^{235}U$ ratio. [e]Quadratic addition of within-run errors (2σ) and daily reproducibility of GJ-1 (2σ). [f]corrected for mass-bias by normalizing to GJ-1 reference zircon (~0.6 per atomic mass unit) and common Pb using the model Pb composition of Stacey & Kramers (1975); [g]degree of concordance = ($^{206}Pb/^{238}U$ age * 100 / $^{207}Pb/^{235}U$ age).

Table A17: Laser Ablation ICP-MS U–Pb data of the Banpo gabbro (sample BA-8).

Sample ID	cPb	$^{207}Pb^{a}$ [cps]	U^{b} [ppm]	Pb^{b} [ppm]	$^{206}Pb/^{204}Pb$	Th/U	$^{207}Pb/^{235}U^{c}$	2σ [%]^{e}	$^{206}Pb/^{238}U^{c}$	2σ [%]^{e}	rho^{d}	$^{207}Pb/^{206}Pb^{f}$	2σ [%]^{e}	$^{207}Pb/^{235}U$ [Ma]	2σ [Ma]	$^{206}Pb/^{238}U$ [Ma]	2σ [Ma]	$^{207}Pb/^{206}Pb$	2σ [Ma]	Conc [%]^{g}
Banpo gabbro																				
BA-8	y	179380	1643	247	5103	0.13	2.1215	3.6	0.1535	2.6	0.72	0.1003	2.5	1156	42	920	24	1629	23	80
BA-8	n	166623	966	236	4530	0.46	3.7652	2.5	0.2296	2.4	0.96	0.1189	0.7	1585	39	1333	32	1940	6	84
BA-8	n	15658	513	43	2393	1.09	0.5363	2.9	0.0692	2.3	0.80	0.0562	1.7	436	13	431	10	462	19	99
BA-8	y	161370	1193	214	3801	0.43	2.5673	3.2	0.1762	2.4	0.76	0.1057	2.1	1291	41	1046	25	1726	19	81

Table A18: Laser Ablation ICP-MS U–Pb data of the Jinghong granodiorite (sample JI-7).

Sample ID	cPb	$^{207}Pb^{a}$ [cps]	U^{b} [ppm]	Pb^{b} [ppm]	$^{206}Pb/^{204}Pb$	Th/U	$^{207}Pb/^{235}U^{c}$	2σ [%]^{e}	$^{206}Pb/^{238}U^{c}$	2σ [%]^{e}	rho^{d}	$^{207}Pb/^{206}Pb^{f}$	2σ [%]^{e}	$^{207}Pb/^{235}U$ [Ma]	2σ [Ma]	$^{206}Pb/^{238}U$ [Ma]	2 s [Ma]	$^{207}Pb/^{206}Pb$	2σ [Ma]	Conc [%]^{g}
Jinghong granodiorite																				
JI-7	n	4758	261	12	15557	0.47	0.3224	3.0	0.0451	1.9	0.63	0.0519	2.4	284	9	284	5	281	27	100
JI-7	n	10288	623	29	22797	0.52	0.3266	2.1	0.0455	1.4	0.65	0.0520	1.6	287	6	287	4	287	18	100
JI-7	n	11584	714	33	20867	0.47	0.3238	2.3	0.0451	1.6	0.67	0.0521	1.7	285	7	284	4	289	20	100
JI-7	n	7455	457	21	50342	0.56	0.3201	2.5	0.0447	1.7	0.67	0.0520	1.8	282	7	282	5	284	21	100
JI-7	n	4338	262	12	16545	0.53	0.3245	2.9	0.0448	2.0	0.67	0.0525	2.2	285	8	283	6	307	25	99
JI-7	n	4226	235	11	22461	0.56	0.3205	3.0	0.0444	1.8	0.62	0.0523	2.3	282	8	280	5	300	27	99
JI-7	n	5355	302	14	8575	0.52	0.3230	2.5	0.0449	1.5	0.58	0.0522	2.1	284	7	283	4	293	24	100
JI-7	y	7853	328	16	590	0.52	0.3196	4.2	0.0447	1.9	0.45	0.0518	3.8	282	12	282	5	277	43	100
JI-7	n	4816	264	12	14549	0.48	0.3243	2.9	0.0451	1.7	0.58	0.0521	2.3	285	8	284	5	291	27	100
JI-7	y	17556	1047	50	2661	0.62	0.3214	2.9	0.0447	1.7	0.58	0.0521	2.4	283	8	282	5	291	27	100
JI-7	y	8235	473	23	1454	0.74	0.3256	5.5	0.0455	2.9	0.54	0.0519	4.6	286	16	287	8	282	53	100
JI-7	y	10098	601	28	1959	0.49	0.3238	3.2	0.0452	1.7	0.53	0.0520	2.7	285	9	285	5	284	31	100
JI-7	y	10757	474	23	2582	0.72	0.3201	3.8	0.0447	1.6	0.43	0.0520	3.5	282	11	282	5	284	40	100
JI-7	n	12155	724	34	27699	0.51	0.3259	2.3	0.0454	1.5	0.67	0.0521	1.7	286	7	286	4	290	20	100
JI-7	n	5755	341	16	17526	0.48	0.3206	3.7	0.0448	2.7	0.72	0.0519	2.6	282	11	283	8	281	30	100
JI-7	n	4333	240	11	30977	0.51	0.3239	3.7	0.0452	2.7	0.73	0.0519	2.5	285	11	285	8	283	29	100
JI-7	n	8695	530	25	28327	0.56	0.3226	2.7	0.0451	2.1	0.76	0.0519	1.8	284	8	284	6	282	20	100
JI-7	n	3879	209	10	9958	0.57	0.3230	3.1	0.0449	1.8	0.57	0.0521	2.6	284	9	283	5	291	29	100
JI-7	n	5313	291	14	10640	0.70	0.3254	2.8	0.0454	1.8	0.64	0.0520	2.2	286	8	286	5	285	25	100
JI-7	y	10094	505	23	2476	0.45	0.3080	9.4	0.0425	3.5	0.37	0.0525	8.8	273	26	269	9	308	100	99
JI-7	n	4151	170	8	12305	0.37	0.3273	6.7	0.0452	6.2	0.94	0.0525	2.3	288	19	285	18	309	27	99
JI-7	n	2825	152	7	8862	0.37	0.3174	2.9	0.0443	1.6	0.53	0.0520	2.5	280	8	279	4	285	28	100
JI-7	n	2917	161	8	146416	0.58	0.3211	3.1	0.0448	2.0	0.63	0.0520	2.4	283	9	283	6	283	28	100
JI-7	n	11773	757	35	317198	0.43	0.3267	2.3	0.0454	1.5	0.63	0.0522	1.8	287	7	286	4	296	21	100
JI-7	y	10122	596	29	14173	0.59	0.3237	3.8	0.0457	3.2	0.84	0.0514	2.1	285	11	288	9	258	24	101

Table A18 continued: Laser Ablation ICP-MS U–Pb data of the Jinghong granodiorite (sample JI-8).

Sample ID	cPb	$^{207}Pb^{a}$ [cps]	U^{b} [ppm]	Pb^{b} [ppm]	$^{206}Pb/^{204}Pb$	Th/U	$^{207}Pb/^{235}U^{c}$	2σ [%]^{c}	$^{206}Pb/^{238}U^{c}$	2σ [%]^{e}	rho^{d}	$^{207}Pb/^{206}Pb^{f}$	2σ [%]^{e}	$^{207}Pb/^{235}U$ [Ma]	2σ [Ma]	$^{206}Pb/^{238}U$ [Ma]	2σ [Ma]	$^{207}Pb/^{206}Pb$	2σ [Ma]	Conc [%]^{g}
Jinghong granodiorite																				
JI-8	n	9823	543	25	11349	0.53	0.3222	2.8	0.0450	2.0	0.71	0.0520	1.9	284	8	283	6	284	22	100
JI-8	n	8717	556	26	5540	0.62	0.3225	3.6	0.0450	3.0	0.84	0.0520	1.9	284	10	284	9	285	22	100
JI-8	y	3428	178	9	1121	0.75	0.3197	8.3	0.0448	2.9	0.34	0.0517	7.8	282	23	283	8	273	89	100
JI-8	y	16075	1009	48	9840	0.57	0.3223	3.4	0.0450	2.2	0.65	0.0519	2.6	284	10	284	6	282	30	100
JI-8	n	9139	559	26	2814	0.46	0.3238	3.4	0.0451	2.8	0.82	0.0521	2.0	285	10	284	8	291	22	100
JI-8	y	11416	579	28	1229	0.58	0.3251	3.3	0.0452	2.3	0.69	0.0522	2.3	286	9	285	6	293	27	100
JI-8	n	3400	187	9	9138	0.58	0.3185	3.4	0.0442	2.1	0.63	0.0523	2.6	281	9	279	6	298	30	99
JI-8	n	4095	234	11	1731	0.61	0.3217	3.0	0.0449	2.1	0.71	0.0520	2.1	283	9	283	6	284	24	100
JI-8	y	10940	217	13	148	0.97	0.3234	6.4	0.0448	3.2	0.50	0.0524	5.6	285	18	283	9	301	64	99
JI-8	y	4598	255	12	2559	0.62	0.3235	5.1	0.0450	3.2	0.63	0.0521	3.9	285	14	284	9	290	45	100
JI-8	n	9042	572	27	2458	0.58	0.3223	3.7	0.0449	3.3	0.90	0.0521	1.6	284	10	283	9	289	18	100
JI-8	y	6347	376	18	1667	0.64	0.3198	5.0	0.0447	2.5	0.50	0.0519	4.3	282	14	282	7	281	50	100
JI-8	n	7602	435	21	2542	0.58	0.3185	3.1	0.0445	2.6	0.84	0.0519	1.7	281	9	280	7	283	19	100
JI-8	y	10297	479	23	778	0.43	0.3220	5.7	0.0449	2.6	0.46	0.0520	5.0	283	16	283	7	285	57	100
JI-8	n	11887	629	31	2709	0.61	0.3251	2.8	0.0453	2.3	0.82	0.0521	1.6	286	8	286	6	288	18	100
JI-8	y	6862	402	19	3313	0.47	0.3204	4.1	0.0447	2.2	0.54	0.0520	3.5	282	12	282	6	285	40	100
JI-8	n	8369	494	22	2242	0.37	0.3205	2.7	0.0447	2.1	0.77	0.0520	1.7	282	8	282	6	284	20	100
JI-8	y	34446	476	31	82	1.27	0.3202	3.4	0.0446	2.5	0.74	0.0520	2.3	282	10	282	7	287	27	100
JI-8	n	8854	530	25	2004	0.47	0.3256	2.5	0.0452	2.1	0.83	0.0523	1.4	286	7	285	6	297	16	100
JI-8	y	4078	234	11	1454	0.57	0.3216	4.8	0.0449	2.7	0.56	0.0520	4.0	283	14	283	8	284	45	100
JI-8	n	4322	247	12	2512	0.64	0.3212	3.4	0.0449	2.3	0.69	0.0519	2.4	283	10	283	7	281	28	100
JI-8	n	4252	235	11	1653	0.52	0.3208	3.0	0.0448	2.3	0.74	0.0520	2.0	283	9	282	6	284	23	100
JI-8	n	6581	382	18	2015	0.52	0.3229	3.2	0.0451	2.3	0.71	0.0520	2.3	284	9	284	7	284	26	100
JI-8	n	8959	474	22	1288	0.51	0.3224	2.8	0.0447	2.2	0.80	0.0523	1.7	284	8	282	6	299	19	99
JI-8	n	8456	464	22	2230	0.61	0.3208	3.1	0.0447	2.4	0.76	0.0520	2.0	283	9	282	7	285	23	100

Table A18 continued: Laser Ablation ICP-MS U–Pb data of the Jinghong granodiorite (sample JI-56).

Sample ID	cPb	$^{207}Pb^{a}$ [cps]	U^{b} [ppm]	Pb^{b} [ppm]	$^{206}Pb/^{204}Pb$	Th/U	$^{207}Pb/^{235}U^{c}$	2σ [%]^{e}	$^{206}Pb/^{238}U^{c}$	2σ [%]^{e}	rho^{d}	$^{207}Pb/^{206}Pb^{f}$	2σ [%]^{e}	$^{207}Pb/^{235}U$ [Ma]	2σ [Ma]	$^{206}Pb/^{238}U$ [Ma]	2σ [Ma]	$^{207}Pb/^{206}Pb$	2σ [Ma]	Conc [%]^{g}
Jinghhong granodiorite																				
JI-56	n	8053	438	20	11760	0.46	0.3198	2.6	0.0447	2.0	0.75	0.0519	1.7	282	7	282	6	281	20	100
JI-56	n	2474	54	3	2716	0.76	0.3217	4.3	0.0447	2.2	0.52	0.0522	3.6	283	12	282	6	293	41	100
JI-56	n	4542	212	10	9951	0.65	0.3205	3.3	0.0443	1.9	0.59	0.0525	2.7	282	9	280	5	305	30	99
JI-56	n	6395	330	16	21475	0.67	0.3306	3.0	0.0452	2.1	0.69	0.0530	2.2	290	9	285	6	330	24	98
JI-56	n	4844	152	8	6255	0.54	0.3233	8.5	0.0450	3.2	0.38	0.0520	7.9	284	24	284	9	287	90	100
JI-56	n	3989	193	9	9610	0.63	0.3199	3.3	0.0445	2.1	0.65	0.0521	2.5	282	9	281	6	290	28	100
JI-56	n	4007	194	9	8642	0.66	0.3213	3.2	0.0448	2.2	0.67	0.0520	2.4	283	9	282	6	288	28	100
JI-56	n	4533	218	10	6727	0.55	0.3211	3.4	0.0448	2.2	0.64	0.0519	2.6	283	10	283	6	282	30	100
JI-56	n	7973	462	22	2349	0.62	0.3195	2.8	0.0446	2.1	0.75	0.0519	1.8	282	8	282	6	282	21	100
JI-56	n	2569	116	6	6152	0.59	0.3220	3.6	0.0449	2.3	0.62	0.0520	2.9	283	10	283	6	287	33	100
JI-56	n	4495	226	11	2288	0.53	0.3215	3.8	0.0446	2.6	0.69	0.0522	2.7	283	11	281	7	296	31	99
JI-56	y	11612	688	32	4547	0.55	0.3218	4.0	0.0448	2.3	0.59	0.0521	3.2	283	11	283	7	288	37	100
JI-56	y	10247	623	29	3491	0.56	0.3199	3.5	0.0447	2.3	0.66	0.0519	2.6	282	10	282	6	282	30	100
JI-56	n	9397	542	25	4462	0.42	0.3203	2.7	0.0448	2.1	0.77	0.0518	1.7	282	8	283	6	277	20	100
JI-56	n	7683	435	21	2114	0.59	0.3221	2.7	0.0447	1.9	0.72	0.0522	1.9	284	8	282	5	296	22	99
JI-56	n	3243	193	9	1746	0.77	0.3223	3.2	0.0448	2.1	0.65	0.0522	2.4	284	9	282	6	294	28	100
JI-56	y	7760	425	20	1503	0.50	0.3209	3.7	0.0446	2.2	0.59	0.0521	3.0	283	10	282	6	292	34	100
JI-56	n	7295	405	19	1124	0.51	0.3206	2.6	0.0444	1.8	0.70	0.0524	1.8	282	7	280	5	302	21	99
JI-56	n	7308	406	19	1486	0.61	0.3214	2.8	0.0445	2.1	0.77	0.0523	1.8	283	8	281	6	299	20	99
JI-56	n	9198	517	24	1896	0.43	0.3203	2.5	0.0447	1.8	0.74	0.0520	1.7	282	7	282	5	283	19	100
JI-56	n	7190	400	18	2187	0.42	0.3229	2.6	0.0449	1.8	0.69	0.0521	1.9	284	7	283	5	292	22	100
JI-56	n	8509	475	22	1819	0.54	0.3180	2.4	0.0443	1.8	0.74	0.0520	1.6	280	7	280	5	287	18	100
JI-56	n	9363	537	25	2322	0.47	0.3204	2.3	0.0447	1.7	0.74	0.0520	1.5	282	6	282	5	286	17	100
JI-56	y	13282	717	34	1174	0.59	0.3189	5.2	0.0445	3.9	0.75	0.0520	3.4	281	15	281	11	283	39	100
JI-56	n	12976	791	36	3828	0.43	0.3203	2.2	0.0447	1.7	0.77	0.0520	1.4	282	6	282	5	284	16	100

Table A19: Laser Ablation ICP-MS U–Pb data of the Paleng amphibole gabbro (sample JI-25).

Sample ID	cPb	$^{207}Pb^{a}$ [cps]	U^{b} [ppm]	Pb^{b} [ppm]	$^{206}Pb/^{204}Pb$	Th/U	$^{207}Pb/^{235}U^{c}$	2σ [%]^{e}	$^{206}Pb/^{238}U^{c}$	2σ [%]^{e}	rho^{d}	$^{207}Pb/^{206}Pb^{f}$	2σ [%]^{e}	$^{207}Pb/^{235}U$ [Ma]	2σ [Ma]	$^{206}Pb/^{238}U$ [Ma]	2σ [Ma]	$^{207}Pb/^{206}Pb$	2σ [Ma]	Conc [%]^{g}
Paleng amphibole gabbro																				
JI-25	n	61502	4117	156	12007	0.05	0.2918	2.9	0.0411	2.7	0.95	0.0515	0.9	260	7	260	7	263	11	100
JI-25	n	129364	7933	298	1621	0.08	0.2831	5.1	0.0398	4.4	0.85	0.0516	2.6	253	13	252	11	267	30	99
JI-25	y	86282	5737	223	22415	0.06	0.2987	3.0	0.0421	2.9	0.95	0.0514	1.0	265	8	266	8	259	11	100
JI-25	y	136950	10988	444	3281	0.08	0.2975	4.5	0.0421	4.4	0.98	0.0513	1.0	264	12	266	12	254	11	100
JI-25	y	146605	9398	353	3402	0.11	0.2861	4.2	0.0406	3.4	0.81	0.0512	2.5	255	11	256	9	248	29	100
JI-25	n	115742	7235	272	13625	0.05	0.2898	3.8	0.0408	3.8	0.98	0.0516	0.7	258	10	258	10	266	8	100
JI-25	y	68855	4040	158	3909	0.08	0.2977	3.7	0.0421	3.5	0.94	0.0513	1.3	265	10	266	9	255	15	100
JI-25	y	128011	7656	292	2435	0.09	0.2913	4.7	0.0411	3.6	0.76	0.0514	3.1	260	12	260	9	257	35	100
JI-25	y	111505	4781	198	502	0.05	0.2926	5.2	0.0413	3.9	0.75	0.0514	3.4	261	14	261	10	260	39	100
JI-25	n	81491	5198	199	20554	0.05	0.2913	3.5	0.0415	3.4	0.98	0.0509	0.8	260	9	262	9	236	9	101
JI-25	n	105375	6877	256	13400	0.04	0.2849	3.3	0.0404	3.1	0.95	0.0511	1.0	255	8	256	8	245	12	100
JI-25	n	496804	23734	304	1956	0.05	0.6157	25.5	0.0062	8.7	0.34	0.7183	24.0	487	124	40	3	4768	172	8
JI-25	y	129397	9041	289	2411	0.04	0.2432	6.3	0.0342	5.8	0.91	0.0516	2.6	221	14	217	12	266	30	98
JI-25	n	205597	22906	210	5966	0.02	0.1939	20.6	0.0062	13.2	0.64	0.2280	15.7	180	37	40	5	3038	126	22
JI-25	n	163166	13157	296	8346	0.07	0.3282	24.0	0.0230	18.8	0.78	0.1036	14.9	288	69	146	27	1690	137	51
JI-25	y	100689	6539	260	4423	1.09	0.3037	4.8	0.0429	4.4	0.92	0.0514	1.9	269	13	271	12	257	22	101
JI-25	n	2676	62	3	142	1.07	0.3871	8.7	0.0409	4.7	0.54	0.0687	7.3	332	29	258	12	889	75	78
JI-25	y	771625	13651	303	27	0.05	0.2036	17.0	0.0151	5.8	0.34	0.0979	16.0	188	32	97	6	1584	149	51
JI-25	y	48299	2270	117	1122	0.17	0.3318	4.7	0.0475	4.5	0.96	0.0507	1.4	291	14	299	13	228	16	103
JI-25	y	182719	10152	259	812	0.06	0.2662	8.6	0.0256	5.9	0.69	0.0755	6.2	240	21	163	10	1082	62	68
JI-25	n	363853	20810	139	58	0.02	0.1576	26.6	0.0039	17.9	0.67	0.2939	19.7	149	39	25	4	3439	153	17
JI-25	n	183359	11366	391	506	-0.15	0.4576	26.7	0.0325	5.9	0.22	0.1022	26.1	383	102	206	12	1665	241	54
JI-25	y	578733	6643	403	57	0.08	0.3533	6.9	0.0486	4.6	0.67	0.0527	5.2	307	21	306	14	315	59	100

Table A19 continued: Laser Ablation ICP-MS U–Pb data of the Paleng amphibole gabbro (sample JI-32).

Sample ID	cPb	$^{207}Pb^{a}$ [cps]	U^{b} [ppm]	Pb^{b} [ppm]	$^{206}Pb/^{204}Pb$	Th/U	$^{207}Pb/^{235}U^{c}$	2σ [%]^{e}	$^{206}Pb/^{238}U^{c}$	2σ [%]^{e}	rho^{d}	$^{207}Pb/^{206}Pb^{f}$	2σ [%]^{e}	$^{207}Pb/^{235}U$ [Ma]	2σ [Ma]	$^{206}Pb/^{238}U$ [Ma]	2σ [Ma]	$^{207}Pb/^{206}Pb$	2σ [Ma]	Conc [%]^{g}
Paleng amphibole gabbro																				
JI-32	y	15401	968	41	119775	0.47	0.2939	4.5	0.0413	3.7	0.82	0.0516	2.6	262	12	261	10	269	30	100
JI-32	y	9839	619	25	35334	0.31	0.2868	4.3	0.0405	3.4	0.78	0.0514	2.7	256	11	256	9	259	31	100
JI-32	n	9839	619	25	115677	0.31	0.2878	5.0	0.0406	4.9	0.97	0.0515	1.3	257	13	256	12	261	14	100
JI-32	n	23403	1533	61	149165	0.28	0.2908	3.9	0.0410	3.7	0.93	0.0515	1.5	259	10	259	9	263	17	100
JI-32	n	15401	990	40	246638	0.29	0.2895	3.6	0.0409	3.3	0.90	0.0513	1.6	258	9	259	8	254	18	100
JI-32	y	10573	678	27	38836	0.31	0.2912	4.7	0.0410	3.3	0.70	0.0515	3.4	259	12	259	9	265	39	100
JI-32	y	11123	674	28	41282	0.44	0.2927	4.0	0.0413	3.3	0.81	0.0514	2.3	261	10	261	9	259	27	100
JI-32	y	11759	710	29	51794	0.39	0.2903	4.5	0.0407	3.7	0.82	0.0517	2.6	259	12	257	9	273	29	99
JI-32	n	14934	930	39	263740	0.52	0.2854	3.8	0.0402	3.4	0.90	0.0514	1.7	255	10	254	9	260	19	100
JI-32	n	37290	94	44	40943	0.88	0.2957	4.2	0.0414	3.6	0.86	0.0518	2.2	263	11	262	10	275	25	99
JI-32	n	8310	478	20	54334	0.41	0.2768	3.6	0.0388	3.1	0.86	0.0517	1.8	248	9	246	8	272	21	99
JI-32	n	15332	930	38	81530	0.54	0.2874	3.9	0.0405	3.6	0.91	0.0515	1.6	256	10	256	9	261	18	100
JI-32	n	18825	1171	49	112693	0.47	0.2844	3.4	0.0400	3.2	0.94	0.0515	1.1	254	9	253	8	264	13	100
JI-32	y	25592	1676	68	63698	0.35	0.2865	3.8	0.0404	3.2	0.85	0.0514	2.0	256	10	255	8	259	23	100
JI-32	y	14991	973	39	66486	0.36	0.2927	4.1	0.0412	3.2	0.78	0.0515	2.5	261	11	260	8	264	29	100
JI-32	y	14928	945	39	113082	0.35	0.2889	3.6	0.0407	3.3	0.90	0.0515	1.5	258	9	257	8	263	18	100
JI-32	n	20710	1323	54	50197	0.35	0.2930	3.4	0.0413	3.1	0.92	0.0515	1.3	261	9	261	8	262	15	100
JI-32	n	14122	869	36	82757	0.35	0.2866	3.4	0.0406	3.1	0.92	0.0512	1.3	256	9	256	8	251	15	100
JI-32	n	8947	531	21	16676	0.31	0.2906	2.6	0.0408	2.1	0.80	0.0517	1.5	259	7	258	5	273	18	99
JI-32	n	13473	735	30	919	0.32	0.2904	2.7	0.0408	2.3	0.84	0.0517	1.5	259	7	258	6	271	17	99
JI-32	n	7276	433	18	39383	0.31	0.2945	2.9	0.0415	2.2	0.75	0.0515	1.9	262	8	262	6	265	22	100
JI-32	n	10112	623	25	23811	0.23	0.2952	2.9	0.0414	2.4	0.81	0.0517	1.7	263	8	262	6	272	20	100
JI-32	y	13585	817	33	5025	0.31	0.2893	3.2	0.0408	2.4	0.76	0.0514	2.1	258	8	258	6	258	24	100
JI-32	n	4974	188	11	74073	0.88	7.3781	3.3	0.3921	3.1	0.94	0.1365	1.1	2158	72	2133	67	2183	10	99
JI-32	n	11916	767	30	9535	0.25	0.3892	6.8	0.0475	3.2	0.47	0.0594	6.0	334	23	299	10	583	65	90

Table A20: Laser Ablation ICP-MS U–Pb data of the Paleng porphyritic basalt (sample JI-26).

Sample ID	cPb	$^{207}Pb^{a}$ [cps]	U^{b} [ppm]	Pb^{b} [ppm]	$^{206}Pb/^{204}Pb$	Th/U	$^{207}Pb/^{235}U^{c}$	2σ [%]^{e}	$^{206}Pb/^{238}U^{c}$	2σ [%]^{e}	rho^{d}	$^{207}Pb/^{206}Pb^{f}$	2σ [%]^{e}	$^{207}Pb/^{235}U$ [Ma]	2σ [Ma]	$^{206}Pb/^{238}U$ [Ma]	2σ [Ma]	$^{207}Pb/^{206}Pb$	2σ [Ma]	Conc [%]^{g}
Paleng porphyritic basalt/in situ zircons																				
JI-26	n	12260	784	31	2976	0.25	0.2914	3.4	0.0402	2.7	0.77	0.0525	2.2	260	9	254	7	308	25	98
JI-26	n	23945	1525	60	7381	0.11	0.2966	3.8	0.0419	3.6	0.93	0.0513	1.4	264	10	265	9	256	17	100
JI-26	n	18965	1146	47	9017	0.21	0.3006	3.3	0.0423	2.8	0.84	0.0515	1.8	267	9	267	7	264	20	100
JI-26	n	14837	911	38	6040	0.33	0.2974	3.3	0.0421	3.0	0.90	0.0512	1.4	264	9	266	8	251	16	101
JI-26	n	14729	910	38	4624	0.37	0.2918	3.2	0.0410	2.9	0.90	0.0516	1.4	260	8	259	7	266	15	100
JI-26	n	13094	776	33	4583	0.41	0.2998	3.1	0.0421	2.6	0.84	0.0516	1.7	266	8	266	7	268	19	100
JI-26	y	8357	365	18	1714	0.52	0.3025	4.9	0.0423	3.7	0.76	0.0518	3.2	268	13	267	10	277	37	100
JI-26	n	51654	3353	149	16545	0.06	0.3027	3.1	0.0427	2.8	0.90	0.0514	1.3	269	8	269	8	260	15	100
JI-26	n	14185	944	40	7011	0.41	0.2963	3.1	0.0416	2.6	0.84	0.0517	1.6	264	8	263	7	272	19	100
JI-26	n	49056	3149	136	13060	0.06	0.2926	3.0	0.0414	2.8	0.92	0.0512	1.2	261	8	262	7	250	13	100
JI-26	n	12361	757	32	3681	0.52	0.2917	3.3	0.0409	2.9	0.90	0.0518	1.4	260	8	258	8	275	16	99
JI-26	n	16300	1034	42	5502	0.27	0.2906	2.8	0.0410	2.5	0.90	0.0514	1.2	259	7	259	7	258	14	100
JI-26	n	11080	708	30	5688	0.53	0.2882	3.3	0.0406	2.9	0.87	0.0515	1.6	257	9	257	7	263	19	100
JI-26	n	13429	823	34	4037	0.38	0.2865	3.8	0.0404	3.5	0.92	0.0514	1.5	256	10	256	9	258	17	100
JI-26	y	12800	782	33	2906	0.43	0.2966	3.9	0.0419	3.1	0.80	0.0513	2.3	264	10	265	8	254	27	100
JI-26	n	14419	918	40	69901	0.62	0.2963	3.4	0.0415	3.0	0.89	0.0518	1.5	264	9	262	8	277	18	99
Inherited zircons																				
JI-26	n	4589	102	16	1719	2.77	0.7701	4.1	0.0931	3.3	0.81	0.0600	2.4	580	24	574	19	604	26	99
JI-26	n	190852	460	196	11121	0.71	7.8096	3.0	0.3547	2.9	0.97	0.1597	0.8	2209	66	1957	57	2452	6	89
JI-26	y	13896	400	33	301	0.62	0.5968	3.9	0.0752	3.1	0.79	0.0575	2.4	475	19	468	15	512	26	98
JI-26	n	13199	151	24	5675	0.36	1.6056	4.2	0.1549	3.8	0.91	0.0752	1.8	972	41	928	35	1073	18	95
JI-26	n	13862	240	27	3606	0.56	0.8616	11.1	0.0907	10.8	0.98	0.0689	2.2	631	70	560	61	895	23	89
JI-26	n	1848	31	3	3918	0.96	0.6891	4.4	0.0867	3.0	0.69	0.0576	3.1	532	23	536	16	516	34	101
JI-26	n	9354	249	26	13122	1.02	0.7043	3.4	0.0884	2.9	0.86	0.0578	1.7	541	18	546	16	520	19	101
JI-26	n	258226	505	313	27238	0.76	13.8068	2.9	0.5400	2.6	0.92	0.1854	1.1	2737	78	2784	74	2702	9	102
JI-26	y	12687	434	32	924	0.23	0.6619	8.2	0.0738	6.7	0.82	0.0650	4.7	516	42	459	31	775	50	89
JI-26	n	23679	304	44	11817	0.22	1.4401	3.0	0.1486	2.8	0.94	0.0703	1.0	906	27	893	25	937	11	99
JI-26	n	19867	274	38	9035	0.24	1.3677	4.5	0.1417	4.2	0.95	0.0700	1.4	875	39	854	36	929	15	98

Table A21: Laser Ablation ICP-MS U–Pb data of the Jinghong dacite (sample JI-49).

Sample ID	cPb	$^{207}Pb^{a}$ [cps]	U^{b} [ppm]	Pb^{b} [ppm]	$^{206}Pb/^{204}Pb$	Th/U	$^{207}Pb/^{235}U^{c}$	2σ [%]^{e}	$^{206}Pb/^{238}U^{c}$	2σ [%]^{e}	rho^{d}	$^{207}Pb/^{206}Pb^{f}$	2σ [%]^{e}	$^{207}Pb/^{235}U$ [Ma]	2σ [Ma]	$^{206}Pb/^{238}U$ [Ma]	2σ [Ma]	$^{207}Pb/^{206}Pb$	2σ [Ma]	Conc [%]^{g}
Jinghong basalt																				
JI-49	n	9449	312	16	124	1.82	0.3004	7.6	0.0393	3.4	0.44	0.0555	6.8	267	20	248	8	431	76	93
JI-49	n	11550	418	21	226	1.21	0.2784	4.2	0.0394	3.4	0.82	0.0512	2.4	249	10	249	9	252	28	100
JI-49	n	5176	172	9	123	1.18	0.2920	4.7	0.0391	3.9	0.84	0.0541	2.5	260	12	247	10	377	29	95
JI-49	n	3601	118	6	108	1.18	0.2957	5.5	0.0393	2.9	0.53	0.0546	4.7	263	15	249	7	395	52	94
JI-49	n	3362	73	5	78	1.93	0.2776	6.4	0.0393	3.3	0.52	0.0512	5.5	249	16	249	8	250	63	100
JI-49	n	3009	30	3	37	0.49	0.2814	17.1	0.0396	4.1	0.24	0.0516	16.6	252	43	250	10	267	191	99
JI-49	n	897	19	1	35	0.59	0.3711	12.5	0.0387	6.6	0.52	0.0695	10.7	320	40	245	16	913	110	76
JI-49	n	3093	16	2	26	2.11	0.4568	8.4	0.0393	8.1	0.96	0.0843	2.3	382	32	249	20	1299	22	65

Table A22: Laser Ablation ICP-MS U–Pb data of the Lincang granite (sample LI-5).

Sample ID	cPb	$^{207}Pb^{a}$ [cps]	U^{b} [ppm]	Pb^{b} [ppm]	$^{206}Pb/^{204}Pb$	Th/U	$^{207}Pb/^{235}U^{c}$	2σ [%]^{e}	$^{206}Pb/^{238}U^{c}$	2σ [%]^{e}	rho^{d}	$^{207}Pb/^{206}Pb^{f}$	2σ [%]^{e}	$^{207}Pb/^{235}U$ [Ma]	2σ [Ma]	$^{206}Pb/^{238}U$ [Ma]	2σ [Ma]	$^{207}Pb/^{206}Pb$	2σ [Ma]	Conc [%]^{g}
Lincang granite																				
LI-5	n	12823	880	40	8940	1.00	0.2727	3.6	0.0372	3.0	0.83	0.0531	2.0	245	9	236	7	335	23	96
LI-5	n	9568	561	22	2222	0.44	0.2746	4.6	0.0387	2.3	0.51	0.0515	4.0	246	11	245	6	263	46	99
LI-5	y	18754	254	15	100	2.08	0.2642	6.7	0.0373	3.4	0.51	0.0514	5.7	238	16	236	8	259	66	99
LI-5	n	7509	494	20	3924	0.59	0.2642	3.4	0.0372	2.9	0.84	0.0515	1.8	238	8	235	7	264	21	99
LI-5	y	8949	592	25	4683	0.86	0.2623	3.4	0.0371	2.5	0.73	0.0513	2.4	237	8	235	6	255	27	99
LI-5	y	7593	356	15	521	1.07	0.2656	5.0	0.0375	2.5	0.50	0.0513	4.3	239	12	238	6	255	50	99
LI-5	y	9124	442	18	643	0.52	0.2695	8.0	0.0382	3.8	0.48	0.0512	7.1	242	19	241	9	250	81	100
LI-5	y	248762	697	125	2	7.81	0.2696	5.8	0.0381	3.8	0.66	0.0513	4.3	242	14	241	9	255	50	99
LI-5	y	12774	768	30	1857	0.38	0.2699	4.2	0.0385	3.1	0.74	0.0509	2.8	243	10	243	8	234	33	100
LI-5	y	16788	303	16	118	1.02	0.2651	6.9	0.0377	3.2	0.46	0.0511	6.2	239	17	238	8	243	71	100
LI-5	y	3152	168	7	806	0.57	0.2645	5.9	0.0376	2.7	0.46	0.0510	5.3	238	14	238	6	240	61	100
LI-5	y	5154	290	11	1188	0.53	0.2620	5.4	0.0372	2.6	0.48	0.0512	4.8	236	13	235	6	248	55	100
LI-5	y	11596	693	28	2487	0.89	0.2662	5.0	0.0371	4.1	0.81	0.0520	2.9	240	12	235	10	285	33	98
LI-5	y	9193	521	21	1355	0.55	0.2712	4.4	0.0385	2.7	0.62	0.0511	3.5	244	11	244	7	243	40	100
LI-5	n	4905	325	13	1409	0.57	0.2635	3.1	0.0373	2.1	0.69	0.0512	2.2	237	7	236	5	248	26	100
LI-5	y	6288	362	15	1753	0.62	0.2742	11.0	0.0387	4.6	0.42	0.0514	10.0	246	27	245	11	257	115	100
LI-5	y	3127	162	7	2201	0.57	0.2730	5.8	0.0389	2.4	0.41	0.0509	5.3	245	14	246	6	238	61	100
LI-5	y	12821	799	34	1454	0.64	0.2640	3.4	0.0376	3.1	0.90	0.0509	1.5	238	8	238	7	235	17	100
LI-5	n	39679	2570	103	12949	0.06	0.2642	2.8	0.0375	2.5	0.88	0.0511	1.3	238	7	237	6	245	16	100
LI-5	y	9414	236	12	187	1.15	0.2715	5.4	0.0384	3.3	0.61	0.0513	4.3	244	13	243	8	254	49	100
LI-5	y	5212	316	12	2303	0.49	0.2630	4.6	0.0374	2.0	0.44	0.0510	4.1	237	11	237	5	242	47	100
LI-5	n	5495	329	15	1339	0.97	0.2689	3.3	0.0380	2.5	0.75	0.0513	2.2	242	8	241	6	255	25	99
LI-5	n	3274	175	8	838	1.04	0.2670	3.8	0.0381	2.5	0.67	0.0508	2.8	240	9	241	6	234	32	100
LI-5	y	18489	1168	45	901	0.39	0.2662	3.6	0.0377	2.3	0.66	0.0512	2.7	240	9	238	6	252	31	99
LI-5	n	6880	419	18	3160	0.84	0.2712	3.1	0.0384	2.3	0.73	0.0512	2.1	244	8	243	6	250	24	100

Table A23: Laser Ablation ICP-MS U–Pb data of the Jinghong basalt (sample JI-52).

Sample ID	cPb	$^{207}Pb^{a}$ [cps]	U^{b} [ppm]	Pb^{b} [ppm]	$^{206}Pb/^{204}Pb$	Th/U	$^{207}Pb/^{235}U^{c}$	2σ [%]^{e}	$^{206}Pb/^{238}U^{c}$	2σ [%]^{e}	rho^{d}	$^{207}Pb/^{206}Pb^{f}$	2σ [%]^{e}	$^{207}Pb/^{235}U$ [Ma]	2σ [Ma]	$^{206}Pb/^{238}U$ [Ma]	2σ [Ma]	$^{207}Pb/^{206}Pb$	2σ [Ma]	Conc [%]^{g}
Jinghong basalt																				
JI-52	n	15621	2198	160	978	0.56	0.2127	4.0	0.0304	3.6	0.91	0.0507	1.6	196	8	193	7	225	19	99
JI-52	n	6012	589	46	306	0.76	0.2193	5.5	0.0308	5.1	0.93	0.0516	2.1	201	11	196	10	267	24	97
JI-52	n	3907	259	14	176	1.84	0.2470	6.4	0.0308	3.9	0.61	0.0582	5.1	224	14	195	8	537	55	87
JI-52	n	2888	126	7	135	2.11	0.2175	5.8	0.0299	4.1	0.71	0.0528	4.0	200	12	190	8	320	46	95
JI-52	n	7435	389	17	146	1.02	0.2093	9.9	0.0306	5.0	0.50	0.0497	8.5	193	19	194	10	179	100	101
JI-52	n	12207	1301	71	947	0.25	0.2118	5.2	0.0304	4.4	0.85	0.0506	2.8	195	10	193	8	221	32	99
JI-52	n	4522	340	16	211	1.64	0.2217	16.2	0.0314	3.8	0.23	0.0512	15.8	203	33	199	8	250	182	98
JI-52	n	3979	394	24	453	2.98	0.2074	12.4	0.0304	4.9	0.39	0.0495	11.4	191	24	193	9	173	133	101
JI-52	n	6487	771	60	482	0.64	0.2084	8.6	0.0301	4.8	0.56	0.0502	7.1	192	17	191	9	202	83	100
JI-52	n	6008	544	24	273	1.42	0.2161	6.2	0.0313	5.0	0.81	0.0500	3.7	199	12	199	10	197	43	100
JI-52	n	4459	201	11	111	2.72	0.2138	8.2	0.0307	6.5	0.79	0.0505	5.0	197	16	195	13	217	58	99
JI-52	n	3060	192	10	184	2.06	0.2311	18.4	0.0311	4.7	0.26	0.0539	17.7	211	39	197	9	366	200	94
JI-52	n	2804	265	15	309	3.58	0.2132	5.9	0.0303	4.3	0.74	0.0510	3.9	196	11	193	8	240	45	98

Table A24: $^{40}Ar/^{39}Ar$ stepped heating data of the Banpo gabbro (sample BA-24).

Temp.	$^{38}Ar^*$	$\pm^{38}Ar^*$	^{39}Ar	$\pm^{39}Ar$	^{40}Ar	$\pm^{40}Ar$	$^{40}Ar^{*4}$	$\pm^{40}Ar^{*4}$	$^{40}Ar^{*4}$	$\pm^{40}Ar^{*4}$	Cl^1	$\pm Cl^1$	Ca^2	$\pm Ca^2$	K^3	$\pm K^3$	$^{40}Ar/^{39}Ar$	$\pm^{40}Ar/^{39}Ar$	$^{40}Ar/K$	$\pm^{40}Ar/K$	Age	±Age
°C	(cc)	(cc)	(cc)	(cc)	(cc)	(cc)	(cc)	(cc)	(mol)	(mol)	(mol)	(mol)	(mol)	(mol)	(mol)	(mol)					(Ma)	(Ma)
BA-24 whole-rock				sample wt = 0.01660g		J = 0.010991 +/- 0.000040																
600	1.11E-10	5.63E-13	1.12E-08	8.49E-12	1.05E-07	8.21E-11	7.47E-08	5.99E-11	3.33E-12	2.67E-15	5.87E-09	4.57E-11	3.51E-07	2.29E-08	3.71E-06	1.38E-08	6.7	0.0	8.99E-07	3.42E-09	127.92	0.56
700	1.03E-10	8.76E-13	7.06E-10	1.43E-12	1.45E-08	1.10E-11	7.81E-09	2.45E-11	3.48E-13	1.09E-15	5.46E-09	5.64E-11	9.38E-07	4.79E-08	2.34E-07	9.75E-10	11.1	0.3	1.49E-06	7.76E-09	207.10	4.94
800	1.81E-11	2.16E-13	6.73E-10	2.73E-12	1.22E-08	1.11E-11	8.81E-09	3.96E-11	3.93E-13	1.76E-15	9.54E-10	1.27E-11	5.87E-07	2.63E-08	2.23E-07	1.22E-09	13.1	0.2	1.76E-06	1.24E-08	242.24	4.31
900	1.28E-11	5.32E-13	8.39E-10	1.74E-12	1.25E-08	1.18E-11	1.03E-08	2.77E-11	4.60E-13	1.24E-15	6.75E-10	2.83E-11	7.31E-07	2.37E-08	2.79E-07	1.17E-09	12.3	0.2	1.65E-06	8.22E-09	228.65	3.71
950	1.39E-11	2.87E-13	1.10E-09	1.18E-12	1.61E-08	1.21E-11	1.32E-08	2.57E-11	5.88E-13	1.15E-15	7.32E-10	1.57E-11	6.78E-07	2.09E-08	3.67E-07	1.39E-09	11.9	0.2	1.60E-06	6.84E-09	222.20	4.14
1000	1.52E-11	4.96E-13	9.06E-10	1.37E-12	1.36E-08	1.07E-11	1.07E-08	2.43E-11	4.78E-13	1.08E-15	8.00E-10	2.66E-11	6.91E-07	3.64E-08	3.01E-07	1.19E-09	11.8	0.2	1.59E-06	7.23E-09	220.58	3.59
1075	3.34E-11	7.21E-13	9.99E-10	1.13E-12	1.52E-08	1.17E-11	1.20E-08	2.50E-11	5.33E-13	1.11E-15	1.76E-09	3.94E-11	9.02E-07	4.01E-08	3.32E-07	1.26E-09	12.0	0.2	1.61E-06	6.99E-09	222.87	4.34
1175	1.31E-10	4.08E-13	7.49E-10	6.67E-13	1.57E-08	1.38E-11	9.83E-09	2.23E-11	4.39E-13	9.96E-16	6.91E-09	4.63E-11	1.69E-06	3.53E-08	2.49E-07	9.31E-10	13.1	0.3	1.77E-06	7.73E-09	243.13	5.44
1300	3.08E-10	5.95E-13	1.62E-09	1.51E-12	3.22E-08	2.45E-11	2.22E-08	2.85E-11	9.91E-13	1.27E-15	1.62E-08	1.01E-10	3.43E-06	2.98E-08	5.38E-07	2.02E-09	13.7	0.1	1.84E-06	7.30E-09	252.75	2.41
1400	2.06E-10	7.45E-13	9.39E-10	9.50E-13	2.37E-08	1.81E-11	1.28E-08	2.36E-11	5.73E-13	1.05E-15	1.09E-08	7.55E-11	2.36E-06	3.68E-08	3.12E-07	1.18E-09	13.7	0.2	1.84E-06	7.72E-09	252.57	4.03
1600	4.48E-11	5.10E-13	2.74E-10	5.23E-13	5.78E-08	6.38E-11	5.82E-09	2.28E-11	2.60E-13	1.02E-15	2.36E-09	3.03E-11	7.50E-07	9.69E-09	9.10E-08	3.74E-10	21.2	0.8	2.86E-06	1.62E-08	378.46	12.86

[1] Determined from $^{37}Cl(n,\gamma,\beta)^{38}Ar$: $Cl = 9.0159\times10^{4}.\frac{^{38}Ar}{\beta\cdot J}\cdot(\text{mole/mole});\ \beta=\left(\frac{K}{Cl}\cdot\frac{^{38}Ar}{^{39}Ar}\right)_{Hb3gr};\ (K/Cl)_{Hb3gr}=5.242;\ \beta=3.46\pm0.06$

[2] Determined from $^{40}Ca(n,\alpha)^{37}Ar$: $Ca = 8.042\times10^{4}.\frac{^{37}Ar}{\alpha\cdot J}\cdot(\text{mole/mole});\ \alpha=\left(\frac{K}{Ca}\cdot\frac{^{37}Ar}{^{39}Ar}\right)_{Hb3gr};\ (K/Ca)_{Hb3gr}=0.1674;\ \alpha=0.52\pm0.02$

[3] Determined from $^{39}K(n,p)^{39}Ar$: $K=\frac{^{39}Ar}{J}\cdot\frac{K}{^{40}K}\cdot\frac{\lambda}{\lambda_e}$ (mole/mole); $\lambda/\lambda_e=0.581;\ K/^{40}K=1.167\times10^{-4};\ J=0.01803\pm0.00010$

[4] $^{40}Ar^* = {}^{40}Ar$ total - $295.5\times{}^{36}Ar$

[5] 2σ errors include uncertainties on the J value.

Table A25: $^{40}Ar/^{39}Ar$ stepped heating data of the Banpo rhyolite (sample BA-12; not discussed in this thesis).

Temp.	$^{38}Ar^*$	$\pm^{38}Ar^*$	^{39}Ar	$\pm^{39}Ar$	^{40}Ar	$\pm^{40}Ar$	$^{40}Ar^{*4}$	$\pm^{40}Ar^{*4}$	$^{40}Ar^{*4}$	$\pm^{40}Ar^{*4}$	Cl^1	$\pm Cl^1$	Ca^2	$\pm Ca^2$	K^3	$\pm K^3$	$^{40}Ar/^{39}Ar$	$\pm^{40}Ar/^{39}Ar$	$^{40}Ar/K$	$\pm^{40}Ar/K$	Age	±Age
°C	(cc)	(cc)	(cc)	(cc)	(cc)	(cc)	(cc)	(cc)	(mol)	(mol)	(mol)	(mol)	(mol)	(mol)	(mol)	(mol)					(Ma)	(Ma)
BA-12	whole-rock			sample wt = 0.01956g		J = 0.010709 +/- 0.000040																
500	7.62E-11	2.32E-13	1.91E-09	1.33E-12	2.54E-08	1.26E-11	6.02E-09	1.85E-11	2.68E-13	8.26E-16	4.12E-09	2.77E-11	1.68E-07	3.42E-08	6.51E-07	2.47E-09	3.15	0.09	4.12E-07	2.02E-09	59.79	1.77
600	2.68E-11	5.72E-13	1.02E-08	4.74E-12	7.08E-08	1.13E-10	6.78E-08	3.83E-11	3.03E-12	1.71E-15	1.45E-09	3.21E-11	3.62E-07	3.49E-08	3.47E-06	1.31E-08	6.65	0.03	8.72E-07	3.32E-09	124.16	0.64
650	1.28E-11	4.59E-13	1.16E-08	4.85E-12	6.61E-08	2.70E-11	6.36E-08	3.25E-11	2.84E-12	1.45E-15	6.94E-10	2.52E-11	3.72E-07	1.20E-08	3.95E-06	1.49E-08	5.48	0.02	7.18E-07	2.72E-09	102.88	0.48
675	1.17E-11	5.66E-13	5.84E-09	2.75E-12	2.91E-08	1.32E-11	2.71E-08	2.20E-11	1.21E-12	9.81E-16	6.32E-10	3.09E-11	3.30E-07	2.68E-08	1.99E-06	7.49E-09	4.63	0.03	6.07E-07	2.34E-09	87.30	0.64
700	8.91E-12	4.05E-13	2.85E-09	1.51E-12	1.33E-08	5.97E-12	1.21E-08	2.16E-11	5.39E-13	9.63E-16	4.82E-10	2.21E-11	6.26E-08	3.99E-08	9.70E-07	3.66E-09	4.24	0.08	5.56E-07	2.32E-09	80.14	1.55
750	1.46E-11	6.19E-13	2.58E-09	1.03E-12	1.13E-08	4.97E-12	1.03E-08	2.14E-11	4.60E-13	9.55E-16	7.91E-10	3.38E-11	7.03E-08	3.90E-08	8.78E-07	3.30E-09	4.00	0.09	5.24E-07	2.25E-09	75.69	1.77
850	2.69E-11	2.42E-13	2.98E-09	1.21E-12	1.32E-08	6.64E-12	1.13E-08	2.01E-11	5.05E-13	8.95E-16	1.45E-09	1.57E-11	1.61E-07	3.00E-08	1.01E-06	3.81E-09	3.80	0.07	4.98E-07	2.07E-09	72.03	1.34
950	6.57E-11	4.67E-13	2.99E-09	1.22E-12	1.50E-08	6.53E-12	1.25E-08	2.34E-11	5.58E-13	1.04E-15	3.55E-09	3.30E-11	7.50E-08	1.93E-08	1.02E-06	3.83E-09	4.18	0.10	5.48E-07	2.30E-09	79.05	1.80
1050	1.85E-10	3.88E-13	2.91E-09	1.28E-12	1.91E-08	9.35E-12	1.35E-08	2.32E-11	6.04E-13	1.04E-15	9.99E-09	6.34E-11	9.80E-08	2.91E-08	9.92E-07	3.73E-09	4.65	0.10	6.09E-07	2.52E-09	87.60	1.78
1150	9.30E-11	4.98E-13	8.39E-10	5.84E-13	8.22E-09	3.21E-12	4.66E-09	2.21E-11	2.08E-13	9.85E-16	5.03E-09	4.04E-11	3.21E-08	4.61E-08	2.86E-07	1.09E-09	5.56	0.31	7.28E-07	4.42E-09	104.25	5.73
1300	8.82E-11	3.27E-13	7.37E-10	4.71E-13	1.14E-08	7.31E-12	4.02E-09	1.86E-11	1.79E-13	8.29E-16	4.77E-09	3.36E-11	4.98E-08	6.04E-08	2.51E-07	9.51E-10	5.46	0.25	7.15E-07	4.27E-09	102.50	4.64
1500	1.84E-10	2.67E-13	1.78E-09	9.35E-13	3.55E-08	1.43E-11	9.38E-09	2.08E-11	4.18E-13	9.27E-16	9.97E-09	6.14E-11	1.73E-07	2.46E-08	6.08E-07	2.29E-09	5.26	0.13	6.88E-07	3.01E-09	98.77	2.33

Table A25 continued: $^{40}Ar/^{39}Ar$ stepped heating data of the Banpo rhyolite (sample BA-23; not discussed in this thesis).

Temp.	$^{38}Ar^*$	$\pm^{38}Ar^*$	^{39}Ar	$\pm^{39}Ar$	^{40}Ar	$\pm^{40}Ar$	$^{40}Ar^{*4}$	$\pm^{40}Ar^{*4}$	$^{40}Ar^{*4}$	$\pm^{40}Ar^{*4}$	Cl^1	$\pm Cl^1$	Ca^2	$\pm Ca^2$	K^3	$\pm K^3$	$^{40}Ar/^{39}Ar$	$\pm^{40}Ar/^{39}Ar$	$^{40}Ar/K$	$\pm^{40}Ar/K$	Age	±Age
°C	(cc)	(cc)	(cc)	(cc)	(cc)	(cc)	(cc)	(cc)	(mol)	(mol)	(mol)	(mol)	(mol)	(mol)	(mol)	(mol)					(Ma)	(Ma)
BA-23	whole-rock			sample wt = 0.02266g		J = 0.010709 +/- 0.000040																
600	1.11E-10	5.63E-13	1.12E-08	8.49E-12	1.05E-07	8.21E-11	7.47E-08	5.99E-11	3.33E-12	2.67E-15	6.03E-09	4.72E-11	3.60E-07	2.35E-08	3.81E-06	1.45E-08	6.69	0.02	8.76E-07	3.41E-09	124.75	0.56
700	4.47E-11	5.14E-13	1.85E-08	1.45E-11	1.37E-07	1.05E-10	1.30E-07	1.04E-10	5.79E-12	4.66E-15	2.42E-09	3.14E-11	5.63E-07	4.88E-08	6.30E-06	2.41E-08	7.01	0.02	9.18E-07	3.58E-09	130.60	0.57
750	1.67E-11	4.66E-13	6.26E-09	4.90E-12	4.49E-08	3.30E-11	4.11E-08	3.87E-11	1.84E-12	1.73E-15	9.06E-10	2.58E-11	1.97E-07	1.42E-08	2.13E-06	8.13E-09	6.58	0.04	8.62E-07	3.39E-09	122.79	0.85
800	2.68E-11	2.84E-13	3.70E-09	2.71E-12	2.80E-08	2.24E-11	2.52E-08	2.53E-11	1.13E-12	1.13E-15	1.45E-09	1.76E-11	1.01E-07	1.66E-08	1.26E-06	4.80E-09	6.82	0.04	8.93E-07	3.52E-09	127.16	0.92
850	2.92E-11	8.57E-13	2.67E-09	2.14E-12	2.18E-08	1.79E-11	1.82E-08	2.47E-11	8.12E-13	1.10E-15	1.58E-09	4.73E-11	8.27E-08	5.36E-08	9.09E-07	3.47E-09	6.82	0.08	8.94E-07	3.62E-09	127.25	1.54
900	3.61E-11	3.29E-13	2.12E-09	2.55E-12	1.58E-08	1.67E-11	1.28E-08	2.57E-11	5.72E-13	1.14E-15	1.96E-09	2.13E-11	6.48E-08	1.51E-08	7.21E-07	2.83E-09	6.05	0.11	7.92E-07	3.49E-09	113.23	2.02
1000	9.47E-11	9.72E-13	1.84E-09	7.59E-12	1.18E-08	3.10E-11	8.60E-09	4.16E-11	3.84E-13	1.86E-15	5.13E-09	6.09E-11	3.77E-08	3.36E-08	6.27E-07	3.49E-09	4.67	0.14	6.12E-07	4.51E-09	88.05	2.67
1050	1.12E-10	9.38E-13	1.63E-09	4.27E-12	9.13E-09	8.90E-11	7.23E-09	2.60E-11	3.23E-13	1.16E-15	6.07E-09	6.25E-11	6.30E-08	4.95E-08	5.54E-07	2.53E-09	4.45	0.11	5.83E-07	3.39E-09	83.93	2.02
1100	1.08E-10	4.90E-13	1.22E-09	1.17E-12	9.78E-09	8.30E-12	5.99E-09	1.98E-11	2.67E-13	8.84E-16	5.83E-09	4.38E-11	8.36E-08	3.01E-08	4.14E-07	1.60E-09	4.93	0.16	6.46E-07	3.28E-09	92.77	3.01
1150	1.09E-10	2.07E-13	9.50E-10	8.89E-13	9.15E-09	6.86E-12	4.94E-09	2.13E-11	2.21E-13	9.51E-16	5.92E-09	3.72E-11	4.71E-08	3.28E-08	3.23E-07	1.25E-09	5.21	0.25	6.82E-07	3.94E-09	97.86	4.60
1250	5.99E-11	2.30E-13	7.35E-10	6.43E-13	9.63E-09	7.13E-12	3.68E-09	1.91E-11	1.64E-13	8.50E-16	3.24E-09	2.30E-11	5.46E-08	2.28E-08	2.50E-07	9.60E-10	5.01	0.26	6.56E-07	4.23E-09	94.22	4.86
1350	6.36E-11	2.75E-13	7.89E-10	6.72E-13	1.28E-08	1.11E-11	4.19E-09	2.15E-11	1.87E-13	9.59E-16	3.44E-09	2.54E-11	6.25E-08	6.43E-08	2.69E-07	1.03E-09	5.31	0.31	6.96E-07	4.45E-09	99.78	5.74
1450	4.51E-11	1.63E-13	5.07E-10	7.96E-13	1.83E-08	2.85E-11	2.57E-09	1.95E-11	1.14E-13	8.71E-16	2.44E-09	1.71E-11	1.39E-07	4.48E-08	1.73E-07	7.00E-10	5.06	0.40	6.63E-07	5.72E-09	95.20	7.28
1600	3.13E-11	4.22E-13	2.76E-10	6.04E-13	2.48E-08	2.52E-11	1.49E-09	2.13E-11	6.65E-14	9.51E-16	1.70E-09	2.50E-11	1.94E-07	2.93E-08	9.39E-08	4.07E-10	5.41	0.89	7.09E-07	1.06E-08	101.59	16.18

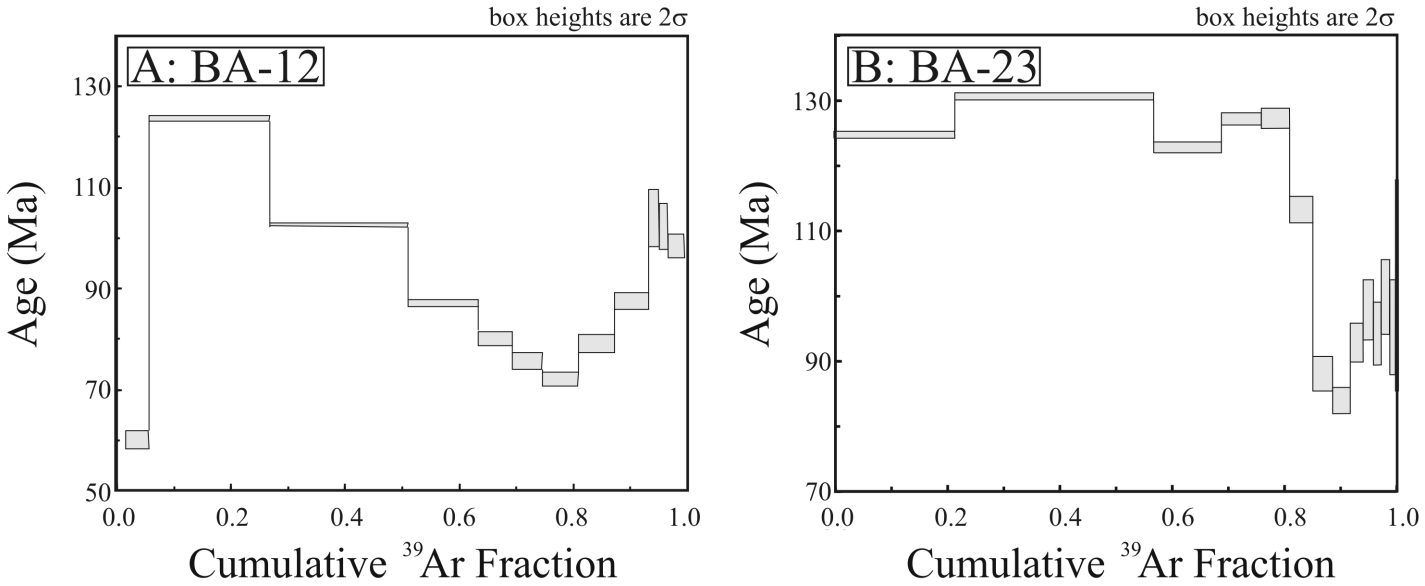

Fig. A1: Ar–Ar age spectra for the Banpo rhyolite samples BA-12 and BA-23.

Table A26: ^{40}Ar/^{39}Ar stepped heating data of the Paleng gabbro (sample JI-27).

Temp.	^{38}Ar*	±^{38}Ar*	^{39}Ar	±^{39}Ar	^{40}Ar	±^{40}Ar	^{40}Ar*[4]	±^{40}Ar*[4]	^{40}Ar*[4]	±^{40}Ar*[4]	Cl[1]	±Cl[1]	Ca[2]	±Ca[2]	K[3]	±K[3]	^{40}Ar/^{39}Ar	±^{40}Ar/^{39}Ar	^{40}Ar/K	±^{40}Ar/K	Age	±Age
°C	(cc)	(cc)	(cc)	(cc)	(cc)	(cc)	(cc)	(cc)	(mol)	(mol)	(mol)	(mol)	(mol)	(mol)	(mol)	(mol)					(Ma)	(Ma)
JI-27 hornblende			sample wt = 0.02105g						J = 0.010149 +/- 0.000038													
400	6.31E-12	4.17E-13	4.05E-12	4.92E-13	1.67E-08	1.89E-11	1.18E-10	2.34E-11	5.28E-15	1.04E-15	3.42E-10	2.26E-11	8.89E-07	1.57E-08	1.46E-09	1.77E-10	29.2	56.0	3.63E-06	8.43E-07	468.64	790.60
500	9.81E-12	2.10E-13	6.63E-12	4.18E-13	8.55E-09	7.72E-12	-8.32E-11	-2.39E-11	-3.71E-15	1.06E-15	5.31E-10	1.18E-11	2.49E-08	1.50E-08	2.38E-09	1.50E-10	-12.6	-45.0	-1.56E-06	nd	nd	nd
600	2.77E-11	3.13E-13	1.87E-11	5.36E-13	6.33E-09	1.33E-11	2.32E-10	2.17E-11	1.04E-14	9.67E-16	1.50E-09	1.90E-11	1.06E-07	4.03E-09	6.73E-09	1.94E-10	12.4	12.5	1.54E-06	1.50E-07	213.94	204.03
700	3.87E-11	2.20E-13	5.51E-11	2.43E-13	1.02E-08	9.01E-12	4.93E-10	2.18E-11	2.20E-14	9.72E-16	2.10E-09	1.70E-11	4.27E-07	8.50E-09	1.98E-08	1.15E-10	8.9	4.7	1.11E-06	4.95E-08	156.77	78.90
800	1.10E-10	2.10E-13	2.07E-10	4.77E-13	1.51E-08	1.20E-11	2.57E-09	2.06E-11	1.15E-13	9.18E-16	5.94E-09	3.63E-11	5.22E-06	2.13E-08	7.44E-08	3.27E-10	12.4	1.0	1.54E-06	1.41E-08	214.36	16.87
900	5.87E-11	5.56E-13	1.88E-10	7.42E-13	4.21E-09	3.39E-12	1.61E-09	1.69E-11	7.17E-14	7.52E-16	3.18E-09	3.53E-11	5.72E-06	2.59E-08	6.76E-08	3.68E-10	8.5	0.7	1.06E-06	1.25E-08	149.81	12.17
1000	4.72E-10	7.94E-13	3.07E-10	7.05E-13	7.29E-09	5.76E-12	3.84E-09	2.29E-11	1.71E-13	1.02E-15	2.55E-08	1.54E-10	4.38E-06	2.74E-08	1.10E-07	4.84E-10	12.5	0.8	1.56E-06	1.15E-08	215.99	13.04
1100	7.94E-10	8.57E-13	5.07E-10	4.85E-13	1.01E-08	7.96E-12	6.82E-09	1.76E-11	3.04E-13	7.87E-16	4.30E-08	2.54E-10	6.83E-06	3.27E-08	1.82E-07	7.03E-10	13.5	0.3	1.67E-06	7.77E-09	231.14	4.71
1200	1.64E-09	1.30E-12	9.34E-10	9.57E-13	1.90E-08	1.79E-11	1.37E-08	2.38E-11	6.12E-13	1.06E-15	8.89E-08	5.21E-10	1.54E-05	5.99E-08	3.36E-07	1.30E-09	14.7	0.2	1.82E-06	7.76E-09	250.74	3.51
1300	7.00E-10	6.53E-13	4.83E-10	7.09E-13	1.01E-08	1.07E-11	6.59E-09	2.46E-11	2.94E-13	1.10E-15	3.79E-08	2.23E-10	9.33E-06	4.12E-08	1.74E-07	6.98E-10	13.6	0.6	1.69E-06	9.29E-09	233.99	9.41
1400	8.91E-11	3.65E-13	2.28E-10	9.03E-13	4.83E-09	4.43E-12	2.58E-09	2.34E-11	1.15E-13	1.04E-15	4.82E-09	3.43E-11	1.53E-06	1.22E-08	8.18E-08	4.46E-10	11.4	1.1	1.41E-06	1.49E-08	196.72	17.67
1600	2.80E-11	2.79E-13	5.70E-11	2.68E-13	1.33E-08	1.19E-11	2.04E-10	2.01E-11	9.09E-15	8.98E-16	1.52E-09	1.75E-11	4.40E-07	4.51E-09	2.05E-08	1.23E-10	3.6	3.9	4.44E-07	4.40E-08	64.36	69.06

Table A26 continued: $^{40}Ar/^{39}Ar$ stepped heating data of the Paleng gabbro (sample JI-31).

Temp.	$^{38}Ar^*$	$\pm^{38}Ar^*$	^{39}Ar	$\pm^{39}Ar$	^{40}Ar	$\pm^{40}Ar$	$^{40}Ar^{*4}$	$\pm^{40}Ar^{*4}$	$^{40}Ar^{*4}$	$\pm^{40}Ar^{*4}$	Cl^1	$\pm Cl^1$	Ca^2	$\pm Ca^2$	K^3	$\pm K^3$	$^{40}Ar/^{39}Ar$	$\pm^{40}Ar/^{39}Ar$	$^{40}Ar/K$	$\pm^{40}Ar/K$	Age	±Age
°C	(cc)	(cc)	(cc)	(cc)	(cc)	(cc)	(cc)	(cc)	(mol)	(mol)	(mol)	(mol)	(mol)	(mol)	(mol)	(mol)					(Ma)	(Ma)
JI-31	**hornblende**		**sample wt = 0.03216g**			**J = 0.010149 +/- 0.000038**																
600	5.82E-11	3.22E-13	4.39E-11	3.83E-13	3.24E-08	2.70E-11	6.26E-10	2.19E-11	2.79E-14	9.78E-16	3.15E-09	2.53E-11	1.20E-07	2.51E-09	1.58E-08	1.50E-10	14.2	5.7	1.77E-06	6.42E-08	243.41	90.53
800	2.85E-10	3.08E-13	4.03E-10	4.14E-13	2.98E-08	2.76E-11	5.32E-09	1.95E-11	2.37E-13	8.71E-16	1.55E-08	9.13E-11	1.07E-06	1.06E-08	1.45E-07	5.62E-10	13.2	0.5	1.64E-06	8.76E-09	226.82	7.75
900	9.43E-11	2.65E-13	3.87E-10	6.01E-13	6.82E-09	6.19E-12	2.98E-09	1.94E-11	1.33E-13	8.64E-16	5.10E-09	3.29E-11	6.30E-07	5.80E-09	1.39E-07	5.64E-10	7.7	0.5	9.55E-07	7.32E-09	135.56	8.56
975	1.52E-10	2.34E-13	4.05E-10	5.26E-13	8.04E-09	7.33E-12	3.44E-09	1.88E-11	1.54E-13	8.40E-16	8.22E-09	4.94E-11	2.18E-06	9.81E-09	1.45E-07	5.76E-10	8.5	0.5	1.06E-06	7.13E-09	149.40	7.68
1050	3.63E-10	4.46E-13	4.80E-10	4.36E-13	1.16E-08	9.47E-12	5.17E-09	1.87E-11	2.31E-13	8.34E-16	1.97E-08	1.17E-10	7.27E-06	2.84E-08	1.72E-07	6.65E-10	10.8	0.4	1.34E-06	7.06E-09	187.08	6.21
1100	2.21E-10	6.38E-13	3.14E-10	3.91E-13	5.92E-09	4.71E-12	3.17E-09	1.78E-11	1.41E-13	7.95E-16	1.20E-08	7.77E-11	3.41E-06	2.38E-08	1.13E-07	4.46E-10	10.1	0.5	1.25E-06	8.60E-09	175.80	8.79
1175	2.22E-09	1.76E-12	2.39E-09	2.04E-12	4.57E-08	4.32E-11	3.63E-08	3.62E-11	1.62E-12	1.62E-15	1.20E-07	7.03E-10	3.32E-05	1.28E-07	8.58E-07	3.30E-09	15.2	0.1	1.89E-06	7.48E-09	258.61	1.32
1250	4.69E-10	5.24E-13	4.14E-10	4.97E-13	1.02E-08	8.39E-12	6.54E-09	1.87E-11	2.92E-13	8.36E-16	2.54E-08	1.50E-10	7.58E-06	3.17E-08	1.49E-07	5.85E-10	15.8	0.4	1.96E-06	9.55E-09	268.46	6.11
1350	2.06E-10	4.00E-13	1.67E-10	3.03E-13	6.09E-09	4.42E-12	2.93E-09	2.10E-11	1.31E-13	9.38E-16	1.11E-08	6.82E-11	5.12E-06	3.01E-08	6.01E-08	2.50E-10	17.5	1.4	2.17E-06	1.80E-08	294.93	21.29
1600	5.04E-11	3.16E-13	3.64E-11	2.79E-13	1.20E-08	1.05E-11	3.35E-10	2.01E-11	1.50E-14	8.96E-16	2.73E-09	2.33E-11	1.73E-06	8.71E-09	1.31E-08	1.12E-10	9.2	6.0	1.14E-06	6.91E-08	161.05	100.49

Table A26 continued: $^{40}Ar/^{39}Ar$ stepped heating data of the Paleng gabbro (sample JI-33).

Temp.	$^{38}Ar^*$	$\pm^{38}Ar^*$	^{39}Ar	$\pm^{39}Ar$	^{40}Ar	$\pm^{40}Ar$	$^{40}Ar^{*4}$	$\pm^{40}Ar^{*4}$	$^{40}Ar^{*4}$	$\pm^{40}Ar^{*4}$	Cl^1	$\pm Cl^1$	Ca^2	$\pm Ca^2$	K^3	$\pm K^3$	$^{40}Ar/^{39}Ar$	$\pm^{40}Ar/^{39}Ar$	$^{40}Ar/K$	$\pm^{40}Ar/K$	Age	±Age
°C	(cc)	(cc)	(cc)	(cc)	(cc)	(cc)	(cc)	(cc)	(mol)	(mol)	(mol)	(mol)	(mol)	(mol)	(mol)	(mol)					(Ma)	(Ma)
JI-33	**hornblende**		**sample wt = 0.04181g**			**J = 0.010149 +/- 0.000038**																
600	3.06E-11	3.45E-13	2.28E-11	8.72E-13	3.02E-08	2.23E-11	6.73E-10	3.18E-11	3.00E-14	1.42E-15	1.66E-09	2.10E-11	1.72E-07	1.57E-08	8.19E-09	3.15E-10	29.5	8.8	3.66E-06	2.23E-07	472.45	123.85
800	6.70E-11	4.28E-13	2.12E-10	4.27E-13	9.53E-09	2.15E-11	2.09E-09	2.23E-11	9.31E-14	9.96E-16	3.63E-09	3.13E-11	1.70E-06	1.31E-08	7.61E-08	3.23E-10	9.9	1.3	1.22E-06	1.41E-08	172.12	20.82
900	3.86E-11	3.16E-13	2.03E-10	4.28E-13	6.22E-09	7.28E-12	2.01E-09	1.85E-11	8.98E-14	8.27E-16	2.09E-09	2.10E-11	3.49E-06	3.26E-08	7.29E-08	3.13E-10	9.9	0.9	1.23E-06	1.25E-08	173.00	14.74
975	7.08E-11	7.74E-13	2.00E-10	6.49E-13	3.95E-09	3.27E-12	1.63E-09	1.81E-11	7.26E-14	8.07E-16	3.83E-09	4.75E-11	4.36E-06	4.01E-08	7.20E-08	3.56E-10	8.1	0.8	1.01E-06	1.23E-08	142.93	14.00
1050	2.08E-10	2.21E-13	2.50E-10	2.22E-13	5.60E-09	4.29E-12	2.32E-09	1.87E-11	1.04E-13	8.36E-16	1.13E-08	6.66E-11	6.96E-06	3.33E-08	8.99E-08	3.46E-10	9.3	0.8	1.15E-06	1.03E-08	162.32	12.80
1110	1.95E-10	6.12E-13	2.33E-10	4.50E-13	5.03E-09	3.92E-12	2.80E-09	1.97E-11	1.25E-13	8.78E-16	1.06E-08	6.98E-11	5.14E-06	2.39E-08	8.37E-08	3.52E-10	12.0	0.9	1.49E-06	1.22E-08	207.68	13.88
1130	1.32E-10	4.04E-13	1.54E-10	2.40E-13	3.77E-09	2.95E-12	1.84E-09	1.45E-11	8.20E-14	6.46E-16	7.12E-09	4.68E-11	2.60E-06	4.29E-08	5.55E-08	2.25E-10	11.9	0.7	1.48E-06	1.31E-08	205.86	11.79
1160	1.73E-10	3.58E-13	2.02E-10	4.01E-13	5.38E-09	4.51E-12	3.29E-09	2.11E-11	1.47E-13	9.42E-16	9.37E-09	5.77E-11	2.88E-06	2.35E-08	7.28E-08	3.08E-10	16.2	1.1	2.01E-06	1.55E-08	275.03	17.29
1200	4.10E-10	3.93E-13	4.38E-10	7.13E-13	9.12E-09	7.10E-12	6.20E-09	2.33E-11	2.77E-13	1.04E-15	2.22E-08	1.31E-10	6.06E-06	3.14E-08	1.57E-07	6.43E-10	14.2	0.6	1.76E-06	9.74E-09	242.12	8.91
1300	1.18E-09	9.86E-13	1.17E-09	9.75E-13	2.44E-08	2.66E-11	1.78E-08	2.30E-11	7.96E-13	1.02E-15	6.37E-08	3.74E-10	1.73E-05	6.90E-08	4.21E-07	1.62E-09	15.2	0.1	1.89E-06	7.65E-09	259.19	2.30
1400	1.72E-10	5.08E-13	1.64E-10	5.05E-13	1.64E-08	1.53E-11	3.45E-09	2.19E-11	1.54E-13	9.79E-16	9.33E-09	6.08E-11	1.14E-05	5.08E-08	5.89E-08	2.85E-10	21.1	1.3	2.62E-06	2.09E-08	349.49	19.44

Table A27: $^{40}Ar/^{39}Ar$ stepped heating data of the Jinbaoshan peridotite/serpentinite (sample JBS-2).

Temp.	$^{38}Ar^*$	$\pm^{38}Ar^*$	^{39}Ar	$\pm^{39}Ar$	^{40}Ar	$\pm^{40}Ar$	$^{40}Ar^{*4}$	$\pm^{40}Ar^{*4}$	$^{40}Ar^{*4}$	$\pm^{40}Ar^{*4}$	Cl^1	$\pm Cl^1$	Ca^2	$\pm Ca^2$	K^3	$\pm K^3$	$^{40}Ar/^{39}Ar$	$\pm^{40}Ar/^{39}Ar$	$^{40}Ar/K$	$\pm^{40}Ar/K$	Age	±Age
°C	(cc)	(cc)	(cc)	(cc)	(cc)	(cc)	(cc)	(cc)	(mol)	(mol)	(mol)	(mol)	(mol)	(mol)	(mol)	(mol)					(Ma)	(Ma)
JBS-2 serpentine				**sample wt = 0.03216g**		**J = 0.010149 +/- 0.000038**																
600	2.08E-12	2.91E-13	2.10E-12	1.16E-12	8.65E-09	6.53E-12	-6.03E-11	-2.36E-11	-2.69E-15	1.05E-15	1.12E-10	1.58E-11	1.99E-06	1.07E-06	7.53E-10	4.17E-10	-28.7	-140.7	-3.57E-06		nd	
700	6.71E-12	1.66E-13	1.34E-12	5.33E-13	8.40E-09	6.57E-12	1.95E-10	2.40E-11	8.70E-15	1.07E-15	3.63E-10	9.21E-12	2.78E-06	4.46E-07	4.81E-10	1.91E-10	145.7	188.2	1.81E-05	7.54E-06	1637.32	1390.39
800	2.85E-11	5.08E-13	2.68E-11	1.58E-12	7.20E-09	5.31E-12	6.15E-12	2.42E-11	2.75E-16	1.08E-15	1.54E-09	2.89E-11	1.75E-06	1.50E-06	9.63E-09	5.70E-10	0.2	12.0	2.85E-08	1.12E-07	4.20	219.17
900	1.08E-10	3.75E-13	7.22E-10	1.10E-12	1.41E-08	9.74E-12	3.76E-09	2.14E-11	1.68E-13	9.55E-16	5.83E-09	3.95E-11	2.47E-06	6.18E-07	2.59E-07	1.05E-09	5.2	0.3	6.46E-07	4.51E-09	92.89	5.73
940	8.19E-11	4.40E-13	7.64E-10	2.30E-12	1.28E-08	8.90E-12	6.61E-09	2.72E-11	2.95E-13	1.21E-15	4.43E-09	3.51E-11	2.01E-06	2.11E-06	2.75E-07	1.32E-09	8.7	0.5	1.07E-06	6.80E-09	151.86	8.47
980	2.23E-10	2.94E-13	4.07E-10	1.08E-12	9.08E-09	6.20E-12	4.43E-09	2.43E-11	1.98E-13	1.09E-15	1.21E-08	7.19E-11	8.65E-07	9.79E-07	1.46E-07	6.72E-10	10.9	0.8	1.35E-06	9.68E-09	189.17	12.70
1025	1.71E-10	8.95E-13	5.49E-10	2.41E-12	1.42E-08	1.06E-11	8.38E-09	2.93E-11	3.74E-13	1.31E-15	9.25E-09	7.23E-11	2.49E-06	2.20E-06	1.97E-07	1.14E-09	15.3	0.7	1.90E-06	1.28E-08	259.85	11.55
1100	1.15E-10	4.19E-13	1.58E-09	3.29E-12	2.11E-08	1.96E-11	1.90E-08	3.23E-11	8.47E-13	1.44E-15	6.21E-09	4.26E-11	2.00E-06	2.94E-06	5.66E-07	2.43E-09	12.0	0.3	1.50E-06	6.90E-09	208.12	4.72
1140	4.70E-11	4.03E-13	8.83E-10	8.95E-13	9.19E-09	6.61E-12	7.38E-09	2.34E-11	3.29E-13	1.04E-15	2.54E-09	2.64E-11	2.62E-06	5.55E-07	3.17E-07	1.23E-09	8.4	0.3	1.04E-06	5.20E-09	146.93	5.37
1180	5.73E-11	3.63E-13	1.02E-09	1.79E-12	1.06E-08	7.22E-12	9.47E-09	2.57E-11	4.23E-13	1.15E-15	3.10E-09	2.67E-11	1.62E-06	1.49E-06	3.66E-07	1.51E-09	9.3	0.3	1.16E-06	5.72E-09	162.91	5.30
1210	6.55E-11	3.25E-13	1.13E-09	1.34E-12	1.21E-08	8.53E-12	1.11E-08	2.41E-11	4.94E-13	1.07E-15	3.54E-09	2.71E-11	2.10E-06	9.84E-07	4.05E-07	1.59E-09	9.8	0.2	1.22E-06	5.48E-09	171.48	4.08
1240	7.01E-11	4.22E-13	1.02E-09	2.11E-12	1.08E-08	7.60E-12	9.33E-09	2.70E-11	4.16E-13	1.21E-15	3.79E-09	3.17E-11	9.46E-07	1.83E-06	3.67E-07	1.57E-09	9.1	0.4	1.13E-06	5.86E-09	159.87	5.95
1280	7.97E-11	4.56E-13	6.29E-10	1.98E-12	6.80E-09	6.90E-12	5.43E-09	2.67E-11	2.42E-13	1.19E-15	4.32E-09	3.52E-11	3.94E-06	1.68E-06	2.26E-07	1.11E-09	8.6	0.6	1.07E-06	7.44E-09	151.41	9.49
1330	1.93E-10	2.94E-13	6.39E-10	8.08E-13	9.04E-09	6.31E-12	7.46E-09	2.41E-11	3.33E-13	1.08E-15	1.05E-08	6.28E-11	4.08E-06	4.85E-07	2.30E-07	9.08E-10	11.7	0.5	1.45E-06	7.40E-09	201.98	7.38
1500	4.28E-10	6.18E-13	6.43E-10	1.35E-12	1.67E-08	3.39E-11	-2.83E-09	-2.46E-11	-1.26E-13	1.10E-15	2.32E-08	1.39E-10	7.61E-06	1.19E-06	2.31E-07	9.93E-10	-4.4	-0.5	-5.47E-07		nd	

Table A28: $^{40}Ar/^{39}Ar$ stepped heating data of the Jinghong basalt sample (sample JI-50).

Temp.	$^{38}Ar^*$	$\pm^{38}Ar^*$	^{39}Ar	$\pm^{39}Ar$	^{40}Ar	$\pm^{40}Ar$	$^{40}Ar^{*4}$	$\pm^{40}Ar^{*4}$	$^{40}Ar^{*4}$	$\pm^{40}Ar^{*4}$	Cl^1	$\pm Cl^1$	Ca^2	$\pm Ca^2$	K^3	$\pm K^3$	$^{40}Ar/^{39}Ar$	$\pm^{40}Ar/^{39}Ar$	$^{40}Ar/K$	$\pm^{40}Ar/K$	Age	±Age
°C	(cc)	(cc)	(cc)	(cc)	(cc)	(cc)	(cc)	(cc)	(mol)	(mol)	(mol)	(mol)	(mol)	(mol)	(mol)	(mol)					(Ma)	(Ma)
BA-24 whole-rock				**sample wt = 0.03434g**		**J = 0.010149 +/- 0.000038**																
500	4.775E-13	2.577E-13	8.696E-13	2.107E-13	9.622E-09	9.74E-12	2.5825E-10	6.3997E-11	1.1522E-14	2.855E-15	2.585E-11	1.395E-11	2.654E-08	1.851E-08	3.125E-10	7.572E-11	296.98	282.63	3.6872E-05	1.278E-05	2507.216	1289.176
600	2.97E-12	4.102E-13	6.5E-13	4.022E-13	1.092E-08	1.245E-11	2.7638E-10	1.6964E-10	1.2331E-14	7.568E-15	1.607E-10	2.223E-11	6.593E-09	3.298E-08	2.336E-10	1.445E-10	425.21	388.25	5.2793E-05	4.601E-05	3013.802	1337.343
700	9.521E-12	5.465E-13	3.935E-12	2.593E-13	4.527E-09	4.457E-12	-4.025E-11	-1.987E-11	-1.796E-15	8.864E-16	5.155E-10	2.974E-11	9.331E-08	3.265E-08	1.414E-09	9.334E-11	-10.23	-52.2	-1.27E-06	nd	nd	nd
800	4.723E-11	2.861E-13	1.607E-11	4.92E-13	3.813E-09	4.134E-12	6.3112E-12	2.1538E-11	2.8158E-16	9.609E-16	2.557E-09	2.146E-11	2.789E-08	1.632E-08	5.776E-09	1.781E-10	0.3926	15.266	4.8747E-08	1.664E-07	7.174207	278.4123
900	3.285E-10	5.334E-13	1.505E-10	4.704E-13	3.345E-09	3.441E-12	3.9903E-10	2.009E-11	1.7803E-14	8.963E-16	1.778E-08	1.072E-10	3.562E-07	1.94E-08	5.407E-08	2.637E-10	2.6517	1.4137	3.2922E-07	1.665E-08	47.90739	25.20595
975	7.605E-11	2.413E-13	1.947E-10	2.386E-13	4.485E-09	6.018E-12	1.1399E-09	2.1243E-11	5.0855E-14	9.477E-16	4.117E-09	2.725E-11	2.515E-07	2.846E-08	6.997E-08	2.756E-10	5.8545	1.221	7.2687E-07	1.385E-08	104.1247	21.10225
1040	1.691E-10	4.435E-13	1.975E-10	3.587E-13	3.322E-09	3.531E-12	1.211E-09	2.1539E-11	5.403E-14	9.609E-16	9.153E-09	5.833E-11	4.63E-07	3.488E-08	7.099E-08	2.954E-10	6.1303	1.2297	7.6111E-07	1.39E-08	108.8854	21.19681
1090	3.272E-10	7.25E-13	1.754E-10	4.583E-13	2.671E-09	2.642E-12	1.4482E-09	2.0266E-11	6.4613E-14	9.042E-16	1.771E-08	1.101E-10	3.322E-07	1.135E-08	6.303E-08	2.878E-10	8.2574	1.1961	1.0252E-06	1.509E-08	145.1808	20.20587
1120	1.074E-09	1.559E-12	3.139E-10	7.697E-13	4.284E-09	1.024E-11	2.5471E-09	2.3079E-11	1.1364E-13	1.03E-15	5.817E-08	3.482E-10	6.107E-07	9.752E-08	1.128E-07	5.048E-10	8.1156	0.8337	1.0076E-06	1.018E-08	142.7836	14.10232
1145	6.474E-10	1.014E-12	2.487E-10	6.489E-13	3.511E-09	4.758E-12	1.8658E-09	2.1242E-11	8.3241E-14	9.477E-16	3.505E-08	2.108E-10	3.682E-07	1.364E-08	8.937E-08	4.079E-10	7.5018	0.9098	9.314E-07	1.142E-08	132.372	15.4795
1170	2.362E-10	4.219E-13	2.853E-10	4.46E-13	3.509E-09	3.515E-12	1.9321E-09	1.9562E-11	8.6201E-14	8.728E-16	1.279E-08	7.771E-11	3.537E-07	3.663E-08	1.025E-07	4.159E-10	6.7728	0.693	8.4088E-07	9.172E-09	119.9253	11.87229
1220	1.305E-10	3.436E-13	2.813E-10	4.228E-13	3.266E-09	3.501E-12	1.7575E-09	2.3887E-11	7.8412E-14	1.066E-15	7.068E-09	4.507E-11	3.499E-07	3.52E-08	1.011E-07	4.078E-10	6.2485	1.0603	7.7578E-07	1.1E-08	110.9207	18.2561
1280	1.969E-10	3.985E-13	5.093E-10	7.129E-13	4.88E-09	4.755E-12	2.9153E-09	1.9713E-11	1.3007E-13	8.795E-16	1.066E-08	6.557E-11	8.864E-07	2.948E-08	1.83E-07	7.316E-10	5.7236	0.3865	7.1062E-07	5.582E-09	101.861	6.687296
1350	2.592E-10	4.617E-13	4.342E-10	5.102E-13	5.905E-09	9.039E-12	2.6814E-09	2.1065E-11	1.1963E-13	9.398E-16	1.403E-08	8.526E-11	1.568E-06	2.491E-08	1.56E-07	6.123E-10	6.1756	0.5503	7.6674E-07	6.733E-09	109.6656	9.481979
1450	7.939E-11	3.4E-13	1.753E-10	3.544E-13	5.585E-09	4.199E-12	1.6254E-09	2.0163E-11	7.2518E-14	8.996E-16	4.298E-09	3.101E-11	1.013E-06	2.738E-08	6.3E-08	2.681E-10	9.2714	1.2438	1.1511E-06	1.51E-08	162.2308	20.81529
1600	5.775E-11	3.37E-13	1.364E-10	2.894E-13	8.669E-09	6.923E-12	1.2805E-09	1.9623E-11	5.7128E-14	8.755E-16	3.126E-09	2.574E-11	7.41E-07	5.337E-08	4.9E-08	2.109E-10	9.3896	1.5267	1.1658E-06	1.856E-08	164.2075	25.52145